SANDIA REPORT

SAND97-0745 • UC-700
Unlimited Release
Printed April 1997

ASSESSMENT OF MICROELECTRONICS PACKAGING FOR HIGH TEMPERATURE, HIGH RELIABILITY APPLICATIONS

Project Leader

Fernando Uribe
Sandia National Laboratories

SANDIA NATIONAL LABORATORIES
Electronic Processing
Ceramic & Glass Processing
Engineering & Manufacturing Mechanics
Thermal & Fluid Engineering
Physical & Joining Metallurgy
Electron Microscopy/Metallography
Reliability Physics
Advanced Packing
Statistics & Human Factors
Digital ASICS

GENERAL MOTORS
Delphi Automotive Systems

UNIVERSITY OF NEW MEXICO
Department of Mechanical Engineering

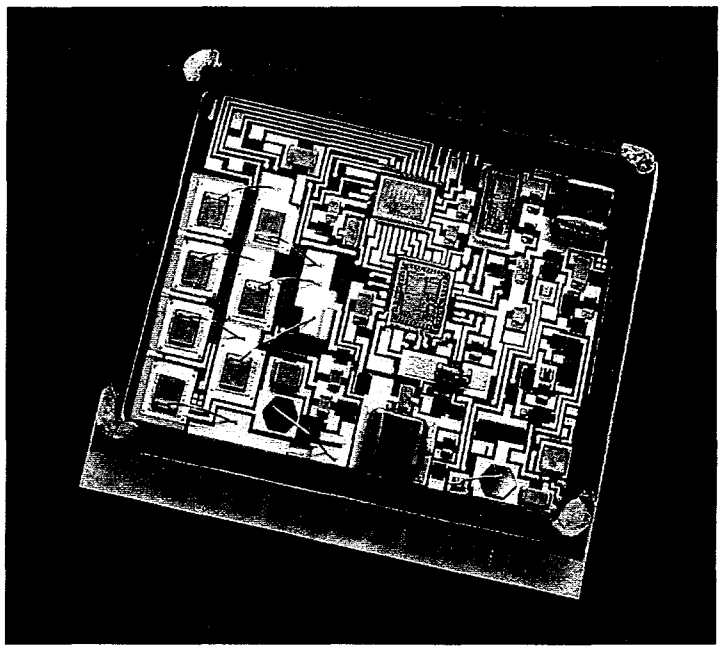

CRADA between Sandia National Laboratories and Delphi, a Division of General Motors

Issued by Sandia National Laboratories, operated for the United States Department of Energy by Sandia Corporation.

Available to DOE and DOE contractors from
Office of Scientific and Technical Information
P.O. Box 62
Oak Ridge, TN 37831

Prices available from (615) 576-8401, FTS 626-8401

Available to the public from
National Technical Information Service
U.S. Department of Commerce
5285 Port Royal Rd
Springfield, VA 22161

NTIS price codes
Printed copy: A17
Microfiche copy: A01

Prepared by
Sandia National Laboratories
Albuquerque, New Mexico 87185 and Livermore, California 94550

Sandia is a multiprogram laboratory operated by Sandia Corporation, a Lockheed Martin Company, for the United States Department of Energy under Contract DE-AC04-94AL85000.

SAND97-0745
Unlimited Release
Printed April 1997

Distribution
Category UC–700

Assessment of Microelectronics Packaging for High Temperature, High Reliability Applications

Fernando Uribe
Electronic Processing Department
Sandia National Laboratories
P.O. Box 5800
Albuquerque, NM 87185-0959

Abstract

This report details characterization and development activities in electronic packaging for high temperature applications. This project was conducted through a Department of Energy sponsored Cooperative Research and Development Agreement between Sandia National Laboratories and General Motors. Even though the target application of this collaborative effort is an automotive electronic throttle control system which would be located in the engine compartment, results of this work are directly applicable to Sandia's national security mission.

The component count associated with the throttle control dictates the use of high density packaging not offered by conventional surface mount. An enabling packaging technology was selected and thermal models defined which characterized the thermal and mechanical response of the throttle control module. These models were used to optimize thick film multichip module design, characterize the thermal signatures of the

electronic components inside the module, and to determine the temperature field and resulting thermal stresses under conditions that may be encountered during the operational life of the throttle control module. Because the need to use unpackaged devices limits the level of testing that can be performed either at the wafer level or as individual dice, an approach to assure a high level of reliability of the unpackaged components was formulated. Component assembly and interconnect technologies were also evaluated and characterized for high temperature applications. Electrical, mechanical and chemical characterizations of enabling die and component attach technologies were performed. Additionally, studies were conducted to assess the performance and reliability of gold and aluminum wire bonding to thick film conductor inks. Kinetic models were developed and validated to estimate wire bond reliability.

Driven by reliability requirements, the baseline design of electronic throttle control module was premised on a hermetic enclosure. Hermetic sealing technology, as it exists today, is not conducive to large volume, low cost production. A viable alternative for creating a hermetic seal based on the use of laser technology was developed. Although thick film multilayer technology was identified as the enabling technology for realization of the throttle control, solder surface mount assembly techniques are a viable alternative. Tin-silver based solder systems including flux, metallization, ands solder were screened for performance in a high temperature environment. Solder compositions resilient to the effects of temperature up to 170 degrees Celsius were identified.

Work performed under this initiative has demonstrated successful realization of an electronic packaging technology for high temperature automotive applications, as well as for high power modules typical in many of the DOE/DP applications.

Acknowledgments

All of the principle investigators involved in this CRADA are indebted to the many people at Sandia National Laboratories who contributed to this program. In particular to TJ Allard who performed the role of Program Manager and whose insight was vital in solving many of the problems that arose in the course of this project. For their efforts Cathy Nowlen, James Gonzales, Mark Stavig, John Emerson, Carl Robinson, Barry Ritchie, James McKinney, and Lorraine Curtis deserve special mention.

Finally, to Dan Sprauer who monitored and helped resolve all the painstaking budget issues, was the liason in all interactions with the DOE, and more importantly developed and updated the project plan which was our road map to success.

This page intentionally left blank

Contents

Contents (continued)

Contents (continued)

Contents (continued)

Contents (continued)

Contents (continued)

Figures

Figures (continued)

Figures (continued)

Figures (continued)

Figures (continued)

Figures (continued)

Tables

Tables (continued)

Tables (continued)

Acronyms

AC	Alternating Current
ATC	Assembly Test Chip
BSEMs	Backscattered Electron Micrographs
BS	Bond Strength (BS)
CHP	Ceramic Hermetic Packaging
CFC	Chlorofluorocarbons
CTE	Coefficient of Thermal Expansion
CMOS	Complementary Metal-Oxide Semiconductor
CRADA	Cooperative Research and Development Agreement
DFT	Design for Testabililty
DSC	Differential Scanning Calorimetry
DC	Direct Currnet (DC)
DMA	Dynamic Mechanical Analysis
DP	Defense Programs
EEPROM	Electonically Erasable Programmable Read Only Memory
ETC	Electronic Throttle Control
EDPMs	Elemental Distribution Photomicrographs
FM	Failure Mode
FET	Field Effect Transistor
GM	General Motors
HTSS	High Temperature Steady State/Burn-In
HAST	Highly Accelerated Stress Tests
HTB	Humidity, Temperature, and Bias
IC	Integrated Circuit
JEDEC	Joint Electronic Device Engineering Council
KGD	Known Good Die
LTCC	Low Temperature Co-fired Ceramic
MCM	Multichip Module
MOS	Metal Oxide Semiconductor
MOSFET	Metal Oxide Semiconductor Field-Effect Transistor
NEG	Nippon Electric Glass
PIND	Particle Impact Noice Detection
PPM	Parts Per Million
RH	Relative Humidity
RGA	Residual Gas Analysis
SEMs	Secondary Electron Micrographs
SBA	Smart Brushless Actuator
STC	Static Temperature Cycling
TGA	Thermal Gravimetric Analysis
TMA	Thermal Mechanical Analysis

1. Executive Summary

Through a Department of Energy sponsored Cooperative Research and Development Agreement (CRADA) a collaborative partnership between Sandia National Laboratories and General Motors, Delphi Automotive Systems was established to characterize electronic packaging technologies for high temperature applications. High temperature electronics are necessary for successful realization of advanced automotive engine control and management systems, as well as for high power modules typical in many of the Department of Energy/Defense Program system designs. The target application of this collaborative effort is an automotive electronic throttle control system which would be located in the engine compartment and would replace the traditional mechanical cable between the drivers accelerator pedal and the throttle valve.

Currently the automotive industry has a robust electronics packaging technology that emphasizes soldering of components on a mother board. Although some of the prepackaged components are hermetic, most automotive modules are molded in epoxy or immersed in a silicone filled well. The high component count associated with the throttle control module dictates the use of high density packaging not offered by surface mount. This project looks at thick film multichip module packaging as the enabling technology for this application. The high packaging density afforded by thick film multichip modules (MCM) makes it a viable near term packaging technology for high reliability DOE weapons applications.

The throttle control module is required to operate in extreme temperature environments. In addition to the high ambient temperature, contributions from self generated heat could possibly raise the junction temperature on some of the components beyond the recommended operating range. A prominent aspect of this collaborative effort involved thermal modeling of the throttle control module and its associated components. A thermal model was defined which characterized the thermal response of the throttle control module in a typical operating environment. This model was used to optimize thick film multichip module layout based on thermal management criteria, as well as for characterization of the thermal signatures of the electronic components inside the module.

Current technologies for manufacturing electronic components for Defense Program (DP) applications are based on surface mount packaging. These technologies rely on the use of components which are packaged and fully tested. However, as the trend toward increased functionality continues to rise, the inherent increase in component count necessitates the use of unpackaged devices which can only be subjected to a limited level of testing either at the wafer level or as individual dice. Coupled with the extreme operating temperature, this causes difficulty in assuring the reliability of systems adopting this technology. A recommended approach to assure some high level of reliability is to use the same sample sizes normally used for other critical electronic devices in the vehicle for qualification and acceptance with demonstrated large margins for each failure. This should be augmented with subjecting the devices to a dynamic accelerated voltage functional test conducted at high temperature wafer sort to screen for gross defects. As the trend toward high density electronics modules continues, a viable cost effective approach to assess long term reliability of electronic systems is essential. The techniques developed for determining component reliability for this application will form the basis for

formulation of predictive models for assessing the long term reliability of future DP electronic assemblies using commercial components.

The use of adhesives is an important element in the realization of high density multichip modules. The selected packaging technology, thick film chip and wire, is premised on the use of organic or inorganic materials for component attachment. Enabling die and component attach technologies, such as eutectic die attach, soft solder attach, silver glass attach, and organic adhesives were considered for this application. Using Sandia developed codes, finite element analysis was performed to determine the thermal performance of these different types of die attach materials. Electrical, mechanical and chemical characterizations were conducted after a variety of thermal and mechanical stresses. The electrical test revealed that all the adhesives performed satisfactorily. The mechanical strength of the adhesives after exposure to temperature cycling was the most critical problem. The results of the mechanical testing suggest that an adhesive with a glass transition temperature higher than the operating temperature may be the best adhesive for this application. The possible use of organics in electronic assemblies targeted for use in high reliability applications has for some years been a controversial issue. The results obtained here establishes a basis for continued research in this area which would in turn have a considerable impact on the use of multichip modules for weapons related applications.

Failures in electronic assemblies are in most cases attributed to faulty interconnections. Driven by large component count associated with the throttle control, chip level interconnection for the proposed packaging technology is premised on wire bonding techniques. Studies were performed to assess the performance and reliability of gold and aluminum wire bonding to gold, silver and silver alloy thick film inks. Data analysis was conducted in two phases. In the first phase, data were summarized and modeled separately for each combination of material and aging temperature/time. The second phase of the analysis modeled the reaction kinetics associated with a fixed combination of thick film inks and alumina substrate. It was shown that these kinetic models can be used to develop estimates of wire bond reliability as a function of specified exposure time at a specified temperature. The methodology used to develop these models can be applied to interconnect methodologies and materials currently used for manufacturing weapons components. The possibility of integrating these chip level interconnect models with existing chip models will enhance Sandia's predictive capability for assessing electronic module reliability.

The throttle control multichip module is based on the use of thick film materials for fabrication of the interconnect network. This type of packaging technology is attractive since its offers economic advantages when producing large volumes. Driven by cost constraints, silver chip level thick film conductors were selected as one of the conductor materials. Other issues, such as interconnect methodology, dictated the possible use of both silver and gold conductor materials. The primary concern of using both silver and gold conductor materials is the integrity and reliability of the material formed at the gold / silver interfaces. Studies were performed to investigate the behavior of gold / silver interfaces. It was determined that voiding at the metallization / ceramic interface caused by the diffusion of silver into gold destroys the strength of the bonding between the substrate and the metallization. It was thus determined that the mixing of silver and gold based metallizations could be extremely detrimental to the integrity of the hybrid module and, if at all possible, should not be used to fabricate the throttle control interconnect network.

An important aspect of this program was development of a process to protect the electronics components from the adverse environments encountered in the engine compartment. Driven by reliability concerns, the preferred approach was to create a hermetic enclosure. This technology, as it exists today, is not conducive to large volume, low cost production. A viable alternative for creating a hermetic seal is based on the use of lasers. A sealing process which relies on the use of a glass composition as the sealing media was developed to fabricate a hermetic ceramic package for high temperature applications. Initial studies focused on the identification and characterization of candidate glass compositions. Follow on development work was performed to determine the feasibility of using a CO_2 laser to produce hermetic glass seals. Results suggest that this process is indeed feasible. Electronics sealed in hermetic enclosures is the baseline technology for most, if not all, the components used for DOE weapons applications. A laser based approach for hermetically sealing electronic packages has the potential for being more agile, robust and cost effective as compared to the currently used process within the DOE complex.

Although the baseline packaging technology for the throttle control is based on thick film multilayer technology with chip and wire assembly methodologies, solder surface mount assembly techniques are a viable alternative. Tin-silver based solder systems including flux, metallization, and solder were screened for performance in a high temperature environment. The emphasis upon Sn-Ag system is derived from the environmental issues surrounding the use of Pb and from the higher melting point of this system as compared to classical Pb-Sn system. Activation energies for the intermetallic growth over the temperature range of interest were obtained through the thickness measurements of the Ag-Sn intermetallic that formed the solder-metallization interface. It was found that Bi containing solders yielded high activation energies for the intermetallic growth, leading to thicker intermetallic layers for given times and temperature than solders free of Bi. The Ag-Sn binary eutectic composition and the Ag-Sn-Cu ternary eutectic composition solders yielded lower activation energies for the Ag-Sn intermetallic formation, less microstructural change with time, and higher peel strength. Unlike the Bi solders, these solders were resilient to the effects of temperature up to 170 degrees Celsius. Results suggest that the Ag-Sn and the Ag-Sn-Cu eutectic compositions should be considered for future service life .

The throttle control module must be designed to withstand the thermal stresses induced over a wide range of temperatures experienced both during manufacturing and in the harsh environment that exists in the engine compartment of an automobile. Three dimensional finite element analysis of a thick film multichip module were performed to determine the temperature field and the resulting thermal stresses under conditions that may be encountered during the operational life of the throttle control. Results of a steady state analysis modeling cold temperature that could be encountered in extremely severe winter indicate the only stresses high enough to be of concern occur in the glass used to seal the electronic module. These stresses occur only over a small area located at the outer corners of the frame and are not likely to cause cracks that propagate through the seal. In addition, analysis of the transient event that could occur while the part is in service in an automobile indicates that most of the detrimental stresses occur only for very short periods of time and are not likely to cause failure of the part. However, the stress level in the die attach material indicates the potential for cracking, even after a relatively long time period.

All the technological issues mentioned in this section are discussed in greater detail in the following chapters. The principal investigators are identified at the beginning of each chapter and may be contacted for further clarification if required.

2. Application and Requirements

Fernando Uribe
Larry Hazelton (Delphi Automotive System)

Approximately $150 billion per year are spent in the purchase of U.S. automobiles and trucks. Over 30% of the total automotive market share is held by the Japanese, and this market share is expected to rise at a rate of 2% per year. Projections for U.S. sales volume are not expected to rise more than 1% annually through the year 2000.

In an effort to maintain a competitive edge, new technologies to improve automobile performance must be developed. Advanced electronic systems for engine control and management have been identified as one area requiring technology development. Driven by mandates by the Automotive Propulsion Research and Development Act of 1978, Clean Air Act of 1990, and Corporate Average Fuel Economy Standards, the need for high combustion efficiency and emissions reduction becomes vital to ensure the competitiveness of the U.S. automotive industry. Successful realization in the area of engine management depends on the development of advanced high temperature electronics packaging technology.

2.1 Engine System Electronics

Many vehicles built today have independent systems that can affect engine air flow rate such as idle air bypass valve, cruise control, traction control, and antilock brakes. Analysis indicates that integrating these functions into a single system improves vehicle safety and reliability. In addition, if throttle position is controlled by the engine control computer, the fuel control algorithm can be proactive instead of reactive. A proactive system may offer reduced emissions and increased fuel economy by anticipating sudden changes in throttle position.

Through a Cooperative Research and Development Agreement (CRADA), General Motors, Delphi Automotive System has teamed with Sandia to evaluate high temperature packaging technologies for automotive under-the-hood applications. The target application is an automotive Electronic Throttle Control (ETC) system (see Figure 2-1). The ETC would be attached to a throttle body assembly which forms the Smart Brushless Actuator (SBA). The SBA would replace the traditional mechanical cable between the driver's accelerator pedal and the throttle valve, and regulate the airflow into the engine. The accelerator is replaced with a position sensor, which is similar to a volume control on a home stereo. Electronics measure the pedal position, and combined with other vehicle information, a desired throttle position is determined. The desired throttle position is used to control the position of an electric motor connected to the throttle valve. Moving these electronics from the automobile cab to the engine compartment increases vehicle performance by enhancing combustion efficiency and reducing nitrous oxide exhaust. Electronics under-the-hood of an automobile also simplify the cabling running from the engine to the electronics under the dashboard.

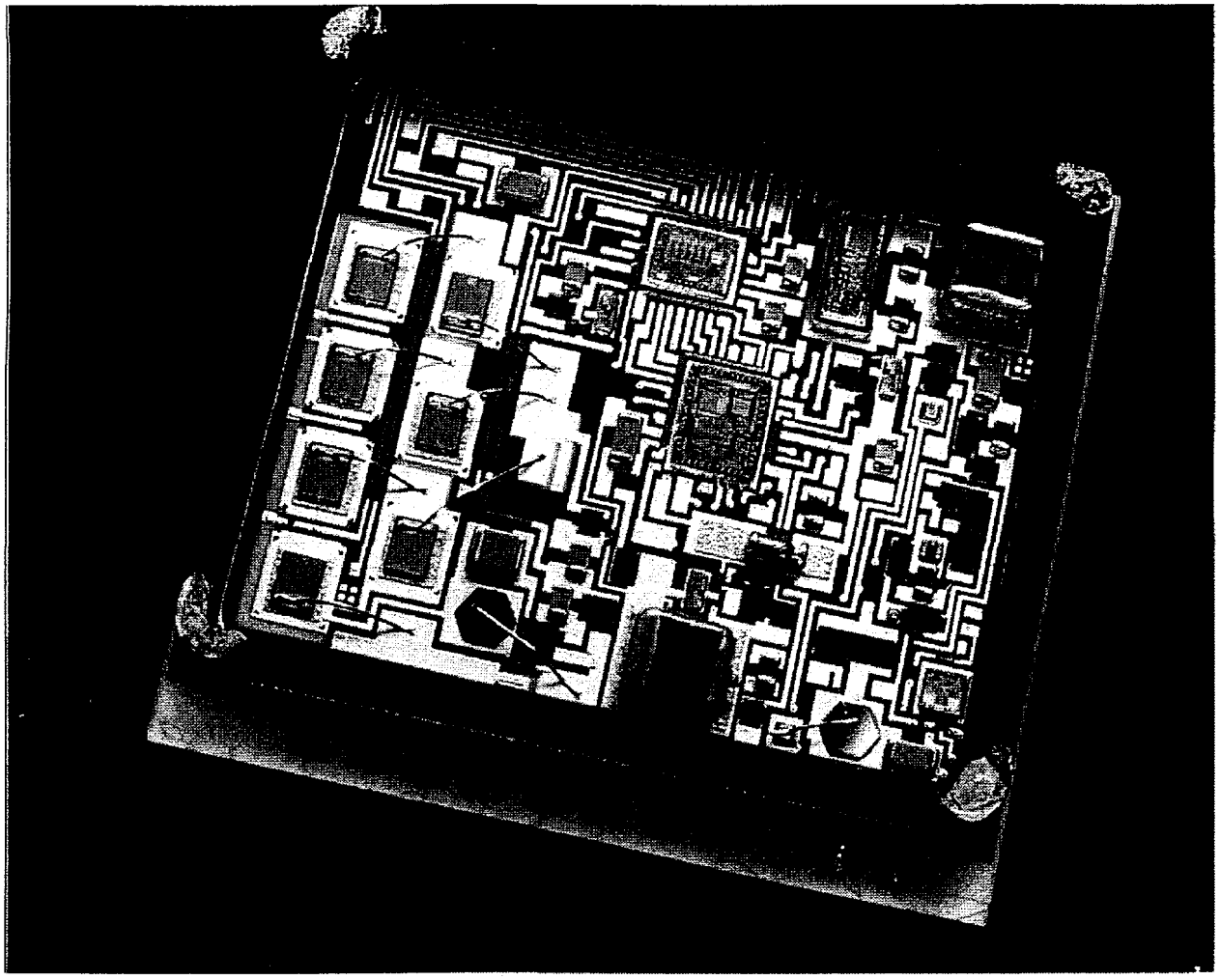

Figure 2-1. Electronic Throttle Control System (ETC)

2.2 Temperature Requirements

The SBA system is attached to the intake manifold of an engine, which causes the electronics to be exposed to temperatures higher than off-engine under-the-hood electronics. The maximum ambient temperature surrounding the SBA was measured at 150°C. Heat sinking was built into the electronics packaging design to limit the internal temperature rise to 10°C for a maximum die temperature of 160°C. The operation of the ETC is 10 years and 150,000 miles. It was estimated that a typical SBA application will operate for a total of 6000 hours over 10 years (88,000 hours). The temperature requirements of these hours would vary greatly with vehicle usage and weather conditions. Table 2-1 lists the estimated temperature requirements of a component of an automobile or other application for severely high temperature exposure. The remaining 82,000 hours of the operations life of the component are unpowered, and the temperature range is estimated at -55 to 85°C depending on the weather.

In addition to temperature, the SBA would be exposed to humidity, salt, dust, and vibration similar to any engine-mounted component. While the module will be protected from dirt splash by a cover, the cover is not hermetic. The full range of humidity and trace amounts of salt and dust were considered in the design.

Table 2-1: Estimated Temperature Requirements of a Component of an Automobile or Other Application for Severely High Temperature Exposure

Temperature (°C)	Hours
130 to 160	500
100 to 130	3500
<100	2000
	6000

*These figures are based on "Delphi Automotive Systems" studies.

2.3 An Electronics Package for Under-the-Hood Applications

The first step in selecting a packaging technology for automotive under-the-hood applications was identification of enabling technologies. Driven by packaging density requirements , cost, volume constraints and operating environments, the two technologies that appeared to have the highest potential for success were low temperature co-fired ceramic (LTCC) and thick-film chip and wire. Feasibility units were produced using LTCC packaging technology. However, substrate cost was higher than expected, driving the total cost per module above Delphi's projected goal. Substrate cost could be reduced by using standard thick film on alumina to manufacture the multilayer interconnect network. This was coupled with the fact that Sandia engineers had considerable experience in the use of thick film chip and wire hybrid modules for high reliability applications. Thick film chip and wire were selected as the baseline packaging technology for the ETC pre-prototype build.

The first lot of parts was designed and manufactured based on an all gold metallization system. However, the contribution to overall cost from the substrate itself was again higher than expected. Cost savings could be attained if the substrate was manufactured using less expensive conductor materials such as silver and silver alloys. Thus, next-generation designs of the ETC module were premised on the use of silver thick films.

An important task in creating the package was selecting adhesive and wire bonding technologies capable of performing under the stresses of elevated temperatures, temperature cycling, and corrosive environments. Choosing the best adhesive available ensured that the electronic components would maintain their mechanical and electrical integrity. Several types of adhesives were subjected to mechanical and thermal stability tests to assess their viability in engine

environments. Ultimately, epoxies were chosen because they maintained the highest strength after high-temperature aging and fatigue due to temperature cycling. Extensive reliability tests were performed on selected epoxies to ensure that the optimum adhesive was chosen.

An airtight hermetic package was developed for the SBA module. This package keeps corrosive liquids and gasses from the engine out of the package and seals in pure nitrogen, which acts as a stabilizing agent. The package design is comprised of an alumina substrate covered by a cup-shaped, glass-sealed alumina lid. A laser sealing technique, developed at Sandia, is used to join the glass to the alumina substrate. This concept is based on using a focusing assembly to reflow the glass seal. To achieve the glass-to-alumina seal, a laser beam is transmitted through lenses that reflect the laser onto a circular mirror. The laser reflects off the mirror creating a uniform 360-degree illumination that is directed at the seam reflowing the glass composition. This laser sealing technique is unique because highly localized glass heating in the range of 450°C can be attained along the glass seal region where the alumina lid joins the alumina plate. This creates an airtight seal without damaging the electronics inside. The electronics inside have a critical temperature tolerance of 150°C. This process has potential applications for high volume sealing of high-density electronics based on multichip module packaging technologies.

3. Enabling Technologies

Cathleen A. Reber
W Doyle Miller
Donald R. Johnson

The first step in the realization of a highly reliable micro-electronic module for use in high temperature applications is the identification and selection of enabling packaging technologies. The selection criteria was driven by many factors, the primary ones being packaging density, technology maturity, cost, reliability, and commercial availability. Among the candidate technologies were Low Temperature Co-fired Ceramic (LTCC), thick film surface mount, direct bond copper, and thick film chip and wire. Of these, thick film multilayer using chip and wire assembly technologies was identified as the packaging technology with the greatest potential for success. This section assesses the reliability implications and environmental vulnerabilities of the materials and processes selected for use in fabricating the thick film multichip module. Inherent failure mechanisms associated with the selected technology are also discussed. A general conclusion is that a high level of reliability can be achieved with thick film multichip module packaging even though new aging mechanisms such as wire corrosion would exist.

This section is organized as follows. Section 3.1 discusses several mounting choices and addresses issues associated with component attach reliability. Section 3.2 discusses wire bond reliability. Section 3.3 covers thermal cycling/fatigue related failure mechanisms. Section 3.4 identifies possible field failure mechanisms. Section 3.5 gives an overview of reliability without hermeticity concerns. Section 3.6 summarizes reliability issues.

3.1 Component Attach and Mount Reliability

Component attach is the process by which a component is affixed to the substrate. This is usually the first process performed during assembly. Historically, the main purpose of attachment is to provide a suitable thermal and electrical path from the component to the substrate and to provide a means of mechanically attaching the component to the substrate. Typically, two classes of adhesives are available for attachment: organic and inorganic materials. These materials are further divided into material classifications.

Attachment failures are of particular concern because of their impact on the stability of the device to perform electrically over the period of time in use during which the device may be subjected to elevated temperatures, thermal cycling, and hostile environments.

This subsection describes common materials used in the mounting procedure and addresses the common concerns related to component attachment reliability: material incompatibility, disbonding or delamination (including interfacial voiding), excess material overflow, and stress-induced cracking. For each of the failure modes, an associated mechanism, the recommended detection method, and possible solutions will be discussed. Most failure modes are classified as

either initial, random, or wearout. In general, effective screening methods, such as those listed in Section 3.1.6, significantly reduce the potential for failures.

3.1.1 Attach Materials

Inorganic adhesive compounds establish a composite (metallurgical, chemical, and mechanical) bond between the component and the substrate. Examples of commonly used inorganic adhesives include Au-Si, silver glass pastes, and soft solder alloys. In a Au-Si eutectic bond, a high degree of silicon diffusion creates a hard soldered joint. Soft solders containing some mixture of Pb, Sn, In, Ge or Ag create a joint based on intermetallic formation. Silver glass pastes bond by three mechanisms: metallurgically, chemically, and mechanically. The metallurgical mechanism is accomplished by forming Au-Ag intermetallics between the thick film gold substrate and the sintered silver matrix formed in the paste. The chemical mechanism is achieved by oxygen bonding between the metal oxides in the glass to the silicon on the backside of the component. Mechanical interlocking takes place as the glass revitrifies upon cooling.

Commonly used organic adhesives include thermoset Ag filled epoxies. The bonding mechanism for the epoxy is mechanical and chemical. When the epoxy is fully cured, it undergoes a phase change and hardens. This phase change also establishes mechanical bonds where the epoxy sticks to microscopic fissures and crevices in the component and substrate. Chemical bonding is responsible for the bulk of the joint strength. As the epoxy cures, portions of the epoxy chains adhere to water absorbed to the surface of the interface. The mechanism of chain attachment is through the Lewis acid-base charge transfer. The epoxy chains become electron acceptors, while the surface film of water acts as the electron donor. The bond sites for the epoxy chains are present uniformly across the interface.

Thermoset and thermoplastic polyimides are also used in some applications. Polyimides have processing characteristics similar to epoxies. However, they tend to be more stable thermally. Filling polyimides with metals, such as silver, tend to lower their thermal stability slightly. Condensation curing produces a thermoplastic polyimide compound whereas additional curing yields a thermoset polyimide compound. As in the epoxies, the bonding mechanism for polyimides is chemical and mechanical.

3.1.2 Material Incompatibility

The selection of appropriate materials is crucial in establishing a reliable attach interface. Improper material selection can eventually lead to one or all of the failure mechanisms discussed in the following sections. Both advantages and disadvantages exist in the selection of a particular attach material. Hard solders tend to have a high onset of plastic flow, which offers excellent fatigue and creep resistance, but the lack of plastic flow tends to create stress at the attach interface due to the thermal expansion mismatch. Soft solders have a high degree of plastic strain capability that allows for a reduction in thermal stresses, but makes the solders susceptible to fatigue and creep rupture failures. Thermoplastic and thermoset organic adhesives tend to lower

thermal stress, but can outgas entrapped solvents during the curing process. Silver filled glass adhesives offer excellent thermal stability, but require higher processing temperatures (>400°C) and ambient oxidizing for optimum adhesion. This creates special processing concerns. A properly cured thermoset organic adhesive is best suited for applications having an operating temperature of less than or equal to 170°C.

Extensive qualification testing should be conducted to characterize selected materials. The following tests should be performed: standard mechanical testing, accelerated environmental testing, analytical destructive testing, and simulated operational testing represented by the system requirements. The results should be carefully analyzed before final material selection.

3.1.3 Disbonding and Delamination

A high degree of interfacial voiding and/or a lack of chemical bonding between the component and substrate can eventually lead to disbonding. The following circumstances can cause disbonding: contamination and/or oxidation at the component or substrate interface or an insufficient amount of adhesive. Degradation of the component or substrate interface can be accelerated when the device is subjected to excessive temperature excursions, constant acceleration, mechanical shock, and random vibration conditions.

Establishing proper processing conditions such as time and temperature are essential to minimize disbonding potential. In general, performing enhanced system-required life tests, constant acceleration, shock, and vibration testing at the qualification level will detect this type of failure mechanism and minimize the occurrence.

3.1.4 Overflow of Conductive Mounting Material

The amount of dispensed adhesive must be controlled to alleviate potentially intermittent shorting. An extensive characterization of the processing parameters and a visual examination of the device after attachment will significantly reduce the overflow occurrence. A lack of surface cleanliness contributes to a condition known as bleedout. Bleedout is described as the overflow of the attachment material onto unintended areas of the substrate and most frequently occurs during the cure cycle. An oxygen or argon plasma clean removes the excess material without negatively affecting the strength of the joint, but there is a remote possibility that the component circuitry can be damaged. An extensive visual examination of the mount area prior to encapsulation can easily detect the bleedout phenomenon.

3.1.5 Stress Induced Cracking

The difference in the thermal expansion mismatch between the component and the substrate is the major cause for residual stresses after attachment. Several key features are associated with this failure mechanism. The cracks typically appear after exposure to extreme temperature excursions and generally propagate from the bottom of the attach interface near the edges or

corners. Stress concentrations on the edges tend to produce horizontal crack initiation while interfacial voiding tends to produce vertical crack initiation. Problems associated with stress-induced cracking can be analyzed using the basic fracture principles of the materials selected for processing. A reliable attach interface should be uniform and void-free to reduce the potential for residual stress.

3.1.6 Summary of Component Attach and Mount Reliability Issues

Table 3-1 represents the recommended critical process and control elements for dispensing and curing attach adhesives.

Table 3-1: Recommended Critical Process and Control Elements for Dispensing and Curing Attach Adhesives

Dispensing	**Curing**
Quantity and Repeatability	Time-Temperature Sensitivity
Pattern Uniformity	Environment- Humidity
Material Pot Life	Shrinkage
Joint Thickness	Fillet Inspection
Visual Examination	Post-Mechanical Strength

Table 3-2 represents analytical tests recommended during the initial evaluation phase as well as an intricate part of process monitoring.

Table 3-2: Analytical Tests Recommended During the Initial Evaluation Phase and as an Intricate Part of Process Monitoring

Test	Purpose
Differential Scanning Calorimetry (DSC)	• Determination of percentage cure and T_g • Thermal stability and reactivity • Phase change versus temperature
Thermal Gravimetric Analysis (TGA)	• Determination of percentage cure and T_g • Thermal stability and reactivity • Weight loss versus temperature
Thermal Mechanical Analysis (TMA)	• Precise determination of T_g • Mechanical performance versus temperature
Residual Gas Analysis (RGA)	• Identification of impurities, gases, and breakdown of products in organics
Scanning Electron Microscopy (SEM)	• Determination of failure mode and microstructure of adhesive

Table 3-3 represents recommended environmental stress testing for evaluating adhesive performance.

Table 3-3: Recommended Environmental Stress Testing for Evaluating Adhesive Performance

Test	Identifiable Problem
Thermal Shock and Temperature Cycling	• Poor adhesion properties • Brittle materials • Accelerates fatigue, and crack generation and propagation
Constant Acceleration	• Poor adhesion properties • Brittle materials • Accelerates fatigue and crack generation and propagation
High Temperature Steady State/Burn-In (HTSS)	• Temperature-related electrical sensitivity • Corrosion sensitivity due to contained residual contaminants
Highly Accelerated Stress Test	• Temperature-related electrical sensitivity • Corrosion sensitivity due to moisture
Mechanical Vibration and Shock	• Mechanical stability and strength • Poor adhesion

3.2 Wire Bond Reliability Issues

Wire bonding techniques such as thermocompression, ultrasonic, and thermosonic were developed to provide interconnections for semiconductor chips to the electronic package contacts and for hybrid circuits to interconnect chip-to-chip, chip-to-passive component, chip to thick film, and to exterior electronic package contacts. The wire bond interconnections have become extremely reliable since the development of automatic wire bonding, improved metallization for bond pads, controlled wire chemistry, effective pad cleaning processes, improved die attach techniques, and reduced temperature bonding processes.

There remains, however, a multitude of potential sources of failure that ultimately affect the high yield and reliability of wire bonds. These include, but are not limited to, stress-strain mismatches, encapsulation or die attach media interactions, atmospheric or process residue corrosion, grain growth coupled to stress induced creep, and the degrading effects of temperature

and temperature cycling. In addition, bonding machine setup parameters, wire metallurgy, and bond pad metallization play critical roles.

Fundamental components necessary for achieving reliable, high yield wire bonds include (a) chip and package metallization compatibility, (b) proper cleaning and storage procedures, (c) parametric control of bonder setup, (d) proper bond evaluation techniques, (e) consistently repeatable bond machine and bond wire characteristics, and (f) compatibility between the bond pads, package pads, and machine capabilities.

This subsection addresses potential failure mechanisms for wire bond interconnections and the prevention of such failures to achieve high reliability. Most reliability failures are related to manufacturing defects. As production processes are refined and controlled, the reliability failures decrease.

3.2.1 Interface-Related Bond Reactions

3.2.1.1 Intermetallic Compound Formation of Gold-Aluminum Bonds

The most widely known reliability problem in wire bonding technology involves the Au-Al interface. That is, purple plague due to intermetallic compound formation. The principal sources of bond failures are the gold-rich phases Au_5Al_2 and Au_4Al and the aluminum-rich phase $AuAl_2$ (purple plague). While it has been generally demonstrated that the intermetallic compounds themselves are not harmful, and these compounds may not necessarily cause bonds to fail, their presence indicates that the integrity of the wire bond may have otherwise been degraded.

Typical bond-failure modes associated with the intermetallic compound formation include: (a) mechanically strong bonds having a high electrical resistance or even an open circuit, (b) a continuous line of Kirkendall voids under the bond resulting in weak mechanical strength, and (c) brittle fracture of bonds exhibiting intermetallics due to wire flexing caused by thermal cycling or vibration.

Achieving good, reliable bonds requires close contact of clean metal surfaces, a large area of intermetallic formation to withstand subsequent stresses on the bond, and thinner metallization that will be used up and, thus, restrict multiple phase formation. For instance, the aluminum metallization for gold wire bonding should be less than 20,000 angstroms thick.

Avoiding bond failures due to the formation of Au-Al intermetallic compounds leading to Kirkendall voiding may be accomplished by restricting process and storage temperatures to less than 300°C for an hour for the gold-rich phases, and less than 400°C for one hour for the aluminum-rich phase. Longer times require even lower temperature exposure by making the metallization thinner or by using thicker wire so that the wire thickness at the heel of a gold-to-aluminum bond is six times greater than the thickness of the metallization.

3.2.1.2 Intermetallic Compound Formation in Non-Gold-Aluminum Bonds

Wires and metallization other than gold and aluminum may introduce similar reliability problems. For instance, the aluminum-silver system, which may be encountered upon the application of silver thick film materials, is quite complex with numerous intermetallic phases. Additional concerns with silver-aluminum include observed humidity corrosion degradation of wire bonds and selective oxidation of the intermetallic layer leading to high electrical resistance. Typically, this oxidation is expected to occur only at temperatures above 400°C, so it is not a critical concern for normal processes and operation.

The utilization of a gold-silver system has been observed to be highly reliable, and this has been established by a history of high-volume production. Intermetallic compounds do not form, and no interface corrosion problems have been reported. The potential problem with this system is encountered by degraded bondability when the silver metalization is tarnished, but this is relatively easily controlled or alleviated.

Yet another highly reliable combination is the aluminum-nickel system. The multitude of intermetallic phases that may be formed are all at temperatures higher than circuit application, and the potential for galvanic corrosion is low. The most serious detriment to bonding aluminum to nickel plating involves the bondability of the easily oxidized nickel surface. Electroless nickel solutions with high-phosphorous content may result in a nickel plating that inhibits both bondability and reliability.

3.2.1.3 Thick Films

Aluminum wire bonds to gold thick film metallization have always resulted in higher failure rates by Kirkendall voiding than aluminum bonds to gold thin films. This occurs because the thick film contains many more grain boundaries, stresses, and impurities than the thin film, all of which lead to an increased number of lattice defects. This combination may result in rapid failure of aluminum wire bonds on thick film gold. The addition of Pd to the gold thick film promotes the formation of a Au-Al-Pd ternary that slows the diffusion of the Au and Al, and thus increases the life and reliability of Al wire bonds.

The utilization of thick film silver for aluminum bonding should be undertaken with caution as this combination results in low interface reliability. Successful application has been enhanced by the addition of Pd to the silver thick film, thorough cleaning of the surfaces to be bonded, and encapsulation in a silicone gel following bonding. This application should be carefully qualified through temperature and humidity testing.

3.2.1.4 Poorly Formed Bonds and Impurity Accelerated Failures

While gold-aluminum wire bond failures due to intermetallic phases, diffusion, and Kirkendall voiding are well-documented, accelerated failures by system impurities have been observed.

Certain of these impurities may be present in the gold plating and may lead to vacancy sinks through the diffusion reactions, and ultimately, to Kirkendall-like voids culminating in weak bond strength. Other observations have identified the degrading effect of halogen reactions with the Au-Al interface; such contamination should be eliminated through process control or cleaning techniques.

Impurity-free but poorly consummated wire bonds should be expected to fail much more rapidly than high-quality, well-controlled wire bonds. Inconsistent and poorly formed bonds may be encountered as a result of improper machine parameters and from surface contamination that restricts intimate contact during the bonding process.

Absolute control of the material received from the wafer fab and/or the hybrid shop, parametric control of the assembly process, and ultimate surface cleanliness are necessary ingredients for achieving well-formed, impurity-free wire bonds.

3.2.1.5 Corrosion

Corrosion must be considered for all combinations of the materials involved. The individual metals, the bond couples, the likely atmosphere, and the galvanic series potential all contribute to the survival and ultimate reliability of the wire bonded device. A definitive test and evaluation procedure for the completed circuit is necessary to determine the contribution of the numerous materials within the assembly. The use of the highly accelerated temperature and humidity stress test (HAST) is one approach for evaluating the reliability of nonhermetic devices (see Section 3.5). Acceptance following this test may be based on compliance with electrical parametric limits and the verification of electrical functionality under both nominal and worst-case conditions.

3.2.2 Surface Cleaning

3.2.2.1 Cleaning Methods

The primary requirement for high yield, high reliability wire bonding is that both the chip metallization and the package/substrate metallization should be clean and bondable. Oxygen plasma and ultraviolet ozone are among the most effective cleaning techniques for wafers, chips, and packages. However, current drawbacks must be considered and factored into the process. Metallization containing silver, copper, or nickel may be oxidized by the plasma and the surface will be rendered unbondable. However, it has been demonstrated that a combination oxygen plasma with argon plasma at the end of the process will remove the black oxide from silver metallization and maintain bondability. A remote possibility exists that the plasma will cause radiation damage to the chip. Plasma will not remove the glass passivation contaminant remaining from the wafer process. With the current emphasis on no chlorofluorocarbons (CFCs), solvent cleaning techniques must be thoroughly developed and evaluated for the specific application.

Storage following cleaning is important because both gold and aluminum surfaces are subject to recontamination almost immediately. While storing in nitrogen-filled cabinets may inhibit recontamination, it is deemed advisable to reclean after a period of two hours. A specific sequence of cleaning, storage, and bonding must be determined and verified for the combination of materials involved and the overall process.

While normal surface contamination may be a problem on thick film materials, they also present bondability issues due to surface defects such as voids and pits. Some approaches have incorporated burnishing, scouring, or coining to counter these surface defects and hopefully improve bondability to the thick film. Though controversial, these techniques are used, and they require careful application so as not to enhance the bondability problem.

3.2.2.2 Sensitivity to Surface Contamination

Good cleaning techniques will obviously improve the bondability and reliability of wire bonds. The degree of cleaning necessary will vary with the bonding method. For organic contaminants produced by photoresists it has been determined that aluminum ultrasonic wire bonding offers far superior results than thermosonic or thermocompression bonding with regard to bondability. Evaluation of the specific contaminant films and bonding processes should be performed to determine the sensitivity of the device manufacturing process to the most probable degradation mechanisms.

3.2.2.3 Plasma Cleaning Damage

As previously stated, the plasma may promote oxidation of surface metallization and degrade bondability. The plasma may also damage the circuit by causing electron-holes at the oxide silicon interface or by resulting in surface damage due to sputtering. The plasma conditions should be evaluated carefully for the specific application.

3.2.3 Mechanics-Related Bond Failures

3.2.3.1 Cratering

Cratering of bond pads during ultrasonic bonding is a phenomenon for which there is little fundamental understanding. However, cratering is known to result in significant yield and reliability issues compounded by higher costs. Typically, a production problem related to cratering is solved, or minimized, by careful parametric control of the bonding process while the root cause of the phenomenon remains undetermined. Cratering may occur as gross damage to the bond pad wherein a divot is removed still attached to the bond wire or it may result in damage that is basically invisible but will ultimately result in degradation of the device's electrical characteristics. Contributing factors to the cratering phenomenon include wire hardness, bond pad thickness and hardness, silicon precipitates in the bond pad, stress due to intermetallic phases, sensitivity of the substrate material (GaAs craters easily), bond pads over polysilicon,

silicon hillocks under the pads, and all of the standard bond machine parameters (force, time, power, temperature, etc.). This is a phenomenon that obviously employs synergism between a multitude of potential culprits.

Whether gross and obvious or minimal and disguised, the cratering phenomenon should be addressed and monitored. Definitive plans for control and evaluation should be defined early in the process development.

3.2.3.2 Heel Cracks in Ultrasonic Wedge Bonds

Aside from cratering, another major concern for aluminum wire bonds is heel cracking. These cracks may be caused by sharp-heeled bond tools, excessive deformation, improper tool angle, bonding machine vibration during or just before tool lift-up from the first bond, or rapid tool movement after the first bond combined with excessive wire looping.

The inherent damage of heel cracking is somewhat subjective. Some heel cracks are actually little more than surface tool marks or readily annealable, nonpropagating surface defects. However, heel cracks can ultimately contribute to the degradation of the bond strength and will undoubtedly effect the long-term reliability of the device. While the extent of the crack is not always obvious, the existence of any crack in the heel of a bond represents a flag showing that some portion of the process and/or equipment is out of control and requires corrective action.

3.2.4 Summary for Wire Bonding Reliability Issues

The development of automatic wire bonding, improved metallization for bond pads, controlled wire chemistry, effective pad cleaning processes, improved die attach techniques, and reduced temperature bonding processes have all contributed to the reliability of wire bond interconnections. Nevertheless, there remain numerous potential sources of failure. Bonding machine setup parameters, wire metallurgy, and bond pad metallization obviously play critical roles for ultimate reliability. Additionally, stress-strain mismatches, encapsulation or die attach media interactions, atmospheric or process residue corrosion, grain growth coupled to stress induced creep, and the degrading effects of temperature and temperature cycling all contribute to interconnection reliability.

Most reliability failures are related to manufacturing defects. As production processes are refined and controlled, reliability failures are minimized to acceptable limits. Proper chip and package metallization, proper cleaning and storage procedures, parametric control of bonder setup, effective bond evaluation techniques, consistently repeatable bond machine and bond wire characteristics, and compatibility between interconnection design and machine capabilities must be rigidly maintained to achieve high reliability for wire bond interconnections.

3.3 Temperature and Humidity Reliability Issues

Product reliability in hybrid components can be significantly impacted by temperature and high humidity environments. These hostile environments are the primary causes of failures in microelectronic packages. Due to these environments, failure mechanisms can range from non-uniform thermal expansion effects of component materials and subsequent thermal fatigue to corroding elements entering the package interior and attacking sensitive parts or critical interfaces. These failure mechanisms must be considered when designing the hybrid module to ensure highly reliable functional performance throughout the intended operational lifetime.

This section will describe common failure mechanisms related to operation in hostile environments and their impact on reliability. Hermetic packages and plastic packages will be discussed in relation to reliability, processing, and cost. Processing steps will be addressed to help minimize local stresses and strains of susceptible elements and minimize moisture permeation of the hybrid component and assembly processes developed to minimize the failure mechanisms.

3.3.1 Temperature and Humidity Failure Mechanisms

3.3.1.1 Thermal Mismatch

Electronic packages are comprised of dissimilar materials that expand and contract at different rates of heating and cooling. Thermal expansions of the various materials will cause repeated strain. If the mismatch is significant, these strains will result in the phenomenon of thermal fatigue. Developments that extend functional lifetime include strain reduction, geometry or shape improvement, and alternate solders, if applicable. Thermal mismatch reliability issues are also discussed in greater detail in Section 3.1, Component Attach and Mount Reliability, and Section 3.2, Wire Bond Reliability Issues with relation to assembly processes.

3.3.1.2 Thermal Fatigue

It is well-known that semiconductor device failures are dependent on temperature. Temperature dependency of the failure rate is a basic parameter used for failure predictions. The primary concern in thermal-cycle reliability is the useful lifetime defined by the first wearout mechanism. This is because the element is unable to bear its share of the mismatch over its lifetime and prematurely fractures. Fatigue will create openings or initiate cracking resulting in reduction of heat radiating efficiency and eventual device failure. Elements that are susceptible to thermal fatigue can include leadframe, package materials, die, and essentially all assembly methods. One example of this type of failure mechanism is the temperature acceleration factor in the degradation of Au-Al bonding strengths. Determination of system forces and deformations, and local stresses and strains of susceptible elements during design stages can optimize thermal-mismatch reliability and the subsequent failure mechanism of thermal fatigue.

3.3.1.3 Moisture

Moisture is one of the major sources of corrosion of semiconductor devices. Electro-oxidation and metal migration are also associated failure mechanisms due to moisture. Moisture is present in ambient atmospheres ranging from zero to 15 percent relative humidity (RH) in arid regions to over 95 percent RH in semitropical areas. Corrosion of aluminum metallization is a primary failure mechanism due to moisture. This is due to aluminum being an extremely chemically active metal and, therefore susceptible to corrosion failure mechanisms.

Typically, three factors contribute to moisture within a package. These factors include (1) the sealed-in water from ambient, absorbed, and dissolved from the sealing materials, lid, or substrate released during the sealing process; (2) leakage or permeation of moisture through the package itself, or (3) leakage or permeation of moisture through the package seal. However, although the connection between moisture and failure rates in microelectronics is known, no direct relationship has been established at this time.

3.3.2 Package Configuration

3.3.2.1 Hermetic Packages

Fully hermetic packages are constructed of metal or dense ceramic. Note, however, that no materials are truly hermetic to moisture. A finite amount of leakage will occur through diffusion and permeation. This permeation is orders of magnitude less than any plastic material. The purpose for using hermetic packages is to exclude moisture and other hostile gasses. Military specifications allow leakage rates less than 10^{-8} cm^3/second and sealed-in moisture limits of 5000 parts per million (ppm). However, the major concern with this package type is retained water in the package, which typically originates from sealed-in adhesives. This failure mechanism was discussed in greater detail in Section 3.1, Component Attach and Mount Reliability.

Overall, hermetic packages are highly reliable packages in relation to moisture failure mechanisms and reliability issues associated with temperature extremes. These packages are seen in applications that require high reliability, such as military applications and certain civilian applications. However, one drawback to hermetic packaging is its cost factor, which is typically two times higher than the cost of alternate package materials.

3.3.2.2 Encapsulation

Plastic-encapsulated devices are discussed in Section 3.5, Reliability Without Hermeticity. The diffusion rate of moisture depends on the encapsulate material. Certain epoxies, polyimides, and imide-siloxanes have shown great promise in reducing diffusion of moisture. However, moisture is known to propagate down the lead interface to the internal package or diffuse directly through the package material. This creates significant reliability concerns. In plastic encapsulated devices, the most significant reliability issue is moisture permeation. Additionally, the packing

of more devices on the same substrate greatly increases the probability of chip-level failure. This factor, combined with failure mechanisms associated with increased device densities, increases the cumulative effect on overall failure mechanisms by an order of magnitude for each doubling in circuit density.

3.3.3 Packaging Processes

3.3.3.1 Component Attach

Component attach is discussed in greater detail in Section 3.1, Component Attach and Mount Reliability. However, note that component attach can be adversely effected by both temperature and humidity. Stress due to temperature extremes is a major factor in determining proper materials to minimize thermal mismatch and maintain reliable attach interface. Materials such as hard solders exhibit large thermal mismatches that create die stresses and cracks. This type of failure mechanism is typical of gold-silicon eutectic attach. Epoxies and polyimides significantly reduce thermal stress. However, the thermal stability of this type of attach is less than the thermal stability of eutectic attach. Outgassing of trapped solvents and other gaseous species can severely degrade long-term reliability.

3.3.3.2 Wire Bonding

As with component attach, wire bonding is discussed in greater detail in Section 3.2,Wire Bond Reliability Issues. However, reliability can be severely degraded due to corrosion effects of aluminum bond interfaces due to moisture. Additionally, degradation in bonding strengths of Au-Al bonds is a typical failure mechanism due to formation of intermetallic bonds and accelerated by temperature.

3.3.3.3 Package Seal

The first function of a semiconductor package is to protect the chip by sealing it from environmental hazards that may be encountered during the component lifetime. The design of the package seal is paramount in minimizing environmental effects, specifically moisture. Additionally, the sealing ambient is crucial to ensure long-term reliability. Various methods of hermetic seals include soldering, brazing, welding, and glass sealing.

Solders for hermetic sealing are based on temperature hierarchy for processes that precede and follow the sealing operation, minimum seal strength, and cost. Straight tin-lead solders are most common for hermetic sealing. However, alloying additions such as indium and silver may improve strength and fatigue resistance over tin-lead solders. Typically, the softer the solder, the less likely it will fatigue. Even with solder improvements, solder seal is typically less desirable than the brazing process due to lower strength. Solder seal typically has half the strength of gold-tin brazing and in most cases requires the use of flux. Flux entrapment during the sealing process is difficult to avoid, can cause corrosion, and can lead to deposition of tin on electrically

active areas of the device. Solder sealing of large-cavity packages also presents a unique reliability concern. Due to the large volume of heated gas inside the package, there is susceptibility to the formation of blow holes in the molten solder or the drawing of solder into the package creating solder balls.

The hermetic sealing process begins with the assembly of a lid and substrate performed with a spring-loaded fixture. The lid and substrate are then reflowed under an inert gas atmosphere. The equipment used is typically a conveyor furnace. Furnaces are generally set up to create a fast preheat period, a peak temperature of 40 to 80 degrees above the solder melting temperature, and a fast cooldown period after solidification that completes the solder seal process. However, all parameters for the sealing process are critical to component reliability. The spring loading tension, metallurgical and surface cleanliness of sealing surfaces, furnace profile, and the ambient must be tightly controlled. Overall, this type of seal is more susceptible to temperature extremes when compared to other sealing methods. With lower strength, the hermetic seal is more susceptible to fatigue failure mechanisms, and specifically more susceptible when used with power devices. Additionally, tightly controlled process parameters are crucial to successful hermetic sealing.

Brazing is typically used in place of soldering due to stronger, greater corrosion resistant seals with no need for flux. The braze is usually used as a thin preform tack welded to a gold-plated kovar lid. This tack consists of a ratio of 80 to 20 gold-tin alloy, respectively. The package or substrate seal ring is also gold-plated for good wettability and corrosion protection. The seal process typically utilizes a seal furnace. Reflow time is between two to four minutes above the eutectic temperature of 280°C with a peak temperature of approximately 350°C. One drawback to brazing is the steep slope of the liquidous curve of Au-Sn on the gold-rich side of the eutectic, which can create significant hermetic failures. A slight increase of 3 to 5 percent in gold above the eutectic composition will significantly raise the liquidous temperature and, thus, potentially create nonwetting and subsequent hermetic failures. By ensuring a brazing alloy richer in tin, this problem is normally avoided. Overall, with proper process control of material flatness, equipment set, and sealing atmosphere, sealing by this technique creates a hermetic package with good yields and long-term reliability to temperature extremes and moisture permeation.

Welding is the most popular method for sealing high-reliability packages. It is estimated that 80 percent of all military packages are sealed by this process. In the welding process, high-current pulses generating localized heat between 1000° and 1500°C fuse the lid to the plating and package. One process advantage of this sealing method is less susceptibility to deviations in flatness for the package and lid. Another process advantage is that, due to the highly localized heating, the interface contaminants can volatize so that cleanliness is not as critical a process parameter. The two most popular methods of welding include parallel seam welding and opposed electrode welding. Other methods with less popularity are electron beam welding and laser welding. Welding equipment does have a higher cost initially, but the benefits of this seal method are high production yields of hermetic components with a history of high reliability.

Glasses in package sealing applications have the versatility of chemical inertness, oxidation resistance, good electrical insulating characteristics, and impermeability to moisture and other gasses. Principal shortcomings include low strength and brittleness. Typical failure mechanisms are due to poor adhesion between glass and the seal surface, high stresses causing fracturing, fracturing due to handling, and the possible failure of the metal or ceramic package or substrate being sealed. It is critical when using this seal method to analyze the seal design, choice of glass, and the actual sealing process.

To avoid high stresses in glass seals, most glasses are modified by devitrification and the addition of certain low-expansivity fillers. One example of a low-expansivity filler would be fused silica. Due to devitrification, increases in seal strength and decreases in thermal expansivity are two factors that have increased overall seal integrity. Conversely, devitrifying solder glasses are associated with increased moisture sealed within the package compared to vitreous seals. This is because crystallized glass has much lower solubility for water than in its glassy state. Therefore, most of the chemically combined water is expelled when devitrification occurs during sealing.

The standard sealing method for glass is furnace sealing. Key factors for successful hermetic sealing with this method include sealing ambient and furnace temperature profiles. Other methods of glass sealing include a graded viscosity seal and focused infrared light to heat the seal area. Both are novel sealing methods not as common as furnace sealing.

3.3.4 Summary of Temperature and Humidity Reliability Issues

Hermetic packages are superior to plastic packages with regard to high reliable applications, but have a significantly higher cost. For economy and mass production, plastic packages have been the logical choice. Currently, 95 percent of all packages produced each year are plastic packages. Yet compared to hermetic packages, plastic packages are more susceptible to moisture permeation and the failure mechanisms associated with hostile and highly humid environments. Therefore, hermetic packages at the present time will tend to be the package of choice in military and highly critical civilian applications regardless of significantly higher costs.

With reliable packages chosen to meet high reliable applications, control of packaging processes is an essential requirement for maintaining high reliability components. The various processes can be susceptible to thermal mismatching, thermal fatigue, and moisture failure mechanisms. As discussed, proper design of starting materials, assembly methods, and process controls are critical for successful production of high reliable hybrid components.

Overall, most reliability failures due to temperature and humidity extremes can be minimized by analyzing design factors, manufacturing factors, and applied environmental factors. Consequently, cost is always a factor in overall design versus reliability.

With all the factors noted, it is still critical to include screening methods to eliminate initial failure mechanisms. These screening methods must be determined according to the required quality,

reliability levels, and associated costs. Methods such as temperature cycle, thermal shock, and high temperature storage represent effective screening methods to identify potential temperature and humidity failure mechanisms, thereby, continually ensuring high reliability hybrid components.

3.4 Possible Field Failures for Hermetic Chip-and-Wire Hybrids in Automobiles

Wire bonded thick film hybrids have been successfully used in large numbers in high reliability military and space applications for decades. The most likely packaging field failures result because manufacturing does not heed proper caution in its process. Thus, the product is susceptible to a well-known failure mechanism. This lack of caution is usually due to (1) cost-driven neglect of controls, (2) workers' insensitivity to the consequences of the neglect, or (3) no feedback from the next assembly or the field to the manufacturing line.

3.4.1 External Inspection

The easiest way to consider the various field failures for hermetic chip-and-wire hybrids in automobiles is to consider the steps taken by failure analysts when a failed module is returned. First, the packaged hybrid must be proven to be the failure cause. For example, the solder connections of the hybrid package to the motherboard must be checked visually and reworked to check whether they are faulty. Historically for electronic modules, approximately 40 percent of parts that are returned from the field are not found faulty because often the wrong part was accused of failure.

Next, a visual inspection of the outside of the extracted package is needed to spot excessive lead corrosion or flaws in the package body. This would indicate a hostile assembly or engine compartment environment (fire or salt) or may indicate improper protection by the next level assembly. This conclusion would suggest that the hybrid manufacturing line is not the source of the problem, but rather, a system problem exists that must be addressed.

The next step is to check the package hermeticity. If the package does not pass a hermeticity test, the failure will probably turn out to be due to moisture or corrosion. Because the package was hermetic when manufactured, a leaky package can either indicate a shock to the package or lid that exceeded the specification, or it can mean a slight contamination on the seal ring or a marginal sealing operation. For example, a manufacturing line can inadvertently become contaminated by low-level presence of silicone grease, which can make the seal lids marginal. The best manufacturing defense against degradation in hermeticity is to perform a quantitative leak check of the package, not just a yes or no check. Typically, a package will pass with several orders of magnitude in leak rate. However, as a manufacturing line starts deteriorating, the margin of passing will begin shrinking. A line that records and plots daily package leakage values will fix the problem before any risk of field failure occurs.

An electrical test on the package is then performed to confirm the failure and determine, with the circuit designer's help, the cause of the faulty electrical response. The electrical test can detect and identify a broken or shorted wire, a dead chip, or a drifted resistor. An optional Particle Impact Noise Detection (PIND) test may be run at this time. This test is to check if any loose particles are in the package. Loose particles do not generally cause failures, but solder or wire debris could momentarily short lines. Most low voltage hybrids and ICs are fairly immune from loose particle failure if a final passivation thick film layer is used. If field results show a marked sensitivity to particle-induced failures, then a thin polymer coating should be applied after wire bonding but before sealing to immobilize particles and insulate all surfaces.

3.4.2 Internal Inspection

The lid is then carefully removed so the undisturbed inside of the package can be viewed. If corrosion products are seen but the package remained hermetic, then either contamination was sealed into the package or the package has a rare intermittent leak. These corrosion products are usually crystal growth on the IC bond pads or discoloration on the hybrid surface. Contamination generated inside can occur if the adhesives used were under-cured, if the samples were not properly cleaned before hermetic sealing, or if the part was accidentally contaminated in a fluke event. One failed part usually is not enough to prove a trend. However, more information can be obtained by checking control parts sealed with each lot produced. Control parts from the same manufacturing lot can be opened with a failed part. The extent of corrosion in these control parts can be used to tell how much margin exists. If the corrosion is caused by internally generated chemicals, then a thin layer of silicone gel before sealing is recommended to prevent the products from pooling on sensitive surfaces. If under-curing adhesives or under-cleaning the assembly are the cause, the processes are easily changed.

Broken or touching wires indicate a handling problem on the line between the wire bonding and the sealing step. This type of failure is difficult to gauge because it is rare to have only one part mechanically disturbed in a whole lot. Normally with semiautomatic or automatic equipment, all parts receive the same care or the same abuse. It is also difficult to screen for wire placement in a nondestructive way (x-ray). Thus, sampling and opening product is the only way to gain insight into the manufacturing quality.

In a rugged automotive environment, wires can possibly undergo resonant vibration leading to failure. The fundamental resonant frequency for typical short wire bonds is typically above 20 KHz, but the harmonics of automotive environment could, in principle, cause problems. Such a failure mechanism must be ruled out before assembly procedures are needlessly changed.

A third way wires can break is for a high current pulse to cause a fuse effect. The melted wire debris is a clue to this event. Again, this failure is not a hybrid manufacturing failure, but rather, a circuit design failure leading to uncontrolled transients.

A fourth wire failure is the cratering failure described in Section 3.2.3.1. The presence of chip material on the wire pad and a crater in the chip are the symptoms. It is important to record the chips that have these failures. Some ICs are much more prone to this failure than others. If cratering is an assembly-induced problem, normally it is noticed by a steady number of rejects on the line in addition to a few that make it through testing to the field. If cratering becomes a major problem, a 100% nondestructive 2 gram wire pull screen may prevent shipment of defective material. However, the cost-effective long-range solution involves IC vendors using correct bond pad design rules, bonding test monitors made and pulled on each shift of a production line, and optimal adjustments to the bonding equipment.

A broken wire at the interface between the wire and the bond pad can be the result of (1) an unclean pad, (2) not enough bonding power, or (3) brittle aluminum gold intermetallics forming at the interface. These mechanisms are well-known and can be avoided by periodic tests to destruction of product in the line. For example, aging of samples at elevated temperature and then wire pull tests are often used to check the strength of the wire-to-pad interface.

The hybrid substrate may be loosened in the hermetic package leading to bent or broken wires. This problem can be caused by incorrect adhesive cure, differential thermal expansion of substrate and package, spotty adhesive coverage, or unclean surfaces. Again, the best defense is to periodically perform a destructive test on the interface strength of randomly selected products. By recording the strength as a function of time, one can spot problems growing on the assembly line before they reach levels that will cause field failures. Due to the large amount of extreme thermal cycles that automotive engine electronics undergo, it is best to minimize the differences in thermal expansion between materials that have a large area interface, such as the substrate and the package.

3.4.3 Individual Component Failures

All failures listed in previous subsections should remain at a low level in an assembly line run using well-established hybrid manufacturing procedures. However, the failure of one particular chip within the hybrid could grow to unacceptable levels. In a chip and wire hybrid, bare chips are typically applied to the module with no more than a partial functional electrical test performed at wafer probe. Once the module is completed, more extensive functional, temperature range, and burn-in qualification can take place. However, the circuit could easily hide the fact that the input leakage of one chip increased at temperature more than one would accept were that chip packaged in a single hermetic package. Thus, a bad or nonstandard chip is included in the module only to drag the module down later in the field. The cures for this problem are twofold: design for testability (DFT) and known good die (KGD).

One designs for testability by making sure the module can be tested to localize any deviance. For example, extra probe points are included so that individual integrated circuit (IC) leakages can be initially monitored during qualification. A little more space is needed for DFT, but the customer receives more reliability. Many known good die approaches, such as extensive wafer

probing, circuit repatterning, and temporary packaging, are under development. The goal is to extensively test the bare chips so they are as dependable as if they had been individually packaged and tested before commitment to the hybrid. Chip manufactures must share their yield and their packaged field failure data with the hybrid manufacturer so the proper trade off of pretesting to field failure can be reached.

3.5 Reliability Without Hermeticity

Plastic IC packaging is replacing ceramic hermetic packaging (CHP) in many high reliability applications. Although plastic packaging has always offered superior performance in shock and vibration environments because of the mechanical stabilization of the die and wire bonds, it does allow moisture access to the die surface with the consequent possibility of moisture-induced IC failures. Because all polymers are permeable to water, there is no way to isolate the die surface from water. However, by judicious choice of packaging materials and die technology, high reliability can be attained in humid environments.

In the early days of plastic packaging, moisture-induced failures were predominately due to corrosion of Al metal on the die or at the Al to Au wire bond-bond pad interface. The early epoxy mold compounds had high ionic impurity contents and high equilibrium water solubilities. Present day mold compounds have low ionics: frequently greater than or equal to 15 ppm Cl^-. In addition, solubility levels have been substantially reduced. Another class of materials, the silicone gels, offers superior protection against corrosion failure in humid environments. Although gel is highly permeable, the molecular bonding mechanism at the gel-die interface appears to prevent the formation of liquid water at the interface. It is widely believed that liquid formation is required for corrosion to occur. However, the gels are soft with a very low elastic modulus and do not offer the mechanical protection of the epoxies.

Sandia has been studying nonhermetic packaging for approximately five years. A family of corrosion sensitive test chips has been designated as Assembly Test Chips (ATCs) and has been used in conjunction with highly accelerated stress testing (HAST) to evaluate the protective properties of both organic coatings and various die passivation strategies. A HAST experiment is typically run at elevated temperature (130°C or higher) and high relative humidity (RH)—typically 85 percent in a pressurized test chamber. The ATCs at Sandia use triple track corrosion test structures that have serpentine, parallel conductor lines. These test chips are usually biased at high voltage to accelerate corrosion failures. A bias of 40 V was usually used across track structures with 2 mm gaps for an effective electric field of 20 MV/m within the track structure.

In these studies, three broad classes of plastic packaging were evaluated: epoxy molded parts, liquid epoxy encapsulates for chip-on-board, and silicone gels. The gels, primarily Dow Corning 6646, offer the best protection against moisture induced failure. Typically, only a few percent fail after approximately 2000 hours in HAST at 140°C and 85 percent RH have occurred. In

cases where failure does occur, it is at the bond pad-wire interface, not in the passivated track structure. The molded parts have the next best performance, but in this case, the 50 percent failure point occurs at »1000 h. In comparison, the liquid epoxy encapsulated parts have a mean time to failure of approximately 200 hours.

The acceleration factor has not been determined that relates the mean lifetime at HAST conditions to conditions at lower temperature, relative humidity, and bias voltage. However, assuming that the Peck temperature and humidity acceleration model is valid, there is a factor of » 30 between mean lifetimes at 140°C and 85 percent RH, and 85°C at 85 percent RH. Another factor of eight would arise from voltage acceleration for a nominal 5 V part for a total acceleration factor of » 240. Thus, even the liquid epoxy encapsulated parts are predicted to have a mean lifetime in excess of five years at 85°C and 85 percent RH.

There remained some interesting unanswered questions about the reliability of plastic ICs in high temperature and humidity conditions:

1. There appear to be two regions in the log normal failure fraction versus time relation in HAST [1]. At early times the bimodal failure curve had a small slope, while at later times a steep slope log normal distribution developed. This type of behavior has been observed in several experiments reported by other investigators using both passive test structures and active digital ICs. This early failure regime is dominated by bond failures, but the specific conditions that caused these early failures are not known. A key to increasing reliability is to reduce the early failure rate.

2. There have been reports of active device failures in HAST that do not appear to be caused by corrosion of metal lines. These failures seemed to occur as a result of MOS transistor threshold voltage shifts and may not have required the presence of ionic contamination. Additional HAST experiments will be performed with 256K static random access memory (SRAM) using 0.6 μm technology in Sandia's Microelectronics Development Laboratory. These experiments will be performed in conjunction with developing new CMOS technology. These SRAM experiments will be run in conjunction with traditional ATCs to compare the failure rates and modes for the two types of parts.

3.6 Summary of Reliability Issues

Currently, the automobile industry has a robust electronics packaging technology that emphasizes soldering of components on a motherboard. Often, surface mount components are used, but through-hole construction is also present. Although some prepackaged components are hermetic, most automotive modules are molded in epoxy or immersed in a silicone-filled well.

The biggest reliability difference between hermetic and nonhermetic packaging is in the use of bare chips instead of prepackaged chips. This impacts reliability in that the chips cannot be easily tested over the predicted temperature range in burn-in for early defect detection. Also,

bare chips cannot be extensively characterized before they are committed to the module. Bare components are subject to more damage in assembly than packaged components. Most testing would occur at the module level requiring higher levels of rework or scrap after testing.

The second biggest reliability difference is the use of fine wire bonding instead of solder connections. Both solder in automobiles and wire bond in high reliability military systems have been shown excellent once manufacturing quality has been achieved on a line. For example, wire bonding has been shown superior to most soldering systems in environments with numerous temperature cycles and high temperature operation.

The third difference is in hermeticity. In general, hermeticity is a great ally to reliability, but is assumed to have no second line of defense. That is, if hermeticity is breached or if enough contamination is inadvertently sealed inside the assembly, the exposed assembly would quickly degrade. With current materials, however, various secondary barriers can be used and will be discussed.

Most field failures do not occur because aging mechanisms were not anticipated. Rather, they occur from expected aging occurring during substandard process control. For example, components could be attached with adhesives with large voids, which were undetected during manufacturing. For this reason, in each subsection process sensitivities were discussed. In addition, it is imperative that during the first five years of fielding these modules, any field failure should be given uniform failure analysis to provide feedback to the assembly and testing processes. Intuition built up through decades of soldering must be augmented by failure analysis on chip-and-wire to continue improving manufacturing.

Thick film hybrid technology is fairly mature with a robust technology base. Several advantages in using this technology are that an abundant supply of resistive inks are available that can be screened onto the substrate to integrate resistors. Also, surface termination inks exist which facilitate the use of wire bonding and component attachment through the use of conductive adhesives.

Reliability is typically measured by evaluating the resistance of the assembled components to degradation of electrical and thermal functions as dictated by system requirements. On completion of the design phase, every program must go through a rigorous test and qualification phase. During this time, the performance properties are measured to verify that the system goals are met. Environmental testing confirms that the design is rugged enough to function reliably over the range of conditions anticipated during its lifetime.

REFERENCES

1. *Packaging,* vol. 1 of *Electronic Materials Handbook.* C. A. Dostal, ed. American Society of Metals (ASM) International, Materials Park, OH, 1989.
2. *Microelectronics Packaging Handbook.* R. R. Tummala and E. J. Rymaszewski, ed., Van Nostrand Reinhold, New York, 1989.
3. G. G. Harman, *Reliability and Yield Problems of Wire Bonding in Microelectronics,* International Society for Hybrid Microelectronics, Reston, VA, 1989.
4. W. Huddleston, D. Cavasin, and C. Seifert, "Wire Bond Process Control," *Quality*, December, 1993, pp. 54-55.
5. T. Ramsey, C. Alfaro, and H. Dowell, "Metallurgy's Part in Gold Ball Bonding," in *Semiconductor International*, April 1991, pp. 99-102.
6. G. G. Harman, "Wire Bonding -- Towards 6-σ Yield and Fine Pitch," in *Institute of Electrical and Electronics Engineers (IEEE) Transactions on Components, Hybrids, and Manufacturing Technology*, vol. 15, no. 6, 1992, pp. 1005-1012.
7. "Welding, Brazing, and Soldering," vol. 6 of *Metals Handbook*, 9th ed. E. F. Nippes, Coord., American Society for Metals, Metals Park, OH, 1983, pp. 746-756.
8. J. L. Jellison and J. A. Wagner, "Role of Surface Contaminants in the Deformation Welding of Gold to Thick and Thin Films," in *Proceedings 29th IEEE Electronics Components Conference,* held in Cherry Hill, NJ, May 14-16, 1979, pp. 336-345.
9. J. J. P. Gagne, "Silver Migration Model For Ag-Au--Pd Conductors," in *Proceedings of the 1992 IEEE Electronic Components Conference*, 1992, pp. 214-219.
10. J. Aday, R. W. Johnson, J. L. Evans, and C. Romanczuk, "Thick Film Silver Multilayers for Under-the-Hood Automotive Applications," in *Proceedings of the 1993 International Society of Hybrid Microelectronics (ISHM) Conference*, Dallas, TX, November 9-11, 1993, pp. 126-131.
11. R. Fillion, and R. Wojnarowski, "Non-Hermetic Embedded Chip MCM Technologies for Automotive and Other Lower Cost Applications," Proceedings 1993 ISHM Conference, Dallas, TX, November 9-11, 1993, pp. 589-596.
12. Evans, J. L., Romanczuk, C., Johnson, R. W., and Aday, J., Using MCM-L Technology for Under-the-Hood Automotive Environmental Conditions, Proceedings 1993 ISHM Conference, Dallas, TX, November 9-11, 1993, pp. 584-588.
13. Simeus, E. J., and Vaughan, G. P., The Use of Buffered Oxide Etch to Enhance Wire bond Performance on Thick Film Gold Conductor, Proceedings 1993 ISHM Conference, Dallas, TX, November 9-11, 1993, pp. 457-462.
14. Noble, R. P., HMC Intraconnections - Some Observations, Problems, and Solutions, International Journal of Hybrid Microelectronics, Vol. 6, No. 1, October 1983, pp. 566-573.
15. Jones, W. K., Liu, Y., and Morrone, A., The Effect of Thermal Exposure on the Structure and Mechanical Properties of Al-1% Si Bonding Wire, Proceedings 1993 ISHM Conference, Dallas, TX, November 9-11, 1993, pp. 445-450.
16. E. Philofsky, "Design Limits When Using Gold-Aluminum Bonds," *9th Annual Proceedings, IEEE Reliability Physics Symposium*, held in Las Vegas, NV, 1971, pp. 114-119.

17. J. K. Nesheim, "The Effects of Ionic and Organic Contamination on Wirebond Reliability," *Proceedings of the 1984 ISHM Symposium on Microelectronics*, held in Dallas, TX, September 17-19, 1984, pp. 70-78.
18. B. L. Gehman, "Bonding Wire Microelectronic Interconnections," in *IEEE Transactions on Components, Hybrids, and Manufacturing Technology*, Vol. CHMT-3, No. 3, September 1980, pp. 375-383.
19. G. G. Harman, "Metallurgical Failure Modes of Wire Bonds," in *12th Annual Proceeding, IEEE Reliability Physics Symposium,* held in Las Vegas, NV, 1974, pp. 131-141.
20. R. Fitzsimmons and E. H. Chia, "Propagation Mechanism and Metallurgical Characterization of First Bond Brittle Heel Cracks in AlSi Wire," *IEEE Transactions on Components, Hybrids, and Manufacturing Technology*, Vol. 15, No. 6, December 1992, pp. 1081-1085.
21. T. S. Liu and H. S. Fraenkel, "Metallurgical Considerations in Tin-Gold Inner Lead Bonding Technology," *International Journal of Hybrid Microelectronics*, Vol. 1, No. 2, July 1978, pp. 69-76.
22. I. Memis, "Quasi-Hermetic Seal for IC Modules," *IEEE Electronic Components Conference, 30th Proceeding*, held in San Francisco, CA, 1980, pp. 121-127.
23. J. F. Graves, and W. Gurany, "Reliability Effects of Fluorine Contamination of Aluminum Bonding Pads on Semiconductor Chips," *Solid State Technology*, October 1983, pp. 227-232.
24. S. Wakabayashi, A. Murata, and N. Wakabayashi, "Effects of Grain Refiners in Gold Deposits on Aluminum Wire-Bond Reliability, Plating and Surface Finishing," *Platinum Surface Finishing*, 69 (1982) pp. 63-68.
25. D. W. Endicott, H. K. James, and F. Nobel, "Effects of Gold-Plating Additives on Semiconductor Wire Bonding, Plating and Surface Finishing," *Platinum Surface Finishing*, 68 (1981) pp. 58-61.
26. J. A. Emerson, J. N. Sweet, D. W. Peterson, "Evaluating Plastic Assembly Processes for High Reliability Applications Using HAST and Assembly Test Chips," Proceedings of the 44th IEEE Electronic Components and Technology Conference, Washington, D. C., May 1994.

4. Thermal Modeling

Vicente Romero
Bruce Bainbridge

During the module design phase special consideration was given to component placement so as to optimize the thermal performance of the throttle control module. Of primary interest was determination of the operating temperature distribution across the hybrid module, as well as estimation of the maximum junction temperature of high power devices. A finite element model was built that characterized the thermal response of the throttle control module and the cyclic thermal signatures of its dice under continuous normal operation and certain operating extremes. This model consisted of several dice attached to a microelectronics hybrid substrate with high-current traces beneath some of the dice. The model quantified the effect of die and trace heating and established a correlation between die electrical resistivity and die temperatures. This correlation enabled the design engineers to prescribe the least expensive die materials to produce reliable ICs for use in the high temperature application. (Generally, dice with greater resistance cost less to produce but generate more heat, thus, experiencing higher temperatures that make them more susceptible to thermal damage.) The thermal effects of increasing the peak current from 3.0 to 3.5 Amps were also investigated since the higher peak current could occur if tolerances stack up undesirably.

The model indicates that die temperatures range from 154.6 to 171.3°C for low-power operation and from 158.5 to 175.2°C for high-power operation. Inclusion of trace heating raises actuator (and die) temperatures almost uniformly by approximately 3.5°C. In contrast, a more localized (in space and time) effect on die temperatures occurs when die resistivity and peak power are increased. Projections indicate that the resistivities of all clustered ICs could be increased by a factor of approximately 5.6 before the peak temperature of any die in the cluster reaches the specified reliability temperature threshold of 175°C. If peak current is increased from the nominal value of 3.0 Amps to the maximum possible value of 3.5 Amps, then the resistivities of all dice in the cluster can only be increased by slightly more than a factor of four before several ICs experience peak temperatures above the 175°C threshold. It is found that a nonlinear compounding effect occurs when die resistivity and peak current are increased simultaneously.

4.1 Numerical Model

The finite-element thermal model was constructed using the commercial finite-element preprocessor PATRAN/2.5a, which was produced by PDA Engineering of Costa Mesa, California.

4.1.1 Housing

Figure 4-1 shows the housing geometry and finite-element model discretization. (For reasons explained below, the bottom of the actuator is not modeled.) The blue part of the housing is referred to as the cylindrical extension. It has a height of 38 mm, a radius of 21.6 mm, and is 2 mm thick at the top and 3 mm thick along the sidewalls. A small electric motor fits into the cylindrical extension of the aluminum housing. The rotor is in direct contact with the housing through a bearing assembly and a plastic stator connector block that holds it in place. The bearing assembly does not conduct heat well to the housing due to the small contact area. The plastic stator connector block does not conduct heat well to the housing due to the low thermal conductivity of plastic. In addition, because the aluminum housing is highly conductive and the motor is relatively remote from the electronics assembly, the actual heat-flow paths from the motor to the housing are not critical. Thus, the heat generated by the motor is evenly distributed over the cylindrical extension of the housing.

Accounting for the motor's heat generation in this manner, the motor and connector block may be neglected to simplify the model. Because the heat capacity of these items (if modeled) would tend to moderate chip temperatures somewhat, ignoring these factors is a conservative approximation, that is, one which leads to less moderate chip temperatures.

The cylindrical extension and other 2-mm-thick housing walls are modeled with 2-D shell elements to eliminate possible numerical stiffness that could arise from the relatively small temperature differences expected through the wall. A convective boundary condition is used to simulate the heat transfer between the actuator and the under-the-hood environment. As specified by GM engineers, a convection coefficient of 24 watts per meter degrees Kelvin (W/m-K) effectively represents the worst-case under-the-hood environment of 150°C and a 3 m/s air velocity. This boundary condition was applied over the housing exterior, except at the top of the cylindrical extension and the bottom of the actuator. Air flow over the top of the cylinder may be obstructed, and heat transfer between the housing and membrane can be ignored for the purposes of this analysis due to their questionable thermal contact. Both of these approximations are conservative and tend to slightly increase chip temperature predictions.

4.1.2 Electronics Assembly

Figure 4-2 is an exploded view of the complete actuator model. The electronics assembly consists of a 3.175 mm (1/8 in.) thick aluminum support plate bolted at its four corners to the housing, and a 0.127-mm-thick layer of adhesive between the plate and the 1.02 mm (40 mil) thick alumina microelectronics substrate. Also, eight 0.0508-mm-thick rectangular patches of adhesive die attaches bond the eight chip dies to the alumina substrate.

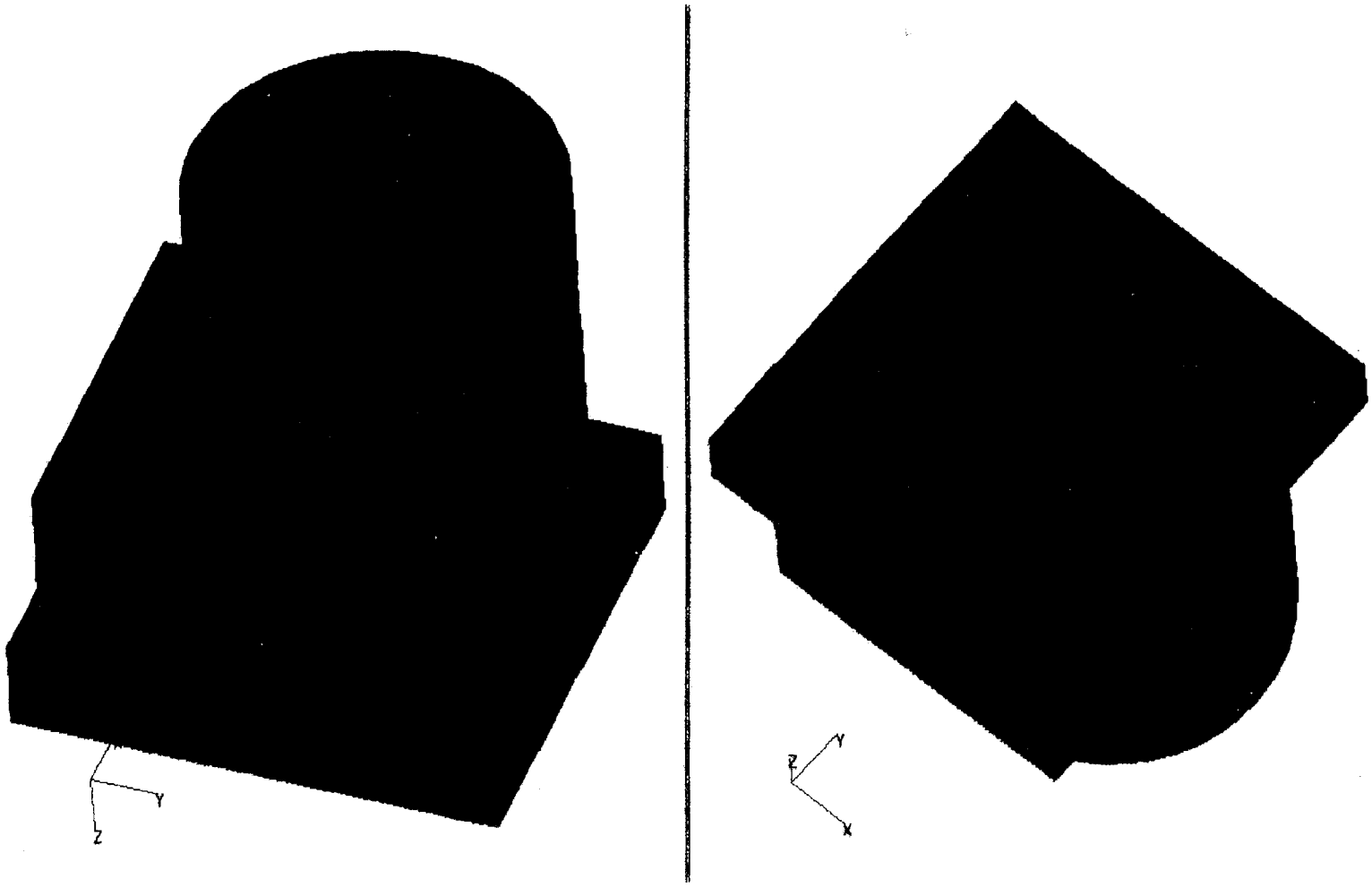

Figure 4-1. Model Geometry and Finite Element Mesh for the Actuator Housing

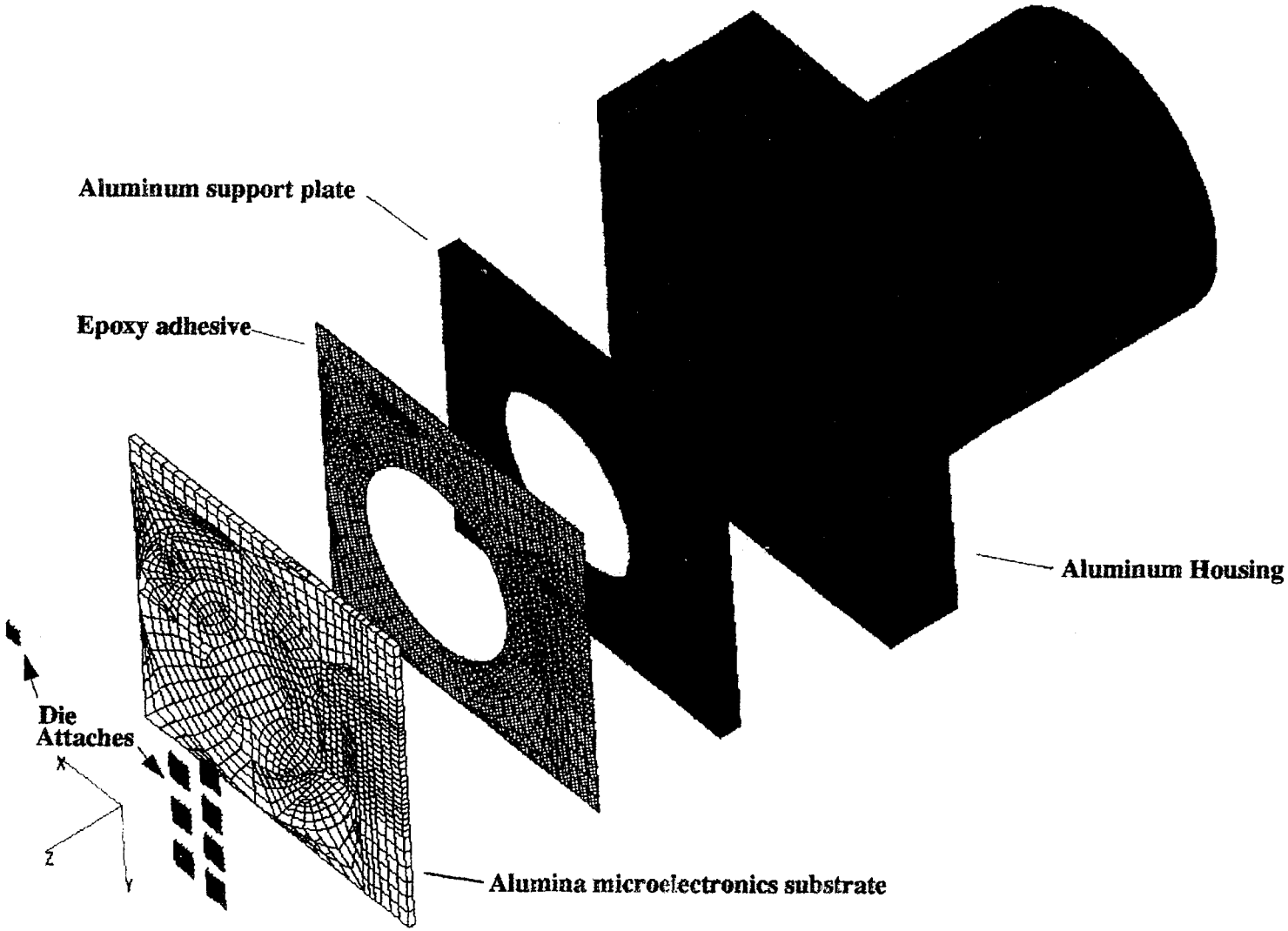

Figure 4-2. Exploded View of the Electronics Assembly Showing Where it Fits into the Actuator Housing

Figure 4-3 shows the die locations on the alumina substrate and the positioning of the electronics assembly within the housing. The individual die attaches are identified according to their labelling in the figure. The substrate and support plate are both modeled as 48 mm in y by 52.1 mm in x. The lateral dimensions of die attaches no. 1 through no. 7 are 4.0 mm in y by 3.5 mm in x, and for die attach no. 8, 2.3 mm by 2.3 mm.

The alumina substrate holds circuitry (exclusive of the eight ICs) that generates distributed heat according to the schedule in Figure 4-4. (The figure is based on a six-second cycle due to the periodicity of the chip duty-schedules described below.) In the model, this heat is distributed evenly over the exposed side of the alumina substrate.

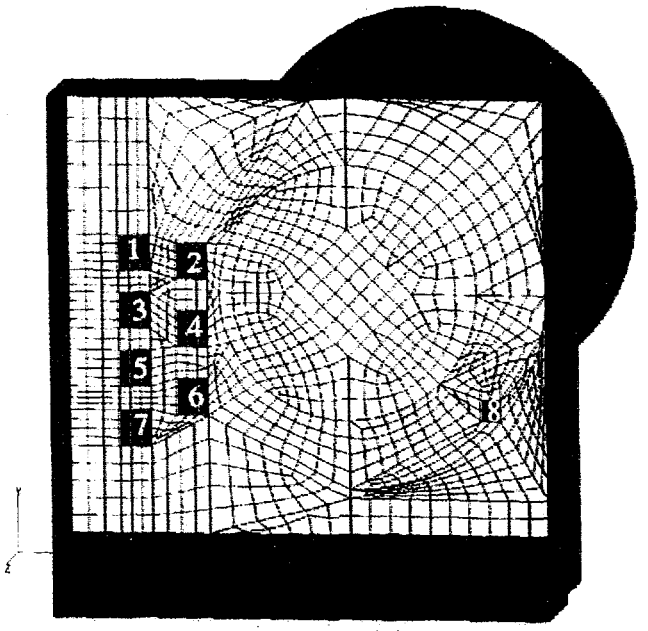

Figure 4-3. Actuator Assembly With Die Attaches Numbered for Future Reference

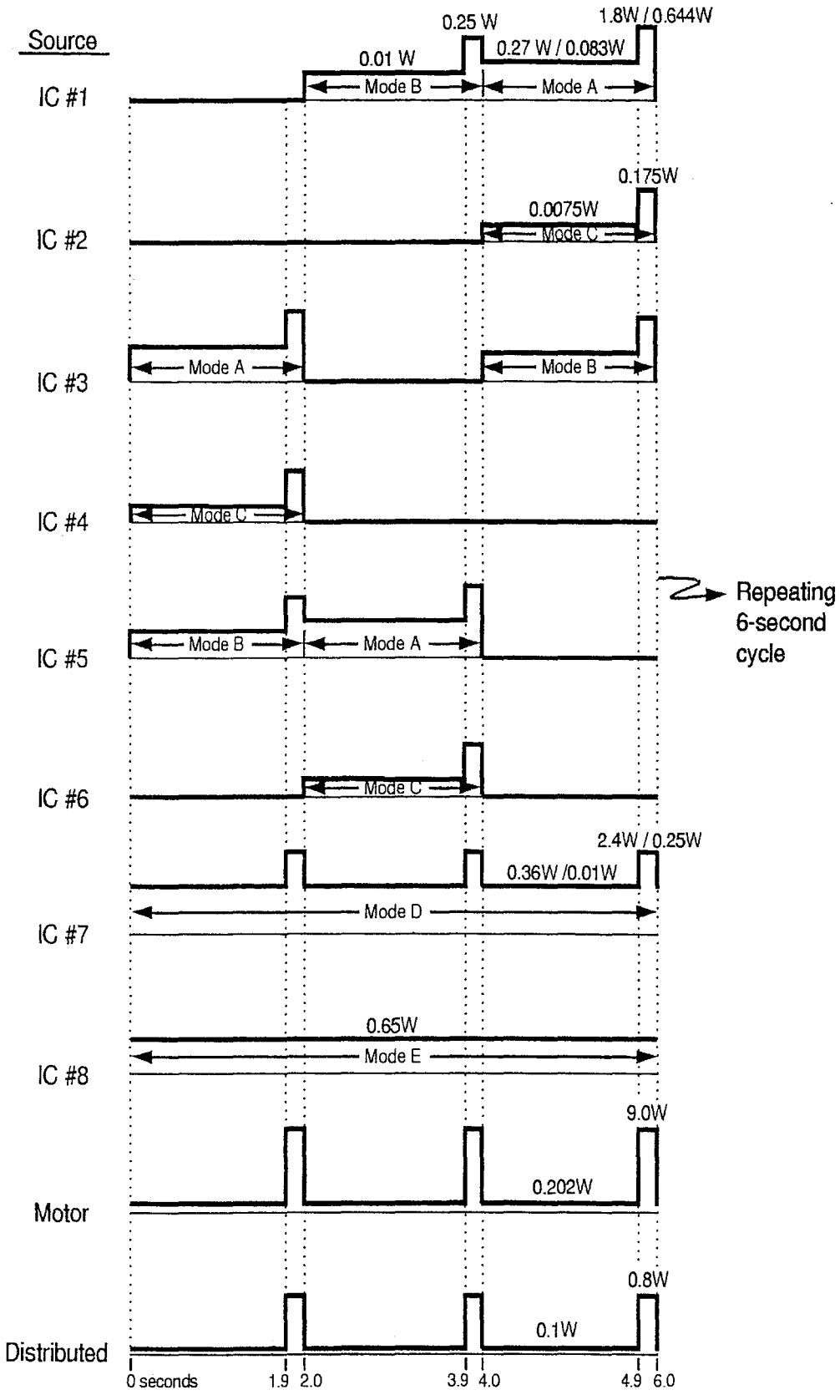

Figure 4-4. Duty Cycles for Heat Sources in the Actuator Model

The dice heat are simulated by applying an equivalent (uniform) heat flux to the exposed side of each die attach. Note that the A and D modes may be operated at either low or high power. Within the parameters set by GM engineers for chip activity, the duty cycles illustrated in Figure 4-4 have been devised to produce the hottest chip temperatures. That is, for chips 1, 3, and 5, the lower-power B mode precedes the higher-power A mode, and within each mode, the time spent at nominal power is fully apportioned in front of the peak pulse. These circumstances combine to maximally preheat the chip before applying the peak A mode pulse. Additionally, the chips have been sequenced so that chips 5 and 6, which surround the continuously-powered chip 7, are on simultaneously. During this time, chip 5 is in its hottest mode (mode A) and all three chips
(5, 6, and 7) reach their peak pulses simultaneously after maximal preheating. Using these parameters, a worst-case-hot scenario for chips 4 through 7 is set up.

4.1.3 Material Properties

Material properties used in this analysis are listed in Table 4-1. These properties were obtained from the 9100 Directorate database at Sandia. Constant properties were used both for the alumina (Material 5281) and the aluminum (Material 2005) due to the narrow temperature range in the analysis. The aluminum properties are for a 2024-T4 alloy, which may differ somewhat from the AA-383 alloy specified in the drawings. The conductivity of the adhesives were provided by DELPHI, but the specific heat and density were not available. Therefore, values appropriate for an epoxy were assumed. The error associated with the assumed values should be low because the unknown parameters only affect the transient performance and not the thermal resistance of the model, and the mass of these layers is low.

Table 4-1: Material Thermal Properties

Name	Material ID	Conductivity (W/m-K)	Density (kg/m^3)	Specific Heat (J/kg-K)
Alumina	5281	14.5	3400	908
Aluminum	2005	155.0	2780	940
Adhesive	7000	0.30	1000	1000
Die Attach	8000	2.1	1000	1000

4.1.4 High-Current Trace

Figure 4-3 shows the locations of the ICs of interest in red; the alumina hybrid device, in yellow. Figure 4-5 shows the alumina substrate on the same side as viewed in Figure 4-3 divided into subregions called hyperpatches. (Decomposition of an arbitrary 3-D geometric region into hyperpatches is required before the region can be discretized into finite elements.) The numbered regions in Figure 4-5 correspond to locations where surface heat fluxes were applied to simulate the heat generated by the substrate's high-current path.

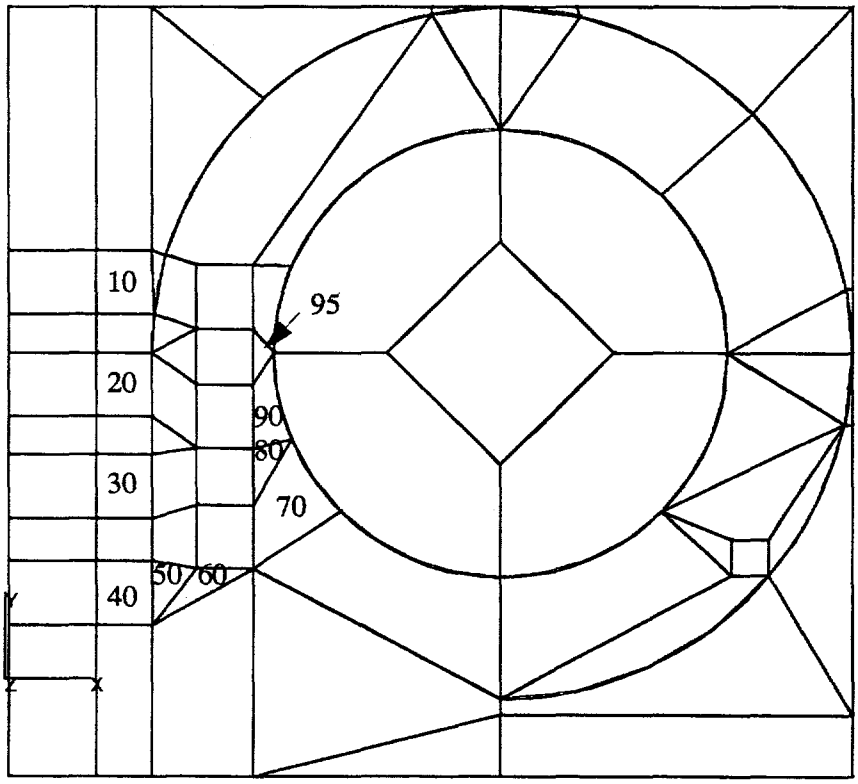

Figure 4-5. Modeled Tracks of High-Current Trace on Alumina Substrate

Regions 10, 20, 30, and 40 are assumed to share equally the heat generated by the 0.0225-ohm track between Q100 (die no. 7) and Q102 (die no. 1) drains. This track lies under dice 1, 3, 5, and 7 and runs from the bottom of die no. 7 to the top of die no. 1 at essentially a constant width equal to the width of the dice. Apportioning all of the heat generated by the trace to only those regions underlying the dice is a slightly conservative approximation; that is, one that tends to increase the predicted temperatures slightly relative to the temperatures that would be predicted if the heat were more realistically apportioned. In the low-power mode, the current through the track follows a repeating two-second square-wave cycle where one-eighth of 0.203 W are dissipated for the first 95 percent of the cycle and 0.203 W are dissipated for the remaining five percent of the two-second cycle.

In regions 50 and 60, a heat flux is applied that derives from the 0.0325 ohm track between external pad D and Q100 (die no. 7) source bond. The current through this track produces, for the 95 percent and 5 percent time-proportions of the two-second cycle, one-eighth of 0.293 W and 0.293 W, respectively. Though some of this track exists outside of regions 50 and 60, it is thinnest and, thus, most resistive and dissipative in these regions. Therefore, concentrating all the heat generated by the track into regions 50 and 60 is a somewhat conservative approximation.

Regions 70, 80, 90, and 95 are assumed to share equally the power generated by

1. the 0.074 ohm track between Q102 (die no. 1) source bond and external pad C, generating, for 95 percent and 5 percent of the time, one-eighth of 0.67 W and 0.67 W, respectively;
2. the 0.054 ohm track between external pad B and Q106 (die no. 4) drain, generating, for 95 percent and 5 percent of the time, one-eighth of 0.486 W and 0.486 W, respectively;
3. the 0.027 ohm track between Q106 (die no. 4) source and external pad E, generating, for 95 percent and 5 percent of the time, one-eighth of 0.24 and 0.24 W, respectively;
4. the unspecified source just to the right of Q107 (die no. 6) that contributes, in the 95 percent and 5 percent time-proportions, one-eighth of 0.4 W and 0.4 W, respectively.

The tracks in items 1 through 3 above lie under and/or just to the right of dice 2, 4, and 6, but the bulk of the heat they generate is concentrated just to the right of dice 4 and 6 where the traces are thinnest and, thus, most resistive and dissipative. Confining the heat generated by items 1 through 4 to regions 70, 80, 90, and 95 in the model is viewed as a good approximation.

The heat generated from the three 0.01 ohm wire bonds are not accounted for because of modeling complications and relatively low heat generation.

4.1.5 Incorporating Die Resistivity

Silicon dice have intrinsic electrical resistance and produce heat according to the total equivalent die resistance multiplied by the square of the applied current. The above-stated dissipation levels are indicative of the applied current cycles and nominal die resistivities. However, using the most resistive dice that can remain below the 175°C reliability threshold is desirable from a cost standpoint. Therefore, the model was used to investigate the effect of increased die resistivities on die temperatures. Because heat generation varies directly with die resistivity, increases in die resistivity are accounted for in the model by proportionately changing the level of heat generation. Accordingly, changes in die resistivity and changes in die power level are referred to interchangeably, but the results can be attributed to purely current-related changes, purely resistance-related changes, or a combination of both types. Because the heat generation of each die has some effect on the temperatures of the other dice, the heat generation of all dice in the cluster of dice 1 through 7 is scaled (multiplied) by a common factor. Uniform scaling of die heat generation in this manner simplifies the parameter study and envelopes the results such that retention of any of the nominally resistive ICs will result in lower projected temperatures than

those temperatures predicted with uniform scaling. Thus, the results that are presented later tend to be conservative if any of the nominally resistive ICs are retained in the final design.

4.1.6 Modification of Peak-Current Levels

A tolerance stackup for the electronics in the actuator has indicated that peak current may rise from the nominal value of 3.0 Amps to a possible maximum value of 3.5 Amps. Because electrical resistance heating is proportional to the square of the applied current, an increase in current from 3 to 3.5 Amps would result in power levels that are approximately 1.36 times greater than in the nominal case. Thus, to investigate the effect of the higher peak current on temperatures, the heat generated by actuator components experiencing current fluctuations (that is, dice 1 through 7, the high-current trace, the distributed circuitry on the alumina substrate, and the motor) were multiplied by a factor of 1.36 for the five percent proportion of time that peak current is applied during their various power cycles.

4.2 Simulations and Results

To predict the transient periodic response of the actuator, the following process was used. First, steady-state solutions were obtained by assigning each chip its average power level over the six-second cycle. This was done for both low- and high-power configurations. Then, using the steady-state temperature distributions as initial conditions, transient simulations were run for 10 six-second cycles using the schedules shown in Figure 4-4. This appeared to be sufficient time for the system to reach a periodically repeating response. The simulations were run using P/THERMAL/2.6 on a Sun SPARC 10-41 compute engine. The steady-state simulations took approximately 15 CPU minutes to complete. The transient simulations each took approximately four CPU hours.

Figures 4-6 and 4-7 show the transient responses of representative (not necessarily the hottest) computational nodes on die attaches 1 through 8 for low- and high-power operation, respectively, for nominal resistivities, 3.0 Amps peak, and no high current trace heating. Figures 4-8 and 4-9 present the temperature distributions in the model at 40 seconds into the low- and high-power simulations, respectively. At this time and at multiples of six seconds from this time as Figures 4-6 and 4-7 show, the hotter nodes attained their peak temperatures.

The peak temperatures attained by the eight die attaches are presented in Table 4-2 for both the low- and high-power simulations. High-power operation significantly increased peak temperatures. Die no. 8 absorbed 0.65 W of steady heat and was by far the hottest.

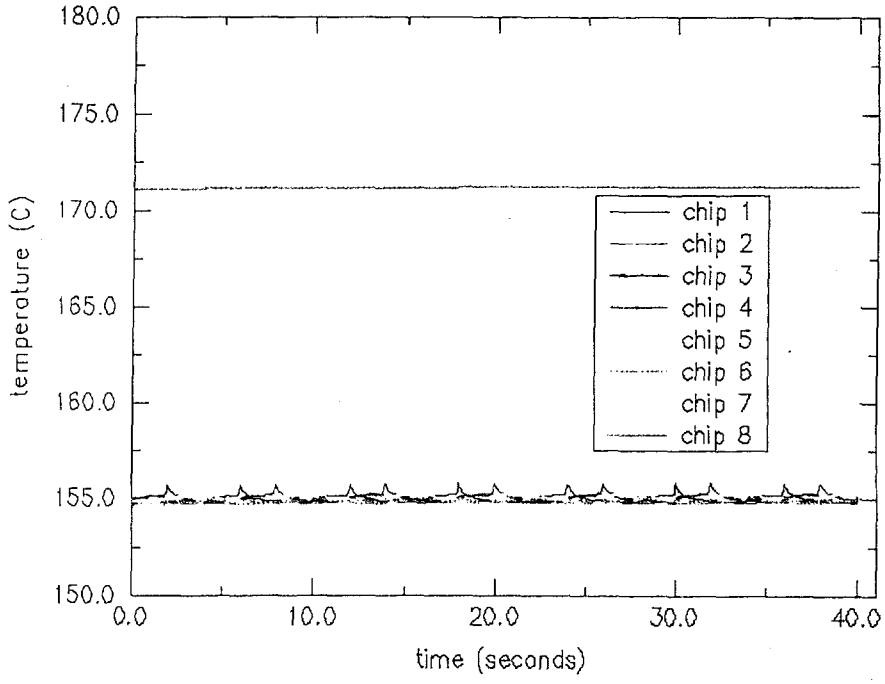

Figure 4-6. IC Temperature Histories for Low-Power Operation

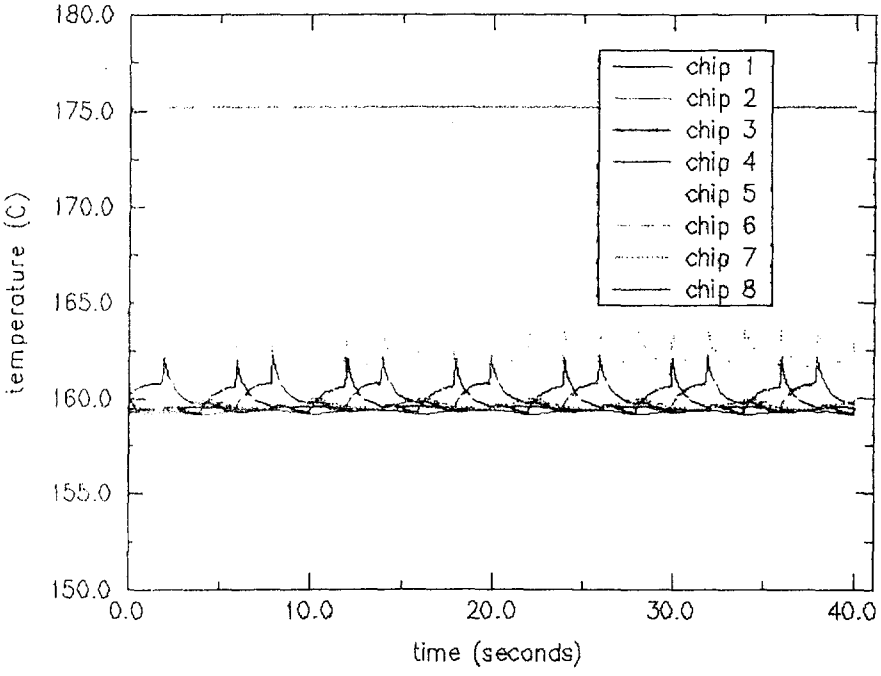

Figure 4-7. IC Temperature Histories for High-Power Operation

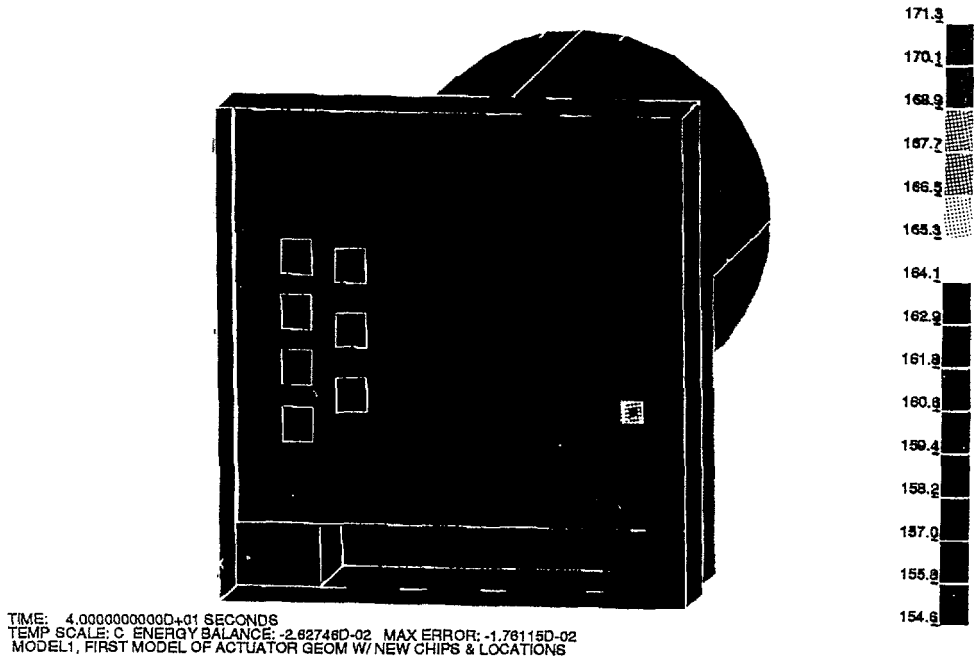

Figure 4-8. Actuator Temperature Distribution at Low Power

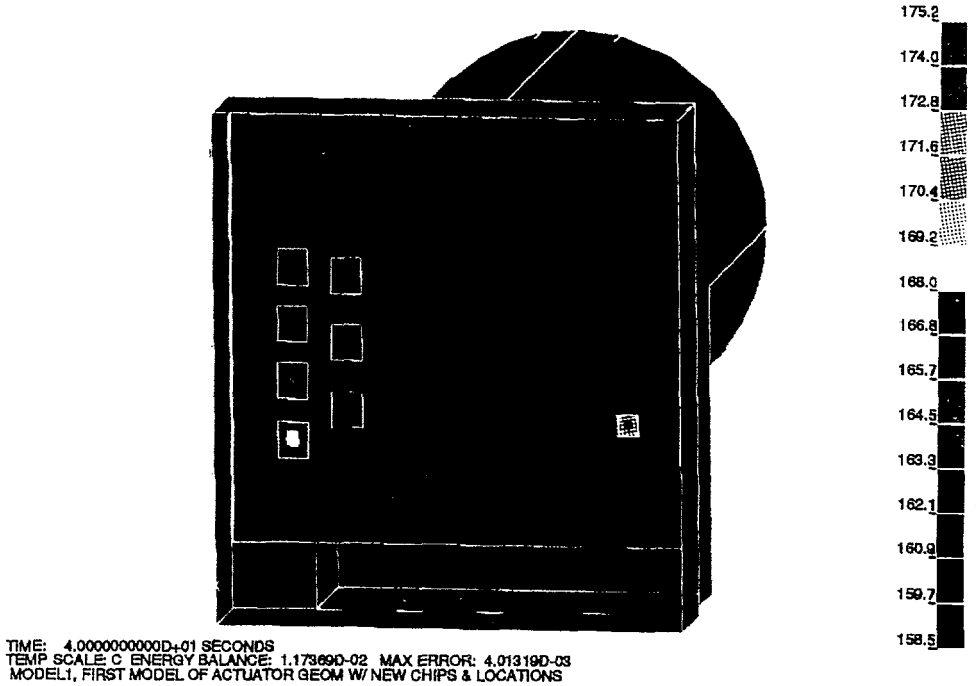

Figure 4-9. Actuator Temperature Distribution at High Power

Table 4-2: Maximum IC Temperatures (°C)

IC	Mode	High-Power Cycle	Low-Power Cycle
1	A/B	159.9	155.1
2	C	159.2	154.9
3	A/B	159.8	155.0
4	C	159.6	155.0
5	A/B	165.0	155.9
6	C	160.0	155.1
7	D	168.7	155.2
8	E	175.2	171.3

Figures 4-8 and 4-9 show that regions of high temperature on the alumina substrate were confined to the near vicinity of the ICs. This indicates that the current design effectively draws IC heat through the alumina layer to the aluminum support plate. Examination of the thermal state of the aluminum plate revealed that there were essentially no in-plane thermal gradients, which indicates good thermal contact with the housing.

Die chip no. 8 is the hottest. The design does not specifically address the intense localized heating there. Because temperature gradients in the aluminum support plate are essentially negligible in the current design, increasing the contact area between the plate and housing will not alleviate the hot spot under die no. 8. Instead, other measures must be taken, such as reducing the thickness of the alumina substrate or thermally coupling the die to the housing, hermetic cover, or cooler areas of the alumina substrate.

To understand the sensitivity of chip temperatures to the die attach, alumina, and epoxy constituents, the temperature distribution through these materials can be examined along a line normal to the plane of the substrate and piercing the center (hottest point) of die attach no. 8. The temperature drop through the adhesive layer of the 0.0508-mm-thick die attach is 3°C, through the 1.02-mm-thick alumina substrate is 6°C, and through the 0.127-mm-thick epoxy layer is 7°C. To first order, these temperature drops scale linearly with the constituent's thickness or inversely with its thermal conductivity. Thus, a doubling of the nominal thickness of the die attach layer will add 3°C to the predicted temperature presented above. In production, it would be difficult to reproduce the nominal thickness of this layer because it is so thin.

An analogous argument can be made for the epoxy layer; its combination of low thermal conductivity and thickness makes it the greatest influence on die temperature. Furthermore, the actual thermal resistance of an adhesive layer is often significantly greater than the thermal resistance predicted using a numerical model. Unaccounted-for thermal resistance appears in the form of voids and contact resistances between the substrate and the adhesive. This is especially

true when gluing pieces with large cross-sectional areas together, such as the alumina substrate and aluminum support plate.

The present analysis neglects the radiative transfer between the actuator housing and its surroundings because of the current lack of definition of the radiative environment in which the actuator will be operating. It is of concern, however, that the environment envisioned will heat ambient incoming air to 150°C. This environment would necessarily have elements at significantly higher temperatures than 150°C. If any of these elements were subjected to the radiant heat generated by the actuator, they could conceivably impart substantial heat to the device through thermal radiation.

Finally, the effect of wire bonds on IC temperatures has not been accounted for in the model. Potentially, these current-carrying wires could provide additional heat to the dice. For example, analyses were performed of a 0.4-in.-long aluminum wire that was 10 mil diameter and carried 10 Amps. The resulting steady-state peak temperature was 224°C. Such a wire bond would contribute to increased die temperatures.

4.2.1 Effect of Trace Heating

Figure 4-10a shows the transient responses of representative computational nodes near the centers of ICs 1 through 8 when the high-current trace is added to the model. (The ordinate of the graph is chosen to facilitate comparison with the other plots presented below. A common scale that envelopes the temperature ranges of all cases that were run is used in all the plots.) The six-second periodic temperature cycles of dice 1 through 7 are evident. Of the ICs in this cluster, dice 1, 3, and 5 had the hottest peak temperatures, but these peak temperatures all rise above the 158°C background temperature by less than 1°C. Compared with Figure 4-11a which does not include the effect of trace heating and is the baseline case, the effect of the high-current path is to raise the temperatures almost uniformly throughout the actuator (including the microelectronics) by approximately 3.5°C.

Figures 4-10b and 4-11b present the associated spatial temperature distributions at 40 seconds into the simulations. In all simulations except one, die no. 5 attained the hottest peak temperature of all those in the cluster of dice 1 through 7. The temperature of die no. 5 peaked at $t = 40$ seconds and six-second multiples thereof. Because in each simulation the temperature of die no. 8 (usually the hottest of all dice) is steady, a temperature snapshot at $t = 40$ seconds contains the most pertinent information available at a single point in time. As with the time-temperature graphs, plots of spatial temperature distribution have a common temperature scale chosen to envelope the temperature ranges of all cases investigated. Comparing Figures 4-10b and 4-11b indicates that essentially the entire actuator was approximately 3.5°C hotter when trace heating is accounted for. Some localized heating of ICs 4 and 6 occurs, but the effect is marginal and inconsequential because of their innately cooler temperatures (due to lower power dissipations) than the dice on the left column of the cluster.

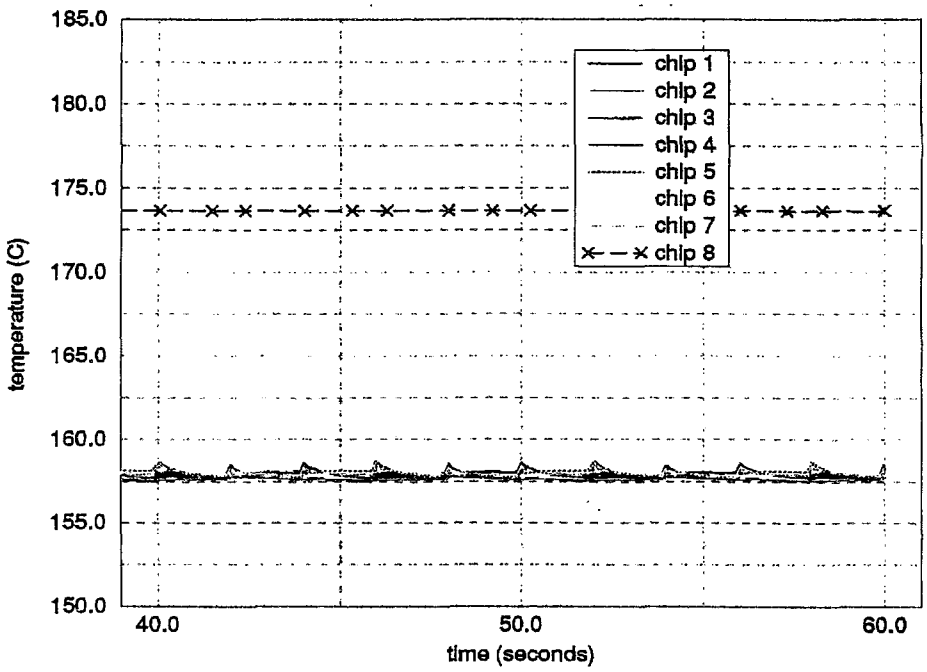

Figure 4-10a. IC Temperature Histories (low power with H-C path added)

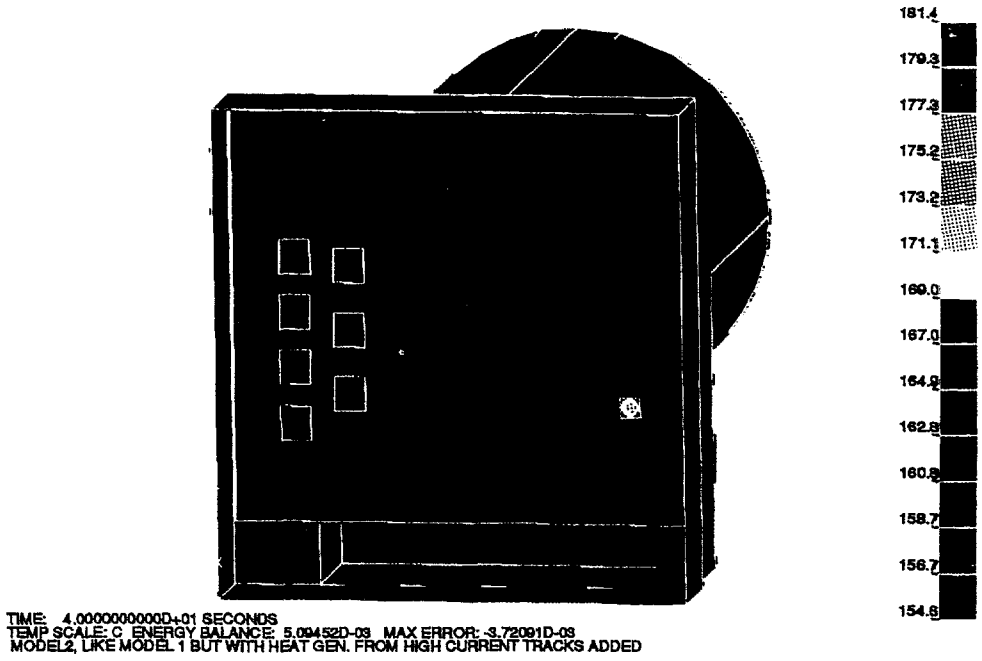

Figure 4-10b. Actuator Temperature Distribution (low power w/H-C path added)

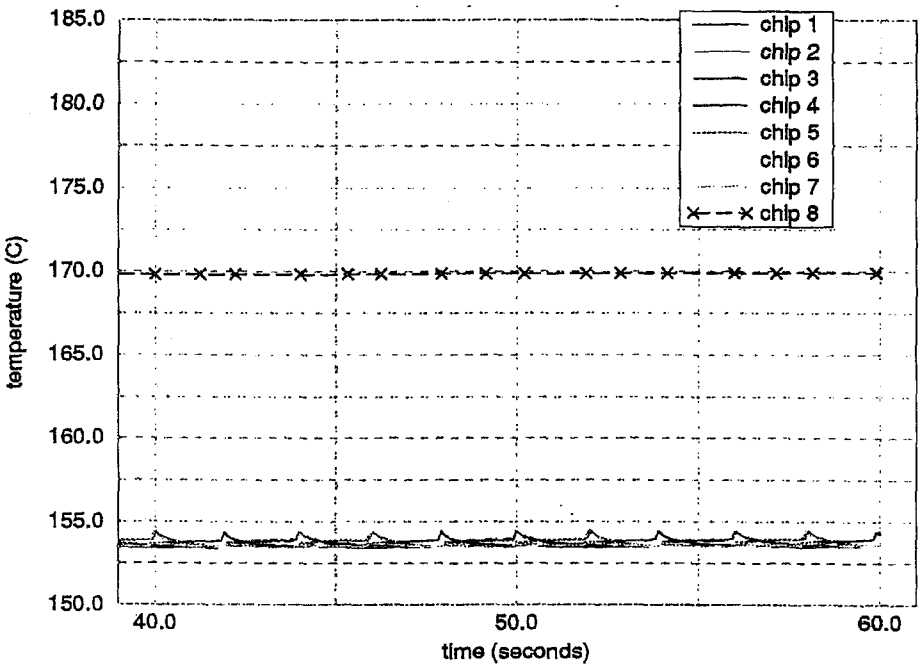

Figure 4-11a. IC Temperature Histories (low power without H-C path)

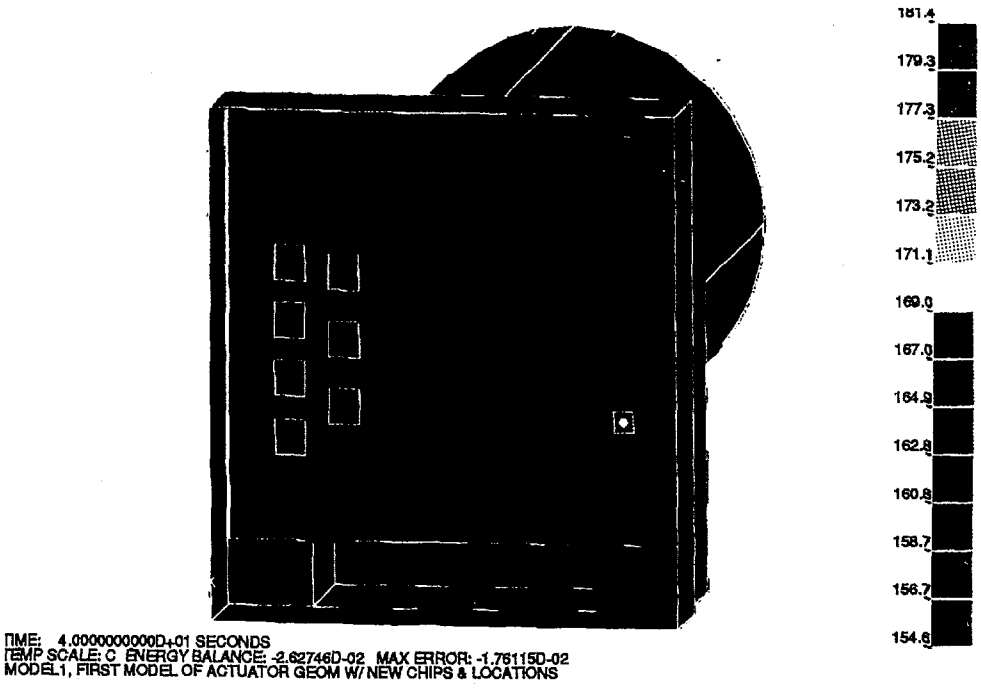

Figure 4-11b. Actuator Temperature Distribution (low power w/o H-C path)

4.2.2 Effect of Die Resistance

Figures 4-12a,b are analogous to Figures 4-10a,b, but with a resistivity scaling factor of five applied uniformly to dice 1 through 7. (To establish a context for comparison, the results in Figures 4-10a,b can be said to correspond to a scaling factor of unity.) Comparing Figures 4-10a and 4-12a, the temperature of die no. 8 is approximately 2.5°C higher with 5X power scaling. The temperature rise of die no. 8 is a convenient and relatively accurate indicator of the rise in bulk or background temperature of the actuator. (Note the difference in background color between Figures 4-10b and 4-12b.) In contrast to the relatively mild rise in bulk temperature, the peak temperatures of dice 1, 3, and 5 increases by approximately 14°C to approximately 172°C. Thus, peak temperatures are much more sensitive to die resistivity than are die background temperatures.

Though the temperatures of the clustered dice are significantly higher with 5X power scaling, their maximum temperatures are less than the threshold temperature of 175°C. Thus, a higher scaling factor of seven was applied. The results are presented in Figures 4-13a,b. Compared with Figures 4-12a,b, respectively, background temperature is approximately 6.5°C higher and peak temperatures are approximately 23°C higher. The hotter dice in the cluster reach temperatures of 180°C, surpassing the 175°C threshold. Thus, the factor by which the resistivity of dice 1 through 7 can be multiplied while maintaining their temperatures below 175°C is somewhere between 5 and 7. An estimate for the crossover factor can be obtained with a parabolic curve-fit of the temperature of die no. 5 versus the resistivity multiplication factor for the cases investigated (1X, 5X, and 7X multiplication). This fit reveals that the temperature of die no. 5 would reach 175°C for a multiplication factor of approximately 5.6. This number can likewise be generated for the other dice in the cluster.

4.2.3 Effect of Peak-Current Level

Figures 4-14a,b display the results of a low-power-operation simulation with trace heating, nominal (1X) die resistivity, and a peak current of 3.5 Amps during the five percent proportion of time that peak current is experienced. Figures 4-10a and 4-10b display the results of a similar simulation but with the nominal peak of 3.0 Amps. A comparison suggests that the higher peak current results in a rise of background temperature of approximately 1°C and in a rise of peak temperatures of approximately 3°C. Thus, peak temperatures are much more sensitive to peak current than are die background temperatures.

4.2.4 Combined Resistivity and Peak Current Effects

Because die resistivity also affects peak die temperatures more greatly than background temperatures, the combination of higher-than-nominal die resistivity and peak current would seem to drive peak die temperatures quite severely. To quantify the compounding effect, a

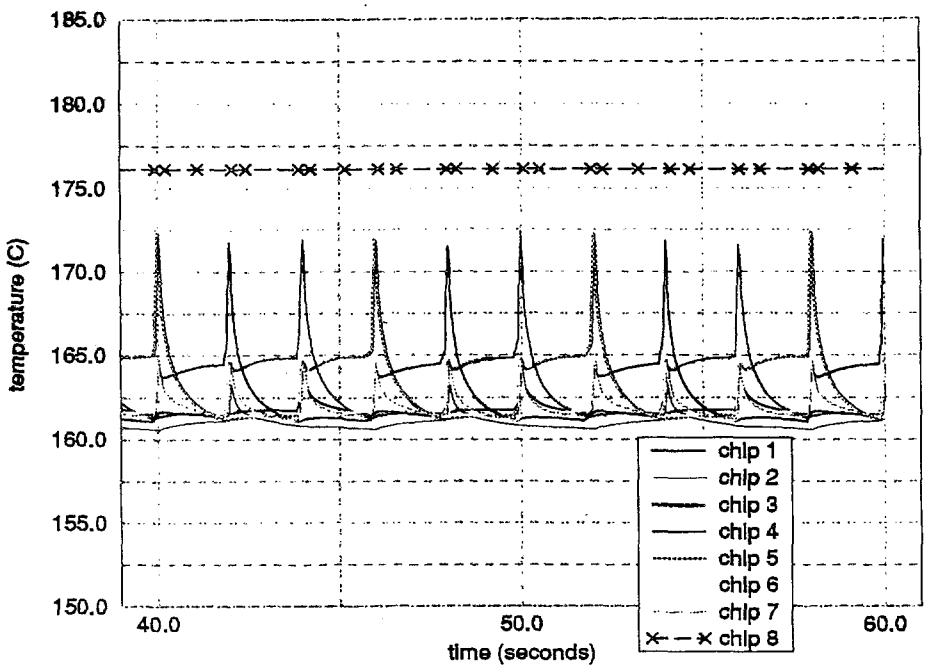

Figure 4-12a. IC Temperature Histories (L.P., H-C path, 5X resistivity)

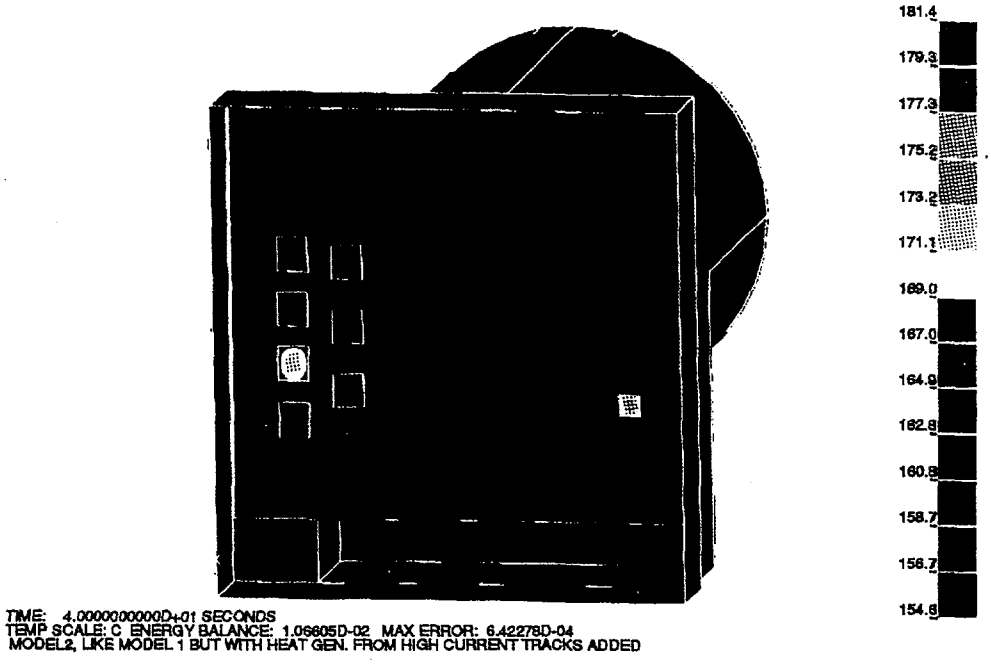

Figure 4-12b. Actuator Temperature Distribution (L.P., H-C path, 5X resistivity)

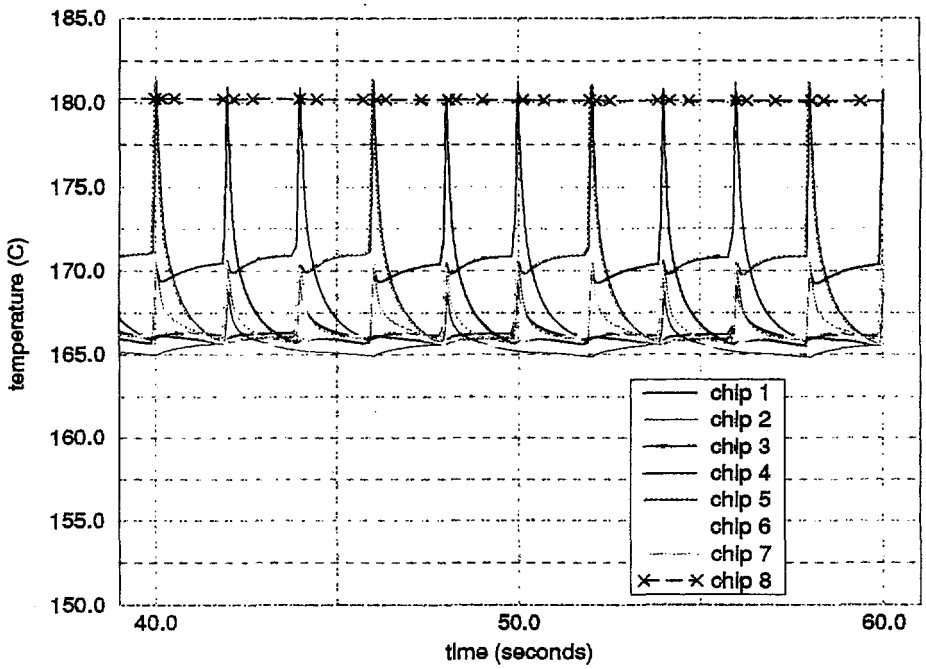

Figure 4-13a. IC Temperature Histories (L.P., H-C path, 7X resistivity)

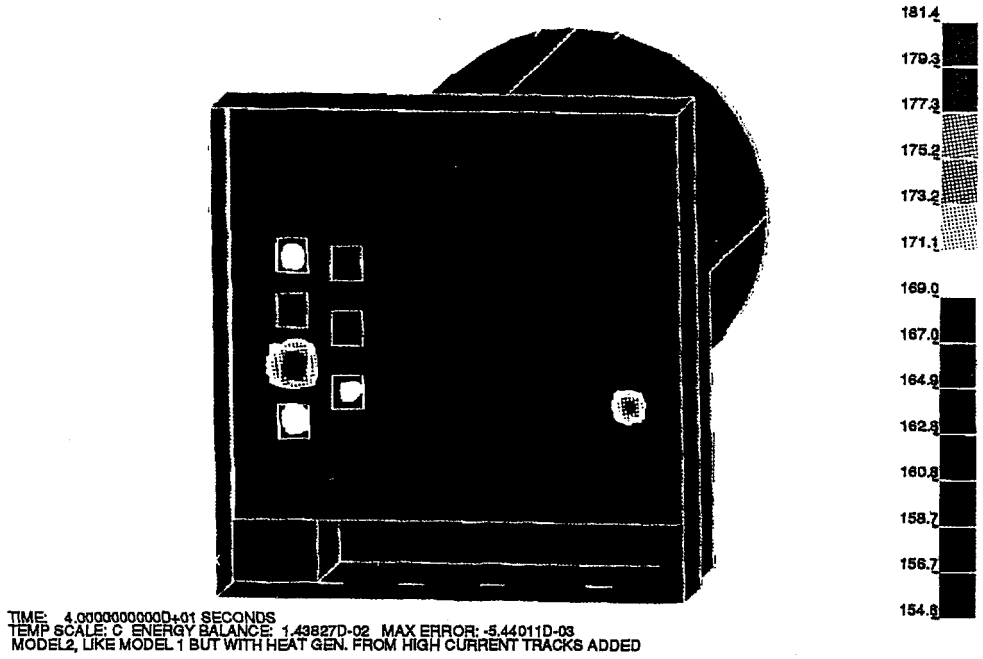

Figure 4-13b. Actuator Temperature Distribution (L.P., H-C path, 7X resistivity)

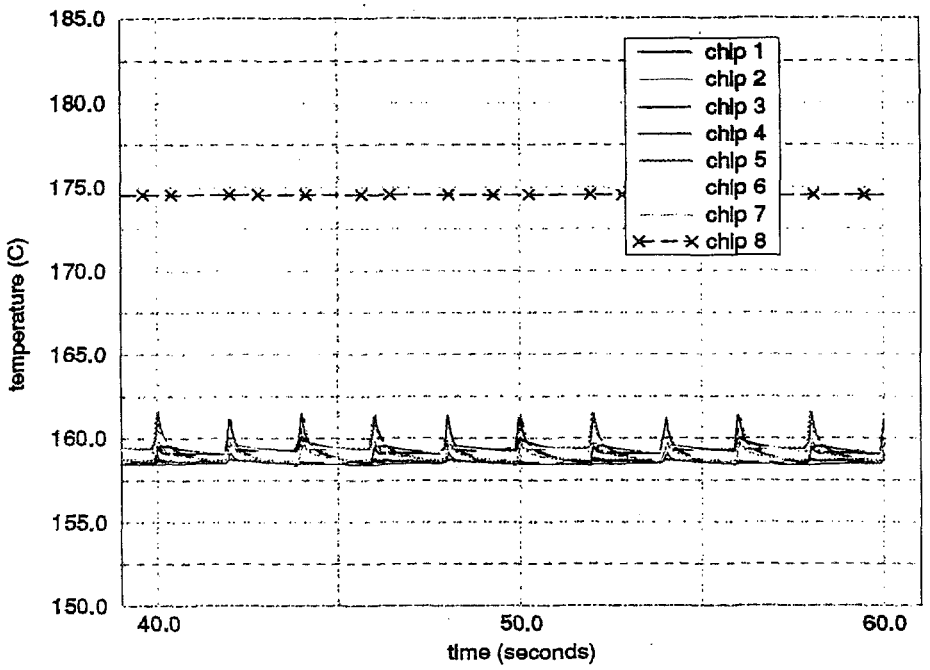

Figure 4-14a. IC Temperature Histories (L.P., H-C path, 1X res., 3.5 Amp pk)

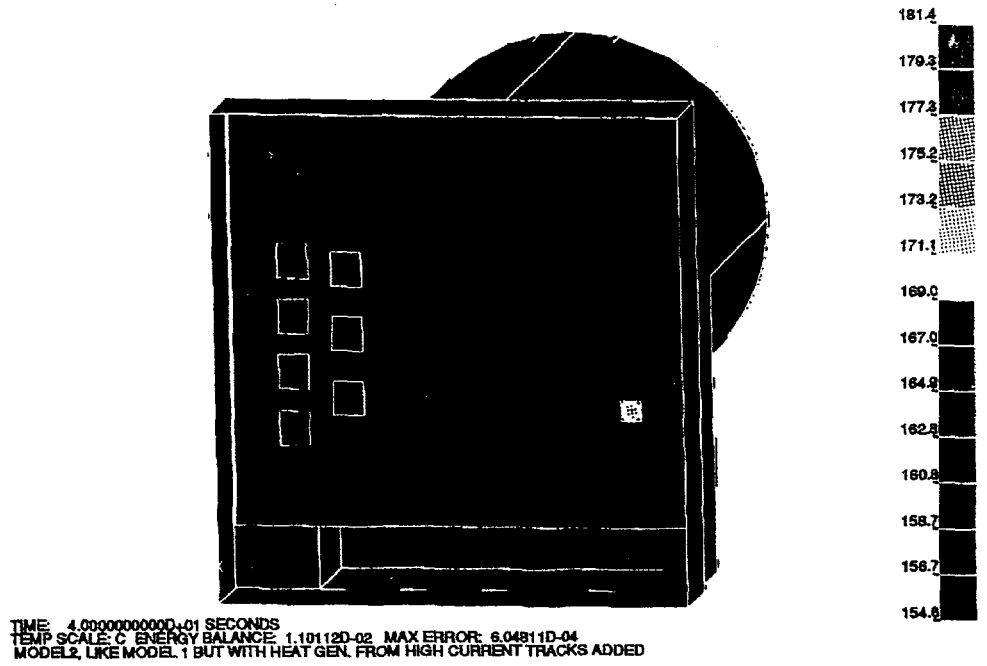

Figure 4-14b. Actuator Temperature Distribution (L.P., H-C path, 1X res., 3.5A pk)

simulation with a peak amperage of 3.5 A and 5X die resistivity of dice 1 through 7 was run. Figures 4-15a and 4-15b present the results. Compared with Figures 4-12a,b (which reflect a similar run with the nominal peak of 3.0 Amps), an increase in peak amperage from 3 to 3.5 A with 5X die resistivity results in a 2°C rise in background die temperatures and a 5°C rise in peak die temperatures. Conversely, as stated previously, at nominal (1X) die resistivity, a similar change in peak current results in only a 1°C rise in background temperature and a 3°C rise in peak temperature. Thus, the compounding effect is clearly evident.

Figures 4-15a,b show that ICs 1, 3, and 5 all reach prohibitively high peak temperatures, which surpass by approximately 2.5°C the reliability threshold temperature of 175°C. Hence, a simulation with 4X die resistivity was run to determine whether acceptable temperatures would result. The result is indicated in Figures 4-16a and 4-16b. All peak temperatures in the cluster of dice 1 through 7 were below the prescribed threshold; the temperatures of ICs 1, 3, and 5 peaked at approximately 173.5°C. Thus, it appears that in the worst-case scenario of 3.5 Amps peak current, the resistivities of dice 1 through 7 may all be increased by as much as a factor of 4 before prohibitively high peak temperatures result.

4.3 Summary and Conclusions

Model predictions indicate that die temperatures range from 154.6 to 171.3°C for low-power operation, and from 158.5 to 175.2°C for high-power operation. Trace heating was added to this model in a manner that probably skews the results toward slightly higher temperatures than more realistic modeling would produce. At low power, the effect of trace heating is to raise actuator (and die) temperatures almost uniformly by approximately 3.5°C. In contrast, a very local (in space and time) effect on die temperatures results from increased die resistivity and peak-power levels. The effect of greater electrical resistivity in the clustered dice 1 through 7 was investigated by increasing their heat outputs by factors of 5 and 7. Projections indicate that the resistivities of all dice in the cluster could be increased by a factor of approximately 5.6 before the die (in the cluster) with the highest peak temperature, die no. 5, reaches the specified reliability temperature threshold of 175°C. If peak current is increased from the nominal value of 3.0 Amps to the maximum possible value of 3.5 Amps (which could occur if tolerances stack up undesirably), then the resistivities of all dice in the cluster can only be increased by slightly more than a factor of four before several dice experience peak temperatures above the 175°C threshold. Die peak temperatures are much more sensitive to both die resistivity and peak applied current than are average or background temperatures. Moreover, a compounding effect occurs when die resistivity and peak current are increased simultaneously. Also, because several confounding factors exist that have a high probability of causing actual chip temperatures to be higher than those temperatures predicted in the model, it is recommended that a reasonable factor of safety be applied to the results presented herein. If chip temperatures are then projected to be unacceptably high, further thermal-management strategies must be employed probably at the surface of the alumina substrate and on the die itself. For example, analyses have indicated that noncurrent-carrying wire bonds have the potential to reduce die temperatures considerably.

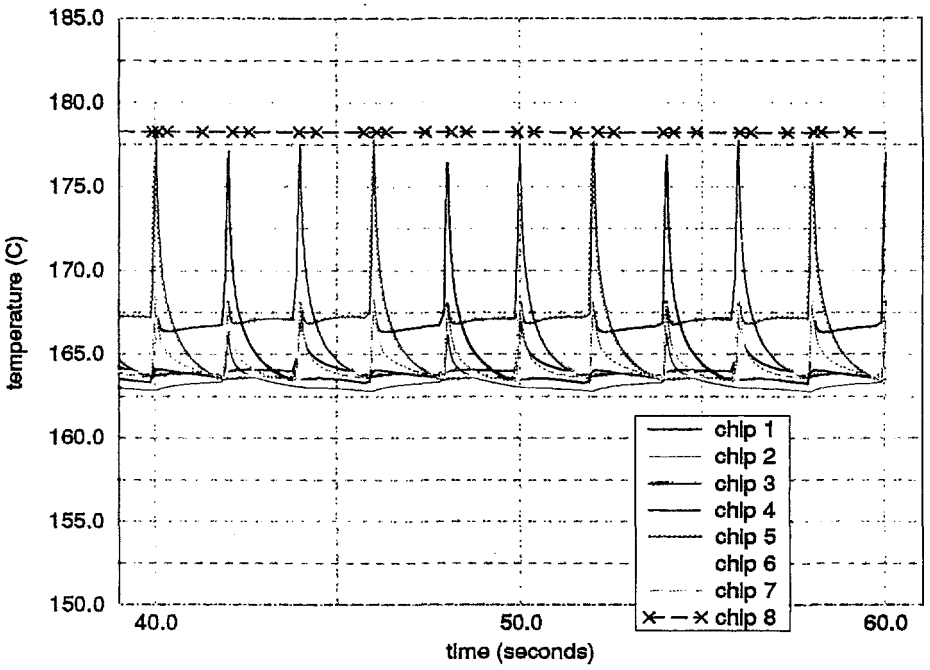

Figure 4-15a. IC Temperature Histories (L.P., H-C path, 5X res., 3.5 Amp pk.)

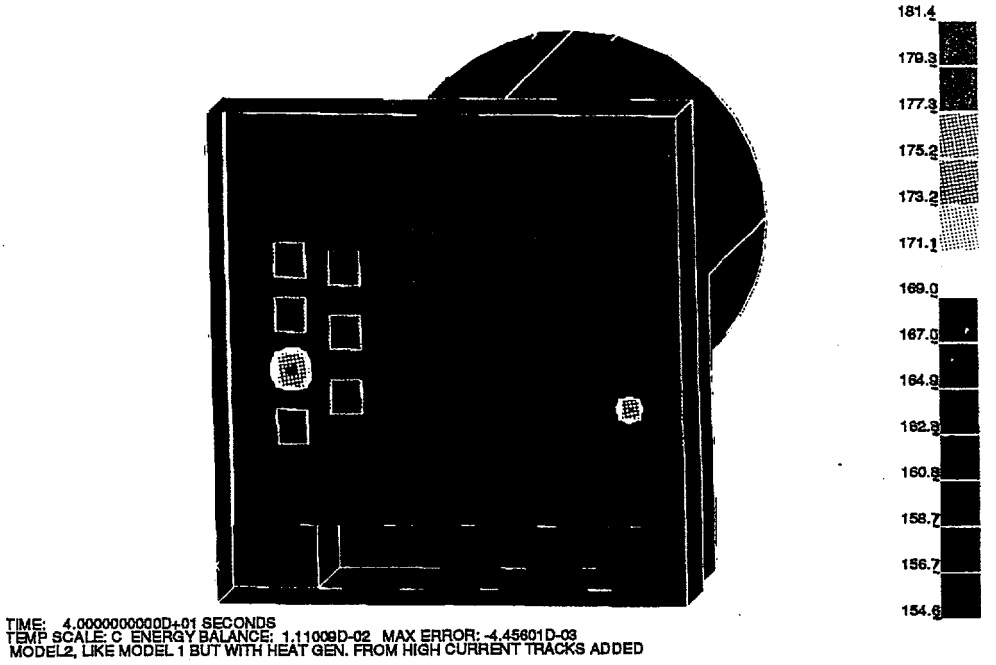

Figure 4-15b. Actuator Temperature Distribution (L.P., H-C path, 5X res., 3.5A pk)

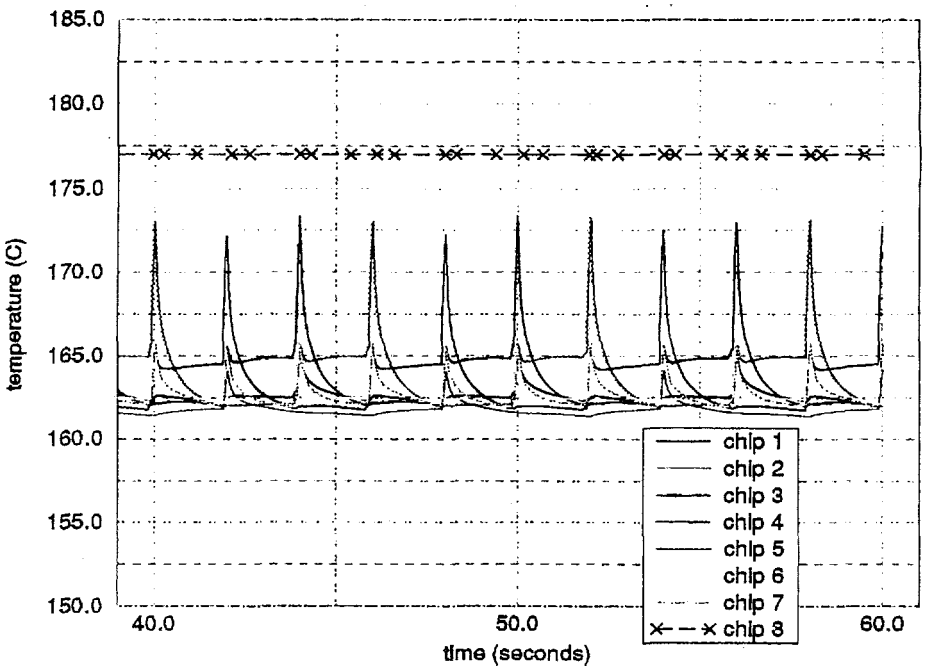

Figure 4-16a. IC Temperature Histories (L.P., H-C path, 4X res., 3.5 Amp pk.)

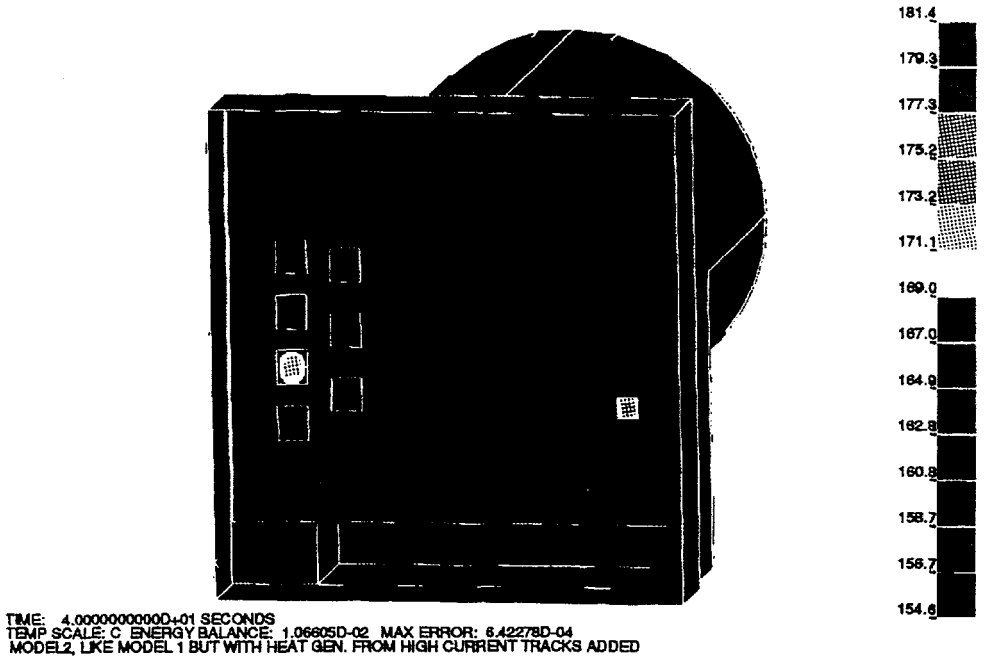

Figure 4-16b. Actuator Temperature Distribution (L.P., H-C path, 4X res., 3.5A pk)

This page intentionally left blank

5. Component Reliability

Donald G Pierce
Eric S Snyder

The throttle control module is expected to reliably operate for a minimum of 10 years, which is the equivalent of 100,000 automotive miles. The ability of the throttle control module to meet the expected lifetime requirement will be largely determined by the performance of the individual components. The selected packaging technology for realization of the throttle control is premised on the use of unpackaged devices which can only be subjected to limited level of testing either at the wafer level or as individual dice. In order to assure the reliability of the throttle control, techniques to assess the reliability of the unpackaged components need to be developed. This chapter formulates an approach based on an understanding of the physics of failure mechanisms and life test data to assess component reliability.

The temperature environment understood by Sandia on the date the assessment was performed is given in Table 5-1. The extreme operating environment cited causes difficulty in ensuring reliability of the multichip module. The first difficulty lies in the area of capability. The most effective way to address whether the IC and package can successfully withstand this environment over the specified life is to focus on the physics of failure for each mechanism and corresponding design rules for each technology.

Table 5-1: Use Conditions for Module

Temperature (°C)	Operating Time (Hours)
130-160	250
105-130	3,000
<105	1,000

A second issue is demonstrating reliability. The high use temperatures greatly diminish the effectiveness of using acceleration factors in life testing. High acceleration factors reduce test time by increasing the number of effective device hours tested. Because of the high temperature use environment, the thermal acceleration factors are close to unity. Thus, the classic approach relying on life test data to measure reliability would cause an enormous test burden. Thus, life test data must be regarded as supplemental to understanding the physics of extrinsic and intrinsic failure mechanisms for each technology and demonstrating large margins for these mechanisms.

An additional issue not related to the extreme operating environment is burn-in. The automotive industry has historically relied on burn-in for lot acceptance. However, as bare die will be used in the module, traditional burn-in approaches are difficult to implement. Novel burn-in approaches or changes in burn-in requirements are necessary.

In summary, the main issue in product qualification and acceptance for the die used in the module is in the tools available to assess capability, demonstrate reliability, and evaluate burn-in requirements. The extreme environments change the basic assumptions used by industry to assess and demonstrate reliability. If it is not possible to reduce the extreme temperatures through cooling or relocation, both supplier and customer must be prepared to use new approaches to qualify and assure the product with regard to reliability. For example, to obtain as much data as possible, much of the qualification should focus on the production line and should make use of historical data on ICs similar to the ICs undergoing qualification. The testing requirements to assure reliability of a specific design can be greatly reduced by using production line data as a supplement.

5.1 Failure Mechanisms

The five IC failure mechanisms that have been considered are dielectric breakdown, hot carrier effects, electromigration, stress voiding, and ionic contamination. A major focus of each discussion is the effect of temperature on the specific failure mechanism.

5.1.1 Dielectric Breakdown

Wear out of dielectrics is accelerated by two factors: the applied electric field and temperature. Because of the field dependence, thin gate oxide on MOS products are the greatest concern from the standpoint of intrinsic wear out. Also, oxide defect densities drive early dielectric failures because the electric field is greatly enhanced by the presence of a defect. Even for thin gate oxides, the intrinsic wear out of defect-free dielectrics is so slow that the reliability evaluation of dielectrics is focused on defects. Because dielectric defects can usually be screened out by burn-in, the issue of dielectric reliability and burn-in are closely linked.

Intrinsic and extrinsic dielectric breakdowns are accelerated by temperature and the activation energy, which is a function of applied field.[1,2,3] For example, a recent large sample test on a 225 Å oxide conducted at Sandia showed the activation energy decreasing monotonically with applied field. The activation energy decreased from 0.90 eV to 0.27 eV as the applied field increased from 8 to 11 MV/cm.[1] Because a typical gate oxide field is approximately 2 MV/cm, extrapolation of this data shows the potential for activation energies is on the order of 2 eV at use conditions. These are potential activation energies because this activation energy has not been verified due to the small acceleration factors and, hence, enormous test times needed for verification.

The acceleration due to temperature is given by Equation (5-1)

$$A_f(T_1 \rightarrow T_2) = e^{\frac{E_a}{k}\left(\frac{1}{T_2} - \frac{1}{T_1}\right)} \tag{5-1}$$

where $A_f(T_1 \rightarrow T_2)$ = Acceleration factor from temperature 1 to temperature 2

T = Temperature (K)

E_a = Activation energy

k = Boltzmann's constant = 8.617×10^{-5} eV/K.

For example, the acceleration factor from room temperature (25°C) to 160 °C at a field of 2 MV/cm ($E_a \approx 2$ eV) is 2.9×10^{-11}. That is, the failure rate due to dielectric wear out of an IC operating at 160°C is 3.4×10^{10} times the failure rate of an IC operating at 25°C. Conversely, cumulative hours under life test are multiplied by this factor when the use condition is room temperature. Thus, given these assumptions, the number of hours under life test to demonstrate a given level of reliability is 3.4×10^{10} times longer when the use condition is 160°C instead of room temperature. Even the smallest estimate of oxide breakdown activation energy, 0.3 eV, leads to test times 38 times longer than when the use condition is 160°C instead of room temperature.

The result above should be viewed with caution because dielectric wear out at low field strengths is not well-understood. The specific model describing oxide failure continues to be a subject of controversy. However, recent data on a 225 Å oxide[1] show that it behaves according to the model of McPherson and Baglee.[3] In any event, careful attention must be paid to high-temperature life test and burn-in results to assure that no intrinsic wear out problem with dielectrics exists. Highly accelerated time-dependent dielectric breakdown data on test structures may be needed to supplement the results given above.

The acceleration factor due to the electric field is

$$A_f(E_1 \rightarrow E_2) = e^{C(E_2 - E_1)} \tag{5-2}$$

where $A_f(E_1 \rightarrow E_2)$ = Acceleration factor going from field 1 to field 2

E = Electric field (V/cm)

C = Temperature dependent empirical constant (cm/V).

At 160°C, the data obtained in Reference 1 yields $C = -4.4 \times 10^{-6}$ cm/V. Because the electric field is proportional to the applied voltage, the acceleration factor at 7 V when the use condition is 5 V equals 0.02. That is, the failure rate due to electric field at 7 V is 50 times greater than at 5 V. This suggests that an accelerated voltage test can be used at the wafer level as a substitute or adjunct to normal burn-in of the IC.

As mentioned above, dielectric reliability is driven by defects. One approach to ascertaining those defect levels is to perform wafer-level testing on large area capacitor test structures using a voltage ramp test, such as specified by the Joint Electronic Device Engineering Council

(JEDEC).[4] Using this type of test, a reliability defect is defined as having a breakdown voltage between the operating voltage and some level slightly below the main population, which is typically 8 MV/cm for oxides. Failures at or below operating voltages are yield limiters and are screened out at wafer sort. The results of this test can be used to calculate dielectric defect densities that, along with the dielectric area of the IC, can be used to calculate the percentage of early failures in the product. These results can then aid in the decision whether burn-in or a burn-in substitute is warranted. Note that a similar procedure can be used on the burn-in fallout history of like product produced on the line provided that proper normalization of dielectric area is performed.

Finally, dielectric defects are mainly due to particulate contamination, silicon crystal defects, and heavy metal contamination. Therefore, an aggressive approach to particulate monitoring, annealing, and gettering can alleviate the need for burn-in related to dielectric defects.

5.1.2 Hot Carrier Effects

Hot carrier induced degradation of metal oxide semiconductor field-effect transistor (MOSFETs) occurs when the channel electric field of a MOSFET is large enough to add sufficient energy to electrons (and/or holes) to cause injection of charge into the gate oxide and/or the generation of interface states at the oxide-silicon interface. As a result, hot carriers can cause threshold voltage shifts, reduction in transconductance, and other degradation of transistor parameters. Unlike dielectric breakdown, hot carrier effects are noncatastrophic. Thus, failure criteria can be somewhat arbitrary and are design-dependent. Because the channel electric field gives rise to the failure mechanism, hot carrier effects are most important in short channel technologies of typically less than 1.0 μm.

Like dielectric breakdown, hot carrier-induced degradation is accelerated by applied voltage. However, unlike other failure mechanisms, hot carrier effects in MOSFETs exhibit a negative activation energy of typically -0.1 eV. Thus, hot carrier effects in MOSFETs are decelerated by temperature. This has an important impact on high-temperature applications in that the techniques used to qualify and assure reliability with respect to hot carrier effects require no modification or special consideration, unlike the other failure mechanisms.

For bipolar technologies, hot carrier effects are accelerated by temperature with a small, positive activation energy. While indications are that the effective activation energy is positive, it has not been quantified in the literature. In most applications, hot carrier effects occur when emitter-base junctions are reverse biased due to excursions on the inputs. Proper signal conditioning and proper circuit design can preclude this from occurring. Also, including a gain margin in the design can mitigate the effects if reverse biased emitter-base junctions are unavoidable. This is because gain reduction is the major degradation mode in bipolar technologies.

The thermal acceleration of hot carrier effects is governed by Equation 5-1. Because of the negative activation energy, the acceleration factor from room temperature (25°C) to 160°C is 3.36. That is, the failure rate due to hot carrier induced degradation of an IC operating at 160°C is 0.297 times less than the failure rate of an IC operating at 25°C. Conversely, cumulative hours under life test are reduced by this factor when the use condition is room temperature. Because of the lack of acceleration with temperature, typical high temperature life tests are not appropriate for hot carrier effects. The life time is usually determined for minimum geometry transistors with this result extrapolated to the entire die. A typical industry goal is 10 years of life under worst-case DC bias with a failure criterion of a 10 percent degradation in transconductance or similar parameter. Because of duty cycle effects in AC operation, this result is conservative.

The acceleration factor due to the applied drain-source voltage[5] is

$$A_f(V_{ds1} \rightarrow V_{ds2}) = e^{b\left(\frac{1}{V_{ds2}} - \frac{1}{V_{ds1}}\right)} \tag{5-3}$$

where $A_f(V_{ds1} \rightarrow V_{ds2})$ = Acceleration factor going from bias 1 to bias 2
V_{ds} = Applied drain-source voltage (V)
b = Empirical constant (V).

Data obtained at Sandia on commercial product yields values of b ranging from 140 to 200 V.[6] Thus, the acceleration factor at 7 V when the use condition is 5 V is 3.4×10^{-4} for b = 140 V. That is, the failure rate due to hot carrier induced degradation of an IC operating at 7 V is 2980 times larger than when operated at 5 V. Because of the negative activation energy, hot carrier tests on test structures are done at room temperature with accelerated drain-source biases.

5.1.3 Electromigration

Electromigration is defined as metal motion under the influence of an applied current density. Failures are catastrophic openings in the metallization or extrusion shorts to another metal layer. Some modern technologies employ a refractory barrier layer between metal 1 and the underlying silicon to prevent aluminum spiking through shallow junctions. Because these barrier layers are not subject to electromigration at low temperatures (<400°C), they will continue to conduct current even after the overlying aluminum has opened. Thus, metallization openings due to electromigration are usually not observed during life tests when barrier layers are employed. Note that the barrier layer provides no additional protection against extrusion shorts.

The thermal acceleration factor for electromigration is governed by Equation 5-1. However, the activation energies are strongly dependent on metallurgy and grain structure of the metal. Sandia has measured activation energies for industrial aluminum based metallizations ranging from 0.35 to 1.1 eV. Those activation energies, coupled with the variation of the intrinsic robustness of the

metal across manufacturing lines, lead to a variation of more than seven orders of magnitude for metal life at room temperature. Because of the potential for such enormous variation in metal reliability across manufacturers, it is critical to measure the electromigration wear out parameters for a given metal process.

The potential for large activation energies makes electromigration a critical concern when high-temperature applications are considered. For example, an activation energy 1.1 eV yields an acceleration factor from room temperature (25°C) to 160°C of 1.6×10^{-6}. That is, the failure rate due to electromigration wear out of an IC operating at 160°C is 624,000 times more than the failure rate of an IC operating at 25°C. Fortunately, experience has shown at Sandia that metal systems which exhibit large activation energies also exhibit a high inherent robustness against electromigration.

Electromigration is also accelerated by the current density as

$$A_f(J_1 \rightarrow J_2) = \frac{J_1^2}{J_2^2} \tag{5-4}$$

where $A_f(J_1 \rightarrow J_2)$ = Acceleration factor going from J_1 to J_2

J = Applied current density (A/cm^2).

Equation 5-4 forms the basis for electromigration design rules where the maximum allowed current density is specified. Also, because the current density depends on the applied current and cross-sectional area, it is important that step coverage is factored into the design rule.

The median time to failure of a metal line is governed by Black's equation:[7]

$$M_{tf} = \frac{A}{j^2} e^{\frac{E_a}{kT}} \tag{5-5}$$

where M_{tf} = Median time to failure (s)

A = Empirical constant ($s\text{-}A^2/cm^4$),

and all other quantities have been previously defined. If A and E_a are known for a metal process, it is possible to estimate reliability when life test data is insufficient to do so.

5.1.4 Stress Voiding

Like electromigration, stress voiding is a failure mechanism based on metal migration. As the name implies, the driving force in stress voiding is built-in tensile stress on the metal due to the surrounding dielectric. Because no bias is needed to cause the effect, stress voiding can occur in unpowered parts and can reduce shelf life. The diffusion mechanism for stress voiding is

expected to follow the diffusion mechanism for electromigration and, hence, will exhibit the same range of activation energies as discussed in the previous section. Stress voiding can be accelerated by temperature because of the positive activation energy of the diffusion processes. However, because the stress on a metal generally decreases with temperature, the decrease in driving force counteracts the increase in diffusivity. Thus, the acceleration factor from room temperature to stress temperature will exhibit a minimum at some temperature, and will, in general, be much more weakly accelerated than electromigration.

Stress voiding is not well understood quantitatively, and accelerating the phenomenon is presently a matter of trial and error. This is largely due to the difficulty in measuring the 3-D stress in patterned metal. A typical stress voiding experiment consists of measuring and counting voids in a patterned, passivated metal; annealing this metal at several temperatures generally from 150 to 250°C; and remeasuring the voids to determine if growth in size or number has occurred. This process is repeated to determine the growth rate as a function of time. Activation energies can be extracted from the temperature dependence. With these parameters available, an estimate of reliability can be made at the use condition if stress voiding occurs. In general, a simpler experiment involving a single anneal is performed first to ascertain the presence of stress voiding.

Some evidence exists that temperature cycling can accelerate stress voiding.[8] Because of the large (in both number and magnitude) thermal cycles the module will undergo, a quick thermal cycle experiment should be performed to check for the presence of stress voiding.

5.1.5 Ionic Contamination

Mobile ions that contaminate a wafer lot cause MOSFET threshold voltage shifts over time as the ions redistribute in the presence of a field. They can cause loss of isolation between transistors by lowering the threshold voltage of parasitic field oxide transistors. Mobile ions are systemic to a lot and, hence, can be spotted through process monitoring.

Because mobile ions move through diffusion processes, they can be accelerated by temperature. They exhibit an activation energy of roughly 1 eV with the acceleration factor governed by Equation 5-1. Thus, the acceleration factor from room temperature (25°C) to 160 °C is 5.4×10^{-6}. That is, the failure rate due to ionic contamination of an IC operating at 160°C is 185,000 times more than the failure rate of an IC operating at 25°C. Thus, for high-temperature applications, it is important to monitor the production line for ionic contamination. Typical approaches for process monitoring include measuring capacitor structure C-V curves and monitoring field transistor threshold voltages and high-temperature anneals of programmed EEPROM cells, if available.

5.2 Dynamic Life Testing

As discussed earlier, high-temperature applications have a large impact on the efficacy of life testing to assure product reliability. To demonstrate this effect, a typical reliability calculation based on life test data is provided.

Assume that a product exhibits a constant failure rate is required to operate t_{use} hours at temperature T_{use} with reliability R at 50 percent confidence. The probability that a device will fail before T_{use} hours is

$$P\{t_f < t_{use}\} = \lambda \int_0^{t_{use}} e^{-\lambda t}\, dt = 1 - e^{-\lambda t_{use}} \tag{5-6}$$

where P = Probability of failure = 1 - R
t_f = Time at failure (hours)
λ = Temperature dependent failure rate (hours^{-1})
t = Time (hours).

The failure rate needed to satisfy the reliability requirement is

$$\lambda \leq -\frac{In(R)}{t_{use}} \tag{5-7}$$

The failure rate for a single mechanism can be obtained from life test data[9] through

$$\lambda(T_{use}) = \frac{\chi^2_{(\alpha,2n+2)}}{2t_{life}A_f\left(T_{stress} \rightarrow T_{use}\right)} \tag{5-8}$$

where n = Number of failures for the mechanism
χ^2 = Chi square distribution
α = Confidence
t_{life} = Cumulative hours under life test
A_f = Acceleration factor from $T_{stress} \rightarrow T_{use}$ for the failure mechanism.

For 50 percent confidence and no failures, $\chi^2 = 1.38629$. Also, if more than one failure mechanism occurs, Equation 5-8 can be summed over the failure mechanisms.

Substituting Equation 5-8 into 5-7 and solving for t_{life} yields the minimum amount of dynamic life testing required to satisfy the reliability requirement

$$t_{life} \geq -\frac{t_{use}\chi^2_{(\alpha,2n+2)}}{2In(R)A_f(T_{stress} \rightarrow T_{use})} \tag{5-9}$$

When the use condition is specified as operating periods at different temperatures, as given in Table 5-1, Equation 5-9 becomes

$$t_{life} \geq -\frac{\chi^2_{(\alpha,2n+2)}}{2In(R)}\sum_i \frac{t_{usei}}{A_{fi}(T_{stress} \rightarrow T_{usei})} \tag{5-10}$$

where the indices are over the operating time at temperature array.

Equation 5-10 can be used to determine the impact of high temperature on life test requirements. Table 5-2 gives the amount of device hours at 150°C needed to meet a reliability requirement of 0.999875 after 4250 operating hours with 50 percent confidence. The table is generated as a function of operating temperature and activation energy. The entry T_{module} is based on the requirements given in Table 5-1. The activation energies span the range discussed in Section 5.1. Note that an activation energy of 0.7 eV is commonly used by manufacturers when the dominant failure mechanism is unknown.

Table 5-2: Number of Life Test Device Hours With Zero Failures Needed at 150°C To Meet a Reliability Requirement of 0.999875 With 50 Percent Confidence at 4250 Hours of Operation

T_{use} (°C)	E_a (eV)			
Activation Energies	0	0.7	1.0	2.0
25	2.36×10^7	7.53×10^3	2.39×10^2	2.43×10^{-3}
65	2.36×10^7	1.89×10^5	2.39×10^4	2.42×10^1
80	2.36×10^7	5.25×10^5	1.03×10^5	4.47×10^2
125	2.36×10^7	7.06×10^6	4.21×10^6	7.53×10^5
T_{module}	2.36×10^7	9.14×10^6	7.09×10^6	6.02×10^6

The difficulty that high-temperature operation imposes in assuring reliability can be seen from inspection of Table 5-2. For example, to meet the reliability requirement for 25°C operation requires roughly 8,000 hours or eight devices subjected to a typical 1000-hour test, assuming an activation energy of 0.7 eV. To meet the module requirements requires 9,140,000 hours, or 9,140 devices subjected to a typical 1000-hour test. Matters become worse when one considers that the 0.999875 reliability requirement applies to the entire module. Because the module contains 60 electrical elements, the test time needed for each is 60 times the amount shown in the table. Also, if higher confidences are needed, the test time increases. For example, to obtain 99.9 percent confidence, the test time increases by a factor of ten.

The 0.999875 reliability requirement stems from the estimated reliability of the mechanical throttle linkage. It may be reasonable to back off from this requirement and require that the ICs in the throttle controller be at least as reliable as other ICs in the vehicle with added physical confidence obtained through detail test data on fundamental failure mechanisms to demonstrate large margins. In that instance, remember that the reliability will not be demonstrated in the classical statistical sense. The throttle controller is a critical item from both a customer satisfaction and safety standpoint. It is the responsibility of Delphi Energy and Engine Management Systems to set the reliability requirement and judge if a more physics-based approach is acceptable. If a demonstrated high reliability is needed, then either test requirements must be increased, as shown in Table 5-2, or the operating temperature must be reduced through active cooling or relocation of the module.

In the case of reliability equivalent to other ICs in the vehicle, Table 5-2 shows that, for an assumed activation energy of 0.7 eV, the acceleration factor for a 150°C life test when the use condition is 65°C is 50 times the acceleration factor for the module environment. Thus, the number of life test device hours needed to demonstrate equivalent reliability is 50 times greater than needed for equivalent ICs. While this may be technically feasible, it greatly increases the cost of qualification and acceptance of the ICs used in the module.

It is clear from this discussion that demonstrating reliability for the module through life test is a hopeless task under the current environment. In this instance, life test qualification of the product will only demonstrate that the chip layout does not contain fundamental flaws that radically reduce life. While normal life testing must be done, the assurance that the product will survive the environment must come from understanding the fundamental failure mechanisms discussed in Section 5.1 and demonstrating large margins with respect to the lifetime requirement. Thus, it is critical to the success of this approach that test structure data be available for each failure mechanism and technology that is used.

5.3 IC Burn-in

Burn-in is similar to life test in its dependence on thermal, and possibly voltage, acceleration to reduce test time. Indeed, a dynamic burn-in may be identical to a dynamic life test except for the

number of hours required for the test. The key difference between burn-in and life test is that burn-in is designed to guarantee a minimum life by removing defects from the population rather than demonstrating a lifetime for a hopefully defect-free population. Because of the emphasis on defects, burn-in requirements can range from 100 percent test sample on a process with a consistent defect problem to no burn-in required for a well-controlled, limited defect process.

While burn-in is useful in detecting any thermally activated failure mechanism, the focus is usually on dielectric failures because they are most sensitive to particulate contamination and silicon faults. If the defect population is well-characterized (through breakdown tests on dielectric test structures, for example) and the intrinsic time-dependent dielectric breakdown of perfect dielectric is also well-characterized, it is possible through sophisticated modeling[10] to select a temperature, time, and voltage for burn-in that will meet precise reliability requirements. This precise information on a process is often not available in real time and will vary from lot to lot. Hence, burn-in requirements are selected based on experience or specification. Another important issue in burn-in for dielectric defects is coverage. For example, in a complementary metal-oxide semiconductor (CMOS) IC, it is important to exercise the part in a manner such that all the gates are subjected to the stress.

As discussed above, burn-in for dielectric defects is subject to the thermal and voltage acceleration factors given in Section 5.1.1. Because the control module is operated at high operating temperatures, more defects may be activated that would not ordinarily cause failure for parts operated at lower temperatures. Thus, the burn-in requirements grow by the factors discussed in Section 5.2 for equivalent defect detection. Again, costs increase dramatically to where assuring such quality is not economically feasible. If reducing the operating temperature of the module is not possible, the most viable approach is to maintain burn-in requirements at levels for normal parts and routinely monitor for dielectric defects by wafer-level testing of dielectric test structures. The dielectric structure testing should be done by the manufacturer as part of his process control.

One difficulty in multichip module fabrication is that bare dice are shipped by the manufacturer. This makes burn-in at the manufacturer impossible beyond small levels for lot acceptance because the device hours needed are not available on wafer probers. One option to help alleviate this difficulty is to apply an accelerated voltage test at the high-temperature wafer sort. This voltage should be chosen to be as high as possible while maintaining device functionality. This test would weed out any severe defects. While not eliminating most defects as a traditional burn-in would, the test would serve as an alert to the presence of a defect population and stimulate further investigation and root cause analysis.

As a final note, any burn-in (or life test) fallout during qualification should be investigated thoroughly. The fallout may not be defect-driven, but may indicate the onset of wear out. Because of the high-temperature operating environment, any evidence of wear out during life test or burn-in can result in an unacceptably high failure rate in the fielded modules.

5.4 Package Reliability

The primary tests used to assure package reliability is temperature cycling and Humidity, Temperature, and Bias tests (HTBs). They are designed to accelerate a wide variety of package related failure mechanisms such as package, thin film, and die cracking; hermiticity failures; bond and wire bond failures; and intermetallic growth. As in the IC failure mechanisms, the high operating temperatures and severe thermal cycling undergone by the throttle control module will impact the effectiveness of package reliability tests.

Thermal cycling is strongly accelerated by the cycle amplitude. This acceleration follows a power law dependence[11]

$$A_f(\delta T_1 \rightarrow \delta T_2) = \left(\frac{\delta T_1}{\delta T_2}\right) \tag{5-11}$$

where $A_f(\delta T_1 \rightarrow \delta T_2)$ = Acceleration factor from δT_1 to δT_2

δT = Magnitude of the temperature cycle.

Equation 5-11 can be convolved with the extrapolated throttle controller thermal cycle environment[12] to yield an equivalent number of 200°C (-50 to 150 °C) thermal cycles. This calculation shows that the controller's thermal cycle environment is equivalent to thirty-six 200° C thermal cycles. This result, coupled with Equation 5-10 (solved for R), can be used to calculate the module package reliability demonstrated from temperature cycling tests. This calculation yields Table 5-3, which gives the demonstrated reliability at 50 percent confidence as a function of the number of 1000-cycle tests.

Table 5-3: Module Package Reliability at 50 Percent Confidence as a Function of the Number of 1000 Temperature Cycle Tests With a 200°C Temperature Amplitude

Number of Tests	20	50	100	200
Reliability	0.99879	0.999515	0.999757	0.999879

The acceleration factor for the HTB test is given by[13]

$$A_f(T_1, H_1 \rightarrow T_2, H_2) = \left(\frac{H_1}{H_2}\right)^{\frac{8}{3}} e^{\frac{E_a}{k}\left(\frac{1}{T_2}-\frac{1}{T_1}\right)} \tag{5-12}$$

where A_f = Acceleration factor from conditions 1 to 2

T = Temperature (K)

H = Relative humidity (%)

E_a = Activation Energy (eV)

k = Boltzmann's constant (8.617×10^{-5} eV/K).

The activation energy for HTB tests has been reported as ranging from 0.79 to 0.9 eV.[11] The lower value, 0.79 eV, will be used here because it is most conservative. Using that activation energy, Equation 5-12 can be convolved with the extrapolated throttle controller temperature and humidity environment[12] to yield an equivalent number of 1000-hour HTB tests with 85 percent RH at 85°C. This calculation shows that the controller's temperature and humidity environment is equivalent to 1.2 of these tests. That result, coupled with Equation 5-10 (solved for R), can be used to calculate the module package reliability demonstrated from a HTB test. That calculation yields Table 5-4, which gives the demonstrated reliability at 50 percent confidence as a function of the number of 1000-hour HTB tests.

Table 5-4: Module Package Reliability at 50 Percent Confidence as a Function of the Number of 1000-Hour HTB Tests with 85 Percent RH at 85°C

Number of Tests	20	50	100	200
Reliability	0.959	0.9835	0.9917	0.9959

As a point of comparison, Table 5-5 gives similar calculations for 1000-hour dynamic life tests performed on the full module at 150°C. In this instance, the environment shown in Table 5-1 was used along with an assumption of 0.7 eV for the activation energy.

Table 5-5: Module Reliability at 50 Percent Confidence as a Function of the Number of 1000-Hour Dynamic Life Tests at 150°C

Number of Tests	20	50	100	200
Reliability	0.944	0.977	0.989	0.9943

Tables 5-3 through 5-5 show that while it is possible to demonstrate reliability equivalent to the original mechanical throttle linkage in the case of thermal cycling, it is cost prohibitive to accomplish that demonstration for the HTB and dynamic life tests on the full module. Note that all reliability calculations assume no observed failures.

5.5 Summary and Conclusions Concerning Component Reliability

It is not economically feasible to demonstrate the reliability of the throttle control module as equivalent to the original mechanical linkage (0.999875) except for temperature cycling tests on the full module. The module may achieve this reliability, but the number of device test hours to prove it is not attainable. It also does not appear possible to demonstrate reliability equivalent to other ICs and modules used in the vehicle due to the extremely high operating temperature environment to which the module will be subjected. The best approach is to change the operating requirements by cooling or relocating the module. If this is impossible, then Sandia recommends that the sample sizes normally used for other critical electronic devices in the vehicle be used for qualification and acceptance with demonstrated large margins for each failure mechanism. The exception is a dynamic accelerated voltage functional test conducted at the high-temperature wafer sort to screen for gross dielectric defects. Any fallout from this test would alert personnel to screen further and perform root cause analysis for dielectric integrity. Note that this test should be performed in addition to, and after, the high-temperature functional test at nominal voltage.

The data gathered above should be supplemented by the following information for each die type to assure that the module components are suitable for the application. This information primarily concerns die quality and fundamental failure mechanisms, and supplements the information from reliability testing on die and the full module.

Construction Analysis

While not mentioned earlier, a detailed, independent destructive physical analysis should be performed on a single sample of each die and the assembled module to verify the overall quality of the workmanship of the product. Sandia has found that such an analysis is invaluable for spotting manufacturing defects that may not show up in electrical testing. Sandia performs this analysis on all of the parts it qualifies for high-reliability applications.

Failure Mechanism Information

The die manufacturers should provide fundamental failure mechanism information on their processes. This information should be obtained from test structure data and should include the following: (Note that hot carrier induced degradation is not included because this phenomenon is suppressed with temperature for MOS devices)

1. Dielectric Breakdown

- Electric field design rules (obtained from dielectric composition, thickness and nominal operating voltage)
- Intrinsic breakdown field
- Defect populations (including sample sizes)
- Time dependent dielectric breakdown response (optional)

2. Electromigration

- Metal used
- Current density design rules
- Activation energy
- Pre-exponential factor (A in Equation 5-5)
- Sigma of the log-normal failure distributions

3. Stress voiding

- Photomicrographs and void densities after passivation (small sample)
- Photomicrographs and void densities after 500 hour, 150 °C anneal (small sample, pre- and post-life test on a single die is sufficient)

4. Ionic Contamination

- Field oxide test structure capacitance-voltage plots, pre- and post-biased anneal

5. Die Reliability--In addition to fundamental failure mechanism results, results of dynamic life test on like product produced with the process would prove useful, including

- Life test conditions
- Cumulative hours
- Analysis of any failures observed.

6. Burn-in Data--Burn-in results on like product produced with the process would prove useful, including

- Life test conditions
- Cumulative hours
- Analysis of any failures observed.

7. Package Reliability

As the package materials and process are still undefined, it is not possible to perform an evaluation on package reliability at this time. The approach will be to carefully monitor reliability tests on the package as that data becomes available.

REFERENCES

1. Statement by W. M. Miller, Dept. 2276, Reliability Physics, in personal interview at Sandia National Laboratories, Albuquerque, NM, February 5, 1993.
2. J. Lee, I-C Chen, and C. Hu, "Statistical Modeling of Silicon Dioxide Reliability," *Proceedings of the 1988 International Reliability Physics Symposium*, 28 (1988) p. 131.
3. J. W. McPherson and D. A. Baglee, "Acceleration Factors for Thin Gate Oxide Stressing," *Proceedings of the 1985 International Reliability Physics Symposium*, 23 (1985) p. 1.
4. "Procedure for the Wafer-Level Testing of Thin Dielectrics," JEDEC Standard No. 35, Joint Electronic Device Engineering Council (JEDEC), symposium held in Lake Tahoe, CA, October 24-27, 1993, pp. 22-34.
5. E. Takeda, "Topic 1, Dynamic Hot-Carrier Effects on Integrated Circuits--Characterization Under ac/dc Stress," *1993 International Reliability Physics Symposium Tutorial*, held in Atlanta, GA, March 23, 1993.
6. Statement by E. S. Snyder, Dept. 2276, Reliability Physics, in personal interview at Sandia National Laboratories, Albuquerque, NM, March 1993.
7. J. R. Black, "Mass Transport of Aluminum by Momentum Exchange with Conducting Electrons," Proceedings of the 1967 Annual Symposium on Reliability Physics, held in Washington, D.C., January 10-12, 1967.
8. C. F. Dunn and J. W. McPherson, "Temperature-Cycling Acceleration Factors for Aluminum Metallization Failures in VLSI Applications," Proceedings of the 1990 International Reliability Physics Symposium, held in New Orleans, LA, March 27-29, 1990, pp. 252-258.
9. P. A. Tobias and D. Trindade, *Applied Reliability*, Van Nostrand Reinhold, New York, 1986.
10. R. Moazzami and C. Hu, "SiO_2 TDDB Testing and Burn-in," *1992 International Reliability Physics Symposium Tutorial Notes*, San Diego, CA, March 30, 1992, pp. 5.1-5.32.
11. R. C. Blish II and J. McCullen, "Package Reliability Physics," *1991 International Reliability Physics Symposium Tutorial Notes*, Las Vegas, NV, April 8, 1991, pp. 1.1-1.35.
12. D. S. Peck and O. D. Trapp, *Accelerated Testing Handbook*, Technology Associates, Portola Valley, CA, 1987, pp. 5.22-5.23.

6. Adhesives for Die and Component Attachment

Stephen E. Garrett
Vicki L. Porter

This chapter describes activities related to the characterization of candidate materials for die and component attachment. As part of this CRADA, a hybrid microelectronic module was designed for an application that would place the module in an automotive under-the-hood environment. The electrical design of the hybrid microelectronic module included ICs, power transistors, and discrete capacitors. Approximately forty die and discrete components were integrated in the module. Enabling die and component attach technologies, such as eutectic-die attach, soft-solder attach, silver-glass attach, and organic adhesive attach were considered for this application. The expected operational environment for this hybrid module is more severe than current thresholds for typical epoxy adhesives.

The outline of this chapter is as follows. First, the results of thermal stress analyses are discussed in Section 6.1. The purpose of these finite element analyses was to provide guidance on the design of the hybrid module and in the selection of die attach materials. The die attach materials being considered had thermal conductivities ranging from 1.7 W/m K for silver-filled epoxy to 293 W/m K for gold-silicon eutectic. It was important to know which types of adhesives had adequate thermal conductivities for this particular application. Based on the results of the thermal analyses, it was concluded that organic adhesives would be suitable for use in this high temperature application.

In Section 6.2, the rationale behind the selection of an organic adhesive for the module and a survey of commercially available adhesives are discussed. The adhesive attach method was chosen as the technology that was most likely to succeed, given the processing limitations of the design and the high temperature environment of an automotive under-the-hood application. A survey of commercially available adhesives was conducted to determine which adhesives would be best suited for this application. Several types of organic adhesive materials (epoxies, polyimides, thermoplastics, and miscellaneous adhesives) were identified for possible use in the hybrid module. Adhesive selection criteria were based on information provided by Delphi and based on the properties of the attachment materials. Twelve adhesives were identified for possible use in the hybrid module. Another three adhesives were also identified as good high temperature adhesives but had processing temperatures higher than the allowable limits. Nevertheless, these three adhesives and a nonconducting adhesive were also included for further testing because they looked promising for DOE/DP applications.

Section 6.3 describes a screen test. To reduce the number of adhesives to a manageable number, a screen test was developed to perform a first order evaluation of the sixteen adhesives. The screen test was designed to determine the mechanical strength, thermal stability, electrical conductivity, and processibility of the adhesives. The results of the screen test enabled the list of sixteen

adhesives to be reduced to just three adhesives. More extensive testing was conducted on the three remaining adhesives.

The final section, Section 6.4, describes the results of the extensive testing that was conducted on the three remaining adhesives. Electrical and mechanical tests were conducted to determine the contact resistance, thermal impedance and mechanical strength of the adhesive joints after a variety of thermal and mechanical stresses. Residual gas analyses were performed to determine the thermal stability of the adhesives after being hermetically sealed. Chemical laboratory tests were also performed to quantify the thermal properties of each adhesive.

6.1 Thermal Analyses

Thermal analyses were performed to provide guidance on the design of the hybrid module, to select the optimum die attach materials, and to provide input for the thermal stress evaluation of Chapter 11[1]. This section summarizes the results of the thermal analyses. Three-dimensional finite element analyses of a hybrid circuit board with a single die were conducted to determine the effects of several design parameters on the temperature rise of the die, die attach, and alumina substrate. The finite element code JACQ3D was used for these thermal analyses because the temperature output can be directly input into JAC3D, a finite element code for quasi-static stress analysis. The parameters investigated included the die attach material and thickness, thermal boundary conditions on the alumina ceramic, alumina purity, and wire bond size. The type and thickness of the die attach materials are shown to have little effect on the temperature increase experienced by the hybrid circuit even for a wide range of thermal conductivities. On the other hand, the thermal condition on the base surface of the alumina substrate and the purity of the alumina can have a significant effect on the temperature increase.

6.1.1 Description of Analyses

The three-dimensional finite element model for a section of the hybrid circuit board with a single die is shown in Figure 6-1. The most critical component was chosen based on the highest steady-state power. The selected die was 0.140 inch by 0.140 inch by 0.025 inch thick with a steady-state power dissipation of 0.75 W. In the finite element model, this power was imposed as a uniform flux over the entire surface of the die. The boundary of the substrate included in the model was assumed to be far enough from the die to represent far-field conditions. In these analyses, the far-field distance was set at ten times the width of the die, so the portion of the substrate included in the model is 1.400 inch by 1.400 inch. The top surface of the alumina substrate was assumed to lie in the xy plane at $z = 0.0$. Because the alumina was 0.050 inch thick, its bottom surface lay in the $z = -0.050$ inch plane.

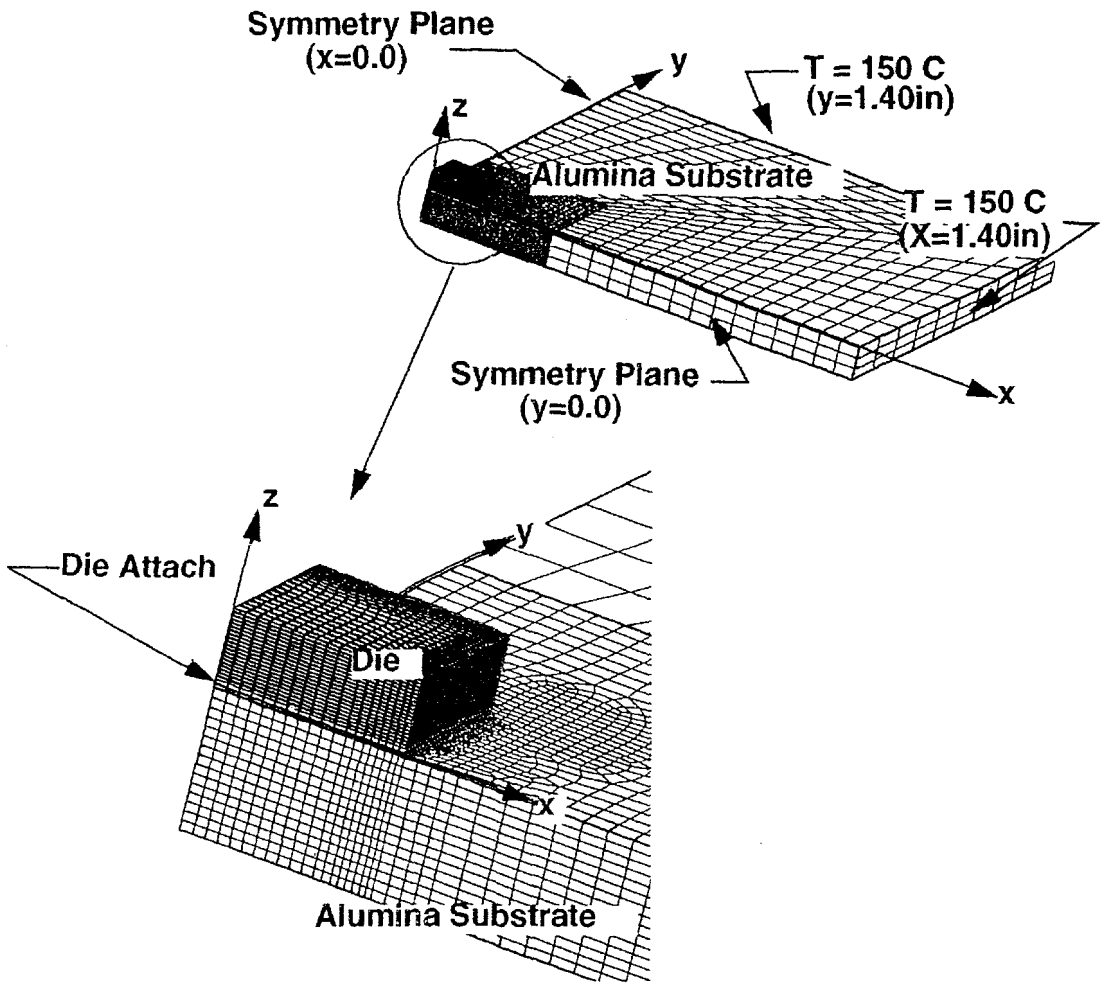

Figure 6-1. Finite Element Model

Due to symmetry conditions, only one-fourth of the geometry was actually modeled in the finite element analyses. Symmetry boundary conditions of no flux were imposed on the edges of the mesh at x = 0.0 and y = 0.0. The outside edges at x = 1.400 inch and y = 1.400 inch were kept at a constant 150°C equal to the maximum ambient temperature during engine operation as specified by the project team.

In the actual assembly, the bottom surface (z = -0.50 inch) of the alumina substrate is joined to an aluminum plate. The aluminum plate is not explicitly included in these analyses. Rather, two different boundary conditions were imposed on the bottom surface (z = -.050 inch) of the alumina ceramic to simulate the bounding cases of a perfectly insulated and perfectly conducting surface, respectively. For the maximum bounding temperature rise, the bottom surface of the alumina was assumed to conduct no heat. This adiabatic boundary condition corresponds to assuming that the alumina is perfectly insulated. To get a lower bound on the temperature rise, a second series of analyses was conducted assuming a constant ambient temperature of 150°C on the bottom surface of the alumina. These analyses simulate the aluminum as a perfect heat sink.

In the actual part, the aluminum backing plate is exposed to the atmosphere in some places and attached directly to the motor housing in others. Therefore, the actual temperatures experienced by the hybrid circuit would be expected to fall between those of the two extreme cases represented in the finite element analyses. In all analyses, the initial temperature was assumed to be a uniform 150°C.

The die attach material forms a thin layer between the die and the alumina. Several different die attach materials with the thermal conductivities and thicknesses shown in Table 6-1 were analyzed. The effects of alumina purity were also investigated using 96% and 99% alumina with the thermal conductivities shown in Table 6-1.

Table 6-1: The Effects of Alumina Purity Using 96 Percent and 99 Percent Alumina and Thermal Conductivities

Component	Thickness mm(inch)	Thermal Conductivity (W/mK)
Silver-Filled Epoxy	0.025 (0.001) and 0.076 (0.003)	1.7
Silver-Filled Polyimide	0.025 (0.001)	2.1
95/5 Pb-Sn Solder	0.127 (0.005)	36
Silver-Filled Glass	0.025 (0.001) and 0.076 (0.003)	78
Gold-Silicon Eutectic	0.025 (0.001)	293
Silicon Die	0.635 (0.025)	148
96% Alumina	1.27 (0.050)	15
99% Alumina	1.27 (0.050)	21

6.1.2 Results of Thermal Analyses

6.1.2.1 Effect of Die Attach Material

The first series of finite element analyses were designed to evaluate the effect of the die attach material on the steady-state temperature rise in the die, the die attach, and the alumina substrate. These analyses assumed a 96% pure alumina with a no-heat-flow boundary condition on the base. These assumptions were the most conservative in that they result in the highest temperatures in the constituent materials.

As shown in Table 6-1 above, five different die attach materials, with thermal conductivities ranging from 1.7 W/mK for silver-filled epoxy to 293 W/mK for gold-silicon eutectic, were considered. A higher thermal conductivity should result in lower temperature of the die and die attach materials because the material is better at conducting heat from the component to the alumina substrate. For all analyses except the solder, the die attach thickness was assumed to be

0.025 mm (0.001 inch). Because this value is unrealistically thin for solder, the solder thickness was assumed to be 0.127 mm (.005 inch).

Figures 6-2 through 6-4 show the steady-state temperature contours in the die, die attach, and alumina substrate, respectively, for the case of the silver-filled epoxy. Although the magnitudes of the temperatures for the other die attach materials will be different, the distribution of temperatures is the same in all cases. The highest temperature, denoted by the asterisk in Figure 6-2, occurs at the center point of the top surface of the die (at the intersection of the symmetry planes in the quarter model). The temperature distribution over the die surface and through the die thickness is nearly uniform; the difference between maximum and minimum temperatures is only 0.6°C. The highest temperatures in the die attach (Figure 6-3) and the alumina (Figure 6-4) are also at the center point of their respective top surfaces. The temperature field in the alumina drops off very rapidly away from the die.

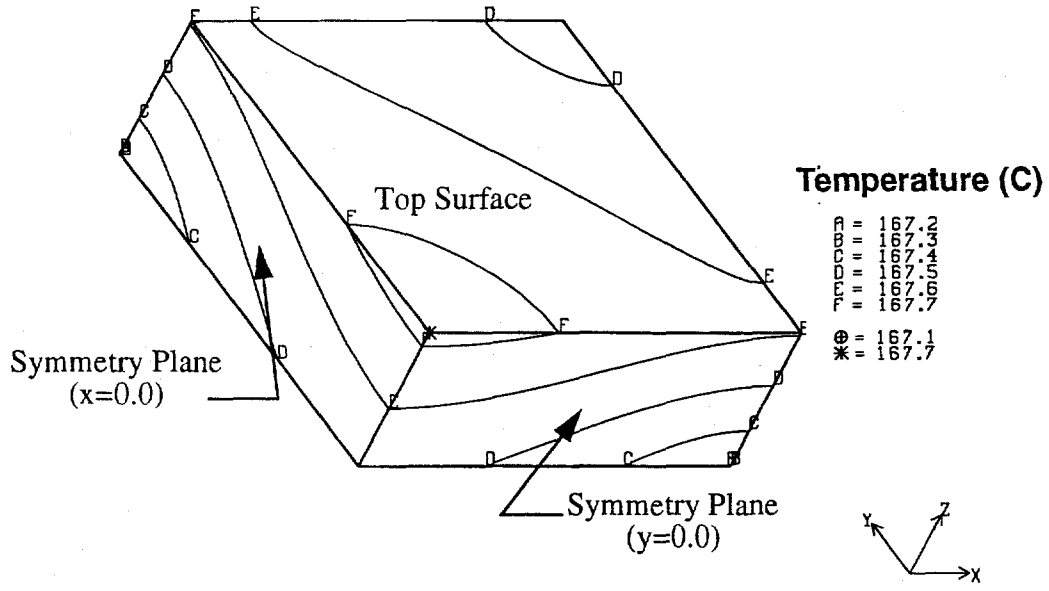

Figures 6-2. Temperature Distribution in Die

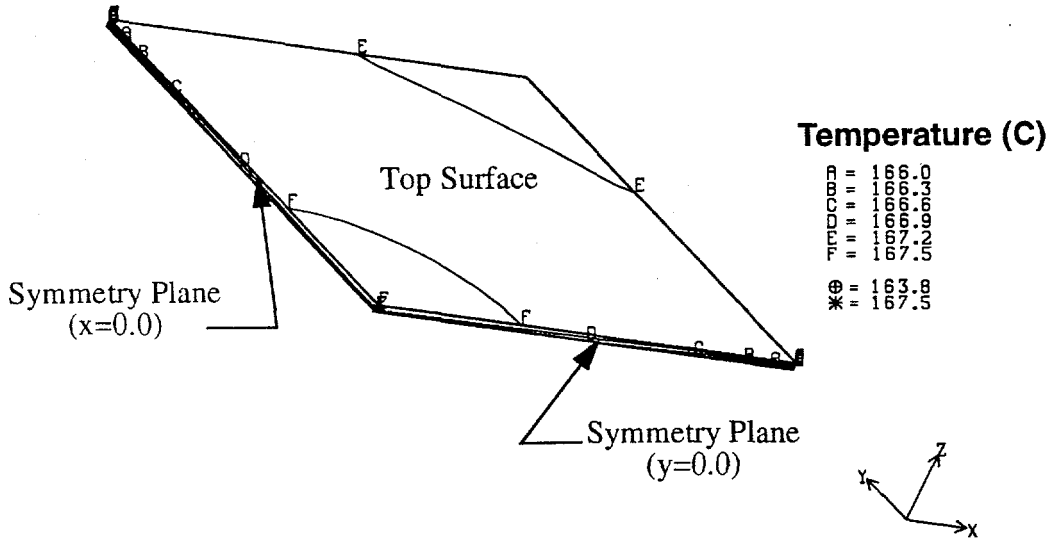

Figure 6-3. Temperature Distribution in the Silver-Filled Epoxy Die Attach

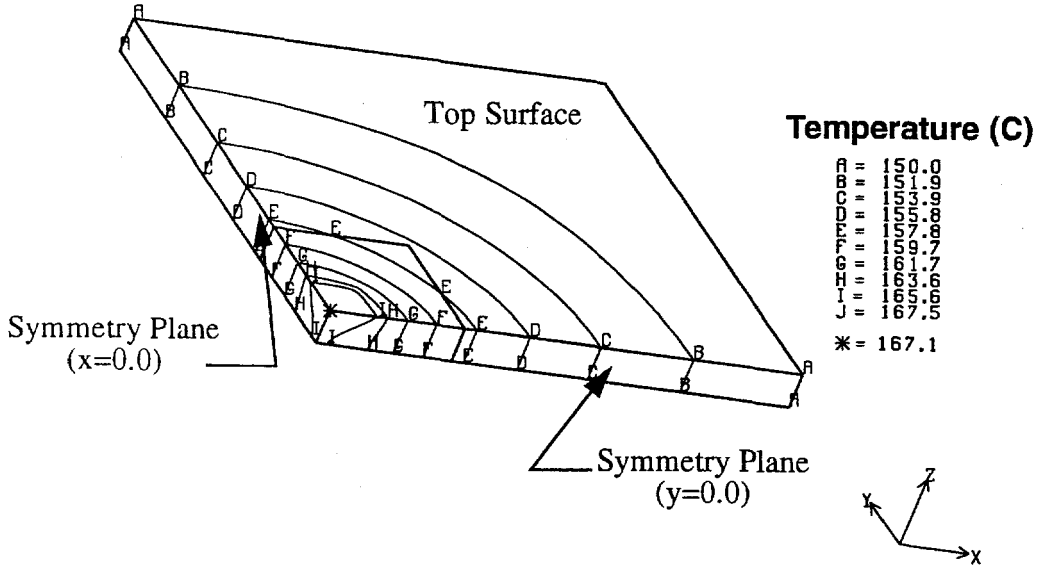

Figure 6-4. Temperature Distribution in the Alumina

Figure 6-5 is a bar chart showing the comparison of maximum temperatures in the constituent materials for each type of die attach material. As expected, the maximum temperatures in the die, die attach material, and the alumina are highest for the silver-filled epoxy, the material with the lowest thermal conductivity. At the other end of the spectrum, the part with gold-silicon eutectic with the largest thermal conductivity displays the lowest temperatures. However, even between these two extremes, the difference in maximum temperatures is less than 1.5°C in all constituent materials. It is apparent that the maximum temperature is not a strong function of the conductivity of the die attach material, probably because this material is so thin and is such a small constituent of the total part.

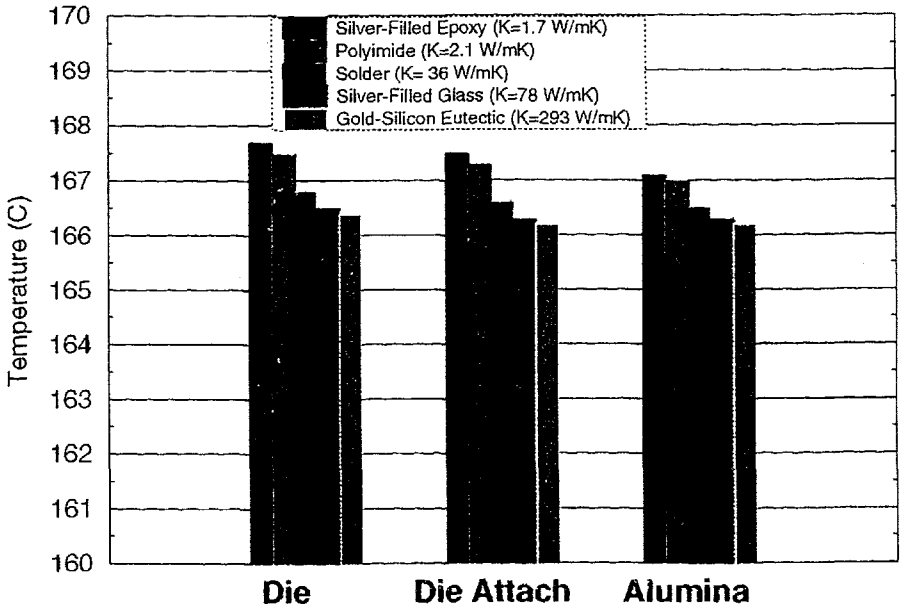

Figure 6-5. Maximum Temperatures in Constituent Materials for Different Die Attach Materials

6.1.2.2 Effect of Die Attach Thickness

The next design parameter studied was the thickness of the die attach layer. Only two different die attach materials, silver-filled epoxy and silver-filled glass, were analyzed. These two materials represent a wide range of thermal conductivities from 1.7 W/m°C for silver-filled epoxy up to 78 W/m°C for the silver-filled glass. The first set of analyses are those discussed in the preceding section in which the thickness of the die attach layer was 0.025 mm (0.001 inch). In the second series, the die attach was 0.076 mm (0.003 inch) thick. In all four analyses the base of the alumina substrate was assumed to be adiabatic.

Figure 6-6 shows the maximum temperatures in the die, die attach, and alumina for the two thicknesses of silver-filled epoxy and silver-filled glass die attach materials. For the silver-filled epoxy (lower thermal conductivity), the die attach thickness has a measurable effect on temperature rise. The increase in temperature is approximately 2°C greater for the thicker die attach material in both the die and the die attach and approximately 0.5°C greater in the alumina substrate. For the silver-filled glass (higher thermal conductivity), the temperature rise is the same for the thin and the thick die attach material. The effect of changing die attach thickness from 0.025 mm (0.001 inch) to 0.076 mm (0.003 inch) is stronger for materials with lower thermal conductivities. By extrapolation, materials with a higher thermal conductivity than silver-filled glass (such as gold-silicon eutectic) should not show a significant difference in temperatures in this range of thicknesses. Furthermore, because the thermal conductivity of a silver-filled polyimide material is very close to that of the silver-filled epoxy, the effect of die attach thickness for polyimide should be very similar to that of the epoxy.

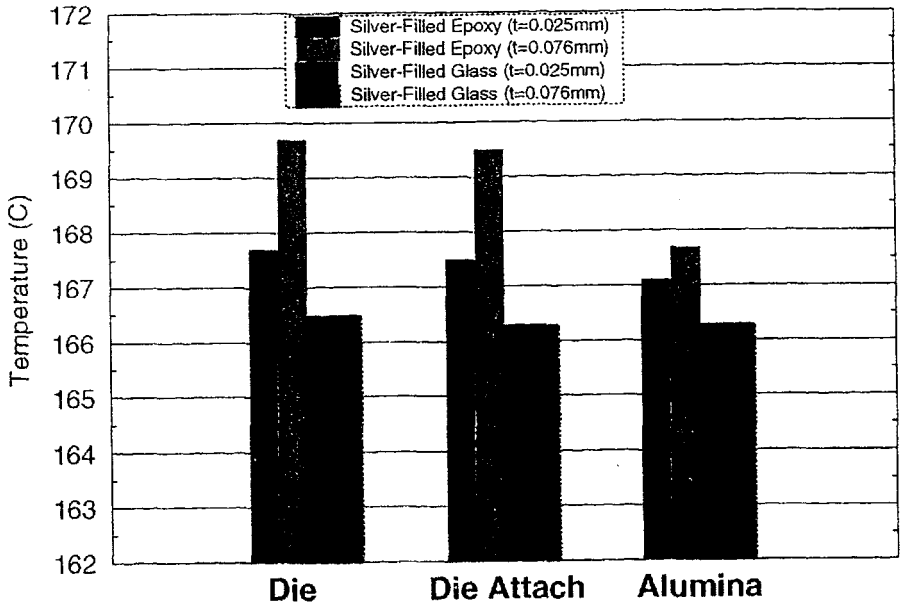

Figure 6-6. Effect of Die Attach Thickness for Silver-Filled Epoxy (K=1.7 W/mC) and Silver-Filled Glass (K=78 W/mC)

6.1.2.3 Effect of Alumina Purity

Purity of the alumina substrate will affect the temperature rise in the constituent materials because the thermal conductivity of the alumina is directly related to its purity. A purer alumina will have a higher thermal conductivity and should produce lower temperatures. For the scope of this study, 96% alumina (K=15 W/m°C) and 99% alumina (K=21W/m°C) were compared. In

both cases, the die attach was assumed to be 0.025 mm (0.001 inch)-thick silver-filled epoxy, and the base of the alumina substrate was assumed to be adiabatic.

As shown in Figure 6-7, the purity of the alumina has a substantial effect on the temperature increase. The total temperature rise in the die and die attach materials was 17.5°C for 96% alumina versus 13°C for 99% alumina; in the alumina the temperature rise is 17°C versus 12.5°C. These represent roughly a 27% decrease in temperature rise when the higher purity alumina is used.

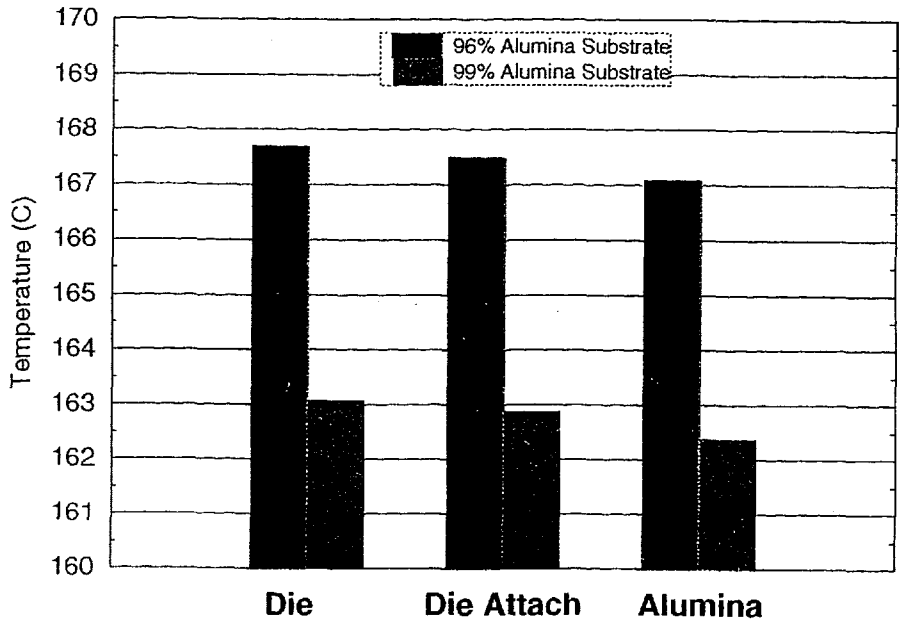

Figure 6-7. Effect of Alumina Purity on Temperature Rise in Constituent Materials

6.1.2.4 Effect of Boundary Condition Applied to Alumina Substrate Base

In all previously described analyses, the base of the alumina substrate was assumed to be an adiabatic surface, i.e., no heat flow was allowed through this surface. This condition simulates a perfectly insulated surface and maximizes the temperature increase in the parts. It thus provides an upper bound to the temperatures. In the actual part, the alumina substrate is bonded to an aluminum plate that will conduct heat away from the part alleviating the temperature increase to some extent. For the purposes of this parameter study, the aluminum plate itself was not modeled. Instead, a series of analyses was conducted assuming that the base of the alumina substrate was held constant at 150°C. This condition corresponds to the aluminum acting as a perfect conductor of heat away from the part and thus provides a lower bound to the temperature rise in the part.

Figure 6-8 shows the temperature rise in the constituent materials for the two bounding cases for both 96% and 99% pure alumina substrate. In these analyses, the die attach was assumed to be 0.025 mm (0.001 inch) thick silver-filled epoxy. As in previously described analyses, the outside edges of the alumina were assumed held at a constant 150°C and the initial temperature was a uniform 150°C. The type of thermal boundary condition on the substrate base has a very pronounced effect on the temperature rise in the part for both alumina purities. For the worst case of a completely insulated base, the temperature rise in all constituent materials is about 17°C for 96% and 13°C for 99% alumina. However, when the base of the alumina is treated as a heat sink, the temperature rise is only 4°C. The actual behavior of the alumina substrate will be between these two bounding cases. For components attached to the alumina where the aluminum backing plate is exposed to the atmosphere, the temperature rise may approach the upper bound. However, for components mounted at points where the backing plate is attached to the motor housing, heat conduction away from the circuit will be enhanced. In these locations, the temperature rise will be closer to the lower bound.

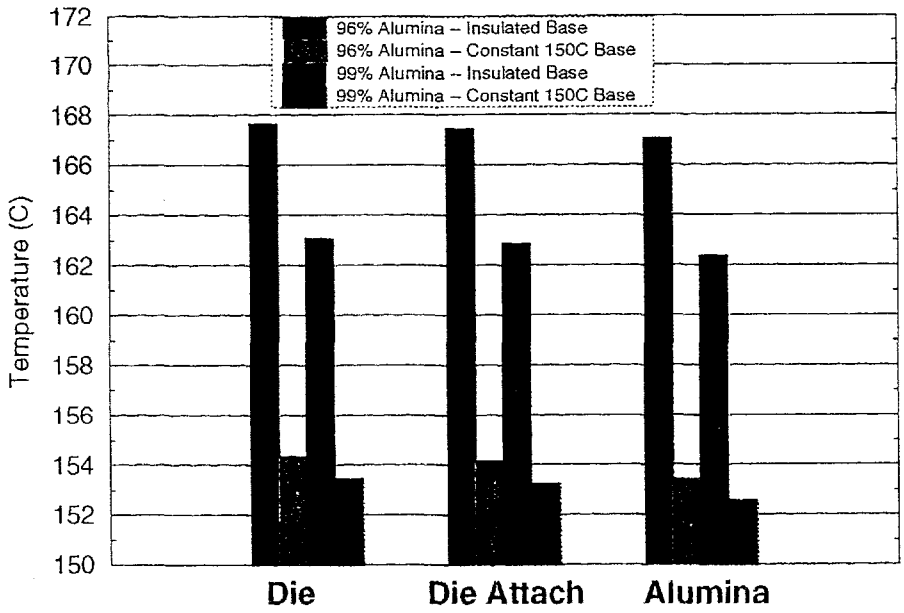

Figure 6-8. Effect of Thermal Boundary Condition Applied to Substrate Base on Temperature Increase in Constituent Materials

6.1.2.5 Effect of Wire Bonds

All previous analyses were performed assuming no wire bonds on the die. To examine the effect of the presence of a wire bond and the size of the wire, the finite element model was modified as

shown in Figure 6-9. Here, a wire (shown in light blue) is explicitly included in the analysis. Due to the symmetry conditions described earlier, only one fourth of the wire cross-sectional area is modeled. This model actually represents two wires of equal cross-sectional area positioned on opposite sides of the plate. The actual part only has a single wire bond. However, modeling the single wire as two wires, each with half the cross-sectional area, should not significantly affect the maximum temperatures computed. As in some of the previously described analyses, the die attach thickness in this series was assumed to be 0.025 mm (0.001 inch), and the base of the alumina substrate was assumed to be adiabatic.

Finite element results for the part without any wire bonds are compared to those for three different sizes of aluminum (K=155 W/m°C) wire in Figure 6-10. Although the maximum temperatures are nearly identical for all three sizes of wire, they are substantially higher for the part with no wire bonds. The presence of even the smallest 0.254 mm (0.010 inch) diameter wire lowered the temperature rise from more than 17°C to less than 11°C for a 35% improvement.

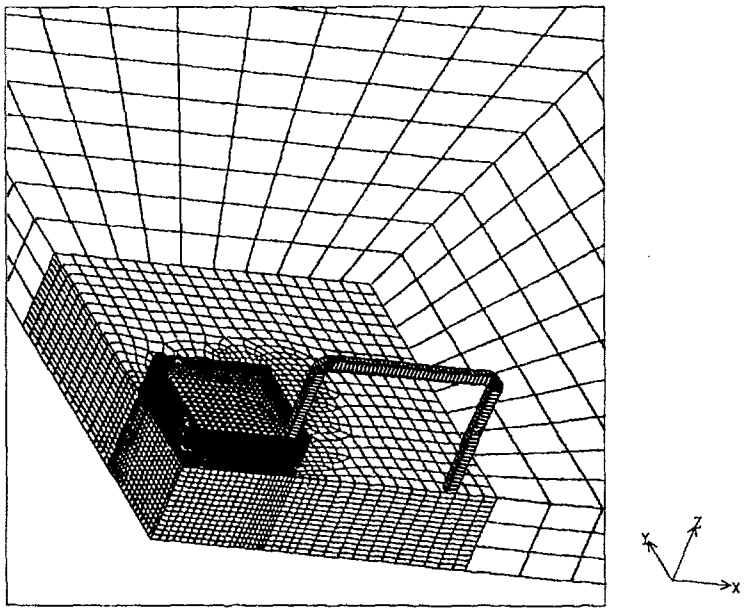

Figure 6-9. Finite Element Model of Single Die With Wire Bond to Alumina Substrate

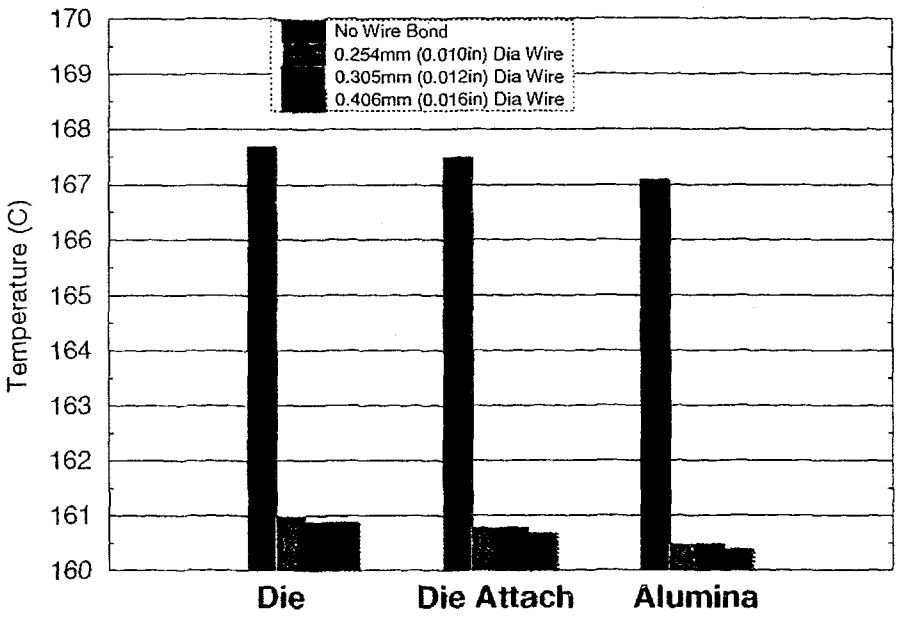

Figure 6-10. Effect of Bonded Aluminum Wire Size on Temperature Increase in Constituent Materials

6.1.3 Summary of Thermal Analyses

Several finite element analyses were performed to assess the effects of several parameters of a hybrid circuit design on the temperature rise during operation. The simplified finite element model consisted of a single die attached to an alumina plate. The factors investigated included the type of die attach material and thickness, alumina plate purity, the thermal boundary condition on the base of the alumina substrate. For all analyses, the die was assumed to have a steady-state power output of 0.75 W.

Results of the finite element analyses indicate that in the worst case, the temperature rise is 17.5°C in the die and die attach and 17°C in the alumina substrate. While the type of die attach material had some effect on the temperature rise, the difference in maximum temperatures was less than 2°C even for two orders of magnitude difference in thermal conductivity. Likewise, the thickness of the die attach had very little effect on the maximum temperatures for a silver-filled glass with a thermal conductivity of 78W/m°C, and only a minor effect (less than 2°C) for the silver-filled epoxy with a conductivity of 1.7W/m°C. The die attach material and thickness probably have little effect on maximum temperatures because these materials form a very thin layer in the part. It is therefore concluded that die attach materials with thermal conductivities in

the range of 1.7W/m°C would be acceptable for the hybrid module from a thermal stress point of view.

On the other hand, the purity of the alumina substrate and the thermal boundary condition on the base of the substrate had a significant effect on the maximum temperatures. Using a 99% alumina substrate reduced the temperature increase by approximately 27% below that of a 96% alumina. While the use of 99% alumina would improve the temperature rise in the die and die attach materials, it can not be used for thick film technology because the rougher surface of the 96% alumina is required to achieve adequate thick film metallization adhesion. The effect of thermal boundary condition was even more dramatic. At the one extreme of an insulated alumina base, the temperature rise was approximately 17°C. At the other extreme, when the alumina base is modeled as a heat sink, the temperature increase was only 4°C. The actual hybrid circuit is mounted on an aluminum plate so the temperature rise would fall somewhere between these two extremes. For a component mounted in an area where the aluminum plate is exposed to the atmosphere, the temperature rise would be expected to be near the upper bound. In areas where the aluminum plate is attached directly to the motor housing, the temperature rise would be closer to the lower bound.

A final design parameter investigated was the effect of the wire bonds on the temperature increase in the constituent materials. Finite element results indicated that even the presence of a single 0.254 mm (0.010 inch) diameter aluminum wire reduced the temperature increase in the part by 35%. However, no significant additional improvement was observed for larger wire sizes up to 0.408 mm (0.016 in) in diameter.

6.2 Technology and Adhesive Selection

6.2.1 Adhesive Selection Criteria

Eutectic die attach was eliminated from consideration for several reasons: (1) eutectic die attach was not considered a high-volume die attach process, (2) inconsistent or poor quality back side metallization can cause die attach problems, (3) it was questionable as to whether the power MOSFETs could withstand the die attach temperature of 400°C, and (4) a single adhesive was desired for use with all the components mainly for reasons of simplicity in processing and materials compatibility. The eutectic die attach process would have been used only for silicon die, and another die attach material would be required for the discrete components. The main advantage in using eutectic die attach was that the gold-silicon eutectic material has a high thermal conductivity as compared to the other types of materials. It also has adequate strength. The eutectic die attach process is not susceptible to stress relief cracking for the small die sizes used in this hybrid and would not add any organic materials to the hermetic package.

Solders with melting points between 183°C and 320°C were also eliminated for several reasons. Solders often require flux to facilitate the soldering operation. Residual flux left on the hybrid due to inadequate cleaning can create both immediate processing problems and reliability problems

later in the life of the hybrid. Another concern with using a solder at an operating temperature of 175°C is that solders will experience an increased rate of grain growth and intermetallic growth. Loss of strength and possibly leaching of the thick film metallization could occur. Back side metallization is also required for solder. The advantages of solders are that they have reasonably high thermal conductivities, adequate strength, and do not add any organic materials to the hermetic package.

Silver-filled glasses also require high processing temperatures of over 350°C, which exceed the 225°C processing limit and were eliminated for the prototype assembly. Some of the glasses also require an additional drying step in the process. The advantages of using these materials are similar to advantages of the solders: they have reasonably high thermal conductivities, adequate strength, and do not add any organic materials to the hermetic package.

6.2.2 Survey of Commercially Available Organic Adhesives

The remaining technology to consider was organic adhesive attachment. Several types of organic adhesives are available, such as epoxies, polyimides, thermoplastics, and other miscellaneous adhesives. A survey of organic adhesives was conducted at Sandia. Due to the time constraints of this CRADA, only commercially available adhesives could be considered. This precluded Sandia from developing its own adhesive or from evaluating experimental adhesives from various vendors. Some of the vendors contacted were developing new adhesives that were reportedly better suited for this application, but they were still in the laboratory stage.

Table 6-2 lists the requirements that were identified for the given application. These requirements were based on the processing, testing, and reliability requirements defined by Delphi. For instance, the electrical design of this module included tantalum capacitors that had a maximum temperature limit of 225°C. This upper temperature limit eliminated the use of some of the adhesives. While not every adhesive vendor was contacted, a large number of vendors were consulted for their recommendations. The following vendors were considered: Ablestik, Alpha, Dexter, Dow Corning, Du Pont, Emerson Cummings, Epo-tek, Furane, Johnson-Matthey, Olin-Hunt, Tracon, and Zymet.

Table 6-2: High Temperature Die/Component Attach Adhesive Requirements

Continuous Operating Temperature	170°C
Maximum Processing Temperature	225°C
Glass Transition Temperature	>175°C (ideally)
Thermal Stability (weight loss)	<1% @ 300°C
Thermal Conductivity	>1.5 W/m°C
Internal Water-Vapor Content	Capable of Passing MIL-STD-883D Method 1018.2
Volume Resistivity	Capable of passing MIL-STD-883D Method 5001.2
Ionic Purity	Capable of passing MIL-STD-883D Method 5011.2
Bond Strength	Capable of passing MIL-STD-883D Method 2019.5
Processing Parameters	Suitable for use a high-volume application.

The requirements for the adhesive were basically the same as the requirements for any organic adhesive. The exceptions were the higher continuous operating temperature and the severe temperature cycling conditions. The adhesive selected must be thermally stable at operating temperatures up to 175°C. The maximum processing temperature must not exceed 225°C. Ideally, the glass transition temperature should exceed the operating temperature range of the module. Outgassing of water vapor and other organic products from the adhesive into the hermetic package must be minimized through proper materials selection and process development, that is, vacuum bake-out prior to hermetic sealing. The adhesive must be low in ionic content to minimize the possibility of corrosion in the hermetic package. Particularly, the corrosion of the aluminum metallization on the silicon devices must be minimized within the package. The strength of the adhesive must withstand the operating temperatures, the temperature cycling requirements, and the mechanical shock and vibration requirements defined by Delphi. Processing considerations are also important, because the hybrid module is a high-volume product. These processing considerations are related to the dispensing and curing of the adhesive. The chosen adhesive material should work well in a high-volume manufacturing line.

The adhesive should be able to be dispensed rapidly and uniformly in thickness and area. The curing time and temperature schedule used should be compatible with high-volume production. Other important parameters are the pot life and shelf life, porosity, and resin bleed out.

6.3 Description of Screen Test

The adhesives evaluated in the screen test are listed in Table 6-3. The three adhesives that had processing temperatures which were greater than the 225°C limit are marked with an asterisk. With the exception of the last entry in the table, all of the adhesives are filled with silver particles for electrical conductivity. The insulative adhesive was added to the screen test because a nonconducting adhesive may be needed to stake the main body of the tantalum capacitors to the substrate for added mechanical strength. The selection of this insulative adhesive was based on a vendor recommendation.

Table 6-3: List of Selected Adhesives for the Screen Test

Adhesive	Glass Transition Temperature	Process Temp/Time
Epoxy		
Ablestik 84-1LMIT	103°C	150°C/1 hr
Ablestik 84-1LMINB1	90°C	150°C/1 hr
Ablestik 8700E	160°C	175°C/1 hr
Ablestik 8175	90°C	150°C/30 min
Ablestik 8175A	80°C	150°C/3 min
Dexter CNB 658-14A	60/? °C[1]	165°C/6 min
Epo-Tek H35-175MP	80/150°C[1]	180°C/1 hr
Miscellaneous		
Johnson Matthey 7000	240°C	150 to 380°C/<30 min
Epo-Tek E-3081	235°C	200°C/1 hr
Polyimide		
*Ablestik 71-1F	240°C	150&275°C/.5&.5 hr
Ablestik 969-1	236°C	200°C/1 hr

Thermoplastic		
Ablestik P86A	125°C	100&195°C/.5 & 1hr
*Stayform 501	180°C	275 to 375°C/~0.1 hr
Stayform 581	85°C	160 to 250°C/~0.1 hr
Glass		
*Johnson-Matthey 6100	390°C	390°C/45 min[2]
Insulative Epoxy		
Ablestik 968-2	139°C	150°C/2 hours

[1] This material has two glass transition temperatures

[2] Total process time is approximately 45 minutes with the time at peak temperature being 7 to 10 minutes

The screen evaluation included the following tests: volume resistivity, mechanical strength at room and elevated temperature, mechanical strength after temperature cycling, thermal stability, and processibility. Three different types of samples were designed for the screen test and are described later. The screen test samples were fabricated with one adhesive at a time. The adhesives were processed according to the vendor's recommendations even though it was recognized that some process improvements might be needed. For the epoxy and miscellaneous adhesives, this processing involved a chemical reaction commonly known as curing. For the thermoplastic and glass adhesives, however, the attachment process did not involve any type of chemical reaction. Rather, these materials undergo a physical change in properties during the attachment process. For instance, the thermoplastic material softens and the glass powders melt, but they never change in chemical composition. For simplicity, this chapter will use the terms "as-processed" or "as-bonded" to include both chemical or physical types of attachment processes. Because the purpose of the screen test was to reduce the number of potential adhesives, not many resources were used for failure analysis. Instead, the results of each test and adhesive were compared to identify the best performers.

6.3.1 Mechanical Strength

The die shear samples used gold-backed silicon ICs. The size of these ICs was 0.085 inch by 0.085 inch. The die were bonded to test samples with each type of adhesive. The test samples were alumina substrates metallized with either Du Pont 5725 gold thick film metal or Du Pont 6262 silver thick film metal. The majority of the adhesives were tested on Du Pont 5725 thick film gold. Two adhesives (6100 and 8175A) were tested on the silver thick film metal. Most of the adhesives were in paste form and were applied with a syringe-dispensing unit. An as-processed bondline thickness from 0.0005 inch to 0.001 inch thick was desired for the paste adhesives. However, two thermoplastic film adhesives (501 and 581) were also included in the

screen test and each had a thickness of 0.003 inch. Thickness measurements were taken after processing to monitor the actual bondline thickness.

Die shear tests were conducted at room temperature and at 170°C to determine the as-bonded shear strength of each adhesive. The 170°C die shear testing was performed to measure the strength of the adhesive at a temperature to which the adhesive could realistically be exposed. (These tests were performed before the upper temperature limit was identified as 175°C.) In most cases, five shear tests were conducted for each adhesive at both temperatures. The results of these tests are shown in Table 6-4 as Groups 1 and 2. The criteria used for this test was MIL-STD-883D Method 2019, which sets the minimum acceptable shear load based on the area of the die. The minimum allowable shear load for the die size used was 5 kg. In some cases, values between 2.5 and 5 kg may be considered acceptable depending on the type of failure mode. For this screen test, adhesives were given a letter grade of A,B,C or D. Adhesives which had shear loads greater than 20 kg were given an A. In this case, the die shear samples did not fail because the maximum load the die shear tester can apply is 20 kg. Adhesives samples which failed at shear loads between 5 and 20 kg were given a B. Adhesives samples which failed at shear loads between 2.5 and 5 kg were given a C. Finally, adhesives which failed at shear loads less than 2.5 kg were given a D. As Table 6-4 shows, only one adhesive received a C for the room temperature shear tests (Group 1). All other adhesives passed this test. Degradation in strength was observed for almost every adhesive when shear tested at 170°C (Group 2). Seven of the sixteen adhesives received a grade of C or D.

Table 6-4: Comparison of Adhesive Properties

Adhesive Type	Group 1 Shear Strength @25°C	Group 2 Shear Strength @170°C	Group 3 Shear Strength Post T/cycle	Group 4 Thermal Stability	Group 5 Volume Resistivity @ 25°C	Group 6 Processing Factors
84-1LMINB1	A	B	B	C	A	A
84-1LMI	A	C	A	D	A	A
8700E	A	B	A	C	B	A
8175	A	C	A	B	B	A
8175A	A	B	A	B	C	A
CNB658-14A	B	C	B	D	D	A
H35-175MP	A	B	B	D	B	A
7000	B	A	B	D	D	A
E-3081	B	B	B	D	A	A
969-1	B	B	B	D	A	D
71-1F	B	B	B	D	B	D
581	B	D	B	D	D	A
501	C	C	B	B	A	A
P-86A	B	D	B	D	A	D

Adhesive Type	Group 1 Shear Strength @25°C	Group 2 Shear Strength @170°C	Group 3 Shear Strength Post T/cycle	Group 4 Thermal Stability	Group 5 Volume Resistivity @ 25°C	Group 6 Processing Factors
6100	B	A	D	C	A	A
968-2	A	C	A	D	N/A	A

Key:
Groups 1 to 4
A = strengths > 20 Kg
B = 5< strengths < 20 Kg
C = 2.5 < strengths < 5 Kg
D = strengths < 2.5 Kg

Group 5
A = values < 1 microohm-meter
B = 1 < values < 3 microohm-meter
C = 3 < values < 5 microohm-meter
D = value > 5 microohm-meter

Group 6
A = voids < 10% of bonded area
B = 10% < voids < 20% of bonded area
C = 20% < voids < 30% of bonded area
D = voids > 30% of bonded area

Group 3 of Table 6-4 lists the results of die shear tests for samples that were temperature cycled for 100 cycles. The cycling conditions were 30 minutes at -65°C and 30 minutes at 180°C. The transfer between hot and cold was immediate air to air. These parameters approach thermal shock conditions. In most case, five shear tests were conducted for each adhesive. Degradation was again observed in shear loads as compared to Group 1 but only one adhesive received a C or D. In retrospect, additional cycling prior to testing may have eliminated some more of the adhesives.

6.3.2 Thermal Stability

Samples identical to those used in the mechanical strength section were used for the thermal stability tests. Samples were aged for 48 hours at three temperatures, 150°C, 225°C and 300°C. Then, each of these samples was shear tested at room temperature. The purpose of the aging was to determine, indirectly, to what extent the adhesive had degraded due to the high temperature aging. For example, if an adhesive is thermally stable up to a particular temperature, then theoretically its shear strength should not be degraded by aging at that temperature. While the 150°C aging temperature was within the expected operating temperature range, the higher temperatures were used to accelerate the degradation for comparative purposes between the adhesives. Adhesives that are more thermally stable should withstand higher temperatures than less stable adhesives. The results of aging at the three temperatures are (1) the 150°C aging had little, if any, effect on the shear strengths of any of the adhesive samples. (2) Approximately half of the adhesives aged at 225°C experienced some degradation in shear strength. (3) Of those that experienced degradation at 225°C, only one adhesive dropped below the 5 kg shear load value. (4) Almost every adhesive had significant drops in shear load values after the aging at

300°C. The samples aged at 300°C are shown as Group 4 in Table 6-4. Ten of the sixteen adhesives were graded as Ds.

6.3.3 Volume Resistivity

Standard test samples were used for the volume resistivity tests and were fabricated according to MIL-STD-883D, Method 5011.2. A controlled amount of each conductive adhesive was applied to glass slides with a doctor blade. The finished samples consisted of an as-processed adhesive area 0.100 inch wide by at least 2.50 inches long. The thickness of the as-processed adhesive was measured for each sample and averaged 0.002 inch thick. Four-wire resistance measurements were then taken of the adhesive samples, and the volume resistivity of the adhesive was calculated. Volume resistivity values less than or equal to 5 microohm-meters were considered acceptable for conductive adhesives. For the screen test, measurements were made at room temperature only. Calculated values of volume resistivity are shown in Group 5 of Table 6-4. Adhesives were given grades of A to D. Volume resistivities of less than 1 microohm-meter were graded as As. Volume resistivities between 1 and 3 microohm-meters were graded as Bs. Volume resistivities between 3 and 5 were graded as C's. Finally, volume resistivities greater than 5 microohm-meters were graded as D's. The three adhesives, graded D's, did not pass this test.

6.3.4 Processibility

All of the die shear samples (30 for each adhesive) were x-rayed after processing to measure the amount of porosity in the adhesive bondline. The amount of porosity (voids in the adhesive bond) was estimated as a percentage of the total die area. Again, letter grades of A to D were given to each adhesive. A was given to adhesives which had voids less than 10% of the bonded die area. B was given to adhesives which had voids between 10% and 20% of the bonded die area. C was given to adhesives which had voids between 20% and 30% of the bonded area. Finally, D was given to adhesives which had voids greater than 30% of the bonded area. Results are listed in Group 6 of Table 6-4. Three adhesives had noticeably more porosity in the adhesive bondline: the polyimide adhesives (71-1F and 969-1) and a paste form of a thermoplastic material (P86-A). Dice were also attached to glass slides to visually determine the amount of porosity in the adhesive bondline. This information is not reported because it generally complemented the x-ray inspection results. Bonding die to glass slides is a useful technique to gain quick information regarding porosity in the adhesive bondline. However, it is not 100% reliable because it can not detect porosity that is trapped within the bulk adhesive or at the epoxy-to-die interface.

The die shear test samples were also visually inspected after processing according to MIL-STD-883D Method 2017. Inspection criteria included the amount of adhesive, cracks in the adhesive, anomalies in the adhesive (that is, stringers, pits, ecetera), and resin bleed out. With the exception of resin bleed out, all the samples passed the visual inspection. All of the epoxy and miscellaneous adhesives experienced some degree of resin bleed out. While bleed out is

undesirable, it was not considered a criteria for elimination because resin bleed out can be removed by plasma cleaning. The assembly personnel were also instructed to record any observations about the ease or difficulty in assembling the test samples with each adhesive. The main observations noted were the differences in the viscosity of the adhesives and the steps taken to control the bondline thickness.

6.3.5 Downsizing the List of Adhesives

Once all of the tests were completed, the results were compared to select the best adhesives for detailed characterization. The selection criteria used was as follows:

(1) Adhesives that failed the volume resistivity tests at room temperature were eliminated. These included 581, 7000, and CNB658-14A. Adhesives 581 and 7000 probably would have passed the volume resistivity test if they were processed at a higher temperature.

(2) Adhesives that failed the high temperature shear test (Group 2 of Table 6-4) were eliminated. Two adhesives failed, 581 and P86-A. Again 581 probably would have passed this test if it had been processed at a higher temperature.

(3) Adhesives that failed the x-ray porosity inspection were eliminated. This involved the two polyimide adhesives and one thermoplastic adhesive, P86-A. Both 969-1 and 71-1F had significant porosity that might have been reduced by improving the processing. However, this would have increased the processing time significantly and therefore would not be well suited for a high volume application. Also, the shear strength values for the polyimides were not as high as the epoxies.

(4) The thermal stability of the remaining adhesives was compared (Group 4 of Table 6-4) and the adhesives with the highest strengths were selected if they had not been previously eliminated. At this point, the selection process became a little subjective and some of the eliminated adhesives may also have been acceptable. Three epoxies performed noticeably better in Group 4 of Table 6-4 and were selected for the second phase of the evaluation. These adhesives were 8700E, 8175, and 8175A.

At this point, volume resistivity tests were repeated for the three remaining epoxy adhesives and two other adhesives, 6100 and E3081. The four-wire resistance measurements were acceptable for all five adhesives when measured at 60°C. At 150°C, the four-wire resistance measurement were slightly erratic for three adhesives (8700E, 8175, and 8175A) but very erratic for two adhesives (E3081 and 6100). The reasons for the erratic behavior were not explored except to verify that there was not a measurement error. A decision was made to include only the three adhesives 8700E, 8175, and 8175A for further evaluation.

Three other adhesives, E3081, 6100, and 7000 looked promising for Sandia applications but were not included for the second phase of the adhesive evaluation. The 6100 adhesive is a silver-filled

glass adhesive and requires a processing temperature of approximately 400°C which was much higher than the maximum limit of 225°C. It is interesting for Sandia applications because it is a nonorganic adhesive. The 7000 adhesive is a cyanate ester based adhesive. The vendor recommended a processing temperature range of 150°C to 380°C for the 7000 adhesive. For the screen test, the 7000 adhesive was processed at 200°C and it failed the volume resistivity tests. However, additional conversations with the vendor revealed that for optimum volume resistivity, processing at 300°C was required. Other than this shortcoming, the 7000 adhesive performed well. Another miscellaneous adhesive which also performed reasonably well was E-3081. Its only shortcoming was it thermal stability at 300°C but may be suitable for other lower temperature environments.

6.4 Main Adhesive Evaluation

6.4.1 Experimental Design

Once results from the screen test were evaluated, the selected adhesives were evaluated more extensively to determine which adhesive(s) would be the optimum choice for use in the high temperature application. The evaluation was designed to accomplish the following goals: (1) to determine the contact resistance and thermal impedance of the adhesive joints, (2) to determine the mechanical strength of the adhesive joints, (3) to determine the thermal stability of the adhesive after being sealed in a hermetic package, and (4) to quantify some of the thermal properties of the adhesives. For the first two goals, the evaluations were performed on as processed samples, after accelerated aging, temperature cycling, thermal shock, and mechanical shock and vibration. In some cases, the samples were exposed sequentially to a predetermined series of the environmental stresses mentioned above. For the third goal, simulated hybrid module samples were evaluated as-processed and after accelerated aging. In the fourth goal, bulk adhesive samples were used to compare the thermal properties of the materials. In each case, the tests required different designs of test samples. With the exception of the bulk adhesive samples, all of the test samples were fabricated using the two main conductor materials of interest, Du Pont 6262 silver or Heraeus 4740 silver-platinum. Test sample design and fabrication are explained in the appropriate sections.

The schedules for the accelerated aging, temperature cycling, thermal shock, and mechanical shock and vibration were based largely on the qualification test specifications obtained from Delphi. The main difference in testing between Delphi and Sandia was that Delphi performed the qualification tests when the hybrid module was assembled in its housing. Testing performed at Sandia was conducted on simulated hybrid modules without the housing. Two different temperature cycling schedules and one thermal shock schedule were used to condition the samples for the electrical and mechanical tests. The standard temperature cycling schedule was from -50°C to 160°C, in dry air, with 90 minute temperature transition times, and a 30 minute dwell at each temperature extreme. The total cycle time was 240 minutes. The static temperature cycle was from -65°C to 180°C, in dry air, with an immediate transfer between temperatures extremes using a shuttle chamber with 30 minute dwell at each temperature

extreme. The total cycle time was 60 minutes. The thermal shock conditions were storage at 150°C in air for 30 minutes with an immediate transfer to 10°C deionized water for 1 minute.

The mechanical shock and vibration tests could not be duplicated because Delphi performed these tests on the hybrid module in its higher assembly configuration. Sandia's Environments Engineering Group was consulted to recommend a test specification that would correctly duplicate Delphi's specification given the differences in sample configuration.[2] A housing was obtained from Delphi to measure transfer functions and determine whether Sandia's test fixture would mimic the boundary conditions for Delphi's next assembly. Sandia's test fixture was shown to be adequate with some minor modifications to the test levels. The Environments Engineering Group also recommended a vibration test schedule that would produce as much fatigue damage in 32 hours as the 66 hour test schedule listed in Delphi's engineering specification. The abbreviated vibration test was generated by using commonly accepted accelerated testing practices. The mechanical shock schedule used by Sandia was 50 g, 11mS half sine, 5 shocks per each axis, 15 shocks total. The vibration schedule used by Sandia is shown in Table 6-5.

Delphi's test specification also called for temperature-humidity cycling. The parameters for this cycling were 10°C to 90°C, with a 90 minute temperature transition time from the two temperature extremes and 30 minutes dwell at each temperature extreme. Relative humidity was maintained at 95% during the complete cycle. The qualification test called for 500 cycles. This qualification test was intended for modules assembled into the next assembly. Test samples designed for Sandia's testing simulated hybrid modules and were usually nonhermetic. Therefore, this environmental stress was not applicable for the evaluations planned for this project.

Table 6-5: Random Vibration Schedule

Level	Breakpoint (Hz)	Intensity (G^2/Hz)	dB	Time (hh:mm)
1	20	0.005	0	00:15
2	200	2.0	-3	02:00
3	300	0.50	-6	02:45
4	500	0.10	-9	05:00
5	1000	0.050	-9	00:36
6	2000	0.010	-9	00:04

6.4.2 Contact Resistance and Thermal Impedance of the Adhesive Joints

6.4.2.1 Electrical Test Design

A thick film sample was designed and fabricated at Sandia to test the contact resistance and thermal impedance of the three adhesives.[3] Thick film samples were fabricated with Du Pont 6262 silver metal and Heraeus 4740 silver-platinum metal printed on 96% alumina substrates, 0.040 inch thick. The primary test vehicle was to be the MTP36N06E FET manufactured by Motorola. The parameter of interest was RDSON at 10 Amps. A diode was also added to the test structures in order to evaluate the thermal characteristics of the die attach adhesives. The diode selected is similar to the 1N4003 manufactured by Sprague. The diode chip is 0.04 inches square, and comfortably handled a 3.5 W power pulse for this evaluation. The substrate test structures were designed to provide electrical connections to each field effect transistor (FET) and diode. The FET connection pattern was designed to provide Kelvin connection close to the substrate end of the wire bonds to isolate the die attach characteristics from test socket contact resistance. In the future, a Kelvin connection to the source bond pad is recommended to eliminate wire bond resistance effects. The test samples were fabricated using standard die attach and wire bonding processes. The components were die attached in equal numbers of the three adhesives, 8700E, 8175 and 8175A. With the exception of one aluminum, 0.010 inch diameter wire bonded to the source pad of the FET, all other wire interconnections were 0.001 inch diameter gold wires. Test samples were sealed with a ceramic cover using a nonconductive epoxy and were not considered to be hermetic. Following the sealing, 0.010 inch aluminum wires were bonded to outside leads of the test sample for electrical connections to the testers.

Approximately 72 samples were fabricated, each containing one diode and one FET for the die attach adhesive study. All of the adhesive samples were electrically tested after

Table 6-6: Outline for Electrical Tests

(1)	Electrical test samples as-assembled for baseline data (24 samples X 3 adhesives) Divide samples into three groups
(2)	Group 1: High temperature aging (6 samples X 3 adhesives) High temperature (180°C) age samples. Electrical test samples at 250 hour intervals up to 1000 hours.
(3)	Group 2: Standard temperature cycling (6 samples X 3 adhesives) Standard temperature cycle samples (1000 cycles / 4000 hours) Electrical test samples at 250 cycle intervals.

(4) Group 3: Sequential environmental exposure (12 samples X 3 adhesives)
Thermal shock samples (6 hours / 10 cycles)
Electrical test
Divide sample into two groups

Group 3A Static temperature cycle samples (100 hrs/100 cycles) (6 samples X 3 adhesives)
Electrical test
(Planned temperature-humidity cycling deleted)

Group 3B Static Temperature Cycle samples (100 hrs/100 cycles) (6 samples X 3 adhesives)
Vibration test samples
Electrical test
Mechanical shock samples
Electrical test

Note: Group 2: Testing at the 500 cycle interval was not conducted because the tester was down.

Note: Group 3B: Testing after vibration was not conducted because the tester was down.

assembly and were then divided into the three test groups outlined in Table 6-6. Exact parameters for the temperature cycling and thermal shock are listed in Section 6.4.1.

Test programs were developed to test the typical electrical characteristics of both the FET and the diode. Control devices of similar electrical function were tested at each test point to monitor test system performance. Most parameters tested were not of interest for the study of adhesives, but were included to insure the validity of the critical parameters of interest. For the FET, RDSON is tested with ID = 10 Amp, and VGS = 20 V. For the diode, the VF was measured with IF = 1 mA. Then the IF was pulsed up to 2 Amp for 75 mS. The VF was then re-measured with IF = 1 mA. The approximate temperature rise of the diode junction was then calculated by dividing the change in VF by 2 mV/°C. Results of both RDSON and approximate temperature rise have been plotted for each test interval.

6.4.2.2 Test Results

A number of the initial test samples contained FETs which failed electrical test parameters. FETs which read over-range on gate to source leakage (IGSS) at 20V were not used for the analysis of RDSON performance as the IGSS over-range condition indicates that the 20V VGS

test condition cannot be successfully applied. In one case, this left only two samples in a group. All the diode samples passed the initial electrical tests.

Results for each group as shown in Table 6-6 are presented in Appendix C1. There are plots for each adhesive for RDSON data and plots for each adhesive for the approximate temperature rise data for each of the test groups. A summary of the results for each test group follows.

Test samples aged for 1000 hours at 180°C (Group 1) survived the accelerated aging with out any evidence of any degradation in the temperature rise of the diode samples. A downward drift in temperature rise of up to 20% can be seen in the plots for Group 1 (Appendix C1) This drift is thought to be real changes in the test samples because the control data changed less than 5%. All of the diode test samples remained functional at the completion of the high temperature aging test. The improvements in temperature rise of the diode samples can be correlated with improvements in the mechanical strength of the die attach joints for samples subjected to accelerated aging. This topic is discussed further in Section 6.4.3. RDSON values for each adhesive also do not show any degradation due to the high temperature aging.

The temperature rise of the diodes and the RDSON values were not negatively effected by the standard temperature cycling process (Group 2). However, the downward drift of the temperature rise of the diodes observed with the aging samples was not noted. The number of samples available to test decreased at the 1000 cycle point because of failed external wire connections. Samples without the external wires were not testable.

No significant changes in the approximate temperature rise of the diodes or the RDSON values were observed in any of the three adhesives for test samples exposed to the thermal shock conditions and the static temperature cycling (Group 3A). Finally, no significant changes in the approximate temperature rise of the diodes or the RDSON values were observed in any of the three adhesives for test samples exposed to the thermal shock, vibration, and mechanical shock conditions (Group 3B).

6.4.2.3 Summary

To summarize the electrical test results, none of the environmental exposures listed in Table 6-6 appear to have caused any detrimental effects on the three adhesives used in this evaluation. In fact, some improvement in electrical and thermal conductivity was observed with the high temperature aging group. Problems were experienced in this test initially due to high leakage currents of the FETs during the initial electrical tests. This is attributed to improper wire bond parameters for bonding the 0.010 inch aluminum wire to the source pad of the FET. While unfortunate, this was Sandia's first attempt at bonding this particular type of die with the bond pad above the active area of the silicon using a new type of large diameter wire bonder. Another problem already mentioned involved losing external wire leads after 1000 cycles. This problem is discussed in greater detail in Section 6.1. Finally, there were no significant differences noted between the three adhesives or the two thick film silver compositions used in the evaluation.

6.4.3 Mechanical Strength Tests

6.4.3.1 Mechanical Strength Sample Fabrication

The mechanical strength samples consisted of a thick film pattern of Heraeus 4740 silver platinum metal printed over areas of dielectric material and bare alumina. The thick film samples were fired six times before any die or capacitors were attached. Both the multiple printings and firings were done to simulate the design and fabrication of a real hybrid circuit. The pattern was basically a matrix of bond pads which allowed the testing of the following components: (1) a Sprague tantalum capacitor (0.230 inch by 0.250 inch) attached to 4740 printed over dielectric, (2) a Kemet ceramic capacitor (0.250 inch by 0.230 inch) attached to 4740 printed over dielectric, (3) a dummy IC, 0.200 inch by 0.250 inch, without any backside metallization attached to 4740 printed over dielectric (4) two dummy ICs without any backside metallization measuring 0.100 inch by 0.100 inch. One IC was attached to 4740 printed over dielectric and the other IC was attached to 4740 printed over alumina The die and capacitors were attached to the samples with the three adhesives using the vendor recommended parameters.

The main focus of the mechanical strength tests was to perform die shear tests on samples of the three types of adhesives. The samples were visually inspected prior to any die shear testing for adequate adhesive material, for cracks in the adhesive fillet, and for discoloration. The room temperature die shear tests were conducted on a Dage BT22 die shear tester. An Instron Series IX Automated Materials Testing System was used to perform the die shear tests at 170°C. Table 6-7 outlines the environmental conditions to which the mechanical test samples were exposed and the periodic die shear tests that were performed. For baseline data, samples were shear tested at room temperature and at 170°C as they were initially processed. The samples were then divided into groups, as described in Table 6-7, and were subjected to a variety of thermal and mechanical stresses. Die shear tests were performed periodically throughout and at the end of environmental stresses.

Table 6-7: Mechanical Strength Tests

Group 1	Shear test 3 samples/adhesive as-assembled for baseline data. Shear test 3 samples/adhesive at 170°C as-assembled for baseline data.
Group 2	High temperature (180°C) age samples. Withdraw 3 samples/adhesive for shear tests at 250 hour intervals. Withdraw 3 samples/adhesive for 170°C shear tests after 1000 hours.
Group 3	Standard temperature cycle samples (4000 hours / 1000 cycles) Withdraw 3 samples/adhesive for shear tests at 250 cycle intervals. Withdraw 3 samples/adhesive for 170°C shear tests at 1000 cycles.

Group 4	Thermal shock samples (5 hours / 10 cycles) Withdraw 3 samples/adhesive for shear test. Withdraw 3 samples/adhesive for 170°C shear test. Split Group 4: (30 samples/adhesive - 4A & 12 samples/adhesive - 4B)
Group 4A	Static temperature cycle samples (100 hours / 100 cycles) Withdraw 3 samples/adhesive for shear test. Withdraw 3 samples/adhesive for 170°C shear test. (Planned temperature-humidity cycling deleted)
Group 4B	Static temperature cycle samples (100 hours / 100 cycles) Vibration test samples Mechanical shock samples Withdraw 3 samples/adhesive for shear test. Withdraw 3 samples/adhesive for 170°C shear test.

6.4.3.2 Results of Visual Inspections and Die Shear Tests

The results of the shear tests and visual inspections are listed in Appendix C2. The general conclusions from these tests are listed below according to the groups outlined in Table 6-7.

Group 1 consisted of the as-processed samples that were shear tested at 25°C or 170°C. Initially, all test adhesives passed the MIL-STD-883D Method 2019 requirements for the large and small die when sheared at room temperature. There were not any distinguishable differences in the adhesion of the small die attached to silver thick film metallization which was printed over dielectric material or printed over the alumina substrate. The small number of shear tests and inherently large standard deviation of the shear test prevented differences, if any, in substrate and thick film composition from being detected. In fact, differences in the adhesion of the adhesives over the different substrate treatments was indistinguishable for all of the groups listed in Table 6-7. The shear test values for all three adhesives were lower at 170°C than at 25°C. This was expected because 170°C is above the glass transition temperatures for three adhesives and the adhesives would naturally be softer at this point. The 8700E adhesive had noticeably greater strength at 170°C than the other two adhesives. This is probably due to the fact that the 8700E adhesives glass transition temperature was reported to be 160°C while the other two adhesives had glass transition temperatures of less than 100°C. Some failures were experienced at 170°C for the small die attached with the 8175 and 8175A adhesives, which may be attributed to the low glass transition temperatures.

Group 2 consisted of shear test samples aged at 180°C for 1000 hours. Room temperature shear tests were conducted at 250 hour intervals up to 1000 hours. Some improvements in adhesion

were noticed early in the aging for all three adhesives. The results reported here, however, are for the complete 1000 hours of accelerated aging. There is some evidence that the strength of the small die did degrade for the 8700E and 8175 adhesives. Sample sizes were not large enough to establish any statistical significance to the numbers. However, all of the shear test values were well above the test criteria of 2.5 kg. There is also some evidence that the strength of the small die increased during the 1000 hours of 180°C aging for the 8175A. Again, sample sizes were not large enough to establish any statistical significance. Increased strength could be due to this particular material curing to a greater degree during the 180°C aging. The strength of the large die exceeded the capability of the shear tester before and after aging for 1000 hours at 180°C. Therefore, it was impossible to determine if the adhesive strength degraded with this size of die. The tantalum and ceramic capacitors were not used in the high temperature aging portion of this evaluation. The 8175 and 8175A adhesives discolored slightly due to the aging process.

Shear tests were performed at 170°C for Group 2, also. The 8700E adhesive still had higher shear values than the 8175 and 8175A adhesives. However, the improvement in strength was not as noticeable as it was with Group 1. Generally speaking, all of the shear values for Group 2 were higher than their corresponding value before the 1000 hours of aging (Group 1).

Group 3 consisted of the samples that were subjected to the standard temperature cycling schedule described earlier. This particular temperature cycling schedule was the most damaging of all the environmental stresses used to qualify the hybrid module. Die shear tests were performed at room temperature after 250 cycle intervals up to 1000 cycles. The tantalum capacitors experienced significant degradation in shear strength. In fact, some degradation in strength was observed after the first 250 cycles. Visible cracks in the adhesive and capacitor body were observed after 500 cycles. By 750 cycles, cracks were prevalent in all samples. The strength of the ceramic capacitors and the large die exceeded the capability of the shear tester before and after 1000 cycles. Therefore, it was impossible to determine if the adhesive strength degraded with this size of die. However, cracks in the adhesive fillets were observed in the ceramic capacitors and large die. Cracks in the adhesive of the ceramic capacitors were observed as early as 500 standard temperature cycles and after 750 temperature cycles were prevalent in all samples. Cracks in the adhesive of the large die were first observed after 750 temperature cycles and were prevalent after 1000 temperature cycles. There is some evidence that the strength of the small die did degrade after 1000 cycles for all three adhesives. Some degradation in strength was observed after the first test period of 250 cycles. All of the shear test values are well above the test criteria of 2.5 kg. Very little in the adhesive of the small die was observed. None of the three adhesives performed particularly better or worse than the other two adhesives.

Adhesive samples were also shear tested at 170°C after 1000 standard temperature cycles. The temperature cycling noticeably degraded the adhesion strength for all five components (tantalum capacitors, ceramic capacitors and the three die) attached with the 8700E adhesive. However, all of the die shear test values were well above the 2.5 kg minimum standard. The temperature cycling slightly degraded the adhesion strength for all five components attached with the 8175A adhesive. Some values were below the 2.5 kg test criteria. The adhesion strengths of all the

components attached with the 8175 adhesive increased after the temperature cycling. While this may indicate a more durable adhesive at high temperatures, the visual inspections revealed that all three types of adhesives experienced cracking in the fillets of the two capacitors and large die at the same test intervals.

Group 4 consisted of the sequential environmental stress exposures listed in Table 6-7. Visual inspections and shear tests were performed after thermal shock and static temperature cycling. Visual inspections after 10 thermal shock cycles revealed some fillet cracks with adhesives 8175 and 8175A when used to attach the tantalum capacitors. Shear tests after 10 thermal shocks also revealed significant degradation in shear strength for the 8700E and 8175 adhesives when used to attach the tantalum capacitors. Visual inspections after 100 static temperature cycles revealed pull back of all three adhesives from the terminations of both types of capacitors. The strength of the ceramic capacitors and the large die exceeded the capability of the shear tester before and after 100 cycles. Therefore, it was impossible to determine if the adhesive strength degraded with this size of die. There is some evidence that the strength of the small die did degrade after 100 cycles for all three adhesives. Some degradation in strength was observed after the first test period of 250 cycles. However, all of the shear test values are well above the test criteria of 2.5 kg.

Visual inspections and shear tests were performed on samples that had been exposed to 100 static temperature cycles followed by vibration. The tantalum capacitors experienced some degradation in shear strength for all three adhesives after the vibration stress. The strength of the ceramic capacitors and the large die exceeded the capability of the shear tester. Therefore, it was impossible to determine if the adhesive strength degraded with this size of die. There is some evidence that the strength of the small die did degrade after vibration for all three adhesives. Nevertheless, all of the shear test values are well above the test criteria of 2.5 kg. None of the three adhesives performed particularly better or worse than the other two adhesives. Visual inspections after vibration revealed cracks in the adhesive fillets of both the tantalum and ceramic capacitors with all three adhesives.

Visual inspections and shear tests were performed on samples that had been exposed to 100 static temperature cycles followed by vibration and then mechanical shock. Visual inspections after mechanical shock revealed cracks in the adhesive fillets of both the tantalum and ceramic capacitors with all three adhesives. The tantalum capacitors experienced some degradation in shear strength for all three adhesives after mechanical shock. The strength of the ceramic capacitors and the large die exceeded the capability of the shear tester in most cases after mechanical shock conditioning. Therefore, it was not possible to determine if the adhesive strength degraded with this size of die. There was some evidence that the strength of the small die did degrade after mechanical shock for the 8700E and 8175 adhesives. All of the shear test values are well above the test criteria of 2.5 kg.

Shear tests were also performed at 170°C for the sequential environmental exposures as listed in Table 6-7. These results parallel the results of the shear tests at room temperature. As

compared to the as-processed shear strengths, the adhesion strengths of the three adhesives improved after the ten thermal shocks. The improvements in strength were most noticeable with the 8700E adhesive which has the higher glass transition temperature. One failure each was noted with the 8175 and 8175A adhesives, which can be attributed to the lower glass transition temperature. Shear tests performed on samples exposed to 10 thermal shock and 100 static temperature cycles revealed degradation in the adhesion strengths of the 8700E and 8175A adhesives and an increase in strength for the 8175 adhesive. This behavior was very similar to the room temperature shear tests. Finally, shear tests performed on samples after exposure to 10 thermal shocks, 100 static temperature cycles, and mechanical vibration and shock also revealed degradation in the adhesion strengths of all three adhesives. However, only the 8175 and 8175A adhesives had failures below the 2.5 kg test criteria, one each for the 8175 and 8175A adhesives.

In comparing the room temperature shear test results of the sequential environmental conditioning, two comments can be made. (1) The strength of the ceramic capacitors and the large die exceeded the capability of the shear tester in almost every case before and after static temperature cycling (STC)/vibration/shock conditioning. Therefore, it is impossible to determine if the adhesive strength degraded with the ceramic capacitor or with this size of die. However, it is known that the adhesion strength of the large die is greater than 20 kg, which is well above the minimum test criteria of 2.5 kg. (2) The adhesive strengths for all three adhesives when used to attach the tantalum capacitors and both of the small die seem to have degraded slightly after each of the three conditioning treatments. Due to the nature of the testing and the small sample sizes, it is impossible to determine if the degradation was due to the first conditioning treatment (static temperature cycling) or if the effect was cumulative (STC/mechanical vibration and shock). It may be that all of the degradation was caused by the 100 static temperature cycles and that the mechanical vibration and shock are relatively benign. Alternatively, each sequential conditioning treatment could have caused a cumulative degrading effect that cannot be distinguished with the small sample sizes. In either case, the degradation was slight, and for the small die all shear loads were well above the Mil-Std 883D test criteria. Similar statements can be said about the 170°C shear tests of the sequential environmental conditioning. The main difference is that some failures were experienced with the small die and adhesives with the lower glass transition temperature.

Failure mode analyses of each shear test were recorded with the shear test data. For the room temperature shear tests, the samples failed within the silicon die on the initial as-processed samples. After the accelerated aging, the failure modes were approximately split between silicon die failures or failures at the interface between the thick film metallization and adhesive. After the initial tests, a shear test failure mode was typically a mixture of different failure modes. For example, a common failure mode might be that 75% of the die area would fail within the silicon die and the remaining 25% would fail at the adhesive to thick film interface. The temperature cycling and sequential environmental exposures caused the failure mode to occur within the adhesive itself (a cohesive failure) or at either interface between the adhesive and die or thick film metallization. Failure modes for the 170°C shear tests were similar to the room temperature tests

with the exception that failures within the silicon die were very rare. This would be expected since the test temperature exceeded the glass transition temperatures.

6.4.3.3 Summary

The following comments can be made to summarize the mechanical strength tests.

(1) Differences in adhesive strength of each adhesive over silver/dielectric and silver/alumina were indistinguishable. There is either no effect of the dielectric material or the shear tests are not sensitive enough to detect the difference.

(2) No problems were encountered that could be attributed to the silver thick film metallization.

(3) The 8700E, with the exception of the standard temperature cycling group, performed better at 170°C than the 8175 and 8175A adhesives. As explained, this material's higher glass transition temperature is higher than the other two adhesives. Strength at high temperature is certainly important for this application.

(4) The phenomena of increased strength due to high temperature aging was observed early during the aging of the samples. Some slight degradation was observed after 1000 hours of aging. High temperature aging is not considered a problem for these adhesives.

(5) The standard temperature cycling (-50°C to 160°C) was particularly damaging for all three adhesive with all five types of components attached. The tantalum capacitors, ceramic capacitors and large die were most negatively affected by the temperature cycling. It was difficult to distinguish one particular adhesive which performed better in this group because all three adhesives did not survive out to 1000 cycles.

(6) An early hypothesis questioned whether an adhesive with a glass transition temperature within the mid-range of the temperature cycling range or an adhesive with a glass transition temperature close to the upper limit of the temperature cycling range would perform better in shear tests. The question remains unanswered primarily because none of the three adhesives satisfactorily survived the standard temperature cycling. However, item 3 above with the temperature cycling results suggests that an adhesive with a glass transition temperature higher than the operating temperature may be the best adhesive for this application.

(7) The effects of the sequential environmental exposures did cause some degradation in shear strengths but no particular adhesive performed significantly better. However, the effects of the sequential environmental exposure may be considered secondary when compared to the effects of the standard temperature cycling.

(8) The tantalum capacitors were by far the most problematic components to be attached because of the mismatch in the coefficient of thermal expansion between the capacitor and the alumina

substrate. As mentioned earlier, cracking of the adhesive or capacitor body and decreased adhesive strength were observed in the tantalum capacitors. Other small experiments were conducted to look at other configurations of tantalum capacitors. These other configurations involved different types of capacitor terminations which could have reduced the mechanical stress on the adhesives during temperature cycling. Unfortunately, these alternative capacitors did not survive the temperature cycling either and were really designed for lower temperature applications.

6.4.4 Thermal Stability of Adhesives in Hermetic Packages

One of the major long-term failure mechanisms that exist in microelectronics are moisture-induced problems such as corrosion, electrochemical metal migrations, and electrical parameter shifts.[4] Electrochemical metal migrations are of particular concern when silver metallization is used. Moisture in a package can occur by a lack of hermeticity, outgassing of materials inside the package, or poor processing controls during assembly of the component. Residual gas analysis (RGA) is used to measure the moisture level within the hermetically sealed package.

Samples of the three adhesives, 8700E, 8175 and 8175A, were processed using a simulated assembly process and then submitted for residual gas analyses. The purpose of this analyses was to identify and measure detrimental products, particularly water, that outgassed from the adhesives after the hybrid module was hermetically sealed. Integrated circuits 0.200 inch by 0.200 inch were attached in 40 pin leadless chip carriers using the vendor recommended processing conditions for the three adhesives. Prior to hermetic sealing, the adhesive test samples were vacuum baked at 175°C at a pressure of 1 Torr for two hours. Resistance seam sealing was used to hermetically seal the leadless chip carriers. Samples of each adhesive type were sent for residual gas analysis after hermetic sealing and after aging the samples at 180°C for 1200 hours.

Table 6-8 lists the RGA results of the samples which were analyzed after hermetic sealing and before the 1200 hour aging at 180°C. All of the adhesives samples passed the MIL-STD-883D Method 1018 criteria of less than 5000 part per million of water vapor. Also, the values of the other gases, nitrogen, oxygen, argon, and carbon dioxide, are typical for a hermetically sealed package. Even though all of the adhesive samples did pass the 5000 parts per million criteria for the water vapor, they were higher than expected. Experience has shown that a vacuum bake out immediately before hermetic sealing can reduce the amount of water vapor within the package. These adhesive samples were vacuum baked at the parameters listed in the previous paragraph. Bake out parameters were based on the highest curing temperature of the three adhesives. From the water vapor results in Table 6-8, it is recommended that additional optimization of the vacuum bake out parameters be conducted to determine if a lower moisture content can be achieved.

Table 6-8: Residual Gas Analysis for Adhesive Samples After Hermetic Sealing

Adhesive	8700E		8175		8175A	
Sample No.	1	2	1	2	1	2
Gas Volume (cc)	0.034	0.039	0.038	0.038	0.038	0.040
N_2 (%)	97+	98+	98+	98+	98+	98+
O_2 (ppm)	6360	1580	600	150	2230	3190
Ar (ppm)	180	230	170	150	230	260
CO_2 (ppm)	11500	9860	8030	8030	7640	5790
H_2O (ppm)	4870	4680	4480	4820	3820	3340
H_2 (ppm)	nd	nd	nd	nd	nd	nd
Organics (ppm)	nd	nd	nd	nd	nd	nd

Table 6-9 lists the RGA results that were analyzed after the hermetic packages had been aged for 1200 hours at 180°C. Unfortunately, the moisture values increased significantly due to the high temperature aging. The volume of the gas inside the package also increased significantly. The RGA samples are leak tested before analyzing to ensure that they are hermetically sealed. Since all of the samples passed the fine and gross leak testing, the increase in the volume of the gases within the package can be attributed to the generation of gases from within the package rather from penetration of gases from outside the package. Evaluating the quantities of other gases present, particularly the oxygen, carbon dioxide, hydrogen and organic gases leads to the conclusion that the adhesives within the package degraded at these temperatures and evolved gases that remained in the hermetic package. These results do not necessarily mean that these adhesives cannot be used for their intended application. It does mean that the vacuum bake out process should be optimized to, in essence, cause a controlled degradation of the adhesive prior to hermetically sealing to reduce moisture content within the hermetic package without degrading other properties such as mechanical strength and electrical and thermal conductivity.

6.4.5 Thermal Analyses of Adhesive

Various analytical tests were performed on the three chosen adhesives to compare specific properties of each adhesive. Samples of 8700E, 8175 and 8175A adhesive were analyzed by Thermogravimetric Analysis (TGA), Thermomechanical Analysis (TMA) and Differential Scanning Calorimetry (DSC), and Dynamic Mechanical Analysis (DMA).[5]

Table 6-9 Residual Gas Analysis for Adhesive Samples Aged 1200 Hours at 180°C

Adhesive	8700E			8175			8175A		
Sample No.	1	2	3	1	2	3	1	2	3
Gas Volume (cc)	.070	.071							
N_2 (%)	64+	61+	64+	58+	57+	54+	71+	72+	71+
O_2 (ppm)	nd	nd	nd	nd	nd	nd	nd	nd	nd
Ar (ppm)	430	50	490	670	750	660	750	700	980
CO_2 (ppm)	291000	310000	244000	146000	140000	136000	113000	109000	118000
H_2O (ppm)	31400	35700	84700	239000	246000	290000	134000	119000	127000
H_2 (ppm)	21900	21800	18800	24100	23400	20200	30100	33500	33300
Organics (ppm)	12800	15700	1130	12200	12300	11200	8810	8540	8880

TGA is a technique in which the mass of a substance is monitored as a function of temperature or time as the sample specimen is subjected to a controlled temperature program in a controlled atmosphere. This technique determines the temperature at which the adhesive begins to degrade as measured by weight loss, the amount of weight lost at a particular temperature, and the weight percent of silver in the adhesive. TMA is a technique in which changes in the dimensions of a sample are measured as it is subjected to a controlled temperature program. The coefficient of thermal expansion and the glass transition temperature (T_g) were measured by this technique. DSC is a technique in which the heat flow, to or from a sample, is measured as it is subjected to a controlled temperature program in a controlled atmosphere. The glass transition temperature was also measured by this method. However, the high silver loading of the adhesive rendered the DSC technique less sensitive than the TMA or DMA techniques. DMA is a sensitive tool for analyzing thermal mechanical transitions in solid polymer samples.[6] These transitions are temperature dependent changes in the molecular structure of motion of a material. DMA testing involves applying a sinusoidal strain to a sample and then measuring the resulting stress while heating the sample to a predetermined temperature at a controlled rate. The glass transition temperature and modulus of elasticity are two properties that can be measured with this technique.

For the thermogravimetric analyses, uncured bulk samples of 8700E, 8175A and 8175 were scanned from room temperature to 700° C, in air, at 10°C per minute. The percent weight loss for the three adhesives and the weight percent of silver are listed in Table 6-10. The MIL-STD-883D, Method 5011 requirement for weight loss at 300°C is less than 1%. There is no particular requirement for the weight percent of silver as long as the other requirements such as mechanical strength and electrical conductivity are acceptable.

Table 6-10: Results of TGA

Adhesive	% Weight Loss @ 300°C	Weight % Silver
8700E	0.5	80.1
8175	0.3	80.6
8175A	0.4	81.6

Bulk samples of the three adhesives were cured for the thermomechanical analyses at the following conditions: 8700E - 1 hour at 175°C, 8175 - 1 hour at 150°C, and 8175A - 10 minutes at 150°C. The TMA samples were scanned from 20°C to 225°C at 10°C per minute in nitrogen. The information gained from the TMA is shown in Table 6-11. The glass transition temperatures (T_g), measured by TMA were within 10°C for the 8175 and 8175A adhesives. However, the measured T_g for the 8700E adhesive, 108°C, was well below the value listed on the vendors data sheet of 160°C. With the exception of the 8700E adhesive, the coefficients of thermal expansion (CTE) are also relatively close to the values stated on the vendor data sheets. It was noted in sample preparation that the 8700E adhesive had many voids within the cured bulk sample while the other two adhesives were relatively void-free. The presence of voids could be the cause of the low T_g value and the discrepant CTE values for the 8700E adhesive.

Table 6-11 Results of TMA and DSC

	TMA	TMA	TMA	DSC
Adhesive	T_g (°C)	CTE α_1 (ppm)	CTE α_2 (ppm)	T_g (°C)
8700E	108	46	154	none detected
8175	83	55	190	84
8175A	84	57	187	86

Bulk samples of the three adhesives were cured for the differential scanning calorimetry at the following conditions: 8700E - 1 hour at 175°C, 8175 - 1 hour at 150°C, and 8175A - 10 minutes at 150°C. The 8175 and 8175A bulk samples were then scanned from 30°C to 150°C at 10°C per minute in nitrogen. The bulk sample of 8700E was scanned from 30°C to 200°C at 10°C per minute. DSC results are also shown in Table 6-11. The glass transition temperatures that were measured for the 8175 and 8175A were close to the values measured by the TMA. However, no glass transition

temperature was detected with the 8700E sample. Again, this was most likely due to the voids that formed in this material during the curing process.

Observations made during the mechanical and electrical tests implied that the adhesives were being cured to a greater degree during subsequent high temperature aging. This was seen as improved mechanical strength and electrical conductivity. Since the measured glass transition temperatures of the 8700E adhesive were much less than expected, a second DSC analysis was performed to measure the glass transition temperature as a function of extended high temperature aging at 175°C. The results of two different lots of 8700E aged for extended times are shown in Table 6-12. These results confirmed that the adhesives were indeed undergoing additional curing during the subsequent environmental conditions that various test samples were exposed to. The glass transition temperatures also approached the 160° value listed on the vendor data sheet. However, void formation in the bulk samples also occurred, casting some doubt on the accuracy of the T_g values.

Table 6-12 Glass Transition Temperature as a Function of Aging Time

Lot 1		Lot 2	
Time (hours)	T_g (°C)	Time (hours)	T_g (°C)
1	104	1	102
10	149	5	110
72	138	40	117
		215	122
		265	122

T_g measured by DSC
Aging Temperature = 175°C

Bulk samples approximately 9 mm by 5 mm by 1.3 mm in length, width and thickness, respectively, were prepared for the Dynamic Mechanical Analysis tests. The adhesives were processed at the following conditions: 8700E - 1 hour at 175°C, 8175 - 1 hour at 150°C, and 8175A - 10 minutes at 150°C. A Polymer Labs DMA was used to run a temperature sweep test from -60 to 180° using a dual cantilever bend geometry. The test frequency was 1 Hz and the temperature sweep rate was 4°C per minute. Figure 6-11 shows the results of the test for the 8175A adhesive in a E' and tan_delta vs temperature plot. This adhesive as well as the 8175 adhesive had values that correlated fairly well with the other tests performed. The glass transition temperatures of the three materials (8700E, 8175 and 8175A) as measured from the peak of the tan_delta are respectively: 64.3°C, 76.5°C, and 90.2°C. Again, the 8700E sample contained many voids which affected the glass transition temperature measurement.

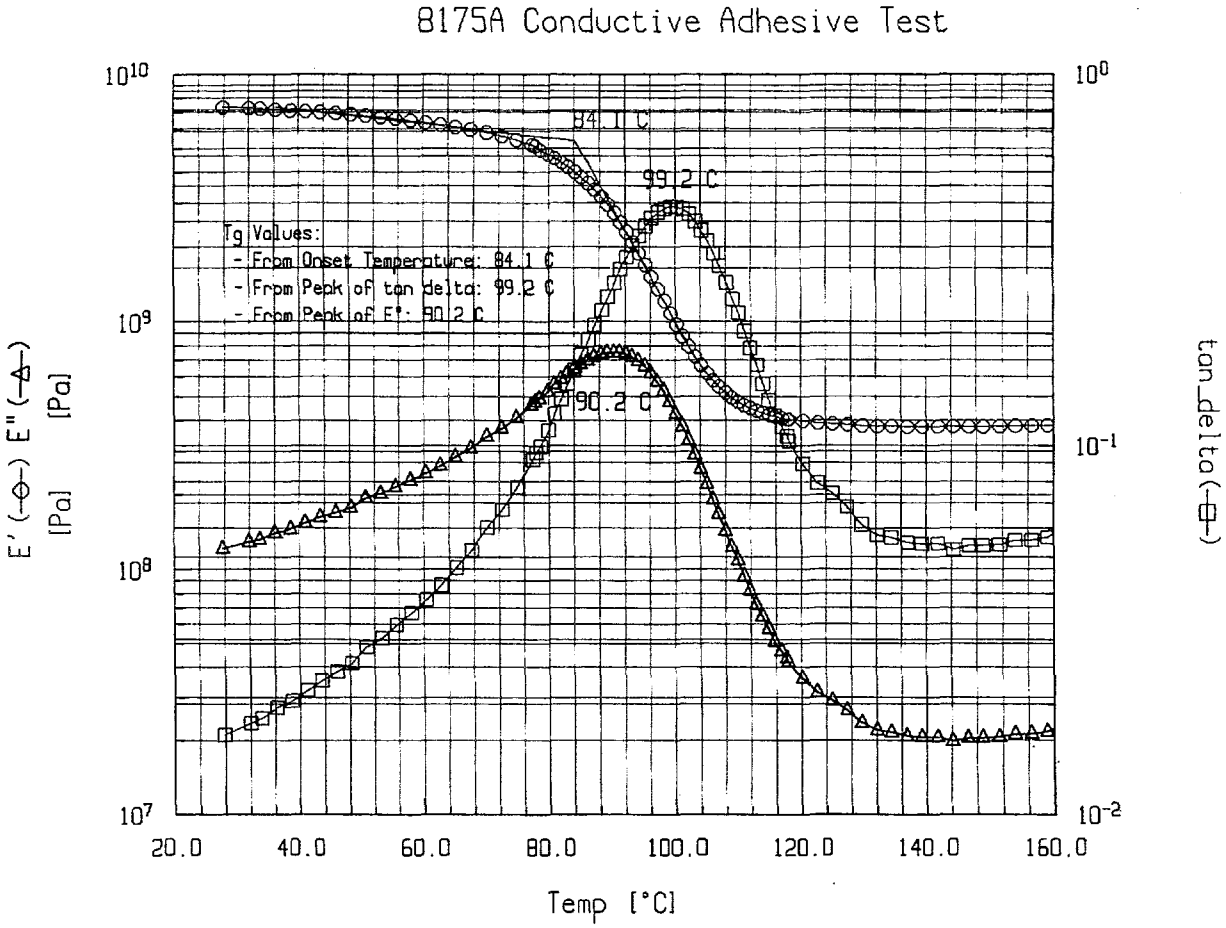

Figure 6-11. Results of the Test for the 8175A Adhesive in a E' and tan_delta Versus Temperature Plot.

As mentioned previously, voiding in the 8700E adhesive samples affected many of the thermal analysis results. However, this voiding that occurred during sample preparation for the thermal analyses was not observed in the die attach samples where the bondline thickness was much thinner. In fact, all three adhesive had low amounts of porosity in the die attach samples (see Group 6 of Table 6-4).

6.4.6 Summary of the Main Adhesive Evaluation

The following section summarizes the main points of the four areas of the adhesive evaluation, the contact resistance and thermal impedance of the adhesive joints, the mechanical strength of the adhesive joints, the thermal stability of the adhesives, and the thermal analyses of the adhesives.

The electrical tests revealed that all three adhesives performed satisfactorily after exposure to the environmental stresses which simulated the high temperature conditions. Problems with increased contact resistance of the die attach joints should not arise with any of the three

adhesives tested in the main evaluation. It is also expected that there should not be any problems with increased thermal impedance of these three adhesives.

The mechanical strength of the adhesives appears to be the most critical problem to overcome. While all of the adhesives experienced some degradation after exposure to the various environmental stresses, the temperature cycling was the most damaging. None of the three adhesives survived the room temperature shear testing after 1000 standard temperature cycles. High temperature strength was also a concern because two of the three adhesives had some failures during high temperature shear testing. The results of the mechanical testing suggest that an adhesive with a glass transition temperature higher than the operating temperature may be the best adhesive for this application. Other adhesives identified in the screen test may have performed better in this evaluation, but could not be considered due to the low processing temperature limit of the tantalum capacitors.

The residual gas analyses revealed that initially all three adhesives had acceptable levels of internal moisture. However, after high temperature aging, all of the adhesive samples had high moisture concentrations. This does not necessarily mean that the adhesives do not have adequate thermal stability, but could indicate that the vacuum bake out process requires further optimization. Further optimization could be achieved by increasing the bake out time and/or temperature. Bake out processes of over eight hours are not uncommon for some applications but may be a bottleneck for high volume production.

Finally, the thermal analyses verified properties for two of the three adhesives. The glass transition temperatures, coefficients of thermal expansion, and weight loss at 300°C all agreed fairly closely with the vendor data sheets. The third adhesive experienced a high degree of voiding during the sample preparation for the thermal analyses which rendered the test results inaccurate. Fortunately, the voiding phenomena only occurred in the bulk test samples and not in the actual die attach joints.

REFERENCES

1. Memo dated 8/20/93, "Effect of Hybrid Circuit Parameters on the Temperature Rise of a Single Die", from V. L. Porter to S. E. Garrett, Sandia National Laboratories.
2. Memo dated 2/24/95, "Random Vibration Test Specification for the GM Electronic Module", from J. S. Cap to S. E. Garrett, Sandia National Laboratories.
3. Memo dated 7/1/96, "Die Attach Adhesive Study", from J. McKenney & L Curtis to S. E. Garrett, Sandia National Laboratories.
4. D. D. Dylis and G. H. Ebel, "Long Term Package Integrity in a Military Environment," Proceedings of the 20th International Symposium for Testing and Failure Analysis, November 1994, pp. 163-168.
5. Memo dated 5/28/96, "Summary of Thermal Analysis Performed on Ablebond Epoxy", from C Robinson to S. E. Garrett, Sandia National Laboratories.
6. Memo dated 7/28/96, "Results of DMA Tests on Ablestik Ag-Filled Epoxies", from M. Stavig to S. E. Garrett, Sandia National Laboratories.

This page intentionally left blank

7. Wire Bond Interconnections for High Temperature Applications

Stephen E. Garrett
Edward V. Thomas

Field failure data has revealed that the majority of failures in electronic systems can be attributed to faulty interconnections. The high component count inherent with the throttle control module requires a large numbers of wire bond interconnections. Thus a thorough understanding of the behavior of this type of interconnect methodology in a high temperature environment is essential to reliably assure system performance.

This chapter describes the activities conducted to characterize wire bond interconnect technologies. Various evaluations were conducted for large diameter aluminum wire and fine gold wire bonded to different thick film metallizations. Experience at Sandia has historically been with fine aluminum and gold wire bonded to gold thick film metallization and aluminum IC bond pads. The design requirements for Delphi's hybrid module necessitated using larger diameter aluminum wire and fine gold wire interconnections. This chapter details the evaluations performed on the new material combinations and/or bonding processes. The large diameter aluminum wire evaluations were started first because they were considered more of a reliability risk than fine gold wires bonded to silver thick film metallization. G. G. Harmon rates the gold to silver intermetallic couple as having higher interface reliability than the aluminum to silver intermetallic couple.[1] Later in this project, the evaluation of fine gold wire to various thick film materials was begun.

Early in this project, Sandia recommended that a gold thick film metallization system be used for this module because of the high reliability requirements. The main concern when using gold thick film was considered to be intermetallic growth between the gold thick film and the large diameter aluminum bonds. While intermetallic growth in itself is not a problem, it can lead to Kirkendall voiding and wire bond failure. Despite the concerns with intermetallic growth, gold was still preferred over silver thick film metallization. Silver thick film metallizations have a history of problems with silver migration in the presence of moisture and corrosion resistance problems. In fact, silver has not been used as a thick film metallization for high reliability applications at Sandia. Based on Sandia's recommendation, the first pre-prototype units were fabricated with a gold thick film materials systems.

It was recognized, however, that the gold metallization may be too expensive for this application. Subsequent conversations with Du Pont and Heraeus, suppliers of thick film materials, suggested that less expensive silver thick film materials may be suitable for this application if they were in a hermetic package. These vendors agreed to perform evaluations on their most promising gold, silver and palladium/silver thick film materials. These evaluations included high temperature aging, temperature cycling, and autoclave testing (similar to 85°C/85% humidity testing). When completed, the vendors presented data that showed that aluminum wire bonds to silver thick film

metal survived high temperature aging, temperature cycling, and autoclave exposures.[2,3] Du Pont stated that their new dielectric material was more hermetic than older dielectric materials. The improvements in hermeticity were due to crystallizable dielectrics which would theoretically minimize problems with silver electromigration. These evaluations suggested that aluminum wire bonds to silver thick film metallization might merit further investigation as a low cost replacement for aluminum wire to gold thick film metal combinations.

In the meantime, viable alternatives to lower the projected cost of the hybrid module were considered. During a design review meeting, an agreement was reached between Sandia, Delphi, and CMAC to use a silver thick film materials system rather than a gold thick film materials system. However, the layout was designed to allow an alternative design if the aluminum wire bonds to silver thick film metal were proven unreliable. This option utilized aluminum tabs between the aluminum wire and the silver thick film metal. The tabs would be attached with a preselected die attach adhesive. The tabs eliminated the aluminum to silver couple. The objective at that point was to prove that the silver thick film system would survive the under the hood environment. If the silver thick film system did not survive, then the hybrid layout design would allow the use of the aluminum tabs. The use of aluminum tabs is a standard technology in the automotive industry and was not considered to be a reliability problem. However, the use of the aluminum tabs would have added extra cost to each unit.

Initial evaluations were based on aluminum wires bonded to gold thick film metallization. Later, other thick film metals compositions of silver, silver-platinum, silver-palladium, and palladium-silver-platinum were added to this evaluation. Even though the gold was too expensive for this application, it was kept in the evaluation to compare its performance with the other materials. The silver or silver-1% platinum metals were the preferred compositions based on their lower cost and higher electrical conductivity. However, the two palladium-silver metal compositions were also included in this evaluation as possible replacements for the silver or silver-1% platinum compositions. Palladium-silver thick film materials are already used extensively in the automotive industry but not in applications where high conductivity is required. For comparison, the sheet resistivity of Du Pont's silver and pallidium-silver materials are 1-2 milliohms/square and 32 milliohms/square, respectively. The Delphi hybrid module design required greater conductivities than the palladium silver metallizations.

Because of the severe environment in the engine compartment, Sandia recommended that the hybrid module be hermetically sealed. Another option, organic encapsulation, was considered later in this project. However, the main evaluations conducted for this program were planned with the intention of the hybrid module being hermetically sealed.

As part of the wire bond evaluation, Sandia was also requested to advise Delphi about minimum wire diameters for high current applications. Calculations were performed at Sandia to determine the minimum wire diameter that would support a 10 amp current load. The analysis included an examination of (1) the appropriate MIL-SPEC document using two different constants, (2) an updated methodology reported in the literature, and (3) the calculated wire

temperatures using an analytical formulation. The results of the different methodologies lead to wire diameters that ranged from 0.008 inch to 0.020 inch with the most accurate results in the range of 0.010 inch to 0.012 inch. The work concluded that a 0.010 inch diameter wire, not over 0.4 inch long when bonded at both ends to fairly conductive substrates, should safely carry a current load of 10 amps. However, due to the uncertainty of the material properties and bond quality, a slightly larger wire diameter of 0.012 inch was recommended for continuous duty. If the duty cycle is less, then the smaller diameter would be appropriate. Based on these thermal calculations conducted at Sandia and the power requirements of the hybrid module, the 0.010 inch diameter aluminum wire was chosen to interconnect the power MOSFETs.

This chapter will first describe the evaluation conducted to determine the reliability of direct bonded, large diameter aluminum wire bonded to various thick film metallizations. Section 7.2 describes the statistical modeling used to predict the life of aluminum wire bonds to particular thick film metals after exposure to particular environmental stresses. Section 7.3 concludes with a description of the evaluation performed with fine gold wire bonded to selected thick film compositions.

7.1 Large Diameter Aluminum Wire Bonding Evaluation

The goals of the large diameter aluminum wire bonding evaluation were to measure the mechanical strength and contact resistance of the aluminum wires directly bonded to the selected thick film materials. The intent was to develop models which would predict the lifetime reliability of the wire bond. Various environmental stresses were developed by Delphi to simulate the environment to which a hybrid module mounted under the hood of an automobile might be exposed. These environments are the same as those environments discussed in Section 6.4.1. Mechanical strength and electrical conductivity tests were conducted periodically throughout the environmental exposures to monitor the strength and contact resistance. The wire bonds were tested as-bonded and after being exposed to the environmental conditions listed in Table 7-1

Table 7-1: Conditioning Groups for Aluminum Wire Bonding Evaluation

160°C Aging for 8000 hours in ambient air
180°C Aging for 8000 hours in ambient air
210°C Aging for 2400 hours in ambient air
225°C Aging for 1200 hours in ambient air
Static Temperature Cycling, -65 to 180°C, with immediate transfer from hot to cold, 1 hour total cycle time, 1000 cycles
Power Temperature Cycling, -50°C to 160°C, with a 90 minute transition from hot to cold, 4 hour total cycle time, 1000 cycles
Highly Accelerated Stress Test (HAST) 140°C, 95% R.H., 3 atmospheres

7.1.1 Design of Experiment/Test Sample

Each thick film test sample consisted of an array of 92 wire loops for pull testing and a daisy chain continuity test loop that included a total of 116 individual wire bonds. Ten mil aluminum wire bonds were bonded to the thick film conductor and tab materials listed in Table 7-2. The nominal thick film metal compositions are also listed in Table 7-2. In all cases, the substrates were 96% alumina. The aluminum wire bond/thick film metallization combinations were tested after a single firing and after multiple firings (six total). The wire bond/thick film combinations were also tested with the thick film metal printed over the alumina substrate and over a printed and fired layer of dielectric material. The differences in the number of firings and in the alumina base versus dielectric base were designed to simulate the processing of an actual throttle control module that has multiple layers of conductor, dielectric, and resistor materials. Two versions of dielectric thick film pastes were used: Du Pont QM42 and Heraeus IP9117. The thick film metal and dielectric materials were fired in an air atmosphere with 10 minutes at a peak temperature of 850°C and a total profile time of 1 hour. Therefore, there were four subgroups for each type of thick film conductor. A group of aluminum wire bonded to aluminum tabs was also tested for a baseline comparison to the thick film materials. Later in the project, another silver thick film material was added to the evaluation at CMAC's request. This material was Du Pont's European version of Du Pont 6262. The European version is called QM15 and does not contain cadmium for ES&H reasons. Only two groups of QM15 were tested: single-fired QM15 printed over dielectric and multiple-fired QM15 printed over the alumina substrates.

Large diameter aluminum bonding had not previously been performed at Sandia. An Orthodyne Model 20B large diameter aluminum wire bonder was acquired for this project. The wire bonder was characterized, and a certain degree of familiarity and expertise with the bonder was gained before the actual evaluation was conducted. Prior to each test group being wire bonded, a designed experiment was conducted to optimize the bonding parameters for each thick film material group. Bond parameter optimization was important to ensure that any degradation of the wire bonds after accelerated aging would be attributed to the accelerated aging rather than poor initial bond quality.

Following the sample preparation, samples were divided into groups for isothermal aging at four temperatures, temperature cycling using Delphi's two temperature cycling schedules (see Section 6.4.1 for greater detail), and for temperature/humidity cycling. As discussed in Chapter 6, the temperature/humidity qualification test was intended for modules assembled into the next assembly. Because the test samples for the wire bonding evaluation were not sealed in a hermetic package, the temperature/humidity cycling was not applicable for this evaluation and was canceled. A new test sample and experiment was proposed to thoroughly study the corrosion resistance of the complete hybrid module hermetically sealed and encapsulated with an organic gel.

Table 7-2: Experimental Matrix for Aluminum Wire Bonding

Group #	Firings	Base Material	Thick Film Material / Composition
1	1	alumina	Du Pont 5725 Au
2	6	alumina	Du Pont 5725 Au
3	1	dielectric/alumina	Du Pont 5725 Au
4	6	dielectric/alumina	Du Pont 5725 Au
5	1	alumina	Du Pont 6262 Ag
6	6	alumina	Du Pont 6262 Ag
7	1	dielectric/alumina	Du Pont 6262 Ag
8	6	dielectric/alumina	Du Pont 6262 Ag
9	1	alumina	Du Pont QM21 75%Ag/25%Pd
10	6	alumina	Du Pont QM21 75%Ag/25%Pd
11	1	dielectric/alumina	Du Pont QM21 75%Ag/25%Pd
12	6	dielectric/alumina	Du Pont QM21 75%Ag/25%Pd
13	1	alumina	Heraeus 4740 Ag/1%Pt
14	6	alumina	Heraeus 4740 Ag/1%Pt
16	1	dielectric/alumina	Heraeus 4740 Ag/1%Pt
17	6	dielectric/alumina	Heraeus 4740 Ag/1%Pt
15	N/A	aluminum tabs	N/A
18	1	alumina	Heraeus 4913 75%Ag/24%Pd/1%Pt
21	6	dielectric/alumina	Heraeus 4913 75%Ag/24%Pd/1%Pt
22	6	alumina	Du Pont QM15 Ag
23	1	dielectric/alumina	Du Pont QM15 Ag

7.1.1.1 Isothermal Aging

Four different temperatures were selected for the isothermal accelerated aging. All of the material groups were aged at these four temperatures: 160°C, 180°C, 210°C, and 225°C. The 160°C temperature was requested by Delphi because it represented actual temperatures that the hybrid module would see. The three remaining temperatures were selected by Sandia. Initially, the temperatures of 180°C and 225°C were selected. The selection of the final temperature was purposely delayed until aging data from the other three temperatures were collected. The options for the final temperature were a temperature greater than 225° or a temperature between 180°C and

225°C. Failures occurred reasonably early for the 225°C samples but relatively late at 180°C. Therefore, a temperature of 210°C was selected as the final temperature.

Aging was conducted in air without the wire bonds being hermetically sealed in an inert atmosphere. Destructive pull tests and electrical conductivity tests were performed as-bonded to provide baseline bond strength characteristics for each material group. Thereafter, pull tests and electrical conductivity test were conducted at periodic intervals throughout the accelerated aging period. Average pull strength, type of failure mode, and electrical conductivity were recorded and grouped according to the thick film processing conditions and type of conditioning for each material combination. Initially, the intervals were as short as 100 hours. As aging progressed, the intervals between testing were larger; for example, 1000 hours. The sample size for each group was 30 with 10 pull tests being taken from three different samples.

Statistical analysis was conducted on initial as-bonded pull strength data for the four main thick film materials: gold, silver, silver-platinum, and palladium silver.[2] The purpose of the analysis was to determine if the sample size of 30 was adequate for the evaluation and to assess the variability of the initial bond pull test data. Because the accelerated isothermal aging was being done to assess the effects of aging, it was important to consider the initial variability of bond strengths within a particular group. The more variability within a group, the more difficult it is to estimate aging effects. This is because the measurement of bond strength is destructive. Thus, for bonds tested after aging, there is no corresponding initial measurement. The initial strengths of such bonds have to be inferred from similar materials that are tested prior to aging. Increased variability in the initial bond strengths will cause increased uncertainty in the estimated aging effects. Two hierarchical levels of variability within a material group can occur: (1) variability among bonds within the same sample, and (2) sample to sample variation. The results of this analysis are the following:

1) The silver-platinum group had the most uniform bond strengths both within individual samples and from sample to sample. The sample size was probably sufficient to make a reasonable assessment of aging effects.
2) The silver group was similar to the silver-platinum group, except that the variability in bond strength within individual samples was greater than the silver-platinum groups. However, the sample size was probably sufficient to make a reasonable assessment of aging effects, also.
3) For the gold and palladium-silver groups, variability of bond strengths from the same sample was greater than the previous two groups. Assessment of aging effects on bonds associated with these material groups may be more problematic.

Table 7-3 lists the aging times and test intervals for each of the aging temperatures. The durations of the higher temperature groups were shorter than the lower temperature groups. As might be expected, some of the aluminum wire/thick film combinations degraded earlier than other material combinations for each aging temperature. In cases of severe degradation, some material combinations were discontinued before the total aging time was completed. Degradation of the wire bond/thick film joints were observed for all of the groups aged at the 225°C and 210°C aging temperatures, even though the point at which the degradation began varied. Groups aged at 180°C

also had some material combinations failing before others, however, at much longer times than the 225°C and 210°C aging temperatures. Some of the material combinations aged at the 160°C time period experienced little degradation. This group was discontinued because of project time constraints.

Table 7-3: Duration of Accelerated Aging at Each Temperature

Temperature (°C)	Aging Time (hours)	Test Intervals (cumulative hours)
225	1200	0, 100, 200, 300, 400, 600, 800, 1000, 1200
210	2400	0, 100, 400, 800, 1200, 1600, 2000, 2400
180	8200	0, 100, 200, 400, 800, 1200, 1600, 2000, 3000, 4300,6200, 7200, 8200
160	8100	0, 100, 200, 400, 800, 1200, 1600, 2000, 3000, 4200,6000, 8100

7.1.1.2 Temperature Cycling

Delphi's hybrid specification called out two different temperature cycling schedules. To distinguish them at Sandia, they were called the standard temperature cycling schedule and the static temperature cycle. Delphi's standard temperature cycling schedule was used to temperature cycle the second group of samples. The standard temperature cycling schedule was from -50°C to 160°C in dry air, with 90 minute temperature transition times, and a 30 minute dwell at each temperature extreme. The total cycle time was 240 minutes. The sample size for each group was 10 pull tests from a single sample. Destructive wire bond pull tests and electrical conductivity measurements were conducted initially and at 250, 500, 750, and 1000 cycle intervals. Delphi's static temperature cycling schedule was used to condition the hybrid module prior to other types of environmental stresses, such as mechanical shock and vibration. The static temperature cycle was from -65°C to 180°C in dry air, with immediate air to air transfers between temperature extremes and a 30 minute dwell at each temperature extreme. Electrical conductivity and destructive pull tests were performed initially and at periodic intervals throughout both types of temperature cycling.

7.1.2 Results

This section discusses the results of the accelerated aging, temperature cycling, and other environmental exposures for each of the material combinations in a qualitative perspective comparing performances of all the different material combinations. Data presented may not include standard deviations. The reader can assume that unless noted, standard deviations of the data

presented are similar. Complete data with statistical analysis and failure mode identification is available from Sandia. This section also summarizes any conclusions reached regarding issues such as the effect of single versus multiple firings and the effect of bonding over metal/alumina and metal/dielectric/alumina. Section 7.2 will then describe in detail some of the statistical analyses performed and predictive models that were developed for selected material combinations.

7.1.2.1 Initial Bondability

The objectives of the designed experiment were to optimize the wire bonder parameters such that the initial as-bonded pull strengths met the following criteria:

(1) the average pull strengths were at least 500 grams (for a 0.010 inch wire diameter)
(2) the standard deviations were as small as possible
(3) the failure modes were either heel breaks or wire span failures
(4) the width of the wire bonds were less than 0.020 inch.

The third criteria describes where the failure occurred for each of the pull tests. There are four general types of failure modes: heel breaks, wire span breaks, wire bond lifts, and metallization failures. Heel breaks are the most common failure mode for good quality wire bonds. The heel portion of the bond is the volume of wire that transitions from the deformed bond foot to the undeformed wire. Heel failures are acceptable but indicate that the original strength of the wire has been altered by the wire bonding process. Wire span failures occur some place within the span of wire between the heels of a bonded wire loop. Wire span failures are ideal because they indicate that the strength of the bonds are at least as strong as the undeformed wire. Two undesirable failure modes also occur: wire bond lifts and metallization failures. These occurred very rarely during the initial as-bonded pull tests. Bond lift failure modes occur at the interface between the wire and the substrate metallization, thus indicating that the initial quality of the bond is poor or that the bond quality has degraded. Metallization failure modes occur at the interface between the substrate metallization and the substrate itself. These types of failure modes indicate that the initial adhesion of the metal to the substrate is poor or that some mechanism has taken place to degrade the adhesion at this interface. The fourth criteria listed above deals with the deformation of the wire in the transverse direction during bonding. Desired deformation ranges are typically from 1.5 to 2 times the original wire diameter. Typical 0.010 inch diameter wire bond loops are shown in Figures 7-1A and 7-1B. Wire heel, bond foot, and wire span locations are identified in these figures.

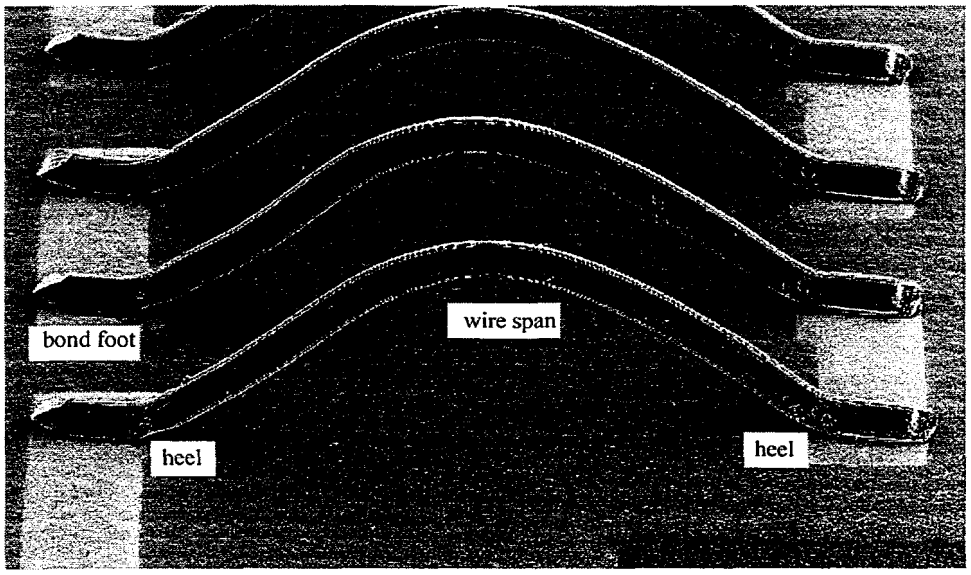

Figure 7-1A. Side View of 0.010 Inch Diameter Aluminum Wire Bonds

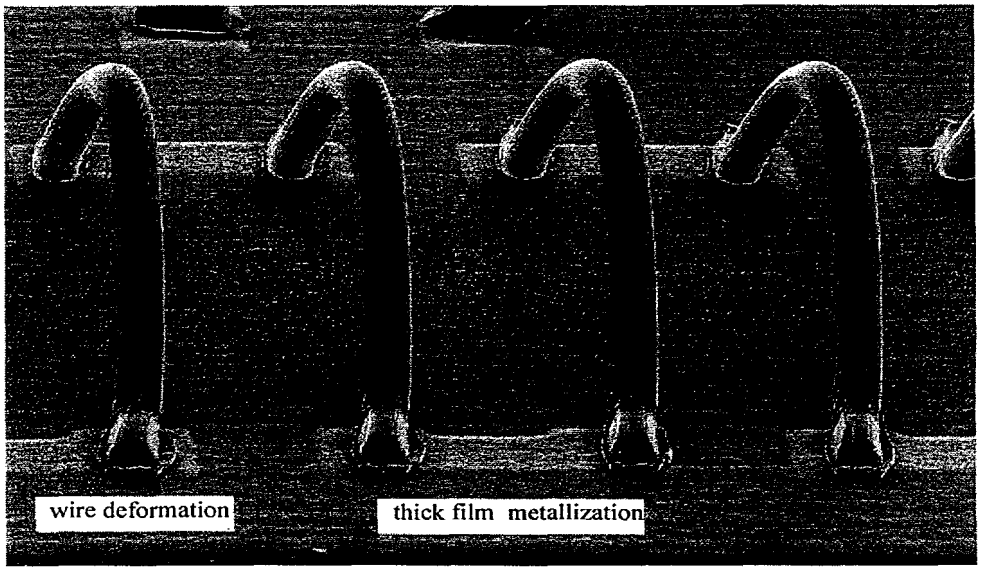

Figure 7-1B. End View of 0.010 Inch Diameter Aluminum Wire Bonds

Argon plasma cleaning of the thick film samples was routinely used to prepare the surfaces before wire bonding. The variables of the designed experiment to optimize the wire bonder parameters were the force, time, and power settings. Other potential variables such as type of tool and condition of the aluminum wire were not varied for this experiment. Vendor preferences were used for both the type of tool and for the condition of the aluminum wire (99.99% aluminum with 10 to 15% elongation and a minimum tensile strength of 400 grams.) One exception was wire with a minimum tensile strength of 300 grams, which was used to bond the silver/palladium thick film and aluminum tab samples. The reason the different wire was used was because the supply of standard aluminum wire was depleted and waiting to purchase additional wire would have delayed the project. The designed experiments were conducted for each material combination grouping all four types of thick film processing conditions together. This was valid as all four processing conditions for a particular materials group had similar strengths, standard deviations, failure modes, and deformation. Two exceptions were the gold and silver/palladium/platinum groups. These two groups required different wire bonder parameters for the alumina and dielectric base subgroups.

Wire bonding to the gold, silver and silver/platinum thick film materials, as well as the aluminum tab samples was relatively easy in that very few iterations of the designed experiment were required before the pull tests met the desired criteria listed above. The two silver/palladium thick film alloys were more difficult to bond to as measured by the number of iterations required to optimize the parameters. Large diameter aluminum wires are routinely bonded to Pd-Ag thick film metallization in automotive hybrids. However, surface preparation before bonding requires solvent washing followed by careful resistivity-monitored cleaning in deionized water.[3] The surface preparation, along with other measures, was reported to improve corrosion resistance of the materials but also could have improved initial wire bondability. It is possible that the palladium/silver thick film materials require more aggressive surface preparation than the other thick film materials prior to wire bonding. Other possible reasons for difficulty in bonding may be due to the higher hardness of the silver/palladium alloys as compared to the other three compositions. This issue wasn't investigated further.

Figure 7-2 compares the as-bonded pull strengths for all of the groups included in this evaluation. An explanation of the legend of Figure 7-2 follows. 1 Fire/Alum. refers to thick film metallization printed directly over the alumina substrate and fired once. 6 Fire/Alum. refers to thick film metallization printed directly over the alumina substrate and fired six times. 1 Fire/Diel. refers to thick film metallization printed and fired once over a previously printed and fired dielectric layer over the alumina substrate. 6 Fire/Diel. refers to thick film metallization printed and then fired six times over a previously printed and fired dielectric layer over the alumina substrate. The standard deviations ranged between 20 and 40 grams for all of the groups in this evaluation except the two gold groups printed over dielectric. Their standard deviations were 80 grams. Because of the softer wire used, the minimum strength requirement of 500 grams criteria was relaxed for the palladium-silver and aluminum tab groups. This evaluation was mainly looking for degradation in bond strength due to the variety of environmental stresses discussed earlier. It was felt that, despite the difference in wire for these two groups, changes in bond strength could still be detected. The failure

modes for the initial groups were predominantly heel breaks with some wire span breaks. Occasionally bond lifts or metallization failures occurred.

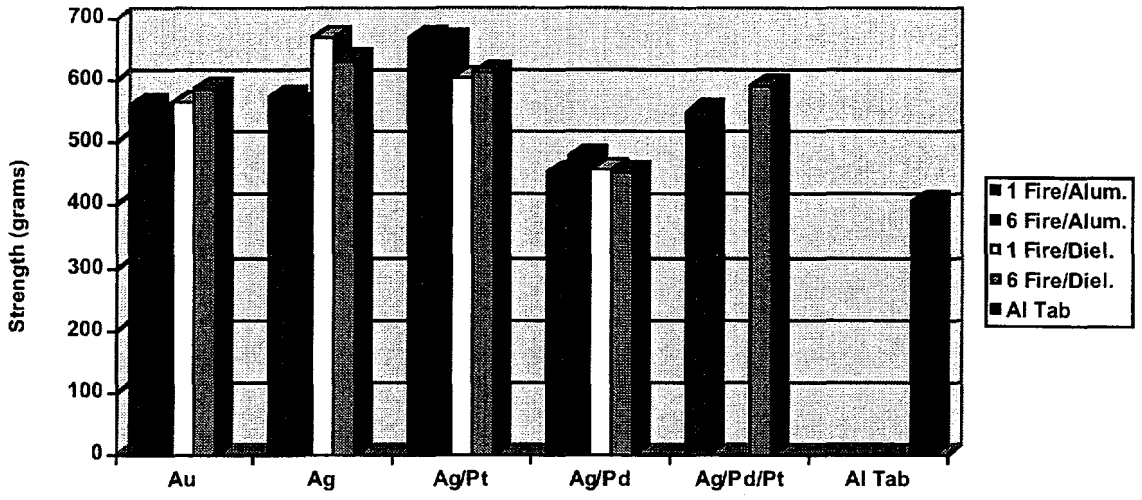

Figure 7-2. Average Pull Strength for 10 Mil Al Wires Bonded to Various Types of Metalization

7.1.2.2 Pull Test Performance Versus Thick Film Processing Conditions

As shown in Figure 7-2, there were not any specific trends in as-bonded pull strengths when comparing the different thick film processing conditions. Differences in bond strength were not discerned between single fired or multiple fired groups. Similarly, different base materials, thick film metal over alumina or thick film metal over dielectric, did not appear to effect the initial bond strength. As shown later in the following sections, differences in base material were a factor in bond strength after various environmental exposures. Because of the similarities between the four groups, later analyses were restricted to the two groups considered the most likely conditions that simulated hybrid processing. These groups were the multiple-fired metal over alumina and the single-fired metal over dielectric/alumina.

7.1.2.3 Pull Test Performance Versus Isothermal Aging

A later section will detail the statistical analysis of the isothermal aging for selected materials. This section is provided to show the general behavior of the different material combinations after aging at the four temperatures described. Pull strength behavior is plotted for the multiple-fired thick film metals over alumina and single-fired thick film metals over dielectric groups. Data for aluminum wires bonded to aluminum tabs are also provided for comparison. Figures 7-3 and 7-4 show the bond strength of each material group after aging out to 8000 hours at 160°C for the two main thick film processing conditions of interest. The two material combinations that were predominantly aluminum wire and silver thick film metal (Ag and Ag/Pt) performed much better

than the other material combinations. The aluminum wire/gold material combination degraded more than any of the other material combinations. As the average bond strengths for the groups decreased, standard deviations and the incidence of undesirable failure modes (bond lifts and metallization failures) increased. This was true for all four aging temperatures but occurred sooner for the higher aging temperatures. Bond strength behavior at 180°C was very similar to the 160°C data and is not shown in this section. Figures 7-5 and 7-6 show the bond strength of each material group after aging out to 2400 hours at 210°C, while Figures 7-7 and 7-8 show the bond strength of each material group after aging out to 1200 hours at 225°C.

The incidence of bond lift and metallization failures were evidence that degradation of the bonds had taken place either by the mechanism of Kirkendall voiding or by degradation of the thick film metal to dielectric interface. Kirkendall voiding was more noticeable in the sample groups with aluminum wire bonds to thick film metal over alumina. Depending on the material and aging temperature, the Kirkendall voiding occurred either at the aluminum wire to thick film interface or at the thick film metal to alumina interface. Kirkendall voiding also occurred with the thick film samples printed over dielectric but complete loss of thick film adhesion to the dielectric was more common. In this case, the interface between the thick film metal and dielectric often failed catastrophically before the Kirkendall voiding was extensive enough to cause a failure. Weakness at the thick film metal to dielectric interface was evidenced by a complete peeling of the entire bond foot area. Examination of the bottom side of the failed surface revealed thick film metallization with little or no presence of aluminum from the wire.

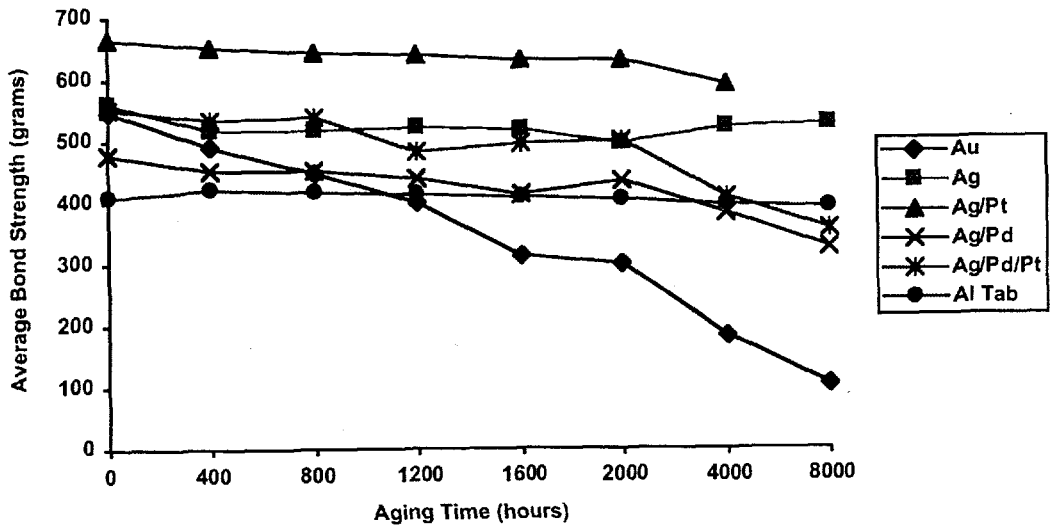

Figure 7-3. Bond Strength vs. Isothermal Aging @ 160°C 10 Mil Al Wires Bonded to Multiple Fired Thick Film Over Alumina

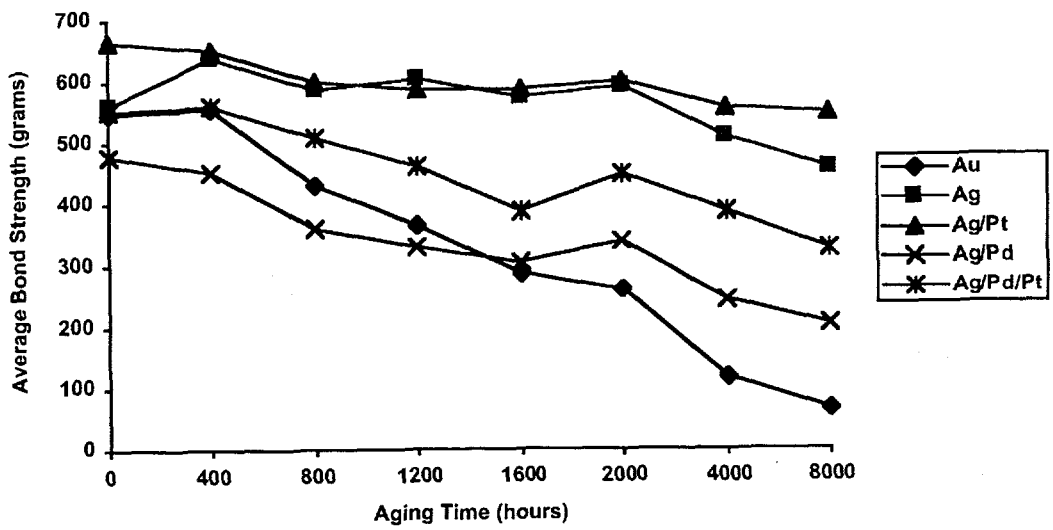

Figure 7-4. Bond Strength vs. Isothermal Aging @ 160°C 10 Mil Al Wires Bonded to Single Fired Thick Film Over Dielectric

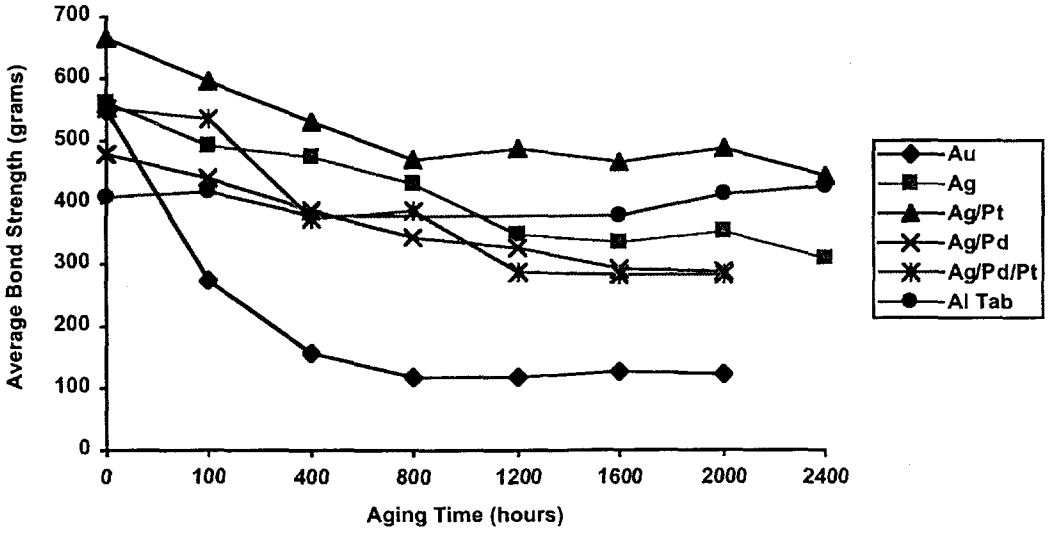

Figure 7-5. Bond Strength vs. Isothermal Aging @ 210°C 10 Mil Al Wires Bonded to Multiple Fired Thick Film Over Alumina

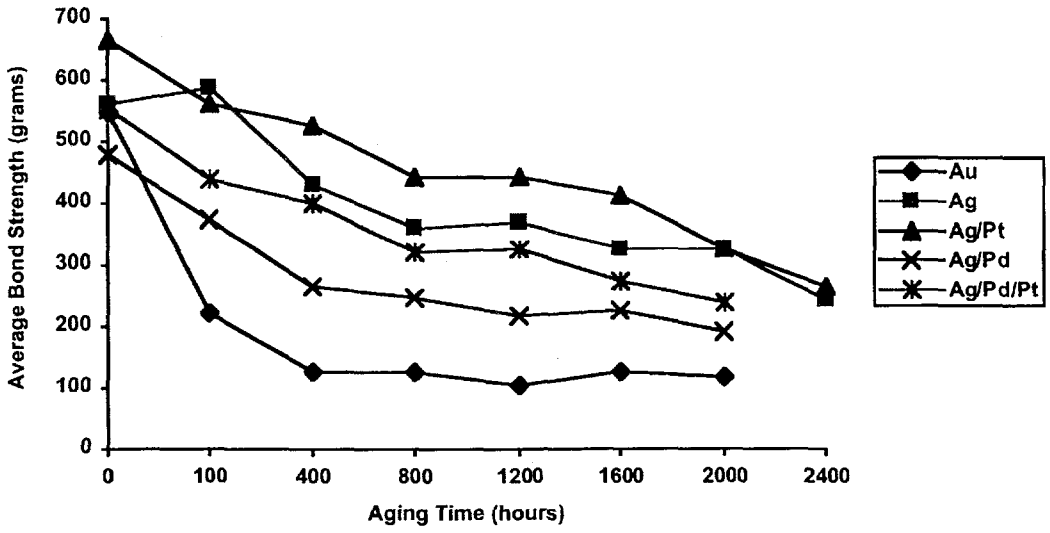

Figure 7-6. Bond Strength vs. Isothermal Aging @ 210°C 10 Mil Al Wires Bonded to Single Fired Thick Film Over Dielectric

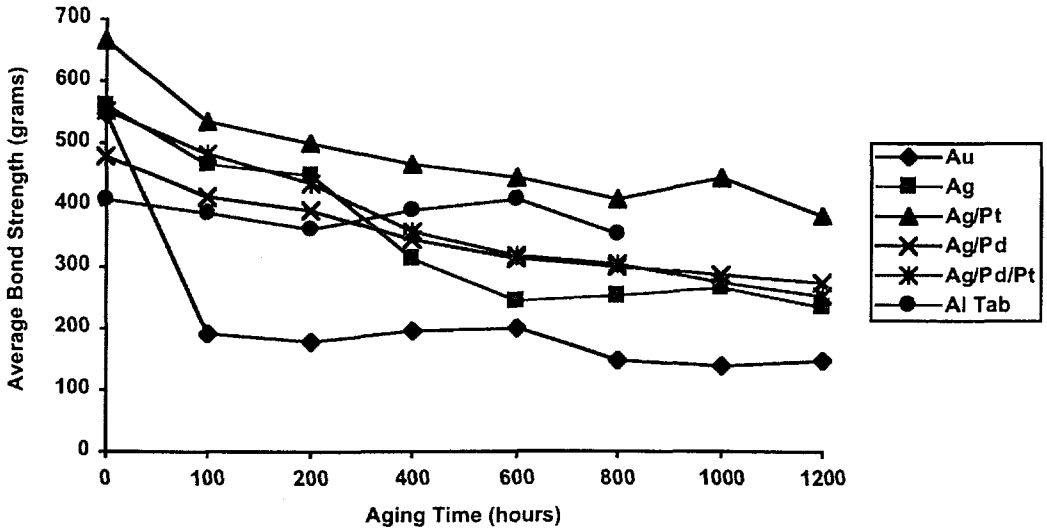

Figure 7-7. Bond Strength vs. Isothermal Aging @ 225°C 10 Mil Al Wires Bonded to Multiple Fired Thick Film Over Alumina

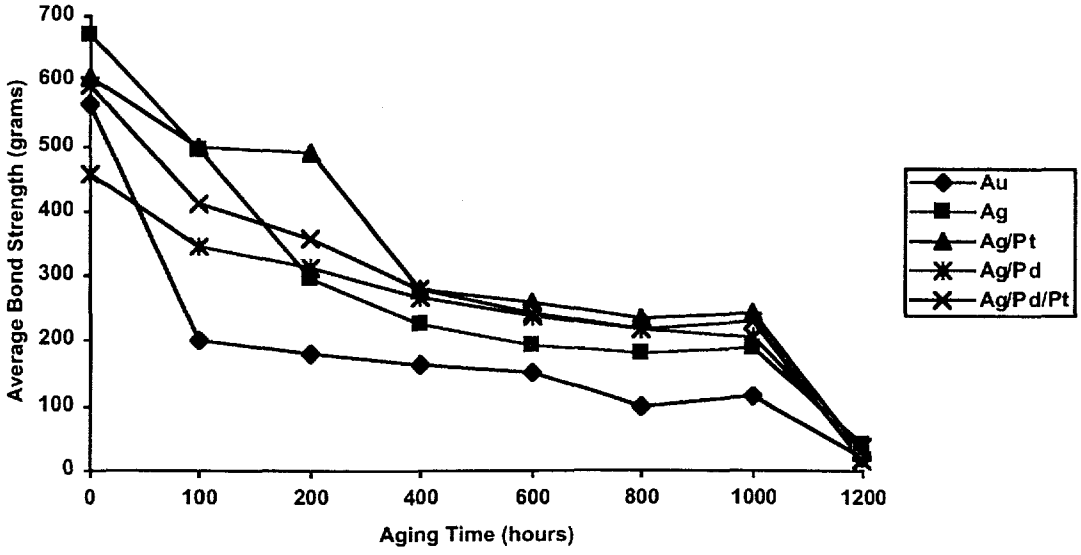

Figure 7-8. Bonded Strength vs. Isothermal Aging @ 225°C 10 Mil Al Wires Bonded to Single Fired Thick Film Over Dielectric

7.1.2.4 Pull Test Performance Versus Temperature Cycling

7.1.2.4.1 Standard Temperature Cycling Results

Initially, the standard temperature cycling was conducted on unprotected thick film samples (non-hermetically sealed samples). Catastrophic failures were experienced after only the first 250 temperature cycles for all the different material combinations.[4] Complete loss of electrical conductivity and significant decreases in wire bond pull strengths were observed. An extensive study of all the existing isothermal aging and cycling data (both cycling schedules) was conducted to compare mean pull strengths as grouped by type of conditioning and failure mode. Auger Electron Spectroscopy was also performed on one of the failed silver thick film samples to look for any evidence of contamination or corrosion. The conclusion to this investigation was that the failures were induced by chlorine contamination and that the temperature cycling conditions did not cause the failures. Therefore, this portion of the evaluation was repeated. The second time, the samples were temperature cycled in an aluminum container that was sealed with a silicone adhesive similar to silicone encapsulants used regularly in automotive applications.

Selected wire bond pull test results for the second round of standard temperature cycling are shown in Figure 7-9 for wire bonds to thick film metallization over alumina. Results were similar for the wire bonds to thick film metallization over dielectric. These results parallel the results obtained in the isothermal aging portion of the evaluation. The material combinations containing predominantly aluminum wire and silver thick film performed the best, while the aluminum wire to gold thick film material combination experienced the greatest decrease in wire bond pull strength. It is interesting to compare the results at 1000 cycles with observations at isothermal aging at 160°C. For example, at 1000 cycles the ten specimens from the multiple fired silver thick film over alumina group tested with an average pull strength of approximately 370 grams. All of the tests failed at the aluminum wire to thick film interface (a bond lift failure mode). In contrast, note that after 8260 hours of 180°C isothermal aging, the average bond strength associated with this type of failure mode is 486 grams. Thus, 1000 cycles (involving 4000 hours at or below 160°C) is much more degrading than 8260 hours at 180°C. Clearly, temperature cycling stimulates an important failure mechanism that is not exercised during isothermal testing. Similar conclusions can be developed by examining the experimental data from the other thick film material combinations. Presumably this mechanism is related to the mismatch of the temperature expansion coefficients of (1) the substrate, (2) the thick film, and (3) the wire.[5]

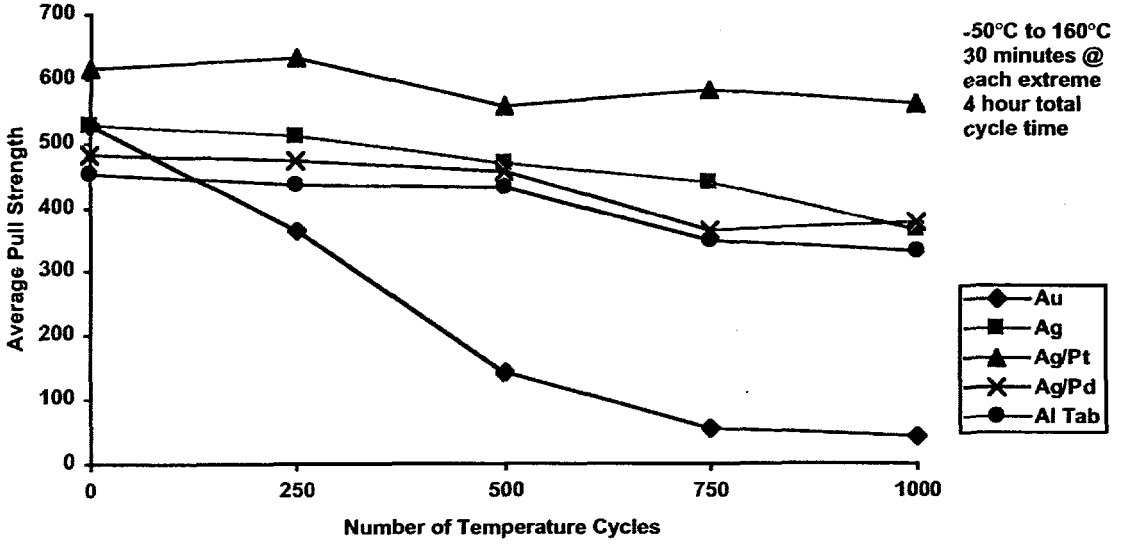

Figure 7-9. Standard Temperature Cycling 10 Mil Diameter Al Wire Bonded to Thick Film Metallization Over Alumina

7.1.2.4.2 Static Temperature Cycling Results

Figure 7-10 shows a comparison of the effect of static temperature cycling for the different material combinations evaluated. The general behavior of all material combinations was reduced bond strength and the onset of the undesirable failure modes after approximately 200 cycles. The degrees of degradation are different for the different materials but all were affected by the cycling. The silver and silver-platinum metals again performed better than the other materials. These samples were not protected by the aluminum containers like the standard temperature cycling and were probably affected somewhat by the unprotected environment. Notice that even the aluminum wire to aluminum tab group experienced degradation in strengths.

By comparing the bond strengths from the standard and static temperature cycles (Figures 7-9 and 7-10, respectively), one can observed that degradation occurred earlier for the static cycling. The temperature extremes of the static temperature cycling condition (-65°C to +180°C) are more severe than the power temperature cycling conditions (-50°C to +160°C). The transition times from hot to cold are also more severe for the static temperature cycling (immediate air to air transfer) than the power temperature cycling conditions (a 90-minute transition in air). The time at temperature for 250 standard temperature cycles is less than 500 hours at 160°C, while the time at temperature for 200 static temperature cycles is only 100 hours at 180°C. These observations would support the earlier comment that temperature cycling stimulates an important failure mechanism that is not exercised during isothermal testing

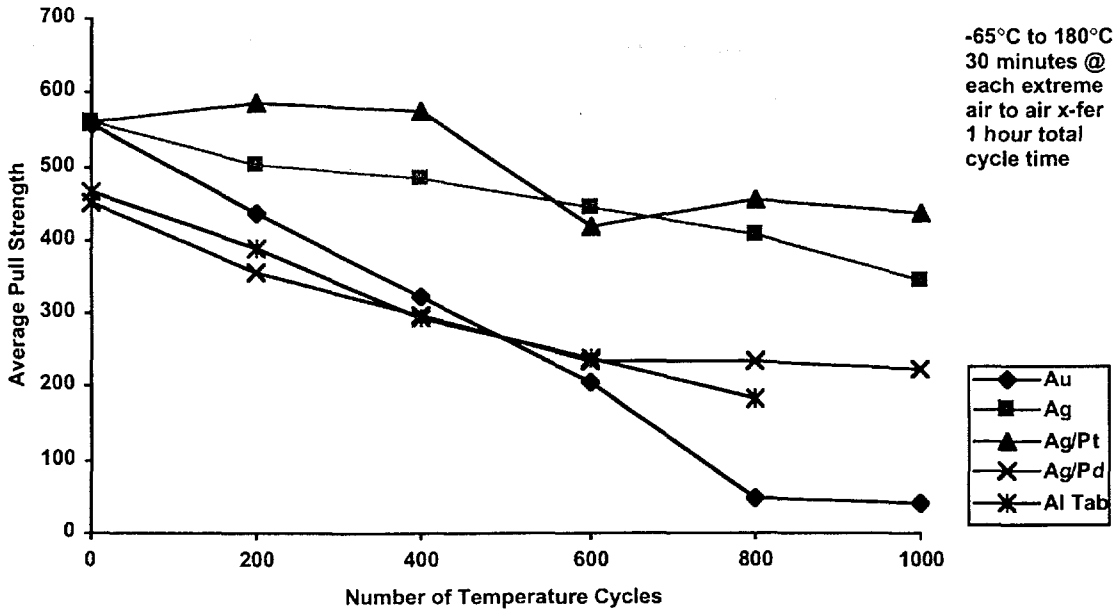

Figure 7-10. Static Temperature Cycling of 10 Mil Diameter Al Wire Bonded to Thick Film Metallization Over Alumina

7.1.2.5 Miscellaneous Evaluations of Large Diameter Aluminum Wire Bonds

Sandia was requested to evaluate a third silver thick film metal, QM15. This is a European version of the Du Pont 6262. The difference between the two compositions is that QM15 does not contain cadmium, presumably for ES&H reasons. Sandia evaluated this material only with two thick film processing conditions, multiple-fired metal over alumina and single-fired metal over dielectric. This evaluation was begun at a later date and joined the main evaluation in progress, therefore, the aging times are not as long as the other materials. Testing performed was identical to the main evaluation with destructive wire bond pull tests and electrical conductivity measurements performed periodically. Because the compositions of Du Pont 6262 and Du Pont QM15 are similar, the average pull strengths of these two materials are plotted in Figures 7-11, 7-12 and 7-13 for isothermal aging temperatures of 160°C, 210°C and 225°C, respectively. These three plots show that at least from the average pull strength data, there is not any significant differences between these two compositions. The standard deviations of both materials at each temperature and time also tracked fairly closely. The only difference observed was that the undesirable failure modes occurred earlier and at a greater frequency for the QM15 material than the 6262 material at the 160°C and 180°C temperatures. This phenomenon was not observed at the two higher temperatures as the first occurrence and frequency of undesirable failure modes were the same. Bond strength after temperature cycling was also monitored. Bond strengths after temperature cycling were comparable for the 6262 and QM15, but are not plotted.

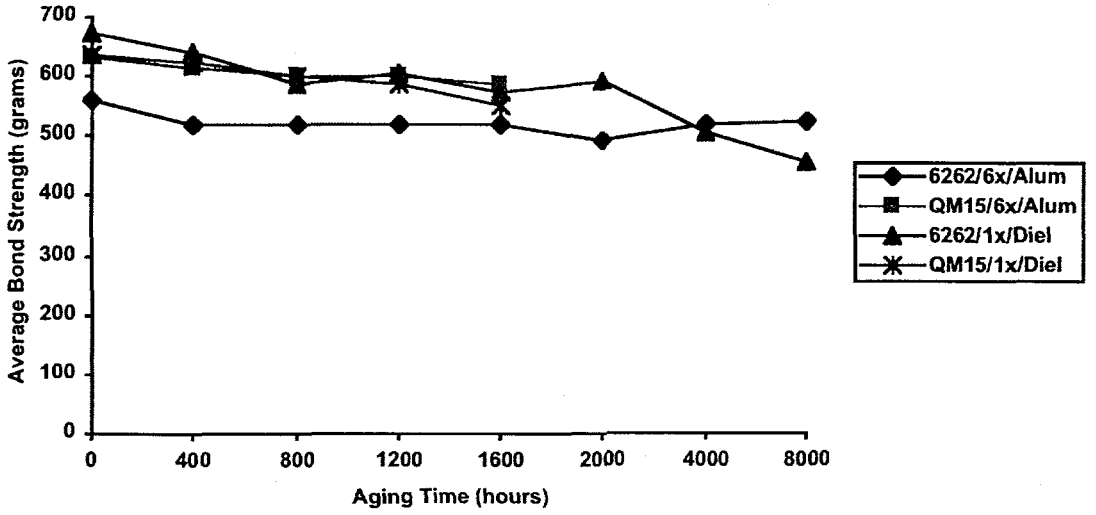

Figure 7-11. Bond Strength vs. Isothermal Aging @ 160°C 10 Mil Al Wires Bonded to Thick Film Over Dielectric

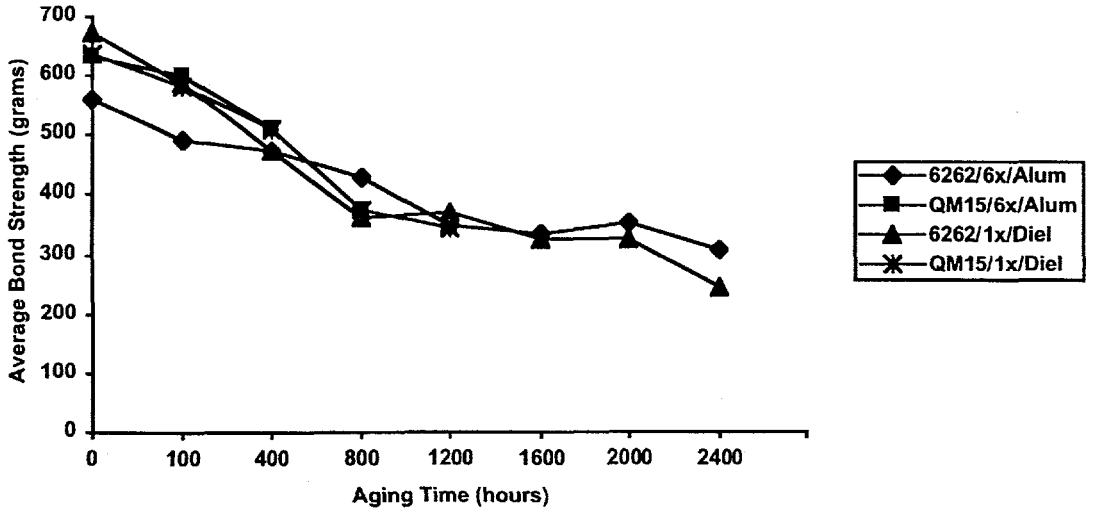

Figure 7-12. Bond Strength vs. Isothermal Aging @ 210°C 10 Mil Al Wires Bonded to Thick Film Over Dielectric

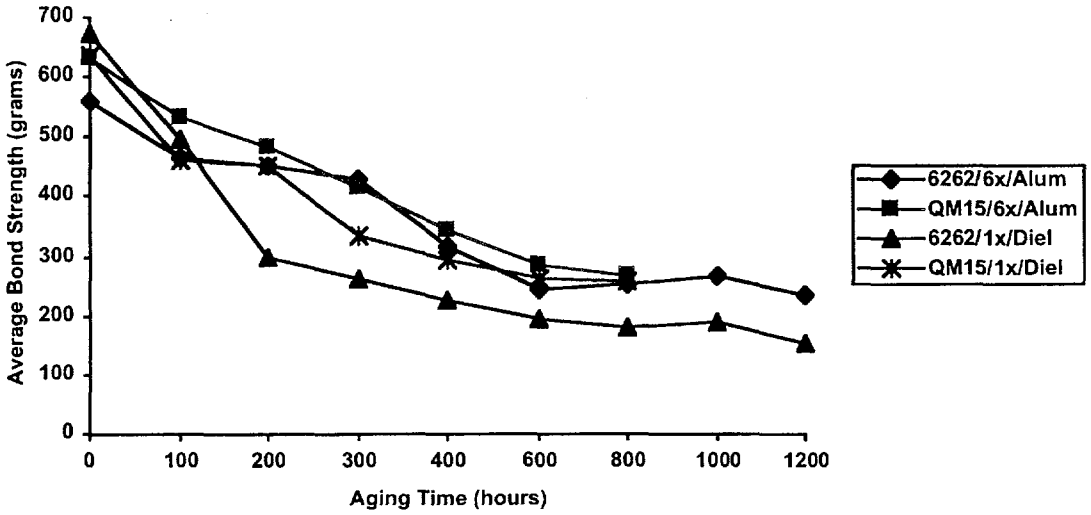

Figure 7-13. Bond Strength vs. Isothermal Aging @ 225°C 10 Mil Al Wires Bonded to Thick Film Over Dielectric

During a design review attended by other automotive companies, a suggestion was made to compare destructive wire bond pull testing with wire bond shear testing. The reasoning behind this suggestion was that ordinarily, the heel breaks in a wire bond pull test and the actual strength of the wire bond is not measured. The actual strength of the wire bond can only be deduced to be greater than the value of the heel break during the wire bond pull test. By directly shearing the wire bond, the actual strength of the wire bond can be measured. Comparison tests of both wire shear and wire pull test methods were conducted when the QM15 thick film composition was tested. Figure 7-14 plots data from pull tests and shear tests for comparison. Data are taken from QM15 samples aged at 225°C. As can be seen, the bond strengths measured by pull test show a steady decrease in strength. Initially, heel breaks were the predominant failure mode. As aging progressed, the incidence of undesirable failure modes increased. In contrast, the shear test data fluctuates somewhat but never show a significant decrease in strength. Failure modes for the shear test were predominantly wire shear failures. (The shear tool cuts through the aluminum metal of the wire but leaves the actual bond between wire and thick film metal intact). In this case, the bulk shear strength of the aluminum wire is being tested rather than the strength of the wire bond. Shear tool heights were varied to determine if an optimum height could be found to ensure that the actual wire bond would fail in shear. These trials were unsuccessful because wire shear failures were always observed. A standard tool height of 30 microns was used for these tests.

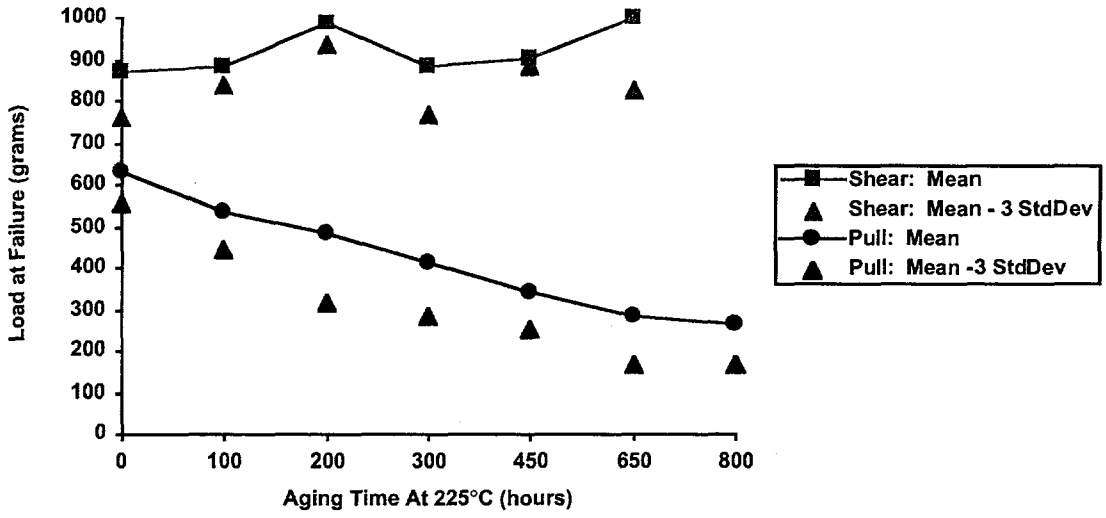

Figure 7-14. Comparison of Shear and Pull Test of Mil Al Wire Bonded to QM15 Over Alumina

For this comparison test, it appears that the softness of the aluminum wire prevented the actual wire bond from being tested. The 225°C aging only caused the wire to soften further due to annealing. However, similar results were observed with the lower aging temperatures, also. To conclude, if the purpose of the accelerated aging is to detect bond strength degradation, then it appears that a wire pull test will detect changes in bond strength much more accurately than the shear test, at least for the large aluminum wire bonds. It is noted that shear testing for fine gold wire ball shear testing is much more accurate in detecting bond strength degradation than pull tests. A possible explanation is the difference in geometries of a fine gold wire ball bond and a large diameter aluminum wedge bond.

Smaller scale evaluations were done throughout the course of the project and are mentioned here. Because the temperature/humidity cycling portion of the test was canceled, the samples originally intended for that portion were available for other types of tests. Other samples were exposed to a sequence of 100 static temperature cycles, vibration, and then mechanical shock, with periodic wire bond pull tests. These results also did not show any degradation in bond integrity, as measured by wire pull tests and conductivity measurements.

A small experiment evaluated the effect of Highly Accelerated Stress Tests (HAST) exposure to various aluminum wire thick film combinations. The HAST conditions were 140°C, 85% R.H., and three atmospheres of pressure. Samples submitted for HAST were not hermetically sealed. Hence, this exposure was not realistic with respect to the exposure of a real hybrid module. However, these tests were performed to provide a comparison measure of corrosion resistance between the different materials and also to have some data to compare with Du Ponts autoclave data.[6] Table 7-4 lists the pull test data and continuity measurements for selected samples from

each material group. The results show that even short exposure times to this humid environment are catastrophic to most of the materials. Comparing before and after HAST exposure data reveals that the aluminum wire to gold thick film material degraded the most after 100 hours of exposure. The other material combinations also lost strength, but not nearly as much. The continuity measurements detected loss of conductivity for the gold, silver, and silver-platinum materials. In this case, the conductivity measurements are more sensitive in detecting changes in bond integrity. This is seen as loss of conductivity for the silver and silver-platinum materials despite that their bond strength remained fairly high. The silver-palladium group maintained electrical conductivity despite losing 50 percent of its initial bond strength. No attempt was made to correlate 85%R.H./85°C autoclave testing with the HAST conditions. In fact, the results of the HAST exposure tests supported Sandia's recommendation that a hermetic enclosure should be used for this hybrid.

7.1.3 Summary and Recommendations

As might be expected, the best performing material combination was the aluminum wire to aluminum-coated tab. If cost and space requirements allow their use, this is the most reliable combination. The aluminum tabs used in this evaluation were larger than necessary for a 0.010 inch diameter wire. Space could be gained by using a smaller tab.

Bond strengths were better for the material groups when the thick film metal was printed over alumina rather than the thick film metal printed over dielectric and alumina. This was true for all materials evaluated.

No significant differences were detected in samples fired once versus samples fired several times. This would indicate that the thick film materials are stable to multiple firings, as measured by bondability and conductivity of the material.

The conductivity measurements recorded for this experiment generally showed no significant increases in resistance. Exceptions were the samples that were corroded either during the first temperature cycling test or with the HAST exposure. These samples experienced significant increases in resistance to the point of complete open circuits (due to bond lifts). Toward the end of the isothermal aging periods at 210°C and 225°C some failures also occurred. Failure analysis revealed that the majority of the bonds were still intact with low resistance readings. Only a small number of bonds had lost conductivity due to bond lifts.

The silver and silver-platinum materials performed the best of all the materials evaluated in the isothermal aging, temperature cycling, and HAST exposures. The silver-platinum material is 99% silver and is comparable to the silver material.

The gold materials did not perform as well as expected. However, expectations were based on previous experience with gold ball bonds to aluminum bond pads rather than large diameter

aluminum wire bonds to gold thick film. Nonetheless, this material combination was usually the first to experience degradations in bond strength or contact resistance.

The performance of the silver-palladium materials (approximately 25% palladium) fell roughly between the silver materials and the gold material. Initial bond strengths were lower due to a different wire being used. Optimized bond parameters were also more difficult to achieve with these metals. Because of their higher sheet resistivities as compared to silver and gold, the use of these materials is limited. Industry, however, uses these materials regularly for surface mount applications, with perhaps selective gold thick film areas in critical areas for chip and wire hybrids.

While the silver thick film materials performed better than the other materials, their performance still was less than ideal. The weakness of these materials seem to be with temperature cycling rather than isothermal aging. The results of the aging are encouraging but the temperature cycling results were not that good. It appears that two different mechanisms of bond degradation can be activated.

Corrosion resistance of all the materials could be another weakness in the materials or hybrid design. All of the materials failed catastrophically when accidentally contaminated with chlorine. In these cases, the aluminum wire corroded rather than the more noble thick film materials. This points out the importance of cleanliness and hermetic sealing. Both cleanliness and hermetic sealing are not foolproof, but can reduce trace amounts of corrosive elements.

To conclude, the results from this evaluation show that while silver performed better than the other material combinations, the temperature cycling performance needs to be improved. Also, using silver might not be considered a robust material for this technology because problems can be experienced if contamination and corrosion are not controlled. A hermetic package can prevent contamination and corrosion and therefore might be the solution to these problems. However, the cost of the hermetic package probably offsets any savings realized by using a silver rather than a gold thick film materials system. The reliability of a hermetic hybrid module must be demonstrated before Sandia can make a recommendation to use direct bonding of aluminum wires to silver thick films.

Table 7-4: Pull Tests and Continuity Measurements for HAST Samples

HAST conditions (140°C, 85% R.H., 3 atm)

							Failure Modes						Resistance
	TIME	N	MEAN	SIGMA	0	1	2	3	4	5	6	RANGE	(ohms)
	(hours)		(grams)	(grams)									
Au / alumina	0	10	631	106	3	0	2	0	2	0	3	345-705	0.616
	120	10	103	65	1	0	0	0	0	2	7*	25-235	OVLD
Ag / alumina	0	10	602	32	0	0	6	0	3	1	0	535-640	0.406
	120	10	548	64	0	0	5	0	2	2	1	395-620	OVLD
AgPt / alumina	0	10	666	25	0	0	4	2	4	0	0	615-700	0.411
	120	10	572	84	2	0	5	0	1	2	0	445-650	0VLD
AgPd / alumina	0	10	459	10	0	0	1	8	1	0	0	435-475	2.045
	120	10	216	33	0	0	0	0	0	0	10	160-255	2.075
Al Tab	0	-	-	-	-	-	-	-	-	-	-	-	0.07
	100	3	393	16	0	0	0	3	0	0	0	375-415	0.076

7.2 Modeling of Wire Bond Failure Data for Large Diameter Aluminum Wire Bonds

7.2.1 Introducton

This section briefly describes the statistical analyses performed on the data associated with selected materials. By the time actual data was available, a decision had already been made that silver thick film (or silver-platinum thick film) materials would have to be used in order to make the hybrid module economically feasible. Therefore the statistical analysis was focused on the two materials of greatest interest, silver (Du Pont 6262) and silver - 1% platinum (Heraeus 4740). The goal of these analyses was to develop models that would allow the accurate lifetime prediction of an aluminum wire bond to a selected material based on an exposure to a particular environment for a particular length of time. The analyses are summarized in the following paragraphs and the complete report is printed in Appendix D.[7]

Test samples were fabricated from the various thick film materials listed in Table 7-5. These samples were fabricated with a variety of material layers and firing schemes before being exposed to accelerated aging via four constant temperature environments (160°C, 180°C, 210°C, and 225°C). Accelerated aging times extended for up to approximately 8000 hours depending on the particular environment and material. Prior to aging, several 0.010 inch diameter, 100% aluminum wires were bonded to each thick-film specimen. Some of these wires were destructively pull-tested immediately to get a feel for the strength of the wire bonds prior to aging.[8] The observed distributions of wire bond strengths prior to aging, by material combination, form a basis for an assessment of the effects of aging. After the initial testing, wire bonds were periodically pull-tested after various amounts of exposure to each of the accelerated temperature environments.

Table 7-5: Thick Film Materials

Material Combination	ID Code
Dupont 6262 silver film multi-fired on alumina	(6262ma)
Dupont 6262 single-fired over dielectric	(6262sd)
Heraeus 4740 silver/platinum film multi-fired on alumina	(4740ma)
Heraeus 4740 silver/platinum single-fired over dielectric	(4740sd)
Dupont-5725 gold film multi-fired on alumina	(5725ma)
Dupont-5725 single-fired over dielectric	(5725sd)
Dupont-QM21 palladium/silver film multi-fired on alumina	(QM21ma)
Dupont-QM21 single-fired over dielectric	(QM21sd)

This analysis was conducted in two phases. At the first phase, data were summarized and modeled separately for each combination of materials with aging temperature and time. With this in hand, the second phase of analysis related to modeling the reaction kinetics associated with a particular material combination, where possible. Finally, the analyses demonstrated (in the case of the 6262ma material) how these kinetics models can be used to develop estimates of wire-bond reliability as a function of a specified exposure time at a specified temperature.

7.2.2 Experimental data

For each wire that was pull-tested, both the bond strength (BS) and failure mode (FM) were observed. Note that the term pull strength is used interchangeably with bond strength. The four general failure modes that were observed are listed below. Note that no attempt was made to distinguish between similar types of failures at the 1st or 2nd bond.

0 - Metallization failure,
1 - Bond lift,
2 - Heel break, and
3 - Wire break (away from heel).

The observed bond strength (BS) depends on the strengths of the various components of the bond. Because only the weakest link is observed,

$$BS = \text{minimum}\{Y_0, Y_1, Y_2, Y_3\}, \text{ where} \qquad (7\text{-}1)$$

Y_0 is the strength of the bond between the metallization and substrate,

Y_1 is the strength of the bond between the wire bond and the metallization,

Y_2 is the strength of the heel, and

Y_3 is the strength of the wire.

Overall, the most common failure modes were modes 0, 1, and 2. Except at the pre-aged condition, failure mode 3 was relatively rare. Generally, for a given film/substrate material, the relative frequency of heel failures (FM = 2) was high initially and then decreased as the aging time increased. Conversely, the relative frequency of failures related to the metallization (FM = 0, FM = 1) increased as the aging time increased. The rate of change from a heel failure regime to a metallization failure regime depended on the aging temperature as well as the material combination. The higher the aging temperature, the more rapid the transition from one regime to another. In general, for a given material combination and aging temperature, there was a smooth

decrease in the mean (or typical) bond strength along with a broadening of the variation in bond strength in time.

At aging temperatures of 160°C and 180°C, the degradation in the observed bond strength over time depended significantly on the material. At these temperatures, even at significant time exposures, heel breaks were the dominant failure modes for some materials (e.g., 6262ma and 4740ma). For other materials, particularly those fired a single time on a dielectric substrate, the degradation was more severe, resulting in metallization-related failures even at relatively benign aging conditions (see e.g., 6262sd and 4740sd).

As expected, the effects of aging at the higher temperatures (210°C and 225°C) was more dramatic for all materials. In general, there was a clear increase in the frequency of metallization-related failures as the exposure time increases. Beyond several hundred hours of aging at these high temperatures, the bond strength is effectively determined by the strength of the metallization. Furthermore, the distributions of metallization strength decreased with increased aging to some steady state level which varied somewhat by material.

7.2.3 Reliability/Unreliability Estimates Derived From Kinetics Modeling

Prior to developing reliability estimates, it is obviously necessary to define reliability. For purposes of discussion here, the reliability (R) of a wire bond (conditional on some specified aging environment [T, t]) is the probability that the bond strength meets or exceeds some strength requirement, S. That is,

$$R(T,t) = \text{Prob}\{BS(T,t) \geq S\} \tag{7-2}$$

A model for overall bond strength (such as given in the previous section) provides a general mechanism for estimating reliability via simulations. This mechanism was used to estimate the unreliability $(1-R)$ of wire bonds associated with the 6262ma material. Figure 7-15 illustrates the resultant estimated unreliability (assuming a 500 gram requirement) as a function of exposure time at 125°C for the 6262ma material. Each point in time in Figure 7-15 is based on 10,000 independent simulations of the models for Y_M and Y_H specific for the 6262ma material (see the model parameter estimates in Appendix D Table D-10). The estimated unreliability is the fraction of the simulations that resulted in an overall bond strength of less than 500 grams. The fact that the points do not fall on a smooth curve (superimposed) is symptomatic of simulation error. Note that the early increase in unreliability (from 0 hours to 1000 hours) is indicative of the annealing process.

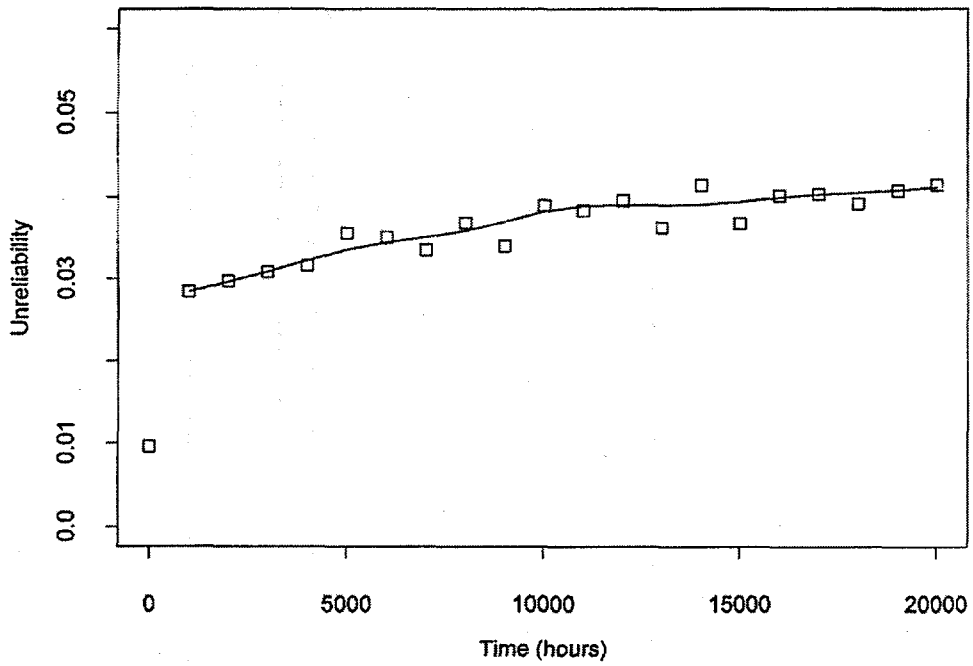

Figure 7-15. Estimated Unreliability Versus Time at 125 Degrees C Assuming 500 gram Requirement With 6262ma Material

In cases where the probability of a heel failure greatly dominates the probability of a metallization failure (or vice versa), one can use a simpler approach to estimate reliability/ unreliability. In cases where heel failures dominate,

$$\hat{R}(T,t) \approx \hat{P}\text{rob}\{Y_H \geq S\}. \tag{7-3}$$

Conversely, when metallization failures dominate,

$$\hat{R}(T,t) \approx \hat{P}\text{rob}\{Y_M \geq S\}. \tag{7-4}$$

Furthermore, in these cases it is relatively straightforward to develop approximate confidence limits for reliability by using a parametric bootstrap procedure.[9] The parametric bootstrap procedure assumes that the model form is correct and utilizes the error magnitudes/correlations among the model parameter estimates as the basis for generating confidence limits. Such confidence limits are developed by constructing N simulated sets of the model parameters that are obtained by perturbing the original model parameter estimates with random normal errors

generated using the magnitudes and correlations that are given in Appendix D Table D-10. Associated with each of the N sets of simulated model parameters, $\{\beta_0, \beta_1, \beta_2\}_i$, is a single value for reliability, R_i. Suppose that these values of reliability are ranked from lowest to highest resulting in $\{R_{(1)}, R_{(2)} \ldots, R_{(N)}\}$. An approximate $\frac{N - k_L}{N} \times 100\%$ lower confidence limit for R is $R_{(k_L)}$. Similarly, an approximate $\frac{k_U}{N} \times 100\%$ upper confidence limit for R is $R_{(k_U)}$. By choosing appropriate values for k_L and $k_{(U)}$ given N, one can construct approximate confidence interval for R given any specified confidence level.

To illustrate the case where Equation 7-3 is appropriate (heel failures dominate), consider Figure 7-16 which indicates the estimated bond unreliability $(1 - R)$ in the case of 6262ma material exposed to a 125°C environment. For this example, the bond strength requirement, S, is assumed to be 450 grams. The solid circles in Figure 7-16 represent the estimated unreliability, while the open circles represent upper and lower 95% confidence limits for the unreliability. That is, based on the experimental data and assuming that the model form is correct, we have 95% confidence that the true unreliability is below the upper limit. These estimated confidence limits were based on a simulation size of N=1000 for each point in time. The fact that the curves denoting the confidence limits are not strictly nondecreasing functions and somewhat noisy is an artifact of the simulation error.

To illustrate the case where Equation 7-4 is appropriate (metallization failures dominate), consider Figure 7-17 which gives $\log_{10}(1 - R)$ in the case of 6262ma material exposed to a 180°C environment with S=300 grams. Here, especially for the longer exposure times, it would be *extremely unlikely* that the overall bond strength would be limited by something other than a metallization failure. As in Figure 7-16, the solid circles represent the $\log_{10}(1 - R)$ while the open circles represent upper and lower 95% confidence limits for log(unreliability). Note the relatively wide limits.

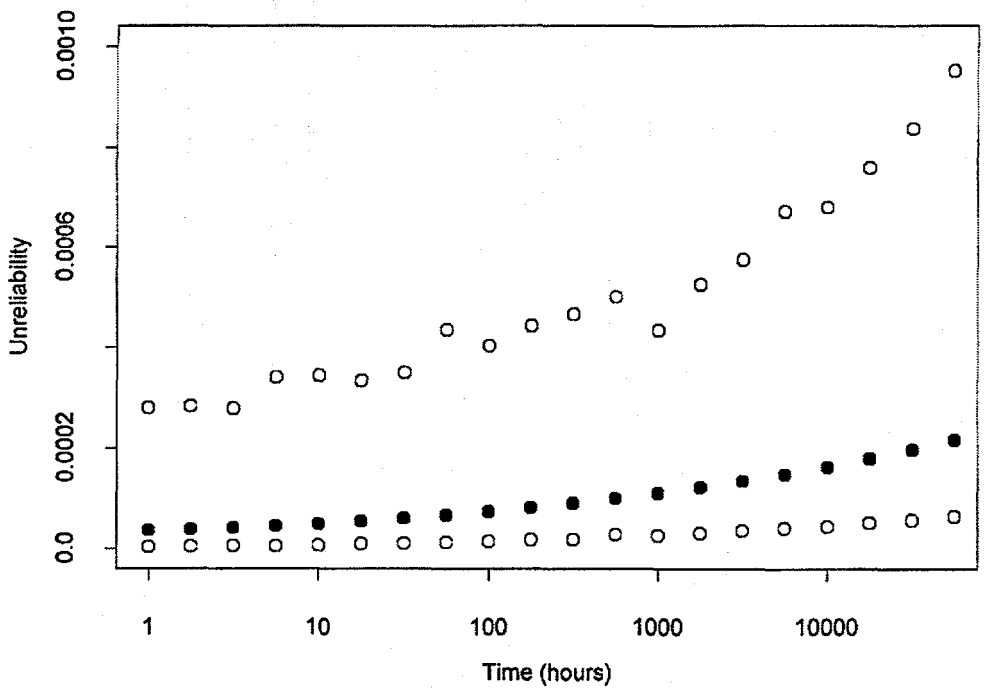

Figure 7-16. 95% Confidence Limits for Unreliability Versus Time Material=6262ma, 125 Degrees C, Required Strength=450 gram

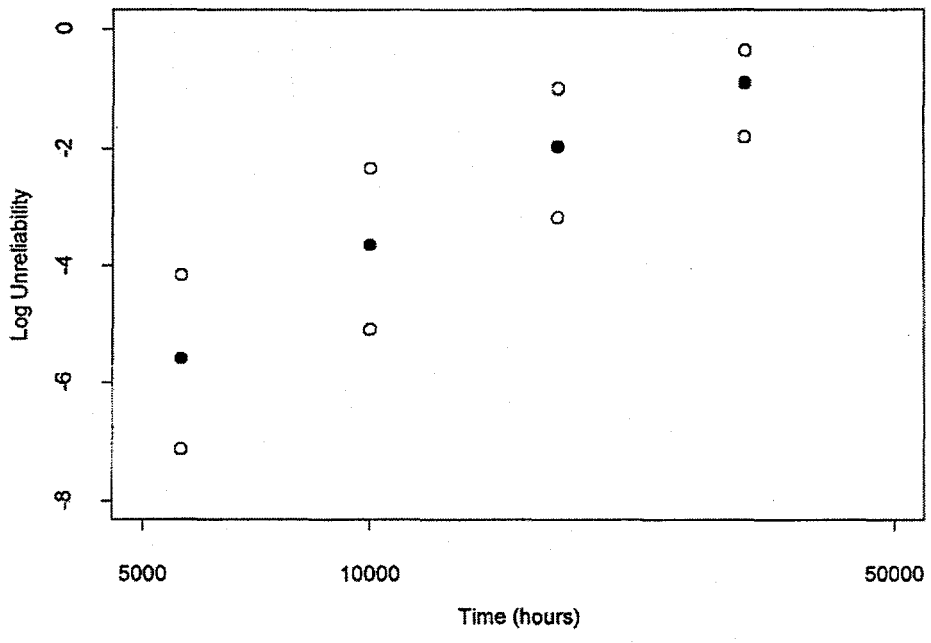

Figure 7-17. 95% Confidence Limits for Log Unreliability Versus Time Material=6262ma, 180 Degrees C, Required Strength=300 gram

Finally, note that in cases where the unreliability is significantly affected by both heel and metallization failures, it is more difficult to estimate upper and lower bounds for unreliability due to the increased computations required. Nevertheless, one could easily adapt the bootstrap procedure (described earlier) to obtain estimates of the upper and lower bounds for this case.

7.2.4 Summary Of Aging Characteristics By Material

The previous sections have dealt primarily with the methodology that was used to estimate reliability. This section is more descriptive in nature, focusing on a comparison between the different material combinations, using Figures D-9 through D-20 of Appendix D as a basis.

First, with respect to heel strength (FM = 2), the materials made with silver (6262) and silver/1% platinum (4740) thick films exhibit similar degradation patterns (as well they should since the same wire material was used in all cases). In these cases, the strength of the bond at the heel degrades to about 450 to 500 grams with increased exposure. Due to the relatively infrequent nature of heel breaks for the other two material types (gold and palladium/silver films), it was not possible to model the heel strength degradation for these cases.

In general, as shown in Figures D-9 through D-20 of Appendix D susceptibility to metallization failures is reduced when the thick-film materials were multi-fired on alumina as opposed to single-fired on dielectric. What follows are some specific comments regarding each thick film.

- 6262ma(sd)/Figures D-9 and D-11--For these materials, there is a clear and systematic dependence of mean bond strength on time and temperature. In both of these cases, the modeling procedures described in earlier sections can provide reasonable estimates of reliability.
- 4740ma(sd)/Figures D-13 and D-15--Compared with all of the different materials tested, the 4740ma material is clearly the least susceptible to metallization failures. Significant numbers of metallization failures were observed only at the two highest temperatures (210° and 225°). Thus, the deviations from linearity regarding the relationship of $\log(K(T))$ versus T^{-1} could not be assessed. With respect to the 4740sd material, the large drop in mean metallization strength from 300 to 400 hours is inconsistent with the smooth nature of the kinetics model given in equation 4. Thus, no model is developed for this case.
- 5725ma(sd)/Figures D-17 and D-18--Compared with the materials fabricated with silver (6262) and silver/platinum (4740) thick films, the materials made with gold films (5725) are much more susceptible to metallization failures, even prior to aging (note in the case of QM21sd material, the relatively low metallization strength prior to aging). At the relatively mild accelerating temperature of 160°, significant and relatively rapid degradation in the metallization strength was observed. If kinetics models were to be developed for these materials (they weren't here), one would choose an asymptotic limit, α (see Equation D4 of Appendix D) close to zero as there does not appear to be as much residual metallization strength in these materials when compared to the other materials.

- QM21ma(sd)/ Figures D-19 and D-20--Like those materials made with gold film, the materials made with palladium/silver film exhibit relatively low metallization strengths prior to aging. However, the metallization strengths of the QM21 materials do not degrade nearly as rapidly as the materials with gold films. Note that kinetics models were not developed for these QM21 materials.

7.2.5 Temperature Cycling

The vast majority of aging was conducted at isothermal conditions. A very limited amount of additional testing, utilizing temperature cycling, was performed with specimens from the 6262ma, 6262sd, 4740ma, and 4740sd groups. For these experiments, a temperature cycle consisted of: 1) a 30 minute dwell at -50°C, 2) a 90 minute ramp to +160°C, 3) a 30 minute dwell at +160°C, and 4) a 90 minute ramp to -50°C. The total cycle time was 240 minutes. After various numbers of cycles had been completed (250, 500, 750, and 1000), 10 specimens were pull tested from each group. Note that no measurements were made on specimens from the 6262sd group at 1000 cycles.

It is interesting to compare the results at 1000 cycles (750 cycles in the case of the 6262sd group) with what was observed at isothermal aging at 160°C. For example, at 1000 cycles the ten specimens from the 6262ma group all failed via mode 1 (bond lift) with an average pull strength of about 370 grams. It is interesting to note that after 8260 hours at 180°C isothermal storage, the average bond strength associated with FM's 0 and 1 (combined) is 486 grams (see Appendix D). Thus, 1000 cycles (involving 4000 hours at or below 160°C) is much more degrading than 8260 hours at 180°. Clearly, temperature cycling stimulates an important failure mechanism that is not exercised during isothermal testing (Note that similar conclusions can be developed by using the experimental data from the other thick film materials). Presumably this mechanism is related to the mismatch of the temperature expansion coefficients of: 1) the substrate, 2) the thick film, and 3) the wire. Thus, it is inappropriate to use the isothermal bond strength model (even if weighted appropriately with respect to the variable temperature levels) as a basis for predicting the reliability of bonds that are exposed to non-isothermal conditions such as would be expected in the vicinity of the engine block of an automobile.

7.2.6 Summary

Based on the experimental data, bond strength is primarily limited by the heel strength and the metallization strength. The heel strength is the primary limitation in the case of benign environments, while the metallization strength is the primary limitation in the case of severe environments. The rate of transition from failures at the heel to failures at the metallization is material dependent. The bonds on multi-fired alumina films appear to be significantly stronger than those on single-fired over dielectric films. The bonds associated with silver and

silver/platinum films appear to be much more resistant to metallization failures than the bonds associated with gold and palladium/silver films.

Kinetics models were used to synthesize the experimental data over the various exposure temperatures for the 6262ma material. These models differ from classical rate models in that there is a log(time) dependence. One might speculate that this log-dependence is due to a situation where the reactants are being consumed relatively quickly or that reaction products might be inhibiting further reaction. Of course, there are other interpretations which are consistent with linear degradation in log(time). These models can be exercised in various ways to produce estimates of reliability. Several examples of what can be done with these models have been provided in Appendix D. However, it should be emphasized that there are limitations of the kinetics models and related estimates of reliability. The estimates of reliability are necessarily model-based due to the fact that they are extrapolated to other than the experimental conditions. Furthermore, the quality of the reliability estimates depends not only on the quality of the experimental data, but also on the quality of the models, which are simply approximations of the observed data. If it is assumed that the model forms are correct and that the errors reside strictly in the parameter estimates, then the estimates of uncertainty are valid. Finally, these kinetics models appear to be valid for only the case of isothermal aging and thus are inappropriate for predicting reliability in a non-isothermal environment.

7.3 Gold Wire Bonding Evaluation

7.3.1 Introduction and Experiment Design

As stated earlier, gold wire bonding to thick film metallization was not considered as large of a reliability risk as the large aluminum wire bond. However, it was desired to evaluate the initial bondability and long-term reliability of the fine gold wire bonded to selected thick film metals of interest. By the time this evaluation was begun, the main materials of interest were the silver and silver-platinum alloys. The evaluation also added the gold thick film material for comparison purposes.

The scope of the gold wire evaluation was not to perform any reliability modeling, but rather to compare long-term performance with other published accounts of fine gold wire bonding to silver containing thick film materials.[10,11] When considering gold ball bonding, more attention has traditionally been placed with the gold ball bond interconnection to an aluminum bond pad of the integrated circuit where a variety of reliability problems can occur. Earlier work performed in support of this CRADA did in fact investigate gold ball bondability issues relating to one of the integrated circuits used in the hybrid module.[12] However, for the main gold wire evaluation the area of interest was specifically focused on the wire to thick film metallization interconnection called the wedge bond. A single aging temperature of 180°C was selected to perform accelerated isothermal aging of the gold bonds rather than the four temperatures used with the aluminum wire evaluation. The samples were aged in an air environment without any hermetic sealing. The goal of the accelerated aging was to demonstrate that the wedge bonds could survive a particular length of time at this temperature. The 180°C temperature was more in line with other published accounts, but still managed to address the high temperature requirements of Delphi's hybrid module. Periodic destructive bond pull test and electrical conductivity measurements were performed at various intervals throughout the conditioning.

Table 7-6 lists the material combinations tested in the gold wire bonding evaluation. The design of the thick film conductor samples allowed for the gold conductor material to be printed over areas of bare alumina and other areas where dielectric material had previously been printed and fired. The thick film firing conditions were the same conditions as those of the aluminum wire evaluation. The design consisted of an array of 100 wire pull test loops, (50 wire loops over alumina and 50 wire loops over dielectric) and a daisy chain continuity loop consisting of 50 wire loops (25 wire loops over alumina and 25 wire loops over dielectric) connected in series with the thick film material. Test samples were assembled using a Hughes 2460 automatic ball bonder. Prior to assembling the test groups, the bond parameters were optimized to yield the highest achievable pull strengths with type 2 failure modes for each of the three thick film metallizations. The stage temperature for the wire bonder was held constant at 180°C during the experiment to optimize bond parameters. Pre bond cleaning consisted of a standard argon plasma cleaning process. The wire used for this evaluation was 99.99% gold, 0.001 inch in diameter with an elongation of 2-5% and a minimum breaking strength of 7.5 grams.

Table 7-6: Gold Wire Bonding Test Groups

Du Pont 6262 Ag on alumina
Du Pont 6262 Ag on QM42 dielectric
Heraeus 4740 Ag/Pt on alumina
Heraeus 4740 Ag/Pt on IP9117 dielectric
Du Pont 5725 Au on alumina
Du Pont 5725 Au on QM42 dielectric

7.3.2 Results of Isothermal Aging

Pull tests and conductivity measurements were performed after the samples were bonded and after intervals of 1000, 2000, and 3000 hours. Pull tests rather than shear tests were performed for this evaluation because the joint of interest was the wedge bond and the pull test is the most accurate way of measuring the bond strength. (Shear testing of wedge bonds from 0.001 inch diameter wire is difficult, if not impossible. This is because the wire is deformed so much that the shear tool has difficulty contacting the wire. By contrast, shear testing of wedge bonds from 0.010 inch aluminum diameter wire can easily be done because there is plenty of wire available for the shear tool can come into contact). Normally, the ball bond would be on the integrated circuit and ball shear testing would be appropriate. For these test samples, the ball bond was also on the thick film metallization.

Isothermal aging at 180°C out to 3000 hours did not have a significant effect on the strength of the wire bonds for any of the three different material groups. Average pull strengths after 3000 hours of aging were still within 10% of their original values for both the gold and silver thick film metallizations. Standard deviation values fluctuated but still do not appear to be significantly different from their original values. Figures 7-18 and 7-19 compare the average strengths of each of the three materials as bonded initially and after aging to 3000 hours. Table 7-7 lists the sample sizes, mean pull strengths, standard deviations, the number of each type of failure mode that occurred (for example, FM2), the minimum pull strength value, and the resistance of the continuity loop for each sample. The reader will notice that the sample size for the as-bonded 6262 silver group was much larger than the other two materials. This was the first silver group bonded for this evaluation. And it was desired to bond a greater amount of samples to gain more experience bonding gold wire to silver thick film metallization.

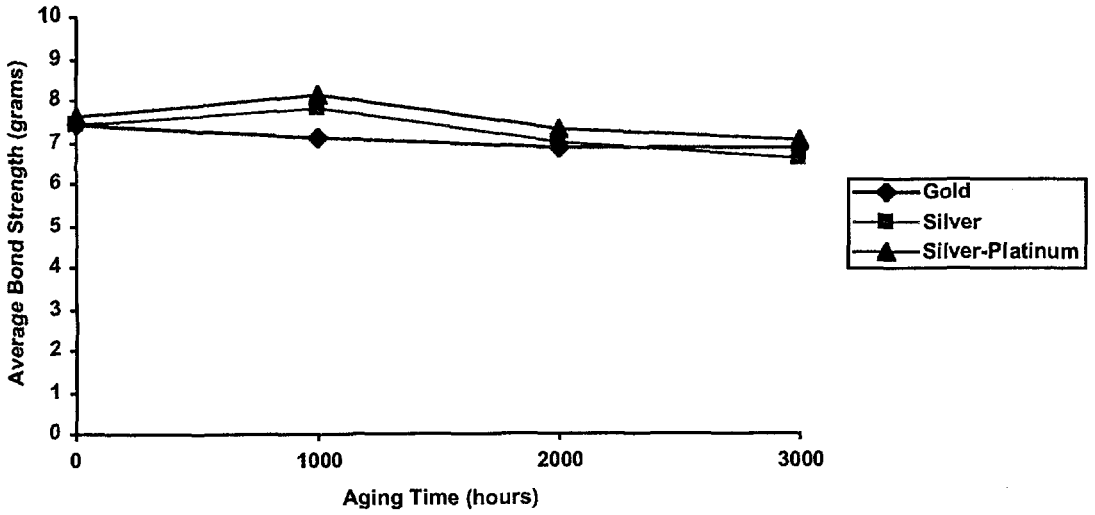

Figure 7-18. Bond Strength vs. Isothermal Aging @ 180°C 1 Mil Gold Wires Bonded to Thick Film Over Alumina

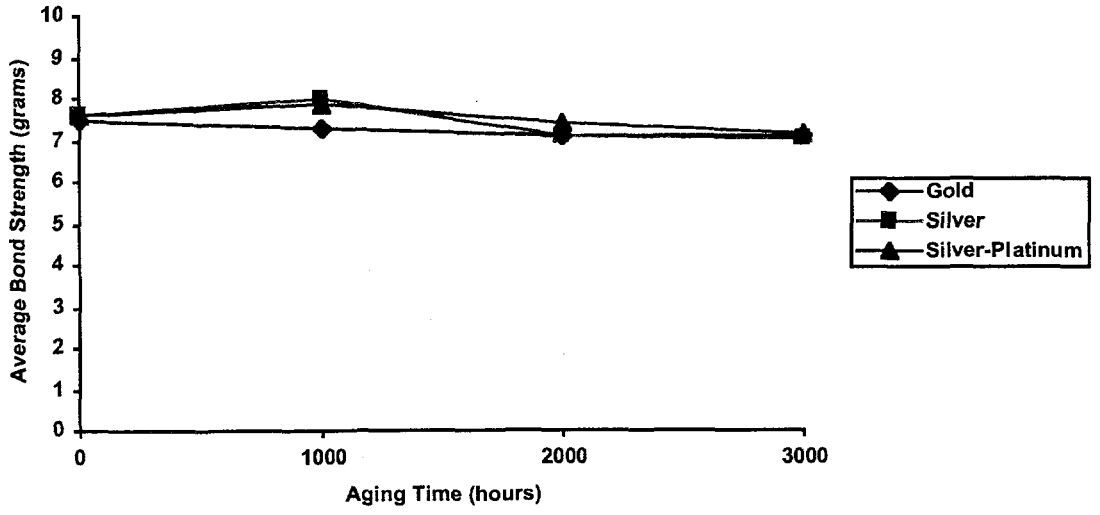

Figure 7-19. Bond Strength vs. Isothermal Aging @ 180°C 1 Mil Gold Wires Bonded to Thick Film Over Dielectric

The only distinguishable difference between the material combinations is that the incidence of wedge bond lifts appears to be more frequent with the silver containing materials than the gold material. Also, these wedge bond lifts occurred mainly on the thick film metal printed over the

dielectric materials. Investigation of individual pull strengths for the wedge bond lifts did not reveal any significant loss in strength for the wedge bond lifts (FM5) as compared with the wire breaks (FM2). This may indicate that some reaction between the silver and gold is taking place, even if at a slow rate. Resistance measurements also did not change much during and after the aging. Due to the lack of degradation in the bond strengths and conductivity, the gold wire to silver thick film material should be a fairly reliable joint.

Test samples were inspected with Scanning Electron Microscopy after 2000 hours. Other published reports[13,14] had indicated that corrosion of the silver thick film occurred in the presence of chlorine during high temperature aging. It is known that silver has a strong affinity for chlorine at high temperatures. The mechanism of this corrosion is that silver from the thick film metal migrates by surface diffusion along the gold wire. Chlorine from the environment reacts with the silver to form silver chloride particles along the surface of the ball bond and extending up the span of wire. SEM analysis at Sandia showed results that were very similar to other published accounts. Energy Dispersive Spectroscopy also verified that the corrosion products on the gold contained silver and chlorine. Figure 7-20 shows silver chloride particles on the surface of the gold wire. Bond strengths from Sandia's evaluation as well as the published accounts did not show any degradation that could be attributed to the corrosion. However, for hermetic applications, it would imply that adequate cleaning to remove all trace of chlorine prior to hermetic sealing is necessary to prevent the silver diffusion and corrosion from occurring.

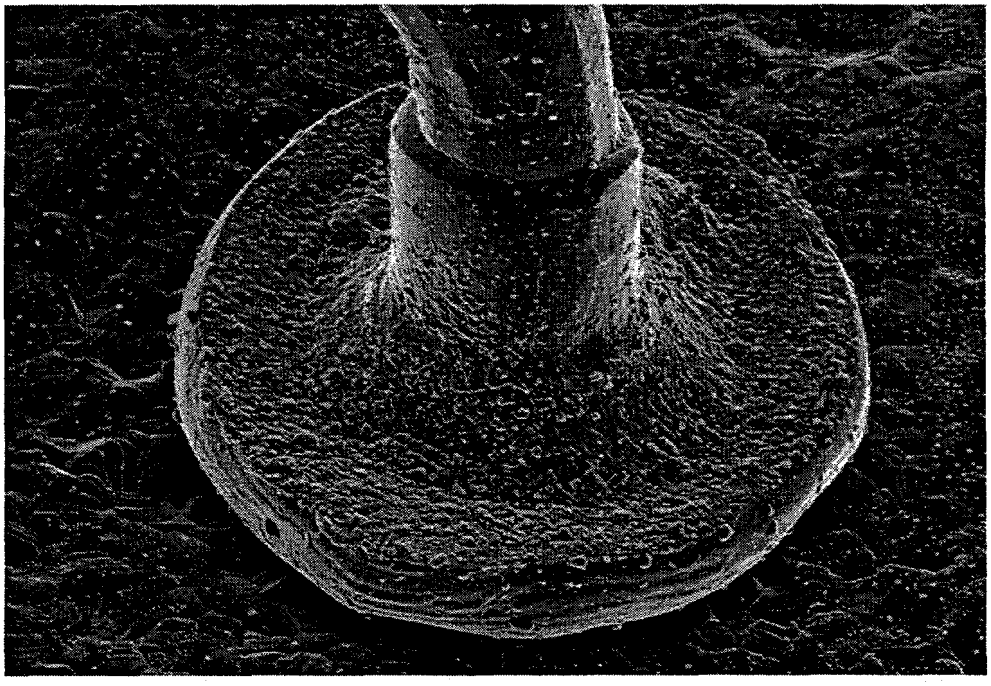

Figure 7-20. Light Particles on the Surface of the Gold Ball Bond and Silver Thick Film Material Were Identified as Containing Silver and Chlorine.

To conclude, the gold wires bonded to the gold, silver and silver-platinum thick films withstood the high temperature aging for 3000 hours at 180°C without any significant degradation in bond strength or conductivity. Although, a full reliability study was not conducted, it doesn't appear that reliability problems would be a major concern. As is always the case, less than ideal cleaning can cause problems that could lead to reliability problems.

Table 7-7: 180°C Aging Data: Bond Strengths and Conductivity Measurements

As-Bonded	N	MEAN	STD DEV	FM 0	FM 1	FM 2	FM 3	FM 4	FM 5	FM 6	Minimum Value	Resistance (ohms)
Au - alum	30	7.4	0.68			30					6.5	4.05
Au - diel	30	7.5	0.52			30					6.6	3.95
Ag - alum	350	7.4	0.65			348	1		1		5.5	3.66
Ag - diel	349	7.6	0.74			333	1		15		5.7	
Ag/Pt - alum	60	7.6	0.51			60					6.5	3.85
Ag/Pt - diel	60	7.6	0.64			59		1			6.3	
1000 hours	N	MEAN	STD DEV	FM 0	FM 1	FM 2	FM 3	FM 4	FM 5	FM 6	Minimum Value	Resistance (ohms)
Au - alum	30	7.1	0.44			30					6.3	4.01
Au - diel	30	7.3	0.49			30					6.3	3.93
Ag - alum	50	7.8	0.68			49	1				5.8	3.68
Ag - diel	50	8	0.63			48			2		6.5	
Ag/Pt - alum	60	8.1	0.64			60					6.8	3.79
Ag/Pt - diel	59	7.9	0.63			53			6		5.8	
2000 hours	N	MEAN	STD DEV	FM 0	FM 1	FM 2	FM 3	FM 4	FM 5	FM 6	Minimum Value	Resistance (ohms)
Au - alum	30	6.86	0.52			29			1		5.7	4.43
Au - diel	30	7.08	0.35			30					6.6	4.62
Ag - alum	50	6.95	0.55			50					5.1	3.73
Ag - diel	50	7.08	0.54			48	1		1		5.8	
Ag/Pt - alum	60	7.3	0.77			59	1				6	3.8
Ag/Pt - diel	59	7.42	0.66			59			1		5.9	
3000 hours	N	MEAN	STD DEV	FM 0	FM 1	FM 2	FM 3	FM 4	FM 5	FM 6	Minimum Value	Resistance (ohms)
Au - alum	30	6.86	0.57			30			0		5.9	4
Au - diel	30	7.11	0.57			30					5.4	3.95
Ag - alum	40	6.58	0.7			40					4.9	3.81
Ag - diel	40	7.05	0.49			39			1		6.2	
Ag/Pt - alum	50	7.01	0.49			50					6.2	3.89
Ag/Pt- diel	50	7.14	0.68			50					5.8	

FM0 is a metallization failure at the 1st bond location
FM1 is a ball bond (1st bond) lift
FM2 is a wire failure within three wire diameters of the exit point of the ball bond
FM3 is a wire failure in the wire between the FM2 and FM4 locations
FM4 is a wire failure within three wire diameters of the wedge bond
FM5 is a wedge bond (2nd bond) lift
FM6 is a metallization failure at the 2nd bond location

REFERENCES

1. "Reliability and Yield Problems of Wire Bonding In Microelectronics" G.G. Harmon, published by the International Society for Hybrid Microelectronics, 1991, pg 75.
2. Memo dated 4/11/94 to Steve Garrett, from Ed Thomas, titled "Analysis of Initial Wire Bond Data."
3. "Reliability and Yield Problems of Wire Bonding In Microelectronics", G.G. Harmon, published by the International Society for Hybrid Microelectronics, 1991, pg 75.
4. Memo dated 11/4/94 to Fernando Uribe, from S.E. Garrett, titled "Evaluation of Temperature Cycled Aluminum Wire Bonds to Thick Film Metallizations."
5. Memo dated 5/23/96 to Steve Garrett, from Ed Thomas, titled "Modeling of Wire Bond Failure Data."
6. Robert C. Mason, Du Pont Electronic Report SSR: 93-152, Part 1 – Lart Aluminum Wire Bond Aging Performance on Silver Thick Film", September 1993.
7. Memo to Steve Garrett from Ed Thomas dated May 23, 1996, titled "Modeling of Wire Bond Failure Data.
8. Memo to Steve Garrett from Ed Thomas dated April 11, 1994 titled "Analysis of Initial Wire Bond Data."
9. An Introduction to Bootstrap, by Efron and Tibshirani, Chapman and Hall Publishers, 1993, pp. 53-56.
10. R.W. Johnson and R.E. Cote, "Thermosonic Gold Wire Bonding to Silver Bearing Conductors", ISHM 1980 Proceedings, New York City, 10/2o to 10/22 1980.
11. J. Aday, R.W. Johnson, J.L. Evans and C. Romanczuk, "Wire Bonded Thick Film Silver Multilayers for Under-the-Hood Automotive Applications", The International Journal of Microcircuits and Electronic Packaging, Volume 17, Number 3, Third Quarter 1994, pp 302.
12. Memo to Fernando Uribe from S.E. Garrett, dated 10/6/1994, titled "Evaluation of CMAC Gold Wire Bonding to the Phillips ASIC."
13. R.W. Johnson and R.E. Cote, "Thermosonic Gold Wire Bonding to Silver Bearing Conductors", ISHM 1980 Proceedings, New York City, 10/2o to 10/22 1980.
14. J. Aday, R.W. Johnson, J.L. Evans and C. Romanczuk, "Wire Bonded Thick Film Silver Multilayers for Under-the-Hood Automotive Applications", The International Journal of Microcircuits and Electronic Packaging, Volume 17, Number 3, Third Quarter 1994, pp 302.

This page intentionally left blank

8. Material Kinetics

Paul F Hlava

Developing multichip modules, such as the throttle control module, that utilize thick film metallization on ceramic substrates is critical to economically producing large volume electronic assemblies. Thick film conductor inks based on either gold (Au) and silver (Ag) alloys are readily available and have different advantages and disadvantages. Gold based inks provide excellent chemical inertness but are expensive. Silver based inks are much less expensive, but are particularly prone to corrosion in an automotive under-the-hood environment, which has high temperature and is sulfur rich.

The first pre-prototype build of the throttle control module was realized using gold conductor materials for fabrication of the thick film multilayer interconnect network. Based on this first build, cost analysis projected the per unit cost of the throttle control module above the desired target value. A viable way of reducing costs was to use silver based inks on the protected layers and gold links only on exposed conductor traces. The question then arises as to the integrity of the material formed at the Au and Ag interfaces. This chapter details investigative efforts designed to determine the extent to which the gold based and silver based inks would alloy with one another.

8.1 Experiments Using Combinations of Silver-Based Inks With Gold-Based Inks

Samples were made of four combinations of silver-based inks with gold-based inks. Two sets of samples were made from essentially pure-silver inks and pure-gold inks. These sets were DuPont 6262 silver ink with DuPont 5725 gold ink, and Heraeus 4740 silver ink with Heraeus 5789 gold ink. The other samples were made from inks containing minor amounts of palladium and with or without platinum, which were intended to act as diffusion inhibitors. These other samples were DuPont QM 21 silver—palladium ink with DuPont 5725 gold ink, and Heraeus 4913 silver—palladium—platinum ink with Heraeus 5789 gold ink. Each sample consisted of a laser-scored alumina substrate printed with broad bands of a silver-based ink, which were partially overprinted with bands of gold-based ink.

After undergoing the appropriate printing and firing operations, the samples were sectioned, potted in epoxy, ground, and polished to expose a suitable cross-section for electron microprobe analysis. A cross-section was suitable if the underlying silver ink had been partially covered by the gold ink. The polished mounts were coated with a thin layer (~200 Å thick) of carbon before examination by the probe.

All of the samples were analyzed with a JEOL 8600 electron microprobe. The analyses consisted of taking photomicrographs at 1000X magnification of three different varieties of

signals coming off of the samples. The photomicrographs include secondary electron micrographs (SEMs) showing the topography of the polished surface, backscattered electron micrographs (BSEMs) showing the distribution of materials of different average atomic number, and identical area elemental distribution photomicrographs (EDPMs) for the elements of interest. SEMs document the distribution of the metallic, ceramic, and epoxy (mounting medium) regions of the area studied and reveal the distribution of voids in the ceramic substrate and between the ceramic substrate and the thick-film metallization. On the BSEM photos, the epoxy is dark because of its low backscatter potential and gold-rich regions are the brightest regions. BSEM is often the most sensitive signal to use in examining subtle chemical changes in diffusion zones. EDPMs are semiquantitative photomicrographs that show where x-rays of the specific wavelength for a particular element are concentrated. Dark areas with only a few points of light show only minor (and unavoidable) background x-rays, while bright areas have a large amount of the element in question.

The exposure conditions can be arranged so that a particular concentration of the element in question is displayed at the optimum white level. EDPMs of several elements showing the same white level but taken to show differing weight percentages can be semiquantitatively related. The ratio of the weight percentages shown on the photo legend is the same as the weight percent ratios of the elements. Areas displaying the optimal white level have approximately the same elemental concentrations as those concentrations listed on the photo.

8.2 Results: Distribution of the Silver and Gold in the Metallization Layers

In all cases, gold and silver were distributed throughout the entire thickness of the metallization layers (see Figures 8-1a and 8-1b). Those samples made with pure silver and gold inks were completely homogeneous. Palladium samples with or without platinum diffusion inhibitors in the silver ink showed diffusion gradients in the Pd and Pt, and some minor Au gradient at the distal side of the layer, but the silver was essentially homogeneous throughout the layers. Samples fired six extra times (see Figures 8-2a and 8-2b) were more nearly homogeneous than those samples fired two times, but they continued to show some gradients in the Pd, Pt, and Au.

In all cases, the gold and silver metallizations combined to form a new alloy of gold and silver (with the palladium with or without platinum, where present). The diffusion inhibitors palladium and platinum tended to diffuse slowly themselves; gold diffused faster. Silver, which was supposed to be inhibited by the palladium and platinum, diffused fastest. The inhibitors were essentially useless in inhibiting the diffusion of silver and/or gold. Because the two metallizations alloyed so thoroughly, no protection existed in the form of a cap or covering of gold over the silver. This was equally true for metallizations from both vendors that were studied.

8.3 Voiding Between the Metallization and Ceramic Substrate

All of the samples studied showed large voids at the metallization and ceramic substrate interfaces where gold overlapped the silver (see Figures 8-3a and 8-3b). The worst of these voids was found in the pure silver metallizations. Voids were essentially nonexistent or small under those parts of the metallization that lacked gold overprint; the presence of voiding could be precisely correlated with gold-bearing regions of the metallization. Samples fired six extra times appeared to have less voiding than their equivalents, which were fired two times (see Figures 8-4a and 8-4b).

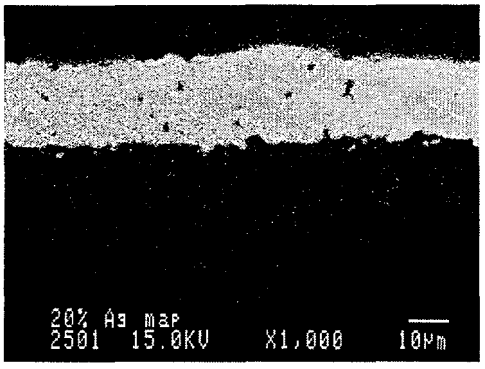

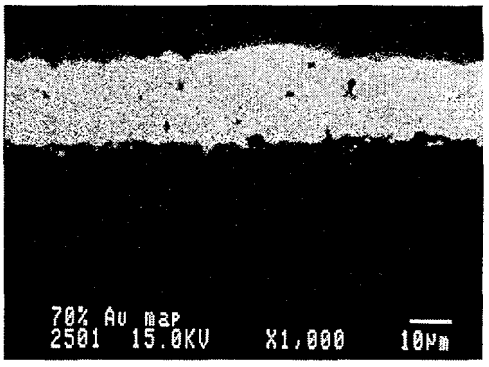

Figures 8-1a and 8-1b. Elemental Distribution Photomicrographs (EDPMs) of a Sample Made With DuPont 6262 Pure Silver Ink and DuPont 5725 Pure Gold Ink in Two Firings.

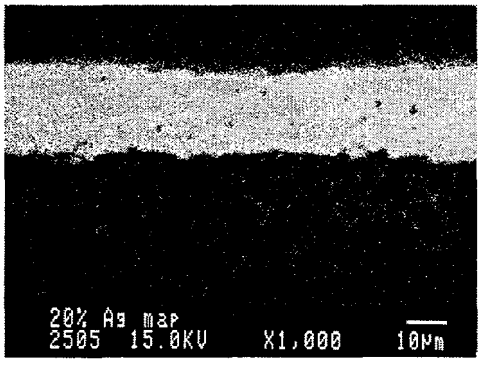

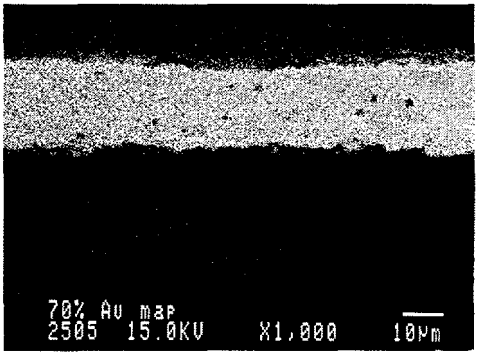

Figures 8-2a and 8-2b. Elemental Distribution Photomicrographs (EDPMs) of a Sample Made With DuPont 6262 Pure Silver Ink and DuPont 5725 Pure Gold Ink in Eight Firings.

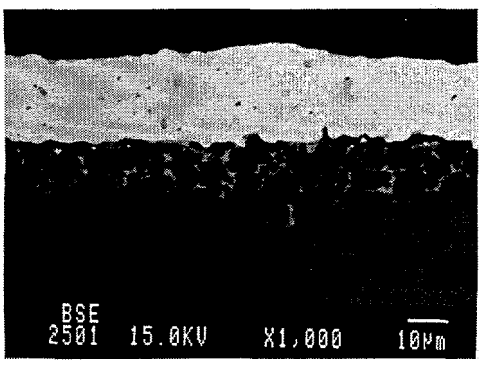

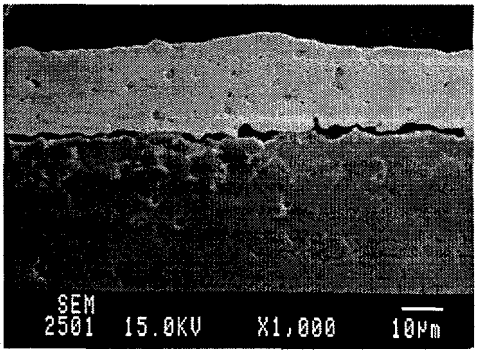

Figures 8-3a and 8-3b. Backscattered Electron Micrograph (BSE) and Secondary Electron Micrograph (SEM) of a Sample Made With DuPont 6262 Pure Silver Ink and DuPont 5725 Pure Gold Ink in Two Firings.

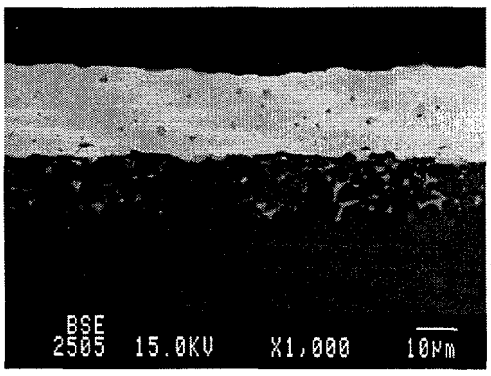

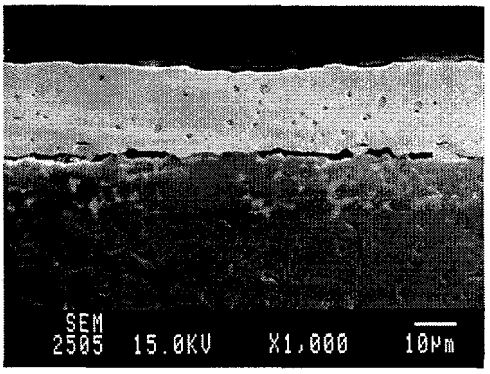

Figures 8-4a and 8-4b. Backscattered Electron Micrograph (BSE) and Secondary Electron Micrograph (SEM) of a Sample Made With DuPont 6262 Pure Silver Ink and DuPont 5725 Pure Gold Ink in Eight Firings.

The voiding along the metallization and ceramic substrate interface appeared diffusion-related and was a form of the Kirkendall effect, or Kirkendall voiding. This effect occurs when metals with different diffusion rates diffuse into one another. The faster species will diffuse so quickly that it will leave voids behind that the other metal can not fill because it diffuses more slowly. In these samples, the effect caused the silver to act as if it were wicked up into the gold to form the silver-gold alloy. This resulted in void formation where the silver was present. The silver metallization layer was then supported by a few pillars of oxide-rich material. (This material was not involved in the diffusion process.) Voiding was worst in the cases of pure silver metallizations because the diffusion was not impeded in any way. Palladium with or without platinum diffusion inhibitors appeared to ameliorate the voiding problem to a minor degree. This is equally true for the metallizations of both vendors that were studied.

8.4 Discussion and Conclusions

Chemical bonding is the primary means by which the oxides in the metallizations studied here join the metallic portions to the underlying ceramic substrates. Total bond strength is related to the total area along the metallization and ceramic substrate interface that is occupied by the metallization oxide. The voiding that was found along these interfaces on all the samples studied is extremely detrimental to the integrity of these metallizations. While the silver-only areas of the metallizations adhered well, the silver-gold areas were weak. This was most evident during sample preparation when the samples were broken along the laser-scored lines. Several of the samples (mainly the pure silver ones) delaminated at the metallization and ceramic substrate interface.

The mixing of silver- and gold-based metallizations is extremely detrimental to the integrity of the hybrid microcircuit modules for several reasons. The two metallizations alloy together wherever they are in contact and as soon as they are fired. Silver, which has diffused to the top surface, is immediately exposed to the corrosive environment. Voiding at the metallization and ceramic substrate interface caused by the diffusion of the silver into the gold destroys the strength of the bonding between the ceramic substrate and the metallization. The choice of thick-film ink vendors is immaterial with regard to the results of this study.

This page intentionally left blank

9. Package Sealing

Larry Kovacic
David M. Keicher
Robert S. Chambers
Steven E. Gianoulakis

The adverse high temperature environments of the throttle control module dictated the need to protect the electronics to assure reliable performance. A preferred approach is to package the electronics in some type of hermetic enclosure. A glass sealing process was developed to fabricate a hermetic ceramic package for high temperature applications. The resulting ceramic package was being developed for use on automobile engines where thermal and mechanical stresses are limiting factors to the package lifetime. Requirements for the sealing glass included mechanical and chemical compatibility with 96% alumina, thermal stability in a high temperature engine environment, and a low sealing temperature to minimize heat input to the electronic components within the package during sealing. Defining the sealing process involved determining screen-printing parameters to control volume and placement of the sealing glass, designing a fixture to align the piece parts, and optimizing the furnace sealing cycle to achieve a consistently robust seal geometry.

Commercially available low-temperature sealing glasses suitable for this application were surveyed. Several glass compositions were selected for investigation (Table 9-1). Sample seals with 96% alumina were made with these candidate glasses. The seals were rated for visual quality, strength, and hermeticity. The sample seals were also used to experiment with variations in processing parameters. Because the alumina substrate was required to have a coating of thick film dielectric material, the sealing glasses were tested for bond integrity with two candidate dielectric materials: DuPont QM42 and Heraeus IP9117. During the sample sealing phase, finite element analyses were performed on the package geometry to determine the magnitude of post-seal residual stresses due to geometrical features and materials mismatches (Section 9.2).

Table 9-1: Sealing Glasses Investigated

Glass	Thermal Expansion RT - 300°C	Sealing Temperature (recommended)
Schott G017-351	65×10^{-7}	630°C
Corning 7583	84×10^{-7}	480°C
Corning 7578	65×10^{-7}	530°C
Corning 7585	68×10^{-7}	415°C
Ferro FX11-036	72×10^{-7}	425°C
Kyocera 1390	71×10^{-7}	none

9.1 First Order Assessment

Glass is a refractory material and usually melts at a relatively high temperature. To reduce the melting temperature of glasses, certain elements are added to the composition. Some of the lowest melting glasses generally contain lead in various percentages and are called solder glasses.

High-lead solder glasses were recommended by Corning, Schott, and Ferro for sealing 96% alumina. These glasses, along with a glass from Kyocera, were characterized for use in the high-temperature package. First, with sections of 96% alumina tubing simulating frame rings (see Figure 9-2), Schott G017-351, Corning 7583, and Corning 7578 were used to bond the rings to bare 96% alumina substrates. All three produced acceptable, crack-free seals, but the sealing temperatures were higher than desired for the sealing process. Schott G017-351 sealed at 630°C, Corning 7583 sealed at 510°C, and Corning 7578 sealed at 530°C. The coefficient of thermal expansion (CTE) of Corning 7583 was also too high for practical consideration, even though the seals appeared functional.

The other glasses, Corning 7585, Ferro FX11-036, and the Kyocera glass, were lower temperature high-lead solder glasses and had acceptable CTEs. Corning recommended their 7585 composition because it is marketed for hermetic sealing on 96% alumina, but for lower service temperatures than the 180°C required in this program. Ferro recommended their FX11-036 composition in paste form for screen-printing and supplied an experimental sample for use in testing. Kyocera 1390 was pre-deposited on 91% alumina ceramic lids. Kyocera 1390 was later identified as a Nippon Electric Glass (NEG) composition, but the NEG code number could not be verified.

These glasses were analyzed for: (1) wetting angle, which is a measure of glass affinity for the material to be sealed; (2) optimal sealing time and temperature for bonding rectangular 96% alumina frames to dielectric-coated substrates; (3) visual characteristics after sealing, including the presence of bubble voids; and seal hermeticity. The 96% alumina frames were ordered from Coors in a configuration that duplicated the package lid proposed by Delphi, but without a lid.

Wetting angles for all three glasses were less than 90 degrees on QM42 dielectric coated substrates, indicating good chemical affinity of the glass for the dielectric material. Hermetic seals with good flow and bonding were made with Corning 7585 at 450°C, Ferro FX11-036 at 450°C, and Kyocera 1390 at 400°C. The 7585 and FX11-036 seals contained bubbles, which could not be completely removed despite numerous processing modifications. The 1390 glass contained no significant bubbles, was sealed at a lower temperature, and produced seals of higher visual quality. Unfortunately, 1390 glass was unavailable from Kyocera, and its product number at NEG could not be verified. Given a greater sealing history with Corning 7585 and comparable results, the 7585 glass was chosen for use in environmental test packages over Ferro FX11-036.

9.2 Thermal Residual Stress Analysis

A stress analysis of the proposed SBA ceramic package was completed to predict residual stresses in the glass seal. The package geometry is depicted in Figure 9-1. It consists of a rectangular alumina frame that is sealed to an alumina substrate using a low-temperature sealing glass (Corning 7585). Using the JAC2D[1] and JAC3D[2] finite element codes, analyses were performed to determine (1) the location and magnitude of the maximum tensile residual stresses generated in the glass during cooling from the sealing temperature, and (2) whether these stresses are sufficiently high to produce cracks. The material properties employed in the finite element computations are recorded in Table 9-2. The elastic properties were assumed to be temperature independent. All subsequently reported stresses are based on cooling from the set temperature of 305°C to 25°C.

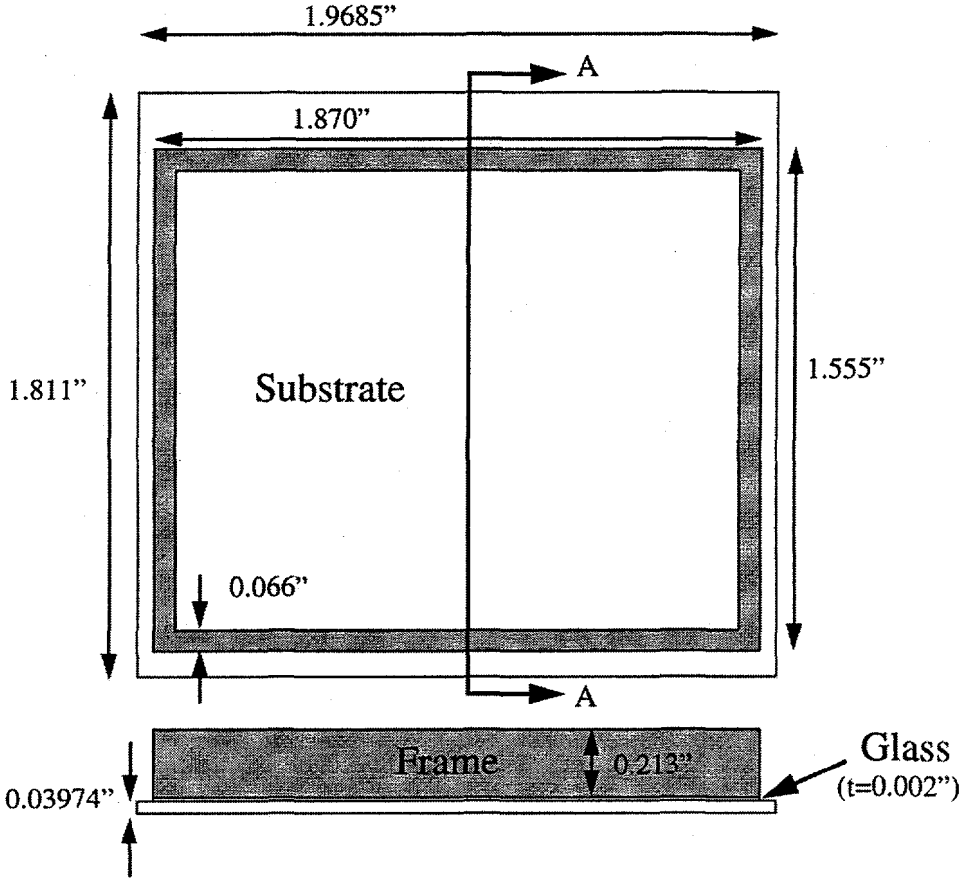

Figure 9-1. Sketch of Frame/Glass/Substrate Assembly in SBA Ceramic Package

Table 9-2: Material Properties Used in Finite Element Analyses

Alumina (96% Al_2O_3)				Corning 7585 Glass			
T (°C)	Thermal Strain	E (psi)	Poisson's Ration	T (°C)	Thermal Strain	E (psi)	Poisson's Ration
25	0.00	44.OE+6	0.21	25	0.0	7.76E+6	0.27
200	1.05E-3			305	1.89E-3		
500	3.51E-3						

9.2.1 Axisymmetric Analyses of Prototype

The Corning 7585 sealing glass was selected after successfully making the prototype seal depicted in Figure 9-2. The prototype consisted of a circular cylinder (made of alumina) sealed to a square alumina substrate. As a first analysis evaluating the compatibility of the alumina and Corning 7585 glass, the thermal residual stresses were computed using an axisymmetric approximation of the prototype. The thickness of the glass seal was assumed to be 0.002 inches. The finite element mesh and a plot of the maximum principal stresses in the glass are shown in Figure 9-3. Note that the magnitude of the maximum tensile stress in the glass is negligible. This is not surprising because the net mismatch between the thermal expansion coefficients of the alumina and the Corning 7585 is quite small when cooling from 305°C to 25°C. The presence of low stresses also is corroborated in that no cracks were detected in the prototypes that were made.

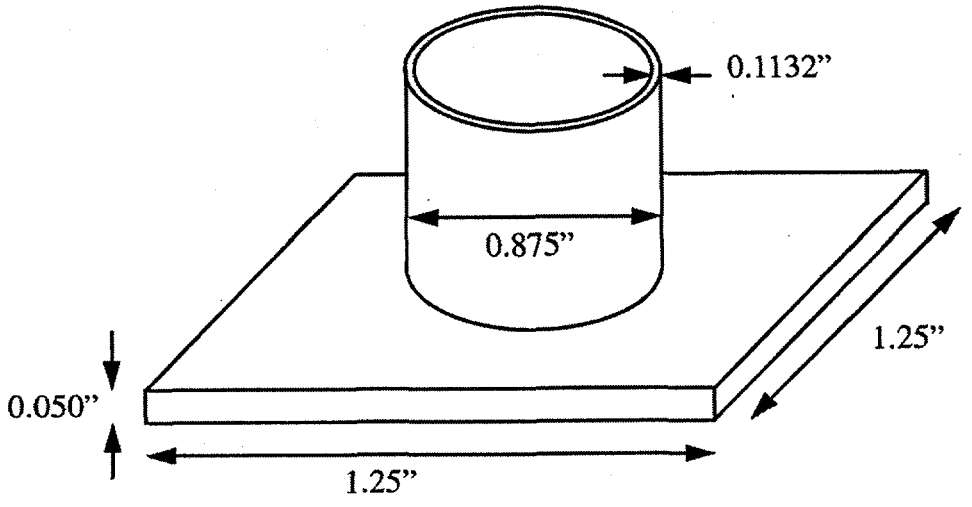

Figure 9-2. Seal Geometry of Prototype

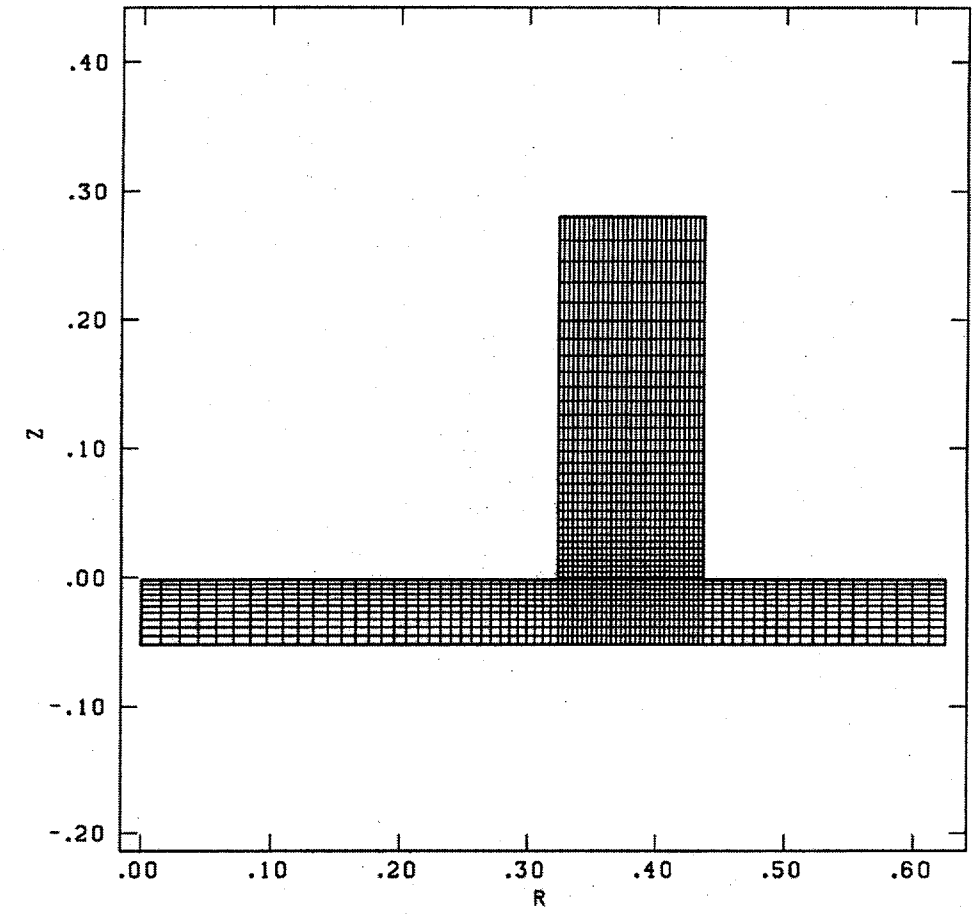

a) Axisymmetric Finite Element Mesh

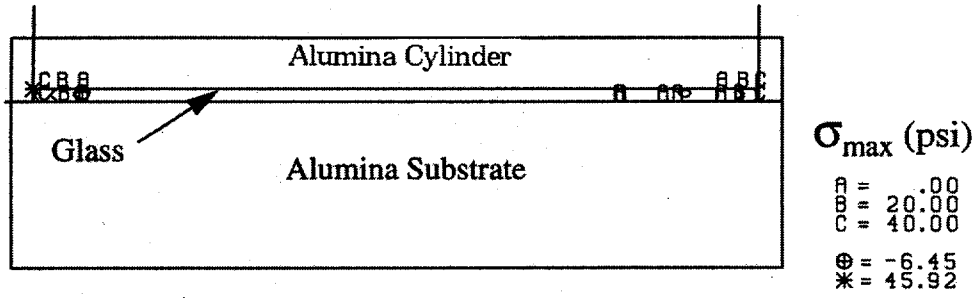

b) Maximum Principal Stresses in the Glass

Figure 9-3. Finite Element Mesh and Maximum Principal Glass Stresses Obtained From Axisymmetric Analysis of Prototype Geometry

9.2.2 Generalized Plane Strain Analyses

The actual sensor geometry does not have an axis of symmetry, but does have two planes of symmetry. With the rectangular frame geometry, there is a possibility of generating peel stresses and bending stresses in the glass if the underlying substrate bends (that is, curvatures in the substrate can induce peeling and bending in the glass seal). One way to investigate the effect of substrate curvature is to analyze a similar model problem that is susceptible to substrate bending. An example problem is illustrated in Figure 9-4 where two rectangular beams are sealed to opposite sides of a plate. The resulting bending deformations through the vertical plane of symmetry are similar to the bending deformations that would be generated in the ceramic package if the rectangular frame were long and narrow and a cross-section far from the ends was examined.

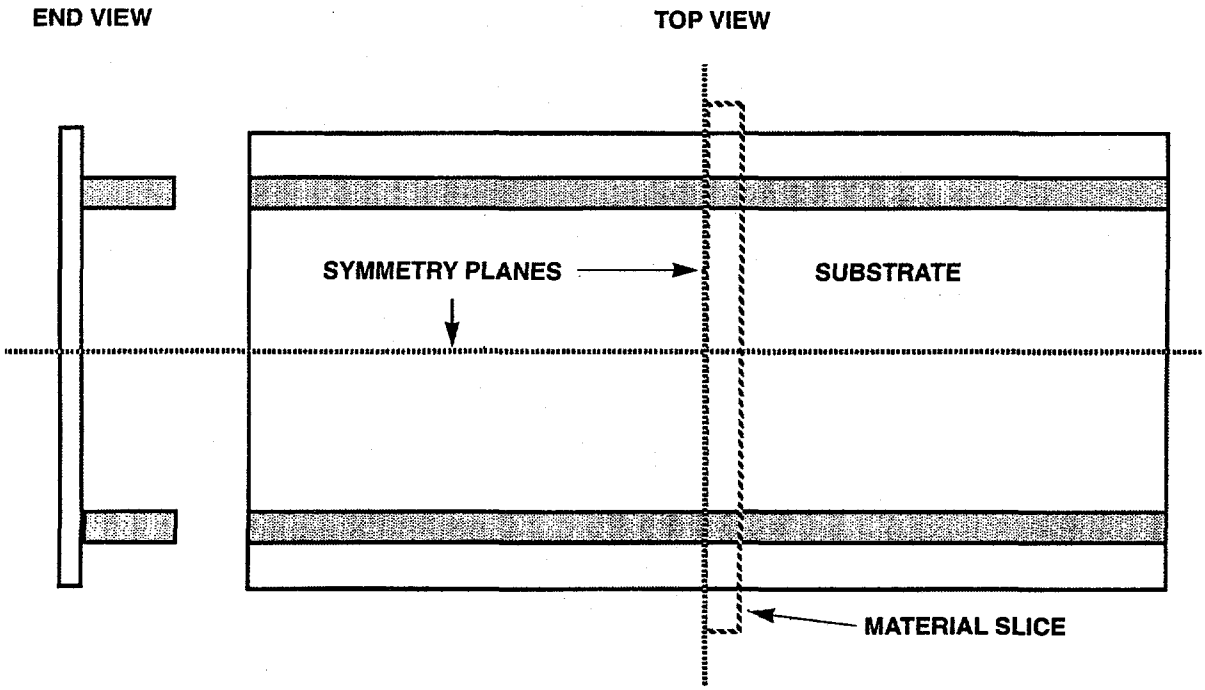

Figure 9-4. Generalized Plane Strain Approximation

Because of the simplicity of the geometry in Figure 9-4, a generalized plane strain analysis was used to approximate the glass stresses found in a slice taken through the vertical plane of symmetry. To do so, a thin slice of the plate was extracted, and plane sections normal to the vertical symmetry plane were assumed to remain plane (that is, the width of the material slice changes uniformly during cooling). This problem was effectively two-dimensional with one extra out-of-plane deformational degree of freedom. Computationally, it was less expensive to model this problem than a quarter of the entire plate in full three dimensions. A generalized plane strain analysis was performed using JAC3D to model a single layer of elements taken from the cross section depicted by the end view in Figure 9-4. Sliding contact against a stiff element block was used to enforce the generalized plane strain condition (that is, uniformity in the out of plane deformation normal to the cross-section). A portion of the finite element mesh and the maximum principal stress contours for the glass are shown in Figure 9-5. These stresses were quite low and were consistent with the findings obtained from the axisymmetric prototype model. Because the flaw sizes and distributions commonly encountered in glass manufacturing processes are able to sustain stresses of 1 to 1.5 ksi over typical service environments, these results are acceptable for design purposes.

When the glass seal is formed, a weight is applied to the top of the frame to make a good seal between the frame and the substrate. As the glass softens during heating, there is a tendency for the weight to squeeze the glass out from under the frame. Figure 9-6 contains a photograph with an enlarged view of the seal. To determine the effect of this geometry change, an additional analysis was performed using the modified geometry depicted by the finite element mesh shown in Figure 9-7. The corresponding stress contours of the maximum principal stresses in the glass are shown in Figure 9-8. As expected, these stresses also were quite low. The only significant difference created by the presence of the squeeze-out was to provide a potential fracture barrier at the location of the maximum principal stress. By embedding this location in a blob of glass and thereby removing it from an exposed surface position, the likelihood of incurring additional damage was reduced.

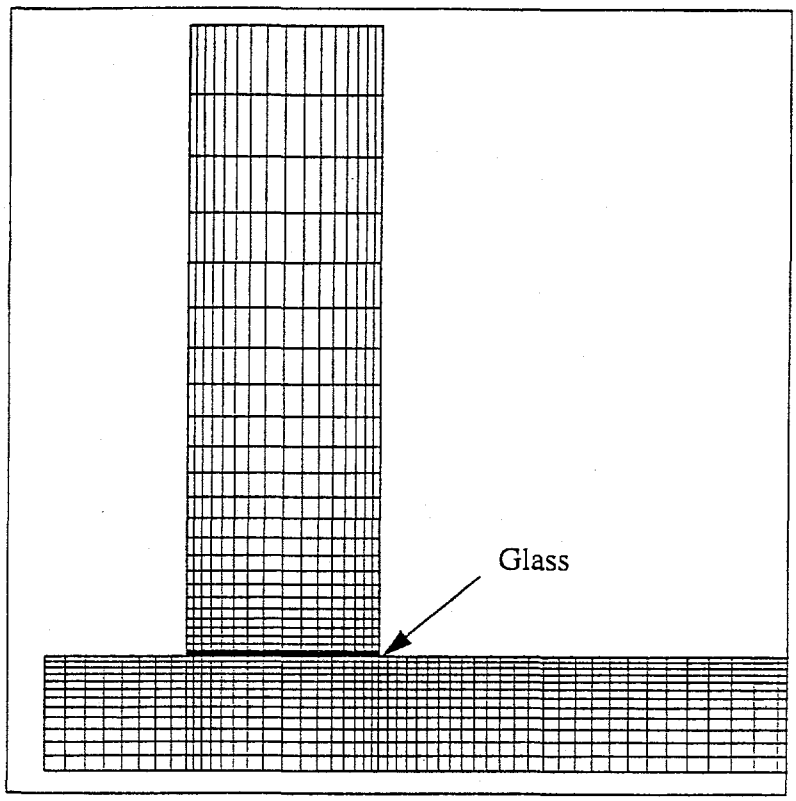

a) Finite Element Mesh

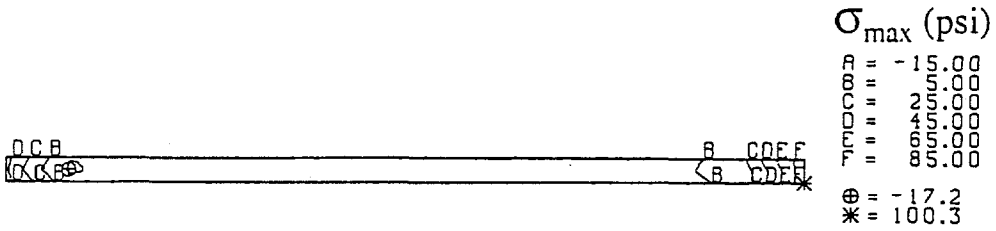

b) Maximum Principal Stress Contours

Figure 9-5. Finite Element Mesh and Stress Contours for the Glass Obtained from the Generalized Plane Strain Analysis

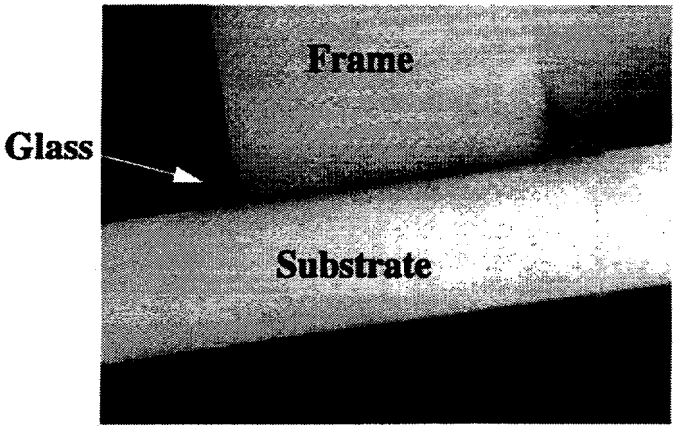

Figure 9-6. Photograph of Glass Seal with Visible Squeeze-Out"

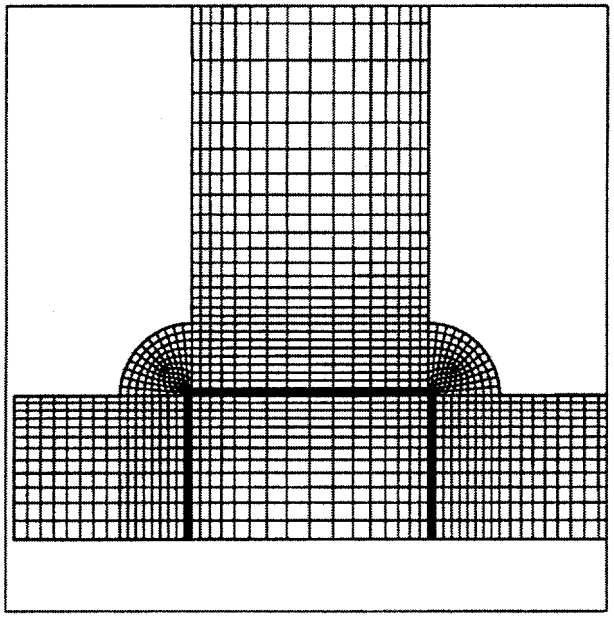

Figure 9-7. Finite Element Mesh of "Squeeze-Out" Glass Geometry

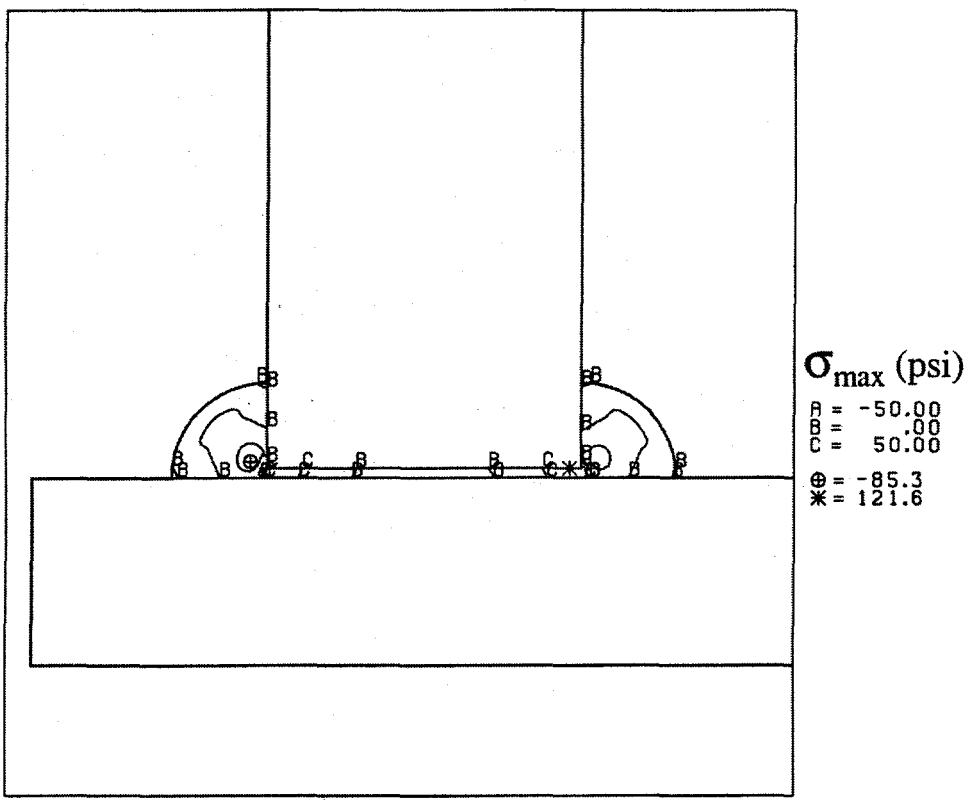

Figure 9-8. Maximum Principal Stress Contours in "Squeezed-Out" Seal Geometry

9.2.3 Three-Dimensional Analyses of the Ceramic Package

The axisymmetric analyses and generalized plane strain results indicate that the Corning 7585 is a satisfactory glass seal for the alumina. However, to identify the location of the maximum glass stress in the ceramic package, a 3-D finite element analysis was performed. Because of the two symmetry planes, only one-quarter of the geometry had to be modeled. The finite element mesh is shown in Figure 9-9. The 3-D computations indicate that the maximum glass stress occurred in the corner of the frame, as shown in the stress contour plot found in Figure 9-10. Although the magnitude of the stress is somewhat higher than that predicted by the other models, it was still well below the desirable design maximum of 1 to 1.5 ksi.

9.2.4 A Ceramic Package with a Dielectric Layer

Another configuration to be examined involved the addition of a 0.0015-inch-thick dielectric layer to the surface of the alumina substrate. In this case, the glass seals the alumina frame to the dielectric layer. Dupont QM42 was proposed for the dielectric. It exhibited thermal expansions closely matching alumina and has a Young's modulus of approximately 10.5E+6 psi with

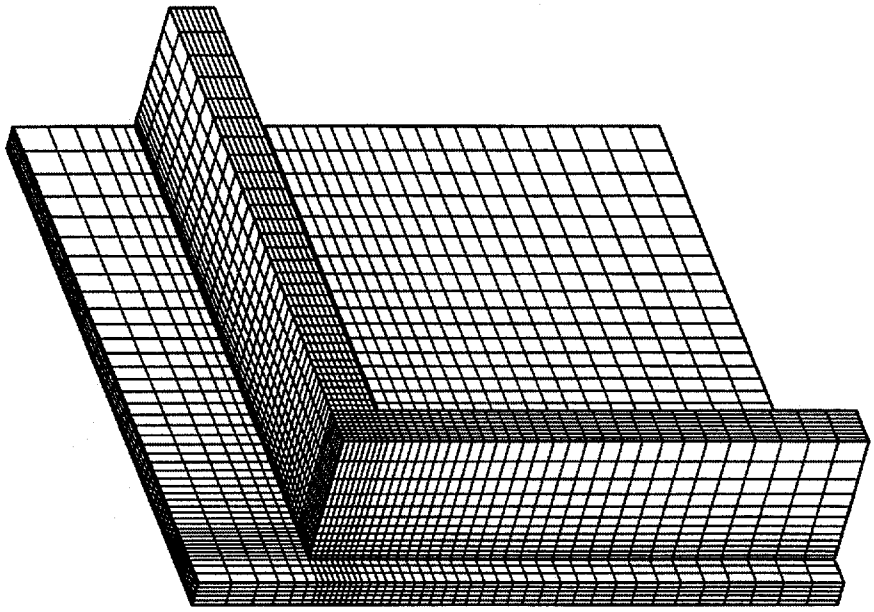

Figure 9-9. 3-D Finite Element Mesh of One-Quarter of Ceramic Package

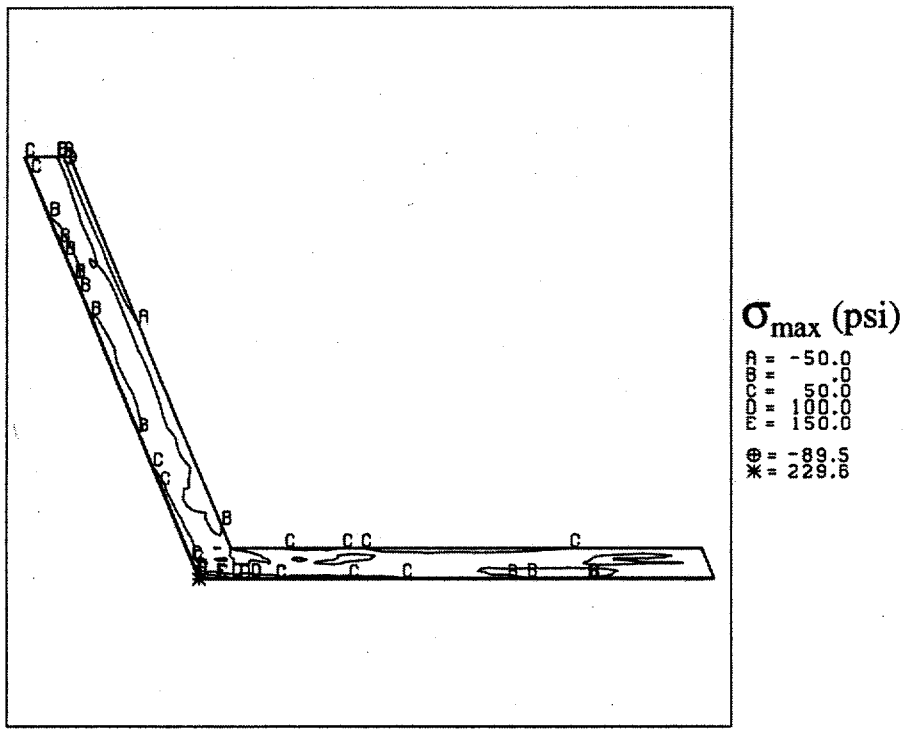

Figure 9-10. Maximum Principal Stresses in Glass Seal Computed with 3-D Model

Poisson's ratio approximately equal to 0.25. With the expansions of the dielectric assumed to be identically matched to the alumina, analyses show that there is no significant increase in stress.

9.2.5 Conclusions of the Thermal Residual Stress Analysis

The thermal residual stresses were computed in the proposed SBA ceramic package to evaluate and document the feasibility of the design. From a mechanical viewpoint, the Corning 7585 glass was determined to be an excellent match to the alumina. The maximum principal stresses in the glass (located adjacent to the substrate at the corners of the frame) were found to be well within acceptable design values. The addition of a dielectric layer was found to have negligible effect on the stress level provided that it too is in fact as closely thermally matched to the alumina as is the Corning 7585.

9.2.6 Material Options for the Frame

Analyses of the initial design (96% alumina frame) were described in Section 9.2. Using the JAC3D [2] finite-element code, analyses of several new material combinations were performed to identify material options for reducing product costs. To evaluate these options, researchers at Sandia computed the location and magnitude of the maximum tensile residual stresses generated in the glass during cooling to room temperature from the sealing temperature. Three new materials were considered for the frame: Kovar, 90% alumina, and 85% alumina. Decreasing the alumina content was a means of lowering the material cost. The material properties employed in the finite element computations are recorded in Table 9-3. The elastic properties were assumed to be temperature independent. All subsequently reported stresses were based on cooling from the set temperature of 305°C to 25°C. Note that the thermal expansion coefficient, α, over this temperature range is also provided in Table 9-3.

Table 9-3: Material Properties Used in Analyses

Alumina (96% Al_2O_3) α = 68.25E-7/°C (25-305°C)			
T (°C)	Thermal Strain	E (psi)	Poisson's Ratio
25	0.0	44.0E+6	0.21
200	1.05E-3		
500	3.51E-3		

Corning 7585 Glass α = 67.5E-7/°C (25-305°C)			
T (°C)	Thermal Strain	E (psi)	Poisson's Ratio
25	0.0	7.76E+6	0.27
305	1.89E-3		

Alumina (90% Al_2O_3) α = 66.625E-7/°C (25-305°C)			
T (°C)	Thermal Strain	E (psi)	Poisson's Ratio
25	0.0	39.0E+6	0.22
200	1.0675E-3		
500	3.3475E-3		

Alumina (85% Al_2O_3) α = 59.25E-7/°C (25-305°C)			
T (°C)	Thermal Strain	E (psi)	Poisson's Ratio
25	0.0	33.0E+6	0.22
200	9.450E-4		
500	2.985E-3		

Kovar α = 49.31E-7/°C (25-305°C)			
T (°C)	Thermal Strain	E (psi)	Poisson's Ratio
25	0.0	21.5E+6	0.31
100	4.000E-4		
200	9.549E-4		
300	1.355E-3		
350	1.611E-3		

9.2.7 Three-Dimensional Analyses of the Ceramic Package Without a Lid

Using the 96% alumina substrate and the Corning 7585 sealing glass, the residual stresses were computed to determine the durability of the glass seal when the substrate was sealed to each of the four proposed frame materials: 96% alumina, 90% alumina, 85% alumina, and Kovar. The finite element mesh of one quarter of the ceramic package (with no lid) is shown in Figure 9-9. The magnitude of the maximum principal stresses obtained from these analyses is summarized in Tables 9-4 and 9-5. These analyses showed that both the 96% and 90% alumina frame materials could be used while still keeping the glass tensile stresses less than about 1200 psi. This was acceptable from a design standpoint. However, the 85% alumina frame and the Kovar frame generated thermal mismatches that increased the stresses in the glass to beyond 5000 psi. This level will most certainly result in cracking. Painted stress contours of the maximum glass tensile stresses found in each of the four cases are shown in Figure 9-11. The viewing direction is identical to that used in Figure 9-9. Note that the location of the maximum principal stress was at the corner.

Table 9-4: Maximum Stresses Obtained in Ceramic Package With No Lid

Frame Material	Maximum Stresses (psi)		
	Frame	Glass	Substrate
96% Alumina	385	230	200
90% Alumina	1470	1130	1150
85% Alumina	6860	5720	5860
Kovar	9300	8760	10800

Table 9-5: Maximum Stresses Obtained in Ceramic Package with Lid

Frame\Lid Material	Maximum Stresses (psi)		
	Frame/Lid	Glass	Substrate
96% Alumina	270	360	400
90% Alumina	1640	1230	1310
85% Alumina	7770	6200	6650

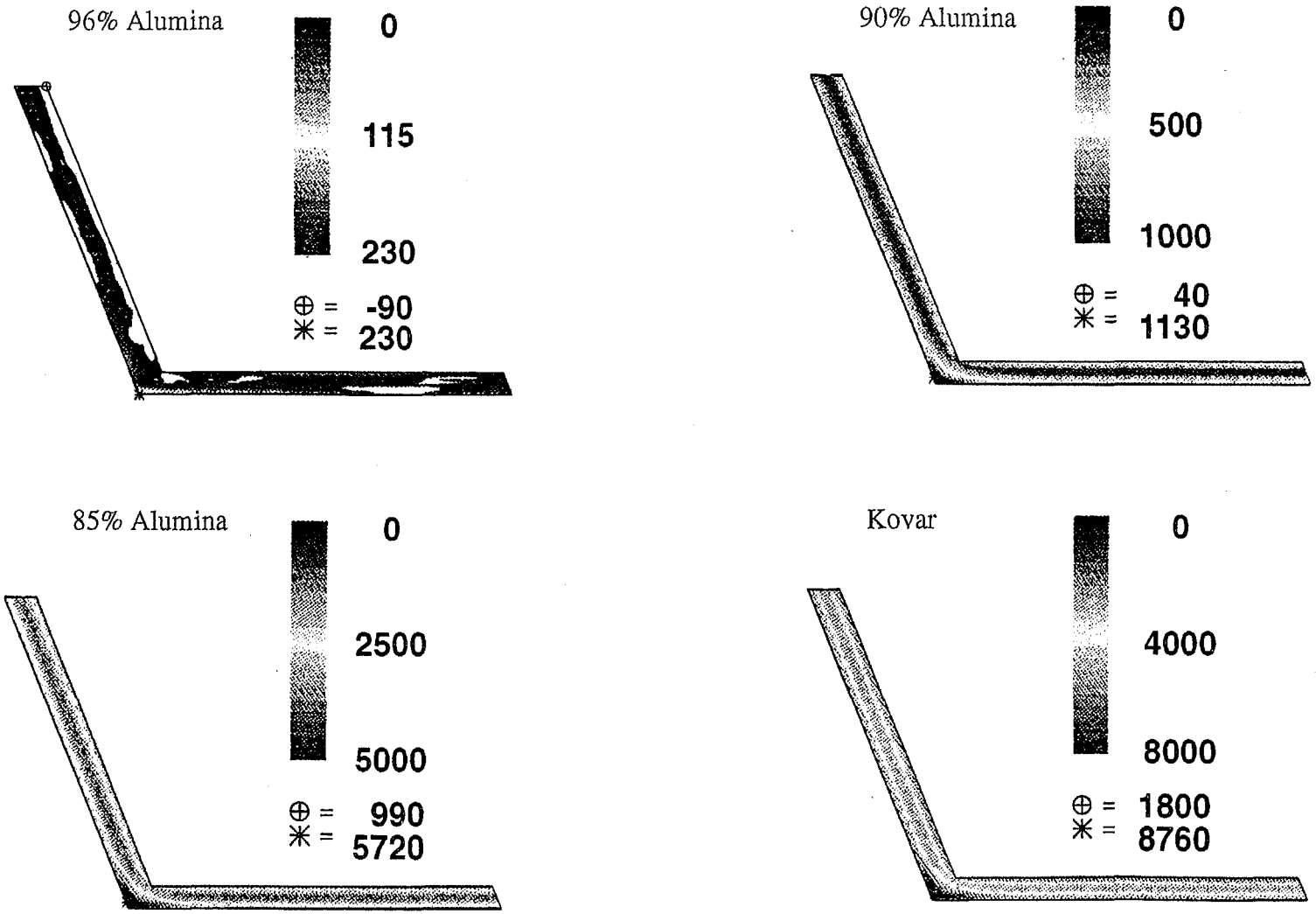

Figure 9-11. Thermal Residual Stresses (psi) in Glass Seal of SBA Ceramic Package Without Lid

9.2.8 Three-Dimensional Analyses of the Ceramic Package With a Lid

The analyses were repeated for some of the material combinations with the design modified to include a one-piece frame with a lid (that is, a box) sealed to the substrate. The modified finite element mesh of one quarter of the model is shown in Figure 9-12. The added stiffness of the lid increased the maximum stresses as indicated by the results provided in Table 9-5.

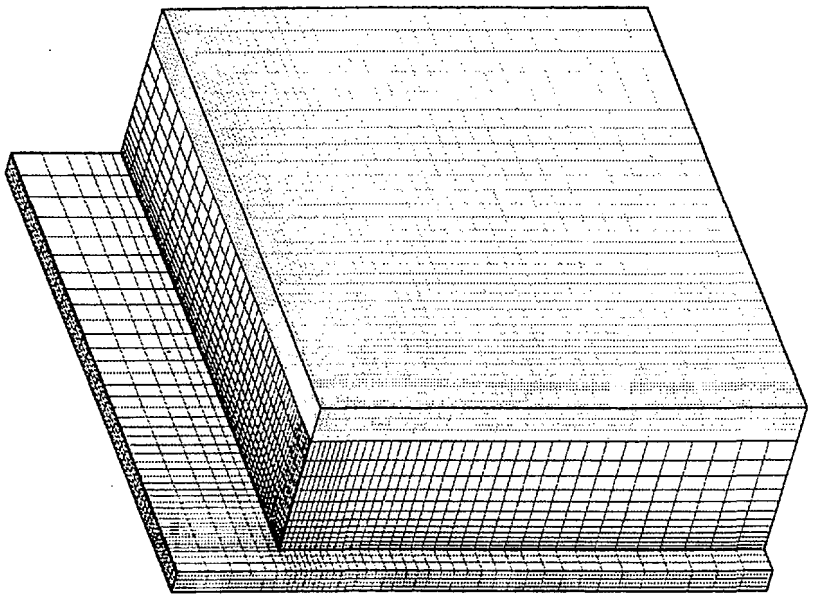

Figure 9-12. 3-D Finite Element Mesh of One-Quarter of Ceramic Package with Box Top (i.e., Frame with Lid)

9.2.9 Conclusions of the Thermal Residual Stress Analysis

The thermal residual stresses were computed in the proposed SBA ceramic package to evaluate and document the feasibility of the design with different frame materials. The results indicated that the frame material could be made from either 96-percent or 90-percent alumina to produce stresses low enough to avoid cracking the glass seal. The added stiffness of a lid on the frame (that is, making the frame a closed box) increased the magnitude of the maximum stresses. However, the increase was not high enough to undermine the design. From a mechanical point of view, note that because the extremely thin glass seal was not stiff and is highly constrained volumetrically at the corner, the maximum stress in the glass was determined by the net mismatch in thermal shrinkage between the frame material and the substrate. The result was not sensitive to the thermal expansion coefficient of the glass. Consequently, different glasses with somewhat different expansion coefficients would yield similar results.

9.3 Process Optimization

Once Corning 7585 was chosen for fabrication of the hermetic ceramic test packages for environmental testing, the sealing process was optimized to the extent possible. This optimization included four primary tasks: (1) The screen-printing process for applying sealing glass paste to the substrates was tailored to achieve a robust seal geometry. This consisted primarily of determining the correct height of glass paste to be printed on the substrate. (2) Times and temperatures were optimized for a glass paste pre-flow operation performed prior to sealing. (3) A fixture was designed to accurately locate the frame on the substrate and prohibit any x-y movement during sealing. (4) A glass sealing profile was defined to achieve optimal glass flow and bonding, while minimizing bubble formation in the glass.

Screen-printing was performed by the Electronics Processing Department at Sandia. Corning 7585 glass paste was screen-printed onto the dielectric coated substrates in a pattern that matched the frame geometry. Two dielectric materials were tested: DuPont QM42 and Heraeus IP9117. Both materials had matching CTEs and were recommended for use with 96% alumina. The correct glass paste height was the height that produced small, continuous glass fillets between the frame and the substrate on all sides of the frame during the sealing cycle. This height was determined to be 0.003 to 0.004 inch after air drying and before pre-flowing. The glass paste height on each environmental test substrate was measured on all four sides before sealing. After printing, the glass paste was air dried at 125°C for 15 minutes. The air drying was followed by a pre-flow operation in which the glass was melted onto the substrate at a temperature that would burn out all the organic binders in the paste. Pre-flowing was done in an air furnace at 400°C for 1 minute. The presence of bubbles in virtually all the previous seals indicates that the organic binder material may not have been burned out during the pre-flow operation, and therefore, a need exists to further investigate this phase of the process.

Sandia designed and fabricated a fixture for sealing the frame to the substrate. The fixture base locates the frame on vertical pins. A counterbore in the top of the base aligns the substrate on top of the frame. A weight is placed on the substrate to press it down uniformly onto the frame, squeeze the glass as it melts, and form a glass fillet around all sides of the frame. Figure 9-13 illustrates the fixture assembly. Three fixtures were fabricated. After initial modifications, two of the fixtures were used to make the sealed units for environmental testing.

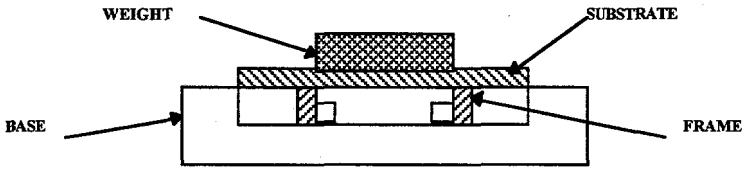

Figure 9-13. Fixture Assembly With Piece Parts

Corning recommended a sealing process time and temperature for the 7585 solder glass of 10 minutes at 415°C. Results from the sample sealing experiments had determined that a temperature of at least 450°C was required to achieve adequate glass flow at the frame and substrate interface. This was, however, without the mass of a fixture to alter the thermal input to the glass paste. Most seals made at 450°C in the fixture exhibited inadequate glass flow, and the temperature was raised to 470°C. At this temperature, glass flow was adequate, but more bubbles were generally visible in the glass. Seals were made in a box air furnace with a ramp rate from room temperature to sealing temperature of 40°C per minute, a 10 minute hold at temperature, and a ramp rate down to room temperature of less than 50°C per minute.

A test matrix was developed to assess the performance of test structures under various types of environmental conditioning. Three package configurations were fabricated:

1. Gold-plated frames sealed to DuPont QM42 dielectric coated substrates with screen-printed Corning 7585;
2. Gold-plated frames sealed to Heraeus IP9117 dielectric coated substrates with screen-printed Corning 7585;
3. Kyocera lids sealed to QM42 dielectric coated Kyocera substrates with Kyocera 1390 glass already applied to the lids.

Section 9.8 lists all environmental test packages used for the testing and indicates their seal characteristics.

The environmental tests performed included temperature cycle, temperature and humidity cycle, liquid thermal shock, mechanical shock, and vibration. See the Glass Seal Environmental Test Sequence in Section 9.9. These tests were condensed from a DELPHI environmental test sequence designed to test the complete electronic package. Only the glass seal was to be tested in this program. Therefore, the tests were modified to retain the extreme temperatures and conditions, but to eliminate redundant or meaningless thermal and electronic conditions.

Before undertaking the extensive (and expensive) environmental test sequence, several feasibility studies were conducted on a number of sealed experimental packages to determine whether they would pass a limited number of cycles of thermal testing. The packages were hermetic at 3×10^{-9} atm cc/sec helium, but included glass seals of various levels of quality.

9.4 Feasibility Studies

Sealed packages from the initial process optimization phase were subjected to a limited number of cycles of each thermal test. The packages were a mixture of bare and gold plated frames, bare and dielectric coated substrates, and Corning 7585 screen-printed in various thicknesses. Some seals were made in a fixture, and some were not. A total of 10 sealed units with varying degrees of seal quality were subjected to up to 300 cycles of the temperature profile -65°C to +180°C.

One package leaked after 100 cycles at an area of the seal with nonuniform glass flow. The remainder of the seals retained hermeticity at 3 x 10^{-9} atm cc/sec helium. Four sealed units were subjected to 250 cycles of the temperature and humidity cycle +10°C to +90°C with 95-percent relative humidity. All units retained hermeticity at 3 x 10^{-9} atm cc/sec helium.

One sealed package from the temperature cycle testing was subjected to three cycles of the liquid thermal shock, 150°C air, and immediate transfer to 10°C distilled water. The glass seal retained hermeticity at 3 x 10^{-9} atm cc/sec helium. The results of the feasibility studies indicated that the sealed packages were of sufficient robustness to fabricate the required number of environmental test packages and initiate the extended test sequence.

9.5 Environmental Testing Results

Thermal, mechanical, and vibration tests were performed at Sandia. A vibration test sequence, determined to be equivalent to the original DELPHI specification, was designed that shortened the time required to perform the testing.

In the final automotive application, it is proposed that the sealed packages be bonded to an aluminum backing plate with Loctite 5402 adhesive. Aluminum has a CTE over three times higher than 96-percent alumina, and there was a concern that bonding an aluminum plate to the substrate could affect the stress condition in the package during thermal cycling. The degree of plasticity of the Loctite 5402 was thought to be critical in absorbing the strain differences between the substrate and backing plate. To check the effect of the backing plate in thermal cycling environments, backing plates were obtained from DELPHI and bonded to some of the sealed packages with Loctite 5402 using process parameters provided by DELPHI. Other packages were left without backing plates for comparison purposes. Packages incorporating the backing plates are indicated in the tables that describe the test results. Section 9.10 lists the sealed packages used for each environmental test and the results of the tests.

9.5.1 Conclusions of Environmental Test Matrix

All sealed packages performed well in the temperature cycle, vibration, and mechanical shock tests. One seal failed in the temperature cycle test. It was characterized as having excessive bubbles in the glass. No seals failed in the vibration test. One seal failed in the mechanical shock test, and it was also characterized as having excessive bubbles in the glass. (Excessive bubbles at this point meant that bubbles were visible on the surface of the glass.) The temperature and humidity cycle test produced more seal failures. Two Kyocera packages, one QM42 package, and one 9117 package failed after the first 100 cycles. Seals in these units were characterized as being marginal, that is, excessive bubbles, low temperature seal, and incomplete glass flow. One more QM42 package failed after 300 cycles; the seal was rated as having excessive bubbles. A final 9117 package failed after 400 cycles. This seal was rated as good with no defects other than the usual bubbles. With the addition of high humidity to the atmosphere, it is likely that

localized cracks in the seals were propagated by the action of water in the crack environment and hermeticity was eventually lost.

The liquid thermal shock testing produced 100% glass seal failures in the packages sealed with Corning 7585 glass. Most of the seals failed after only one cycle. All of the corning 7585 samples failed by the third cycle. Two Kyocera seals failed after one cycle, and two Kyocera seals retained hermeticity through the complete ten cycles. One Kyocera package was damaged during vacuum bake-out and removed from the test.

No pattern of glass cracking was observed due to the presence or absence of an aluminum backing plate on the substrate. The Loctite 5402 adhesive absorbed the strain differential between the aluminum and the 96% alumina during thermal cycling.

Visual inspection of the glass seals at high magnification revealed minute cracks in and adjacent to the corners of the frames. However, these cracks were in the thin area of glass along the edge of the seal, not in the main body of glass that forms the interface between the frame and substrate. This type of crack is not likely to result in failure of seal hermeticity.

Seal failures in the Corning 7585 packages were related to bubbles in the glass, which were most likely caused by failure to completely burn out the organic binder in the glass paste after the screen-printing process. Cross-sectioning seals to expose the glass interface between the frame and substrate revealed bubbles in the glass throughout the bulk (Figure 9-14) The bubbles in the glass form strings through the frame and substrate interface. Individual bubbles were separated by a thin web of glass. These webs can be cracked relatively easily during thermal testing, forming a leak path through the seal.

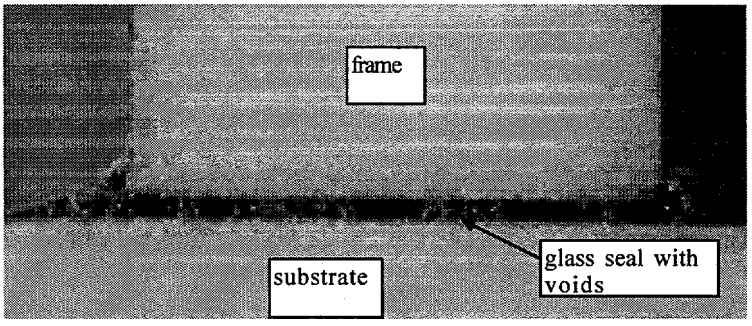

Figure 9-14. Corning 7585 Package Cross-Section

The same configuration of glass without bubbles would probably not fail during testing. This is suggested by the better performance of the Kyocera packages. Two things were different about the Kyocera assemblies: (1) The Kyocera lid was a more integrated structure—essentially, a frame with a lid as opposed to merely a frame. This may have affected the residual stress state of the glass after sealing, although stress analyses of the two designs indicated a negligible contribution to the stress state of the seal from the presence of a lid on the frame (Section 9.2). Cross-sections of Kyocera 1390 packages did not exhibit significant bubbles in the glass after

sealing (Figure 9-15) This may have been the result of the pre-flow process used on the Kyocera lids by the manufacturer or the composition of the glass itself. The pre-flow process may have burn out of the organic binders in the glass paste more completely.

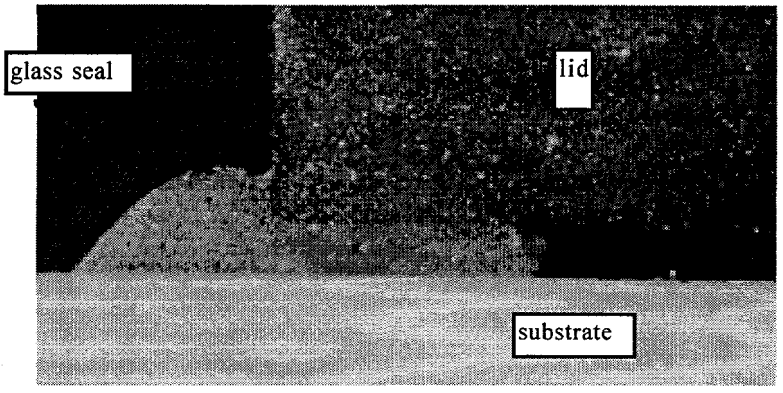

Figure 9-15. Kyocera Package Cross-Section

In general, the results of the testing indicate that the materials and processing chosen for the package perform well in the temperature cycling, mechanical shock, and vibration tests. Minimum dropout due to loss of hermeticity of the glass seal was experienced in these tests. These failures were predominantly associated with seal geometry defects, that is, bubbles in the glass or nonuniform areas of glass flow. Glass performances in the temperature and humidity test and the liquid thermal shock test were less positive, with more seals failing the hermeticity check. Packages with visually marginal glass seals were included in the testing to determine a range of acceptability for the glass processing parameters. These seals fell out first and were easily accounted for. Other seals that eventually failed were cross-sectioned and analyzed for the cause of failure.

The ceramic packages subjected to these tests failed due to cracking in the glass seal, which resulted in a loss of hermeticity in the package. Two reasons for the cracking were postulated: (1) Bubbles in the glass weakened the integrity of the seal and prevented the glass from withstanding the stress associated with the thermal excursions with water present. (2) The geometry of the frame without a supporting lid allowed the ceramic to flex during the thermal cycling, causing cracking in the glass seal. Experiments were undertook to determine the relative contribution of each factor, and funding was provided to look at ways to reduce the bubble count in the glass and improve seal integrity.

Inadequate binder burnout of the glass paste used to make the hermetic seal was the suspected cause of bubbles in the glass after sealing. Residual organic binder material in the seal area burns and outgasses at the elevated temperatures used to melt the glass to form the seal. The gasses emitted became trapped in the molten glass and remained as bubble voids when the glass was a

solid at room temperature. Consultation with the paste vendor resulted in several modifications of the binder burnout process, but the bubbles remained.

9.6 Follow-On Process Development

A different binder and liquid vehicle were used to make a paste with Corning 7585 glass powder. The glass powder was mixed with DuPont thick film composition thinner 9450 to form a glass paste, which was then screen-printed onto alumina substrates in the same manner as before. The paste was printed twice, with a resulting thickness of 0.006 to 0.007 inch. The DuPont thinner contained a lower temperature binder than the previous paste, and it was burned out at 138°C during the drying operation.

Sample seals were made in an air furnace with bare alumina frames and bare alumina screen printed substrates. The same sealing fixtures as in previous experiments were used. The screen-printed substrates were run through a glazing cycle to adhere the glass to the substrates and make them suitable for handling. The following glazing cycle was used:

RT $\rightarrow$ 400°C @ 25°C/min., hold 10 min.
400 $\rightarrow$ RT @ $\approx$ 10°C/min.

After glazing, the alumina substrate and frame were sealed together with the following thermal cycle:

RT $\rightarrow$ 480°C @ 25°C/min., hold 15 min.
480 $\rightarrow$ RT @ $\approx$ 10°C/min.

The DuPont paste produced seals with good glass flow and wetting to the alumina, continuous glass fillets around the frame, and very few bubbles in the bulk of the glass. Cross sections of glass seals showed optimum seal geometry and a few small bubbles, as would be expected from a glass powder melting process. The massive bubbling resulting from inadequate binder burnout was not present.

Thirteen sample frame seals were fabricated with the above processing and subjected to the two thermal cycling sequences that had caused failures in previous tests. Eleven assemblies were run through three sets of 50 temperature/humidity cycles and functionally leak checked between each 50 cycles. Two separate assemblies were liquid thermal shock tested twice and leak checked after each shock. All units retained hermeticity at 1×10^{-9} atm cc/sec helium after all thermal testing. Cracking was not visually apparent in any of the seals.

Results from this follow-up work showed that the bubbles in the glass were the root cause previous failures. Frame flex was not a factor since no evidence of cracking was seen in the

follow-on units. The binder burn-out operation is critical to the success of glass paste sealing and must be carefully investigated when making seals for extreme use conditions.

9.7 Laser Enhanced Process

A series of tests and analysis were performed to determine the feasibility of using a CO_2 laser to produce a glass closure seal between an alumina substrate and cover. There were several requirements which needed to be satisfied by this process: (1) the seal must be able to withstand the high temperature associated with the environment in immediate contact with a hot engine, (2) the seal needed to be hermetic and (3) while creating a seal, the substrate temperature must be maintained to below 150°C to avoid damaging heat sensitive electronics on the base substrate. To satisfy the high temperature requirement, a glass seal between the two alumina components was preferred. Because the sealing operation was the final process to be performed, conventional furnace sealing processes would not provide the localized heating required to satisfy requirements 2 and 3 above. The laser sealing process was chosen as a potential process for satisfying all three system requirements. The localized heating provided by lasers allows very large thermal gradients to be obtained. Exploitation of this feature will allow the glass seal region to be heated to a sufficiently high temperature to flow the sealing glass while heat sinking will maintain a low temperature at the heat sensitive components. In addition, a zoom-axicon lens assembly will allow the entire package periphery to be heated simultaneously.

Before the preliminary sealing experiments were initiated, a series of finite element analyses for the laser sealing process using the throttle control geometry were performed. This modeling effort was aimed at evaluating the feasibility of maintaining a low bias temperature on the substrate to avoid damage to heat sensitive electronics while achieving a sufficiently high temperature at the seal region to flow the glass. These results are described in Section 9.7.1. Based on these results, experiments were performed to determine the feasibility of using the laser to create a seal between two alumina components.

9.7.1 Thermal Simulation of a Laser Sealing Process

A thermal analysis of the proposed laser process was performed to optimize the laser schedule, to predict the transient temperature distribution through the devices, and to aid in the placement of the temperature sensitive components within the throttle control module. The throttle control module will be located near the carburetor and therefore subjected to elevated temperatures during normal operation. The throttle control module consists of an alumina frame and substrate. Conductor traces are printed on the top surface of the substrate and pass between the frame and the substrate. The frame is glass soldered to the substrate providing a hermetic environment for the electronic components. The throttle control module is essentially square measuring approximately 49 mm on a side. The frame is 5.5 mm high and 1.5 mm thick. The substrate is 5.5 mm thick and the glass is 0.25 mm thick.

The proposed method to join the substrate to the frame was with glass solder using a CO_2 laser as the heat source. Because the frame and substrate move together during the soldering process, the glass-solder has to be uniformly heated along its entire length. This was accomplished

through the use of a Zoom-Axicon focusing assembly. An appropriate laser schedule had to be determined to accomplish the soldering using this assembly.

9.7.1.1 Analysis and Results

A series of finite element thermal simulations of the soldering process was performed using P3/Thermal [1] to identify an appropriate laser schedule. Quarter symmetry was used for the simulations. The model consisted of 7152 finite elements. The material properties for the alumina and glass-solder are provided in Table 9-6. The boundary conditions for the simulations consisted of natural convection and thermal radiation to the ambient. The emissivities used are also provided in Table 9-6.

Table 9-6: Material Properties

Material	Density [kg/m^3]	Specific Heat [J/kg K]	Thermal Conductivity [w/m k]	Emissivity
96% Alumina	3720.0	1005.0		0.60
20°C			26.0	
100°C			20.0	
400°C			12.0	
Glass Solder	304.0			0.90
0°C		502.4		
100°C		586.2	1.172	
500°C		711.8	1.424	

During the soldering process, the throttle control module was placed on a 150°C heat sink. This sink was modeled using gap conductances on the bottom of the throttle control module. The heat source for the soldering was modeled as a uniform heat flux along the length of the glass. The first simulation modeled a laser operating at a power level that ramped from zero to 300 W in 1 minute, held at 300 W for 10 minutes, and ramped back to zero W in 1 minute. The laser was focused down to a 1.25 mm (0.005 inch) beam size. The resulting heat flux from the laser was 1.39 W/mm^2. The resulting temperature history for the glass solder at the corner and center-side is shown in Figure 9-16. From this figure it can be seen that the glass solder does not reach the desired softening temperature of 450°C, and that an approximate 100°C difference exists between corner and center-side solder temperatures. This temperature difference is highly undesirable because the corner would have to be heated to a temperature significantly above its softening point for the center-side to reach the softening point. This excessive heating may result in crystallization of the glass. The excessive temperature difference was caused by the uniform heat flux along the solder. Near the corners, the heat was incident from two directions, resulting in a significantly larger volumetric energy deposition. At the center-side, the energy was incident from only one direction.

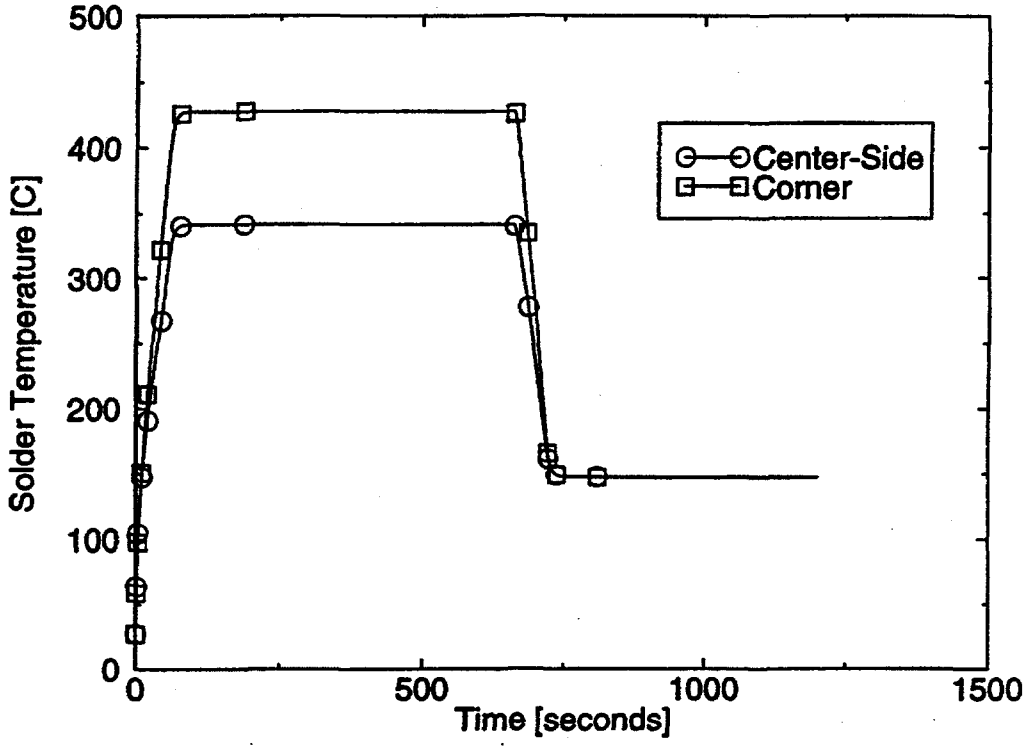

Figure 9-16. Temperature History for 300 W Laser Power

To investigate reducing the temperature difference between the corner and center-side regions of the throttle control module, a simulation was performed with the laser shielded from the corners. In addition to the shielding, the laser power was increased to a maximum of 350 W with the same ramping profile as before. This laser power level resulted in a heat flux of 1.62 W/mm^2. The increase in laser power was necessary because the 450°C softening point was not achieved at 300 W. The temperature history of the glass solder at the corner and center-side with the laser shielded at the corners is shown in Figure 9-17. From this figure it can be seen that the temperature difference has been reduced to approximately 5°C by preferentially shielding the laser. However, the softening point was not reached using a laser power of 350 W. A third simulation was performed using a maximum laser power of 400 W (1.85 W/mm^2), and a similar ramping profile. The laser was also shielded from the corners in this simulation. The temperature history for the 400 W laser is shown in Figure 9-18. From this figure it can be seen that the softening point of 450°C was reached and the corner and center-side solder temperatures were within a few degrees. Figures 9-19 and 9-20 show the isotherms on the throttle control module at 11 minutes into the soldering process. From these figures it can be seen that the higher temperatures tended to occur near the corners of the throttle control module. Placement of temperature sensitive components should therefore be near the center of the throttle control module.

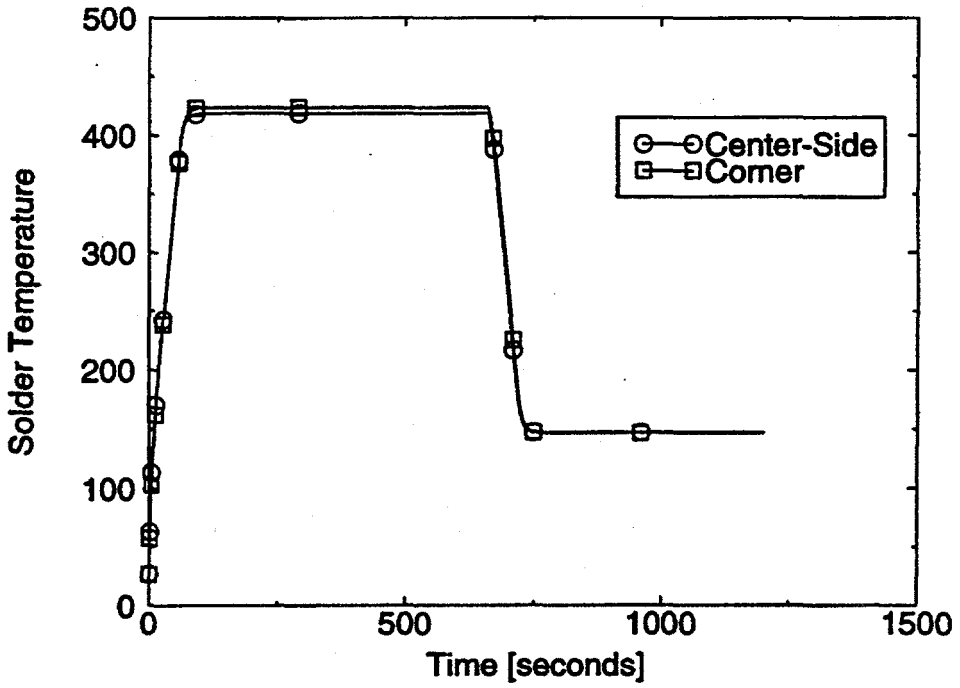

Figure 9-17. Temperature History for 350 W Laser Power

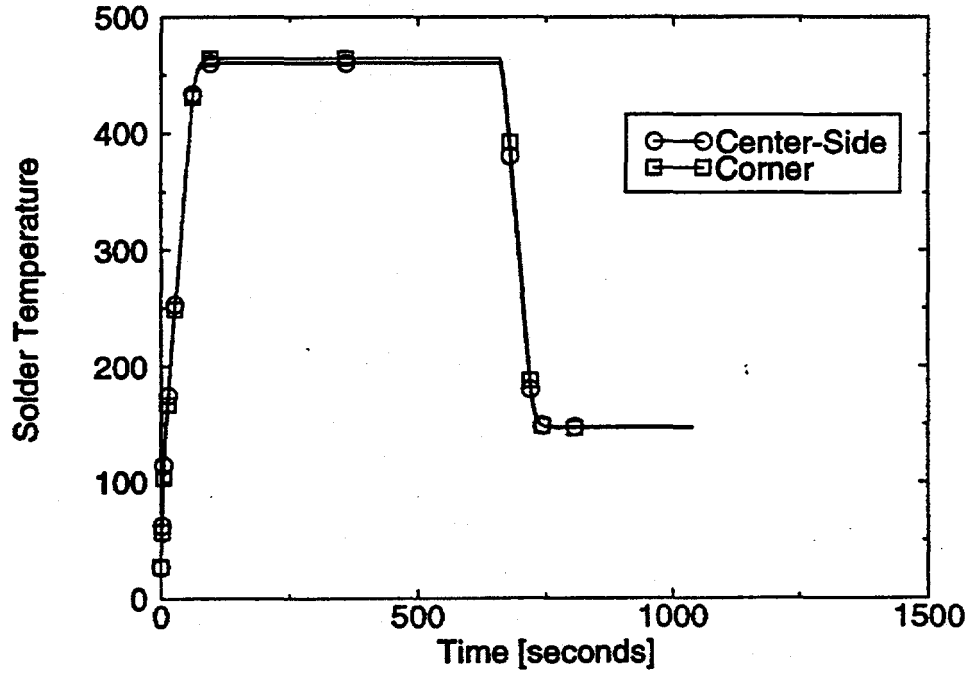

Figure 9-18. Temperature History for 400 W Laser Power

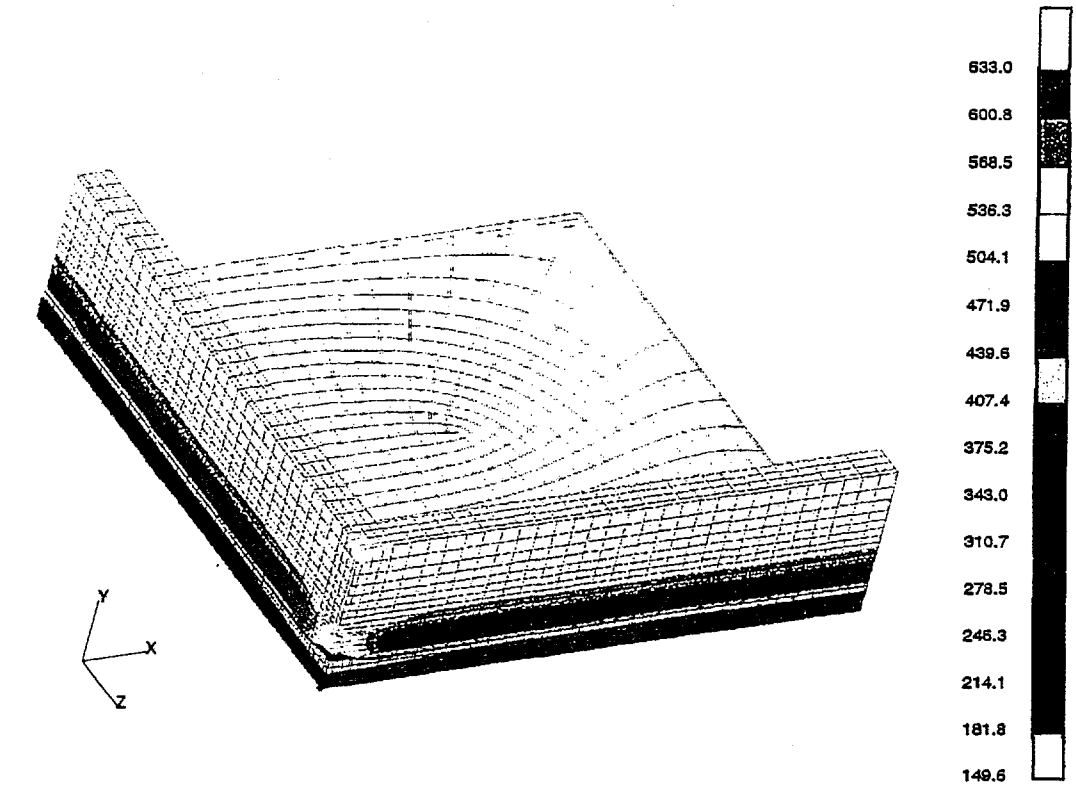

Figure 9-19. Isotherms [°C] at 11 Minutes into Soldering Process-Exterior View

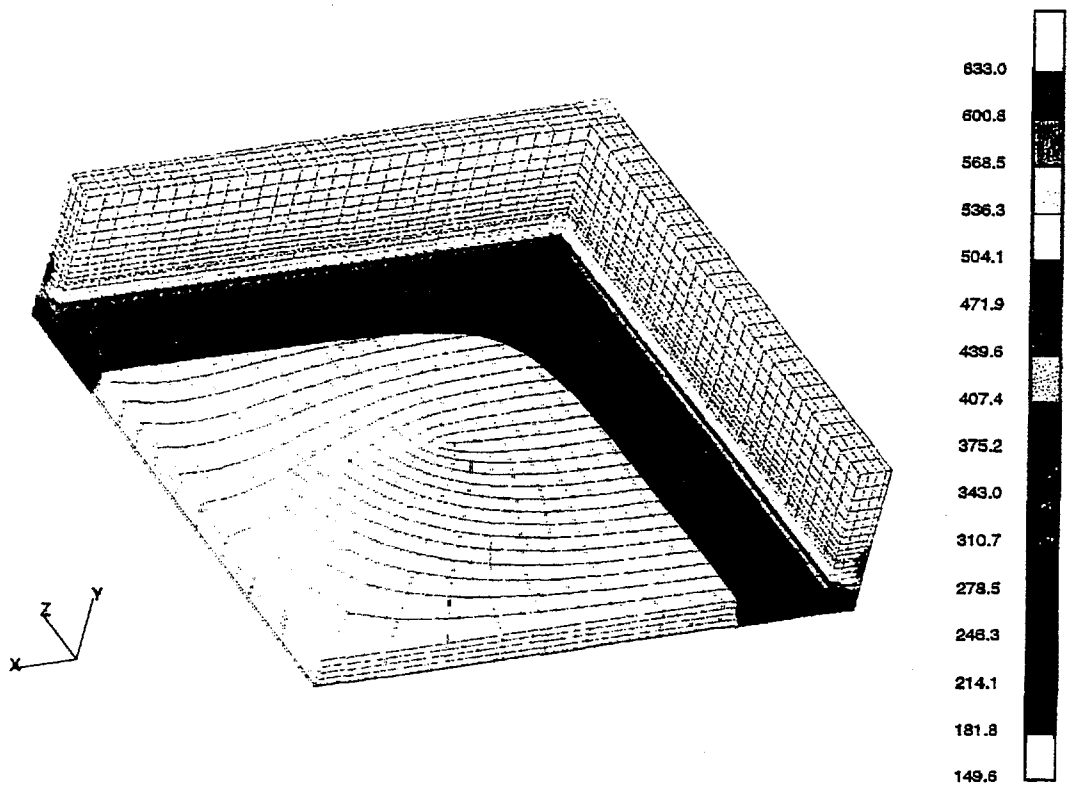

Figure 9-20. Isotherms [°C] at 11 Minutes into Soldering Process-Interior View

9.7.1.2 Conclusions

A series of thermal simulations were performed to examine the joining process of alumina components of the throttle control module using glass solder with a laser heat source. It was found that to achieve sufficient temperature in the glass solder, a 400 W laser had to be used. To minimize differences between the corner and center-side temperatures in the glass solder, the corners had to be shielded from the laser. For all simulations, the sensor was placed on a 150°C heat sink during the glass reflow process. If preferentially shielding the laser is found to be undesirable from a manufacturing standpoint, the heat sink design should be examined in an effort to minimize the temperature differences found in the solder.

9.7.2 Experiment and Testing

The test specimens used in these experiments are shown in Figure 9-21. This geometry was chosen because it is a recommended geometry from the ASTM standard for four- point bend testing and the wall thickness closely approximated that of the housing which would be sealed for the DELPHI component. The material was 95% Al_2O_3; the same material which was to be used for the final housing assembly. Each sample was ground to a uniform finish to insure consistency during testing. Each of the specimens were cleaned using a standard four-step cleaning process prior to applying the sealing glass to the end of the specimen. The sealing glass was a Corning 7585 glass powder which was applied in a slurry form. The solvent and binder used in the slurry was polyvinyl alcohol. The sealing glass slurry was applied to one end of each test specimen. After application, the specimens were placed in a furnace at 450°C for 10 minutes. This allowed the glass powder to flow and the organic binder to be burned out prior to performing the sealing experiments. It was determine that this step was essential to insure the integrity of the seal. If the binder was not burned out prior to sealing, the joints created by the laser process contained large voids and were especially low in strength.

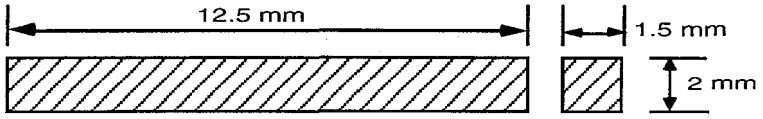

Figure 9-21. Schematic Representation of Test Vehicle Used in Process Feasibility Studies

After the samples were prepared, they were placed in a fixture with the solder glass surfaces contacting each other. This configuration is shown in Figure 9-22. A spring was brought into contact with the top specimen to apply a downward pressure to bring the samples together as the sealing glass flowed. The fixture maintained close alignment between the samples yet also allowed the top sample to move downward as the glass in the joint flowed. The fixture maintained the seal region in free space to simulate conditions expected for the final sealing operation. The laser beam was focused using a two cylindrical lenses to create a line source to approximate the periphery sealing process. The cross-sectional dimensions of the focused laser beam were 1 by 3 mm providing an irradiance range of 100 to 1500 W/cm^2. The parameters

varied during experiments included ramp-time, beam position, peak temperature and hold time at temperature. The exact values for laser power and irradiance at any given time were not known precisely since the laser system functions as a closed-loop process. The user defines the thermal profile of the heating cycle and a personal computer serves to monitor the process and provide a feedback signal to maintain the desired heating cycle. A schematic representation of the laser system is given in Figure 9-23. The thermal profile information measured during processing was recorded to a data file for verification of potential anomalies.

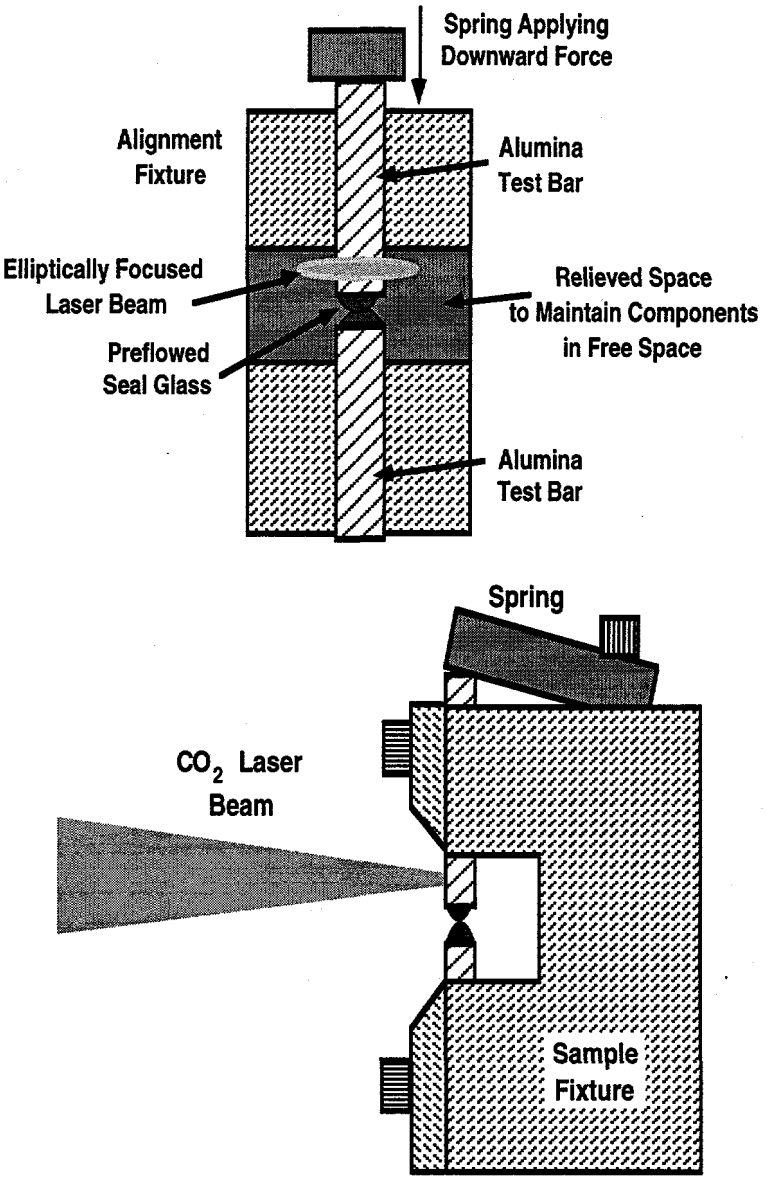

Figure 9-22. Schematic Representation of Fixturing Used in Performing Feasibility Studies, (a) Front View (Clamp Removed), (b) Side View

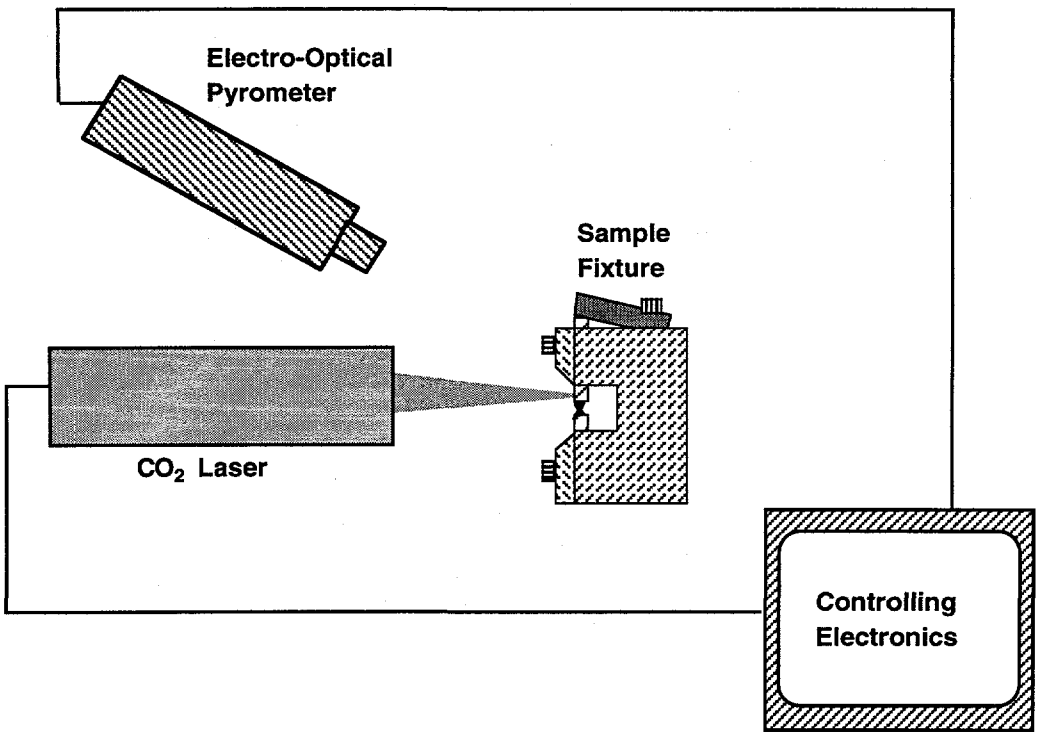

Figure 9-23. Schematic Representation of Closed-Loop Laser Sealing System

A statistically designed experiment was developed and executed to identify the process parameters that significantly influenced the laser sealing process and for use in developing a response surface model for process optimization. The parameters varied during this experiment are given in Table 9-7. After the samples were sealed, they were tested in four-point bend. To reduce scatter in the results due to surface variations and corner stress points, each of the samples was ground flat on the front face and the two front corner were also ground slightly to break all sharp corners. During the grinding operation some of the samples were broken; however, a significant number of specimens survived for the bend testing.

Table 9-7: Process Variables Used in Performing Statistically Designed Experiment

Process Variable	Variable Values		
	Low	Mid Point	High
Hold Temperature (°C)	460	485	510
Time at Temperature (min.)	3	6.5	10
Ramp Down Rate (°C/min.)	50	100	150
Beam Position Above Joint (mm)	1	2	3

9.7.3 Conclusions

The bend strengths of the laser sealed sampled varied from 3 kpsi to almost 18 kpsi. Because a satisfactory bend strength value for a typical lead glass is 8 kpsi, these results suggest that this process is indeed feasible. Preliminary analysis of the results show that the bend strength is a function of the total exposure or input energy. This is shown in Figure 9-24. Although there is a fair amount of spread in the measured data, there is an obvious trend showing increased strength with increased input energy. The scatter observed is typical of glass data for four-point bend testing. Although these results demonstrate process feasibility, further analysis of the data is required in generating a response surface model of this process.

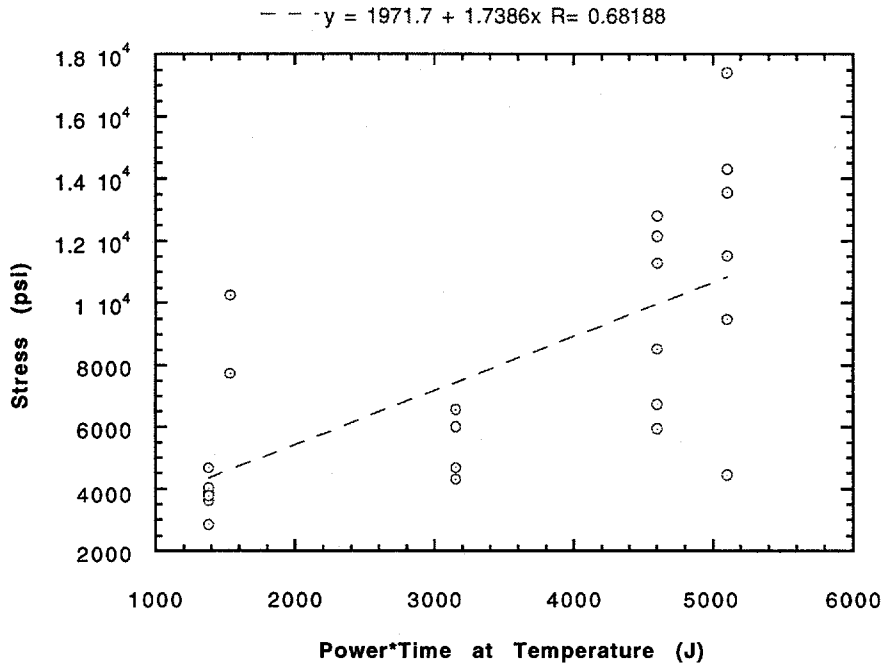

Figure 9-24. Measured Bend Strength Values Plotted as a Function of Total Input Energy

9.8 Environmental Test Packages

Table 9-8 lists all test packages used for the testing and indicates their seal characteristics.

Table 9-8: Environmental Test Packages

Sample Identification[1]	Frame[2]	Fixture Number	Seal Temperature (°C)	Comments[3]
QM42-1	used, gold	2	450	2 glass layers, continuous fillets, bubbles, good seal
QM42-2	new, gold	2	470	2 glass layers, continuous fillets, bubbles, good seal
QM42-3	new, gold	3	470	2 glass layers, continuous fillets, bubbles, good seal
QM42-7	new, gold	2	470	1 glass layer, continuous fillets, bubbles
QM42-10	?, gold	3	470	1 glass layer, continuous fillets, bubbles
QM42-12	used, gold	3	450	2 glass layers, continuous fillets, bubbles, less flow
QM42-21	used, gold	3	450	2 glass layers, incomplete fillets, bubbles, not optimal
QM42-22	used,	3	450	2 glass layers, continuous

Sample Identification[1]	Frame[2]	Fixture Number	Seal Temperature (°C)	Comments[3]
	gold			fillets, bobbles, good seal
QM42-23	new, gold	2	470	2 glass layers, continuous fillets, bubbles, good seal
QM42-24	new, gold	2	470	2 glass layers, continuous fillets, many bubbles, good seal
QM42-25	new, gold	2	470	2 glass layers, continuous fillets, many bubbles, good seal
QM42-27	used,?	2	450	2 glass layers, incomplete fillets, bubbles, not optimal
QM42-28	new, gold	3	470	2 glass layers, continuous fillets, bubbles, good seal
QM42-29	new, gold	3	470	2 glass layers, continuous fillets, bubbles, good seal
QM42-30	new, gold	3	470	2 glass layers, continuous fillets, bubbles, good seal
9117-1	new, gold	2	470	2 glass layers, continuous fillets, bubbles, good seal
9117-1B	new, gold	2	470	Re-run, new ID, old ID lost, min. fillet 2 sides, bubbles, not optimal
9117-3	new, gold	2	450	2 glass layers, continuous fillets, bubbles, good seal
9117-3B	used, gold	3	470	Re-run, new ID, old ID lost, continuous fillets, bubbles, good seal
9117-4B	used, gold	2	470	Re-run, new ID, old ID lost, continuous fillets, bubbles, good seal
9117-5	new, gold	2	470	2 glass layers, continuous fillets, bubbles, good seal
9117-6	new, gold	3	470	2 glass layers, continuous fillets, many bubbles, good seal
9117-7	new, gold	3	450	2 glass layers, continuous fillets, bubbles, good seal
9117-31A	new, gold	3	450	1 glass layer, continuous fillets, bubbles, good seal

Sample Identification[1]	Frame[2]	Fixture Number	Seal Temperature (°C)	Comments[3]
9117-32	new, gold	2	450	2 glass layers, min. fillet 1 side, bubbles, not optimal
9117-34	new, gold	3	450	2 glass layers, continuous fillets, bubbles, good seal
9117-34A	new, gold	2	450	1 glass layer, continuous fillets, bubbles, good seal
9117-35	new, gold	3	470	2 glass layers, continuous fillets, bubbles, good seal
9117-35A	new, gold	2	450/470	1 glass layer, re-sealed once, min. fillet 1 side, not optimal
9117-36A	new, gold	3	450/470/470	1 glass layer, re-sealed twice, min. fillet 2 sides, gold tarnish, bubbles, not optimal
K3	N/A	none	425	Sealed in 2411 belt furnace, uniform fillets, no bubbles, good seal
K5	N/A	none	400	Low weight on assembly, lid stayed on center, uniform fillets, marginal seal
K6	N/A	none	400	Low weight on assembly, lid slid off center, min. fillet 1 side, marginal seal
K7	N/A	none	400	Lid slid off center, min. fillet 1 side, not optimal
K8	N/A	none	400	Lid stayed on center, uniform fillets, good seal
K9	N/A	none	400	Lid moved off center, 1 corner underfilled, not optimal
K10	N/A	none	400	Lid stayed on center, continuous fillets, good seal
K12	N/A	none	400	Lid slid off center, still continuous fillets, good seal
K13	N/A	none	400	Lid slid off center, continuous but min. fillet 1 side, not optimal

Sample Identification[1]	Frame[2]	Fixture Number	Seal Temperature (°C)	Comments[3]
K15	N/A	none	400	Lid slid off center, continuous but min. fillet 1 side, not optimal

[1]QM42 and 9117 denote dielectric material on substrate; K = Kyocera piece parts.
[2]Used = recycled frame from previous seal; gold = gold-plated frame.
[3]Continuous fillets = no gaps in the glass fillet between the frame and substrate

9.9 Glass Seal Environmental Test

The following thermal and mechanical tests are based on the qualification tests specified by Delphi for the completed electronic package. These tests qualify the glass-to-ceramic package seal only. They incorporate those conditions from the DELPHI specifications which will subject to seals to maximum environmental conditions without unnecessary repetition of tests.

Qualification Tests

1 Static Temperature Cycle. -65°C to +180°C, dry air, immediate transfer between temperatures, 30 minutes dwell at temperature extreme, 60 minute temperature cycle. Functional check: visual inspection for glass cracking, seal hermeticity at 1×10^{-9} atm cc/sec Helium.

Qualification: 1000 cycles
Extended Durability: 2000 cycles
Functional Check: After every 100 cycles.

1.2 Temperature/Humidity Cycle. +10°C to 90°C, 30 minute temperature transfer cold to hot, 90 minute temperature transfer hot to cold, 30 minute dwell at each temperature extreme, 180 minute temperature cycle. Relative humidity ± 95%. Functional check: visual inspection for glass cracking, seal hermeticity at 1×10^{-9} atm cc/sec Helium.

Qualification: 500 cycles
Extended Durability: 1000 cycles
Functional Check: After every 50 cycles.

1.3 Liquid Thermal Shock. 150°C air for 30 minutes, immediate transfer to 10°C distilled water for 1 minute. Functional check: visual inspection for glass cracking, seal hermeticity at 1×10^{-9} atm cc/sec Helium.

Qualification: 10 cycles
Functional Check: after first, fifth, and tenth cycles.

1.4 Vibration. Mount device to approximate attachment used for application. Apply filtered random noise with the following spectrum at the following level schedule. Functional check: visual inspection for glass cracking, seal hermeticity at 1 x 10^{-9} atm cc/sec Helium. Apply the schedule in Table 9-9 to three perpendicular axes. Total test time is 66 hours.

Table 9-9: Vibration Testing Schedule

	Breakpoint Frequency (Hz)	Intensity G^2/Hz
	<20	0
0 db = 20.8 Grms	20	0.0005
	200	2.000
	300	0.500
	500	0.100
	1000	0.050
	2000	0.010
	>2000	0

Qualification: 1 pass through this schedule
Functional Check: at end of test

1.5 Mechanical Shock. 50 g., 11 mS half sine, five shocks per each axis, 15 shocks total. Functional check: visual inspection for glass cracking, seal hermeticity at 1 X 10^{-9} atm cc/sec Helium.

2. TEST MATRIX

2.1 Sample Description.

Sample A: 96% alumina frame with Corning 7585 glass, 96% alumina substrate with Dupont QM42 dielectric.

Sample B: 96% alumina frame with Corning 7585 glass, 96% alumina substrate with Heraeus IP9118 dielectric.

Sample C: 91% alumina Kyocera lid with Kyocera 1390 glass, 96% alumina substrate with Dupont QM42 dielectric from C-MAC.

2.2 Test Sequence.

Sample A, 10 each.	Step 1. Static Temperature Cycle per 1.1, 5 each
	Step 2. Temperature/Humidity Cycle per 1.2, 5 each.
	Step 3. Liquid Thermal Shock per 1.3, 5 each
	Step 4. Vibration per 1.4, 5 each.
	Step 5. Mechanical Shock per 1.5, 5 each
Note:	Steps 1 and 2 conducted concurrently.
Sample B, 10 each.	Repeat Sample A sequence.
Sample C, 10 each.	Repeat Sample A sequence.

9.10 Temperature Cycle

Tables 9-10 through 9-14 list the sealed packages used for each environmental test and test results.

Table 9-10: Temperature Cycle

Package Identification	Aluminum Back Plate	Results and Comments
QM42-10	yes	hermetic 3 x 10^{-9} atm cc/sec helium after 1000 cycles
QM42-23	yes	hermetic 3 x 10^{-9} atm cc/sec helium after 1000 cycles
QM42-24	no	leaked 10^{-7} range after 700 cycles, excessive bubbles in seal
QM42-27	no	hermetic 3 x 10^{-9} atm cc/sec helium after 1000 cycles
QM42-29	yes	hermetic 3 x 10^{-9} atm cc/sec helium after 1000 cycles
9117-1B	yes	hermetic 3 x 10^{-9} atm cc/sec helium after 1000 cycles
9117-5	yes	hermetic 3 x 10^{-9} atm cc/sec helium after 1000 cycles
9117-7	no	hermetic 3 x 10^{-9} atm cc/sec helium after 1000 cycles
9117-35	yes	hermetic 3 x 10^{-9} atm cc/sec helium after 1000 cycles
9117-35A	no	hermetic 3 x 10^{-9} atm cc/sec helium after 1000 cycles

Table 9-11: Temperature and Humidity Cycle

Package Identification	Aluminum Back Plate	Results and Comments
QM42-1	no	leaked 10^{-7} range after 100 cycles, low temperature seal
QM42-3	yes	hermetic 3 x 10^{-9} atm cc/sec helium after 500 cycles
QM42-22	no	hermetic 3 x 10^{-9} atm cc/sec helium after 500 cycles
QM42-25	yes	leaked 10^{-9} range after 300 cycles, excessive bubbles in seal
QM42-30	no	hermetic 3 x 10^{-9} atm cc/sec helium after 500 cycles
9117-3	no	hermetic 3 x 10^{-9} atm cc/sec helium after 500 cycles
9117-3B	no	hermetic 3 x 10^{-9} atm cc/sec helium after 500 cycles
9117-31A	no	leaked $>10^{-6}$ range after 100 cycles, low temperature seal
9117-32	yes	hermetic 3 x 10^{-9} atm cc/sec helium after 500 cycles
9117-34A	yes	leaked 10^{-7} range after 400 cycles, was rated good seal
K3	N/A	hermetic 3 x 10^{-9} atm cc/sec helium after 400 cycles
K5	N/A	leaked 10^{-8} range after 100 cycles, marginal seal
K6	N/A	leaked 10^{-6} range after 100 cycles, marginal seal
K9	N/A	hermetic 3 x 10^{-9} atm cc/sec helium after 400 cycles
K12	N/A	hermetic 3 x 10^{-9} atm cc/sec helium after 400 cycles

Table 9-12: Liquid Thermal Shock

Package Identification	Aluminum Back Plate	Results and Comments[2]
QM42-10	yes	leaked after 1 cycle, will not pump down
QM42-23	yes	leaked 10^{-7} range after 1 cycle
QM42-27	no	leaked 10^{-7} range after 1 cycle
QM42-29	yes	leaked 10^{-6} range after 1 cycle
9117-1B	yes	leaked 10^{-7} range after 3 cycles
9117-7	no	leaked after 1 cycle, will not pump down
9117-35	yes	leaked 10^{-8} range after two cycles
9117-35A	no	leaked after 1 cycle, will not pump down
K3	N/A	hermetic 3 x 10^{-9} atm cc/sec helium after 10 cycles
K9	N/A	hermetic 3 x 10^{-9} atm cc/sec helium after four cycles, then damaged in vacuum oven, out of test
K12	N/A	hermetic 3 x 10^{-9} atm cc/sec helium after 10 cycles

[1]All packages are from previous thermal tests.
[2]Kyocera packages were baked out in a vacuum oven overnight before leak checking and leak checked after each cycle.

Table 9-13: Vibration [1]

Package Identification	Aluminum Back Plate	Results and Comments
QM42-2	no	hermetic 3 x 10^{-9} atm cc/sec Helium after test
QM42-7	no	hermetic 3 x 10^{-9} atm cc/sec Helium after test
QM42-12	no	hermetic 3 x 10^{-9} atm cc/sec Helium after test
QM42-21	no	hermetic 3 x 10^{-9} atm cc/sec Helium after test
QM42-28	no	hermetic 3 x 10^{-9} atm cc/sec Helium after test
9117-1	no	hermetic 3 x 10^{-9} atm cc/sec Helium after test
9117-4B	no	hermetic 3 x 10^{-9} atm cc/sec Helium after test
9117-6	no	hermetic 3 x 10^{-9} atm cc/sec Helium after test
9117-34	no	hermetic 3 x 10^{-9} atm cc/sec Helium after test
9117-36A	no	hermetic 3 x 10^{-9} atm cc/sec Helium after test
K7	N/A	hermetic 3 x 10^{-9} atm cc/sec Helium after test
K8	N/A	hermetic 3 x 10^{-9} atm cc/sec Helium after test
K10	N/A	hermetic 3 x 10^{-9} atm cc/sec Helium after test
K13	N/A	hermetic 3 x 10^{-9} atm cc/sec Helium after test
K15	N/A	hermetic 3 x 10^{-9} atm cc/sec Helium after test
[1]All packages were proven in with 100 cycles of temperature cycle prior to this test.		

Table 9-14: Mechanical Shock

Package Identification [1]	Aluminum Back Plate	Results and Comments
QM42-2	no	hermetic 3 x 10^{-9} atm cc/sec Helium after test
QM42-7	no	hermetic 3 x 10^{-9} atm cc/sec Helium after test
QM42-12	no	hermetic 3 x 10^{-9} atm cc/sec Helium after test
QM42-21	no	hermetic 3 x 10^{-9} atm cc/sec Helium after test
QM42-28	no	hermetic 3 x 10^{-9} atm cc/sec Helium after test
9117-1	no	hermetic 3 x 10^{-9} atm cc/sec Helium after test
9117-4B	no	hermetic 3 x 10^{-9} atm cc/sec Helium after test
9117-6	no	leaked >10^{-6} range after test, excessive bubbles in seal
9117-34	no	hermetic 3 x 10^{-9} atm cc/sec Helium after test
9117-36A	no	hermetic 3 x 10^{-9} atm cc/sec Helium after test
K7	N/A	hermetic 3 x 10^{-9} atm cc/sec Helium after test
K8	N/A	hermetic 3 x 10^{-9} atm cc/sec Helium after test
K10	N/A	hermetic 3 x 10^{-9} atm cc/sec Helium after test
K13	N/A	hermetic 3 x 10^{-9} atm cc/sec Helium after test
K15	N/A	hermetic 3 x 10^{-9} atm cc/sec Helium after test
[1]Packages from vibration testing were used again for mechanical shock testing.		

REFERENCES

1. J. H. Biffle, "JAC2D - A Two-Dimensional Finite Element Computer Program for the Nonlinear Quasi-Static Response of Solids with the Conjugate Gradient Method," Sandia National Laboratories, Albuquerque, New Mexico, (to be published).
2. J. H. Biffle, "JAC3D - A Three-Dimensional Finite Element Computer Program the Nonlinear Quasi-Static Response of Solids with the Conjugate Gradient Method," SAND87-1305, Sandia National Laboratories, Albuquerque, New Mexico, February, 1993.

10. High Temperature Solders

Julie A. Kern
Martin W. Weiser
Celest A. Drewien
Frederick G. Yost
Susan J. Sackinger

The automotive industry has traditionally relied on the use of lead-tin (Pb-Sn) solder based surface mount technologies for the manufacture of electronic systems. There are many attributes inherent with this attachment technology that makes it a logical choice for automotive applications, primarily, low cost. However Pb-Sn solders can not be used in the manufacturing of systems targeted for use in high temperature environments. In these instances the more expensive organic die attach adhesives are required. This chapter investigates silver-tin (Ag-Sn) solder systems as a possible economical solution to the organic die attach materials.

10.1 Introduction

This study was a continuation of a CRADA with GM, in which Sn-Ag based solder systems including flux, metallization, and solder were screened for performance in a high temperature, under-the-hood application. The emphasis upon the Ag-Sn system is derived from the environmental issues surrounding the use of Pb and from the higher melting point of this system as compared to the classical Pb-Sn system. In typical operations for an under-the-hood environment, solder joints must survive temperatures greater than 80°C. Based upon reports in the literature, [1-4] it is believed that solder alloys in the Ag-Sn system can fulfill this role because of the higher melting point of the Ag-Sn eutectic as compared to the Pb-Sn eutectic, higher creep resistance, higher tensile strength and ductility, better low cycle fatigue resistance, and higher impact resistance.

This section summarizes the effects of thermal aging upon microstructural evolution and peel strength of the solder joint for the solder systems chosen through the screening study in an effort to recommend systems for service life and reliability testing. The initial study[5] provided a screening mechanism for establishing which systems should be considered for subsequent thermal aging studies based upon processing and microstructural issues alone. Six Sn-rich solders, five Ag-rich metallizations, and four commercially available fluxing agents were screened in an experimental matrix whereby every combination was used to make sessile drops utilizing standard thermal processing techniques. The systems were chosen for subsequent testing allowed formation of sessile drops with contact angles of less than 30 degrees while exhibiting a fine, uniform microstructure without evidence of degradation in a humid, chlorine, and sulfur-containing environment. In the event that the fluxing agents did not influence the sessile drop, environmentally conscious (no volatile organics or remaining debris) fluxes were chosen. Table 10-1 shows the solder systems tested and the systems selected for thermal aging studies.

Table 10-1: Solder Systems Considered for High-Temperature, Under-the-Hood Application

Solder Alloy	Metallization	Fluxing Agent
*Sn-Ag-Cu (SAC)	*5081/5082	RMA
*Sn-Ag-Cu-Bi (SACB)	6160	Water Soluble
*Sn-Ag-Bi (SAB)	6175	Citric
*Sn-Ag (121)	6277	*No Clean
Sn-Ag-Bi-Sb (SABSb)	7484	
Castin		
*Solder Alloys Chosen for Thermal Aging Studies	*Metallization Chosen for Thermal Aging Studies	*Fluxing Agent Chosen for Use

Based upon desirable sessile drop formation utilizing standard processing procedures, the four solders were formed on the Ag-Pt 5081/5082 metallization using a no clean flux. Isothermal aging studies were performed, and the effects of time and temperature upon the microstructure and strength of the solder system were investigated. Ultimately, the strength of the solder joint determines its usefulness, and the solder joint strength depends upon the solder and the solder/metallization joint microstructure. Microstructural changes are expected to occur as a function of time and temperature through diffusional processes between solder constituents and metallization, so the solder joint strength is also expected to change. Thus, mechanical tests to determine the influence of the thermal treatment upon the peel strength were performed. Accelerated aging tests such a isothermal aging cannot duplicate the service life of a solder joint. However, they provide one method of screening solder systems that potentially will provide the desired service life and reliability needed.

The purpose of this study was to examine the mechanical integrity of four Pb-free, Ag-rich solder systems on a Ag-Pt metallization for possible use in under-the-hood applications. This analysis focused on the kinetic growth rate of the intermetallic layers that formed in these systems and how the strength was ultimately affected. The parameters involved isothermally aging the systems from 134°C to 190°C.

10.2 Background

The growth of intermetallic layers and other factors that affect joint integrity are discussed in this section.

10.2.1 Intermetallics

Analysis of the solder joint microstructure is important for determining the factors that lead to failure. One such entity that has the propensity of existing, changing over time, and influencing the integrity of the solder joint is the growth of intermetallic layers.

The presence of an intermetallic layer is not a strict requirement for wetting to occur, but most solders containing Sn do form intermetallics with Ag. From previous documentation in a Sn-based solder, Sn is the active component, contributing to the formation of intermetallics that act as an association between the metallization and the solder.[6] Sn is known to have a high affinity for dissolving Cu or Ag into itself. Therefore, a system containing Sn, Cu and/or Ag will have a high probability of containing Cu-Sn and Ag-Sn intermetallics.

During soldering of Cu substrates using Sn-based solders, an intermetallic layer of Cu_6Sn_5 forms at the solder/metallization interface.[7] Based on the Cu-Sn equilibrium phase diagram,[8] Cu_3Sn (ε) should also form. However, this intermetallic has not been visible at annealing temperatures below 135°C.[7, 9, 10] This has led researchers to conclude that Cu_3Sn is observed following high temperature annealing, only.

Similar behavior has been documented in the Ag-Sn system.[11] In viewing a Ag-Sn equilibrium phase diagram,[8] both the ε and the ζ (composition) phases should form when Sn and Ag interact. However, only the reaction phase Ag_3Sn (ε) is observed, even after annealing temperatures between 20°C and 170°C. Therefore, in the assessment of possible intermetallics that would appear in Sn, Ag, and Cu containing solder alloys, the Ag_3Sn, the Cu_6Sn_5, and the Cu_3Sn intermetallics exhibit a high propensity to form.

The growth of intermetallic compounds by a diffusion controlled process is illustrated in Figure 10-1. The Sn must diffuse through a continuously increasing thickness of the intermetallic layer and then react with the Ag; the Ag must diffuse through the intermetallic layer to react with the Sn. The growth, therefore, is limited by diffusion through the intermetallic layer.

10.2.2 Joint Strength

A soldered joint is required to provide bonds sufficiently strong and durable in meeting the design life of an assembly.[1] Microstructural analysis to detect the presence of brittle layers and/or voids in the microstructure provide important information on joint integrity. Kirkendall voids form as a result of different diffusion fluxes.[12, 13] Other factors that result in voids are

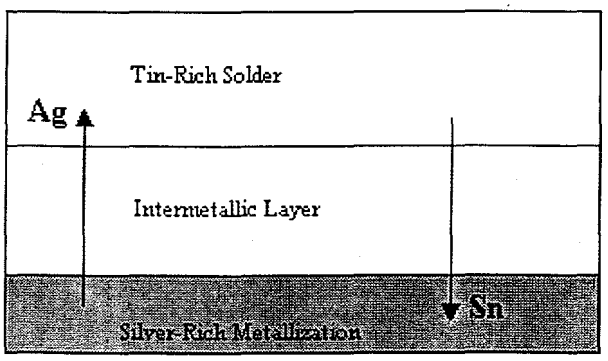

Figure 10-1. A Schematic of a Diffusion-Controlled Process with a Sn-Rich Solder on a Ag-Rich Metallization

contaminants in the metallization, gas becoming trapped when the metals are molten, or shrinkage of the constituents due to solidification as the system cools.

Through mechanical testing, the influence that voids, along with microstructural coarsening, and intermetallic formation have on the mechanical properties of the solder joint are exposed. There are many forms of mechanical testing and they are all designed in attempts to simplify the actual conditions that exist during the service life of a device. Tensile strength[14-16] and thermal shock[14] tests have been documented. However, shear testing appears to be a popular means of measuring the solder joint's strength. [17-20] The ring and plug shear,[17, 21, 22] the double-lap shear,[18, 22, 23] and the single-lap shear[22, 24] are among the different ways that shear testing is performed. Shearing involves stresses that act parallel to the surfaces. It is imposed on a joint that is under thermal cycling conditions where the solder bonds of two materials with different coefficients of thermal expansion exist. When one side is heated, the joint expands more that the other; upon cooling, it contracts further than the other resulting in shear strain in the solder. This shear strain results in heterogeneous coarsening of the microstructure, where cracks form resulting in joint failure.

Some solder joints in electronic systems also experience strains that act to tear or peel them apart. Because the scope of this study is not thermal cycling, the peel test which is important in exposing a brittle interface has been chosen. There are many different geometric configuration of peel tests,[20] but the peel tests that were explored for this study had to give strength values that were representative of a wire bonded to a solder/metallization system. DuPont[25] defined an in-board peel test that appeared to appropriately measure the strength of a wire/solder system. It is quick and easy to perform and produces a reasonable set of results.[26] The only concern was that the wire could be weaker than the joint, producing measured stress in breaking the wire instead of a straight forward response of a failure load as applied to the joint.[6] Fortunately this was not the case in this study.

10.3 Experimental Procedure

The four different Pb-free solder alloys and a single, two layer Ag-Pt metallization, 5081/5082, that was selected from a preliminary study[5] were used in this project. The solders are shown in Table 10-2, with their varying weight percent in Sn, Ag, Cu, and Bi. These solder/metallization systems were exposed to isothermal aging after which a microstructural analysis of the intermetallic growth was completed and an in-board peel test was performed. These tests gave necessary information in determining the individual mechanical integrity of the solder/metallization systems.

Table 10-2: The Sn-Ag Solder Alloys Used in This Experiment. They will be denoted by the notation in the parenthesis, hereafter.

Solder Alloys	Composition (Wt%)
Sn-Ag (121)	96.5 Sn, 3.5 Ag
Sn-Ag-Cu (SAC)	93.6 Sn, 4.64 Ag, 1.76 Cu
Sn-Ag-Bi (SAB)	91.9 Sn, 3.33 Ag, 4.8 Bi
Sn-Ag-Cu-Bi (SACB)	88.9 Sn, 4.5 Ag, 1.6 Cu, 5.0 Bi

10.3.1 Metallization

The E.I. DuPont metallization 5081/5082, comprised of two different metallizations (weight percents of 75 Ag-7 Pt, and 79 Ag-6 Pt, respectively[5] and will be referred to by this numerical identification, hereafter), was in the form of pastes or thick-film conductor inks. These pastes were printed onto a ceramic substrate using a patterned wire screen (325 openings per inch). Initially this mesh screen was covered with a 4 to 12 mil thick photosensitive emulsion. Using an Instant Mercury Printer, this system was then exposed to a pattern via ultraviolet light. The emulsion not exposed to light was then washed off with water, leaving behind a pattern on the screen. A Presco thick film screen printer was then used to apply the thick-film ink metallization through this patterned screen onto an alumina substrate. Squeegee blade pressure on the Presco screen printer was controlled to produce a consistent thickness of the thick-film ink while printing.

The 5081/5082 was applied as a two-stage process. First, metallization 5081 was screened printed, dried in a 150°C oven for 10 minutes, and fired. To bond the metallic conductor to the ceramic surface, this system was fired in a furnace, ramping the temperature for one hour to a peak temperature of 850°C for ten minutes. The same procedure was repeated again for the application of metallization 5082. When the firing had been completed on the two different metallization patterns, the substrates were stored in a container with an inert atmosphere. This prevented oxidation and sulfidation of their surfaces.

This two-stage process occurred for the two different test patterns: one pattern for the specimens that would be used for the cross-sectional analysis and the other pattern to be used for the in-board peel test, as shown in Figure 10-2 and Figure 10-3, respectively. Figure 10-2 illustrates a pattern of 16 one cm squares where laser scribed lines were applied around the perimeter and through the center of each pad on the nonprinted side of the substrate. These scribe marks allowed easy separation of pads to form individual aging samples. Figure 10-3 shows the in-board peel test pattern that consisted of 21 two mm square metallization pads: 3 pads in 7 rows. Pad sizes of two mm square were chosen to enable the wires to be kept vertical during the testing.[26] Fourteen small markers located at each end of a row were used to align the wires, insuring that the wires were centered on the test pads. The center strip of pads served as a buffer when the peel test was performed, since the middle pad absorbed the tensile shock when the bond broke keeping the opposite outer pad from being affected.

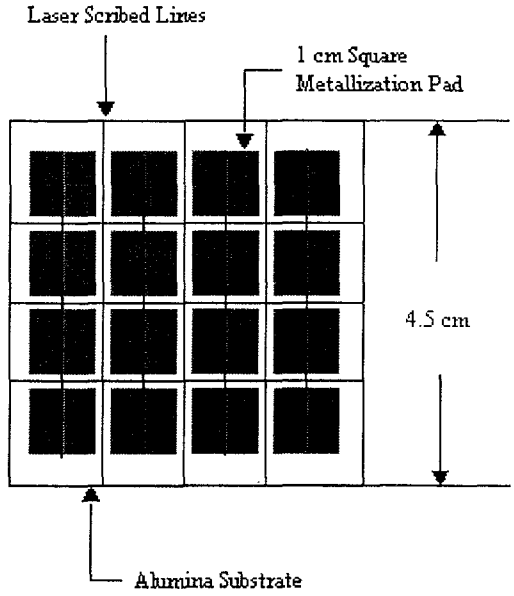

Figure 10-2. The Pattern Used to Make the Aging Samples. The lines designate the lines that were laser scribed onto the back of the alumina substrate used for separating the pads individually and in half.

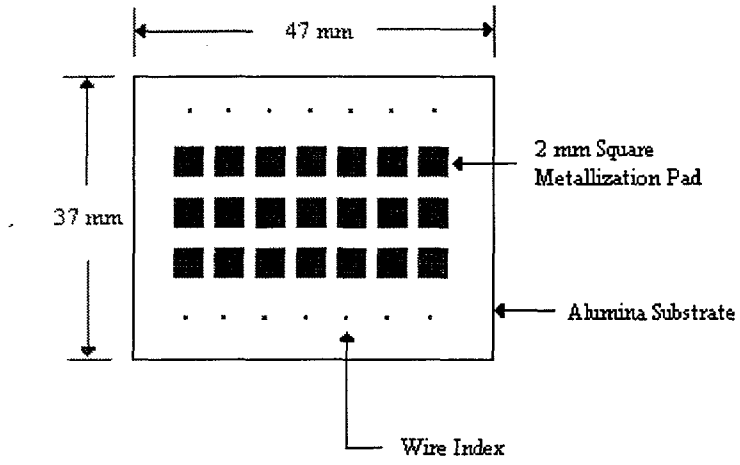

Figure 10-3. The Screen Print Design Used for the In-Board Peel Test. Approximately 170 ceramic boards were printed with this design to allow for testing of the four solder alloys in each time and temperature increment.

10.3.2 Solder

The solder, which was in the form of a paste, was comprised of solder particles and a no clean flux binder. This no clean flux was chosen because it is commonly used in industry. The 121 solder paste was purchased from Indium Corporation of America, and the SAB paste was purchased from AIM (American Iron and Metal Company). The SACB and the SAC solder pastes were processed from AMES laboratory.

Aging specimens were formed with 20 ± 1 mg of solder paste individually placed onto the one cm square metallization pad. Beforehand, these solder quantities were weighed out, placed on plastic sheets, and placed in air permeable containers. Until they were ready to be used, these quantities were stored in a refrigerator at 3.3°C (38°F) to prevent the solder paste degradation by reaction of the flux with the solder. Thermal treatment to form the aging samples is described below.

For the mechanical testing samples, the solder paste was screen-printed to a thickness of approximately 150 μm (6 mils) on the 2 mm square metallization pads (see Figure 10-3). Standard Sn-plated, 20 gauge (0.8 mm diameter) Cu wire was cleaned and hand-placed across three pads as shown in Figure 10-4. This procedure does not follow the preparation parameters defined by DuPont, where solder baths were used to coat the metallizations. Instead, screen-printing of the solder was chosen because it offered a consistent thermal processing of the system and a constant volume application of the solder, i.e., a volume that did not depend on the straightness of the wire. It was anticipated that the stress distribution in the

wire/solder/metallization assembly would be quite reproducible due to the constant thickness of solder and controlled thermal history.

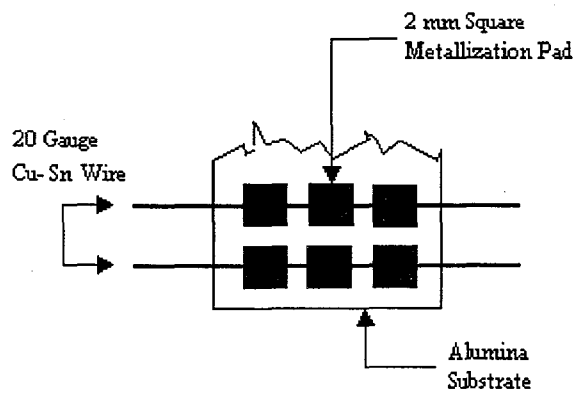

Figure 10-4. Placement of the Cu-Sn Wire on the Metallization Pads

10.3.3 Reflow Heat Treatment

A Heller 988C reflow oven was used to reflow all samples. This oven consisted of four inert atmosphere convection heated zones and two infrared panels where the temperatures could be programmed for a desired profile. Compressed nitrogen, stored in cylinders, was used to keep the atmosphere inside the oven inert, the infrared panels clean, and the effects of oxidation of the molten solder reduced. A motor/gear driven conveyor belt moved the samples through the heated zones of the reflow oven at designated speeds.

The cooling rate determines the initial solder microstructure. The faster cooling rate allows less time for diffusion to occur, resulting in a finer microstructure. The preliminary study[5] showed that microstructural differences existed between the two heat treatments: the hot plate microstructure versus the reflow oven microstructure. The hot plate produced a finer eutectic microstructure of Ag_3Sn and Sn. It was clear that the finer microstructure was a result of the rapid cooling rate experienced by the solder during the thermal processing.

To achieve a finer microstructure, a faster cooling rate temperature profile was made for the reflow oven. This involved increasing the belt speed from 25 cm per minute to 35 cm per minute while keeping the time above the liquidus temperature of the 121 solder alloy (221°C) at 68 seconds. This new temperature profile is shown in Figure 10-5. Performing this change in the profile proved to be a success. This can be seen when comparing microstructures resulting from the old temperature profile shown in Figure 10-6, and the new temperature profile used in the reflow oven, as shown in Figure 10-7. Here, the microstructure is seen to be fine and homogenous. Both of these figures show the 121 reflowed on metallization, 5081/5082.

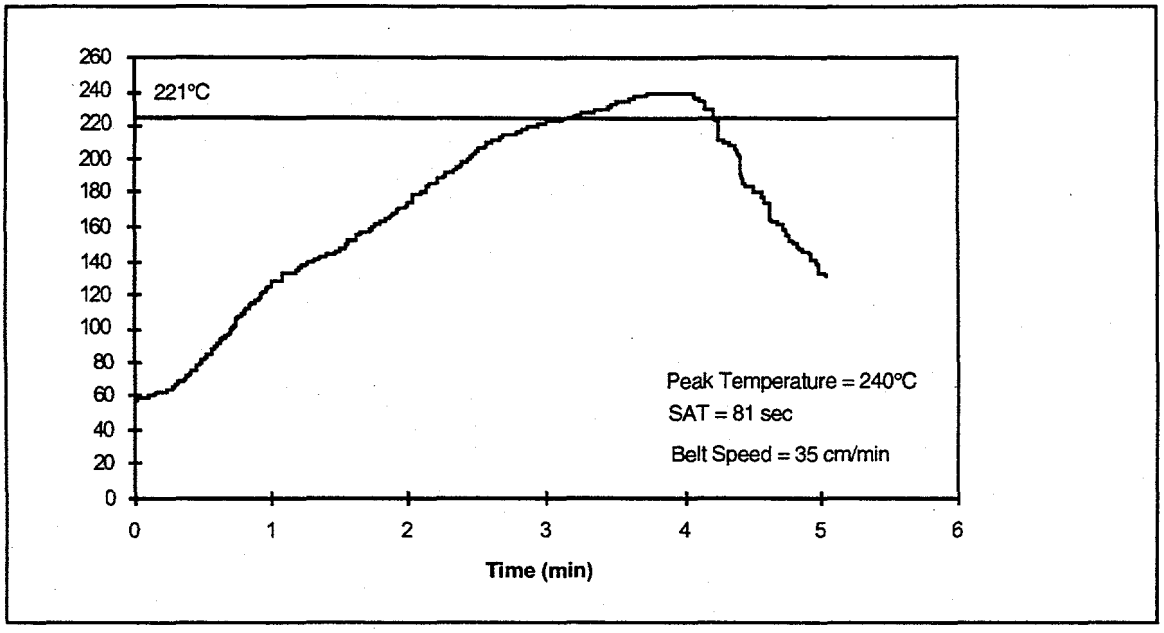

Figure 10-5. Temperature Profile for the Heller Reflow Oven. The saturation time (SAT) denotes the time that the solder/metallization system was above 221°C.

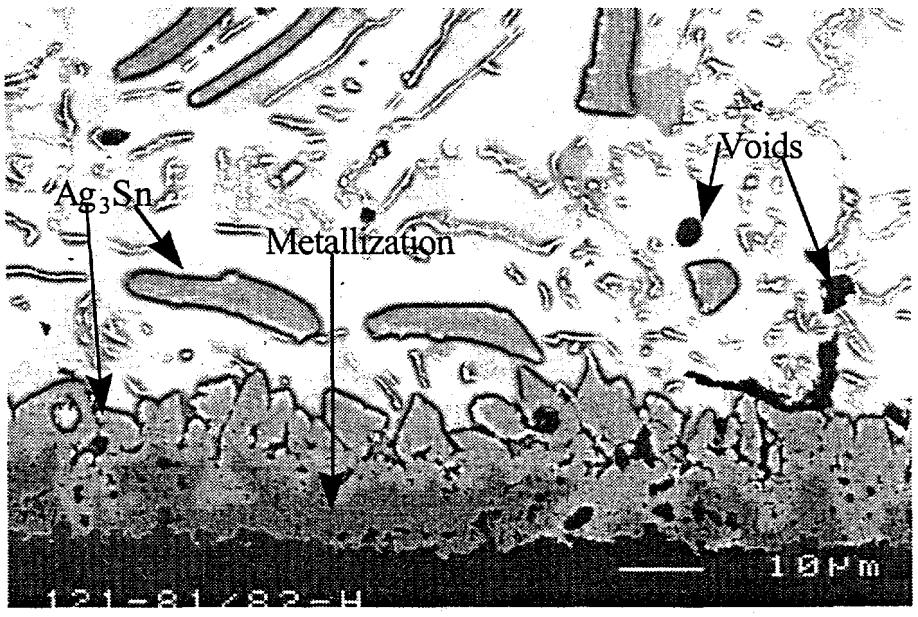

Figure 10-6. The 121 Has Been Reflowed on the 5081/5082 Metallization Using the Reflow Oven Resulting in a Coarse Microstructure

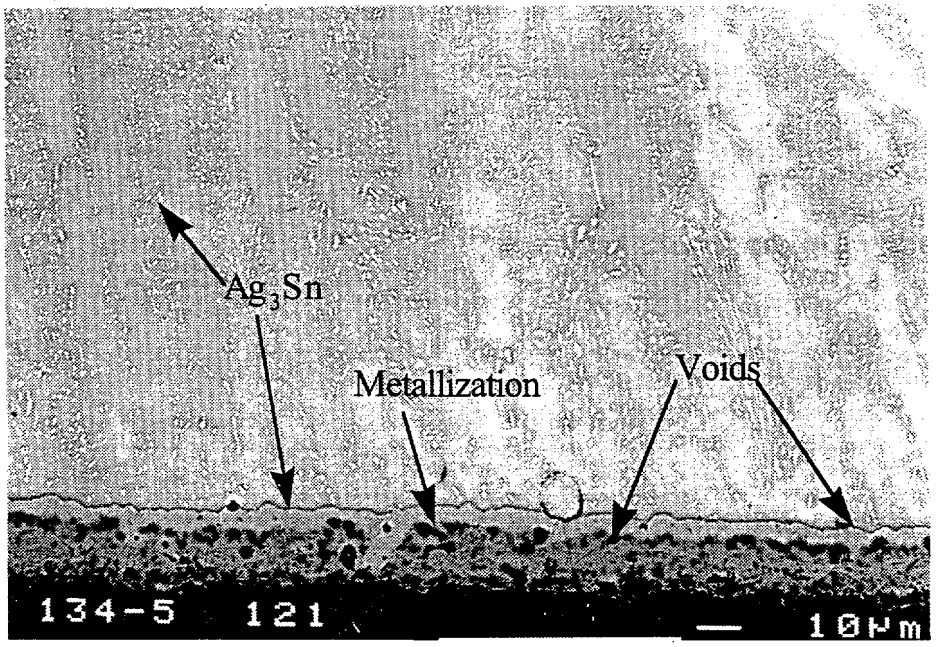

Figure 10-7. The Fine, Homogeneous Microstructure of Indalloy 121 is Indicative of a Faster Cooling Rate.

To reduce the variation in the sample preparation, the preceding temperature profile was used to reflow both the aging samples and the in-board peel test samples for all four alloys.

10.3.4 Isothermal Aging

Accelerated aging tests were constructed to simulate a period of natural aging in an under-the-hood environment. These tests consisted of five different temperatures with eight different time intervals. The parameters were selected based on previous data and the Arrhenius equation, as shown in Equation (10-1)

$$x(t,T) = x_o + At^n e^{-Q/RT} \tag{10-1}$$

where t is the time, T is the temperature (Kelvin), A is a constant, Q is the activation energy, and n is the empirical power-law constant. Previous aging of intermetallics has been performed on Sn-Ag (100% Sn and 100% Ag) systems,[27] using Equation (10-1). This study covered a temperature range from 20°C to 170°C using a multivariable regression to determine the values of A, n, and Q. To effectively examine the growth process at both high and low temperatures in accelerated isothermal aging conditions, these values were used to design this experiment. These parameters are shown in Table 10-3 for Sn-plated on Ag.

Table 10-3: Values That Were Used in Equation (10-1) To Design the Isothermal Aging Experiment[27]

Parameters		Units
A	8.62×10^{3}	$\mu m/t^{n}$ (time in days)
n	0.416	dimensionless
Q	28.31	KJ/mol

Since the under-the-hood temperatures in automobiles range from 150°C to 180°C, a median temperature of 160°C was chosen. A maximum time of 1,000 hours with the minimum time of 2 hours (which equated to 0.2% of the maximum time) was selected using the temperature of 160°C. Rearranging Equation (10-1) to give Equation (10-2) gave a growth formula that could be applied to other temperatures giving corresponding maximum aging times.

$$\frac{x - x_o}{A} = t^n e^{-Q/RT} \tag{10-2}$$

Four other aging temperatures, 134°C, 146°C, 175°C, and 190°C, were chosen so that they were distributed evenly in terms of 1/T (Kelvin). The annealing time periods are distributed uniformly in terms of ln(t) and are listed for all of the temperatures in Table 10-4 ranging from 0.6 hour to 3,401 hours.

Table 10-4: Different Aging Temperatures and Their Corresponding Time Intervals. There are five different temperatures, each with eight time intervals.

Temperature	134°C	146°C	160°C	175°C	190°C
Time	Hours	Hours	Hours	Hours	Hours
1	6.8	3.7	2	1.1	0.6
2	16.5	9	4.9	2.6	1.4
3	40.2	21.8	11.8	6.4	3.5
4	97.6	53	28.7	15.6	8.4
5	237	128.6	69.7	37.8	20.5
6	576	312.4	169.4	91.9	49.8
7	1400	759	411.6	223.2	121
8	3401	1844	1000	542.2	294

Three different ovens were used to perform the accelerated isothermal aging: a Hot Pack, a Blue M, and a Lindberg. The latter two were computer controlled which allowed the ovens to be programmed to a desired profile; however, only one temperature could be obtained for the oven compartment at any given time. The Hot Pack and Blue M ovens were of the forced convection type while the Lindberg was natural convection.

The Hot Pack, which was not computer controlled, was used for the 134°C temperature tests. The 146°C and 190°C temperatures were performed in the Blue M, while the other aging temperatures, 160°C and 175°C, were achieved in the Lindberg. To ensure that the temperatures were calibrated to within ± 3°C between the three ovens, a portable thermocouple was used.

During both aging cycles, the 134°C and the 146°C temperature intervals, power failure occurred in the ovens, using the Hot Pack and the Blue M, respectively. The Hot Pack, operating at 134°C lost its power due to a blown fuse. This occurred after the sixth time increment (576 hours) for approximately one to three days; the exact duration is unknown. The Blue M operating at 146°C lost its power due to a power outage in the building. This happened approximately 75 hours into the fifth time interval of 128.5 hours. The duration of power loss was approximately four hours. However, the percentage of time lost in either oven was small when compared to the total time at the aging temperature: two percent lost time in the Hot Pack and less than one percent lost time in the Blue M. Therefore, these interruptions should have minimal effect on the results.

10.3.5 In-Board Peel Test

The mechanical testing was performed using a modification of the in-board peel test specified by DuPont,[25] which is believed to represent a realistic failure mode that is similar to failures occurring in hybrid microcircuits.[28]

The test apparatus consisted of two sections: grips that maintained the position of the wire and a slotted holder that maintained the stability of the alumina substrate during the peel test. Both items were made out of 3031 aluminum and 1040 steel. These dimensions are shown in Appendix E. The section that held the wire during a peel test was mounted to an Interface load cell (Model No. SM-50; 50 pound maximum load), and the slotted holder was positioned onto an actuator situated in a computer controlled MTS load frame (closed loop system for mechanical testing of materials and structures, MTS Systems Corp., Model No. 661.234-01). The vertical displacement of the actuator was measured by an linear-variable differential transformer (LVDT). This setup is shown in Figure 10-8.

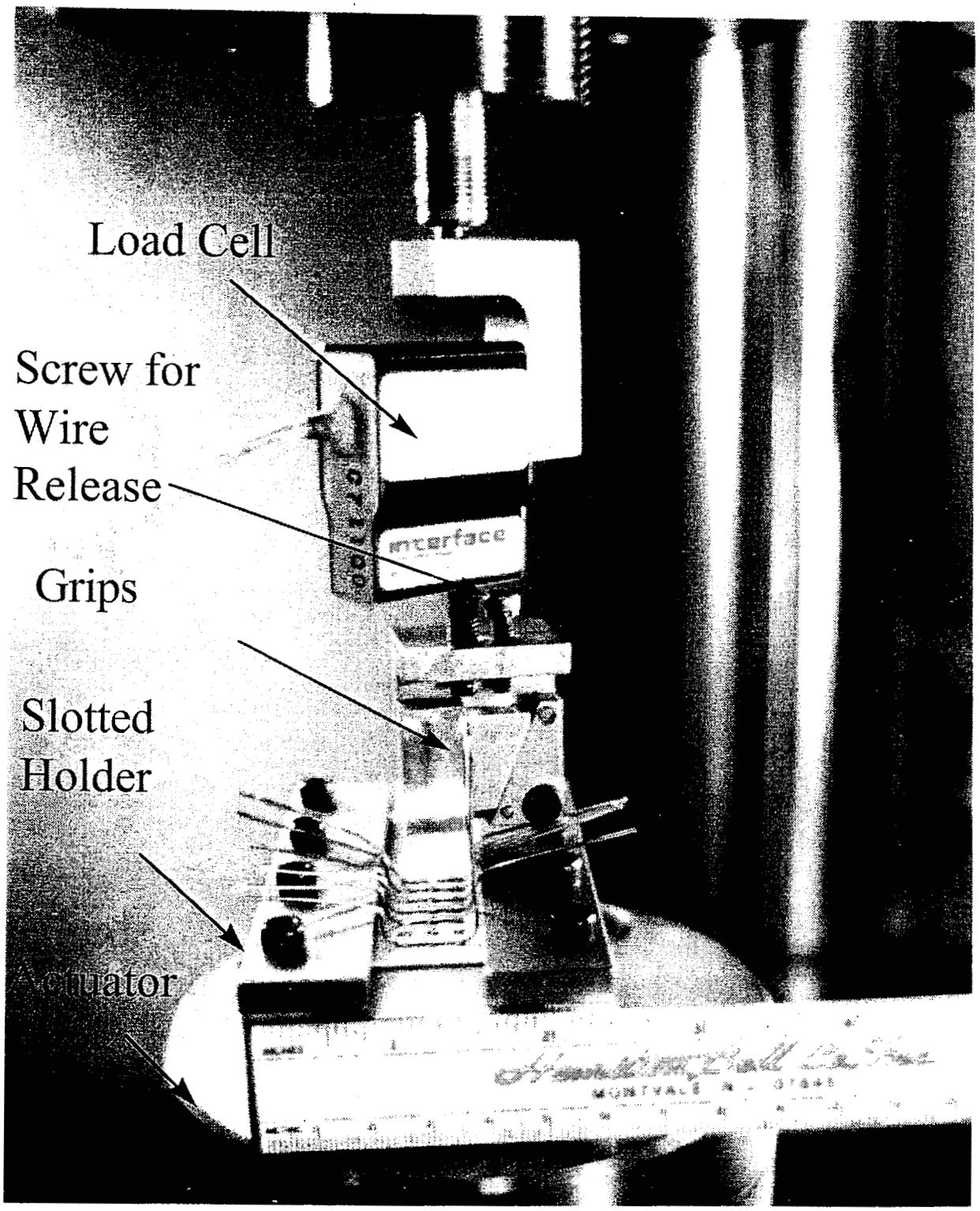

Figure 10-8. Schematic Set Up of the In-Board Peel Test Using a MTS Loading Frame

After the specific aging had been performed on a sample, the wires on the mechanical testing boards were bent up 90° using a fixture to control the location of the bend, as shown in Figure 10-9. The substrate was then inserted into the slot of the substrate holder, as shown in Figure 10-8. This holder was critical in supplying support for the substrate so that the substrate itself did not fracture during the in-board peel test. Each wire was individually pulled at a rate of 3.81 cm per minute in a direction normal to the plane of the substrate (see Figure 10-10). The in-board peel test program was set to acquire data every second. When a distance of 0.3 cm had been reached, the LVDT stopped the peel test. This distance guaranteed failure of the bond between the wire and the solder pad, since the diameter of the wire was 0.8 mm and the approximate thickness of the solder was 150 μm. The actuator then held that position for 10 seconds, while the wire was manually released. The actuator then returned to its original starting position, which insured that the end of the wires were gripped at exactly the same point every time to prevent any deviation in the length of the moment arm.[28] A total of fourteen load failure values were obtained from each solder/metallization system for each time at a given aging temperature unless some of the joints had failed during isothermal aging.

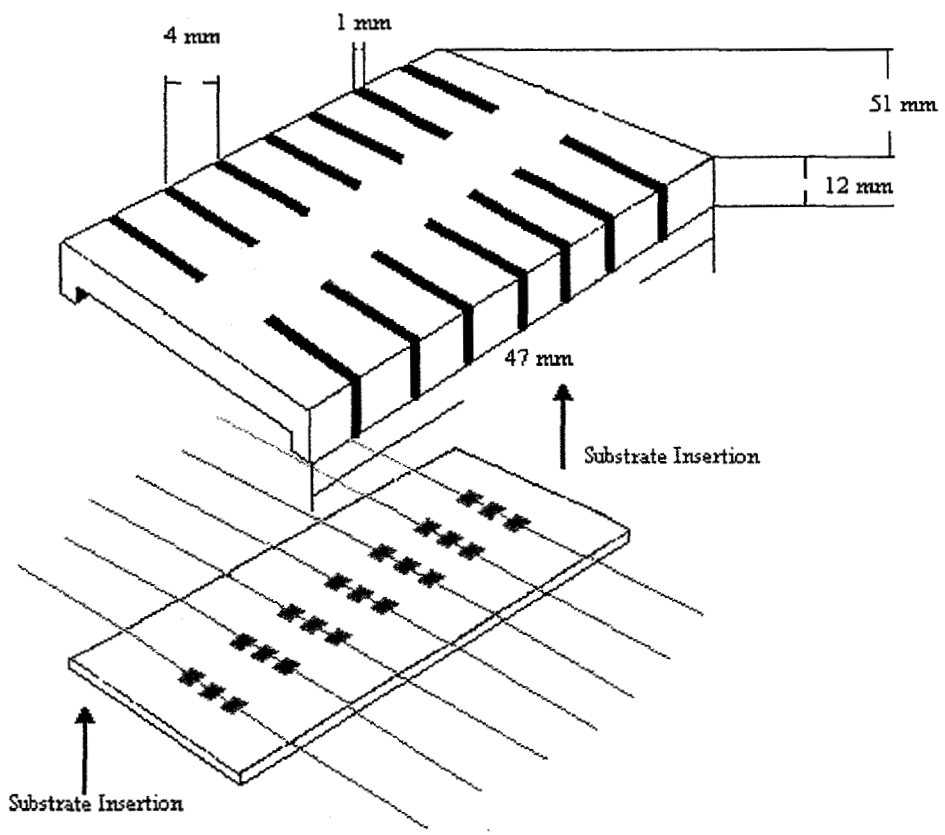

Figure 10-9. The Apparatus Used for Controlling the Location of the 90° Bend on the Wires

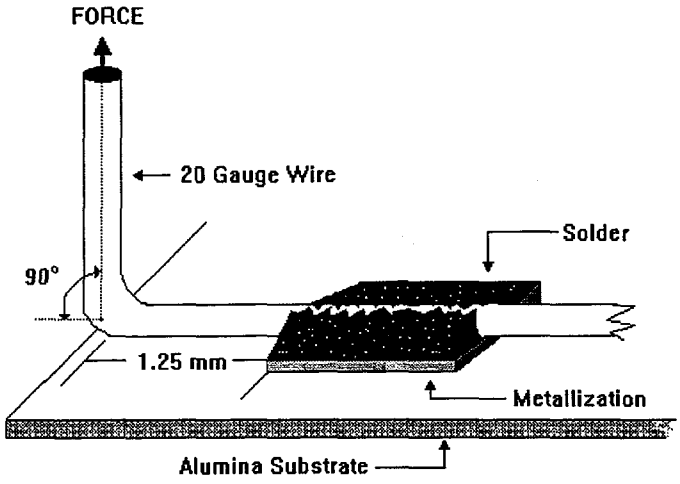

Figure 10-10. A Schematic Drawing of the In-Board Peel Test on One 2 mm Square Metallization Pad. Redrawn from the DuPont test document.[25]

10.3.6 Measurement of Intermetallic Growth

The measurement of the intermetallic growth was performed on a micrograph containing a cross-sectional view of the solder/metallization system. This view was obtained by the sectioning of the aged solder/metallization systems along the laser-scribed line on the alumina substrate into two segments. Each of the segments were cold mounted in alumina (Al_2O_3) filled Castolite epoxy and polished on a 20 μm fixed diamond wheel. They were then polished with 6 μm and 1 μm Metadi diamond paste using Buehler's Metadi extender on a nylon cloth. Secondary and back-scattered electron images were obtained on the polished surface using a JEOL 6400 scanning electron microscope (SEM).

From these micrographs, the intermetallic thickness in the image was measured in mm with a resolution of 0.5 mm and converted into the actual thickness in μm based upon the magnification of the micrograph. A total of thirty measurements were taken at random locations along the interface for each sample at each time and temperature increment. Using the method of least-squares,[29] a multivariable regression analysis was performed on these data using Equation (10-1). A general model of this regression is shown in Equation (10-3)

$$Y = \beta_o + \beta_1 x_1 + \beta_2 x_2 + \varepsilon \qquad (10\text{-}3)$$

where Y is the dependent variable (intermetallic growth), β_o is the intercept, x_1 and x_2 are the independent variables (temperature and time), β_1 and β_2 are the unknown coefficients, and ε is the random error term that is added to allow for deviation between the dependent and independent part of the model.

Due to the computational difficulty of fitting data to a multivariable regression model, an EXCEL[30] computer spreadsheet was used. This enabled the ease in determining the values of the unknown coefficients A, n, and Q and the intercept and values of β_1 and β_2, respectively. Prediction of the intermetallic growth rate of each solder alloy was then possible once these parameters were calculated.

10.4 Results

10.4.1 Intermetallic Growth

In conducting the isothermal aging, only four of the eight time increment samples from the five temperatures were examined due to limited financial resources. In the temperatures 134°C, 160°C, and 190°C, the odd numbered time increments (times 1, 3, 5, and 7) were analyzed. For the remaining temperatures, 146°C and 175°C, the even numbered time increments (times 2, 4, 6, and 8) were analyzed.

While examining the micrographs obtained from the cross-sectional views of the solder/metallization systems, an intermetallic layer was visible for all of the different temperature and time conditions. This layer was also apparent in the as-soldered condition, where no isothermal aging had been performed. Figure 10-11 is a schematic of the typical behavior that was exhibited as a solder/metallization system isothermally aged; from the initial as-soldered state (without aging) to the final aged state. The intermetallic and the metallization systems have a jagged interface that runs parallel to the substrate. As the aging time and temperature increased, this intermetallic layer observed to increase in thickness. In severe cases, the complete reaction of the solder with the metallization occurred leaving behind only an intermetallic layer where the metallization originally existed.

Voids apparent at the interfacial regions of the intermetallic layer and metallization were assumed to be Kirkendall vacancies. Other voids could be seen in the as-soldered condition throughout the metallization and the intermetallic/metallization interface. As the aging continued on any one solder/metallization system, these voids appeared to grow and coarsen. Small colonies of precipitates could also be seen in the solder itself with varying composition of elements that were dependent on the type of solder used.

In the following four sections, the microstructure of the four solder alloys will be discussed. Note that this analysis did not cover the compositional study of the microstructure of the sessile drop or the intermetallics that formed. Therefore, the constituents of the solder microstructure and intermetallics are identified based upon limited compositional studies. This is justified by the limited number of phases and relatively unique backscattered images that they produce.

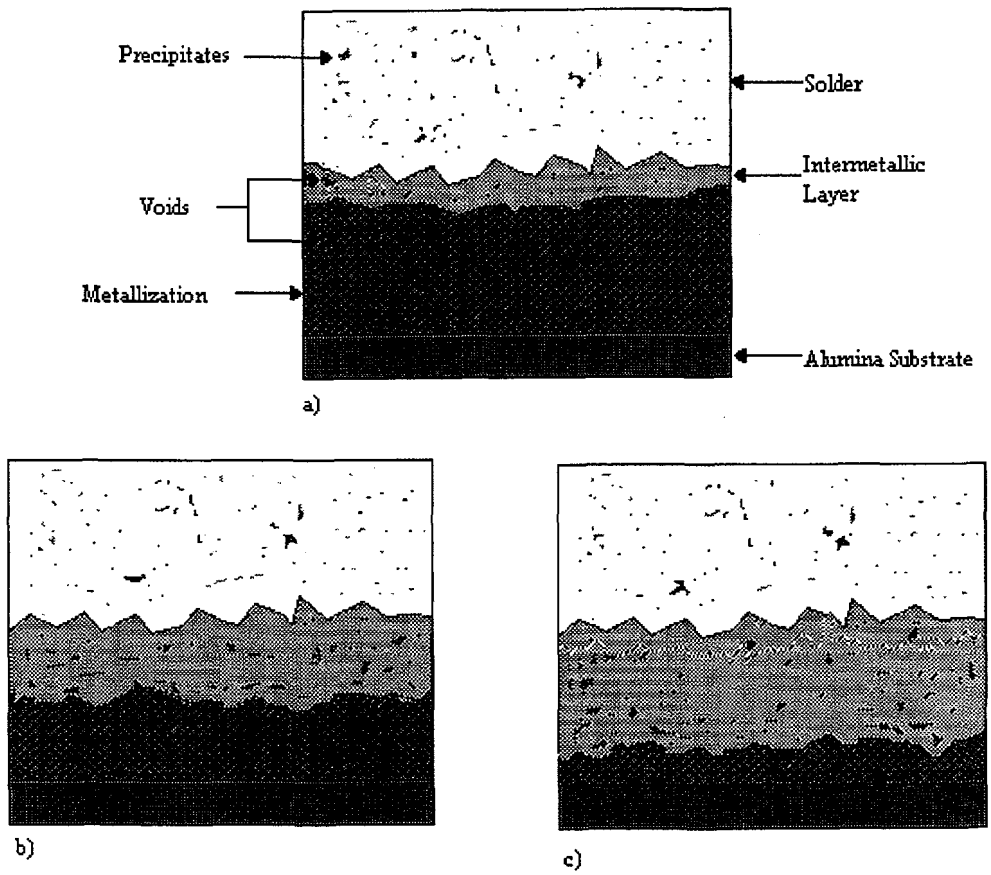

Figure 10-11a-c. A Typical Progression of Intermetallic Growth. (a) The As-Soldered Condition, t = 0, Shows Precipitates, Voids, and an Intermetallic Layer. (b) The solder/metallization after exposure to some time and temperature duration, t > 0, shows the coarsening of the voids and increase of intermetallic growth. (c) The solder/metallization was exposed to a long time and temperature condition, t >> 0, showing a significant increase of the intermetallic thickness.

10.4.1.1. Sn-Ag (121)

The 121 solder alloy, shown in Figure 10-12, had a fine-grained microstructure. Grains of Sn are surrounded by Ag_3Sn near the metallization. Voids are apparent at the intermetallic/metallization interface and throughout the metallization. The intermetallic layer that was measured is assumed to be comprised of Ag_3Sn.

Previously, a Pt-Sn phase containing traces of Ag was observed in this system.[5] The compositional analysis of this phase indicated a stoichiometry near $PtSn_7$. In the binary equilibrium Pt-Sn phase diagram, no such phase has been identified; so this phase may be

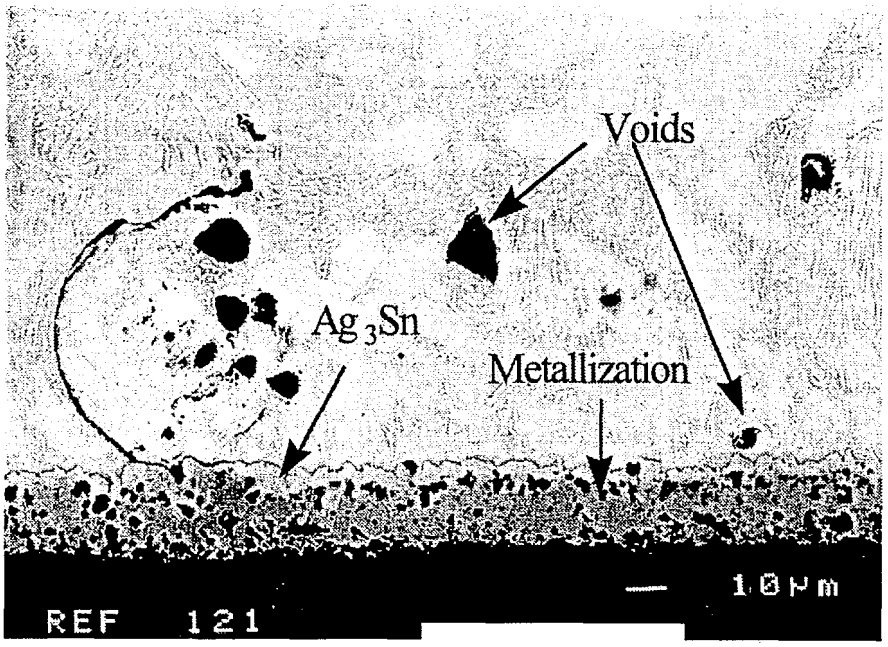

Figure 10-12. A Cross Sectional View of the 121 Solder Aloy in the As-Soldered Condition.

metastable. No attempt was made to determine the presence of this phase in the as-deposited or aged microstructures.

Upon examination of the metallization over all the time and temperature increments, the metallization was still identifiable even at the highest temperature, 190°C. This is shown in Figure 10-13 and Figure 10-14, where the metallization is visible after one hour and 121 hours of aging at 190°C, respectively. From the observations of the aged samples, there appeared to be no visible coarsening of the microstructure or voids.

10.4.1.2 Sn-Ag-Cu (SAC)

The SAC solder alloy also exhibited a fine grained microstructure. In Figure 10-15, large primary Ag_3Sn, coarse eutectic Sn (light gray), and Cu_6Sn_5 (dark structures) can be seen.
A layer of large grains of Ag_3Sn is present on top of the metallization. Voids throughout and along the interface of the metallization are also seen, and they are observed to coarsen over time at a given temperature.

The average intermetallic thickness ranged from 3.4 to 25.1 μm, where the latter value was obtained in the 190°C temperature at 121 hours. In this sample, the metallization had been completely consumed by the intermetallic growth. This is shown in Figure 10-16.

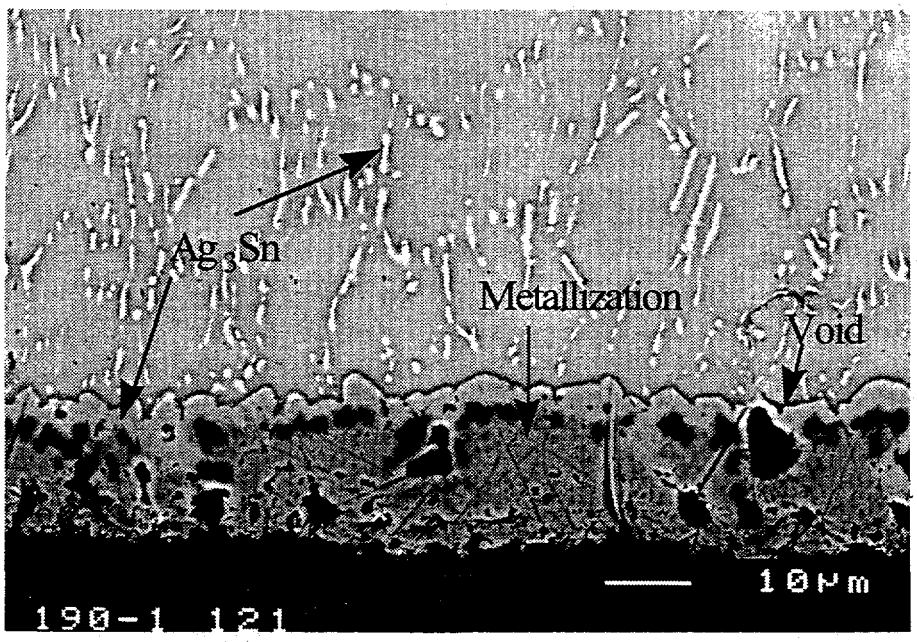

Figure 10-13. A Micrograph Showing the Cross Sectional View of the 121 Solder Alloy Isothermally Aged for One Hour at 190°C

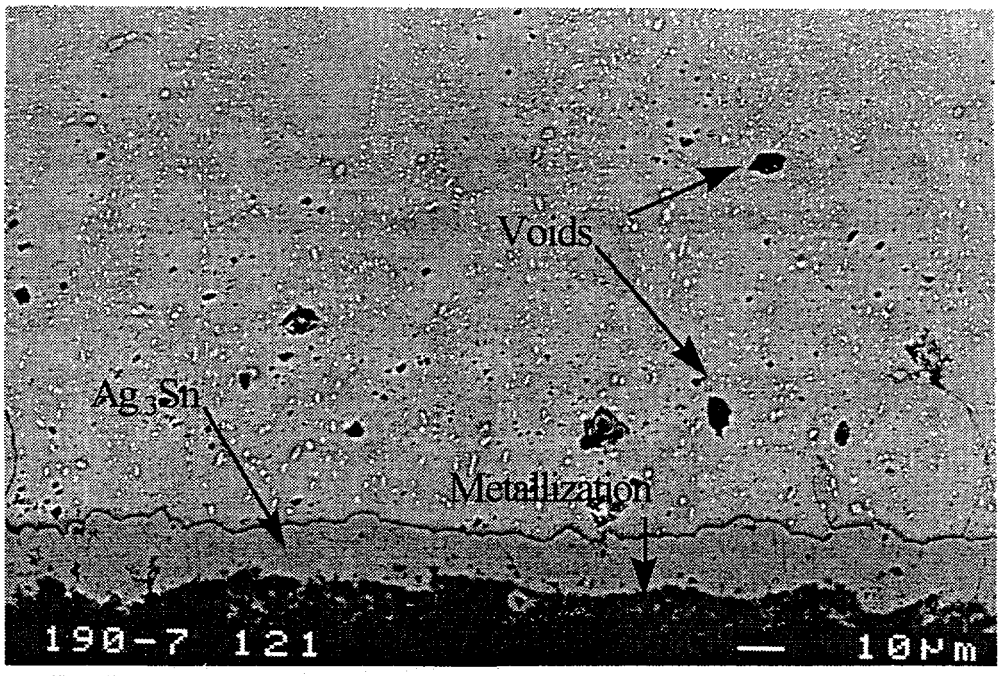

Figure 10-14. A Micrograph Showing the Cross Sectional View of the 121 Isothermally Aged for 121 Hours at 190°C. The metallization is still apparent.

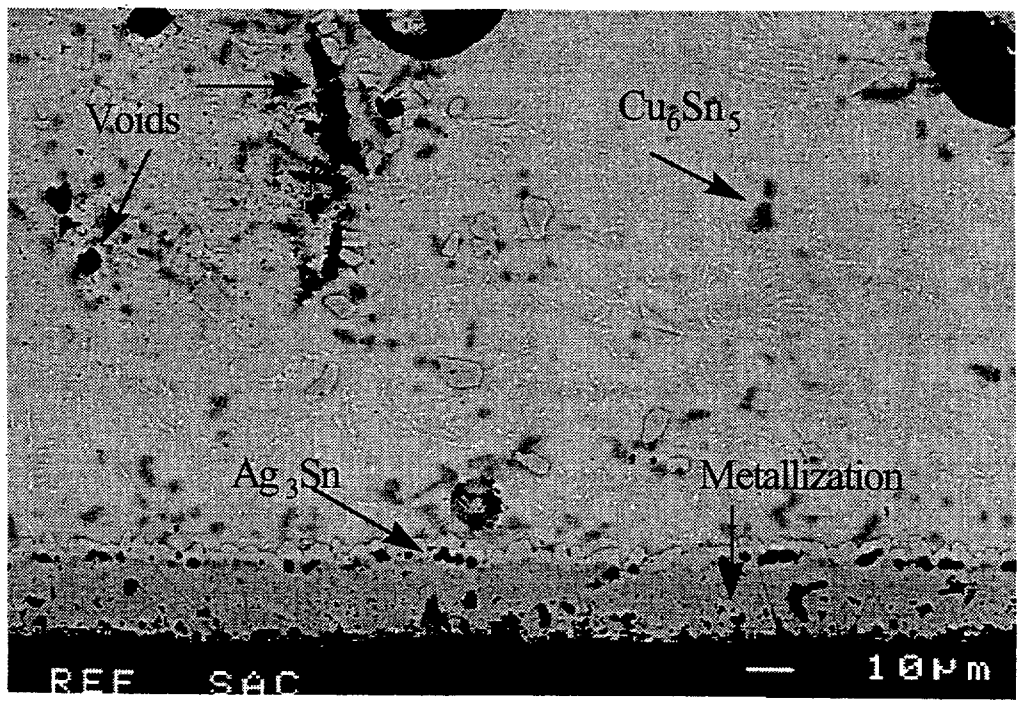

Figure 10-15. A Cross Sectional View of the SAC Solder Alloy in the As-Soldered Condition

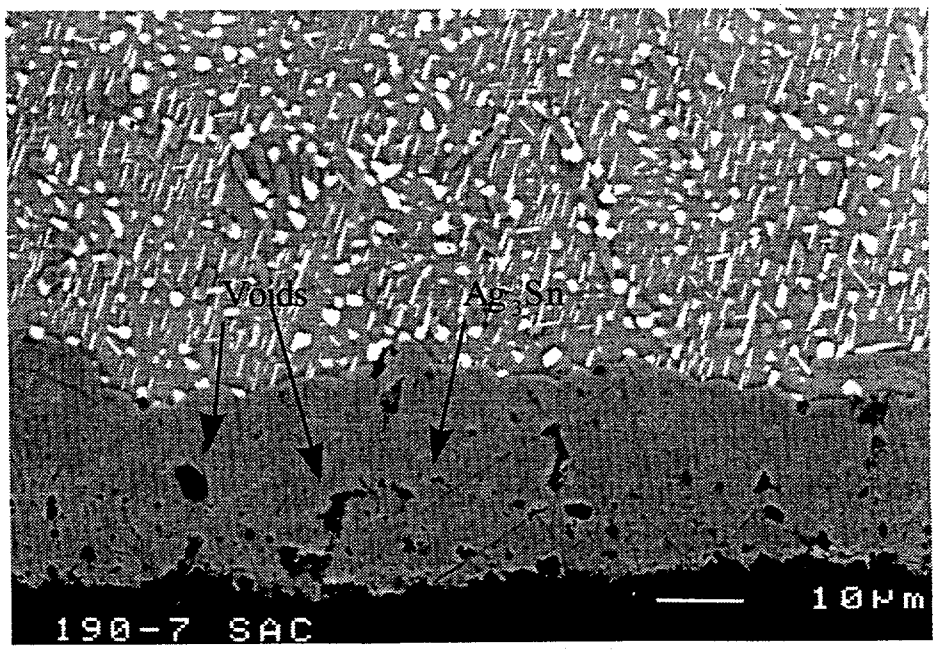

Figure 10-16. The Metallization in the Cross Sectional View of the SAC was Fully Consumed. This sample was aged for 121 hours at 190°C.

10.4.1.3 Sn-Ag-Bi (SAB)

The microstructure of the SAB shows small round white regions that are essentially pure Bi, as seen in Figure 10-17. It is believed that during cooling, this Bi precipitated in the solder matrix. The Sn-Ag eutectic is surrounded by primary Sn and Bi phases. Close to the metallization, large grains of Ag_3Sn form a continuous layer over the metallization. Voids in the metallization and its interface with the intermetallic layer are visible and appear to coarsen as time and temperature increase.

The SAB caused a total reaction of the metallization in the 175°C temperature cycle, unlike the SAC where a total reaction of the metallization by the intermetallic growth occurred in the 190°C temperature cycle. Figure 10-18 shows the SAB after 2.6 hours at 175°C where the metallization is visible. Figure 10-19 shows the SAB at the end of the 175°C aging temperature, 542 hours, where the metallization is no longer apparent and only the intermetallic layer can be seen. Again, as seen with the SAC after high temperatures and extended time, the SAB microstructure coarsened.

10.4.1.4 Sn-Ag-Cu-Bi (SACB)

The microstructure of the SACB, shown in Figure 10-20, is similar to the microstructure of the SAB solder alloy where the same small round white regions of Bi can be seen. The large dark regions in the microstructure are primary Cu_6Sn_5. Below the Sn-rich region there is a layer of large Ag_3Sn grains near the remaining metallization. Voids are visible in the intermetallic layer, intermetallic/metallization interface, and solder matrix. These voids and the solder microstructure appear to coarsen with time and temperature.

Total reaction of the metallization into the intermetallic growth also occurred in the 175°C temperature range, which was similar behavior to the other solder alloy containing Bi, SAB. Figures 10-21 and 10-22 show the observation of the visible metallization after 92 hours at 175°C and then the total reaction of the metallization into intermetallic growth 450 hours later at 175°C, respectively. Visible in Figure 10-22 is a dark region at the interface of the solder matrix and the intermetallic layer. This formation is assumed to be the Cu_6Sn_5 intermetallic.

10.4.1.5 Intermetallic Growth Discussion

The interface of the intermetallic between the solder matrix and the metallization was rough and nonuniform; therefore, measuring the intermetallic thickness was not a straight forward process. Large voids were visible at the interface of the intermetallic and metallization with smaller voids, in comparison, throughout the microstructure. When measuring the intermetallic layer, these small voids were included, but the voids present at the interface were not and an effort was made to avoid these areas. It was assumed that a variety of intermetallics existed, but a compositional analysis was not performed to confirm this. However, it was assumed that most of the

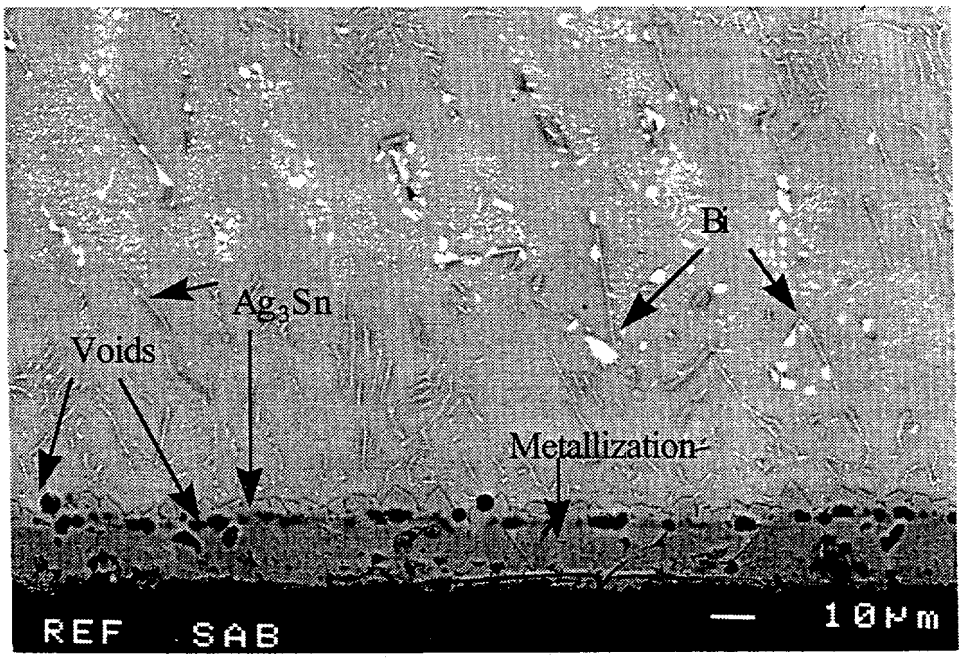

Figure 10-17. A Cross Sectional View of the SAB Solder Alloy in the As-Soldered Condition

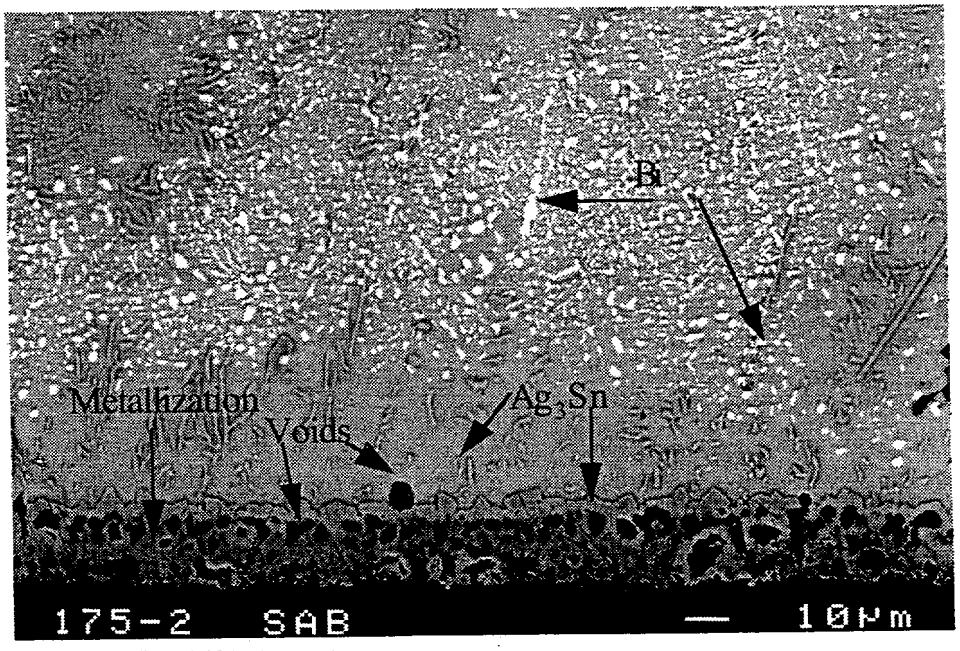

Figure 10-18. A Micrograph Showing the Cross Sectional View of the SAB Isothermally Aged for 2.6 Hours at 175°C

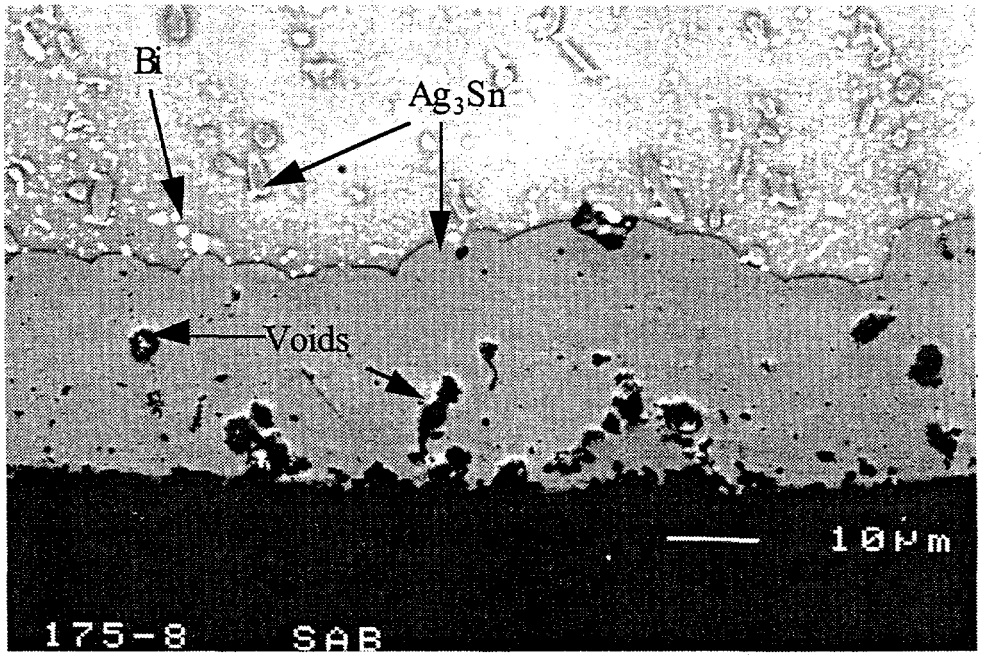

Figure 10-19. A Micrograph of the SAB Aged for 542 Hours at 175°C. Complete dissolution of the metallization has occurred and only the intermetallic layer is present.

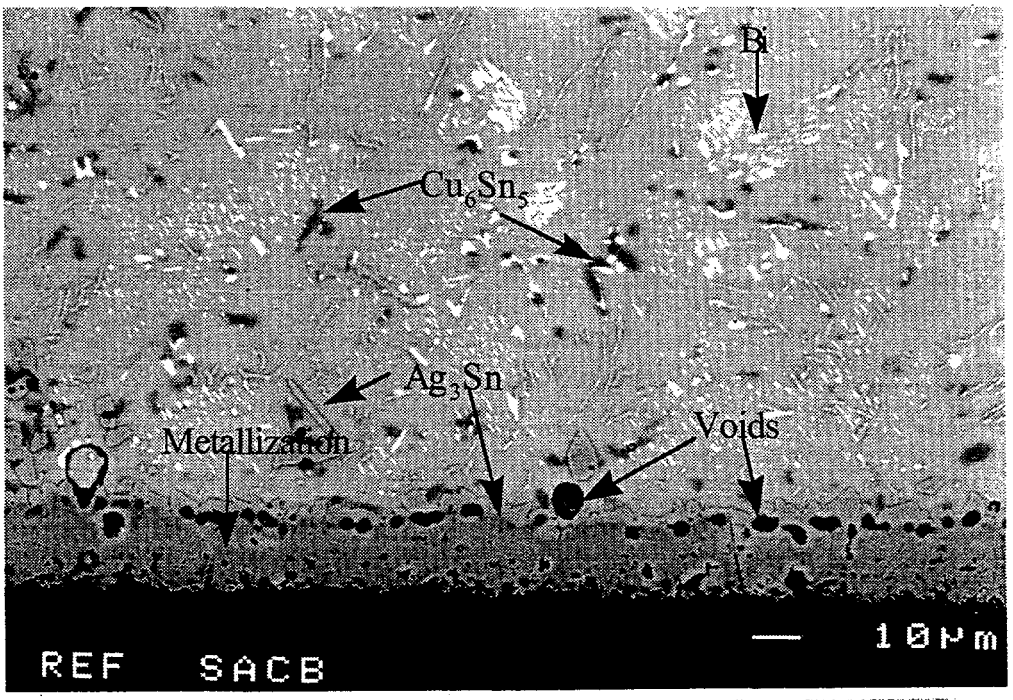

Figure 10-20. A Micrograph Showing the Cross Sectional View of the SACB Solder Alloy in the As-Soldered Condition

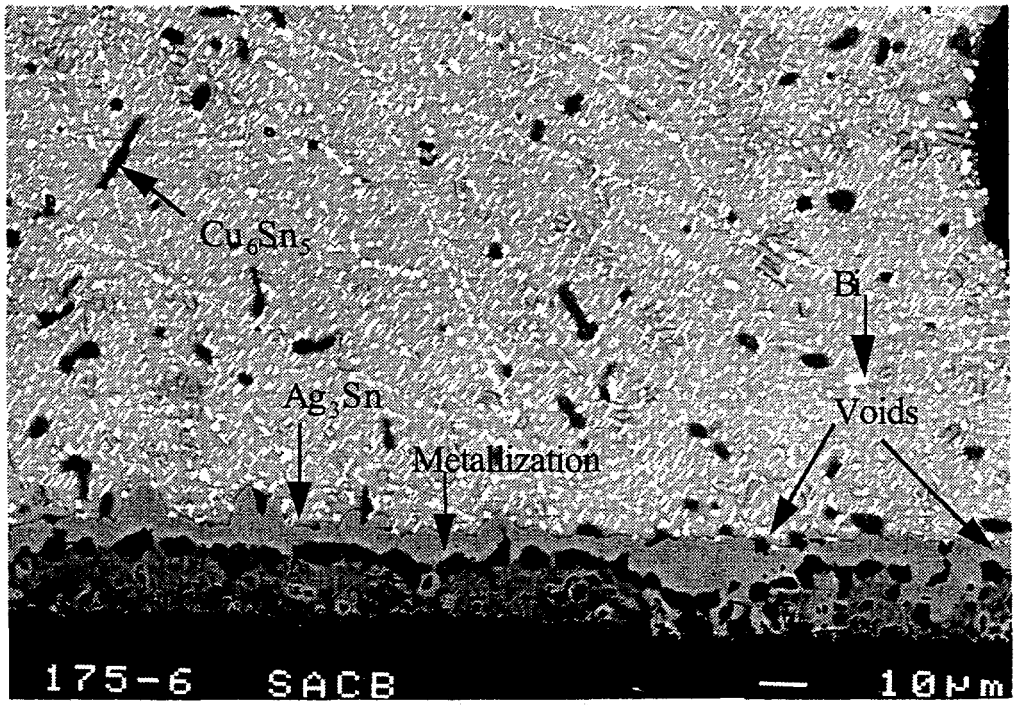

Figure 10-21. A Cross Sectional View of the SACB Solder Alloy Aged at 175°C for 92 Hours. The metallization is still visible beneath the intermetallic layer

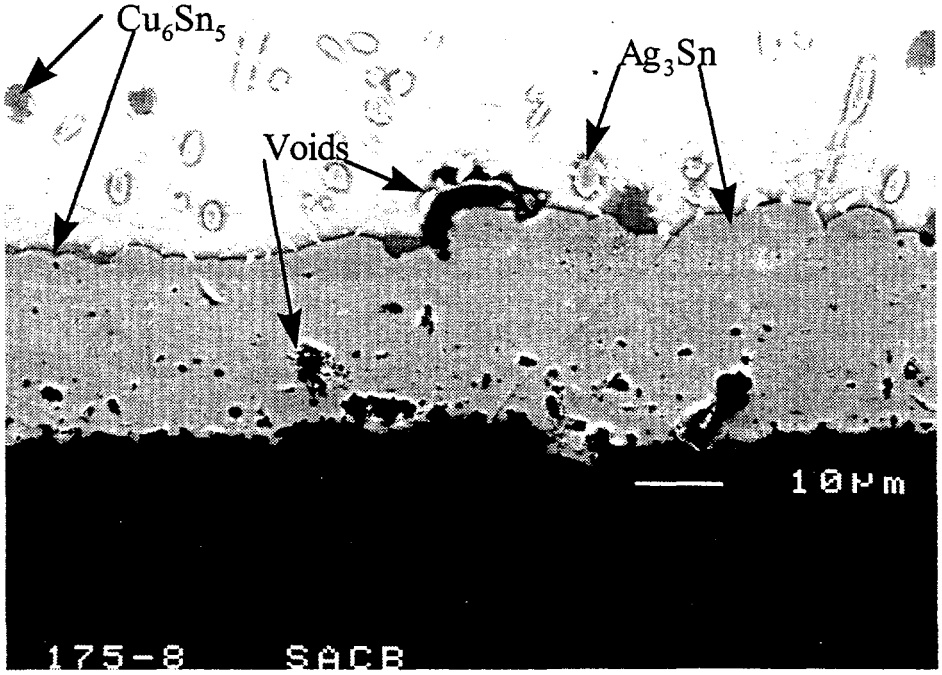

Figure 10-22. A Micrograph Showing the Cross Section of the SACB Solder Alloy Aged at 175°C for 542 Hours. The metallization is no longer visible and only the intermetallic layer, Ag_3Sn, is seen.

intermetallic layer was comprised of the Ag_3Sn intermetallic. Cu_6Sn_5 intermetallics were also present if the solder alloy contained Cu; therefore, the Cu-based intermetallic was included in these measurements and not viewed as a separate entity. The data appear in Table 10-5. The measured values where total reaction of the metallization occurred are denoted by shading. The x_o values, also shown in Table 10-5, are the averages calculated the as-soldered states of the four solder alloys.

At the onset of any one aging cycle, the intermetallic layers x_o measured between 2.2 to 3.1 μm thick. In the higher temperatures, 175°C and 190°C, towards the end of these aging cycles, it was found that in most of the Pb-free solders (except for the Indalloy 121), the metallization had completely reacted. Occurring at a faster rate as the temperature increased, this complete reaction gave a 21.6 to 26 μm thick layer of intermetallic.

The data that were obtained on the samples that involved total reaction of the metallization were included in the multivariable regression analysis. These data points held statistical significance for the constants used in predicting the growth rate of the overall system. Using the t statistic, it was found that all the coefficients determined were highly significant (94.6% and greater).

In performing the multivariable regression analysis, values for the unknown coefficients of Equation (10-1) were found for each of the solder alloys (the 121 solder, SAC, SAB, and SACB); the pre-exponential constant, A; the time exponent, n; and the apparent activation energy, Q; ranging from 0.7×10^{8} to 1.9×10^{8} $\mu m/t^n$ (time in hours), 0.26 to 0.48, and 27.6 to 88.5 kJ/mol, respectively. The multiple correlation coefficient, R^2, was used to determine the adequacy of the regression model, a perfect fit occurring when R^2 equals 1.0. For this analysis, the R^2 values ranged from 0.72 to 0.84. The value of the unknown constants found through regression, their t-statistics, and the values calculated for R^2 are summarized in Table 10-6.

Table 10-5: Average Thickness Values of the 30 Total Intermetallic Thickness Measurements That Were Obtained for Each Solder Alloy After the Accelerated Isothermal Aging. The shaded values denote the situation involving complete reaction of the metallization. Average thickness values determined from the as-soldered conditions of each solder alloy is noted by x_o.

Temp (°C) Time (Hours)		Mean Thickness (μM)			
		121	SAC	SAB	SACB
x_o	0	2.2 ± 0.8	3.0 ± 1.2	2.2 ± 1.1	3.1 ± 1.8
134	6.8	2.8 ± 0.8	3.4 ± 1.3	2.6 ± 0.9	3.3 ± 1.5
	40.2	6.3 ± 0.9	4.5 ± 1.8	4.5 ± 0.9	5.4 ±1.1
	237.1	4.7 ± 1.1	5.5 ± 2	4.4 ± 0.8	5.4 ± 1.9
	1400	7.1 ± 1.4	6.7 ± 1.6	6.9 ± 1.1	7.3 ± 1.7
146	8.9	4.4 ± 1.1	4.6 ± 1.7	4.5 ± 1.1	3.8 ± 1.9
	52.9	4.4 ± 1.3	5.3 ± 1.4	5.3 ± 1.1	4.5 ± 1
	312.4	6.1 ± 1.4	5.9 ± 1.4	6.2 ± 0.9	6.7 ± 1.3
	1844	9.6 ± 1.8	8.6 ± 1.6	10.8 ± 2.5	9.9 ± 1.6
160	2.0	3.5 ± 1.4	4.3 ± 1.1	4 ± 1.3	3.9 ± 2.4
	11.8	3.9 ± 0.9	3.8 ± 0.9	4.9 ± 1.2	4.8 ± 1
	69.7	5.2 ± 1.3	5.3 ± 1.5	5.9 ± 1.2	4.9 ± 1.3
	411.6	5.6 ± 1.8	5.3 ± 1.5	7 ± 1.4	7.5 ± 1.5
175	2.6	4.3 ± 1.4	4 ± 1.7	3.9 ± 1.2	4.5 ± 1.5
	15.6	4.9 ± 1.7	5.7 ± 1.9	5.5 ± 1.4	6.1 ± 1.8
	91.8	5.7 ± 1.5	7.4 ± 6.8	8.6 ± 3.4	8 ± 2
	542.2	7.2 ± 2.3	7.8 ± 2.4	25.2 ± 3.3	23.5 ± 2.5
190	1.0	3 ± 1.2	4.5 ± 1.6	3.9 ± 1.3	4.5 ± 2.1
	3.5	4.3 ± 0.8	5.2 ± 1.4	6.6 ± 1.5	6.5 ± 1.8
	20.5	6.7 ± 1	6.9 ± 1.7	21.6 ± 2.9	24.7 ± 1.6
	121	15.3 ± 2.2	25.1 ± 2.7	23.8 ± 3.6	26.3 ± 3

Table 10-6: Values That Were Obtained for A, n, and Q in a Regression Analysis Performed on the Data Obtained From the Four Solder Alloys During the Accelerated Aging Environment.

Constants	121	t statistic	SAC	t statistic
A ($x10^8$ μm/t^n)	0.6 ± 0.2	96.5%	1.2 ± 0.2	95.2%
n	0.26 ± 0.04	93.4%	0.31 ± 0.05	95.0%
Q(kJ/mol)	27.6 ± 8.3	96.7%	52.3 ± 10.8	94.1%
R^2	0.73		0.72	
Constants	SAB	t statistic	SACB	t statistic
A ($x10^8$ μm/t^n)	1.7 ± 0.2	92.2%	1.9 ± 0.3	93.5%
n	0.36 ± 0.04	92.0%	0.48 ± 0.08	94.5%
Q(kJ/mol)	71.0 ± 9.4	92.4%	88.5 ± 13.6	93.5%
R^2	0.84		0.84	

These values were then substituted into Equation (10-1) to obtain a model predicting the kinetic growth rate of the intermetallic layer. A trend was seen with the four solder alloys when the average raw data values were compared to the predicted values from the regression analysis. This is shown on a log-log plot in Figure 10-23 with the SAC solder. Deviation can be seen in the higher temperature 160°C, 175°C, and especially at 190°C.

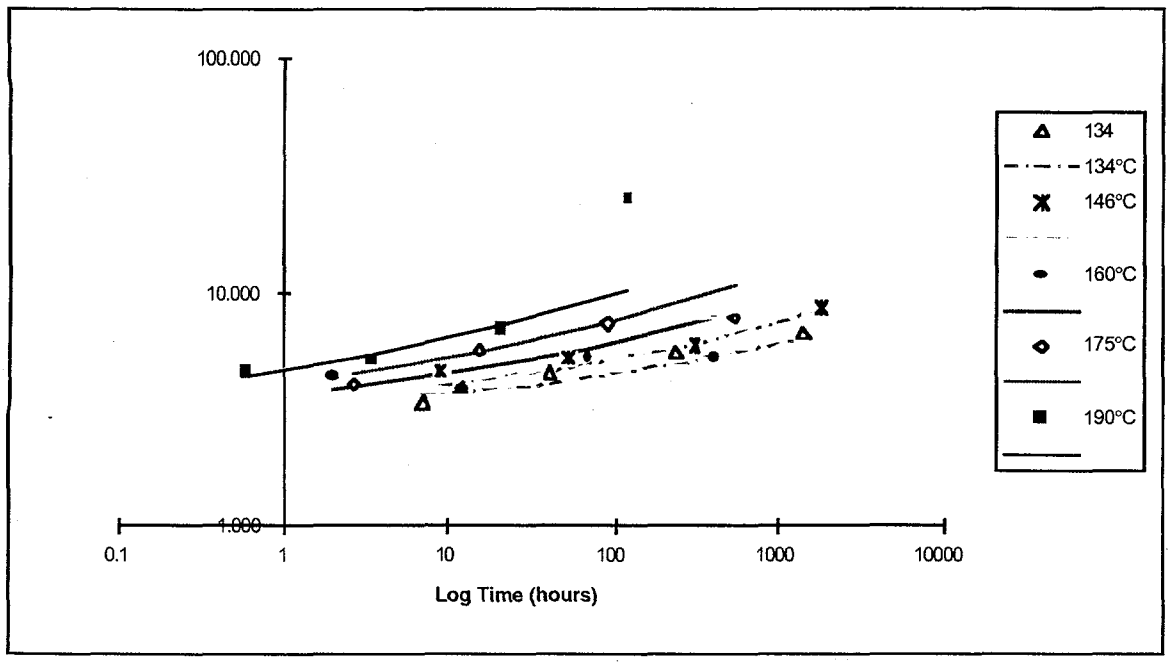

Figure 10-23. A Log-Log Plot of SAC, Showing the Intermetallic Growth, in μm, at the Five Different Aging Temperatures. The symbols represent the average of the raw data obtained and the lines show the predicted regression model.

The values in Table 10-6 found from the regression corresponded well to the growth behavior that was evident at the 160°C temperatures for each solder alloy. The solder alloys containing Bi had higher values of A, n, and Q and were characterized by the high growth rate of intermetallics. In comparison to the other alloys, the SAC solder had a slower growth rate mechanism, while SACB had a faster intermetallic growth rate. This behavior is portrayed in Figure 10-24, where a comparison is made between the four solder alloys' raw values obtained in measuring the growth intermetallics for the 160°C temperature.

Upon further observation at this temperature at 160°C, SAB, SAC, and 121 solder show a subparabolic growth. Without more data measurements, it is impossible to determine, based on one data point, why the SACB did not exhibit subparabolic growth at this temperature. Perhaps a different mechanism was present, or there was experimental error because this behavior of the SACB was not apparent in the other temperatures.

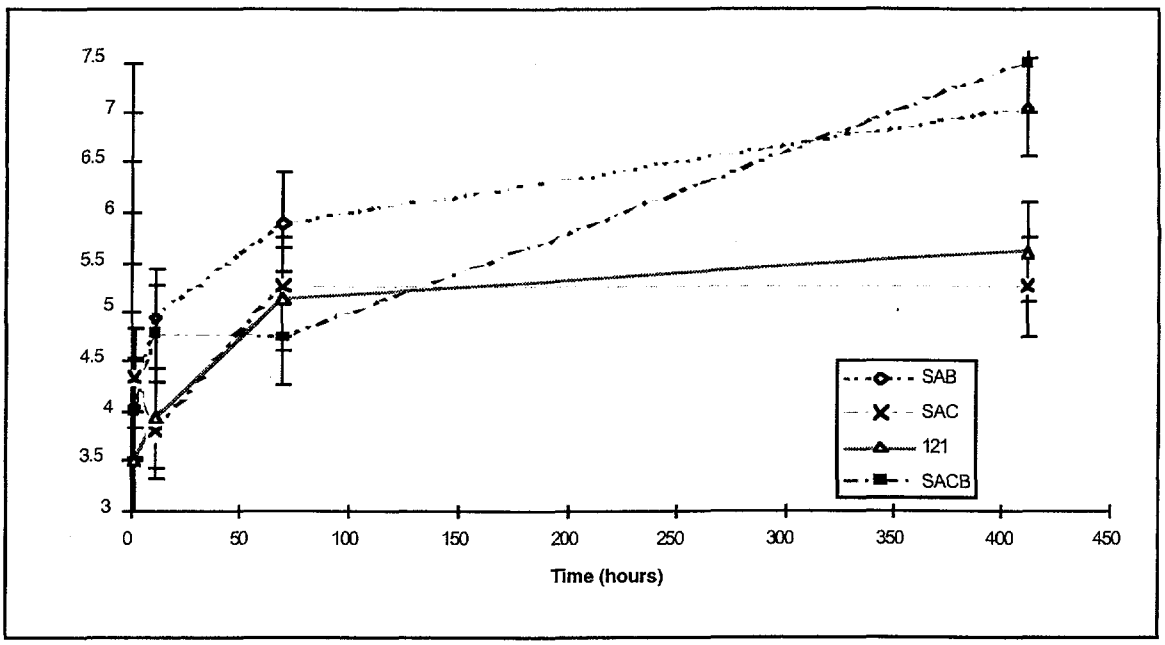

Figure 10-24. A Comparison of Intermetallic Growth, in μm, is Shown Between the Four Solder Alloys in the 160°C Temperature Cycle Using the Raw Measurement Values.

In analyzing solid-state growth (intermetallic), three types can be identified based on the values that are found through regression for the time exponent, n: (1) linear growth kinetics where n = 1, (2) parabolic growth kinetics where n = 0.5, and (3) subparabolic growth where n < 0.5. Parabolic growth kinetics are a result of bulk diffusion, while subparabolic growth has an inclination of exhibiting formation of more than one intermetallic compound.[27]

The intermetallic growth proved to be nonlinear from the n values obtained from the regression model. These values indicated subparabolic controlled kinetics growth (n < 0.5), where the growth is assumed to be composed of more than one intermetallic compound growing in solid state. In the two alloys containing Cu, SAC, and SACB, the possible intermetallics could be Cu_6Sn_5, Ag_3Sn, or Cu_3Sn. The Cu-Bi phase equilibrium diagram[8] shows that an intermetallic phase does not exist between the Bi and Cu. However, a metastable compound Cu_5Bi_2 has been reported.[31] In SAB and the 121 it is uncertain at this time, other than the Ag_3Sn intermetallic compound, what other intermetallics exist; it was not determined if another intermetallic phase was present. Nevertheless, recalling from the preliminary study, a nonequilibrium phase of $PtSn_7$ was found in this Sn-Ag solder alloy joined to a Ag-Pt metallization.

The regression model produced activation energies that varied by a factor of 3.2 between the four different solder alloys. This type of difference is fully expected to result in a change in the growth rate as the temperature increases. In general, the alloys with a high activation energy would be expected to grow slower at low temperatures and faster at high temperatures compared to those alloys with a low activation energy. This trend is shown in Figure 10-25, where the 121 solder having a low activation energy value exhibits a faster growth rate at lower temperatures

while the SACB, having a high activation energy value, is seen to have a slow rate of intermetallic growth at the lower temperatures. These activation energies were plotted using the Arrhenius equation while keeping time constant at 100 hours.

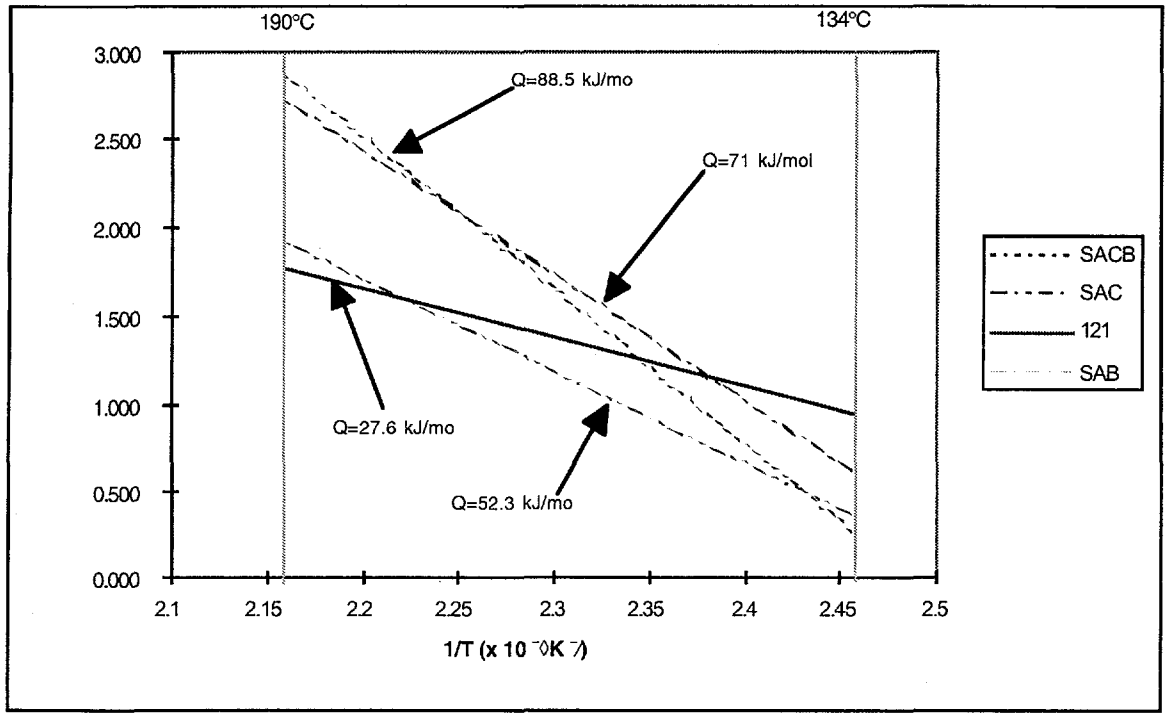

Figure 10-25. A Comparison of Activation Energies (kJ/mol), is Shown Between the Four Solder Alloys Keeping the Time Constant at 100 Hours.

In performing the regression analysis, 121 yielded an activation energy of 27.6 kJ/mol. This agrees with another study reporting an activation energy of 28.3 kJ/mol in which Sn-Ag was annealed on Cu substrates and aged in an air furnace at constant temperatures.[32]

For the SAC solder alloy, the regression analysis yielded an activation energy of 52.3 kJ/mol. This value corresponds with a similar study where the combined activation energy for the Ag-Sn-Cu-interfacial intermetallics was 59 kJ/mol.[10] The isothermal aging was performed in air furnaces with temperatures ranging from 70°C to 205°C. Both the Cu_6Sn_5 and Ag_3Sn intermetallics were present, but the Cu_3Sn was only observed at annealing temperatures above 170°C.

A literature review was performed to find documentation on activation energies involving the SAB and SACB solder alloys annealed in a similar fashion, but was unsuccessful. In comparison to the 121 solder and the SAC solder alloys that did not contain Bi, the SAB and the SACB solders yielded the highest activation energy. Why does the addition of Bi appear to boost the activation energy? At present, intermetallics that contain Bi have not been identified, and there is belief that Bi will not readily combine to form compounds because it appears to precipitate out

of the solder matrix. An answer arises from the fact that the Bi lowers the melting point of a system, thus increasing the activation energy. Activation energy is defined as the minimum energy needed to form products from the reactants. Perhaps in exploring this further it can be determined that the Bi works as a catalyst in the formation of the intermetallic compounds. With this increase of energy added to the system, the fraction of atomic mobility collisions increase leading to more reactions that form the intermetallics.

The activation energy is weakly temperature dependent;[33] lower melting temperatures induce higher activation energies (in an extreme case an activation energy of zero indicates that the process is independent of temperature). Therefore, the activation energy can be varied when different alloys, melting at different temperatures, are combined. This dependence between the melting point and the activation energy was apparent in these four solder alloys. The 121 solder had a melting point at 221°C, the highest out of the four solders, and yielded the lowest activation energy. Likewise, the SACB and the SAB, with melting points at 208°C and 211°C, respectively, had the highest activation energies, with the SACB yielding the highest value.

In summary, the activation energies obtained through the regression analysis clearly demonstrate that solder alloy composition contributes to the apparent intermetallic growth rate. The 121 solder, consisting of only Ag and Sn, had the propensity to only form the Ag_3Sn intermetallic. Due to the limited solubility of Ag into Sn,[10] the apparent growth rate of this intermetallic was lower when compared to solders containing Cu and/or Bi. It is evident that the Cu and especially the Bi that was added to the solder matrix increased the sensitivity of the intermetallic growth rate.

10.4.2 In-Board Peel Test

Failure of the solder joint was achieved when the initial separation of the wire from the solder/metallization pad occurred. In assessing the collected values from each peel test, the maximum strength value (also known as the point of maximum stress or ultimate strength of the joint) obtained in a run was used as defining the system inoperable. This value represented the force that was required to completely detach a wire from the solder/metallization pad. Subsequent lower strength values from that maximum value signified the pulling on a wire that was no longer attached to the system.

A typical peel test, shown in Figure 10-26, was performed on SAB aged for 128 hours at 145°C. An observation was made that the joint was weaker then the wire because there was no deformation of the wire as the peel test was performed; therefore, the data collected described the properties of the joint and not the wire.

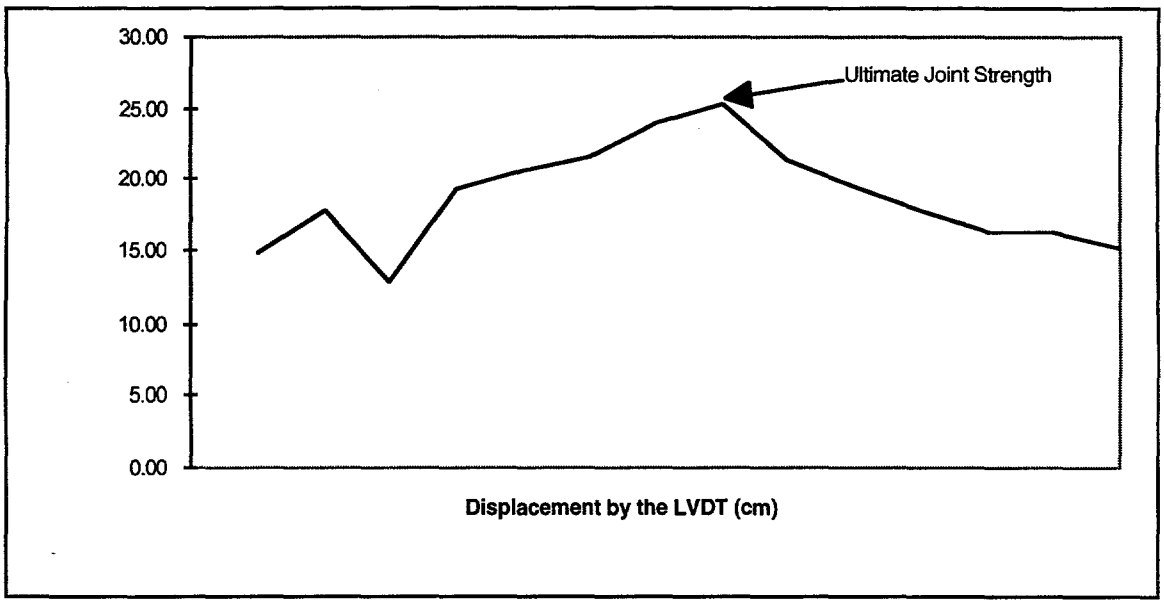

Figure 10-26. A Typical Peel Test That Was Obtained on all the Four Solder Alloys. This represents the data that was obtained on SAB aged for 128 hours at 145°C.

Different properties existed between the solder, the intermetallic layer, the Cu-Sn wire, and the metallization; therefore, an assumption was made that the failure occurred by joint fracture along or through the intermetallic layer interface at the metallization or solder matrix. However, this was not verified. Failure could also have occurred along the surface area of the wire where intermetallic layers could have formed. There is documentation stating that failure results from the formation of shrinkage voids, which divert the fracture path away from the intermetallic/solder interface and into the solder itself.[34] Other studies have indicated that if the intermetallic layer is thin, fracturing will occur through the solder.[35]

At the onset of the in-board peel test, it was anticipated that a total of 14 failure values would be obtained for each solder/metallization system from each time in a given temperature; however, this was not the case. Factors that contributed to lost data were: (1) improperly bending the wire at 90°, causing the wire to crumple, (2) improper insertion of the alumina substrate into the holder, causing the substrate to fracture, (3) human error in operating the load frame, and (4) degeneration of the solder/metallization joint, resulting in the wires detaching from the solder pad. Except for the Indalloy 121 solder, all the other Pb-free solder pads did not maintain the adhesion of their wires in the 190°C increment. The two solders that contained Bi had lost most of their wires after 50 hours (the wires were no longer attached to the solder pads), and lost all their wires after 294 hours. This would indicate that the metallization was completely dissolved resulting in a nonexistent bond between the wire and the board. Table 10-7 summarizes the average strength value for a set of data for each solder alloy at a time and temperature increment. The actual number of data points that were obtained from the anticipated 14 values is denoted by the italicized font located in the shaded columns.

Although the in-board peel tests were well controlled, much deviation in the measured values existed. Some of these deviations could be explained by the uneven solder thickness when it was screen-printed due to the consistency of the solder paste, or the alignment of the wire not being centered on the pad. Other factors to consider were the apparent jagged and uneven thickness of the intermetallic layer, and voids that were possibly present at the interfacial regions of the solder and/or the metallization.

Nonetheless, there were obvious trends that were observed with the solder alloys, except for the 121 solder. The average values calculated from the 121 solder's data sets obtained from the in-board peel test at each temperature and time cycle ranged from 23.1 to 26.3 N. A decreased strength was seen in the 190°C temperature, 17.3 N. However, since complete reaction of the metallization did not occur with the 121 solder and coarsening of the microstructure was not visible, the reason for this lower strength is not apparent.

At the end of an aging cycle at 134°C, 146°C, and 175°C, the SAC maintained a constant strength value of approximately 20.5 N. However, at the end of the 190°C temperature cycle, a 40% decrease in strength, from the initial strength of 20.3 N, was seen. This decreased strength would appear dependent on the total reaction of the metallization that was evident at this temperature.

The Bi-containing solders exhibited a similar strength degradation behavior. The SAB and SACB kept a constant strength of approximately 18.6 N ± 1.4 N and 16.1 N ± 1.1 N, respectively, for the 134°C, 146°C, and 160°C temperatures. However, by the end of the aging cycle of 190°C, the strengths of the SAB and SACB decreased to 3.6 N ± 1.6 and 2.1 ± 2.4 N, respectively. This behavior is illustrated in Figure 10-27, where comparison is made on SAB between the 160°C and 190°C temperatures. The extreme decrease in strength at 190°C is characteristic of two different stages of strength degradation occurring.

In comparison between the four solder alloys, a repeating behavior was seen at any given temperature over the eight different time intervals. A representative example of this trend is shown in Figure 10-28, where the SAB and SACB produced lower values of strength when compared to the other solder alloys, SAC, and 121 solder for the 146°C temperature. Between the average strengths of the SAB and SACB, the SAB was 13% stronger; between the SAC and the 121 solder, the 121 solder was 14% stronger.

Table 10-7: The Average Values Calculated From Data Sets Obtained From the In-Board Peel Test on the Four Solder Alloys.

The number of data points in each set is denoted by the italicized font in the shaded columns (*).

		AVERAGE STRENGTH (NEWTONS)							
TEMP (°C)	TIME (hrs)	*	121	*	SAC	*	SAB	*	SACB
	0.0	*14*	22.1 ± 2.3	*14*	20.3 ± 1.8	*13*	17.7 ± 2.1	*14*	15.6 ± 0.9
134	6.8	*14*	24.5 ± 3.9	*14*	20.1 ± 3.6	*11*	20.2 ± 2.1	*14*	15.9 ± 2.2
	16.5	*14*	21.3 ± 3.3	*13*	22.3 ± 4.3	*14*	18.2 ± 2.6	*14*	15.9 ± 1.9
	40.2	*14*	23.7 ± 3.8	*14*	22.1 ± 2.8	*14*	17.9 ± 1.9	*14*	16.1 ± 1.0
	97.6	*14*	25.6 ± 3.6	*14*	26.1 ± 2.9	*14*	17.6 ± 2.1	*14*	17.4 ± 2.2
	237.1	*14*	25.2 ± 4.9	*14*	23.5 ± 2.6	*14*	17.0 ± 2.7	*14*	16.1 ± 2.9
	576.1	*14*	29.0 ± 6.2	*14*	22.8 ± 2.3	*14*	18.8 ± 2.5	*14*	15.6 ± 1.9
	1400	*14*	24.7 ± 3.3	*14*	21.9 ± 2.1	*0*		*14*	16.7 ± 2.3
	3401	*14*	24.8 ± 2.9	*14*	20.6 ± 2.0	*14*	19.4 ± 4.3	*14*	15.7 ± 2.6
146	3.7	*14*	24.6 ± 6.3	*12*	19.9 ± 2.3	*14*	17.8 ± 2.5	*14*	15.3 ± 1.9
	8.9	*14*	24.2 ± 4.2	*14*	21.7 ± 2.1	*14*	20.0 ± 3.1	*14*	16.0 ± 3.5
	21.8	*14*	23.8 ± 5.9	*14*	23.4 ± 1.3	*14*	18.4 ± 1.9	*13*	17.1 ± 1.0
	52.9	*14*	24.5 ± 3.7	*14*	22.1 ± 2.8	*14*	17.8 ± 1.5	*14*	17.0 ± 2.0
	128.6	*14*	27.1 ± 6.6	*14*	22.7 ± 4.8	*14*	18.8 ± 3.6	*13*	16.7 ± 1.0
	213.4	*14*	24.7 ± 1.7	*14*	23.6 ± 2.9	*14*	19.9 ± 4.9	*14*	15.3 ± 2.7
	759	*14*	26.3 ± 2.6	*14*	22.6 ± 2.1	*14*	18.1 ± 2.0	*12*	15.8 ± 2.4
	1844	*14*	23.1 ± 2.9	*14*	21.6 ± 3.5	*13*	18.1 ± 2.7	*14*	15.1 ± 2.7
160	2.0	*14*	25.8 ± 3.3	*14*	19.8 ± 1.9	*14*	20.6 ± 2.9	*14*	15.7 ± 1.6
	4.9	*14*	24.4 ± 2.1	*12*	22.8 ± 1.4	*14*	20.9 ± 3.3	*14*	17.0 ± 2.9
	11.8	*14*	24.7 ± 4.4	*14*	20.1 ± 2.3	*14*	18.5 ± 2.3	*14*	15.4 ± 1.2
	28.7	*14*	24.8 ± 3.2	*14*	24.6 ± 2.9	*14*	17.8 ± 3.5	*14*	15.8 ± 1.7
	69.7	*14*	25.8 ± 2.6	*14*	23.5 ± 3.2	*12*	20.7 ± 4.0	*14*	18.9 ± 2.8
	169.4	*14*	27.5 ± 4.0	*13*	23.1 ± 3.2	*14*	19.2 ± 2.4	*14*	17.8 ± 2.7
	411.6	*14*	24.9 ± 4.2	*14*	22.8 ± 1.3	*14*	17.4 ± 3.7	*14*	13.9 ± 3.3
	1000	*13*	24.8 ± 3.7	*13*	25.5 ± 2.5	*14*	15.1 ± 4.6	*14*	14.3 ± 2.2
175	1.1	*14*	25.2 ± 5.4	*14*	22.9 ± 1.9	*14*	18.9 ± 3.7	*14*	16.1 ± 1.6
	2.6	*14*	24.8 ± 4.2	*14*	22.2 ± 1.9	*14*	18.2 ± 3.6	*14*	16.1 ± 1.5
	6.4	*14*	25.1 ± 2.2	*14*	23.1 ± 2.2	*14*	18.6 ± 3.4	*14*	16.8 ± 3.1
	15.6	*14*	25.9 ± 5.2	*14*	23.2 ± 1.7	*14*	18.2 ± 2.8	*14*	16.8 ± 2.4
	37.8	*14*	24.9 ± 3.6	*14*	21.8 ± 2.6	*11*	21.0 ± 2.5	*14*	16.4 ± 2.1
	91.8	*12*	23.1 ± 3.4	*14*	22.1 ± 3.1	*0*		*14*	16.4 ± 2.6
	223.2	*14*	25.2 ± 3.4	*14*	23.8 ± 2.4	*14*	19.4 ± 2.6	*13*	16.7 ± 2.1
	542.3	*14*	26.3 ± 3.9	*14*	20.5 ± 1.5	*14*	16.9 ± 4.3	*14*	11.5 ± 4.0
190	1.0	*14*	26.7 ± 3.9	*14*	22.4 ± 2.2	*14*	19.4 ± 2.4	*14*	16.0 ± 1.6
	1.4	*14*	25.1 ± 2.0	*12*	23.3 ± 1.6	*14*	18.9 ± 2.2	*13*	16.6 ± 2.6
	3.5	*14*	25.7 ± 2.0	*14*	23 ± 2.8	*14*	20.9 ± 3.2	*13*	16.1 ± 2.5
	8.4	*14*	23.7 ± 3.6	*14*	24.3 ± 2.5	*12*	17.8 ± 3.2	*13*	15.8 ± 1.4
	20.5	*14*	25.3 ± 4.9	*14*	21.9 ± 3.5	*12*	9.9 ± 5.3	*4*	6.3 ± 5.4
	49.8	*14*	21.6 ± 4.5	*14*	21.1 ± 1.4	*13*	8.8 ± 2.3	*5*	6.5 ± 1.5
	121	*14*	17.1 ± 6.3	*14*	16.7 ± 2.1	*4*	3.6 ± 1.6	*4*	2.1 ± 2.4
	294	*14*	17.3 ± 5.7	*13*	12.2 ± 2.9	*0*		*0*	

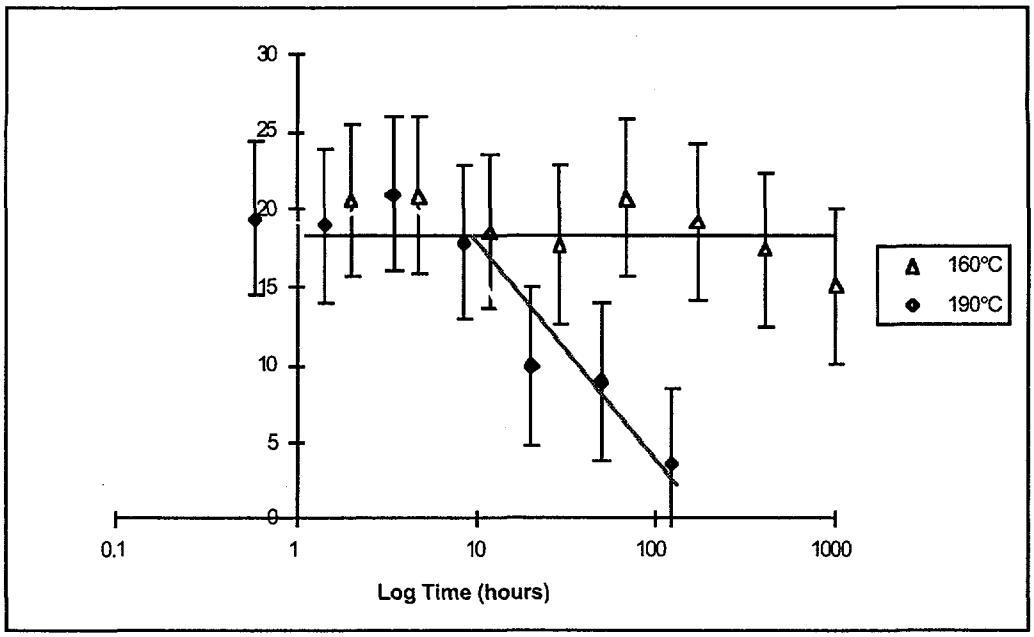

Figure 10-27. A Comparison of the Strengths at the 190°C and the 160°C Temperature Increment of the SAB. These values are the averages obtained from the in-board peel test.

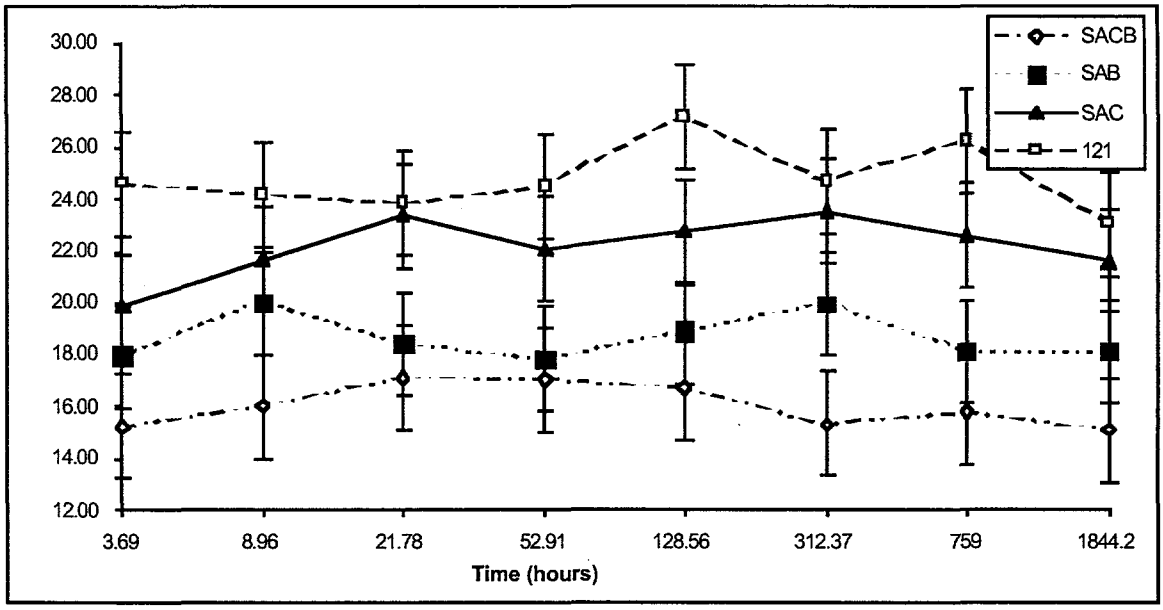

Figure 10-28. Comparison of the Bond Strength of the Four Different Solder Alloys at 146°C. The Bi-containing solders, SAB and SACB, can be seen as having lower strengths than the other two solder alloys, SAC and 121.

When comparing the overall strengths between the 121 and SAC and between the SAB and SACB, there appeared to be a correlation that the solder alloys containing Cu, SAC, and SACB presented a lower strength when compared to their counterpart; i.e., the SAC was weaker in strength to the 121 solder. Similarly, the SACB was weaker in strength compared to the SAB. In viewing the micrographs of the Cu containing solders, SAC, and SACB and the solders that did not contain Cu, 121 and SAB, a comparison was made to see if the intermetallic layer revealed a different microstructure. However, no apparent differences, i.e., difference in voids or coarsening, were noted from these visual inspections. Nonetheless, throughout the solder matrix and along the interfacial region of the intermetallic layer in the Cu containing alloys, dark, somewhat elongated grain formations were visible in these microstructures (see Figure 10-15 and Figure 10-20, respectively). Their size was substantial in giving the structure a nonhomogeneous appearance. It is believed that these formations are Cu_6Sn_5 particles and that they weakened the systems. Analysis was not performed to substantiate this, but documentation shows that Cu_6Sn_5 are hollow hexagonal rods and under testing conditions, the formation of these brittle rods appear to expedite the failure of the joint. [16, 36] Voids which also have the bias to weaken a system were also compared between the SAC and SACB solders and the 121 and SAB solders. There appeared to be voids throughout all the microstructures of the four solders, and it was not apparent if the Cu-containing solders had a larger number of voids. Without further analysis, it was not apparent if the voids found in the Cu-containing solders were larger in size when compared to the voids in the other two solders, not containing Cu. In addition to the voids, solid solution and precise image analysis for size and shape of microstructural constituents must also be considered.

In the same manner, when the strengths of the Bi solders, SAB, and SACB were compared to SAC and 121 solder, the Bi appeared to lower the overall strength. Despite the potential solid solution strengthening provided by the Bi in the Sn, it is believed that these lower strengths are the result of the Bi that precipitated out into the microstructure. The Bi occurred in the microstructure as large white grains resulting in a nonhomogeneous microstructure. Another factor that needs consideration is the Bi also appeared to increase the kinetic growth rate of the intermetallic layer in these Bi-containing solders. A fast growing brittle compound in a solder system would have the tendency to challenge the joint integrity.

To better understand the influence that temperature and time had on the solder alloys' strength, Analysis of Variance (ANOVA)[37] was performed on the strength values that were acquired from the in-board peel test. This was not a straightforward analysis due to missing data points (sometimes as much as twelve values) from a fourteen set replication. An alternative method was chosen to create a simulated data set based on the mean and standard deviation of the existing data.

Random values of probability between zero and 1 were selected and converted into standardized values, or z-scores, that are based on a normal distribution. Using the mean and standard deviation of the present data, these z-scores were used to fabricate strength values. These dummy values could then be used to fill a deficient data set with the same number of data points

as an average data set. This method was performed using EXCEL, a software spreadsheet, for data sets that had less then nine values.

In performing the ANOVA, the average data set size (nine to twelve values) was used instead of a full fourteen value set that may or may not contain simulated data. Data sets that contained fourteen values were reduced to the average data set size by randomly dropping strength values from the set. Using full size data sets would over estimate the true significance of the factors. It was believed that by using the average data set size a reasonable estimate of the significance would be obtained.

A summary of the ANOVA tables calculated for each of the four alloys is shown in Table 10-8 where SS is the sum of the squares, *df* is the degrees of freedom, MS is the mean square equal to SS/*df*, and F calc is the Fisher F statistic that is calculated for each factor. F crit is the value obtained from statistical tables[38] based on the df of the system and the level of desired significance of 95%. If F calc is greater than F crit, then the factor and/or interaction does have a significant effect on the bond strength. The p-value, also shown in Table 10-8, indicates that the probability of achieving the same results due to random variation is very low.

Table 10-8: An ANOVA for Time, Temperature, and Time-Temperature Interactions Influencing Intermetallic Growth of the Four Solder Alloys

	Source	*SS*	*df*	*MS*	*F calc*	*F crit**	*P-value*
Alloy 121							
	TIME	179.5	7	25.64	**1.43**	**2.03**	0.19
	TEMP	350.1	4	87.53	**4.89**	**2.39**	7.32E-04
	TIME*TEMP	1324.5	28	47.30	**2.64**	**1.5**	1.8E-05
	ERROR	7155.2	400	17.89			
	Total	9009.3	439				
SAB	TIME	1375.6	7	196.43	**21.24**	**2.03**	2.44E-24
	TEMP	2727.72	4	681.93	**73.73**	**2.39**	9.1E-47
	TIME*TEMP	4219.37	28	150.69	**16.3**	**1.5**	4.79E-50
	ERROR	3699.58	400	9.24			
	Total	12021.732					
SAC	TIME	612.76	7	87.54	**13.9**	**2.03**	2.3E-16
	TEMP	311.27	4	77.82	**12.4**	**2.39**	1.45E-09
	TIME*TEMP	1642.1	28	58.64	**9.34**	**1.5**	5.2E-30
	ERROR	2760.92	440	6.27			
	Total	5327.06	479				
SACB	TIME	1417.1	7	202.44	**38.35**	**2.03**	6.07E-42
	TEMP	2684.1	4	671.0	**127.14**	**2.39**	4.82E-72
	TIME*TEMP	3079.01	28	109.96	**20.84**	**1.5**	1.08E-63
	ERROR	2322.3	440	5.28			
	Total	9502.42	479				

*This is based on using a 95% confidence interval.

From Table 10-8, all factors except time for the 121 solder were significant for the solder alloys. This is demonstrated by the F calc being greater than the F crit indicating the significant effect that time, temperature, and time-temperature had on the strength. However, there was greater significance in these variables for some alloys than for others. This is illustrated in Figure 10-29, were the F crit values are compared to the F calc values for each of the two factors and their interaction.

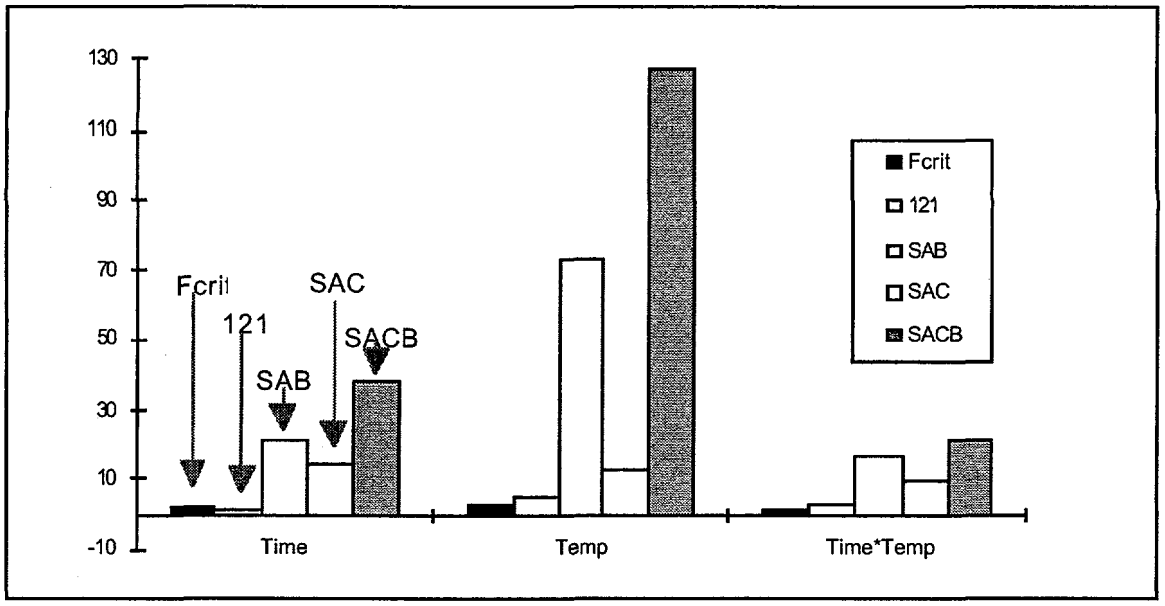

Figure 10-29. Comparison of F crit to F calc Values Obtained in an ANOVA

The value of significance given for all the factors appear to support the hierarchy of strength that was exhibited by the four solder alloys. From the ANOVA, the weakest strength alloy, SACB appeared to have low resistance to the effects of time, temperature, and time-temperature interaction while the strongest alloy, 121, appeared to be only slightly affected by the factors.

In viewing the significance that time and temperature had on 121 solder, it can be seen that time was irrelevant. When compared to the other three alloys, 121 solder appeared to maintain a lesser significance in the temperature and time-temperature interaction. This supports the data obtained on the 121 solder, where its strength sustained a fairly average constant strength of 25 N up until the 190°C temperature.

Time and temperature had more significance on the bond strength with the solder alloys containing Bi (SAB and SACB). This was reflected in the overall lower strengths of these solders. Both solder alloys had a lesser significance in time than temperature, but this significance proportionally increased for the temperature factor. For the time-temperature interaction, the F calc was greater than the F crit, but it was not as significant as the individual factors.

Overall, the significance was similar for all the factors on the SAC. There was only 1.5 units difference of significance between the time and temperature; time being more, and 3 units difference between the temperature and time-temperature interaction. In comparison to the other alloys, the SAC showed lesser significance in time and temperature when compared to SAB and SACB, but when compared to the 121, the factors contributed more to the SAC.

The most significant effects the time and temperature factors had on the bond strength of the solder alloys containing Bi was that they may not be strong candidates in replacing the Pb-Sn

systems. The results indicate they were not resistant to isothermal aging and may not have mechanical strengths required for under-the-hood applications.

10.4.3 Comparison of Intermetallic Layer Growth Versus Strength

A comparison among the four solder alloys was made between the strengths and their corresponding growth rate of intermetallics. It is believed that the continuous Ag_3Sn formation along the interface may have influenced the integrity of the joint because this intermetallic is brittle. For the most part, the anticipation that the solder alloy strength would decrease as the growth rate increased was proven correct at the higher temperature. However, finding a behavioral pattern became impossible in the 134°C , 146°C, and 160°C temperatures for all the alloys. The difference in the thickness of intermetallic appeared to have little or no affect on the strength. This was especially prominent with 121 solder where there seemed too little correlation of how thick the intermetallic was in regards to the strength in all the temperatures.

This trend can easily be seen with the SACB solder alloy, shown in Figure 10-30, where the average intermetallic thickness is compared to the average strength obtained from the in-board peel test performed at the last time cycle of each aging temperature. At the 134°C, 146°C, and 160°C temperatures, the intermetallic growth does not correlate with the strength, i.e., the smaller growth seen should indicate a higher strength. However, the association between the intermetallic thickness and strength becomes significant at 190°C. At this temperature the strength decreased approximately 17 N, as a noticeable increase in the intermetallic layer occurred.

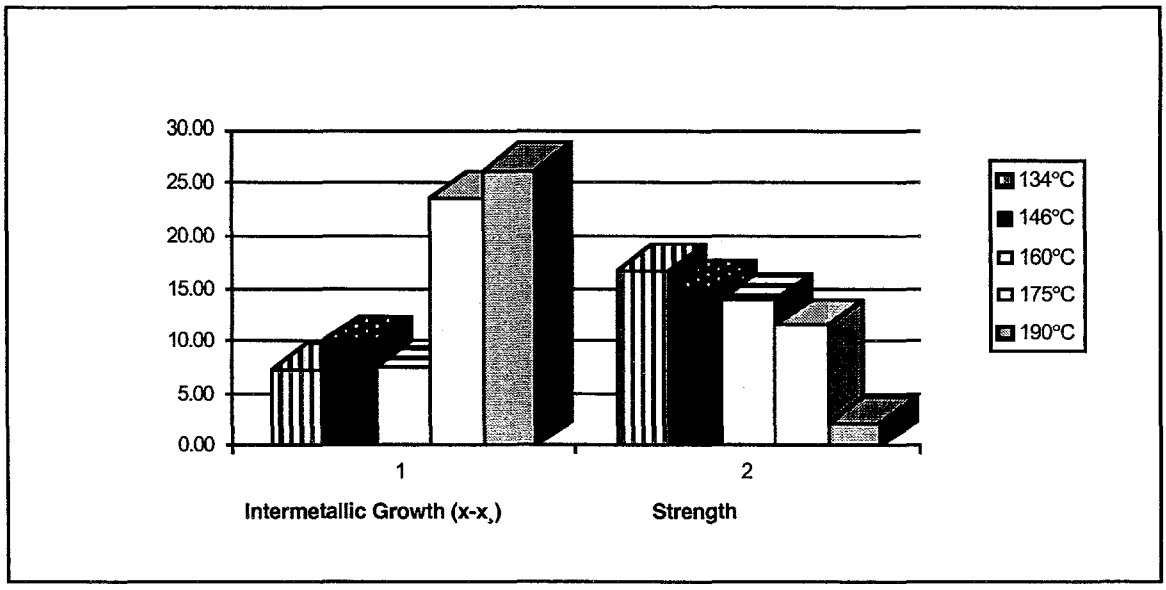

Figure 10-30. Comparison of the Average Intermetallic Growth, in μm, and the Average Strength, in Newton, that the SACB Solder Alloy Exhibited at the Last Time Increment for Isothermal Aging Temperatures.

It was of interest to analyze the 190°C temperature further. In performing the peel test, eight values were obtained from each of the eight time intervals. However, as discussed earlier, only four time intervals were examined for the measurements of the intermetallic growth. To compensate for the lack of thickness data, the coefficients determined from the multivariable regression were used to simulate the nonexistent data, using Equation (10-1). This calculation gave an intermetallic thickness value for each strength value. In plotting the strength versus the intermetallic growth a correlation between the intermetallic thickness and the strength became apparent after the thickness had exceeded 7.3 (ln 1.9) μm. This behavior is illustrated with SAC and SAB in Figure 10-31. Nonetheless, it was observed that at the smaller aging times there appeared to be a wide variation of intermetallic thickness, resulting in little effect on the strength. It appears that a linear correlation can be used to fit the dependence of the peel strength on intermetallic thickness of 7.3 μm or greater.

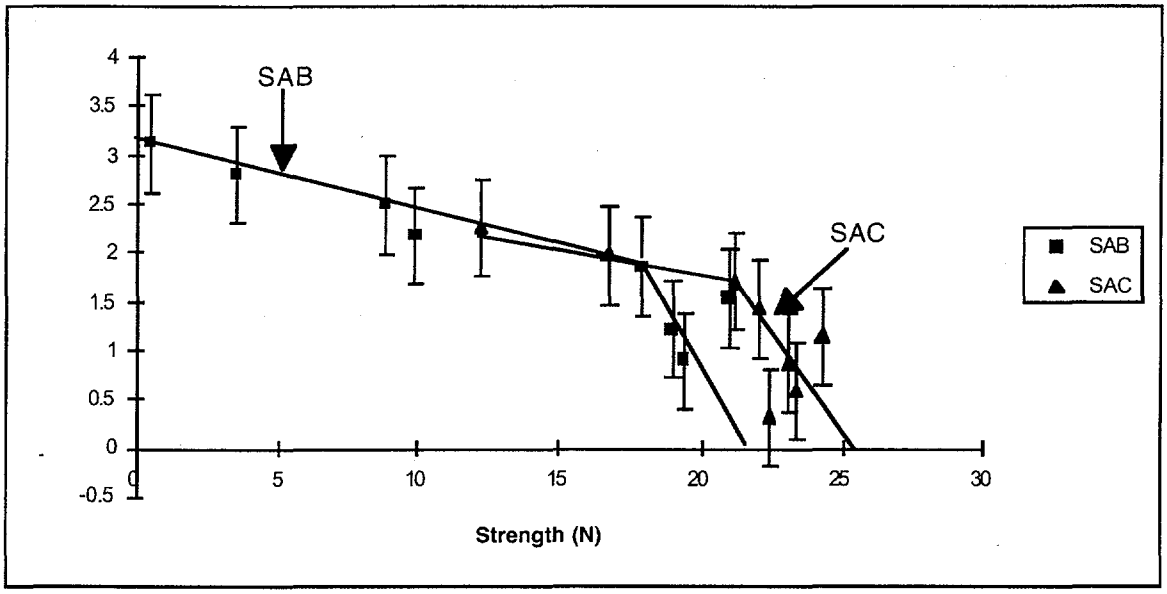

Figure 10-31. Comparison of SAB and SAC and the Affect of Their Intermetallic Growth on Their Strength at 190°C

The total reaction of the metallization that was observed at higher temperatures left behind a brittle intermetallic compound phase, perhaps disabling the adhesion of the wires to the solder/metallization system and causing the wires to become detached. However, there are other considerations to investigate when determining the reasons for the lower strength values that were obtained. One possibility is that there was degradation of the Cu-Sn wire. This degeneration would result in formation of Cu-Sn brittle intermetallics and/or the reduction of the cross-sectional area of the wire causing an increase in the sensitivity of forces that act on the joint. If the difference in the diffusional fluxes are significant between the wire and the solder/metallization system, Kirkendall voids form resulting in a severe reliability issue.[27]

Without further investigation it is not known at this time if perhaps this difference in flux existed between the elements present in the solder/metallization system and the wire.

Even though there appeared to be a correlation between the intermetallic thickness and strength at higher temperatures, the voids that were visible throughout the microstructures of the solders should not be overlooked. These voids that were visible throughout the solder matrix, intermetallic layer, and metallization appeared to coarsen at longer times and higher temperatures. Not only do these voids give the microstructure a nonhomogeneous entity, but they have the potential to initiate failure. A dependence of the solder joint strength may also exist between the size and amounts of voids.

10.5 Summary and Conclusion

For high-temperature applications for under-the-hood components, four Pb-free solders comprised of varying weights of Sn, Ag, Cu, and Bi were chosen based upon previous screening of low contact angles and desirable sessile drop appearances and microstructures. The four solders, Sn-Ag eutectic (Indalloy 121), Sn-Ag-Cu eutectic, Sn-3.33 Ag-4.8 Bi, and Sn-1.6 Cu-4.5 Ag-5.0 Bi, were reflowed using no clean flux onto a double-layer Ag-rich Pt metallization using a Heller reflow oven. The initial appearances, contact angles, and microstructure were analyzed. The samples were subjected to accelerated isothermal aging at five different temperatures. An analysis was performed to determine the mechanical integrity of these four solder alloys by examining the kinetic growth rates and strengths of the intermetallic layers that formed. The results are summarized as follows:

1. The constant thermal processing produced fine and homogeneous initial microstructures in the four solder alloys, even though the melting points were different in each system. For the initial processing and subsequent aging treatments that were used in this experiment, it was found that the increase in intermetallic thickness maintained a subparabolic growth rate ($n < 0.5$). As the aging temperature and time increased in any given cycle, voids and microstructure coarsening were observed in the solder alloys, except for the Indalloy 121.
2. From measurements of the intermetallic thickness as a function of time and temperature of aging, activation energies were obtained over the temperature range of 134 to 190°C. The activation energy for the binary eutectic Sn-Ag was found to be 27.6 kJ/mole. An increase in activation energy was found with the addition of alloying elements. The activation energies for the other solder systems were 52.3 kJ/mole, 71 kJ/mole, and 88.5 kJ/mole for the SAC, SAB, and SACB solders, respectively. The actual mechanism(s) contributing to the activation energies found here are not fully understood, but represent the overall interfacial behavior for the systems studied.
3. In correlation to the activation energies obtained, the increase in intermetallic layer thickness varied from solder to solder with greater intermetallic thickness observed in the systems with higher activation energies. The average joint strengths in the as-soldered condition, presumably of the solder system and substrate, as determined by the DuPont in-board peel

test were about 22, 20, 18, and 16 N for the 121, SAC, SAB, and SACB systems, respectively. With aging, the values remained constant within the limit of experimental error unless an intermetallic layer thickness of 7.3 μm or greater had been reached. This correlation was observed in the solder alloys, SAC, SAB, and SACB, but due to limited data and slower growth of the intermetallic, it was not observed for 121.

4. An ANOVA demonstrated the relative influence that time, temperature, and time-temperature interactions from the aging experiments had on the peel strength. The analysis showed little influence of time, temperature, and time-temperature interactions upon the peel strength of the 121 solder, which was substantiated by the limited growth of the intermetallic over the time and temperature aging regime investigated. The lack of influence by these variables upon the peel strength suggest that this solder system is resilient to these aging conditions and may prove useful as a reliable joint for under-the-hood applications.

5. For Bi containing solders, the following observations were made:
   (a) Higher activation energies were obtained for these two solder alloys, when compared to SAC and 121. Fast growth of the intermetallic layer was observed. Perhaps the Bi acted as a catalyst in expediting the intermetallic growth.
   (b) Total reaction of the metallization occurred during aging at 175°C and 190°C. This resulted in wires becoming detached and/or low strength values obtained from the in-board peel test performed at these temperatures.
   (c) Bi was seen clearly in the microstructure, because it had precipitated out from the solder matrix. This left the microstructure as a nonhomogeneous entity.
   (d) Out of the four solder alloys, SAB and SACB provided the lowest strengths in the in-board peel test at all the temperatures; SACB had the lowest strength value.
   (e) In performing the ANOVA, these solders exhibited significant sensitivity to time, temperature, and time-temperature interactions.
   (f) These solders do not appear to provide joints that would be mechanically reliable after aging.

6. For the solders without Bi, the following observations were made:
   (a) Lower activation energies were obtained for 121 solder and SAC, the 121 solder having the lowest value.
   (b) Total reaction of the metallization only occurred with the SAC solder at 190°C.
   (c) The SAC and 121 solders demonstrated higher in-board peel strength; 121 solder yielded the highest average values in the initial and aged conditions.
   (d) In performing the ANOVA, the time, temperature, and time-temperature interactions had only a slight effect on SAC, while no significant effect was noted with the 121 solder.

7. When comparing solders with Cu to those solders without Cu, it appears that Cu weakens the peel strength of the system. The SAC and the SACB, both containing Cu, exhibited lower strengths when compared to their non-Cu containing counterparts--121 solder and the SAB, respectively. Even though the 121 solder and the SAC gave higher strengths when

compared to the SAB and the SACB, between the 121 solder and the SAC, the SAC was lower. Likewise with the SAB and the SACB, the lower strength solders, in comparison SACB was lower in strength. The influence of Cu upon the strength is not fully understood. However, the microstructure revealed Cu_6Sn_5 intermetallics, which may have been present not only as large grains in the bulk of the solder but possibly also as a thin, continuous layer of intermetallic.

At the onset of this project there was belief that a strong correlation would exist between the increasing intermetallic thickness and the peel strength of the solder systems. However, based on the results this only holds true to an extent. Other methodologies were apparent such as coarsening of the microstructure, large formations of intermetallics existing in the solder matrix, voids that were visible throughout the microstructure, and possible reactions with the wire. The correlation only became evident between the intermetallic thickness and the peel strength when the intermetallic thickness had reached a certain thickness.

Nonetheless, from these results, the SAC and the 121 solder systems appear to show promising potential for use in high temperature, under-the-hood applications. They have low activation energies for intermetallic growth and consequently yielded thinner intermetallic layers. They were resilient to the effects of temperatures up to 175°C; the 121 solder showed little change in peel strength and microstructure even at 190°C. Through all the aging temperatures, the SAC and the 121 solder maintained higher strengths than the Bi-containing solders, even at the elevated temperature of 190°C.

10.6 Future Work

The isothermal aging that was used in this project is only the first step in giving a comparative test between solders. This accelerated isothermal aging should not be used to predict the service life but only as a relative reference in the reliability of solder joints. There are many questions where answers could be supplied if further investigations were performed.

After the regression analysis had been performed, there appeared to be intermetallic growth of some of the solder alloys that did not fit the model well. For example, in the 160°C temperature the SACB initially did not exhibit a subparabolic growth curve. Further studies would include a larger collection of data points that would either lessen the deviation effect seen or discover an aging mechanism that SACB has at this temperature.

The kinetic rates that were obtained on the intermetallic growth for each solder were a general estimate in a given temperature range. Future work could include identifying the individual intermetallics and determining each of their activation energies and their contribution to the overall kinetic rates.

It is believed that the subparabolic growth rate that was apparent with the solder alloys was indicative of more than one intermetallic phase being present. In the Cu containing solders, it would appear to be a straight forward assumption of what the second or third intermetallic constituent would be. However, with the 121 and the SAB solder, an analysis could determine if the $PtSn_7$ compound that was identified in the preliminary study and the metastable compound, Cu_5Bi_2, that has been documented is actually present.

In the samples that exhibited total reaction of the metallization, a repeated accelerated aging test could be employed along with a rigorous compositional analysis to determine the cause of this event. It would be interesting to determine the outcome of this total dissolution had the time been extended at the 190°C temperature to see when cracks between the solder matrix and intermetallic layers began to appear.

In performing the in-board peel test, it was not clear where the actual failure of the joint occurred. Investigating the cross-sectional view of these destroyed specimens may give insight into the failure mechanism, i.e., did the failure occur in the interfacial region between the intermetallic layer and metallization or propagate into the solder matrix or was there actual degradation of the wires themselves causing a faster failure rate? Thus, cross-sectional analysis may also expose possible effects the voids that were present throughout the microstructure of the solder had on the ultimate strength of the joint.

If the failure had occurred in the solder matrix, hardness tests could be performed on the intermetallics that had been identified along the fracture path. For example, would the Cu_6Sn_5 that was believed to be present prove to be more ductile or brittle than the other intermetallics such as Ag_3Sn?

Performing these tests would enhance the knowledge that was obtained from this study. In turn, this information could lead to a more knowledgeable development of future Pb-free solders.

REFERENCES

1] G. Humpston and D. M. Jacobson, *Principles of Soldering and Brazing*, (ASM International, OH, 1993).

2] J.S. Hwang, R.M. Vargas, *Soldering and Surface Mount Technology*, **5** (1990), p. 38.

3] H.D. Soloman, "Low Cycle Fatigue of Sn96 Solder with Reference to Eutectic Solder and a High Pb Solder", *Trans. ASME*, **113** (1991), p. 102.

4] R. L. Davies, "High Strength, Low Temperature Bonding with Silver-Tin Solders", *Welding Journal*, **55**, No. 10 (1976) p. 838.

5] C.A. Drewien, et al., "Progress Report: High Temperature Solder Alloys for Underhood Applications", *Sandia National Laboratory,* Report, #SAND95-0196 (1995).

6] C. Luchinger, et al., "Inside Solder Connections", *Advanced Packaging*, (1994), p. 14.

7] Yujing Wu, et al., "The Formation and Growth of Intermetallics in Composite Solder", *Journal of Electronic Materials*, **22**, No. 7 (1993), p. 769.

8] T.B. Massalski, Binary Alloy Phase Diagrams, 2nd Edition, (AMS International, OH, 1990), Vol. 1 - Vol. 2.

9] P.T. Vianco, P.F. Hlava, A.C. Kilgo, "Intermetallic Compound Layer Formation Between Copper and Hot-Dipped 100In, 50In-50Sn, 100Sn, and 63Sn-37Pb Coatings", *Journal of Electronic Materials*, **23**, No. 7 (1994), p. 583.

10] P.T. Vianco, K.L. Erickson, P.L. Hopkins, "Solid State Intermetallic Compound Growth Between Copper and High Temperature, Tin-Rich Solders - Part I: Experimental Analysis", *Journal of Electronic Materials*, **23**, No. 8 (1994) p. 721.

11] B. Ozmat, *Proc. 40th Electr. Comp. & Techn. Conf.*, (Las Vegas, NV, 1990), pp. 959-972.

12] D.R. Frear, F.G. Yost, "Reliability of Solder Joints", *MRS Bulletin*, **18**, No. 12 (1993), p. 49.

13] W. Yang, R.W. Messler, "Microstructure Evolution of Eutectic Sn-Ag Solder Joints", *Journal of Electronic Materials*, **23**, No. 8 (1994), p. 765.

14] M. McCormack, S. Jin, "New, Lead-Free Solders", *Journal of Electronic Materials*, **23**, No. 7 (1994), p. 635.

15] G.B. Greeman, et al., "Intermetallic Embrittlement of Thin Unsupported Tin/Copper Specimens", *Journal of Electronic Materials*, **23**, No. 9 (1994), p. 919.

16] D.R. Frear, D. Grivas, J.W. Morris, "Thermal Fatigue in Solder Joints", *Journal of Metals*, **40**, No. 6 (1988), p. 18.

17] J.L. Goldstein, J.W. Morris, "Microstructural Development of Eutectic Bi-Sn and Eutectic In-Sn During High Temperature Deformation", *Journal of Electronic Materials*, **23**, No. 5 (1994), p. 477.

18] S.P.S. Sangha, G. Humpston, "Shear Strength of Diffusion Soldered Joints", *GEC Journal of Research*, **10**, No. 3 (1993), p. 174.

19] D. Tribula, et al., "Microstructural Observations of Thermomechanically Deformed Solder Joints", *Welding Journal*, **68**, No. 10 (1989), p. 404-s.

20] L. Chadwick, "Solder Alloy Data: Mechanical Properties of Solders and Soldered Joints", *International Tin Research Institute*, #ITRI 656 (undated).

21] D. Frear, et al., "Fatigue and Thermal Fatigue Testing of Pb-Sn Solder Joints", *Center for Advanced Materials, Berkeley, CA* (1983), p. 269.

22] J.J. Ramon, S.F. Dirnfeld, "A Practical Way to Measure the Strength of Small Soldered Joints", *Welding Journal*, **67**, No. 10 (1988), p. 19.

23] C.H. Raeder, et al., "The Effect of Aging on Microstructure, Room Temperature Deformation, and Fracture of Sn-Bi/Cu Solder Joints", *Journal of Electronic Materials*, **23,** No. 7 (1994), p. 611.

24] K. Shimizu, et al., "Solder Joint Reliability of Indium-Alloy Interconnection", *Journal of Electronic Materials*, **24**, No. 1 (1995), p. 39.

25] "Method of Test for Wire Peel Adhesion of Soldered Thick Film Conductors to Ceramic Substrates", *DuPont Electronic Materials* Report #SS309297 (1992).

26] K.J. Williams, "Adhesion Test Methods for Solderable Thick Film Conductors", *Brazing & Soldering*, No. 15 (1988), p. 10.

27] D.R. Frear, W.B. Jones, K.R. Kinsman, Solder Mechanics: A State of the Art Assessment, (TMS, Warrendal, PA, 1991).

28] T.L. Crandell, J.E. Sergent, "Some Aspects of the Measurement of the Adhesion of Thick Film Conductor Inks to Alumina Substrates", *Marshall Space Flight Center*, Report #NAS8-31172 (undated).

29] R.L. Scheaffer, J.T. McClave, Probability and Statistics for Engineers, (Duxbury Press, Belmont, CA, 1995).

30] Microsoft Excel for Windows 95, Software Package System Version 7.0, Microsoft Corp. (1995).

31] Z. Mei, J.W. Morris, Jr., "Characterization of Eutectic Sn-Bi Solder Joints", *Journal of Electronic Materials*, **21**, No. 6 (1992), p. 599.

32] F.G. Yost, F.M. Hosking, D.R. Frear, The Mechanics of Solder Alloy Wetting and Spreading, (Van Nostrand Reinhold, NY, 1993).

33] P.W. Atkins, Physical Chemistry, 4th Edition, (W.H. Freeman and Company, NY, 1990).

34] W.J. Tomlinson, N.J. Bryan, "The Strength of Brass/Sn-Pb-Sb Solder Joints Containing 0 to 10% Sb", *Journal of Materials Science*, **21** (1986), pp. 103-109.

35] D.R. Frear, P.T. Vianco," Intermetallic Growth and Mechanical Behavior of Low and High Melting Temperature Solder Alloys", *Metallurgical and Materials Transactions*, **25A** (1994), p. 1509.

36] D. Frear, D. Grivas, J.W. Morris, Jr., "The Effect of Cu_6Sn_5 Whisker Precipitates in Bulk 60Sn-40Pb Solder", *Journal of Electronic Materials*, **16**, No. 3 (1987), p. 181.

37] T.P. Ryan, Statistical Methods For Quality Improvement, (John Wiley & Sons, NY, 1989).

38] D.C. Montgomery, G.C. Runger, Applied Statistics and Probability For Engineers, (John Wiley & Sons, NY, 1994).

11. System Level Stress and Thermal Model

Vicki L. Porter

Throughout the lifetime of an automotive electronic component, there are many instances in which the electronic module can be subjected to extremes in temperature during operation.

This chapter describes analyses performed to assess the critical thermal stresses in the hybrid microcircuit during the operational life of a vehicle. During the manufacturing process, the part is heated to allow assembly of the components and then cooled back to room temperature. Because the part is assembled with the aluminum plate at 100°C, this temperature is taken as the stress-free initial condition. While it is in operation in a vehicle, the module may experience cold temperatures (-65°C) in a severe winter or hot temperatures (150°C) when the engine is running during a hot summer. Because both of these conditions occur in a slow, steady-state manner, the temperature at any time can be assumed to be uniform over the entire part. However, the various components of the hybrid module expand and contract at different rates with increasing or decreasing temperature. Therefore, thermal stresses are induced in the part with any change in temperature over time. Thermal stresses are thus caused by mismatches in the coefficients of thermal expansion even in a part with a uniform temperature field. The maximum steady-state thermal stresses will occur at the most extreme temperature change from the stress-free state at 100°C. Therefore, the critical temperature to be analyzed is -65°C.

The scenario chosen to represent the worst-case transient event for the part during operation is the scenario of a hot engine that undergoes a thermal shock due to a sudden dousing with cold water, such as may occur in a car wash. In this case, the temperature is not uniform in the part. This type of transient event required thermal finite element analyses to compute the temperature at any point in the part at any given time. This was followed by structural finite element analysis to determine the stresses. In such transient events, thermal stresses resulted from both the mismatch in coefficients of thermal expansion and from the temperature gradient throughout the part.

In both the steady-state and the transient events, the goal is to prevent failure in any of the components of the hybrid microcircuit. Potential modes of structural failure considered here include cracking of the glass seal between the microcircuit and its ceramic cover, cracking of the die or the substrate on which it is mounted, and yielding of the aluminum backing plate.

11.1 Steady-State Analysis

A 3-D finite element analysis was performed to evaluate the thermal stresses resulting from a steady-state decrease in operational temperature to -65°C. The part was assumed to be stress-free at 100°C because this would be approximately the temperature at which the aluminum plate

is attached to the microcircuit during the manufacturing process. The lower bound was provided by DELPHI as the coldest temperature at which the part is required to survive.

11.1.1 Model Description

The Sandia-developed finite element code JAC3D[2] was used for the thermal stress analysis. An initial, uniform, stress-free temperature of 100°C was assumed. Subsequent uniform temperatures of 50°C, 10°C, 30°C, and -65°C were used as input. The analysis was performed in several steps rather than a single step because the epoxy material used for the die attach has a nonlinear coefficient of thermal expansion.

Electronic components were mounted on a substrate that was 96% pure alumina. The components were then sealed by attaching an alumina frame to the substrate using a glass layer. The hybrid microcircuit, glass, and frame were heated to above the glass transition temperature (305°C). Then the entire assembly was cooled to room temperature to set the glass. These analyses were performed for the substrate-frame assembly process only and indicated acceptable residual stresses in the glass seal at room temperature.

In the next step of the assembly, the substrate-frame assembly was attached to an aluminum base plate using a Loctite adhesive layer. To perform this process, the Loctite was applied to the bottom side of the substrate, and the aluminum plate is put in place. This substrate-frame-plate assembly was heated to 100°C, held for approximately 25 minutes, and then cooled back to room temperature. In the final step of the assembly, the four corners of the aluminum base plate were bolted to an aluminum motor housing. It is this entire assembly that must be able to withstand temperature extremes of -65°C to 150°C during the operational lifetime.

The 3-D finite element model for the hybrid module is shown in Figure 11-1. To keep the size of the analysis reasonable, quarter symmetry was assumed and only one-fourth of the assembly was modeled. The aluminum base plate was included but not the motor housing. None of the electronic components were included in the steady-state finite element model. Symmetry boundary conditions of no displacement were imposed on the edges of the mesh at $x = 0.0$ and $y = 0.0$. The other two edges and the top of the cover and the bottom of the aluminum plate were free surfaces. An enlarged view in Figure 11-2 shows the mesh used for each of the component parts. Material properties used in the analyses for all the components of the assembled part are shown in Table 11-1.

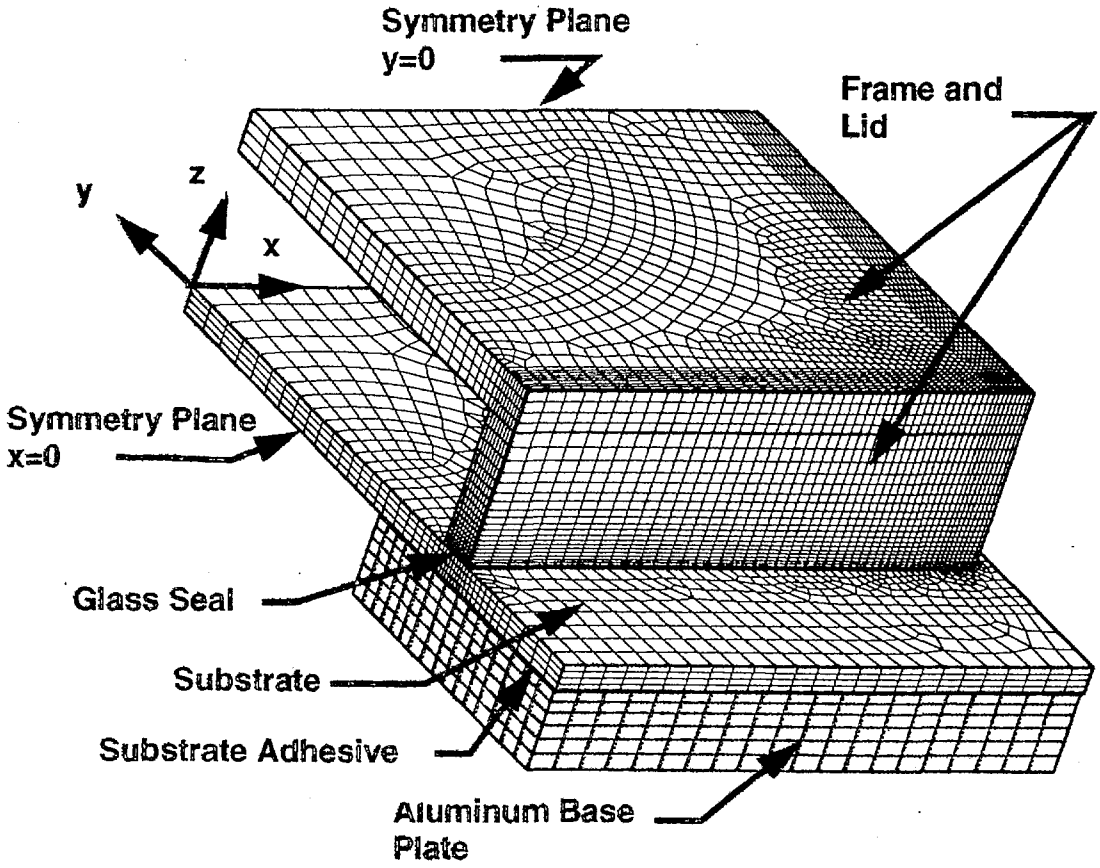

Figure 11-1. Finite Element Model of Hybrid Microcircuit with Frame and Aluminum Base Plate

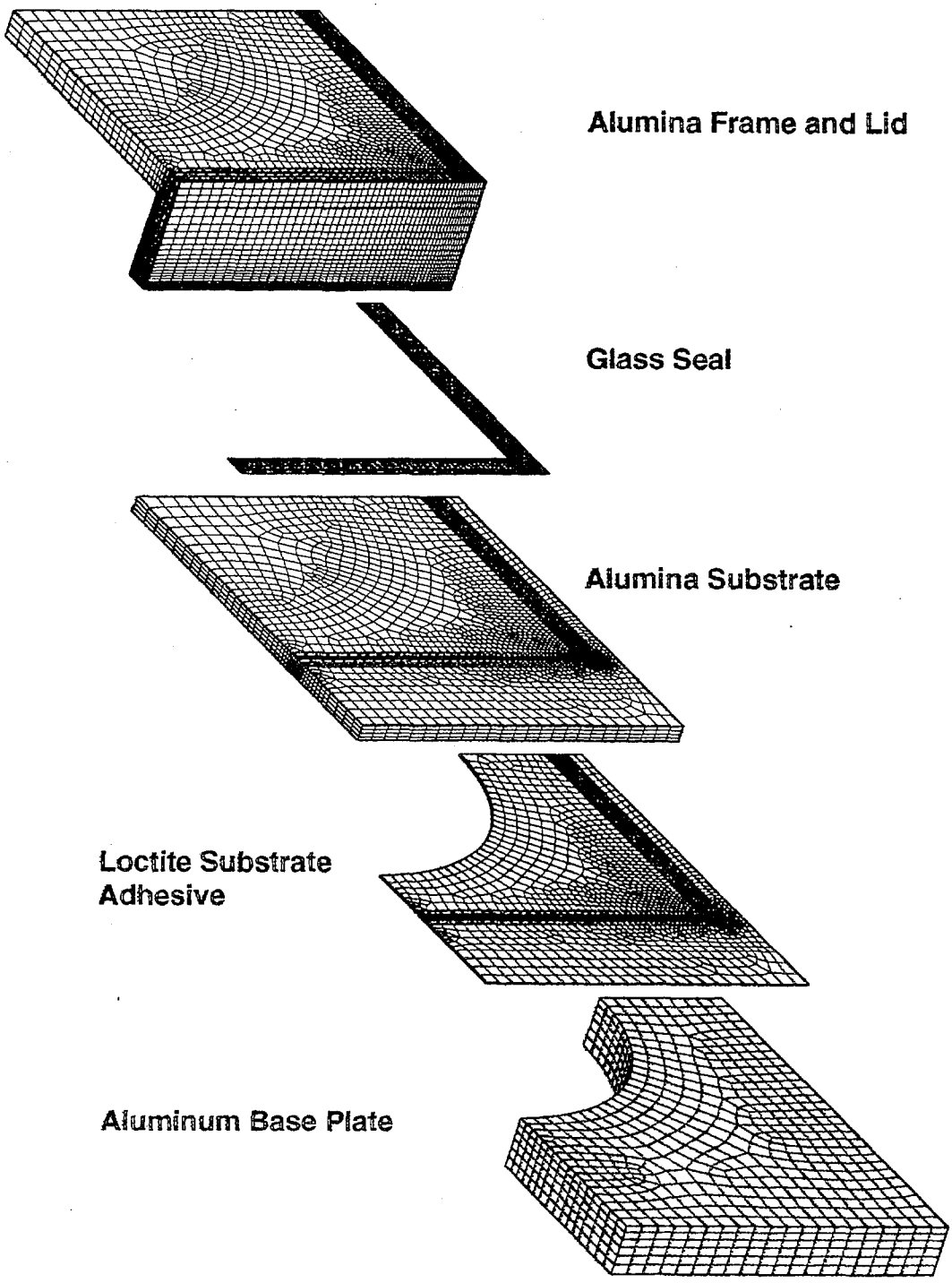

Figure 11-2. Exploded View of Finite Element Mesh

Table 11-1: Structural Material Properties

Material	Use	Young's Modulus (MPa)	Poissons Ration	Coefficient of Thermal Expansion (10^{-6}/K)	Specific Heat (J/kg/K)	Density (kg)/m^3)	Thermal Conductivity (W/m/K)
Alumina (96%)	Substrate, Frame	300,000	0.21	6.70	908	3400	14.5
Epoxy	Die Attach	7580 @ -70C 6030 @ 20C 4190 @ 132C 500 @ 150C	0.34	45	1000	5100	0.80
Silicon	Die	200,000	0.32	3.0	712	1000	2.1
Glass	Ring Seal	53,500	0.27	6.75	600	2330	148
Loctite	Substrate Adhesive	3.5	0.49	290	1000	1000	0.30
Aluminum	Base Plate	68,950	0.30	23.2	875	2780	177

11.1.2 Results

Results for the steady-state finite element analysis are shown in Figures 11-3 through 11-5. Figure 11-3 shows the distribution of maximum principal stress in the alumina frame and lid. Figure 11-4 shows the same stress in the alumina substrate. The results indicate that the maximum tensile principal stress is 4.8 ksi in the alumina frame (including the lid) and 4.1 ksi in the substrate. Both of these are acceptable stress levels, and neither should cause cracking.

In contrast, the maximum tensile stress in the glass seal shown in Figure 11-5 is 7.6 ksi, which is well above a desirable limit of less than 2 ksi. This level of stress indicates that the glass may crack. However, note that the area of high stress in the glass is concentrated at the corner and along the outside edges. Therefore, the damage may be limited to the surface and may not pass entirely through the glass thickness to destroy the seal.

The analysis described here evaluated the glass during assembly of the hybrid microcircuit, frame, and the aluminum base plate. The analysis also considered cooling to an extreme temperature of -65°C. The stresses in the assembled part under operating conditions were much worse than the residual stresses in the part before it had been attached to the aluminum plate. These results suggest that the critical test for structural integrity is temperature cycling of the entire assembled part, not only the microcircuit and cover.

11.2 Analysis of the Car Wash Event

The worst-case transient event is the car wash scenario in which a hot engine is suddenly doused with cold water. During this type of event, extreme temperature gradients occur in the part. These temperature gradients were computed using the heat transfer finite element code JACQ3D.[1] The results for the temperature distribution history were then used as input to compute the thermal stresses using the structural finite element code JAC3D.[2]

11.2.1 Model Description

Figures 11-6 and 11-7 show the finite element model used for both the heat transfer and the stress analyses for the transient event. Due to the asymmetric nature of the boundary conditions, the full microcircuit board was modeled. Figure 11-6 shows the overall assembly with the frame, substrate, and aluminum base plate. Figure 11-7 shows an enlarged view of the model in which the glass seal, the substrate adhesive, and the die and die attach can be seen.

The bottom of the aluminum base plate attaches to an aluminum motor housing. However, to accomplish an analysis at reasonable cost, this housing was not explicitly included in the analysis. Because the temperature transient through the aluminum housing was not modeled, it must be assumed as a boundary condition for the heat transfer analysis. In the analysis, a

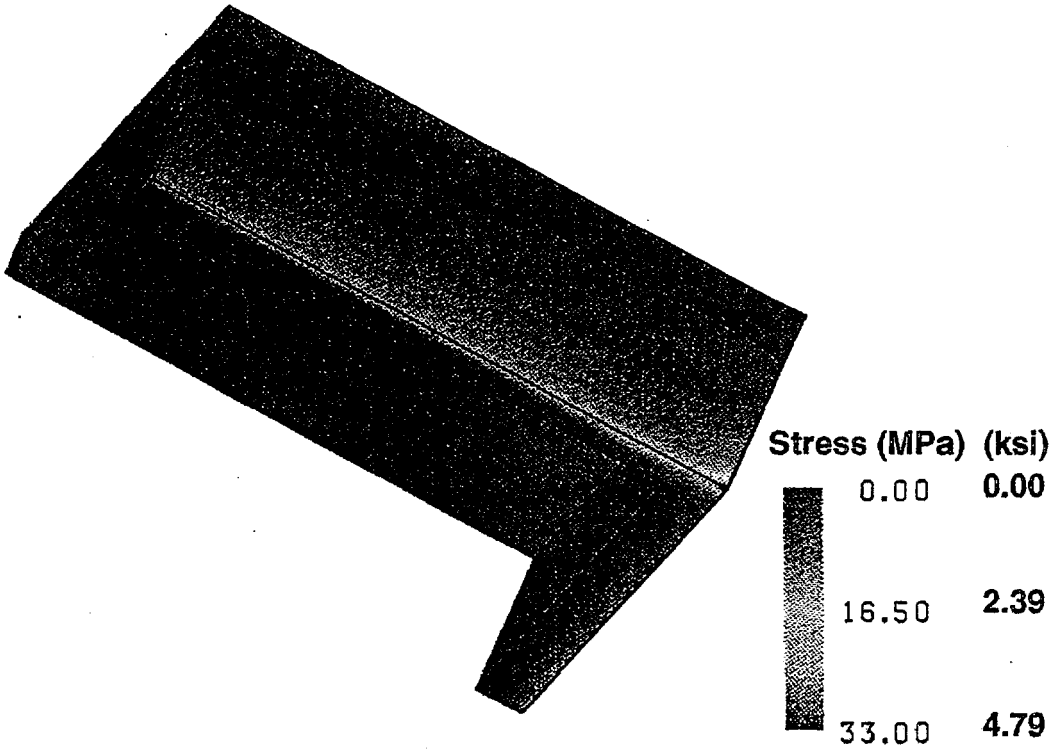

Figure 11-3. Maximum Principal Stress in the Alumina Frame

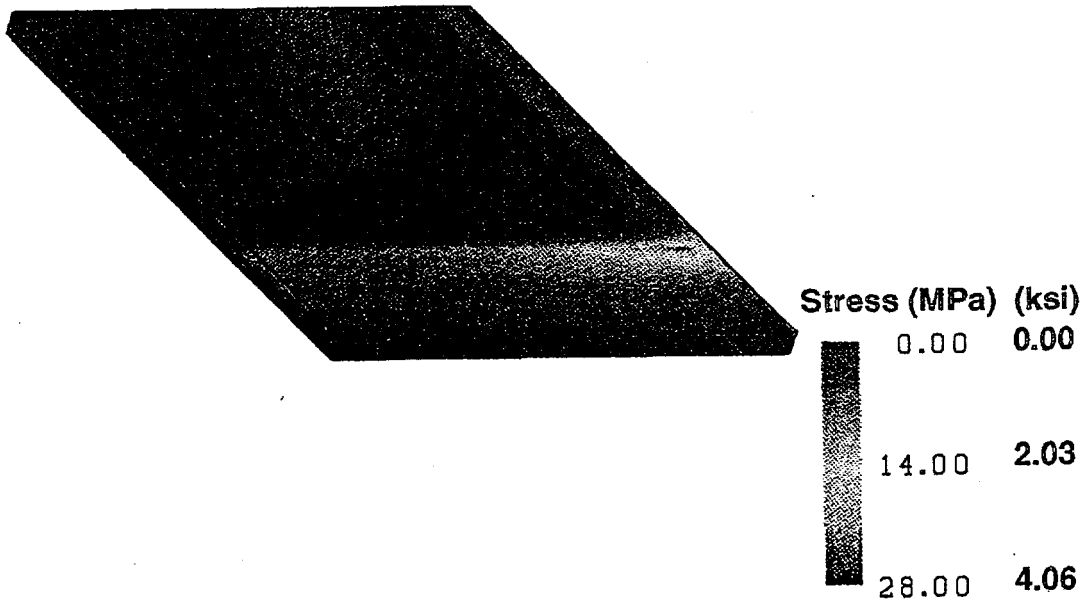

Figure 11-4. Maximum Principal Stress in the Alumina Substrate

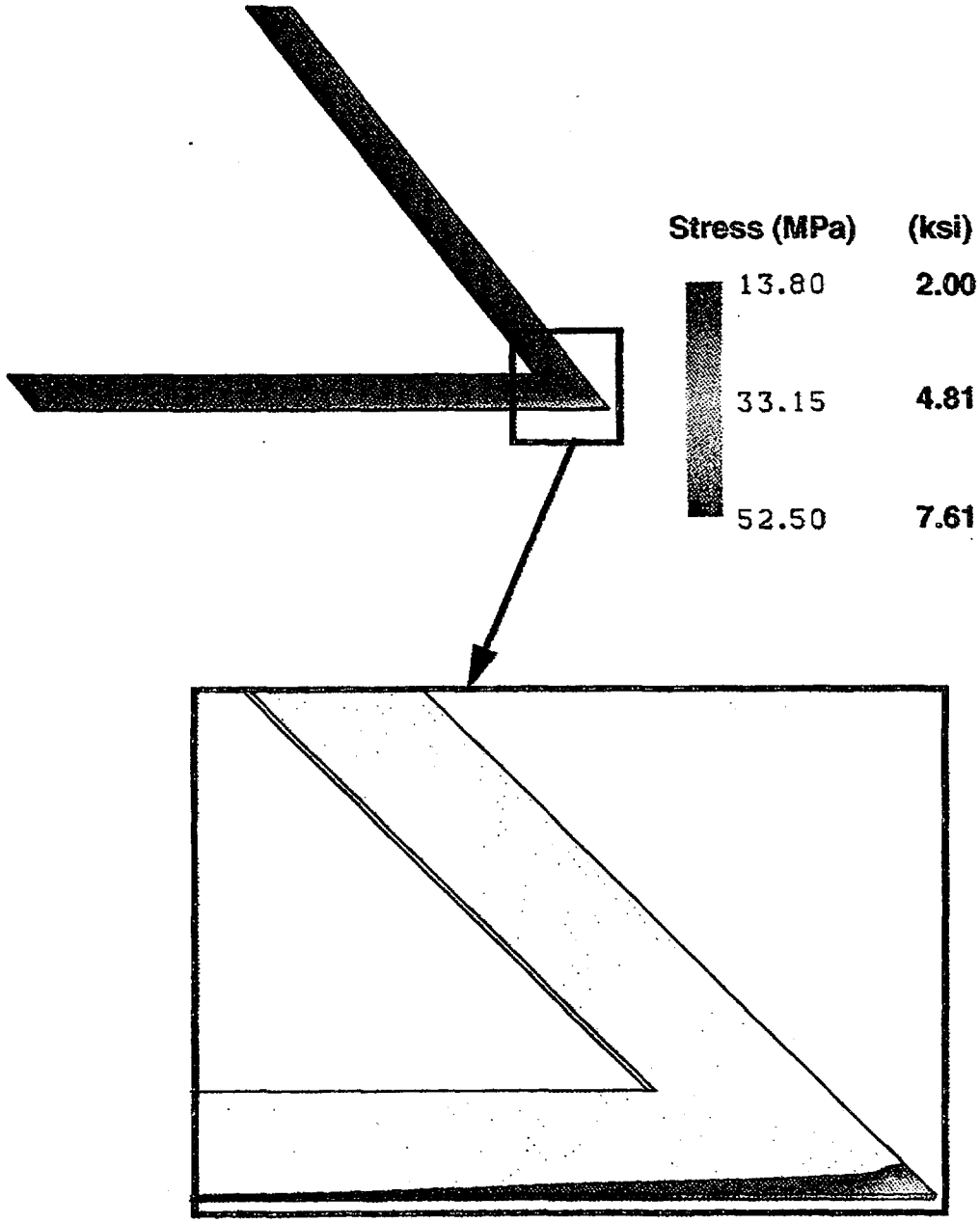

Figure 11-5. Maximum Principal Stress Distribution in the Glass Seal

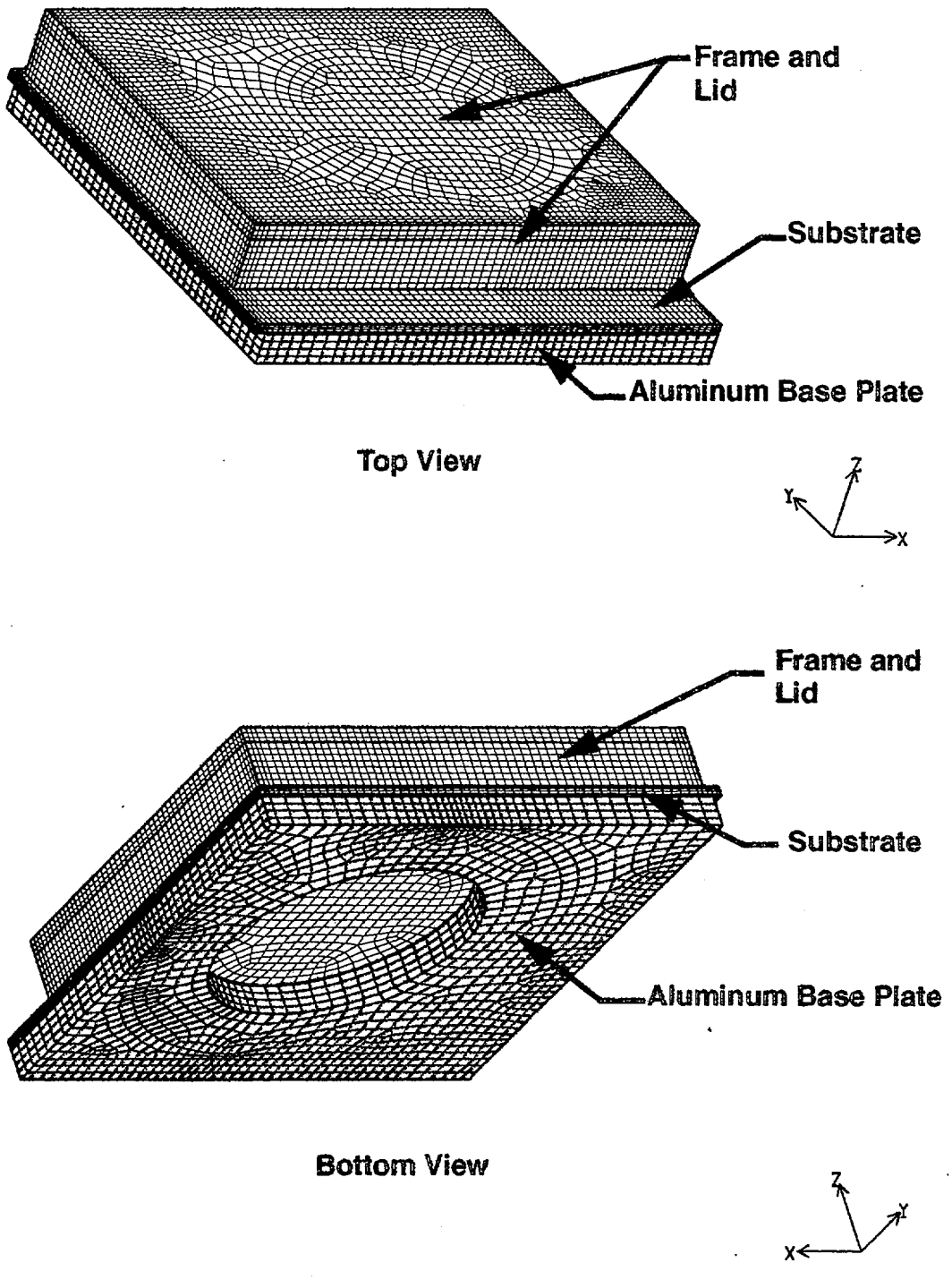

Figure 11-6. Finite Element Model for the Transient Analyses

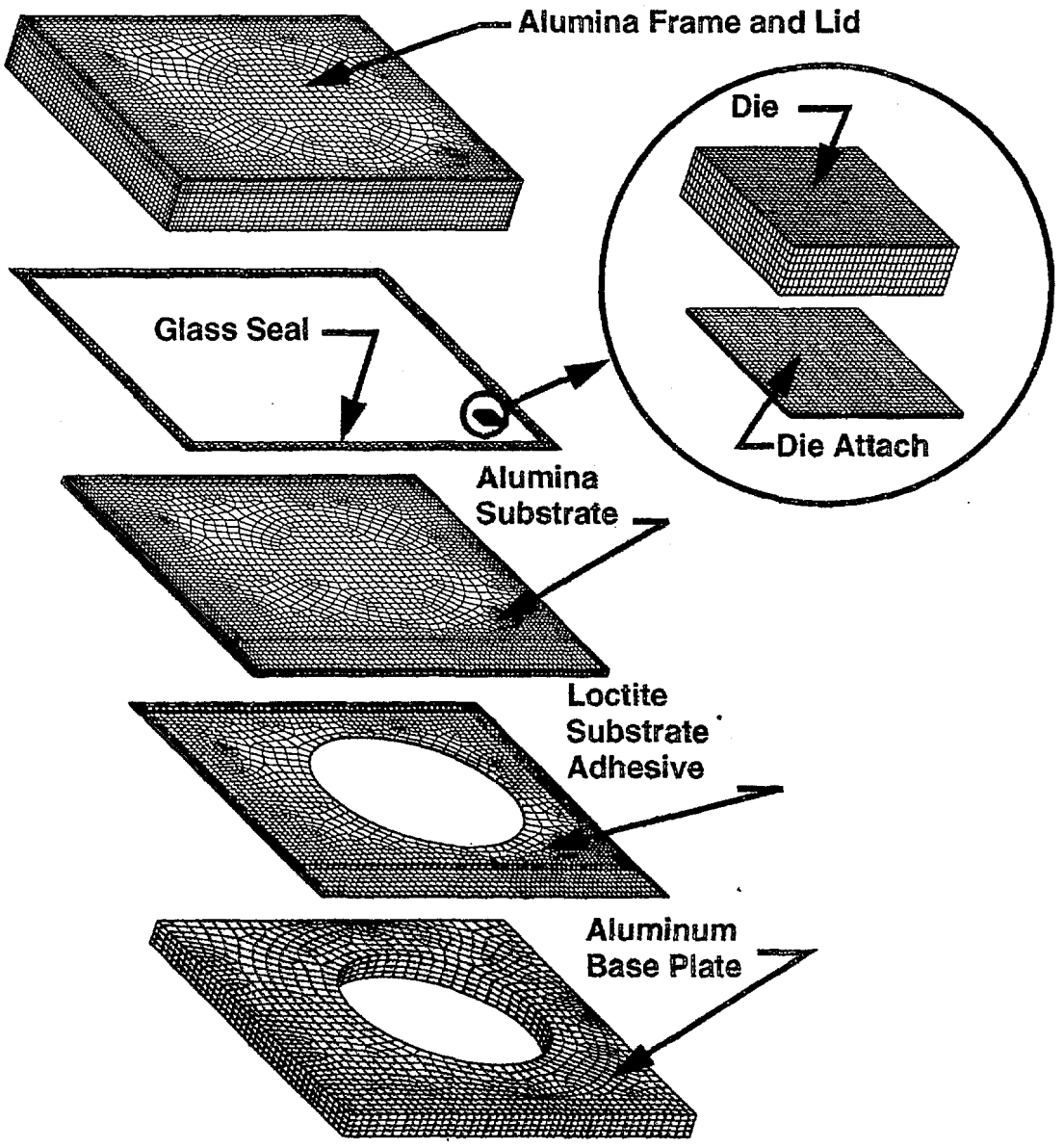

Figure 11-7. Exploded View of Model Used for Transient Analyses

temperature boundary condition (heat sink) was placed directly on the area of the bottom of the backing plate that was in contact with the motor housing. In this area, the temperature was conservatively assumed to drop from the initial temperature of 150°C to 10°C in one-half sec. Figure 11-8 shows an enlarged view of the modeled part at t = 0.50 sec. The blue area shown on the bottom of the aluminum plate is roughly the area over which the temperature boundary condition has been applied. This area was that which is in direct contact with the aluminum housing. Boundary conditions must also be assumed for the stress analysis. In this case, all edges of the part were assumed to be free to move.

11.2.2 Temperature Results

Figures 11-8, 11-9, and 11-10 show the temperature distribution at three different times during the car wash event. Figure 11-8 shows the temperature distribution in the part at t = 0.50 sec. At this time, the temperature boundary condition on the bottom of the aluminum plate reached 10°C by imposing the assumed boundary condition. This is represented by the blue color and is the area that would be in contact with an aluminum housing. The area of the plate not in direct contact with the aluminum housing was near 150°C. The same qualitative temperature pattern can be seen on the bottom of the Loctite adhesive layer, although the minimum temperature in this layer only dropped to 50°C. Only a slight variation from 150°C can be seen on the bottom of the alumina substrate near the outer edges where the temperature dropped to 130°C.

Temperature distributions at t = 1.0 sec are shown in Figure 11-9. By this time, the temperature distribution in the aluminum plate was more uniform. The area that was then at the minimum 10°C was substantially larger. The maximum temperature dropped to 108°C. Likewise, the minimum temperature in the Loctite adhesive dropped to 28°C, and the maximum dropped to 138°C. In addition, more temperature variation was now visible in the alumina substrate, although the frame and lid were still fairly uniform at 150°C. The maximum temperature in the substrate was also still 150°C, but the minimum dropped to 97°C.

The temperature distribution at the end of 60 sec is shown in Figure 11-10. This represents a relatively long time compared with the time for temperature transients in the part. Therefore, the temperature was a nearly uniform 10°C in all components. The only part displaying any variation was the alumina frame and lid because this part was the farthest away from the heat sink. Even here, however, the maximum temperature was only 69°C and occurred in the center of the lid.

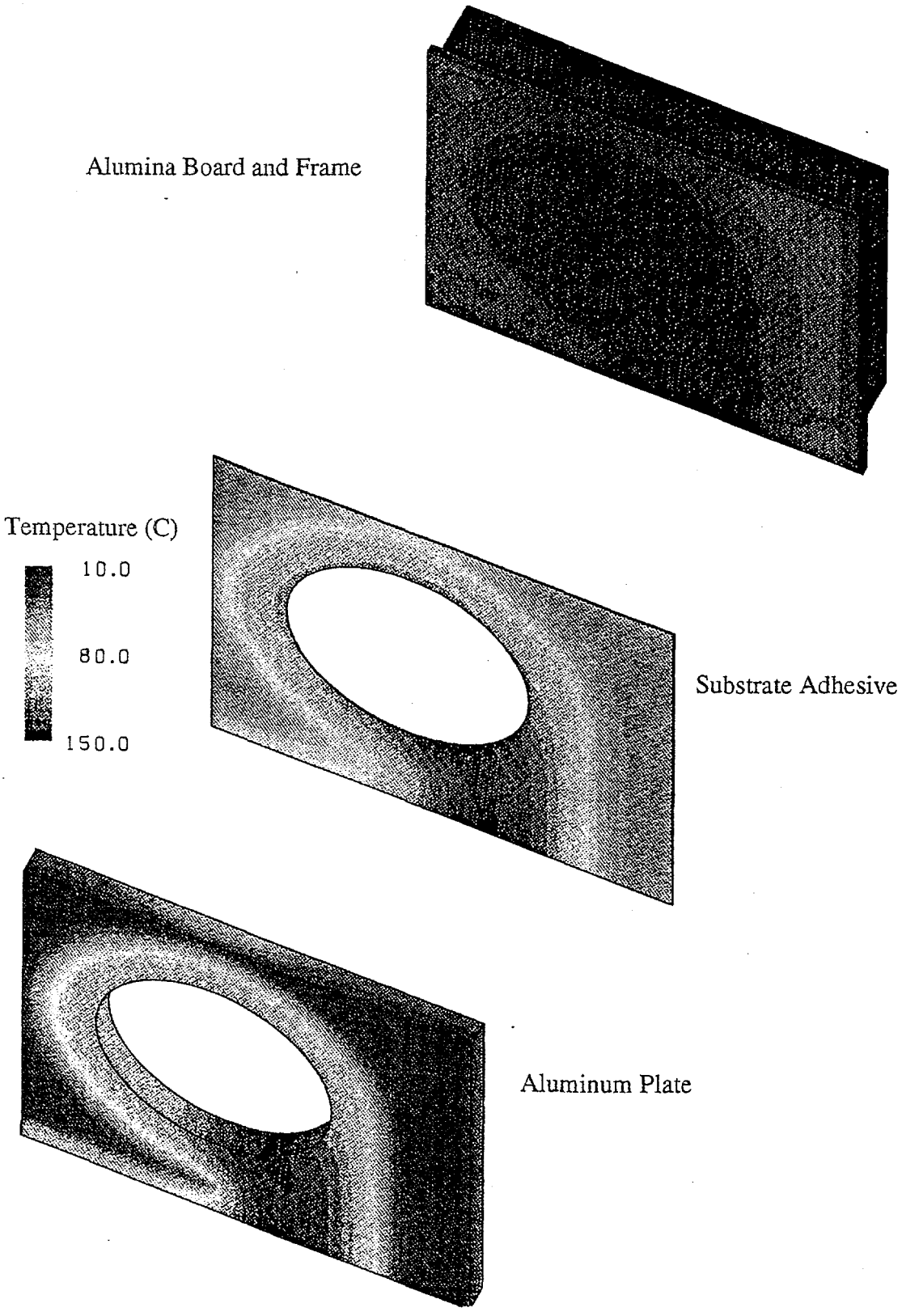

Figure 11-8. Temperature Distribution in Part at 0.50 Seconds

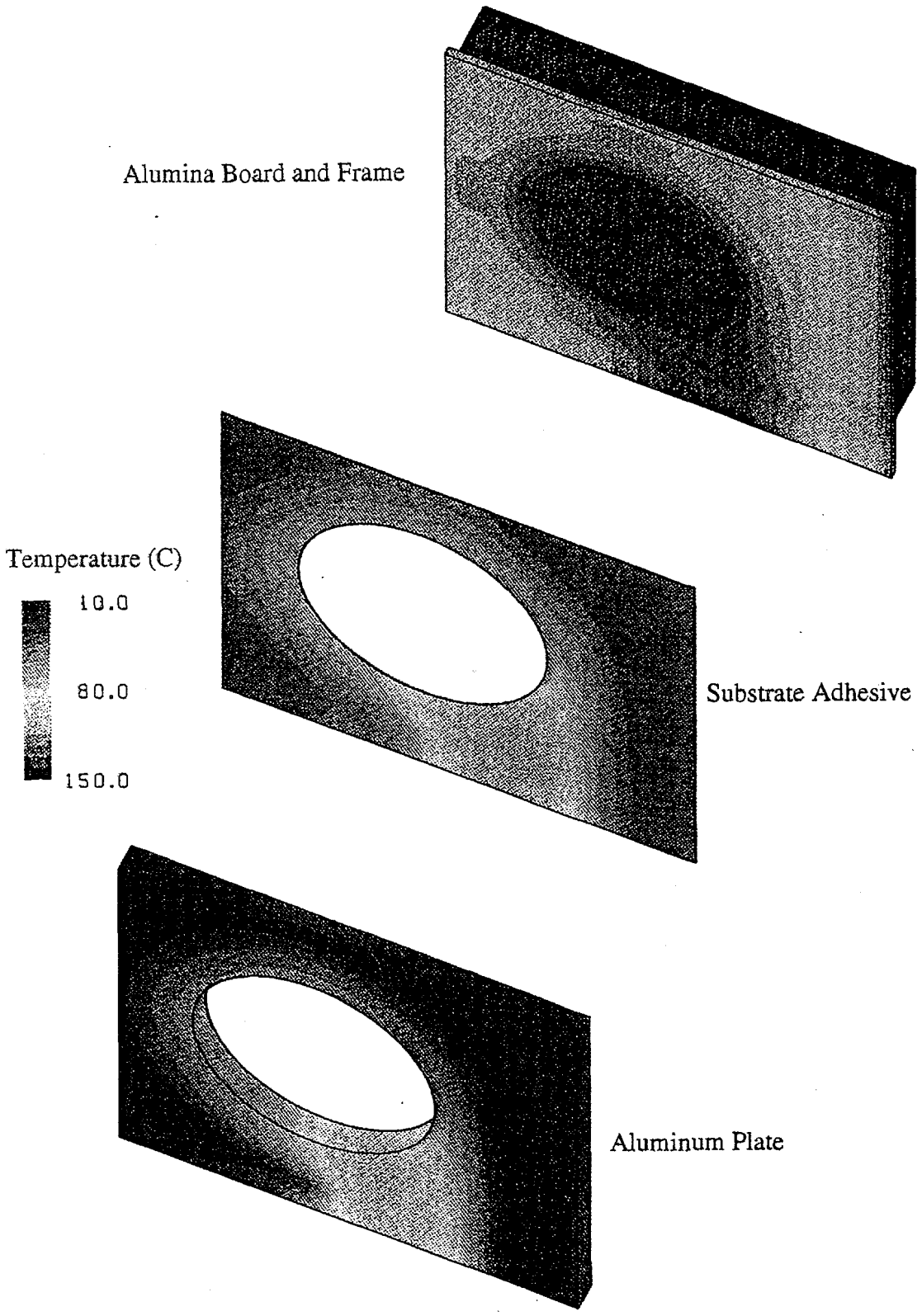

Figure 11-9. Temperature Distribution at 1.0 Seconds

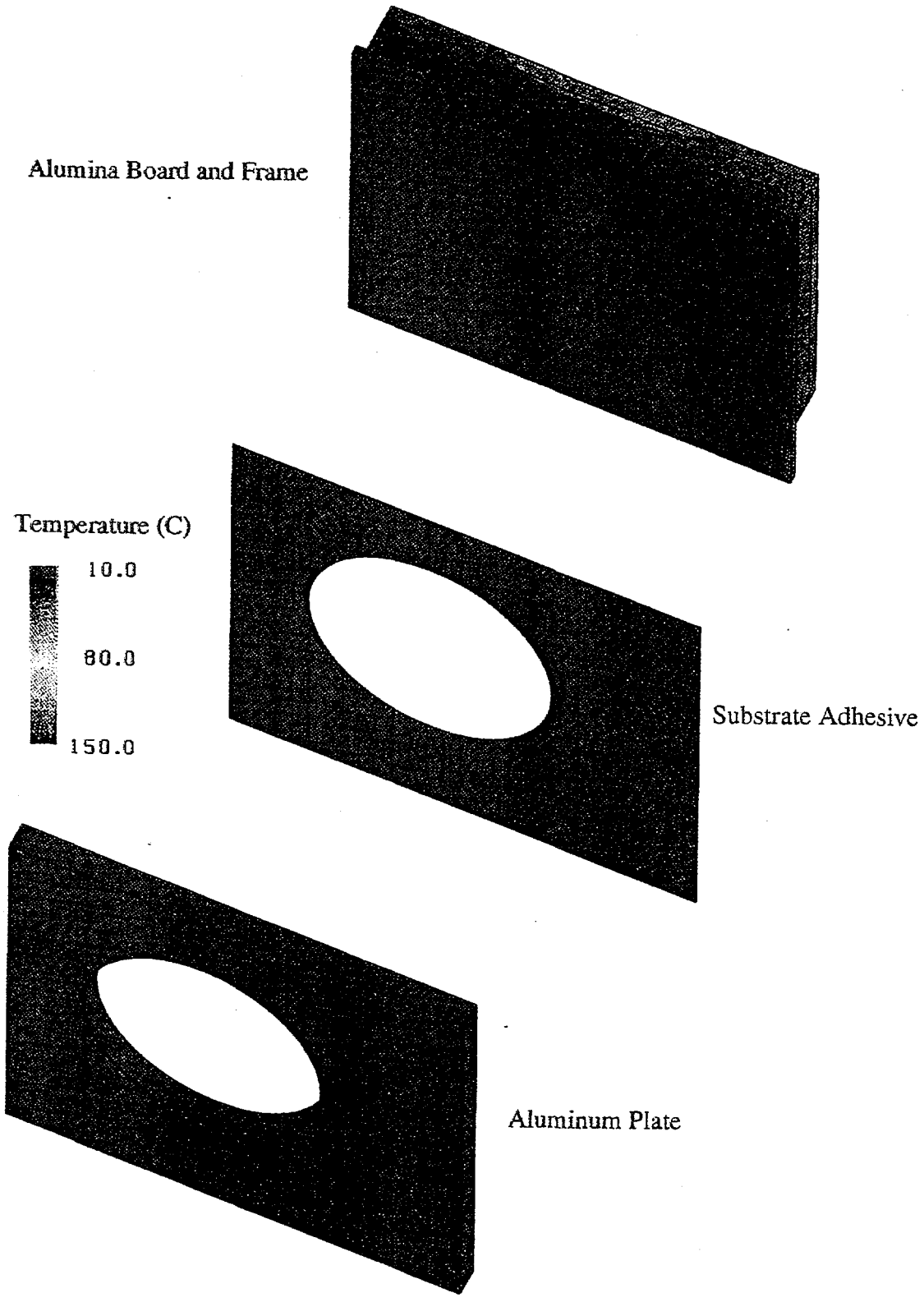

Figure 11-10. Temperature Distribution at 60 Seconds

Finally, the temperature distribution in the die and die attach mounted on top of the alumina substrate is shown in Figure 11-11 for the same times. The thin layer on the bottom is the die attach. The rectangular box represents the die. These parts are small compared to the scale of the microcircuit (Figure 11-7). Thus, the temperature distribution at any point in time was relatively uniform, but some variation can still be seen. At t = 0.5 sec, the effect of the heat sink on the bottom of the aluminum plate was to reduce the maximum temperature to 144°C, while the minimum only dropped to 141°C. At 1.0 sec, the maximum dropped to 120°C and the minimum to only 115°C. Finally at 60 sec, the maximum temperature dropped to 12°C and the minimum temperature dropped to 11.5°C representing a nearly uniform temperature field.

11.2.3 Stress Results

With the temperature history results discussed above as input, the thermal stresses were computed using the structural analysis finite element code JAC3D. As in the steady-state analysis, unacceptably high values of tensile stress indicate the potential for cracking. However, in this transient event, thermal stresses can be induced by both the mismatch in the coefficients of thermal expansion and by the temperature gradients in the part.

Figure 11-12 shows the time history of maximum principal stresses in the alumina substrate, glass seal, and alumina frame and lid. The maximum tensile stress in the alumina substrate occurred slightly over 14 ksi and occurred at t = 4.0 sec. The maximum stress in the alumina frame and lid was 13.5 ksi, but it did not occur until t = 20 sec. These values were higher than the desirable design range of 6 to 8 ksi and may have induced cracking. However, in both cases, these maximum values were transient quantities. The transient nature of these stresses made them less likely to cause cracking than steady-state stresses of the same values. By the end of 60 sec, the stress in the substrate was only slightly more than 1.0 ksi, while the stress in the frame had dropped to 7 ksi and was still declining. Both of these stress levels met the design criterion.

The maximum tensile stress in the glass seal was 9 ksi and occurred early at t = 0.5 sec. This was a value that would certainly indicate cracking in the glass seal. However, as shown by the sharp spike, this stress was transient and almost immediately settled back down to a value of 5 ksi. Furthermore, similar to the steady-state stress results, this maximum stress was concentrated at the corners and along the outside edges of the seal. The stress distribution at t = 0.5 sec is shown in Figure 11-13. Except for the stress near the corners, the stress in the glass seal was below the acceptable value of 2.0 ksi.

Figure 11-14 shows the stress history in the aluminum plate. Because the plate is made of a ductile material, the relevant stress measure is the von Mises stress. A von Mises stress above the yield strength of the material will cause permanent plastic deformation and is undesirable in this part. The results of the finite element analysis indicated that the maximum von Mises stress

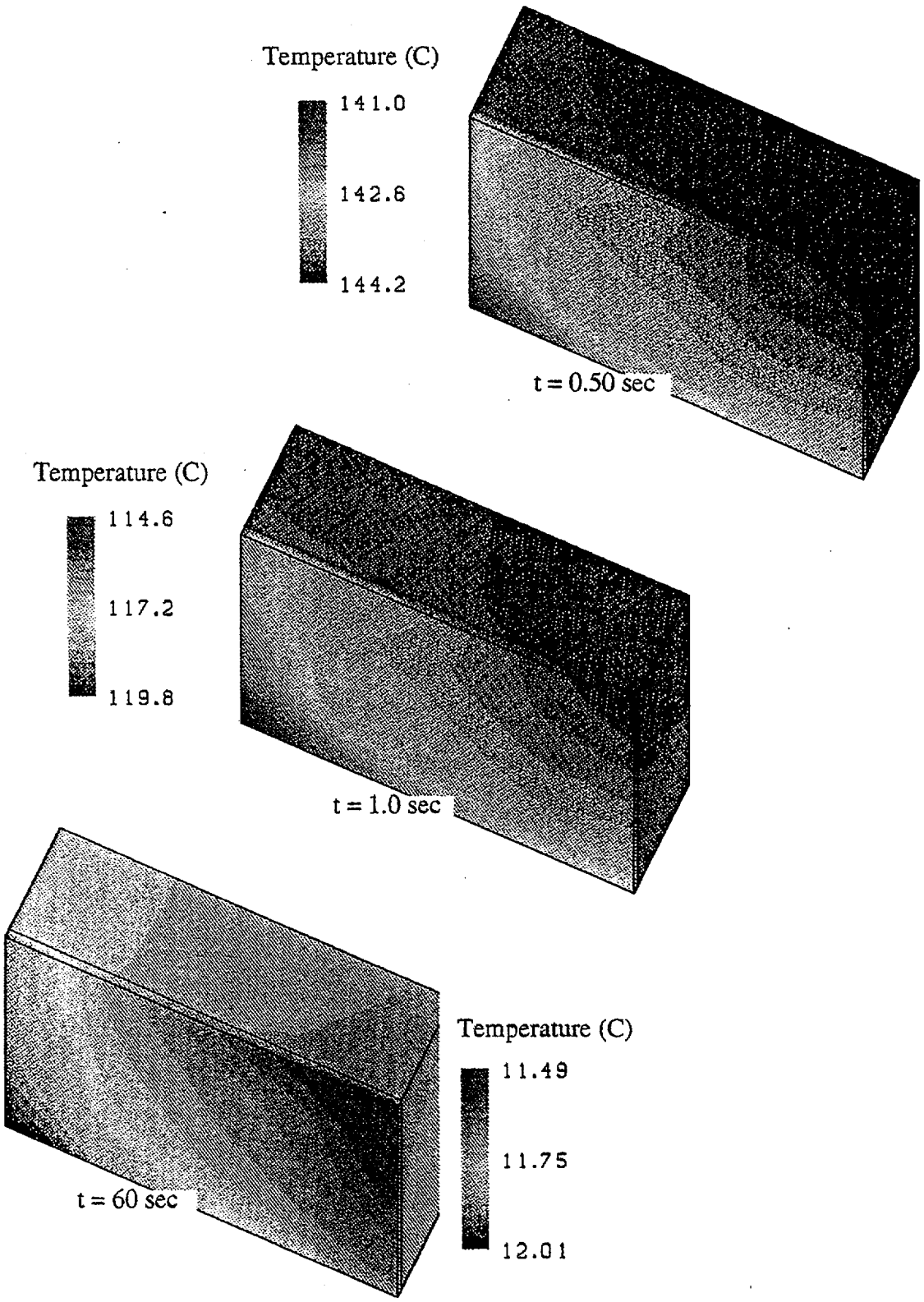

Figure 11-11. Temperature Distribution in Die and Die Attach at Various Times

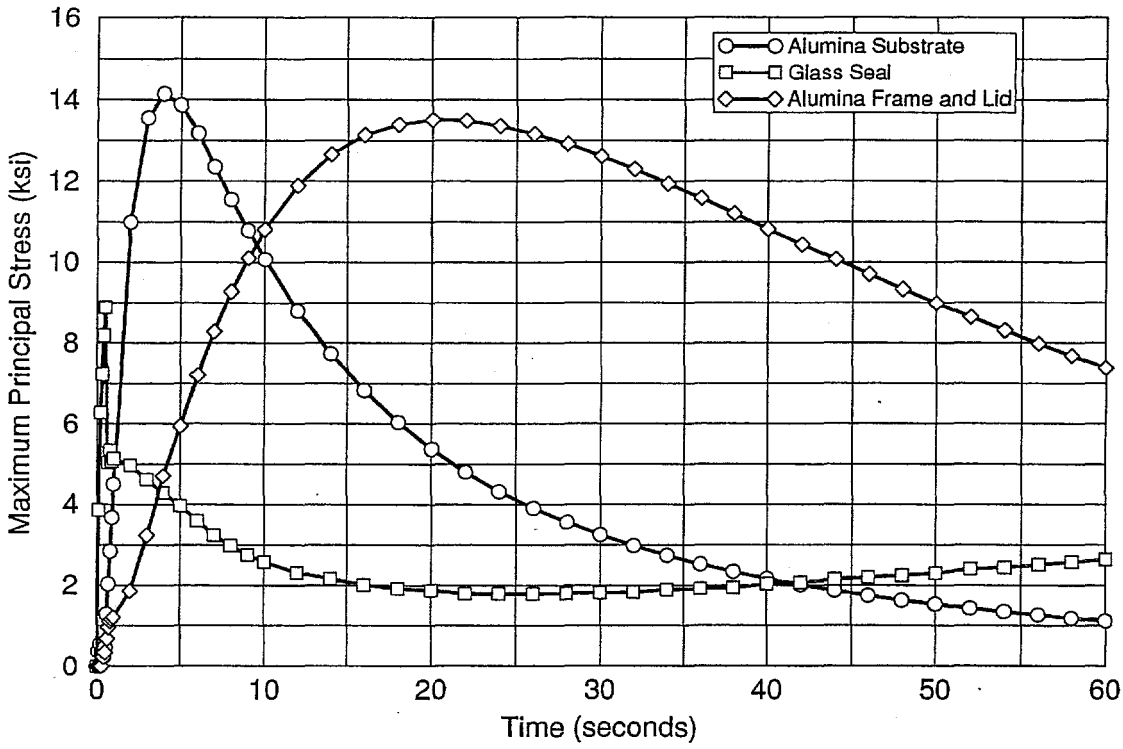

Figure 11-12. Maximum Principal Stress in the Alumina Substrate, Glass Seal, and Alumina Frame and Lid

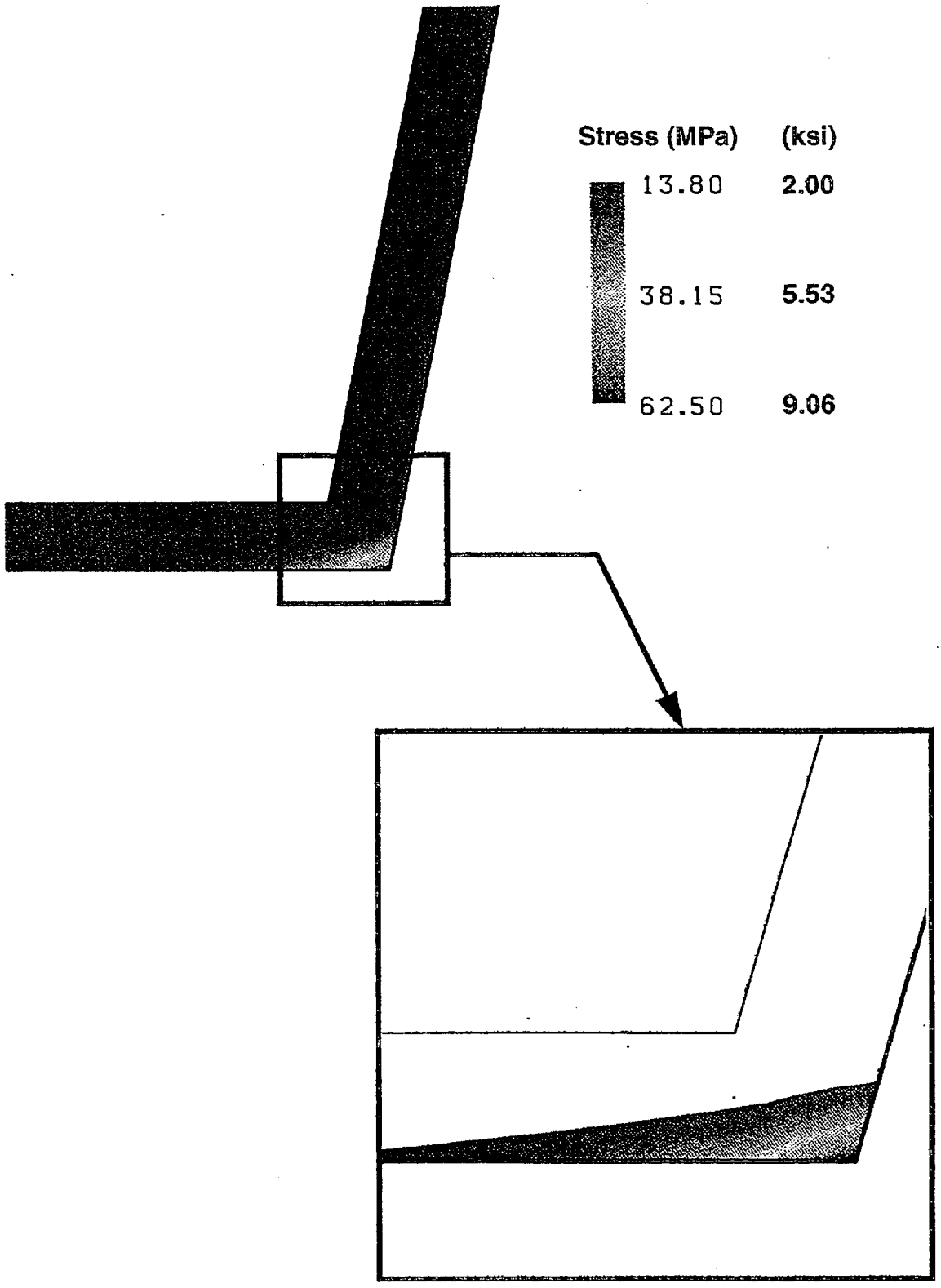

Figure 11-13. Distribution of Stress in the Glass Seal at t=0.50 Sec.

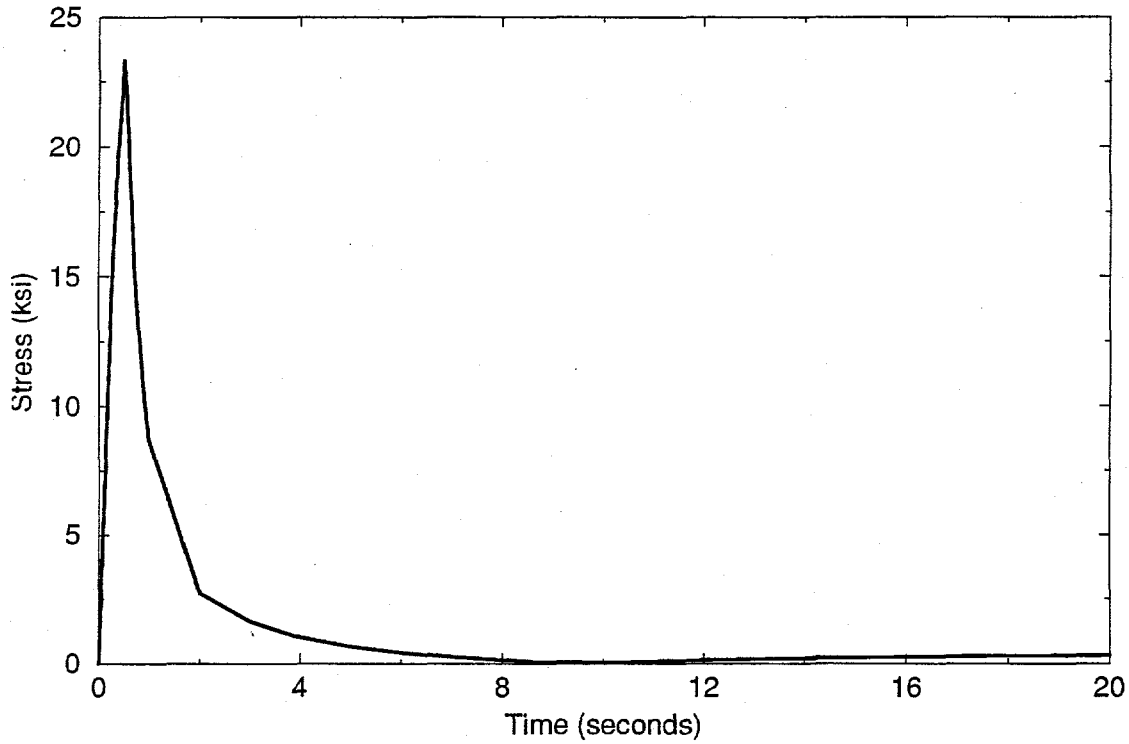

Figure 11-14. Maximum Stress (VonMises) in the Aluminum Base Plate

maximum von Mises stress in the aluminum plate was 23 ksi, which is well below the yield strengths of most common aluminums (30 to 45 ksi). Therefore, plastic deformation of the aluminum backing plate should not occur.

Finally, the history of the maximum tensile stresses in the die and die attach are plotted in Figure 11-15. Because both of these materials were located far from the heat sink, the stresses rose asymptotically to a maximum value at t = 60 sec. The stress reached a level of nearly 11 ksi in the die attach and 3 ksi in the die itself. While the stress in the die was within an acceptable range, the stress in the die attach was high enough that it may have caused cracking. Furthermore, this stress was not concentrated in one location but was fairly uniform through the die attach layer.

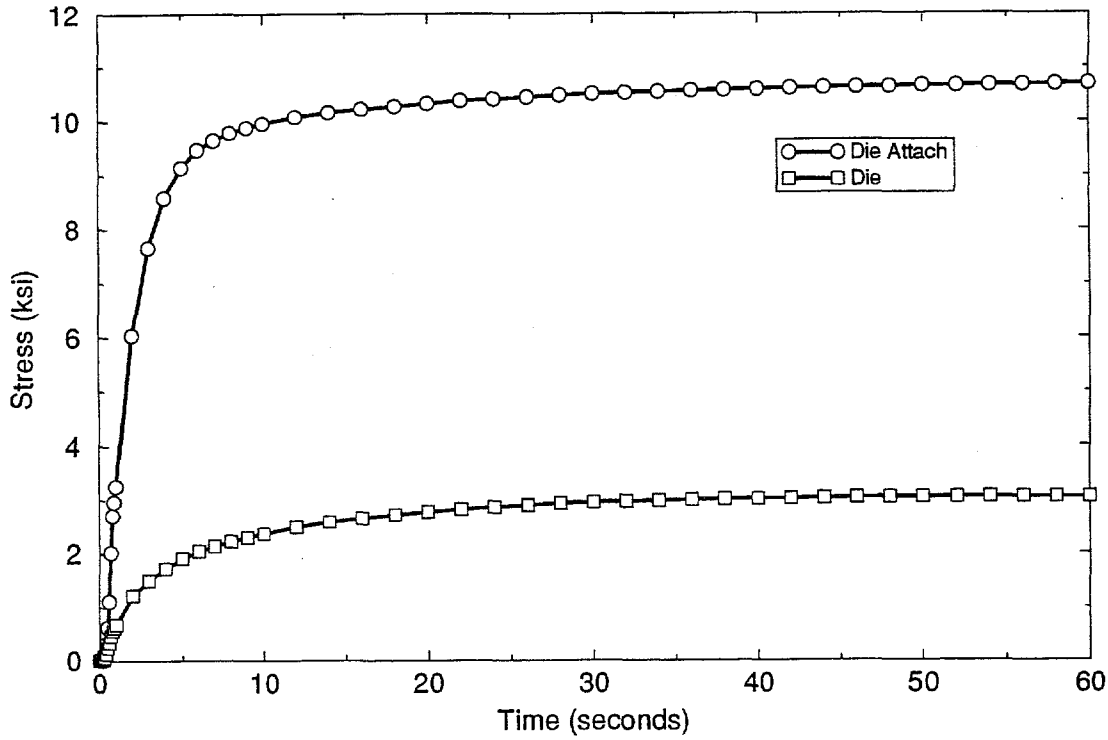

Figure 11-15. Maximum Principal Stress in the Die and Die Attach

11.3 Conclusions

This chapter describes finite element analyses performed to assess the stresses in an under-the-hood hybrid module under environmental conditions that may occur in both the manufacturing process and during the operation of the part. In the analysis of the manufacturing process, the part was assumed to slowly drop in temperature from a stress-free 100°C to -65°C. Because the temperature is assumed to drop slowly, the temperature field is assumed to be uniform throughout the part at any point in time. Results of a 3-D finite element analysis of the part under these conditions indicate that the tensile stress in the glass seal may cause cracking. However, note that these high stresses occur only in a concentrated area near the outside edge at the corners of the frame. Stresses in the alumina substrate and alumina frame and lid are within acceptable design limits.

A transient thermal event that could occur during the operational life of the part was also analyzed. This event assumes that a hot engine running at 150°C is suddenly cooled to 10°C. Results of the finite element analyses for this event indicate that tensile stresses in the alumina substrate and the alumina frame and lid may cause cracking. However, these maximum stresses are transient quantities, and by a time of 60 sec, the stress levels have dropped off to acceptable values. In addition, the stress in the glass seal reaches a level that indicates cracking. However, this is a transient value that drops off almost immediately after 0.50 sec. Similar to the steady-state results, the stress in the glass seal is highly concentrated at the outside corners.

For the transient event, a simple model of a single die and die attach was included. Results indicate that the stresses in these two components rise monotonically to asymptotic values. The maximum stress reached in the die is within acceptable design limits, while the level of stress in the die attach may indicate the potential for cracking.

REFERENCES

1. J. H. Biffle, "JACQ3D - A Three-Dimensional Finite Element Computer Program for Non-Linear Heat Conduction Problems with the Conjugate Gradient Method," In preparation.
2. J. H. Biffle, "JAC3D - A Three-Dimensional Finite Element Computer Program for the Nonlinear Quasi-Static Response of Solids with the Conjugate Gradient Method," SAND87-1305, Sandia National Laboratories, Albuquerque, New Mexico, 1993.

This page intentionally left blank

APPENDIX A

STEVENSON-WYDLER (15 USC 3710)
COOPERATIVE RESEARCH AND DEVELOPMENT AGREEMENT
(hereinafter "CRADA") NO. SC92/01113

BETWEEN

Sandia Corporation
(hereinafter "Sandia")
AND
General Motors Corporation
(hereinafter "GM")

a corporation of the State of Delaware having a principal office in Detroit, Michigan, both being hereinafter jointly referred to as the "Parties."

Background - The U.S. Department of Energy (DOE) is the agency responsible for the federally-owned facility known as Sandia National Laboratories. Sandia National Laboratories is managed and operated by American Telephone and Telegraph Company (AT&T) through its wholly owned subsidiary Sandia Corporation. Sandia operates at no-profit or loss to AT&T under a prime contract between AT&T and DOE designated Contract DE-AC04-76DP00789.

ARTICLE I. DEFINITIONS

A. "Government" means the United States of America and agencies thereof.

B. "DOE" means the Department of Energy, an agency of the United States of America.

C. "Contracting Officer" means the DOE employee administering Sandia's DOE Contract.

D. "Generated Information" means information produced in the performance of this CRADA.

E. "Proprietary Information" means information which embodies trade secrets developed at private expense outside of this Agreement and commercial or financial information which is privileged or confidential under the Freedom of Information Act (5 USC 552(B)(4)) and which is marked as Proprietary Information.

F. "Protected CRADA Information" means Generated Information which is marked as being Protected CRADA Information by a Party to this Agreement and which would have been Proprietary Information had it been obtained from a non-federal entity.

G. "Subject Invention" means any invention of Sandia or GM conceived or first actually reduced to practice in the performance of work under this CRADA.

H. "Intellectual Property" means patents, trademarks, copyrights, mask works, and other forms of comparable property rights protected by Federal law and other foreign counterparts.

I. "Trademark" means a distinctive mark, symbol or emblem used in commerce by a producer or manufacturer to identify and distinguish their goods or services from those of others.

J. "Mask Work" means a series of related images, however fixed or encoded, having or representing the predetermined, three-dimensional pattern of metallic, insulating or semiconductor material present or removed from the layers of a semiconductor chip product; and in which series the relation of the images to one another is that each image has the pattern of the surface of one form of the semiconductor chip product. (17 USC 901(a)(2))

ARTICLE I.1 SPECIAL GM REPRESENTATION - RESERVED

ARTICLE II. STATEMENT OF WORK, EFFECTIVE DATE AND PERIOD OF PERFORMANCE

Appendix A, Statement of Work, version February 18, 1993, is hereby incorporated into this CRADA by reference.

The effective date of this CRADA shall be the latter date of (1) the date on which it is signed by the last of the Parties hereto or (2) the date on which it is approved by DOE. The work to be performed under this CRADA shall be completed within four years from the effective date.

ARTICLE III. FUNDING & COSTS

A. GM's estimated total contribution is $2,308,000. The Government's estimated total contribution, which is provided through Sandia's contract with DOE, is $2,997,400, and includes $2,308,000 for Sandia, subject to available funding, and $689,400 for Depreciation and DOE Overhead.

B. Neither Party shall have an obligation to continue or complete performance of its work at a cost in excess of its estimated cost as contained in Article III.A. above, including any subsequent amendment.

C. Each Party agrees to provide at least thirty (30) days' notice to the other Party if the actual cost to complete performance will exceed the estimated cost.

ARTICLE III.1 SPECIAL PAYMENT TERMS AND CONDITIONS - RESERVED

ARTICLE IV. PROPERTY

All tangible personal property produced under this CRADA shall become the property of GM or the Government depending upon whose funds were used to obtain it. Such property is identified in Appendix A, Statement of Work. Personal Property shall be disposed of as directed by the owner at the owner's expense. All jointly funded property shall be owned by the Government.

ARTICLE IV.1 SPECIAL PROPERTY TERMS AND CONDITIONS - RESERVED

ARTICLE V. DISCLAIMER

THE GOVERNMENT, GM, AND SANDIA MAKE NO EXPRESS OR IMPLIED WARRANTY AS TO THE CONDITIONS OF THE RESEARCH OR ANY INTELLECTUAL PROPERTY OR PRODUCT MADE OR DEVELOPED UNDER THIS CRADA, OR THE OWNERSHIP, MERCHANTABILITY OR FITNESS FOR A

PARTICULAR PURPOSE OF THE RESEARCH OR RESULTING PRODUCT. NEITHER THE GOVERNMENT, GM, NOR SANDIA SHALL BE LIABLE FOR SPECIAL, CONSEQUENTIAL OR INCIDENTAL DAMAGES.

ARTICLE VI. PRODUCT LIABILITY

A. Except for any liability resulting from any negligent or intentional acts or omissions of Sandia, GM indemnifies the Government, AT&T, and Sandia for all damages, costs and expenses, including attorney's fees, arising from personal injury or property damage occurring as a result of the making, using or selling of a product, process or service by or on behalf of GM, its assignees or licensees, which was derived from the work performed under this CRADA. In respect to this Article, neither the Government, AT&T, nor Sandia shall be considered assignees or licensees of GM, as a result of reserved Government, AT&T, and Sandia rights. The indemnity set forth in this paragraph shall apply only if GM shall have been informed as soon and as completely as practical by Sandia, AT&T, and/or the Government of the action alleging such claim and shall have been given an opportunity, to the extent afforded by applicable laws, rules, or regulations, to participate in and control its defense, and Sandia, AT&T, and/or Government shall have provided reasonably available information and reasonable assistance requested by GM. No settlement for which GM would be responsible shall be made without GM's consent unless required by final decree of a court of competent jurisdiction.

B. For licenses granted by Sandia to any third party in Intellectual Property derived from Generated Information, such licenses shall include the requirement that the third party shall indemnify the Government, Sandia, AT&T, and GM for all damages, costs and expenses, including attorneys' fees, arising from personal injury or property damage occurring as a result of the making, using or selling of a product, process or service by or on behalf of such third party, its assignees or licensees, provided, however, such third parties shall not be required to indemnify GM for any negligent or intentional acts or omissions of GM.

ARTICLE VII. OBLIGATIONS AS TO PROPRIETARY INFORMATION

A. If Proprietary Information is orally disclosed to a Party, it shall be identified as such, orally, at the time of disclosure and confirmed in a written summary thereof within twenty (20) days as being Proprietary Information.

B. Sandia agrees to use Proprietary Information only in the performance of this CRADA and not to further disclose such information to others, except to Government employees who are subject to 18 USC 1905. GM will not receive Proprietary Information from Sandia except in accordance with a specific nondisclosure agreement approved by GM.

C. All Proprietary Information shall be returned to the provider thereof at the conclusion of this CRADA at the provider's expense.

D. All Proprietary Information shall be protected, unless and until such Proprietary Information shall become publicly known without the fault of the recipient, shall come into recipient's possession without breach of any of the obligations set forth herein by the recipient, or shall be independently developed by recipient's employees who did not have access to Proprietary Information.

ARTICLE VIII. OBLIGATIONS AS TO PROTECTED CRADA INFORMATION

A. Each Party may designate as Protected CRADA Information, as defined in Article I, any Generated Information produced by its employees, and with the agreement of the other Party, mark any Generated Information produced by the other Party's employees. All such designated Protected CRADA Information shall be appropriately marked.

B. For a period of five years from the date Protected CRADA Information is produced, Parties agree not to further disclose such information except:

(1) as necessary to perform this CRADA;

(2) other than as provided in Article XI, as requested by the DOE Contracting Officer to be provided to other DOE facilities for use only at those DOE facilities with the same protection in place; or

(3) as mutually agreed by the Parties in advance.

C. The obligations of (B) above shall end sooner for any Protected CRADA Information which shall become publicly known without fault of either Party, shall come into a Party's possession without breach by that Party of the obligations of (B) above, or shall be independently developed by a Party's employees who did not have access to the Protected CRADA Information.

D. Either Party may disclose to a third party those portions of Protected CRADA Information necessary for the third party to make (including develop), use or sell any product, and/or practice any process on behalf of or for the disclosing party.

ARTICLE IX. RIGHTS IN GENERATED INFORMATION

The Parties understand that the Government shall have unlimited rights in all Generated Information or information provided to the Parties under this CRADA which is not marked as being Copyrighted (subject to Article XIII) or as Protected CRADA Information (subject to Article VIII.B.) or Proprietary Information (subject to Article VII.B.).

ARTICLE X. EXPORT CONTROL

THE PARTIES UNDERSTAND THAT MATERIALS AND INFORMATION RESULTING FROM THE PERFORMANCE OF THIS CRADA MAY BE SUBJECT TO EXPORT CONTROL LAWS AND THAT EACH PARTY IS RESPONSIBLE FOR ITS OWN COMPLIANCE WITH SUCH LAWS. FAILURE TO COMPLY WITH SUCH LAWS MAY RESULT IN CRIMINAL LIABILITY.

ARTICLE XI. REPORTS AND ABSTRACTS

A. The Parties agree to produce the following deliverables:

(1) initial abstracts suitable for public release;

(2) other abstracts (final when work is complete, and others as substantial changes in scope and dollars occur);

(3) a final report; and

(4) other topical/periodic reports where the nature of research and magnitude or dollars justify.

B. The Parties acknowledge that DOE has the right to require delivery of reports and abstracts produced under this CRADA, subject to Article IX.

ARTICLE XII. PRE-PUBLICATION REVIEW

The Party proposing a public disclosure of data that may include Protected CRADA Information shall submit a publication text or a presentation abstract to the other Party for review. Such pre-publication review shall not be unreasonably withheld or denied beyond 45 days. If, however, the reviewing Party modifies or rejects the proposal, the Parties shall negotiate the content of proposed publications and presentations, endeavoring in good faith to reach a mutually satisfactory result within 45 days of the submission of the initial proposal. If the reviewing Party, by written notification and justification, finally rejects a proposal for public disclosure of Protected CRADA Information, the proposing Party shall not publish or present the Protected CRADA Information, except as provided in Article VIII B.

ARTICLE XIII. COPYRIGHT

A. The Parties may assert copyright in any of their generated information.

B. Each Party shall have the first option to retain ownership of copyrights in works created by its employees. If either Party decides not to retain ownership of copyright in a work created by its employee(s), that Party agrees to assign such copyright to the other Party, at the other Party's request. GM agrees to notify Sandia if it decides not to retain ownership of copyright in any work created by its employee(s); Sandia agrees to notify DOE if GM or Sandia decide not to retain ownership of copyright in any work created by its employee(s). The Parties agree to assign to the DOE, upon request, copyrights not retained by either Party.

C. For Generated Information, the Parties acknowledge that the Government has for itself and others acting on its behalf, a royalty-free, nonexclusive, irrevocable worldwide copyright license to reproduce, prepare derivative works, distribute copies to the public, and perform publicly and display publicly, by or on behalf of the Government, all copyrightable works produced in the performance of this CRADA, subject to the restrictions this CRADA places on publication of Proprietary Information and Protected CRADA Information.

D. For all copyrighted computer software produced in the performance of this CRADA, the Party owning the copyright will provide the source code, an expanded abstract as described in Appendix B, Abstract Format Description, and the object code and the minimum support documentation needed by a competent user to understand and use the software to DOE's Energy Science and Technology Software Center. The expanded abstract will be treated in the same manner as Generated Information in subparagraph C of this Article.

E. Sandia and GM agree that, with respect to any copyrighted computer software produced in the performance of this CRADA, DOE has the right, at the

end of the period set forth in paragraph B of Article VIII hereof and at the end of each two-year interval thereafter, to request Sandia and GM and any assignee or exclusive licensee of the copyrighted software to grant a nonexclusive, partially exclusive, or exclusive license to a responsible applicant upon terms that are reasonable under the circumstances, provided such grant does not cause a termination of any licensee's right to use the copyrighted computer software. If Sandia or GM or any assignee or exclusive licensee refuses such request, Sandia and GM agree that DOE has the right to grant the license if DOE determines that Sandia, GM, assignee, or licensee has not made a satisfactory demonstration that it is actively pursuing commercialization of the copyrighted computer software.

Before requiring licensing under this paragraph E, DOE shall furnish Sandia/GM written notice of its intentions to require Sandia/GM to grant the stated license, and Sandia/GM shall be allowed 30 days (or such longer period as may be authorized by the cognizant DOE Contracting Officer for good cause shown in writing by Sandia/GM) after such notice to show cause why the license should not be required to be granted.

Sandia/GM shall have the right to appeal the decision by the DOE to the grant of the stated license to the Invention Licensing Appeal Board as set forth in paragraphs (b)-(g) of 10 CFR 781.65 "Appeals."

F. The Parties agree to place Copyright and other notices, as appropriate for the protection of Copyright, in human readable form onto all physical media, and in digitally encoded form in the header of machine readable information recorded on such media such that the notice will appear in human readable form when the digital data are off loaded or the data are accessed for display or printout.

ARTICLE XIV. REPORTING INVENTIONS

A. The Parties agree to disclose to each other each and every Subject Invention, which may be patentable or otherwise protectable under the Patent Act. The Parties acknowledge that Sandia will disclose Subject Inventions to the DOE within two (2) months after the inventor first discloses the invention in writing to the person(s) responsible for patent matters of the disclosing Party.

B. These disclosures should be in such detail as to be capable of enabling one skilled in the art to make and use the invention under 35 USC 112. The disclosure shall also identify any statutory bars, i.e., printed publications describing the invention or the public use or on sale of the invention in this country. The Parties further agree to disclose to each other any subsequent statutory bar that occurs for an invention disclosed but for which a patent application has not been filed. All invention disclosures shall be marked as confidential under 35 USC 205.

ARTICLE XV. TITLE TO INVENTIONS

A. Whereas the DOE has granted rights to inventions under this CRADA, each Party shall have the first option to elect to retain title to any invention made by its employees. If a Party elects not to retain title to any invention of its employees, then the other Party shall have the second option to elect to retain title to such invention under this CRADA. The DOE shall retain title to any invention that is not retained by any Party.

B. The Parties acknowledge that the DOE may obtain title to each Subject Invention reported under Article XIV for which a patent application or applications are not filed and for which any issued patents are not maintained by any Party to this CRADA.

C. The Parties acknowledge that the Government retains a non-exclusive, non-transferable, irrevocable, paid-up license to practice or to have practiced for or on behalf of the United States every Subject Invention under this CRADA throughout the world.

ARTICLE XV.1 AT&T INTELLECTUAL PROPERTY RIGHTS

A. Patents - AT&T shall have non-exclusive, irrevocable, royalty-free licenses under patents or inventions made solely or jointly by Sandia employees. Said licenses shall be limited to make and have made, use, lease, and sell products and services.

B. Technical Data - AT&T shall have, subject to patent, data and security provisions of prime contract DE-AC04-76DP00789 between DOE and AT&T, the right to use technical data first produced under the prime contract for its private purposes, provided that as of the date of such use all reporting requirements, if any, of the prime contract have been met. The AT&T rights apply to all Generated Information under this CRADA deemed to be technical data under the prime contract.

ARTICLE XV.2 SPECIAL LICENSE TERMS AND CONDITIONS

Sandia and GM will resolve license provisions for intellectual property rights in a separate agreement.

ARTICLE XVI. FILING PATENT APPLICATIONS

A. The Parties agree that the Party initially indicated as having an ownership interest in any Subject Inventions shall have the first opportunity to file U.S. and foreign patent applications; but, if such Party does not file such applications within six months after disclosure, then the other Party to this CRADA may file patent applications on such inventions.

B. GM agrees to notify Sandia if it decides not to file a patent application for any invention; Sandia agrees to notify DOE if GM or Sandia decide not to file a patent application for any invention. Both Parties agree to make their respective notifications within nine (9) months after the initial disclosure of such invention or not later than 60 days prior to the time when any statutory bar might foreclose filing of a U.S. patent application.

ARTICLE XVII. TRADEMARKS

The Parties may seek to obtain trademark/service mark protection on products or services generated under this agreement in the United States or foreign countries. [The ownership and other rights relating to this trademark shall be as mutually agreed to in writing by the Parties.] The Parties hereby acknowledge that the Government shall have the right to indicate on any similar goods or services it produces, that such goods or services were

derived from and are a DOE version of the goods or services protected by such trademark/service mark with the trademark and the owner thereof being specifically identified.

ARTICLE XVIII. MASK WORKS

The Parties may seek to obtain legal protection for mask works fixed in semiconductor products generated under this agreement as provided by Chapter 9 of Title 17 of the United States Code. The rights to any mask work covered by this provision shall be as mutually agreed to in writing by the Parties. Parties acknowledge that the Government or others acting on its behalf shall retain a nonexclusive, paid-up, worldwide, irrevocable, nontransferable license to reproduce, import, or distribute the covered semiconductor product by or on behalf of the Government.

ARTICLE XIX. COST OF INTELLECTUAL PROPERTY PROTECTION

Each Party shall be responsible for payment of all costs relating to copyright, trademark, and mask work filing, U.S. and foreign patent application filing and prosecution, and all costs relating to maintenance fees for U.S. and foreign patents hereunder which are owned by the Party.

ARTICLE XX. REPORTS OF INVENTION USE

The Parties agree to submit, upon request of DOE, reports no more frequently than annually on the efforts to obtain utilization of any Subject Invention.

ARTICLE XXI. DOE MARCH-IN RIGHTS

The Parties acknowledge that the DOE has certain march-in rights to any Subject Inventions in accordance with 48 CFR 27.304-1(G).

ARTICLE XXII. U.S. COMPETITIVENESS

A. The Parties agree that any products, processes, or services for use or sale in the United States under any United States Patent resulting from a Subject Invention shall be manufactured, practiced, or provided substantially in the United States.

B. The Parties also agree that any products, processes, or services using intellectual property arising from the performance of this CRADA shall be manufactured, practiced, or provided substantially in the United States.

ARTICLE XXIII. ASSIGNMENT OF PERSONNEL

A. It is contemplated that each Party may assign personnel to the other Party's facility as part of this CRADA. Such personnel assigned by the assigning Party, to participate in or observe the research to be performed under this CRADA shall not during the period of such assignments be considered employees of the receiving Party for any purposes.

B. The receiving Party shall have the right to exercise routine

administrative and technical supervisory control of the occupational activities of such personnel during the assignment period and shall have the right to approve the assignment of such personnel and/or to later request their removal by the assigning Party.

C. The assigning Party shall bear any and all costs and expenses with regard to its personnel assigned to the receiving Party's facilities under this CRADA. The receiving Party shall bear facility costs of such assignments.

ARTICLE XXIV. FORCE MAJEURE

No failure or omission by Sandia or GM in the performance of any obligation under this CRADA shall be deemed a breach of this CRADA or create any liability if the same shall arise from any cause or causes beyond the control of Sandia or GM, including but not limited to the following, which, for the purpose of the CRADA, shall be regarded as beyond the control of the Party in question: Acts of God, acts or omissions of any government or agency thereof, compliance with requirements, rules, regulations, or orders of any governmental authority or any office, department, agency, or instrumentality thereof, fire, storm, flood, earthquake, accident, labor problems (including lockouts, strikes, and slowdowns), acts of the public enemy, war, rebellion, insurrection, riot, sabotage, invasion, quarantine, restriction, transportation embargoes, or failures or delays in transportation.

ARTICLE XXV. ADMINISTRATION OF THE CRADA

It is understood and agreed that this CRADA is entered into by Sandia under the authority of its Prime Contract with DOE. Sandia is authorized to and will administer this CRADA in all respects unless otherwise specifically provided for herein. Administration of this CRADA may be transferred from Sandia to DOE or its designee with notice of such transfer to GM, and Sandia shall have no further responsibilities except for the confidentiality, use and/or nondisclosure obligations of this CRADA and the provisions of Articles XIV, XV, XVI, and XIX.

ARTICLE XXVI. RECORDS AND ACCOUNTING SYSTEM

GM shall maintain records of receipts, expenditures, and the disposition of all Government property in its custody, related to the CRADA.

ARTICLE XXVII. NOTICES

A. Any communications required by this CRADA, if given by postage prepaid first class U.S. Mail, return receipt requested, and addressed to the Party to receive the communication, shall be deemed made as of the day of receipt of such communication by the addressee, or on the date given if by verified facsimile. Address changes shall be given in accordance with this Article and shall be effective thereafter. All such communications, to be considered effective, shall include the number of this CRADA.

B. The address, telephone numbers and facsimile numbers for the Parties are as follows:

1. For Sandia:

U.S. Mail Only:
Sandia Corporation
P.O. Box 5800, CRADA SC92/01113
Albuquerque, NM 87185-5800

Fed. Ex., UPS, Freight:
Sandia Corporation
Bldg. 957, CRADA SC92/01113
1515 Eubank Blvd. SE
Albuquerque, NM 87123

a. FORMAL NOTICES AND COMMUNICATIONS, COPIES OF REPORTS

Attn: Carla Chirigos Org. No. 2402
Tel: (505) 845-8645
Facsimile: (505) 844-6584

b. TECHNICAL CONTACT, REPORTS, COPIES OF FORMAL NOTICES AND COMMUNICATIONS

Attn: DuWayne Branscombe Org. No. 2274
Tel: (505) 844-1707
Facsimile: (505) 844-8480

2. For GM:

U.S. Mail Only:
AC Rochester Division
Dept. 32-31, Bldg. B
1300 Dort Highway
Flint, MI 48556

Fed. Ex., UPS, Freight:
AC Rochester Division
Dept. 32-31, Bldg. B
1300 Dort Highway
Flint, MI 48556

a. FORMAL NOTICES AND COMMUNICATIONS, COPIES OF REPORTS

Attn: Carl E. Miller
Tel: (313) 257-7402
Facsimile: (313) 257-2001

b. TECHNICAL CONTACT, REPORTS, COPIES OF FORMAL NOTICES AND COMMUNICATIONS

Attn: Larry A. Carol
Tel: (313) 257-5807
Facsimile: (313) 257-2001

ARTICLE XXVII.1 INFORMATION REQUESTED FROM GM

In order to evaluate the success of this CRADA and Sandia's CRADA program, the following information shall, upon request, be provided by GM:

A. An annual estimate of additional sales dollars or, if the effort of this CRADA can not be linked to sales, cost savings realized by GM as a result of the contributions made to GM's technology that are attributable to Sandia's efforts under this CRADA. The annual estimate is requested within 30 days of the end of each calendar year from inception of this CRADA through the calendar year following termination or completion of work under this CRADA.

B. With the final annual estimate, a projection of anticipated additional sales dollars or cost savings that are expected by GM for each of the next five years and that are attributable to Sandia's efforts under this CRADA.

ARTICLE XXVIII. DISPUTES

The Parties shall attempt to jointly resolve all disputes arising from this CRADA. If the Parties are unable to jointly resolve a dispute within a reasonable period of time, the dispute shall be referred to a process of nonbinding alternate dispute resolution to be agreed by the Parties at the time. To the extent that there is no applicable United States Federal law, this CRADA and performance thereunder shall be governed by the law of the State of New Mexico.

ARTICLE XXVIII.1 BUSINESS RELATIONS WITH OTHERS

Because Sandia is obliged to transfer technology widely to U.S. industry, GM(s) accepts that other commercial entities, including competitors of GM(s), may have business relationships with Sandia before, during, or after this CRADA. Such business relationships may involve work similar to the work under this CRADA, subject to obligations concerning use and nondisclosure of Proprietary Information and Protected CRADA Information.

ARTICLE XXIX. ENTIRE CRADA AND MODIFICATIONS

A. It is expressly understood and agreed that this CRADA with its Appendices contains the entire agreement between the Parties with respect to the subject matter hereof and that all prior representations or agreements relating hereto have been merged into this document and are thus superseded in totality by this CRADA. This CRADA shall not be effective until approved by DOE.

B. Any agreement to change any terms or conditions of this CRADA or the Appendices shall be valid only if the change is made in writing, executed by the Parties hereto, and approved by DOE.

ARTICLE XXX. TERMINATION

This CRADA may be terminated by either Party upon 30 days written notice to the other Party. In the event of termination by either Party, each Party shall be responsible for its share of the costs incurred through the effective date of termination, as well as its share of the costs incurred after the effective date of termination, and which are related to the termination. The confidentiality, use, and/or nondisclosure obligations and the obligations under Articles XIV, XV, XVI, and XIX of this CRADA shall survive any termination of this CRADA.

FOR Sandia:

BY _____
C. Paul Robinson

TITLE Vice President of Laboratory Development

DATE _____

FOR GM:

BY _____

TITLE

DATE _____

Appendix A
CRADA SC92/01113
February 18, 1993

Engine System Electronics for High Temperature Electronics for Under Hood Applications

The objectives of this CRADA are to develop high temperature materials, electronic systems, and components critical to the automotive manufacturing industrial community. Vital knowledge will also be transferred to the automotive and electronic systems, and components manufacturing communities.

This CRADA teams the capabilities of Sandia National Laboratories (SANDIA) and General Motors, AC Rochester (GM/ACR). SANDIA will provide expertise in the areas of High Temperature (HT) packaging technologies, HT component performance, advanced materials for HT, manufacturing and reliability assessments, and prototypes to proof of concept. GM/ACR will provide expertise in automotive engine electronics, under hood environments, mandated fuel economy, and emission standards.

The U.S. automobile industry sells approximately $150 billion per year in new cars and trucks in this country; the total automaker market in the U.S. for autos, trucks, and parts is estimated to be in excess of $600 billion per year. In recent years, the number of U.S. vehicles, most notably the Japanese vehicles, have continued to increase. A significant market share, approximately 26% with a 1991 increase of 1.8% over the previous year, is held by the Japanese. The problem is compounded by a weak U.S. economy causing more Americans to keep their vehicles for longer periods of time. The U.S. sales volume is not expected to rise more than 1% annually for the remainder of the decade.

To maintain a competitive edge, new technologies for use in automobiles must be developed. One major area requiring new technology development is Engine System Electronics (ESE). ESE improves the management of high combustion efficiency and emissions reduction. Development of high temperature electronics, materials, and components for under hood applications are an important area in which DOE research laboratories can help U.S. auto manufacturers meet new requirements and maintain their competitive edge.

Cost effective engine management is essential to increasing performance and efficiency of internal combustion engines. The development of enabling technologies for under hood applications is pivotal to advanced engines and thus to the competitiveness of the U.S. auto industry. This CRADA draws on the research, development and manufacturing technology available at SANDIA; it will result in the bridging of scientific developments to practical systems usable by industry. GM/ACR will use technology developed through this program for improving the design of automotive engine systems, and U.S. industrial suppliers will use the technology for manufacturing.

A three-year, four-phase development schedule is proposed for this project. In Phase I, existing and near-term HT component and packaging/interconnect technologies will be compared against automotive needs to determine the preferred technologies for further development. Required materials, processes, and design developments will be pursued in Phase II. In Phase III, the Parties will demonstrate proof of concept and ensure the availability of the technology for manufacture. Finally, in Phase IV, prototype units will be

produced and evaluated. The four phases will be executed concurrently.

Phase I. Development of Components and Packaging/Interconnects

Objectives - Establish the use requirements such as environment and expected life, and determine technologies to develop.

Discussion - Candidate technologies will include low temperature and high temperature co-fired, multi-chip ceramic modules; thick-film or thin-film hybrids on ceramic, silicon, or other substrates; high temperature printed wiring boards; active (ASIC gate arrays and FPGAs) and passive components; and interconnect options (MCMs) between modules.

Responsibilities

- SANDIA and GM/ACR will meet to clearly document the use conditions and expected life.

- SANDIA and GM/ACR will meet to identify an existing project that will serve as a development vehicle. Initial selection of active/passive components, substrates, attachments and interconnects and packaging will be accomplished.

- SANDIA will propose reduction of component parts with a smaller family of devices.

- SANDIA and GM/ACR will build and test electronic assemblies using proposed designs. Also, test results will be analyzed and modifications will be proposed.

- SANDIA and GM/ACR will begin certification of supplier base for HT electronic component suppliers.

Phase II. Development of Advanced Materials

Objectives - To evaluate materials for components, chip attachment, and interconnection and to classify them according to their maximum use temperature.

Discussion - Assessments will include: thick film conductors, resistors, and capacitors; materials for attachment of semiconductor die; wire, TAB, or solder bump interconnections; and thermally conductive adhesives and potting materials for removal of self-generated heat from the circuit. Compatibility with several substrates will be investigated.

Responsibilities

- SANDIA and GM/ACR will assess and report on organic dielectrics, alternate inorganic dielectric substrates, proposed manufacturing processes, and environmentally conscious manufacturing processes.

- SANDIA will iterate competing technologies with selection of best fit, and development as required.

- SANDIA will identify failure modes and issues related to reliability and producibility.

Phase III. Production Readiness

Objectives - To provide assurance that the technologies are manufacturable and available from U.S. suppliers.

Discussion - The successful auto suppliers, chosen by GM/ACR, will be evaluated, certified and qualified to ensure delivery of prototypes for use in production.

Responsibilities

- GM/ACR will develop engineering and material specifications for all critical materials.
- GM/ACR will quantify process specifications for the generic materials.
- SANDIA will provide analytic, design, and certification methodologies.
- SANDIA will provide product assurance and process qualification. Test engineering will complete product evaluation of proposed generic designs.

Phase IV. Proof of Concept

Objectives - To determine that technologies and components meet the required GM/ACR auto industry environmental and performance requirements.

Discussion - When the components, packaging/interconnect, and advanced materials have been developed, SANDIA and GM/ACR will evaluate and test the prototypes in the auto environment.

Responsibilities

- SANDIA will determine critical parameters of materials used in HT environments.
- SANDIA will obtain prototype units.
- GM/ACR will perform dyno-engine tests of prototype designs for temperature (+175C) and life (150,000 KM).
- GM/ACR will certify circuitry in vehicle tests for federal fuel and emission standards.

APPENDIX B

PRINCIPAL CONTACTS

Collaborative Partnerships with Sandia National Laboratories:

Dave Larson
Sandia National Laboratories
National Security Partnership Development
Mail Stop 1380
Albuquerque, New Mexico 87185
Tel (505) 843-4165

TJ Allard
Sandia National Laboratories
Integrated Electronics
Mail Stop 1071
Albuquerque, New Mexico 87185
Tel (505) 844-5581

Electronic Packaging Applications:

Fernando Uribe
Sandia National Laboratories
Electronic Processing Department
Mail Stop 0957
Albuquerque, New Mexico 87185
Tel (505) 845-8802

Jim Jorgensen
Sandia National Laboratories
Electronics Modeling
Mail Stop 1071
Albuquerque, New Mexico 87185
Tel (505) 844-1023

Dave Palmer
Sandia National Laboratories
Advanced Packaging
Mail Stop 1082
Albuquerque, New Mexico 87185
Tel (505) 844-2138

Paul Dressendorfer
Sandia National Laboratories
Multichip Module Applications
Mail Stop 1073
Albuquerque, New Mexico 87185
Tel (505) 844-5373

APPENDIX C

Appendix C

Appendix C1:
Electrical Test Data

Group 1

High temperature aging to 1000 hours at 180°C is complete with no evidence of any degradation in the temperature rise of the diode samples, as shown in Figures C-1 through C-3. Up to 20 percent downward drift can be seen in the plots. This drift is thought to be real changes in the test samples because control data have changed less than 5 percent. All 18 diode test samples remained functional at completion of the high temperature aging test.

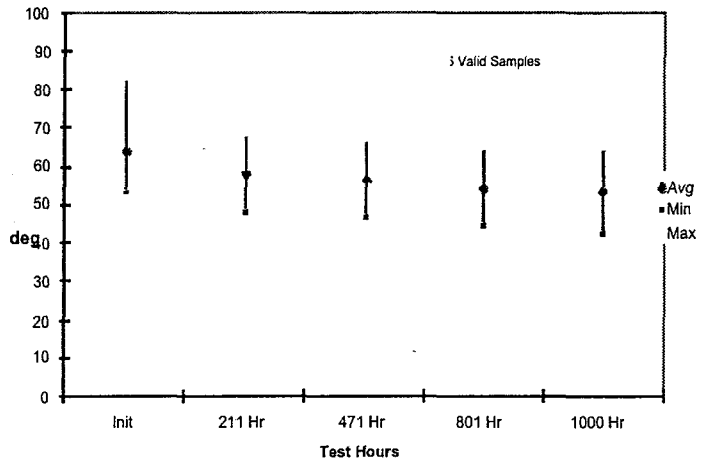

Figure C-1. Die Attach Test, Adhesive 8175, 75 mS Power Pulse = 325 W/cm^2

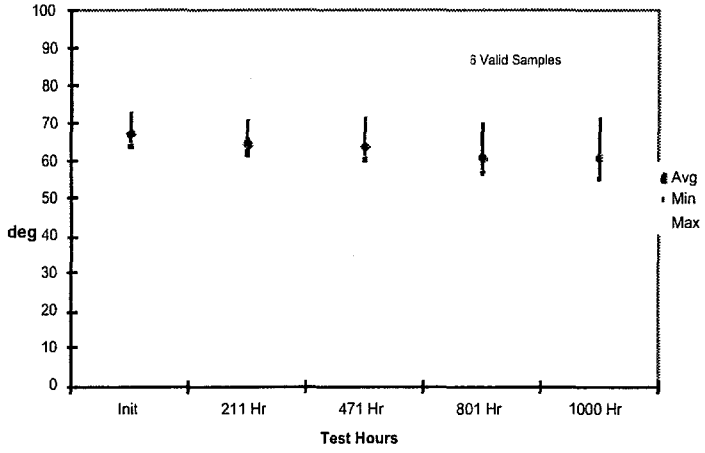

Figure C-2. Die Attach Test, Adhesive 8175A, 75 mS Power Pulse = 325 W/cm^2

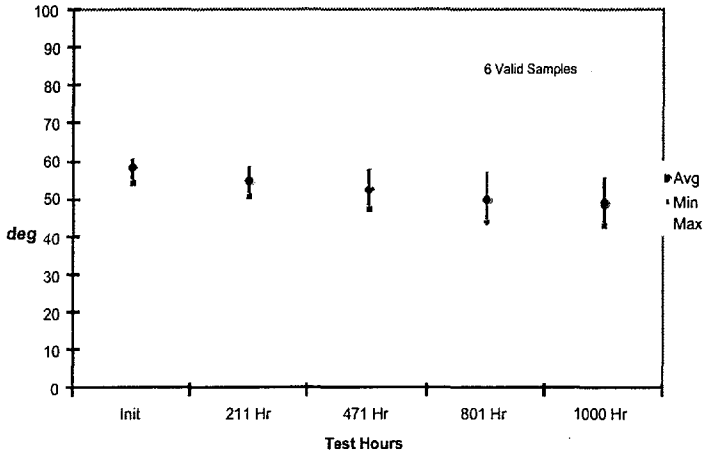

Figure C-3. Die Attach Test, Adhesive 8700E, 75 mS Power Pulse - 325 W/cm^2

Figures C-4 through C-6 below show RDSON for each adhesive. The shock/vibration data are from only two samples in each of the charts.

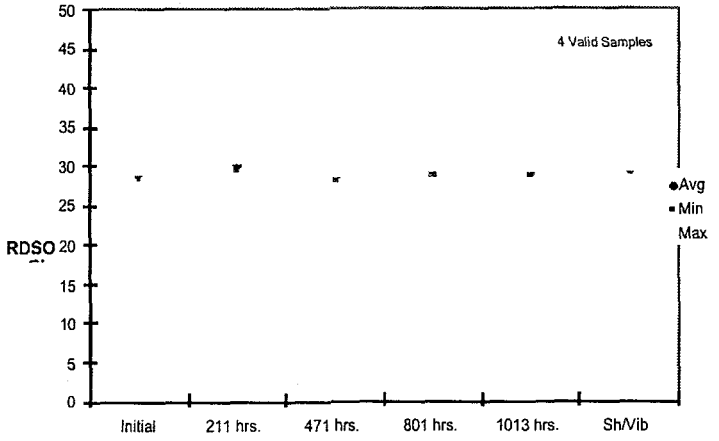

Figure C-4. Die Attach Test, Adhesive 8175, RDSON at 10 Amp, Storage at 180°C

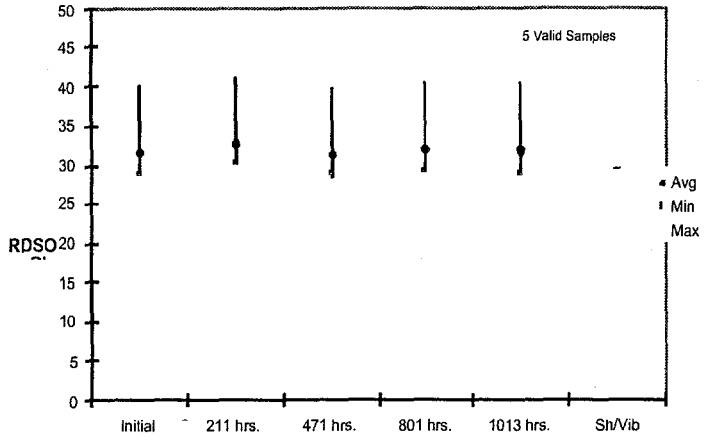

Figure C-5. Die Attach Test, Adhesive 8175A, RDSON at 10 Amp, Storage at 180°C

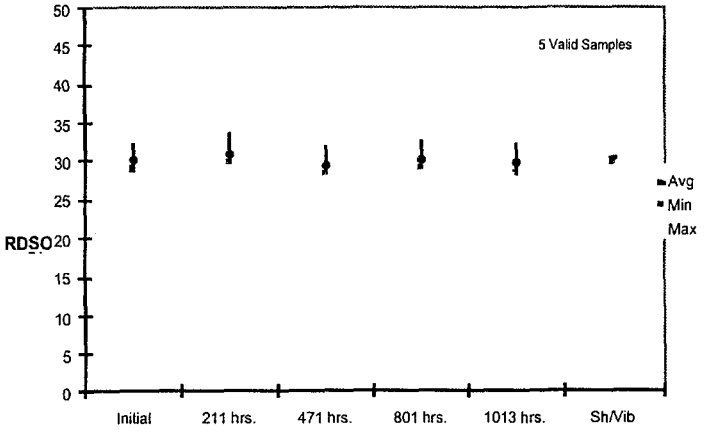

Figure C-6. Die Attach Test, Adhesive 8700E, RDSON at 10 Amp, Storage at 180°C

Group 2

Temperature cycling was taken to the 1000 cycle point. Figures C-7 through C-9 below show approximate temperature rise for each adhesive.

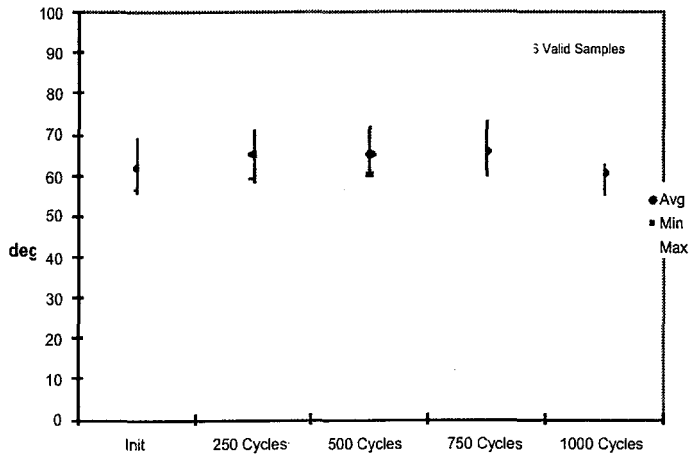

Figure C-7. Die Attach Test, Adhesive 8175, 75 mS Power Pulse = 325 W/cm^2

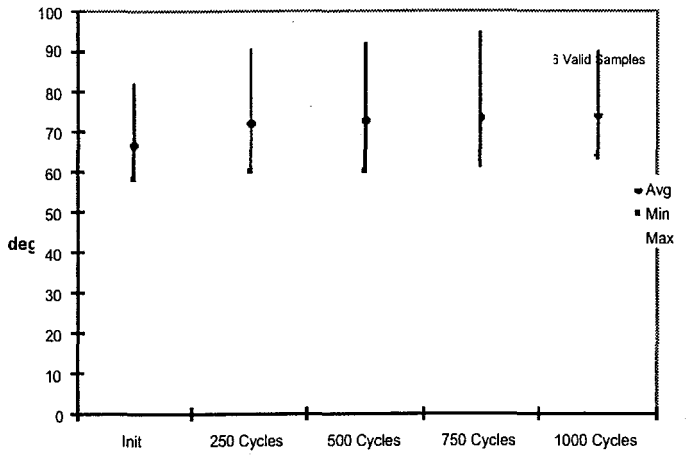

Figure C-8. Die Attach Test, Adhesive 8175A, 75 mS Power Pulse = 325 W/cm^2

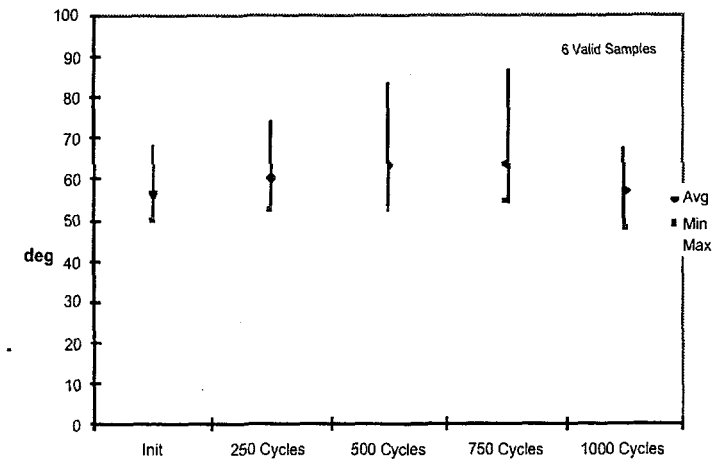

Figure C-9. Die Attach Test, Adhesive 8700E, 75 mS Power Pulse = 325 W/cm^2

Group 2

Temperature cycling was taken to the 1000 cycle point. Figures C-10 through C-12 below show RDSON for each adhesive. One of four functioning FETs in the 8700E sample has doubled in value. This was caused by a bad wire bond which degraded during test. This sample was removed from the chart because its changes had nothing to do with die attach.

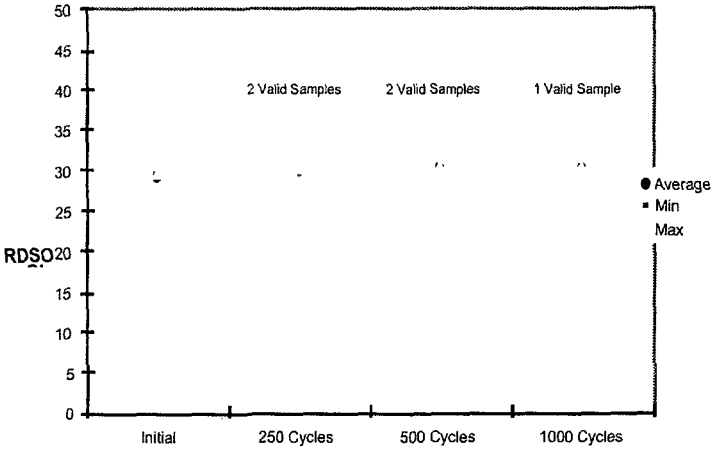

Figure C-10. Die Attach Test, Adhesive 8175, RDSON at 10 Amp

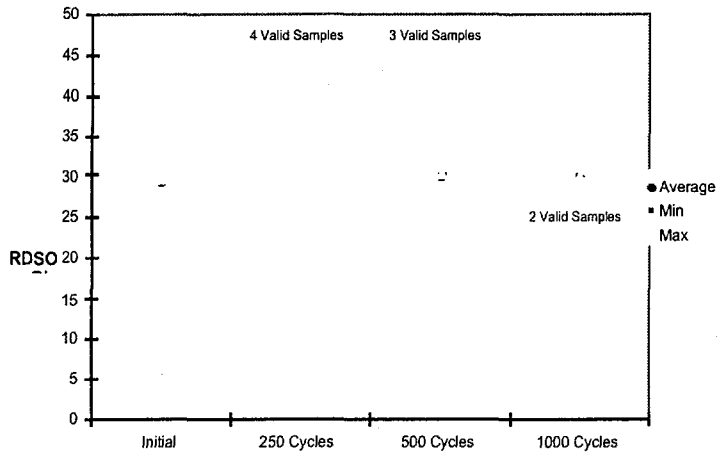

Figure C-11. Die Attach Test, Adhesive 8175A, RDSON at 10 Amp

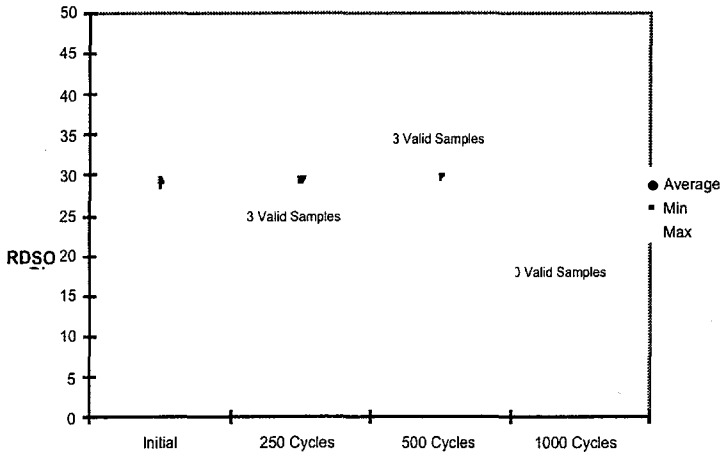

Figure C-12. Die Attach Test, Adhesive 8175A, RDSON at 10 Amp

Group 3A

Group 3A completed the thermal shock test and 100 cycles of the static temperature cycle. There have been no significant changes in the samples. Figures C-13 through C-15 below show approximate temperature rise for each adhesive.

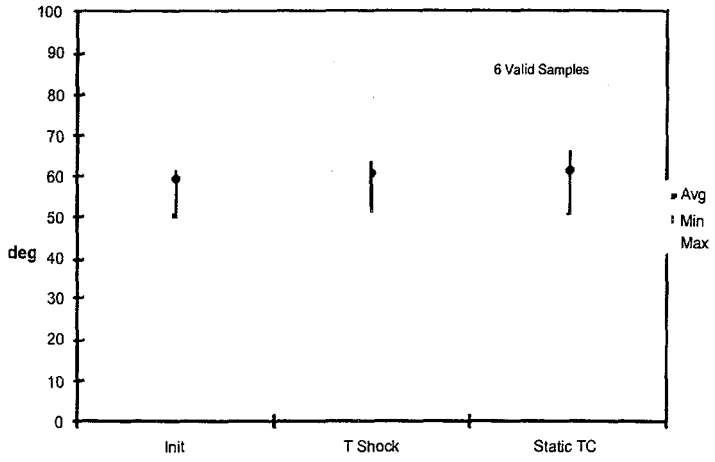

Figure C-13. Die Attach Test, Adhesive 8175, 75 mS Power Pulse = 325 W/cm^2

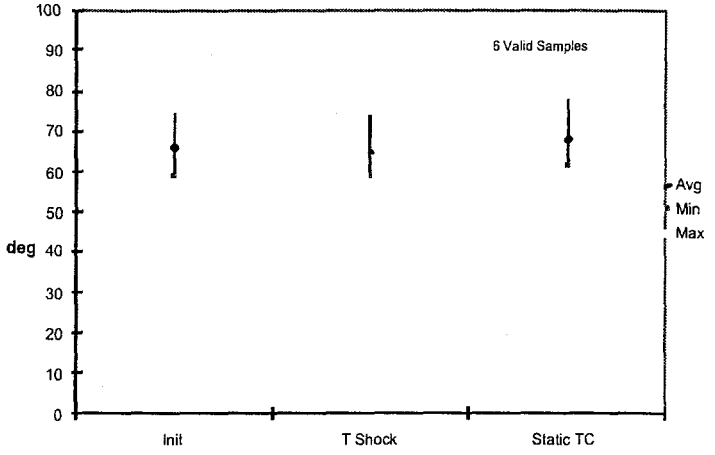

Figure C-14. Die Attach Test, Adhesive 8175A, 75 mS Power Pulse = 325 W/cm^2

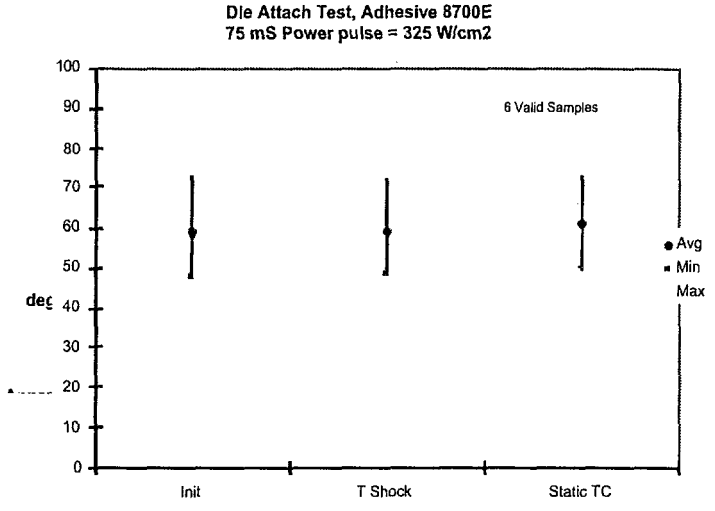

Figure C-15. Die Attach Test, Adhesive 8700E, 75 mS Power Pulse = 325 W/cm^2

Group 3A

Group 3A completed the thermal shock test and 100 cycles of the static temperature cycle. There have been no significant changes in the samples. Figures C-16 through C-18 below show RDSON for each adhesive.

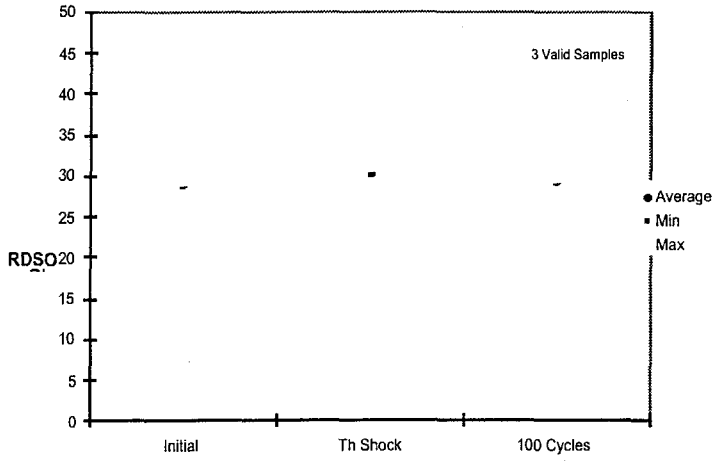

Figure C-16. Die Attach Test, Adhesive 8175, RDSON at 10 Amp

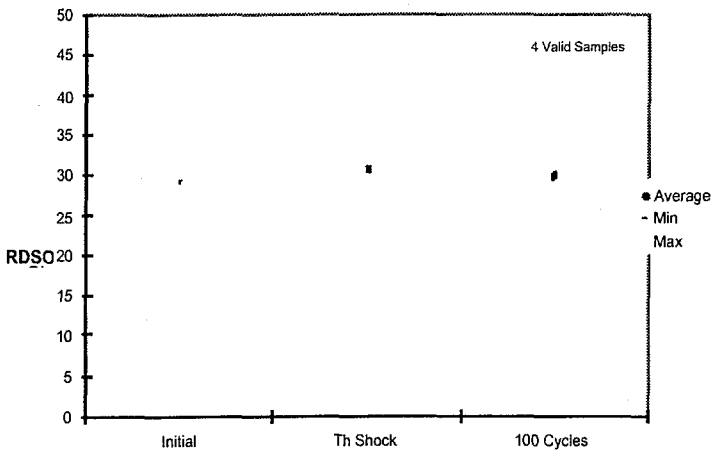

Figure C-17. Die Attach Test, Adhesive 8175A, RDSON at 10 Amp

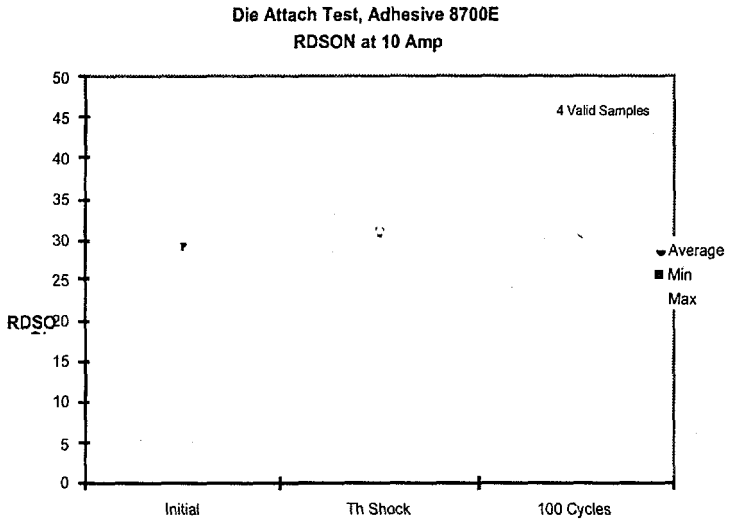

Figure C-18. Die Attach Test, Adhesive 8700E RDSON at 10 Amp

Group 3B

Group 3B completed the static temperature cycling, vibration and mechanical shock tests. There have been no significant changes in the samples. Figures C-19 through C-21 below show approximate temperature rise for each adhesive.

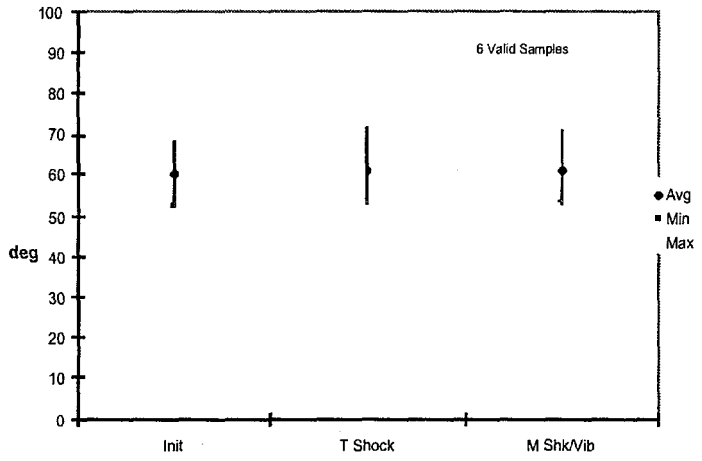

Figure C-19. Die Attach Test, Adhesive 8175, 75 mS Power Pulse = 325 W/cm^2

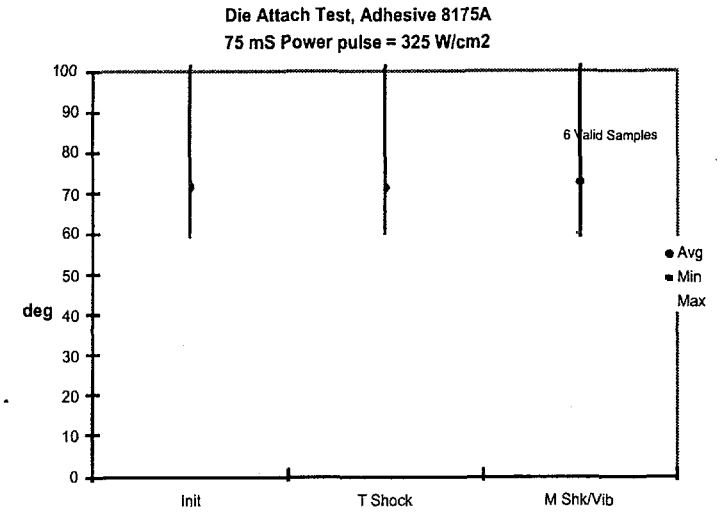

Figure C-20. Die Attach Test, Adhesive 8175A, 75 mS Power Pulse = 325 W/cm^2

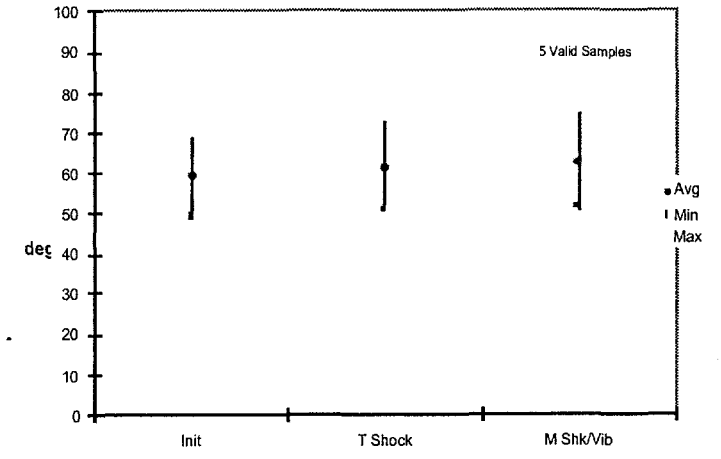

Figure C-21. Die Attach Test, Adhesive 8700E, 75 mS Power Pulse = 325 W/cm^2

Group 3B

Group 3B completed the static temperature cycling, vibration and mechanical shock tests. There have been no significant changes in the samples. Figures C-22 through C-24 below show RDSON for each adhesive.

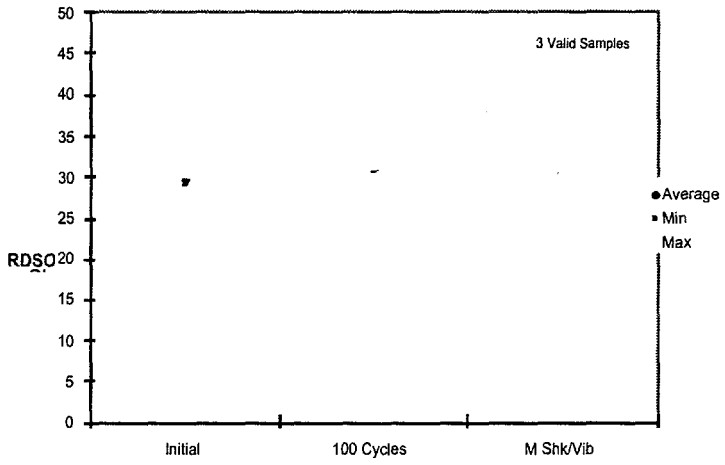

Figure C-22. Die Attach Test, Adhesive 8175, RDSON at 10 Amp

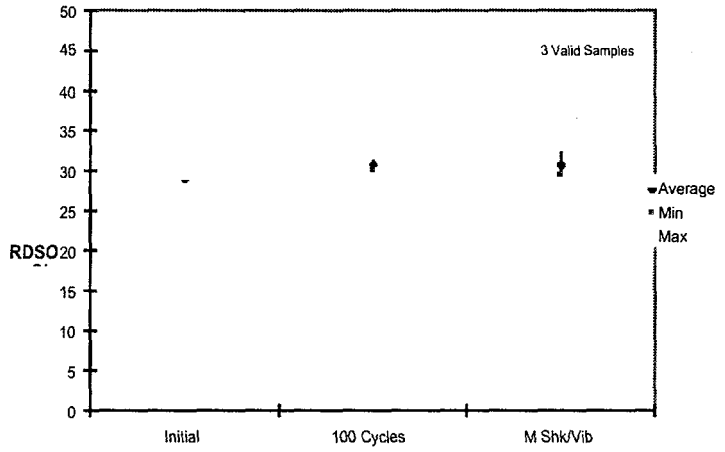

Figure C-23. Die Attach Test, Adhesive 8175A, RDSON at 10 Amp

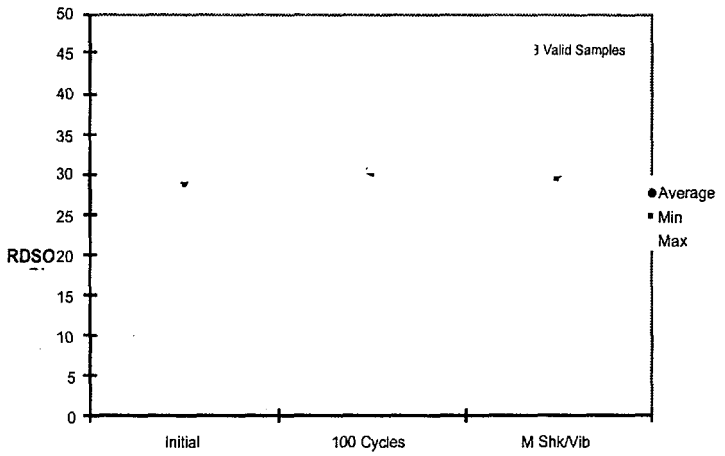

Figure C-24. Die Attach Test, Adhesive 8700E, RDSON at 10 Amp

Appendix C2 Mechanical Strength and Visual Inspection Data

Group 1

Table C-1 describes the results of Group 1, 25°C and 170°C Die Shear Tests as processed.

Table C-1: Group 1: As-Processed 25°C and 170°C Die Shear Test Results.
(Values listed are shear loads in kilograms)

8700E					
25°C	TCap/Diel	CCap/Diel	LgDie/Diel	SmDie/Diel	SmDie/Alum
	>20	>20	>20	>20	>20
	>20	>20	>20	9.5	20
			>20	9.3	7.2
170°C	TCap/Diel	CCap/Diel	LgDie/Diel	SmDie/Diel	SmDie/Alum
	13.5	29.2	25.3	8.6	15.2
	13.4	24.5	20.5	9.4	7.7
			22.9	11.1	11.5
8175					
25°C	TCap/Diel	CCap/Diel	LgDie/Diel	SmDie/Diel	SmDie/Alum
	>20	>20	>20	>20	17.3
	>20	>20	>20	11.4	6.5
			>20	6.3	18.7
170°C	TCap/Diel	CCap/Diel	LgDie/Diel	SmDie/Diel	SmDie/Alum
	2.77	6.7	16.2	2.9	2.4
	3.1	13.0	13.5	no test	2.5
			13.5	2.6	no test
8175A					
25°C	TCap/Diel	CCap/Diel	LgDie/Diel	SmDie/Diel	SmDie/Alum
	>20	>20	>20	9.5	7.6
	>20	>20	>20	8.9	9.4
			>20	no test	12.7
170°C	TCap/Diel	CCap/Diel	LgDie/Diel	SmDie/Diel	SmDie/Alum
	8.2	12.6	16.1	2.7	2.8
	7.6	10.8	17.6	2.3	2.2
			25.3	4.2	2.4

Group 1 - The following observations were made concerning the samples shear-tested at 25°C and 170°C as-processed (Table C-1):

(1) The shear values for all three adhesives are lower at 170°C than at 25°C, which is expected because 170°C is above the glass transition temperatures for three adhesives.
(2) The 8700E adhesive had greater strength at 170°C than the other two adhesives.
(3) The 8175 and 8175A adhesives had some failures with small die at 170°C according to MIL-STD-883D Method 2019.
(4) Comparisons of the adhesion of small die over dielectric and alumina were inconclusive.
(5) Visual inspection did not reveal any mentionable defects.

Group 2

Table C-2 describes Group 2, Shear Test Results of 1000 Hour Storage at 180°C

Table C-2: Group 2: 1000 Hour Storage at 180°C Shear Test Results
(Values listed are shear loads in kilograms)

8700E					
0 Hrs	TCap/Diel	CCap/Diel	LgDie/Diel	SmDie/Diel	SmDie/Alum
			>20	>20	>20
			>20	9.3	20
			>20	9.5	7.2
1000 Hrs	TCap/Diel	CCap/Diel	LgDie/Diel	SmDie/Diel	SmDie/Alum
			>20	11.5	8.5
			>20	8.8	10.8
			>20	6.6	5.1
8175					
0 Hrs	TCap/Diel	CCap/Diel	LgDie/Diel	SmDie/Diel	SmDie/Alum
			>20	>20	17.3
			>20	11.4	18.7
			>20	6.3	6.5
1000 Hrs	TCap/Diel	CCap/Diel	LgDie/Diel	SmDie/Diel	SmDie/Alum
			>20	18.5	16.1
			>20	12.3	12.8
			>20	6.6	5.9
8175A					
0 Hrs	TCap/Diel	CCap/Diel	LgDie/Diel	SmDie/Diel	SmDie/Alum
			>20	9.5	7.6
			>20	8.9	9.4
			>20	no test	12.7
1000 Hrs	TCap/Diel	CCap/Diel	LgDie/Diel	SmDie/Diel	SmDie/Alum
			>20	16.2	14.4
			>20	10.5	9.3
			>20	6.4	8.8

Group 2 - The following observations were made concerning high temperature aged samples shear tested at 25°C (Table C-2):

(1) Die shear tests were also performed at 250, 500 and 750 hours, but only the data from the 1000 hours aging are reported here.
(2) The strength of the large die exceeded the capability of the shear tester before and after aging for 1000 hours at 180°C. Therefore, it is impossible to determine if the adhesive strength degraded with this size of die.
(3) There is some evidence that the strength of the small die did degrade due to the 180°C aging for the 8700E and 8175 adhesives. Sample sizes were not large enough to establish any statistical significance to the numbers. However, all of the shear test values are well above the strength criteria of 2.5 Kg.
(4) There is some evidence that the strength of the small die increased due to the 180°C aging for the 8175A. Again, sample sizes were not large enough to establish any statistical significance. Increased strength could be due to this particular material curing to a greater degree during the 180°C aging.
(5) The 8175 and 8175A adhesives discolored slightly due to the aging process.

Group 3

Table C-3 describes the results of Group 3, Shear Test Results of Standard Temperature Cycling (4000 hrs/1000 cycles). (Values listed are shear loads in kgs):

Table C-3: Group 3: Shear Test Results of Standard Temperature Cycling (4000 hrs/1000 cycles) (Values listed are shear loads in kilograms)

8700E					
0 Cycles	TCap/Diel	CCap/Diel	LgDie/Diel	SmDie/Diel	SmDie/Alum
	>20	>20	>20	>20	>20
	>20	>20	>20	9.3	20
			>20	9.5	7.2
1000	TCap/Diel	CCap/Diel	LgDie/Diel	SmDie/Diel	SmDie/Alum
Cycles	20.5	>20	>20	11.9	17.8
	6.4	>20	>20	11.6	16.3
			>20	6.0	5.1
8175					
0 Cycles	TCap/Diel	CCap/Diel	LgDie/Diel	SmDie/Diel	SmDie/Alum
	>20	>20	>20	>20	17.3
	>20	>20	>20	11.4	18.7
			>20	6.3	6.5
1000	TCap/Diel	CCap/Diel	LgDie/Diel	SmDie/Diel	SmDie/Alum
Cycles	10.8	>20	>20	20.5	11.5
	8.9	>20	>20	8.6	9.9
			>20	6.6	6.7
8175A					
0 Cycles	TCap/Diel	CCap/Diel	LgDie/Diel	SmDie/Diel	SmDie/Alum
	>20	>20	>20	9.5	7.6
	>20	>20	>20	8.9	9.4
			>20	no test	12.7
1000	TCap/Diel	CCap/Diel	LgDie/Diel	SmDie/Diel	SmDie/Alum
Cycles	14.6	>20	>20	8.4	7.2
	13.3	>20	>20	4.4	6.7
			>20		4.2

Group 3 - The following observations were made concerning Table C-3:

(1) Die shear tests were also performed at 250, 500 and 750 cycles, but only the data from the 1000 cycles are reported here.
(2) The tantulum capacitors experienced significant degradation in shear strength. In fact, some degradation in strength was observed after the first test period of 250 cycles. Visible cracks in the adhesive and capacitor body were observed as early as 500 standard temperature cycles. By 750 temperature cycles, cracks were prevalent in all samples.
(3) The strength of the ceramic capacitors and the large die exceeded the capability of the shear tester before and after 1000 cycles. Therefore, it is impossible to determine if the adhesive strength degraded with this size of die. However, cracks in the adhesive fillets were observed in the ceramic capacitors and large die. Cracks in the adhesive of the ceramic capacitors were observed as early as 500 standard temperature cycles and after 750 temperature cycles were prevalent in all samples. Cracks in the adhesive of the large die were first observed after 750 temperature cycles and were prevalent after 1000 temperature cycles.
(4) There is some evidence that the strength of the small die did degrade after 1000 cycles for all three adhesives. Some degradation in strength was observed after the first test period of 250 cycles. Sample sizes weren't large enough to establish any statistical significance to the numbers. However, all of the shear test values are well above the strength criteria of 2.5 kg. Very little cracking was observed in the small die.
(5) None of the three adhesives performed particularly better or worse in the shear tests than the other two adhesives.

Group 4A

Table C-4 describes the results of Group 4A, static temperature cycle (100 Hrs/100 Cycles) shear test results.

Table C-4: Group 4A: Static Temperature Cycle (100 Hrs/100 Cycles) Shear Test Results. (Values listed are shear loads in kilograms)

8700E					
0 Cycles	TCap/Diel	CCap/Diel	LgDie/Diel	SmDie/Diel	SmDie/Alum
	>20	>20	>20	>20	>20
	>20	>20	>20	9.3	20
			>20	9.5	7.2
100 Cycles	TCap/Diel	CCap/Diel	LgDie/Diel	SmDie/Diel	SmDie/Alum
	>20	>20	>20	19.2	17.6
	15.0	>20	>20	9.7	11.2
	14.9	>20	>20	6.5	8.9
8175					
0 Cycles	TCap/Diel	CCap/Diel	LgDie/Diel	SmDie/Diel	SmDie/Alum
	>20	>20	>20	>20	17.3
	>20	>20	>20	11.4	18.7
			>20	6.3	6.5
100 Cycles	TCap/Diel	CCap/Diel	LgDie/Diel	SmDie/Diel	SmDie/Alum
	>20	>20	>20	9.7	>20
	12.6	>20	>20	9.5	11.3
	11.5	>20	>20	8.1	9.1
8175A					
0 Cycles	TCap/Diel	CCap/Diel	LgDie/Diel	SmDie/Diel	SmDie/Alum
	>20	>20	>20	9.5	7.6
	>20	>20	>20	8.9	9.4
			>20	no test	12.7
100 Cycles	TCap/Diel	CCap/Diel	LgDie/Diel	SmDie/Diel	SmDie/Alum
	>20	>20	>20	16.4	19.1
	>20	>20	>20	14.2	18.6
	>20	>20	>20	6.2	no test

Group 4A - The following observations were made concerning the static temperature cycled samples (Table C-4):

(1) Die shear tests were also performed after 10 thermal shock cycles prior to the static temperature cycling. The shear test data are not reported here; however, some cracks were observed with adhesives 8175 and 8175A when used to attach the tantalum capacitors.
(2) The tantulum capacitors experienced significant degradation in shear strength for the 8700E and 8175 adhesives. This phenomena was also observed after the 10 thermal shock cycles.
(3) The strength of the ceramic capacitors and the large die exceeded the capability of the shear tester before and after 1000 cycles. Therefore, it is impossible to determine if the adhesive strength degraded with this size of die.
(4) There is some evidence that the strength of the small die did degrade after 1000 cycles for all three adhesives. Some degradation in strength was observed after the first test period of 250 cycles. Sample sizes weren't large enough to establish any statistical significance to the numbers. However, all of the shear test values are well above the strength criteria of 2.5 Kg.
(5) None of the three adhesives performed particularly better or worse than the other two adhesives.
(6) Visual inspections after 100 static temperature cycles revealed general pull back of all three adhesives from the terminations of both types of capacitors.

Group 4B

Table C-5 describes Group 4B, Shear Test Results of Post Static Temperature Cycle/ Vibration.

Table C-5: Group 4B: Shear Test Results of Post Static Temperature Cycle/Vibration
(Values listed are shear loads in kilograms.)

8700E					
Initial	TCap/Diel	CCap/Diel	LgDie/Diel	SmDie/Diel	SmDie/Alum
	>20	>20	>20	>20	>20
	>20	>20	>20	9.3	20
			>20	9.5	7.2
Post STC/	TCap/Diel	CCap/Diel	LgDie/Diel	SmDie/Diel	SmDie/Alum
Vibration	>20	>20	>20	9.5	16.9
	>20	>20	>20	7.3	7.8
	13.3	>20	>20	no test	6.1
8175					
Initial	TCap/Diel	CCap/Diel	LgDie/Diel	SmDie/Diel	SmDie/Alum
	>20	>20	>20	>20	17.3
	>20	>20	>20	11.4	18.7
			>20	6.3	6.5
Post STC/	TCap/Diel	CCap/Diel	LgDie/Diel	SmDie/Diel	SmDie/Alum
Vibration	>20	>20	>20	>20	>20
	>20	>20	>20	16.0	19.3
	16.2	>20	>20	13.6	16.3
8175A					
Initial	TCap/Diel	CCap/Diel	LgDie/Diel	SmDie/Diel	SmDie/Alum
	>20	>20	>20	9.5	7.6
	>20	>20	>20	8.9	9.4
			>20	no test	12.7
Post STC/	TCap/Diel	CCap/Diel	LgDie/Diel	SmDie/Diel	SmDie/Alum
Vibration	>20	>20	>20	15.3	16.5
	>20	>20	>20	9.9	14.2
	18.4	>20	>20	7.6	12.7

Group 4B - The following observations were made concerning the post-static temperature cycle/vibration samples (Table C-5):

(1) The tantulum capacitors experienced some degradation in shear strength for all three adhesives.
(2) The strength of the ceramic capacitors and the large die exceeded the capability of the shear tester before and after STC/vibration. Therefore, it is impossible to determine if the adhesive strength degraded with this size of die.
(3) There is some evidence that the strength of the small die did degrade after STC/vibration for all three adhesives. Sample sizes weren't large enough to establish any statistical significance to the numbers. However, all of the shear test values are well above the strength criteria of 2.5 Kg.
(4) None of the three adhesives performed particularly better or worse than the other two adhesives.
(5) Visual inspections after mechanical vibration revealed cracks in the adhesive fillets of both the tantulum and ceramic capacitors with all three adhesives.

Table C-6 describes Group 4B Post Static Temperature Cycle/Vibration/Mechanical Shock Shear Test Results.

Table C-6: Group 4B: Post Static Temperature Cycle/Vibration/Mechanical Shock Shear Test Results (Values listed are shear loads in kilograms)

8700E					
Initial	TCap/Diel	CCap/Diel	LgDie/Diel	SmDie/Diel	SmDie/ Alum
	>20	>20	>20	>20	>20
	>20	>20	>20	9.3	20
			>20	9.5	7.2
Post STC/	TCap/Diel	CCap/Diel	LgDie/Diel	SmDie/Diel	SmDie/ Alum
Vibration/	>20	>20	>20	15.9	15.1
Shock	>20	>20	>20	11.9	12.8
			18.5	5.2	12.1
8175					
Initial	TCap/Diel	CCap/Diel	LgDie/Diel	SmDie/Diel	SmDie/ Alum
	>20	>20	>20	>20	17.3
	>20	>20	>20	11.4	18.7
			>20	6.3	6.5
Post STC/	TCap/Diel	CCap/Diel	LgDie/Diel	SmDie/Diel	SmDie/ Alum
Vibration/	>20	>20	>20	11.5	7.8
Shock	19.1	>20	>20	9.2	7.7
			>20	9.1	6.0
8175A					
Initial	TCap/Diel	CCap/Diel	LgDie/Diel	SmDie/Diel	SmDie/ Alum
	>20	>20	>20	9.5	7.6
	>20	>20	>20	8.9	9.4
			>20	no test	12.7
Post STC/	TCap/Diel	Ccap/Diel	LgDie/Diel	SmDie/Diel	SmDie/ Alum
Vibration/	>20	>20	>20	11.8	19.0
Shock	>20	>20	>20	10.2	13.4
		>20	>20	8.1	8.0

Group 4B - The following observations were made concerning post-static temperature cycle/vibration/mechanical shock samples (Table C-6):

(1) The tantulum capacitors experienced some degradation in shear strength for all three adhesives.
(2) The strength of the ceramic capacitors and the large die exceeded the capability of the shear tester in most cases before and after STC/vibration/shock conditioning. Therefore, it is impossible to determine if the adhesive strength degraded with this size of die.
(3) There is some evidence that the strength of the small die did degrade after STC/vibration for the 8700E and 8175 adhesives. Sample sizes weren't large enough to establish any statistical significance to the numbers. However, all of the shear test values are well above the strength criteria of 2.5 Kg.
(4) Visual inspections after mechanical shock revealed cracks in the adhesive fillets of both the tantulum and ceramic capacitors with all three adhesives.

Tables C-7 through C-11 show 170°C shear test results after various environmental treatments.

Table C-7: Group 1: As-Processed 170°C Die Shear Test Results (Values listed are shear loads in kilograms):

8700E					
170°C	TCap/Diel	CCap/Diel	LgDie/Diel	SmDie/Diel	SmDie/ Alum
	13.5	29.2	25.3	8.6	15.2
	13.4	24.5	20.5	9.4	7.7
			22.9	11.1	11.5
8175					
170°C	TCap/Diel	CCap/Diel	LgDie/Diel	SmDie/Diel	SmDie/ Alum
	2.77	6.7	16.2	2.9	2.4
	3.1	13.0	13.5	no test	2.5
			13.5	2.6	no test
8175A					
170°C	TCap/Diel	CCap/Diel	LgDie/Diel	SmDie/Diel	SmDie/ Alum
	8.2	12.6	16.1	2.7	2.8
	7.6	10.8	17.6	2.3	2.2
			25.3	4.2	2.4

Table C-8: Group 2: 170°C Die Shear Test Results After 1000 hours Aging at 180°C (Values listed are shear loads in kilograms):

8700E 170°C	TCap/Diel	CCap/Diel	LgDie/Diel	SmDie/Diel	SmDie/Alum
			51.3	13	7.8
			40.8	11.8	5.4
			37.9	4.8	5.2
8175					
170°C	TCap/Diel	CCap/Diel	LgDie/Diel	SmDie/Diel	SmDie/Alum
			32.7	10.6	6.8
			25.5	7.8	5.3
			24.6	7.2	2.8
8175A					
170°C	TCap/Diel	CCap/Diel	LgDie/Diel	SmDie/Diel	SmDie/Alum
			17.6	7.3	6.5
			11.3	3.9	6.0
			11.1	no test	3.7

Conclusions

(1) For Group 1, the 8700E adhesive had higher strengths for all five components than 8175 and 8175A. This would correspond to the higher glass transition temperature of the 8700E versus the other two adhesives.
(2) For Group 2, the 8700E adhesive still appears to have had higher strengths for the three die components than 8175 and 8175A. However, the improvement in strength is not as noticeable as with Group 1.
(3) The strengths for Group 2 are generally higher after 1000 hours of aging at 180°C than the strengths of the as-processes samples of Group 1.

Table C-9: Group 3: 170°C Die Shear Test Results After 1000 Standard Temperature Cycles
(Values listed are shear loads in kilograms)

8700E					
170°C	TCap/Diel	CCap/Diel	LgDie/Diel	SmDie/ Diel	SmDie/ Alum
	6.7	19.4	12.3	6.3	7.6
	4.3	12.6	8.7	3.7	5.9
			6.2	3.4	5.4
8175					
170°C	TCap/Diel	CCap/Diel	LgDie/Diel	SmDie/ Diel	SmDie/ Alum
	11.4	19.0	29.0	6.9	3.0
	10.1	17.8	23.0	5.3	3.0
			19.3	2.7	3.0
8175A					
170°C	TCap/Diel	CCap/Diel	LgDie/Diel	SmDie/ Diel	SmDie/ Alum
	7.5	10.9	7.1	7.8	3.2
	5.1	7.4	5.3	5.2	2.4
			3.6	2.3	1.5

Conclusions

(1) The temperature cycling noticeably degraded the adhesion strength for all five components attached with the 8700E adhesive. However, all of the die adhesion strengths were well above the 2.5 kg criteria.
(2) The temperature cycling slightly degraded the adhesion strength for all five components attached with the 8175A epoxy. Some values were below the 2.5 kg criteria.
(3) The adhesion strengths of the components attached with the 8175 increased after the temperature cycling.

Table C-10: Group 4: 170°C Die Shear Test Results After 10 Thermal Shock Cycles
(Values listed are shear loads in kilograms)

8700E					
170°C	TCap/Diel	CCap/Diel	LgDie/Diel	SmDie/ Diel	SmDie/ Alum
	31	43.6	43.9	14.9	17.0
	22.9	38.8	28.3	14.0	13.6
			26.2	no test	13.2
8175					
170°C	TCap/Diel	CCap/Diel	LgDie/Diel	SmDie/ Diel	SmDie/ Alum
	7.0	10.0	16.0	4.6	3.0
	3.8	7.3	13.5	3.8	2.8
			11.3	3.5	1.8
8175A					
170°C	TCap/Diel	CCap/Diel	LgDie/Diel	SmDie/Die l	SmDie/ Alum
	10.6	15.0	18.2	4.1	4.2
	10.6	12.3	15.3	3.5	2.7
			11.7	2.5	1.4

Conclusions

(1) Compared to the as-processed shear strengths, the adhesion strengths for all three adhesives increased after the 10 thermal shocks.
(2) The improvements in adhesion strength were most noticeable with the 8700E epoxy.
(3) Two samples failed at a shear loads below the acceptable 2.5 kg criteria (One with 8175 and one with 8175A adhesives).

Table C-11: Group 4A: 170°C Die Shear Test Results After 10 Thermal Shock Cycles and 100 Static Temperature Cycles (Values listed are shear loads in kilograms)

8700E					
170°C	TCap/Diel	CCap/Diel	LgDie/Diel	SmDie/Diel	SmDie/ Alum
	17.8	29.7	12.5	10.0	11.3
	17.1	26.1	8.0	9.7	9.4
	10.7	24.9	7.6	9.3	7.7
8175					
170°C	TCap/Diel	CCap/Diel	LgDie/Diel	SmDie/Diel	SmDie/ Alum
	15.0	21.2	24.5	6.5	5.1
	15.0	18.8	22.9	4.2	4.3
	12.8	17.1	22.5	3.5	3.3
8175A					
170°C	TCap/Diel	CCap/Diel	LgDie/Diel	SmDie/Diel	SmDie/Al um
	10.1	24.1	5.1	3.8	3.4
	6.8	13.1	4.0	3.2	3.0
	4.0	8.5	1.6	3.2	2.8

Conclusions

(1) Group 4A results show that the adhesion strength of the 8700E and 8175A epoxies degraded after the 100 static temperature cycles.
(2) Group 4A results show that the adhesion strength of the 8175 epoxy increased after the 100 static temperature cycles.

Table C-12: Group 4B: 170°C Die Shear Test Results After 1000 Standard Temperature Cycles and Mechanical Vibration/Shock (Values listed are shear loads in kilograms)

8700E					
170°C	TCap/Diel	CCap/Diel	LgDie/Diel	SmDie/Diel	SmDie/ Alum
	19.2	26.9	27.0	7.6	5.0
	16.0	25.3	13.7	5.9	5.0
	12.5	19.1	10.0	5.4	4.4
8175					
170°C	TCap/Diel	CCap/Diel	LgDie/Diel	SmDie/Diel	SmDie/Alum
	9.1	14.5	13.5	3.0	4.7
	5.4	11.3	7.4	3.0	3.1
	5.3	9.5	5.3	3.0	2.4
8175A					
170°C	TCap/Diel	CCap/Diel	LgDie/Diel	SmDie/Diel	SmDie/Alum
	5.1	9.6	7.1	3.2	3.2
	4.1	5.5	5.2	2.4	3.0
	3.9	5.5	5.1	1.5	2.5

Conclusions

(1) Additional degradation in the adhesion strengths are seen after the mechanical vibration and shock conditions.
(2) Two samples were below the 2.5 kg criteria.

APPENDIX D

Appendix D:
Modeling of Wire Bond Failure Data for Large Diameter Aluminum Wire Bonds

This appendix describes the statistical analyses performed on selected materials. By the time actual data were available, a decision had already been made that silver thick film (or silver-platinum thick film) materials would have to be used to make the hybrid module economically feasible. Therefore, the statistical analysis was focused on the two material of greatest interest - silver (Du Pont 6262) and silver - 1% platinum (Heraeus 4740). Portions of the analysis are reported in the following paragraphs. However, the complete analysis with statistical data are available in a separate report.[1] The goal of these analyses was to develop models that would allow the accurate lifetime prediction of an aluminum wire bond to a selected material based on an exposure to a particular environment for a particular length of time.

Specimens of various thick film materials subjected to a variety of firing schemes and material layers were subjected to accelerated aging via four constant temperature environments (160°C, 180°C, 210°C, and 225°C) for up to approximately 8000 hours depending on the particular environment and material. Prior to aging, several 0.010 inch diameter, 100% aluminum wires were bonded to each thick-film specimen. Some of these wires were destructively pull-tested immediately to get a feel for the strength of the wire bonds prior to aging [2]. The observed distributions of wire bond strengths prior to aging, by material combination, form a basis for an assessment of the effects of aging. After the initial testing, several wires were periodically pull-tested after various amounts of exposure to each of the accelerated temperature environments. The following paragraphs summarize the analysis of the resulting data associated with thick film specimens listed in Table D-1.

Table D-1: Thick Film Specimens Evaluated

Material Combination	ID Code
Dupont 6262 silver film multi-fired on alumina	(6262ma)
Dupont 6262 single-fired over dielectric	(6262sd)
Heraeus 4740 silver/platinum film multi-fired on alumina	(4740ma)
Heraeus 4740 silver/platinum single-fired over dielectric	(4740sd)
Dupont-5725 gold film multi-fired on alumina	(5725ma)
Dupont-5725 single-fired over dielectric	(5725sd)
Dupont-QM21 palladium/silver film multi-fired on alumina	(QM21ma)
Dupont-QM21 single-fired over dielectric	(QM21sd)

This analysis was conducted in two phases. At the first phase, data were summarized and modeled separately for each combination of materials with aging temperature and time. With this in hand, the second phase of analysis related to modeling the reaction kinetics associated with a particular material combination, where possible. Finally, this section demonstrates in the

case of the 6262ma material how these kinetics models can be used to develop estimates of wirebond reliability as a function of specified exposure time at a specified temperature.

1.1 Experimental data

For each wire that was pull-tested, both the bond strength (BS) and failure mode (FM) were observed. Note that the term pull strength is used interchangeably with bond strength. The four general failure modes that were observed are listed below. Note that no attempt was made to distinguish between similar types of failures at the first or second bond.

0 - Metallization failure,
1 - Bond lift,
2 - Heel break, and
3 - Wire break (away from heel).

The observed BS depends on the strengths of the various components of the bond. Because only the weakest link is observed,

BS = minimum $\{Y_0, Y_1, Y_2, Y_3\}$, where (D-1)

Y_0 is the strength of the bond between the metallization and substrate,
Y_1 is the strength of the bond between the wire bond & the metallization,
Y_2 is the strength of the heel, and
Y_3 is the strength of the wire.

Figures D-1(a-d) through D-8 (a-d) indexed by material (6262ma, 6262sd, 4740ma, 4740sd, 5725ma, 5725sd, QM21ma, and QM21sd) and temperature (160°C, 180°C, 210°C, and 225°C), display the distributions of observed bond strength (with associated failure modes) as a function of time. For reference, the distributions of the bond strengths of the wires that were tested prior to aging (zero hours) are displayed in each figure.

Overall, the most common failure modes were modes 0, 1, and 2. Except at the pre-aged condition, failure mode 3 was relatively rare. Generally, for a given film/substrate material, the relative frequency of heel failures (FM = 2) was high initially and then decreased as the aging time increased. Conversely, the relative frequency of failures related to the metallization (FM = 0, FM = 1) increased as the aging time increased. The rate of change from a heel failure regime to a metallization failure regime depended on the aging temperature as well as the material combination. The higher the aging temperature, the more rapid the transition from one regime to another. In general, for a given material combination and aging temperature, there was a smooth decrease in the mean (or typical) bond strength along with a broadening of the variation in bond strength in time. There were a few inconsistencies in the data, however. For example, there was a number of apparent measurement anomalies at the 1200 hour measurement point. Figure D-1b. shows an unusual number of metallization failures (FM = 0), one at approximately 300 grams.

Also, in Figure D-2b, it is curious why at 1200 hours there is such a large number of metallization failures (FM = 0). Perhaps this is explained by the inability to distinguish metallization failures from bond lifts (FM = 1). With regard to Figure D-4d, it is also curious why there is such an abrupt change in the nature of the failures and the corresponding bond strengths from 300 hours to 400 hours at 225°C. These inconsistencies are problematic when attempting to model these particular data.

At aging temperatures of 160°C and 180°C, the degradation in the observed bond strength over time depended significantly on the material. At these temperatures, even at significant time exposures, heel breaks were the dominant failure modes for some materials (e.g., 6262ma and 4740ma--see Figures D-1a., D-3a., and D-3b.). For other materials, particularly those materials fired a single time on a dielectric substrate, the degradation was more severe, resulting in metallization-related failures even at relatively benign aging conditions (Figures D-2a, D-2b, and D-4b).

As expected, the effects of aging at the higher temperatures (210°C and 225°C) was more dramatic for all materials. In general, there was a clear increase in the frequency of metallization-related failures as the exposure time increases. Beyond several hundred hours of aging at these high temperatures, the bond strength is effectively determined by the strength of the metallization. Furthermore, the distributions of metallization strength decreased with increased aging to some steady state level which varied somewhat by material.

1.2 Data analysis

Ultimately, the objective in analyzing this aging data was to be able to estimate the reliability of a wire bond after it had been exposed to accumulated temperature environments that were consistent with its lifetime in a product. Prior to meeting this objective, however, one needs an understanding of the degradation in time of the strengths of each of the various bond components for each of the acceleration temperatures (in this case 160°C, 180°C, 210°C, and 225°C). With this in hand, it may be possible to develop an Arrhenius model for specific bond components which in turn can form the basis for estimating lifetime reliability by extrapolating to temperature environments that were not considered experimentally.

The general approach was to analyze the effects of aging on each interface/component separately. This was important because the effects of aging are likely to be different for the various interfaces/components as different aging mechanisms are expected to be involved. Unfortunately, each pull test yields complete information with respect to only a single interface/component. For example, the pull-testing of a single wire yielded the outcome {BS, FM}{Y, j}. In this case, the complete information relates only to interface/component j, that is,. $Y_j = Y$. Note, however, as seen in Equation D-1, one can also develop incomplete (or censored) information regarding the other failure modes, i.e., $Y_{k \neq j} \rangle Y$. With respect to the k^{th} interface/component (where $k \neq j$), the inherent strength of that wire bond component is said to be *right* censored at the value, Y.

For a particular material and an aging temperature/time, one can use a mixture of complete and incomplete information to characterize the distribution of the inherent strength of a particular interface/component. Obviously, complete information is more valuable than incomplete information in this regard. The degree to which a particular interface/component can be characterized depends on the relative amounts of the complete and incomplete data the total number of observations.

For example, with regard to aging at the two lower temperatures (160°C and 180°C), the predominate failure mode for some materials was the heel break (FM = 2). Thus, the distribution of the heel strength can be reasonably well characterized for these cases. Conversely, for these cases, it is difficult to characterize the strength distributions associated with the metallization interfaces (FM = 0, FM = 1) at the lower temperatures due to the lack of relevant complete information for these failure modes. At the two higher temperatures (particularly for the longer exposure times), the predominate failure modes were associated with metallization failures (FM = 0 and FM = 1). Thus, in these cases it is possible to characterize the strength distributions associated with the metallization interfaces.

Overall, there were few wire breaks (FM = 3). This is expected since the wire is presumably weakest where it is deformed (at the heel). Because this failure mode did not occur with much regularity (except at the pre-aged condition), one would suspect that the undeformed wire will not ultimately limit bond strength. Because of this and the lack of relevant complete data, no attempt was made to analyze the data specifically with respect to this failure mode.

Failure modes 0 and 1 were combined to form a single class because (1) failure modes 0 and 1 are hard to distinguish (see earlier note in Section 1.2), (2) both failure modes involve the metallization, and (3). the combination into a single class mitigates the difficulties with incomplete data. Thus, for the remainder of the analysis, we will consider only the heel strength (FM = 2) and the metallization strength (FM = 0 and FM = 1).

1.2.1 Modeling Specific to Aging Condition (Temperature/Time) and Material

In cases where all of the information is complete with respect to a particular failure mode for fixed aging condition and material, there are straightforward procedures that can be used to characterize the strength distribution for a particular interface/component. Because this was generally not the case here, less straightforward procedures were used. These procedures require the specification of a distributional form (e.g., normal, lognormal) before proceeding. Based on goodness-of-fit testing, the bond strength distributions for a fixed material, aging condition (i.e., time and temperature) and failure mode were found to be consistent with a normal probability model. That is,

$$\text{Prob}\{Y_j > W\} = \int_W^{\infty} \frac{1}{\sqrt{2\pi}\cdot\sigma} \cdot \exp\left\{-.5\cdot\left(\frac{z-\mu}{\sigma}\right)^2\right\} dz. \qquad \text{(D-2)}$$

Given this distributional form, PROC LIFEREG (Statistical Analysis System [SAS]) was used to estimate the model parameters (μ and σ) for each combination of material, aging condition, and failure mode class where there was sufficient complete data. Tables D-2 through D-8 provide the estimated model parameters (with associated standard errors) for each of these combinations.

The estimated mean strengths ($\hat{\mu}$) versus aging temperature and time are displayed in Figures D-9 through D-20, by material and failure mode class (heel and metallization). In general, the values of $\hat{\mu}$ yielded reasonably smooth patterns when plotted versus time for each temperature. This smoothness facilitated the modeling process. There were exceptions, however (e.g., see Figure D-11 [180°C, 3000 hours]). Consistent with the relative infrequency of metallization failures (FM = 0, FM = 1) for benign aging conditions, there was a scarcity of estimates of mean strength ($\hat{\mu}$) associated with metallization failures at these conditions (especially for the multi fired on alumina groups). This is in contrast to the estimates of mean strength associated with heel failures. For this class of failures, estimates of mean strength are generally available at all conditions, except the most accelerated aging conditions.

Note that the estimated mean bond strengths (conditional with respect to the failure mode) were plotted with respect to time on a log scale. This approximate linearity with respect to a log(time) scale was exploited to develop temperature-dependent kinetics models for each material and failure-mode class. Note that this approximate linearity holds until $\hat{\mu}$ becomes sufficiently small where it appears to converge with increasing exposure to some value greater than zero (say 150 grams in the case of metallization failures for 6262ma material). For example, with 6262sd material aged at 225°C (see Figure D-11), additional exposure beyond 600 hours did not seem to affect the metallization strength. In this particular case, aging at 225°C was continued well beyond 1200 hours to 2300 hours without further degradation in bond strength. With respect to the failures at the heel (FM = 2), a very slow reduction in the mean strength over time was apparent for the various materials. As in the case of metallization strength, the heel strength appears to converge with increasing exposure to a value greater than zero, in this case about 450 grams. It has been speculated that this is indicative of an annealing process within the aluminum wire. Because the wire is the same across all film/substrate combinations, one should expect that this asymptotic value should be consistent and independent of the film/substrate. Qualitatively (from Figures D-10, D-12, D-14, and D-16), this value appears to be consistent. While there was an obvious degradation of the heel strength with increasing exposure, it appears to be relatively benign when compared to the degradation of the metallization interface.

1.2.2 Modeling of Reaction Kinetics

To be useful for extrapolation to lower temperatures and thus be useful for estimating reliability over normal use conditions, it was necessary to consider a parametric model. The following model attributes were deemed reasonable and necessary. Suppose that $\mu(t,T)$ is the true (but unknown) average strength associated with a particular bond component (heel or metallization) at time, t, and temperature T. It would seem that $\mu(t,T)$ should be a smooth decreasing function in both t and T. Furthermore, $\alpha = \mu(t = \infty, T)$ should not depend on T. That is, when given enough exposure at any $T > 0$, the component strength should reach some common asymptotic limit, α. Furthermore, the data indicate that α is greater than zero.

A general model that meets these requirements and is often used in these types of situations is a model of the form,

$$\mu(t,T) = \alpha + \exp\{\beta_0 - \beta_1 \cdot K(T) \cdot t\} \qquad \text{(D-3)}$$

where

$K(T) = \exp\left\{-\beta_2 \cdot \left(\frac{1}{T}\right)\right\}$ defines the Arrhenius relation,

α, β_0, β_1, and β_2 are unknown parameters.

Some interpretation of these parameters is possible. As was mentioned earlier, α is the asymptotic limit of $\mu(t,T)$ with respect to infinite exposure. Prior to aging $(i.e., t = 0)$, $\mu(t = 0, T) = \alpha + \exp\{\beta_0\}$. β_1 is often referred to as the pre-exponential term. β_2 is related to the activation energy (E), where $\beta_2 = \frac{E}{\kappa}$ and κ is Boltzman's constant $\left(\kappa = 8.616 \times 10^5 ev \cdot \deg^{-1}\right)$.

As mentioned earlier in section 1.2.1, the estimated mean bond strengths (conditional with respect to the failure mode) were empirically found to be approximately linear with log(time). Thus, the standard kinetics model (equation D-3) was modified to account for this behavior. That is t was replaced with $\log(t+1)$, so that

$$\mu(t,T) = \alpha + \exp\{\beta_0 - \beta_1 \cdot K(T) \cdot \log(t+1)\} \qquad \text{(D-4)}$$

Note that $t+1$ was used to avoid the singularity of $\log(t)$ at $t = 0$. Also, to stabilize the computational procedure used to estimate the model parameters, a modification of K(T) was used. That is, $K(T) = \exp\left\{-\beta_2 \cdot \left(\frac{1}{T} - \frac{1}{T_0}\right)\right\}$, where $T_0 = 498$. Note that reparameterization only affects the pre-exponential rate term, β_1 This model form was used to compactly summarize the experimental results and form the basis for estimating reliability.

The strategy used for estimating the model parameters was as follows.

1. By inspection, estimate α.
2. Check that $\log(K(T))$ is approximately linear with respect to T^{-1}. For each material, estimate $K(T)$ point-by-point for each temperature (without assuming the T^{-1} form of the relationship). That is, estimate the parameters $\beta_0, \beta_1, \gamma_1, \gamma_2, \cdots, \gamma_p$ by weighted linear regression, where the goal is to find the set of model parameters that minimize the sum of the squared weighted deviations,

$$W \cdot \left\{ \log\{\mu(t,T) - \alpha\} - \left\{ \beta_0 - \gamma_1 \left(I_{T_1}\right) \log(t) - \gamma_2 \left(I_{T_2}\right) \log(t) - \cdots - \gamma_p \left(I_{T_p}\right) \log(t) \right\} \right\}^2$$

over the relevant observations. The weights, W, were derived from the error in $\hat{\mu}$, $(i.e., \hat{s}_{\hat{m}})$ given in Tables D-2 through D-9. The indicator variables, I_{T_i}, take the following values: 1 if the observation is associated with temperature, T_i, otherwise 0. Then, plotting $\log(\gamma_i)$ versus T^{-1} reveals the form of K(T).

3. Next, given that the model form for K(T) looks good, use weighted nonlinear regression conditioned on a value for α (PROC NLIN [SAS]) to estimate the other parameters $(\beta_0, \beta_1, \beta_2)$ in Equation D4. Without the conditioning on α, the nonlinear regression procedure fails to converge due to the strong correlation among α, β_0, and β_1. Estimates of the parameters used to start the iterative nonlinear procedure were obtained from analysis of the results from the previous step.

To illustrate the strategy, consider the case of metallization failure (FM = {0, 1}) of the 6262ma material. By inspection, α is set to 100 (see Figure D-9). Figure D-21 displays the relationship between $\log(\hat{\gamma}_i)$ and T^{-1} with $\alpha = 100$. The Xs represent the estimates of $\log(\gamma_i)$, and the vertical lines describe approximate 70% confidence intervals for each $\log(\gamma_i)$. Since K(T) appears to be reasonably linear with T^{-1} given $\alpha = 100$, the form of Equation D4 was accepted and the remaining parameters in Equation D4 $(\beta_0, \beta_1, and \beta_2)$ were estimated by using nonlinear regression (Table D-10. Note that other values for were considered. Given the uncertainty in the data, values of α between 50 and 150 worked about as well in producing a linear relationship between $\log(\hat{\gamma}_i)$ [given α] and T^{-1}. Perhaps with more reliable estimates spread out in time, it would have been possible to simultaneously estimate all of the parameters in Equation (D4), including α. As it turns out, conditioning on a different value of (for example 50 or 150) has relatively little effect on the resulting reliability estimates given in Section 1.2.4.

The estimates of μ are used to model the deterministic portion of the metallization strength. Thus, these models produce a single point estimate of the bond component strength given a

particular exposure time and temperature. These estimates represent the typical performance expected within the population of bonds.

It is difficult (if not impossible) to differentiate between measurement error and bond-to-bond strength variation due to the nature of the destructive testing. By assuming negligible measurement error, σ represents the magnitude of bond-to-bond variation present in the population. This, in a sense, is the stochastic portion of the metallization strength. To discuss the distribution of bond component strength, both the *deterministic* and *stochastic* portions need to be considered.

In the case of the 6262ma material, an estimate of the deterministic portion of metallization strength is

$$\hat{\mu}_M(t,T) = 100 + \exp\left\{8.916 - .560 \cdot \exp\left(-2706 \cdot \left(\frac{1}{T} - \frac{1}{T_0}\right)\right) \cdot \log(t+1)\right\},$$

where the M subscript refers specifically to metallization. Note that in Table D-2, the estimates of σ are relatively consistent across the various exposure conditions. A good overall estimate of the variation about $\hat{\mu}_M(t,T)$ is $\hat{\sigma}_M(t,T) = 46 grams$. [Note that for other materials, σ clearly depends on t. For these cases, one would not want to assume that σ is constant]. Furthermore, as was mentioned earlier (Section 1.3.1), the variation of the experimental data within a given exposure condition is consistent with a normal distribution. Thus, the estimated distribution of metallization strength as a function of exposure time and temperature is

$$\hat{\Pr}ob\{Y_M \geq W\} = \int_W^\infty \frac{1}{\sqrt{2\pi} \cdot \hat{\sigma}_M(t,T)} \cdot \exp\left\{-.5 \cdot \left(\frac{z - \hat{\mu}_{M(t,T)}}{\hat{\sigma}_M(t,T)}\right)^2\right\} dz. \qquad \text{(D5)}$$

An approximation for this integral may be obtained by computing $Q = \dfrac{W - \hat{\mu}_M(t,T)}{\hat{\sigma}_M(t,T)}$ and then entering a table for the standard normal distribution to obtain $\Pr ob\{Z > Q\} \approx \hat{\Pr} ob\{Y_M \geq W\}$, where Z is the standard normal variate. An alternative approximation (see *Handbook of Mathematical Functions*, by Abramowitz and Stegun, National Bureau of Standards Applied Mathematics Series #55, 1972) can be obtained as follows:

1. $c_1 \leftarrow .196854$
2. $c_2 \leftarrow .115194$
3. $c_3 \leftarrow .000344$
4. $c_4 \leftarrow .019527$

5*a*: If $Q \geq 0$: $\text{Prob}\{Z > Q\} \leftarrow \dfrac{.5}{\left(1 + c_1 \cdot Q + c_2 \cdot Q^2 + c_3 \cdot Q3 + c_4 \cdot Q^4\right)^4}$

5*b*: If $Q \leq 0$: $\text{Prob}\{Z > Q\} \leftarrow 1 - \dfrac{.5}{\left(1 - c_1 \cdot Q + c_2 \cdot Q^2 - c_3 \cdot Q3 + c_4 \cdot Q^4\right)^4}$

It is important to point out that if metallization failures dominate, then Equation D5 (and its approximation) can be used as the basis for deriving an estimate for the reliability of the wire bond (see 1.3.4) given exposure at temperature, T, for time, t.

1.2.3 Modeling Overall Bond Strength by Combining Individual Failure Mode Models

Given the two classes of failure modes, the overall (observed) bond strength is BS = minimum $\{Y_M, Y_H\}$. Thus, a model of the overall bond strength will necessarily involve models for metallization strength and heel strength. The model for metallization strength of 6262ma material is given in the preceding section. A similar modeling strategy resulted in the following model, which is specific to the heel strength of 6262ma material (see Table D-10). That is,

$$\hat{P}\text{rob}\{Y_H \geq W\} = \int_W^{\infty} \frac{1}{\sqrt{2\pi} \cdot \hat{\sigma}_H(t,T)} \cdot \exp\left\{-.5 \cdot \left(\frac{z - \hat{\mu}_H(t,T)}{\hat{\sigma}_H(t,T)}\right)^2\right\} dz, \text{ where}$$

$$\hat{\mu}_H(t,T) = 450 + \exp\left\{4.69 - .376 \cdot \exp\left(-6354 \cdot \left(\frac{1}{T} - \frac{1}{T_0}\right)\right) \cdot \log(t+1)\right\}, \text{ and}$$

$\hat{\sigma}_H(t,T) = 25$ grams.

One can develop a convolution integral that gives the estimated distribution of the overall bond strength. However, there is neither an analytical expression for this integral nor relevant tabled approximations. Given that Y_M and Y_H are assumed to be independent normal random variables, simulations can be used to approximate the distribution of BS. In general, the (100) th percentile of BS, is that value of W such that $\text{Prob}\{BS(T,t) > W\} = 1 - \rho$. Figure D-22 provides estimates of selected percentiles (10^{th}, 50^{th}, and 90^{th}) of the distribution of BS for various exposure conditions in the case of 6262ma material. Figure D-23 summarizes the results of 30 independent samples from the estimated overall bond-strength model for 6262ma material at each of seven exposure times at 210°C. These simulated results can be directly compared with the experimental results in Figure D-1c.

1.2.4 Reliability/Unreliability Estimates Derived From Kinetics Modeling

Prior to developing reliability estimates, it is necessary to define reliability. For purposes of discussion here, the reliability (R) of a wire bond (conditional on some specified aging environment [T, t]) is the probability that the bond strength meets or exceeds some strength requirement, S. That is,

$$R(T,t) = \text{Prob}\{BS(T,t) \geq S\} \tag{D6}$$

A model for overall bond strength (such as given in the previous section) provides a general mechanism for estimating reliability using simulations. This mechanism was used to estimate the unreliability $(1-R)$ of wire bonds associated with the 6262ma material. Figure D-24 illustrates the resultant estimated unreliability (assuming a 500 gram requirement) as a function of exposure time at 125°C for the 6262ma material. Each point in time in Figure D-24 is based on 10,000 independent simulations of the models for Y_M and Y_H specific for the 6262ma material (see the model parameter estimates in Table D-10). The estimated unreliability is the fraction of the simulations that resulted in an overall bond strength of less than 500 grams. The fact that the points do not fall on a smooth curve (superimposed) is symptomatic of simulation error. Note that the early increase in unreliability (from 0 hours to 1000 hours) is indicative of the annealing process.

In cases where the probability of a heel failure greatly dominates the probability of a metallization failure (or vice versa), one can use a simpler approach to estimate reliability/unreliability. In cases where heel failures dominate,

$$\hat{R}(T,t) \approx \hat{P}\text{rob}\{Y_H \geq S\}. \tag{D7}$$

Conversely, when metallization failures dominate,

$$\hat{R}(T,t) \approx \hat{P}\text{rob}\{Y_M \geq S\}. \tag{D8}$$

Furthermore, in these cases it is relatively straightforward to develop approximate confidence limits for reliability by using a parametric bootstrap procedure [3]. The parametric bootstrap procedure assumes that the model form is correct and utilizes the error magnitudes/correlations among the model parameter estimates as the basis for generating confidence limits. Such confidence limits are developed by constructing N simulated sets of the model parameters that are obtained by perturbing the original model parameter estimates with random normal errors generated using the magnitudes and correlations that are given in Table D-10. Associated with each of the N sets of simulated model parameters, $\{\beta_0, \beta_1, \beta_2\}_i$ is a single value for reliability, R_i. Suppose that these values of reliability are ranked from lowest to highest resulting in $\{R_{(1)}, R_{(2)} \ldots, R_{(N)}\}$. An approximate $\frac{N-k_L}{N} \times 100\%$ lower confidence limit for R is $R_{(k_L)}$.

Similarly, an approximate $\frac{k_U}{N} \times 100\%$ upper confidence limit for R is $R_{(k_U)}$. By choosing appropriate values for k_L and $k_{(U)}$ given N, one can construct approximate confidence interval for R given any specified confidence level.

To illustrate the case where Equation D7 is appropriate (heel failures dominate), consider Figure D-25, which indicates the estimated bond unreliability $(1-R)$ in the case of 6262ma material exposed to a 125°C environment. For this example, the bond strength requirement, S, is assumed to be 450 grams. The solid circles in Figure D-25 represent the estimated unreliability, while the open circles represent upper and lower 95% confidence limits for the unreliability. That is, based on the experimental data and assuming that the model form is correct, we have 95% confidence that the true unreliability is below the upper limit. These estimated confidence limits were based on a simulation size of N = 1000 for each point in time. The fact that the curves denoting the confidence limits are not strictly nondecreasing functions and somewhat noisy is an artifact of the simulation error.

To illustrate the case where Equation D8 is appropriate (metallization failures dominate), consider Figure D-26 which gives $\log_{10}\left(1-\hat{R}\right)$ in the case of 6262ma material exposed to a 180°C environment with S300 grams. Here, especially for the longer exposure times, it would be extremely unlikely that the overall bond strength would be limited by something other than a metallization failure. As in Figure D-25, the solid circles represent the $\log_{10}\left(1-\hat{R}\right)$ while the open circles represent upper and lower 95% confidence limits for log(unreliability). Note the relatively wide limits.

Finally, note that in cases where the unreliability is significantly affected by both heel and metallization failures, it is more difficult to estimate upper and lower bounds for unreliability due to the increased computations required (see the complications discussed in Section 1.2.3) Nevertheless, one could easily adapt the bootstrap procedure (described earlier) to obtain estimates of the upper and lower bounds for this case.

1.3 Summary of Aging Characteristics by Material

The previous sections have dealt primarily with the methodology that was used to estimate reliability. This section is more descriptive in nature, focusing on a comparison between the different material combinations, using Figures D-9 through D-20 as a basis.

First, with respect to heel strength (FM = 2), the materials made with silver (6262) and silver/1% platinum (4740) thick films exhibit similar degradation patterns (as well they should because the same wire material was used in all cases). In these cases, the strength of the bond at the heel degrades to approximately 450 to 500 grams with increased exposure. Due to the relatively

infrequent nature of heel breaks for the other two material types (gold and palladium/silver films), it was not possible to model the heel strength degradation for these cases.

In general, as shown in Figures D-9 through D-20, susceptibility to metallization failures is reduced when the thick-film materials were multi-fired on alumina as opposed to single-fired on dielectric. The following are some specific comments regarding each thick film.

- 6262ma(sd)/s D-9 and D-11 - For these materials, there is a clear and systematic dependence of mean bond strength on time and temperature. In both of these cases, the modeling procedures described in earlier sections can provide reasonable estimates of reliability.
- 4740ma(sd)/Figures D-13 and D-15 - Compared with all of the different materials tested, the 4740ma material is clearly the least susceptible to metallization failures. Significant numbers of metallization failures were observed only at the two highest temperatures (210°C and 225°C). Thus, the deviations from linearity regarding the relationship of $\log(K(T))$ versus T^{-1} could not be assessed. With respect to the 4740sd material, the large drop in mean metallization strength from 300 to 400 hours is inconsistent with the smooth nature of the kinetics model given in Equation D4. Thus, no model is developed for this case.
- 5725ma(sd)/Figures D-17 and D-18 - Compared with the materials fabricated with silver (6262) and silver/platinum (4740) thick films, the materials made with gold films (5725) are much more susceptible to metallization failures, even prior to aging (note in the case of QM21sd material the relatively low metallization strength prior to aging). At the relatively mild accelerating temperature of 160°C, significant and relatively rapid degradation in the metallization strength was observed. If kinetics models were to be developed for these materials (they weren't here), one would choose an asymptotic limit, α (see Equation 4), close to zero because there does not appear to be as much residual metallization strength in these materials when compared to the other materials.
- QM21ma(sd)/ Figures D-19 and D-20 - Like those materials made with gold film, the materials made with palladium/silver film exhibit relatively low metallization strengths prior to aging. However, the metallization strengths of the QM21 materials do not degrade nearly as rapidly as the materials with gold films. Note that kinetics models were not developed for these QM21 materials.

1.5 Temperature Cycling

The vast majority of aging was conducted at isothermal conditions. A very limited amount of additional testing, utilizing temperature cycling, was performed with specimens from the 6262ma, 6262sd, 4740ma, and 4740sd groups. For these experiments, a temperature cycle consisted of (1) a 30 minute dwell at -50°C, (2) a 90 minute ramp to +160°C, (3). a 30 minute dwell at +160°C, and (4) a 90 minute ramp to -50°C. The total cycle time was 240 minutes. After various numbers of cycles had been completed (250, 500, 750, and 1000), 10 specimens

were pull tested from each group. Note that no measurements were made on specimens from the 6262sd group at 1000 cycles.

It is interesting to compare the results at 1000 cycles (750 cycles in the case of the 6262sd group) with observations of isothermal aging at 160°C. For example, at 1000 cycles the ten specimens from the 6262ma group all failed using mode 1 (bond lift) with an average pull strength of approximately 370 grams. Note that after 8260 hours at 180°C isothermal storage, the average bond strength associated with FM's 0 and 1 (combined) is 486 grams (see Table D-2). Thus, 1000 cycles (involving 4000 hours at or below 160°C) is much more degrading than 8260 hours at 180°C. Clearly, temperature cycling stimulates an important failure mechanism that is not exercised during isothermal testing (note that similar conclusions can be developed by using the experimental data from the other thick film materials). Presumably this mechanism is related to the mismatch of the temperature expansion coefficients of (1) the substrate, (2) the thick film, and (3) the wire. Thus, it is inappropriate to use the isothermal bond strength model (even if weighted appropriately with respect to the variable temperature levels) as a basis for predicting the reliability of bonds that are exposed to nonisothermal conditions such as would be expected in the vicinity of the engine block of an automobile.

1.5 Conclusions/Future Activities

Based on the experimental data, bond strength is primarily limited by the heel strength and the metallization strength. The heel strength is the primary limitation in the case of benign environments, while the metallization strength is the primary limitation in the case of severe environments. The rate of transition from failures at the heel to failures at the metallization is material dependent. The bonds on multi-fired alumina films appear to be significantly stronger than those on single-fired over dielectric films. The bonds associated with silver and silver/platinum films appear to be much more resistant to metallization failures than the bonds associated with gold and palladium/silver films.

Kinetics models were used to synthesize the experimental data over the various exposure temperatures for the 6262ma material. These models differ from classical rate models in that there is a log(time) dependence. One might speculate that this log-dependence is due to a situation where the reactants are being consumed relatively quickly or that reaction products might be inhibiting further reaction. Also, there are other interpretations which are consistent with linear degradation in log(time). These models can be exercised in various ways to produce estimates of reliability. Several examples of what can be done with these model have been provided. However, it should be emphasized that there are limitations of the kinetics models and related estimates of reliability. The estimates of reliability are necessarily model-based due to the fact that they are extrapolated under other than the experimental conditions. Furthermore, the quality of the reliability estimates depends not only on the quality of the experimental data, but also on the quality of the models, which are simply approximations of the observed data. If it is assumed that the model forms are correct and that the errors reside strictly in the parameter estimates, then the estimates of uncertainty are valid. Finally, as was discussed in section 1.5

these kinetics models appear to be valid for only the case of isothermal aging and thus are inappropriate for predicting reliability in a nonisothermal environment.

---

[1] Memo to Steve Garrett from Ed Thomas dated May 23, 1996, titled "Modeling of Wire Bond Failure Data
[2] Memo to Steve Garrett from Ed Thomas dated April 11, 1994 titled "Analysis of Initial Wire Bond Data"
[3] *An Introduction to the Bootstrap*, by Efron and Tibshirani, Chapman and Hall Publishers, 1993, pp. 53-56

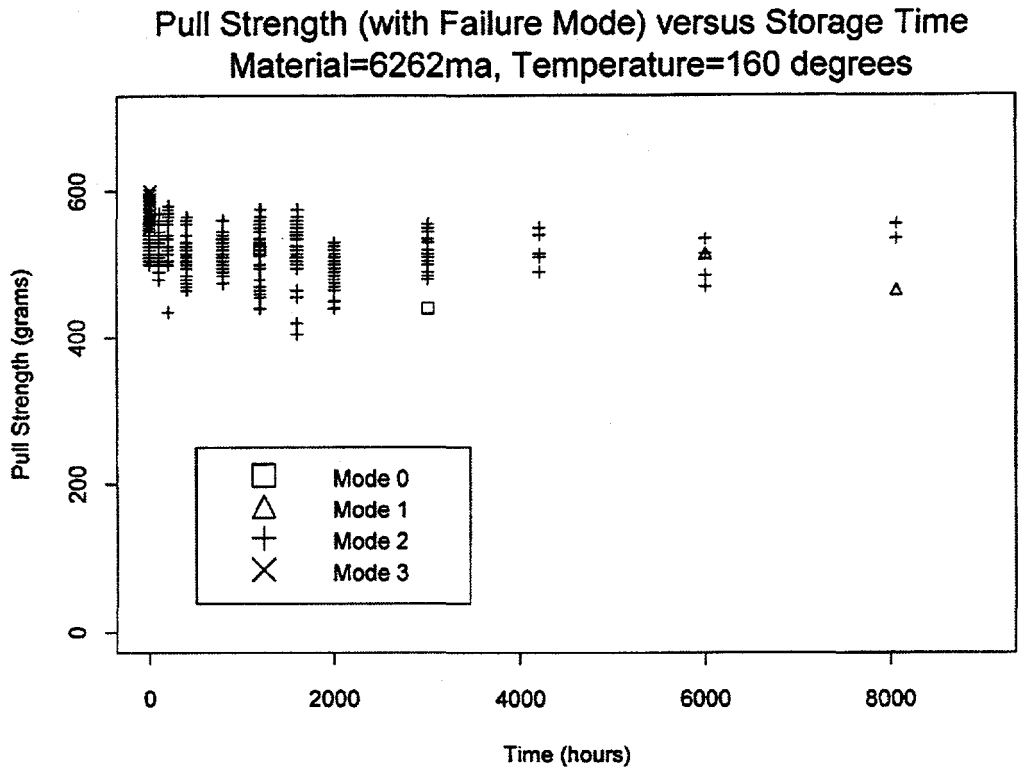

Figure D-1a

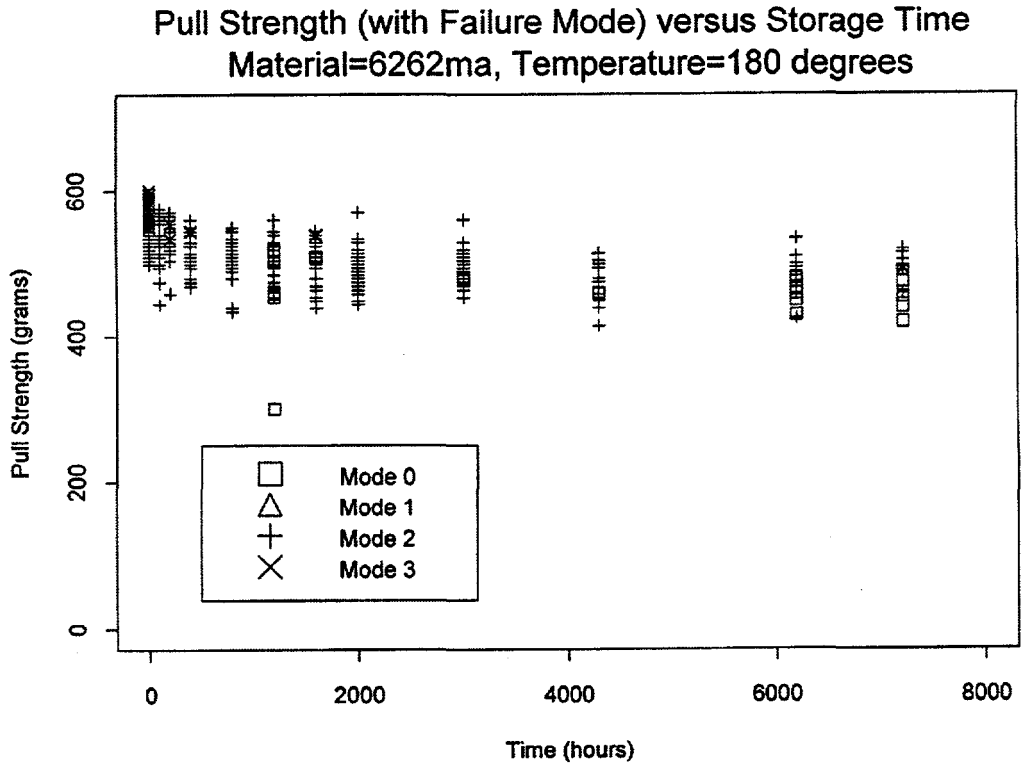

Figure D-1b

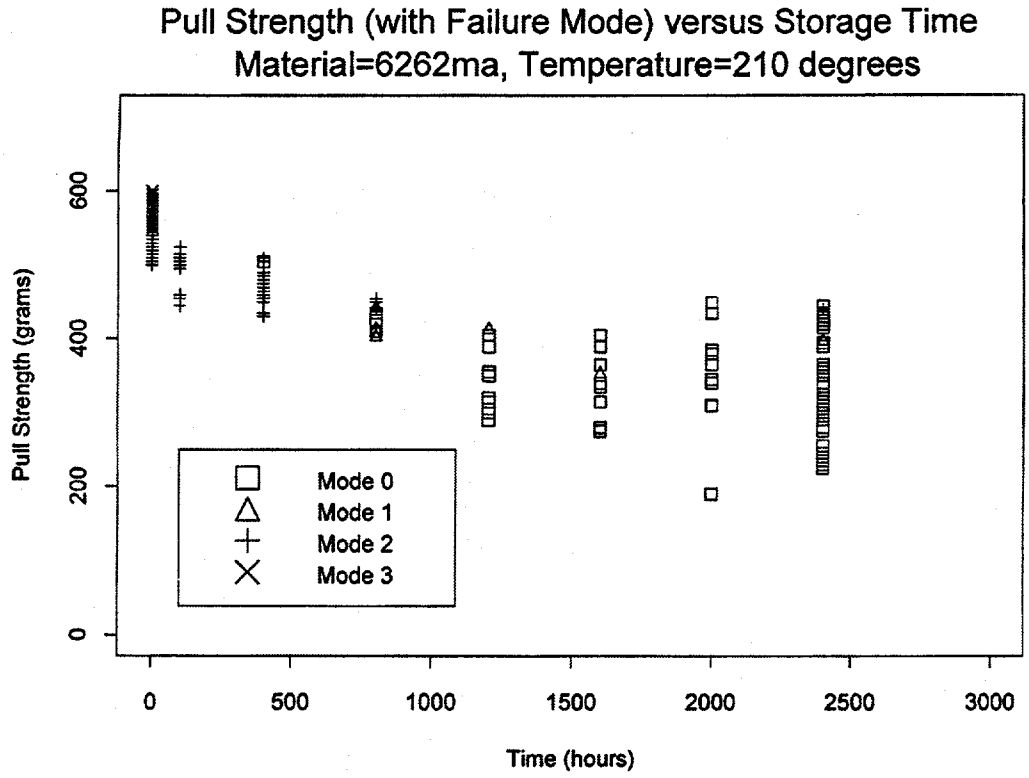

Figure D-1c

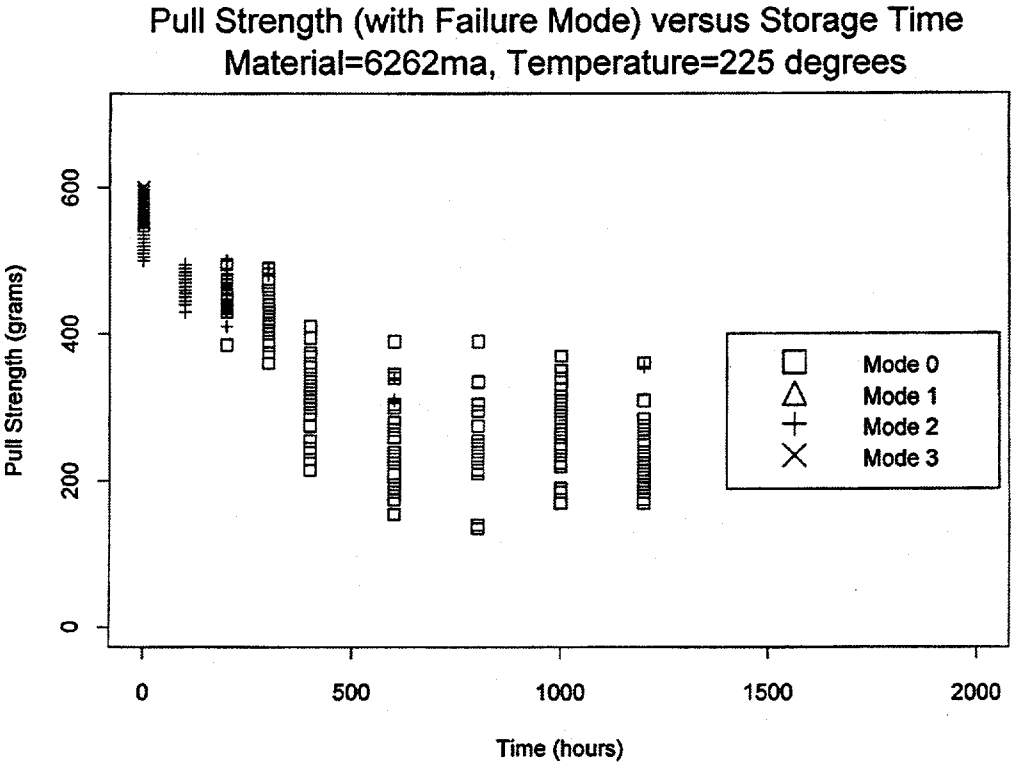

Figure D-1d

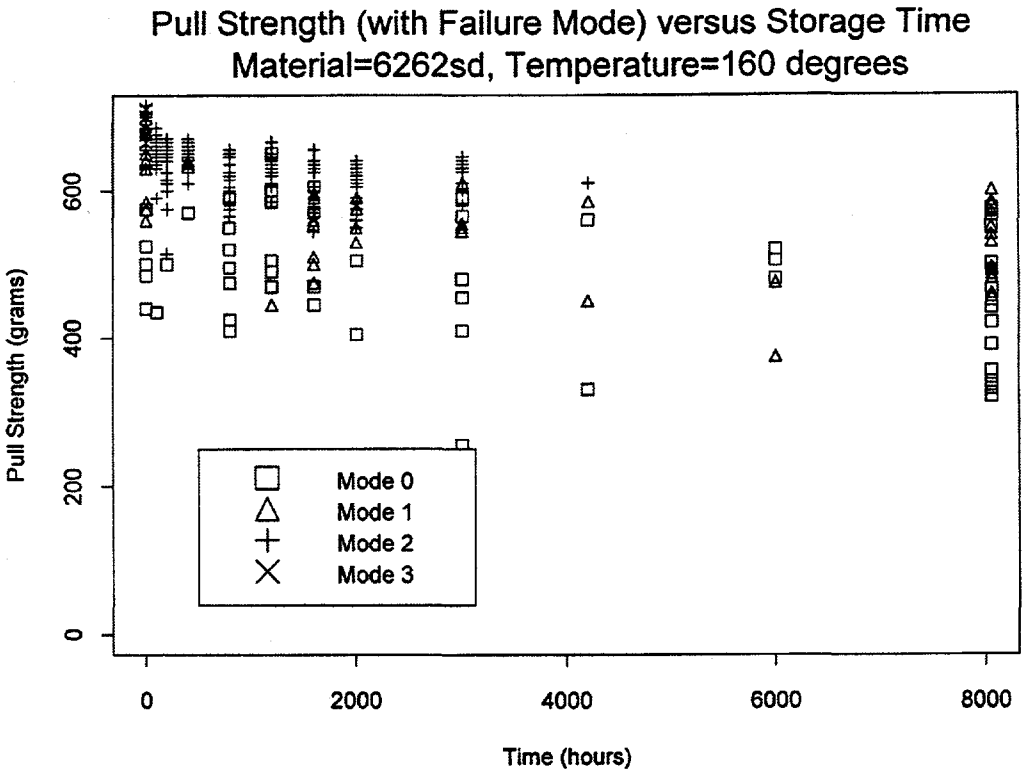

Figure D-2a

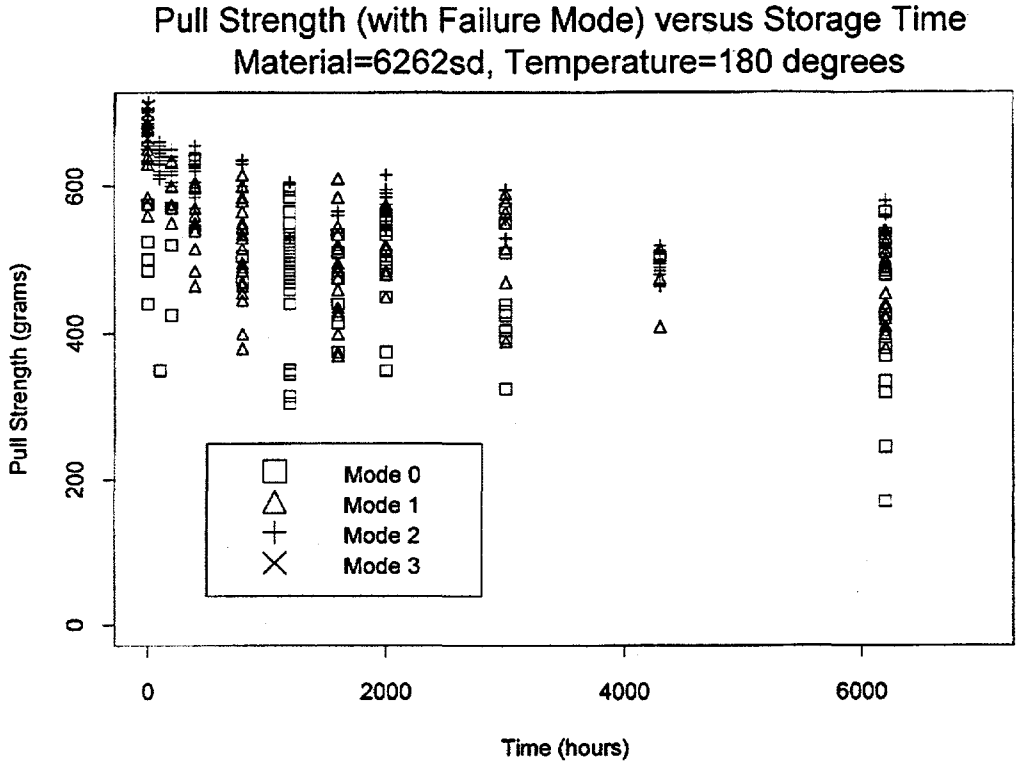

Figure D-2b

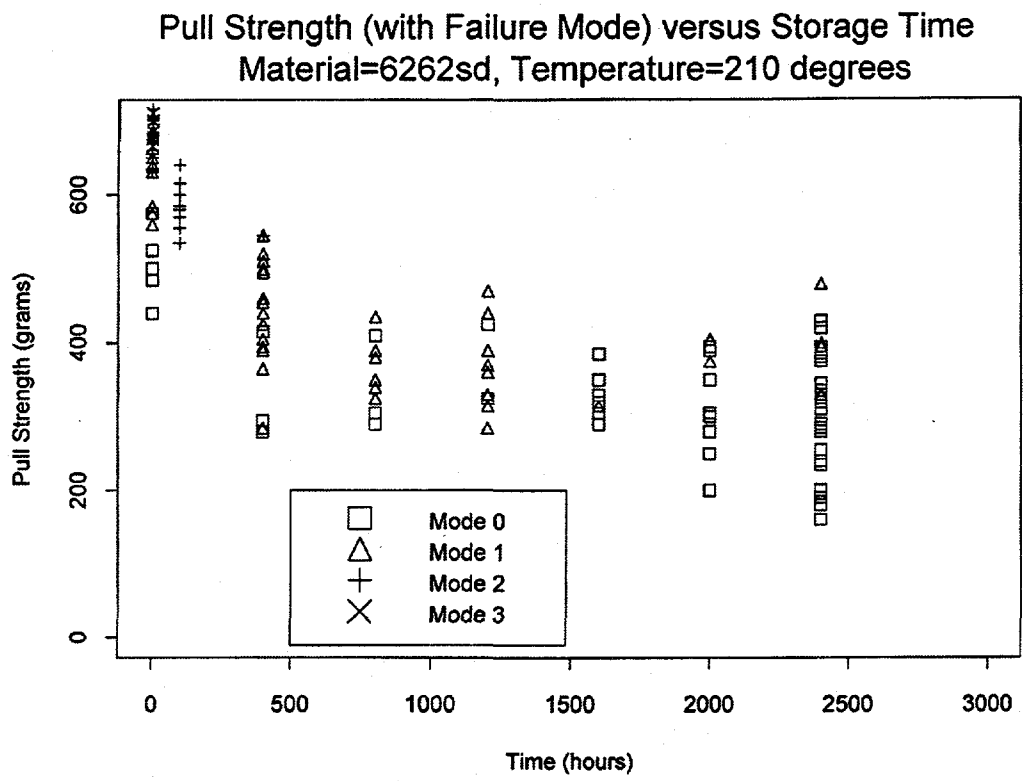

Figure D-2c

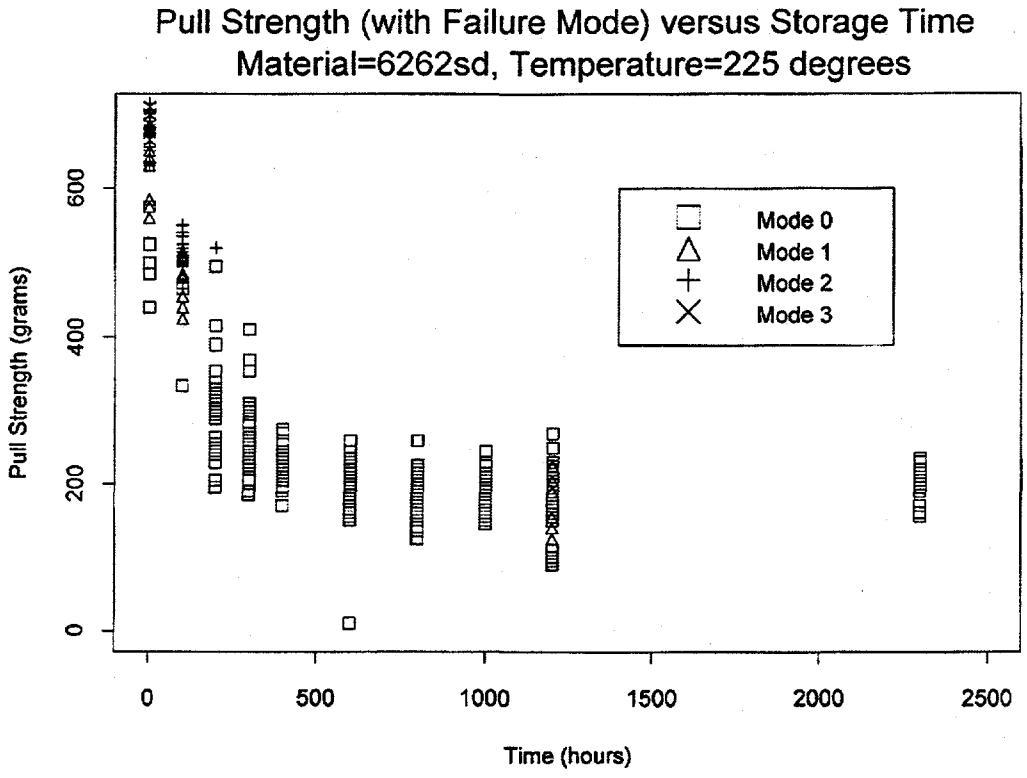

Figure D-2d

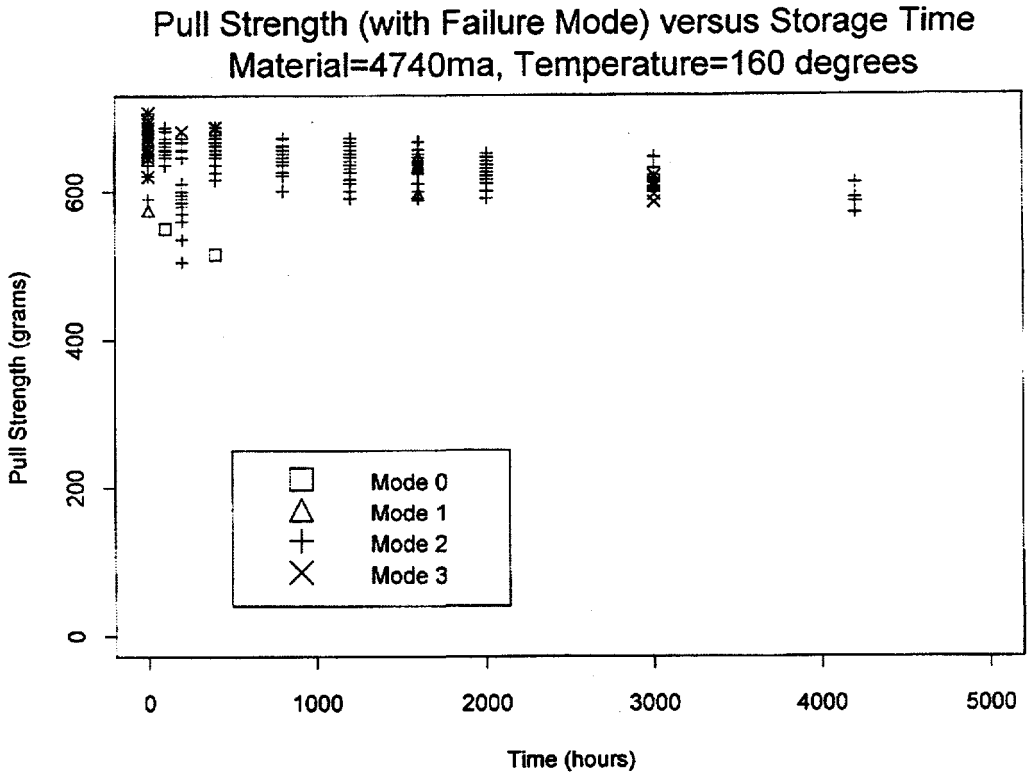

Figure D-3a

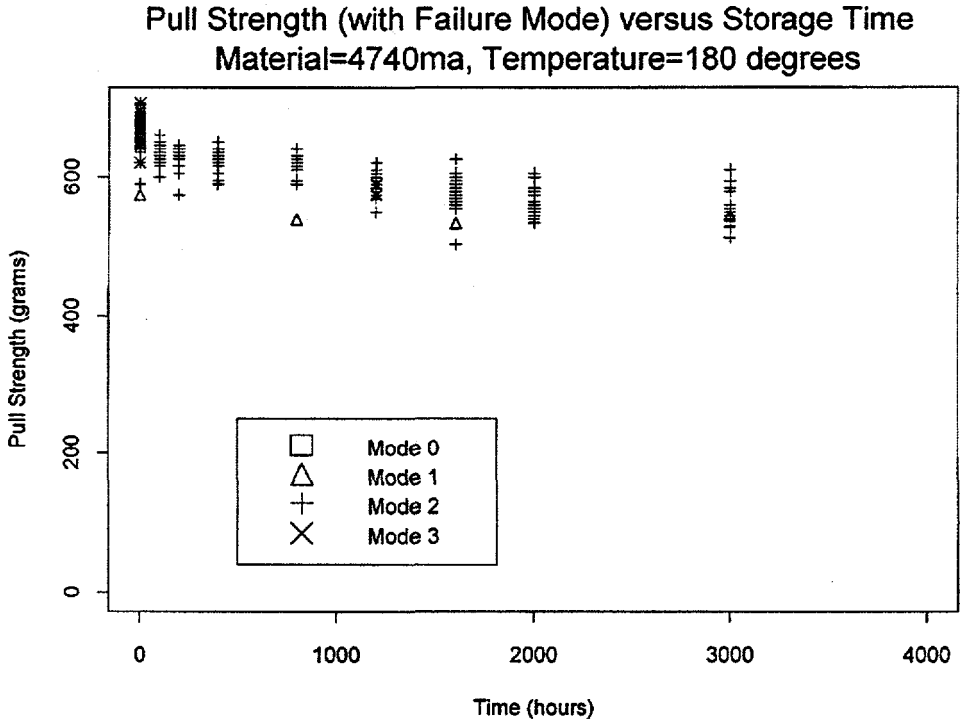

Figure D-3b

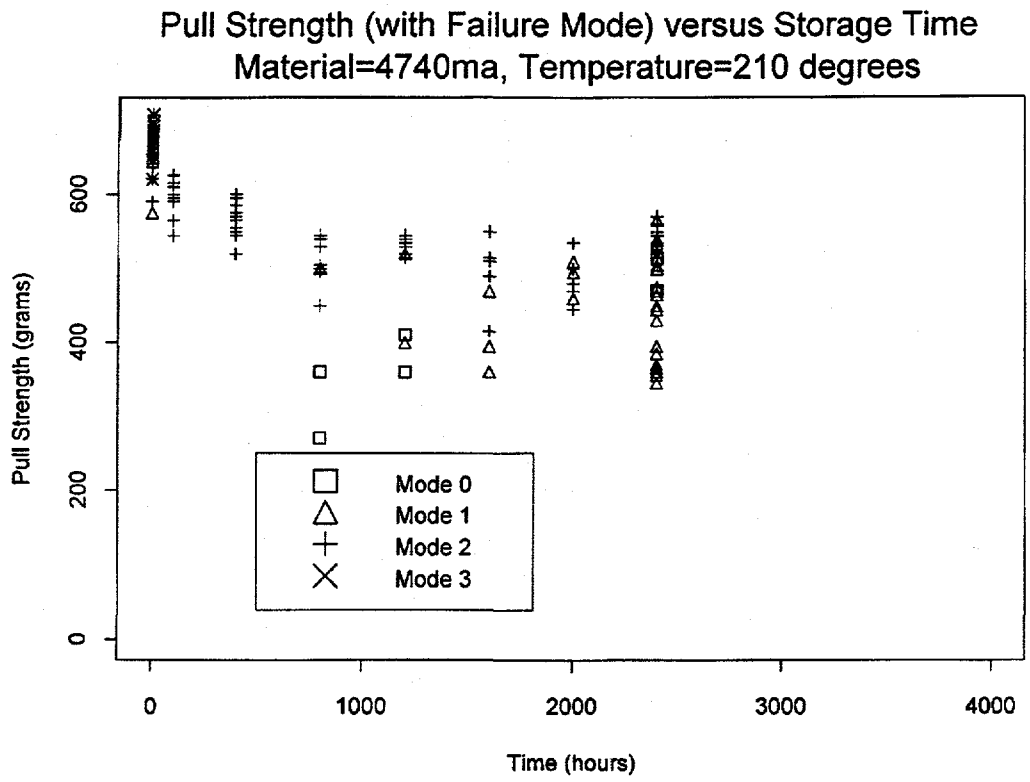

Figure D-3c

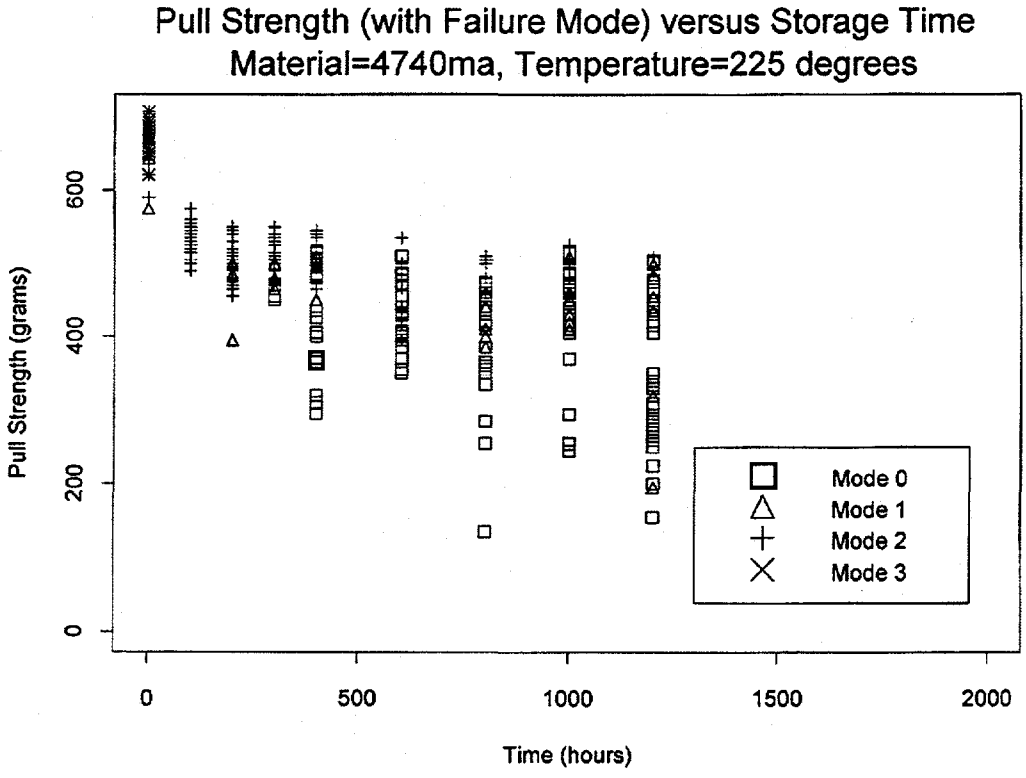

Figure D-3d

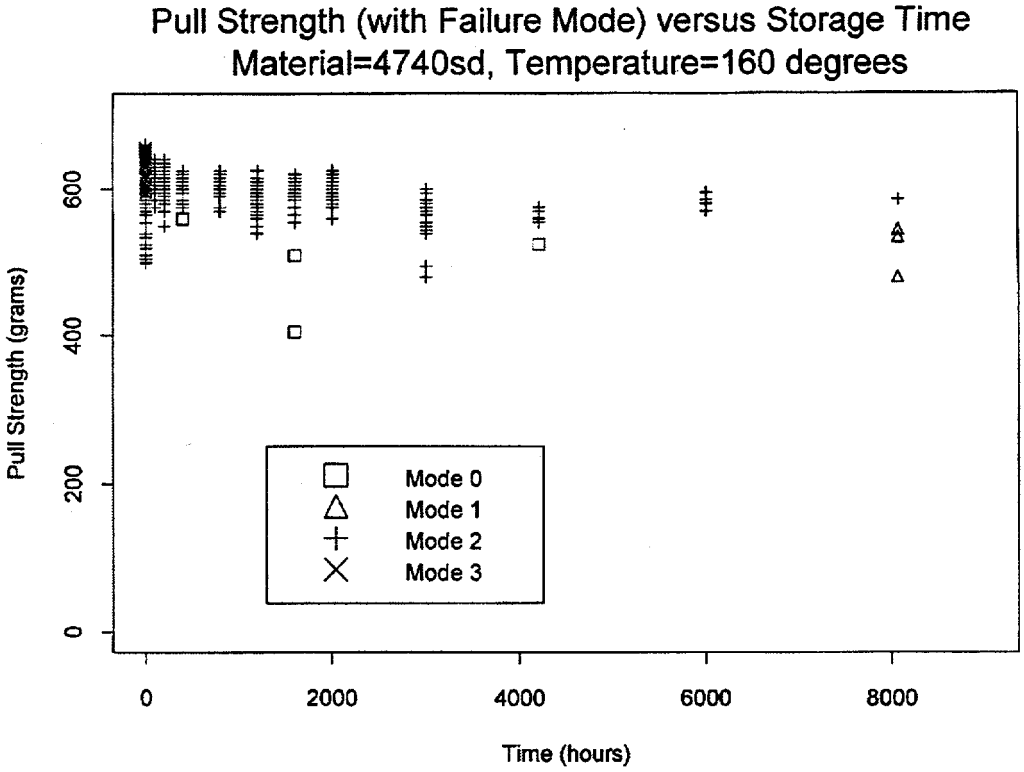

Figure D-4a

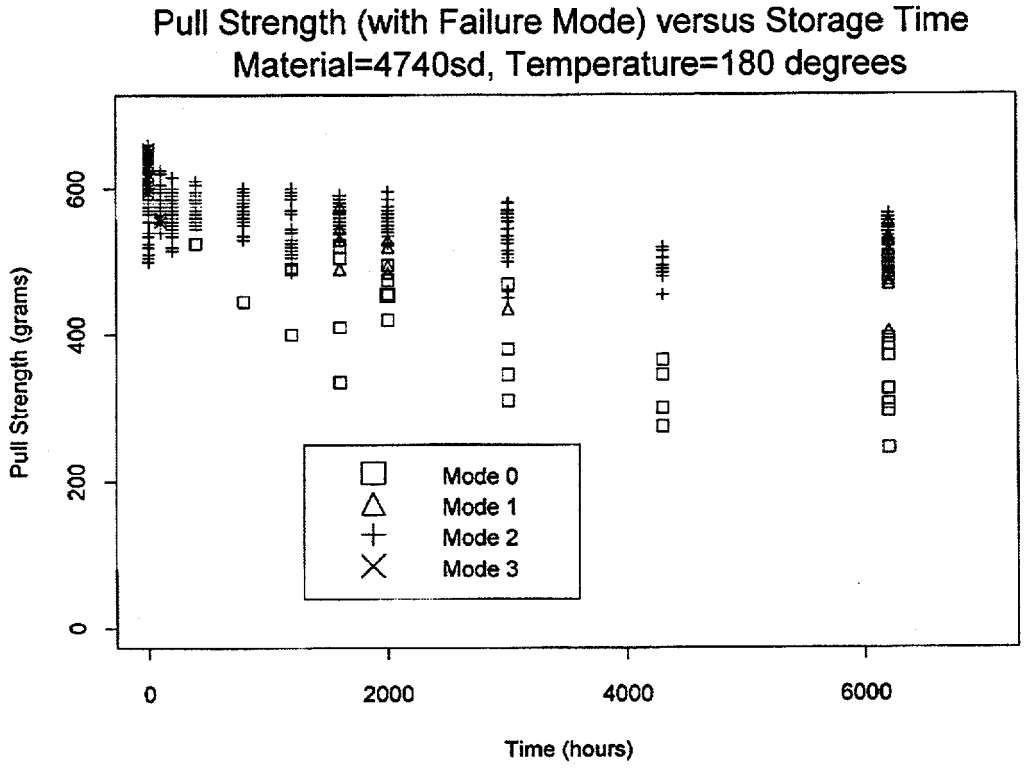

Figure D-4b

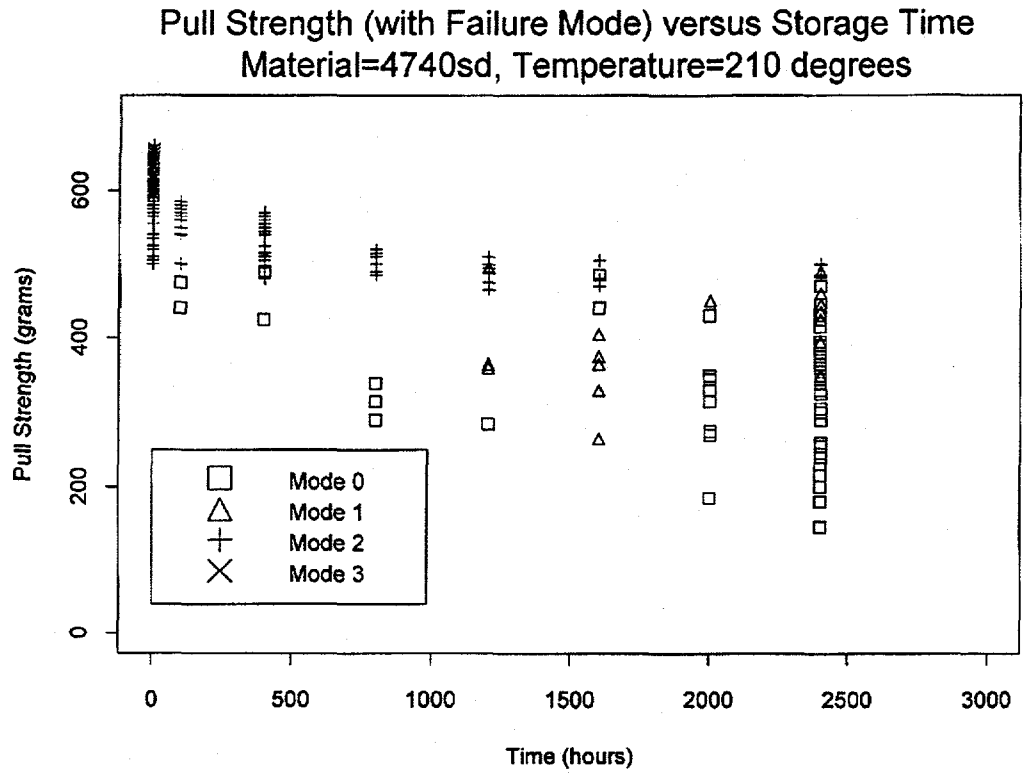

Figure D-4c

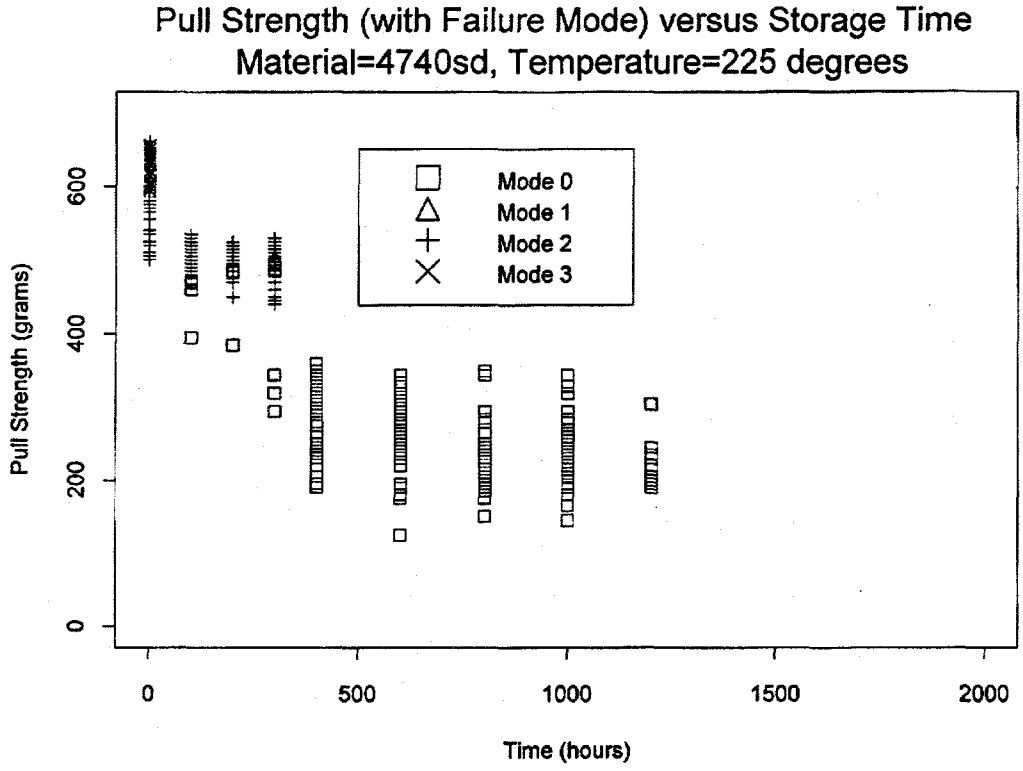

Figure D-4d

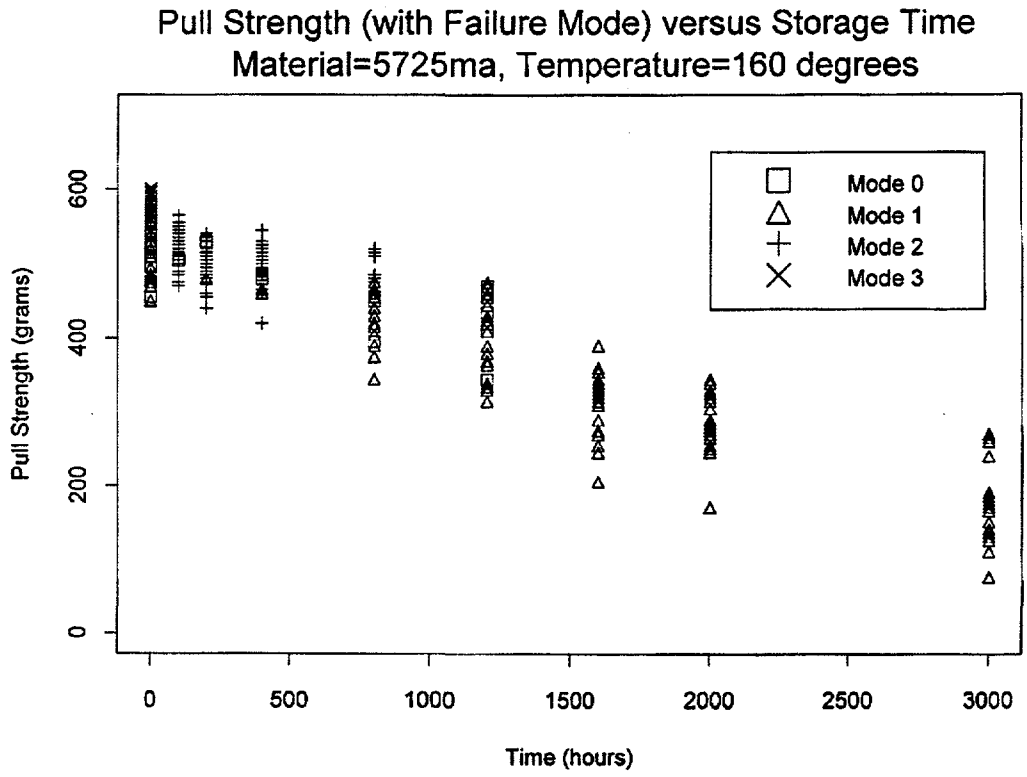

Figure D-5a

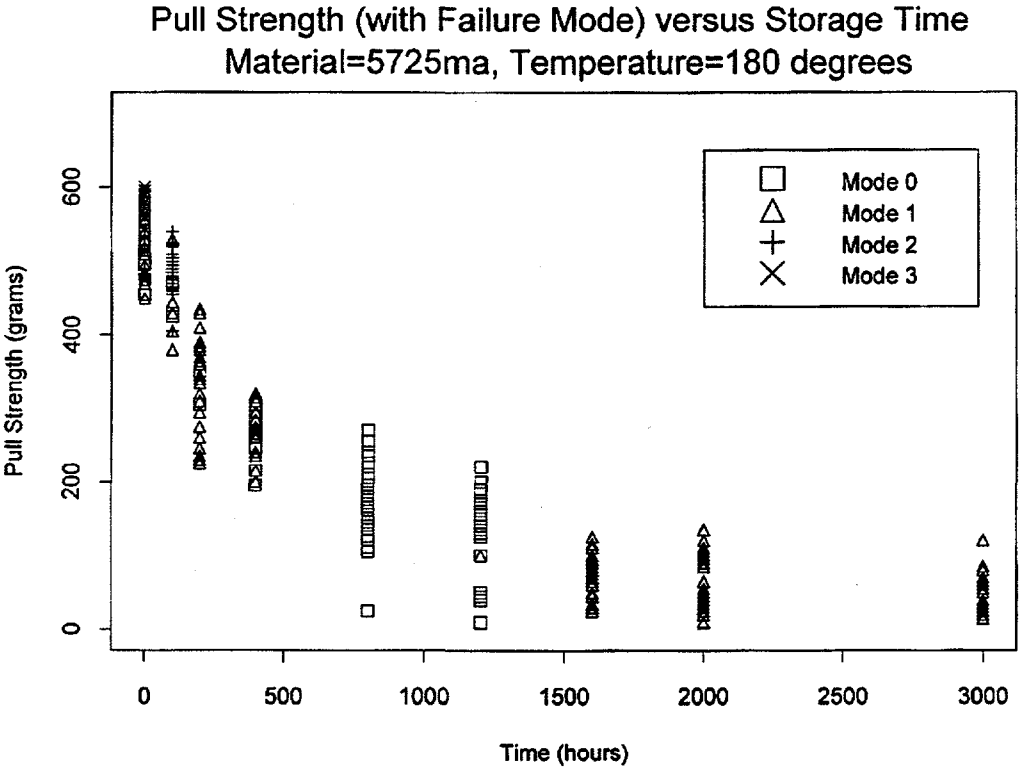

Figure D-5b

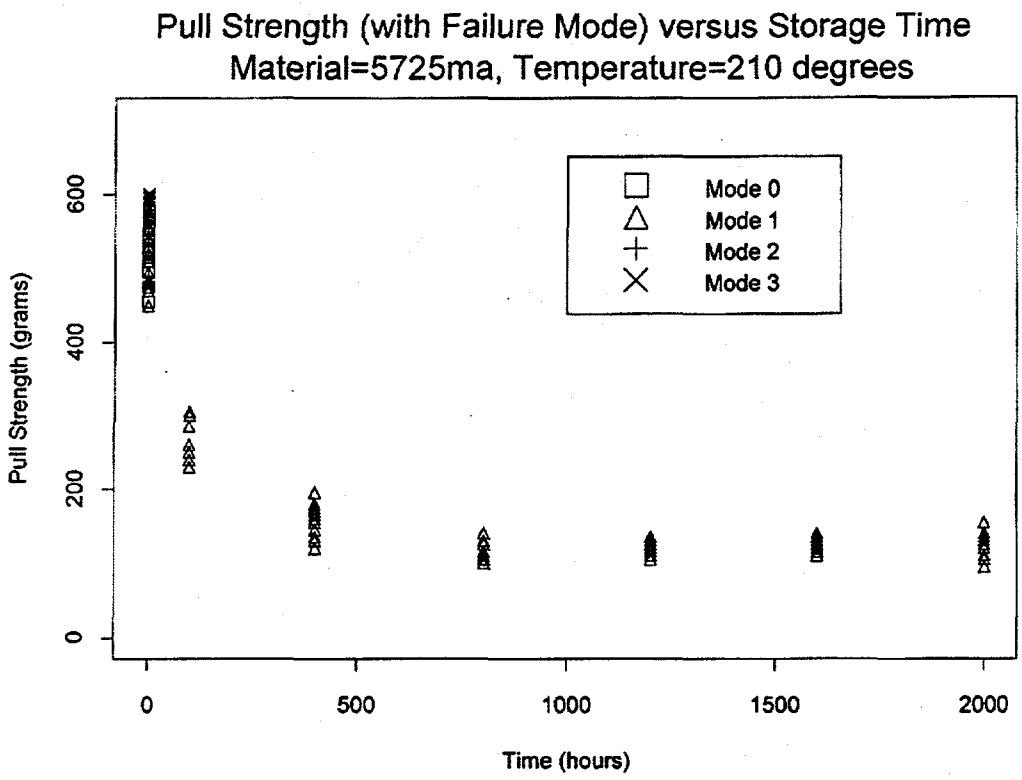

Figure D-5c

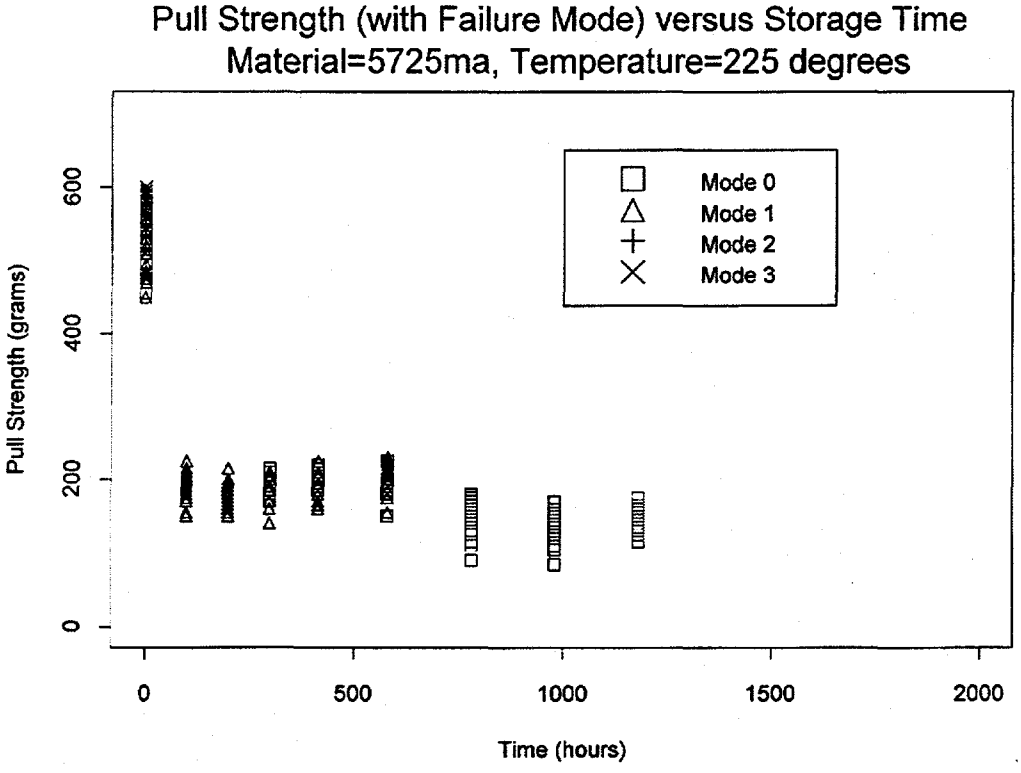

Figure D-5d

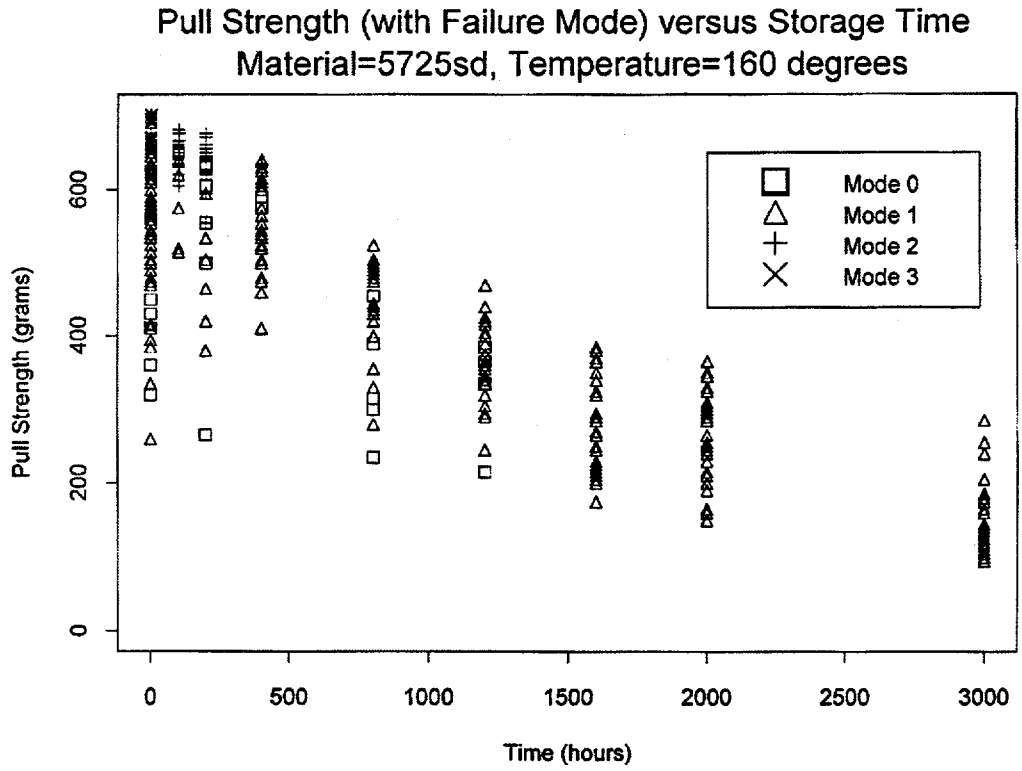

Figure D-6a

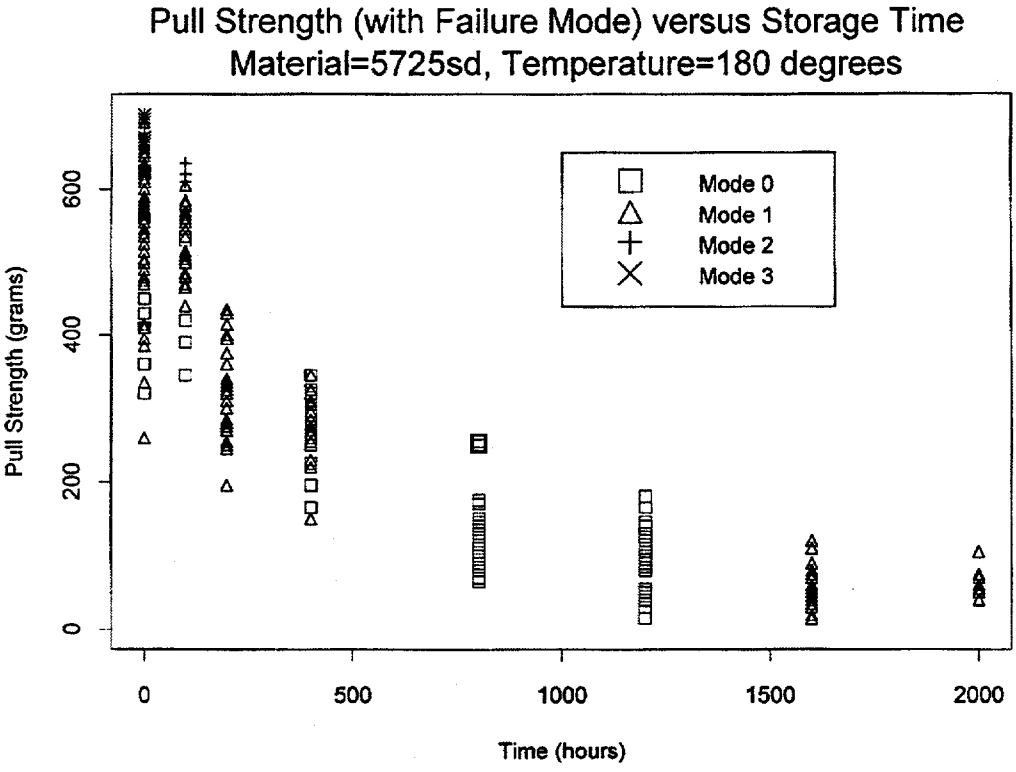

Figure D-6b

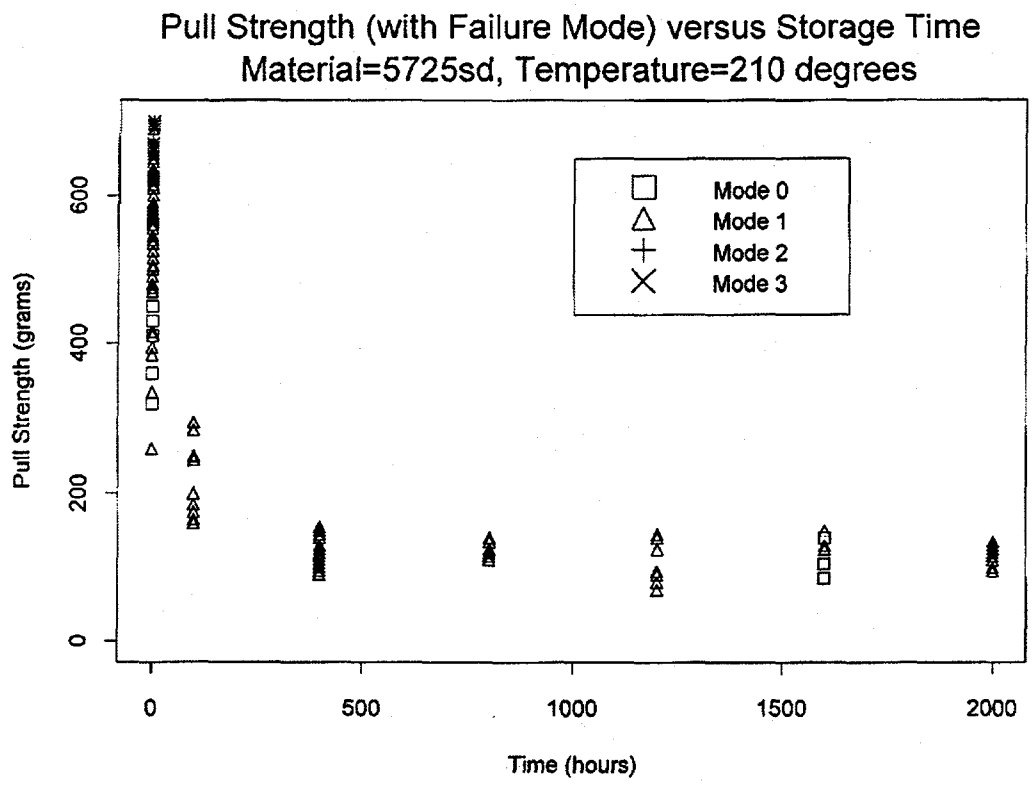

Figure D-6c

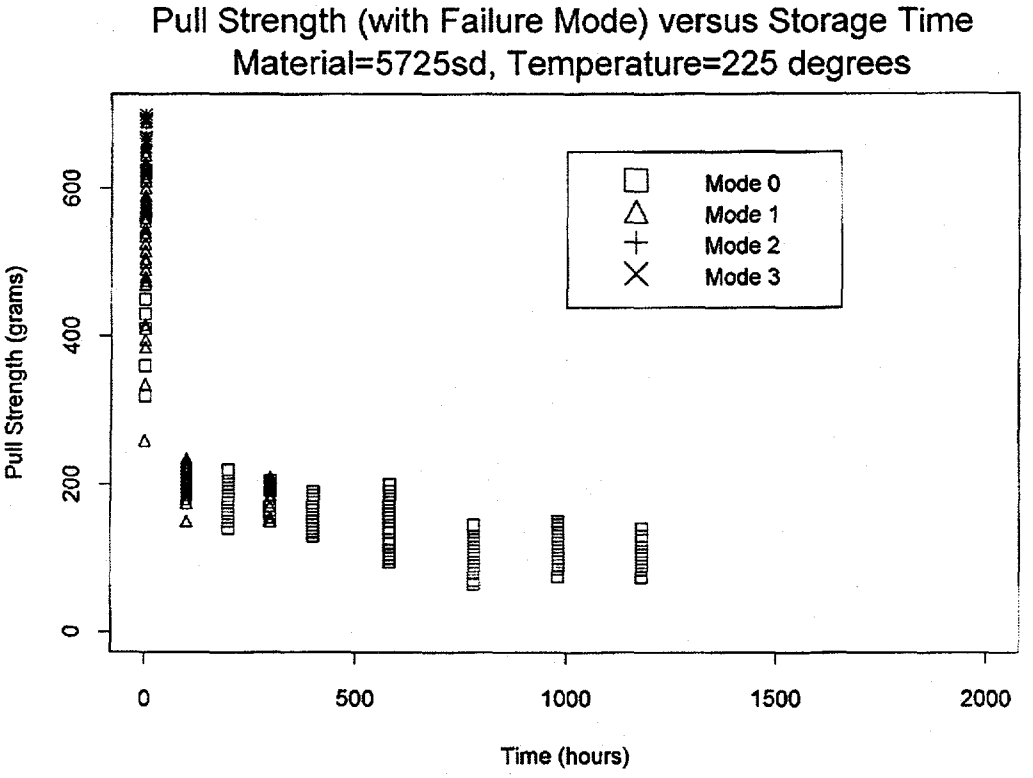

Figure D-6d

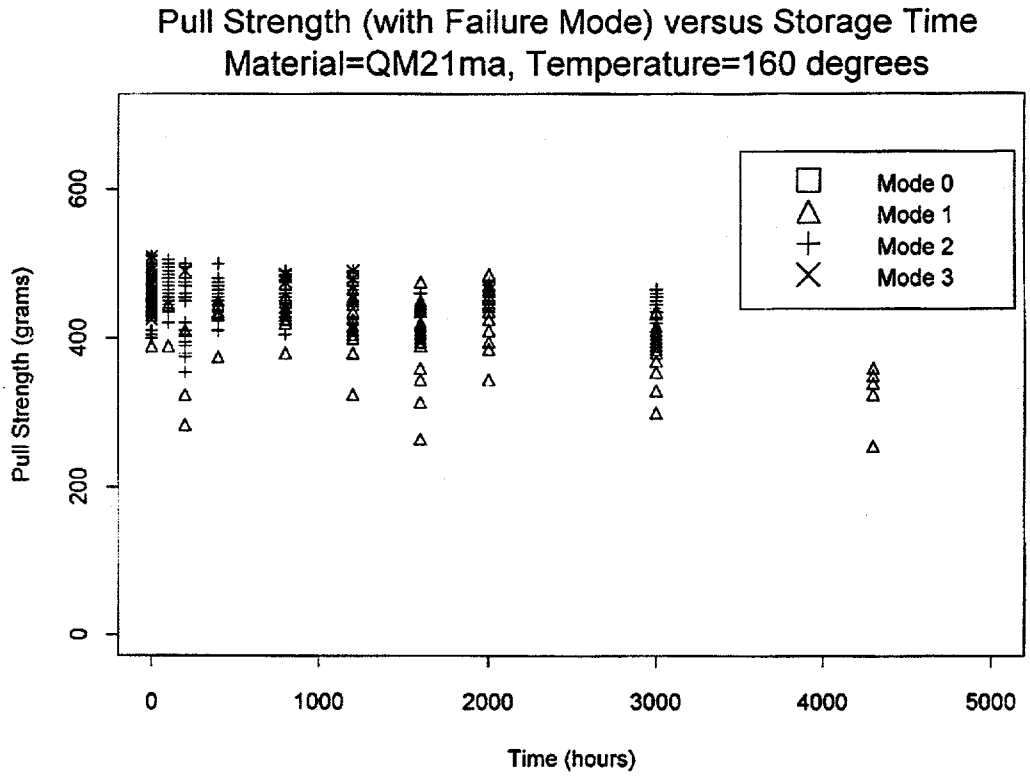

Figure D-7a

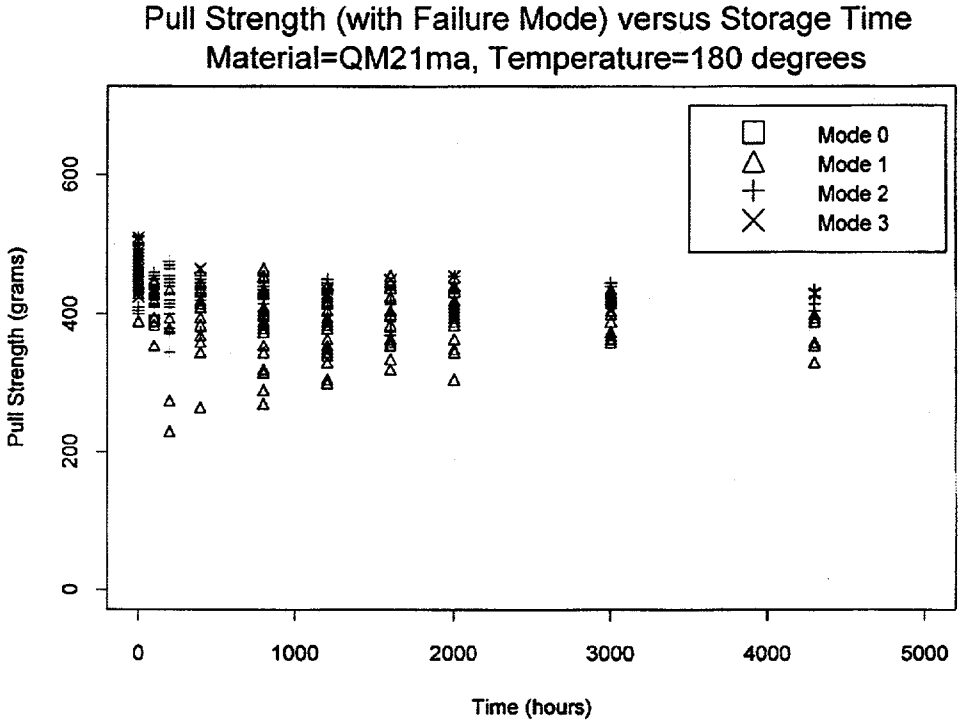

Figure D-7b

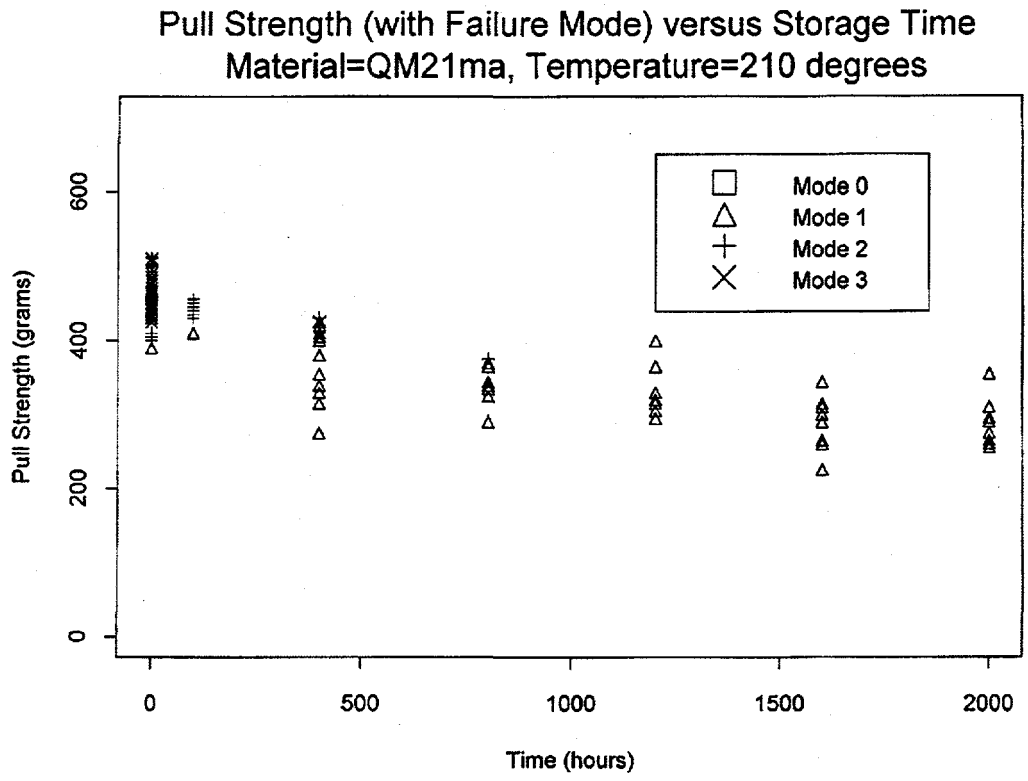

Figure D-7c

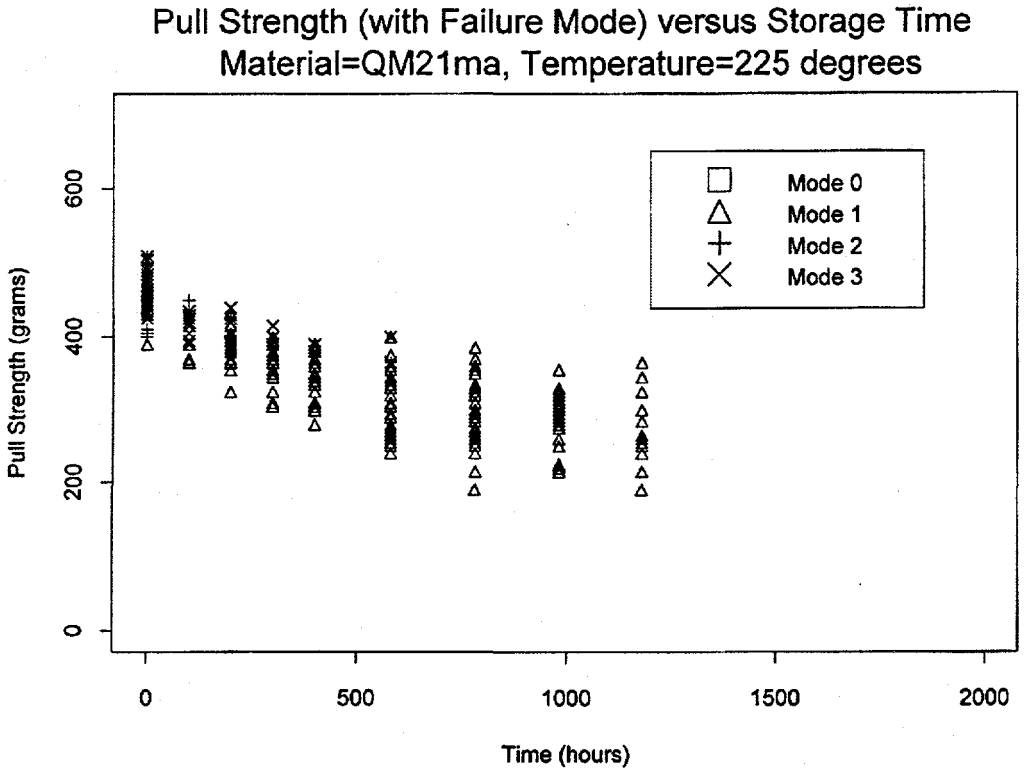

Figure D-7d

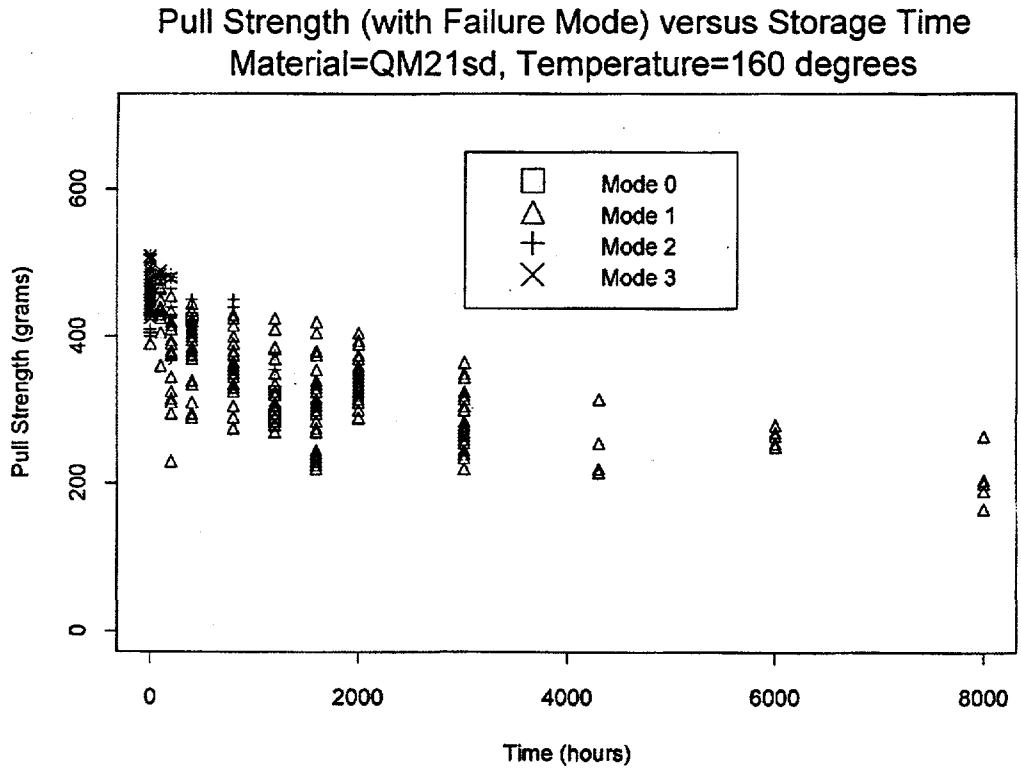

Figure D-8a

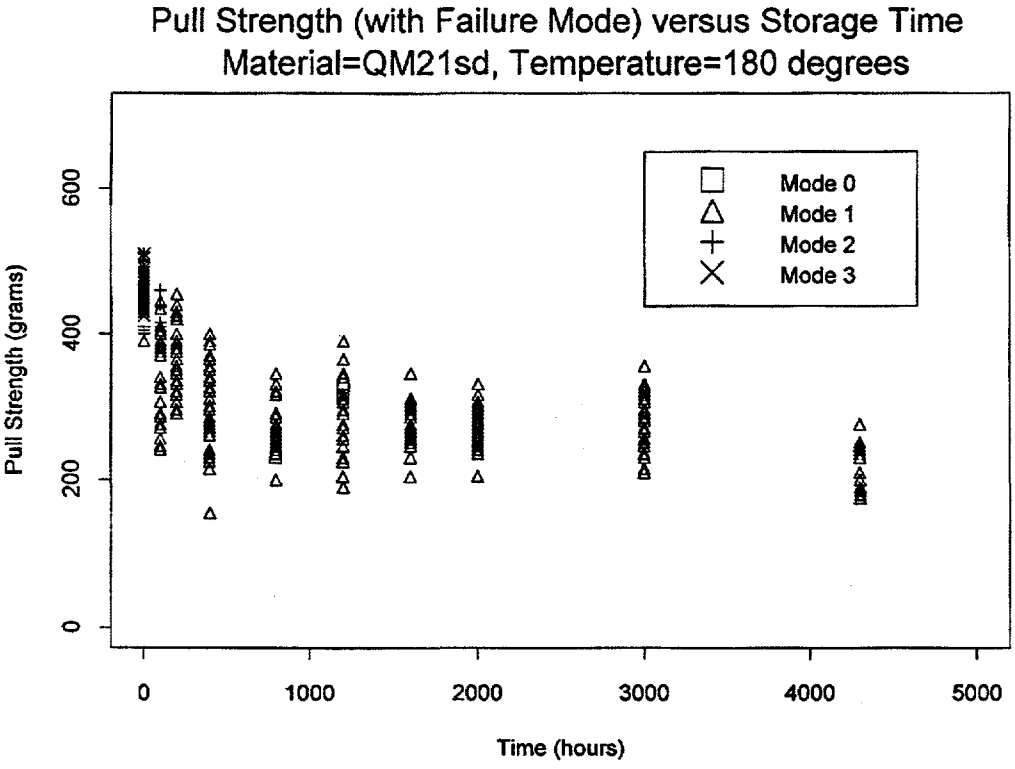

Figure D-8b

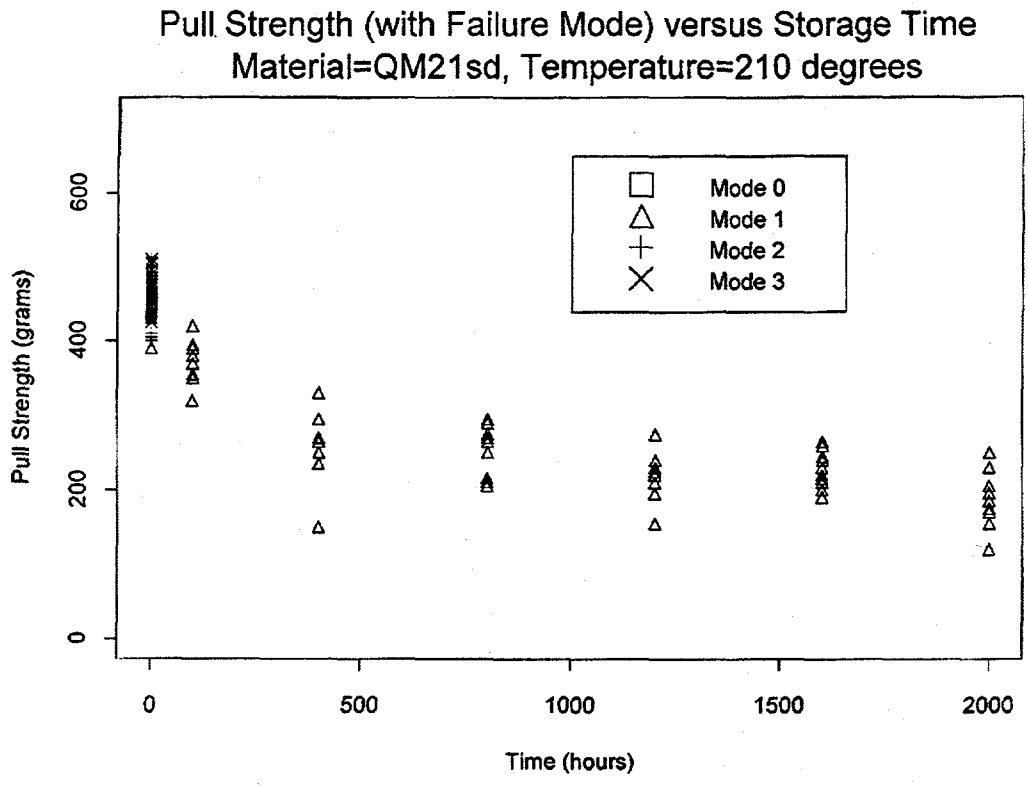

Figure D-8c

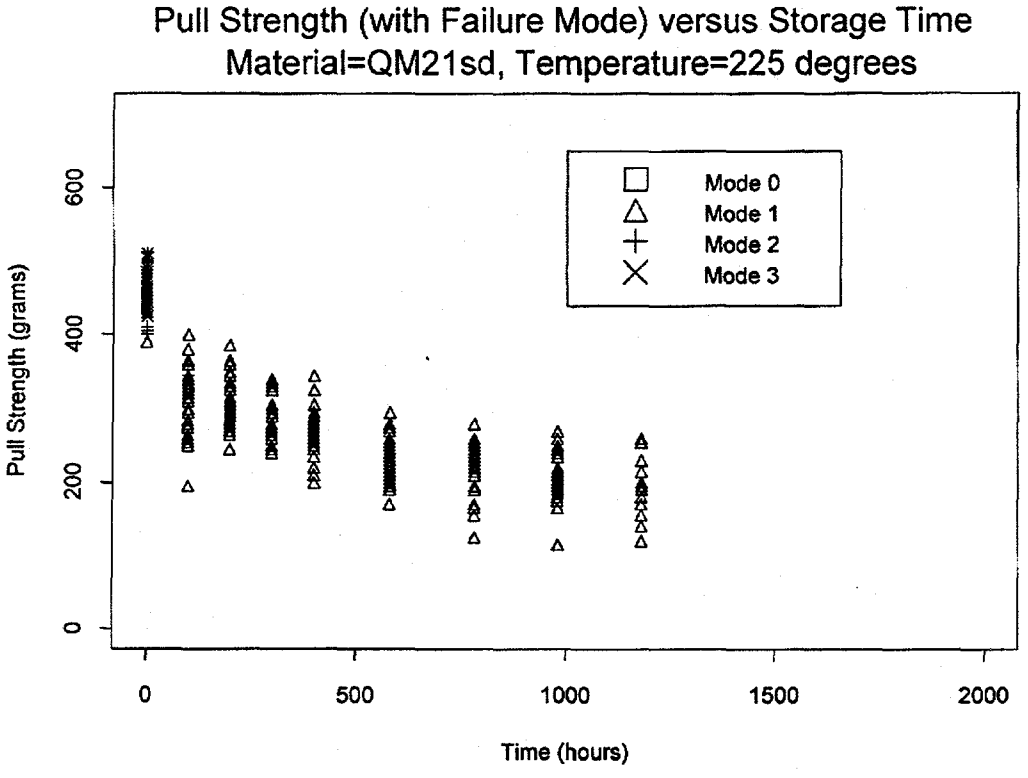

Figure D-8d

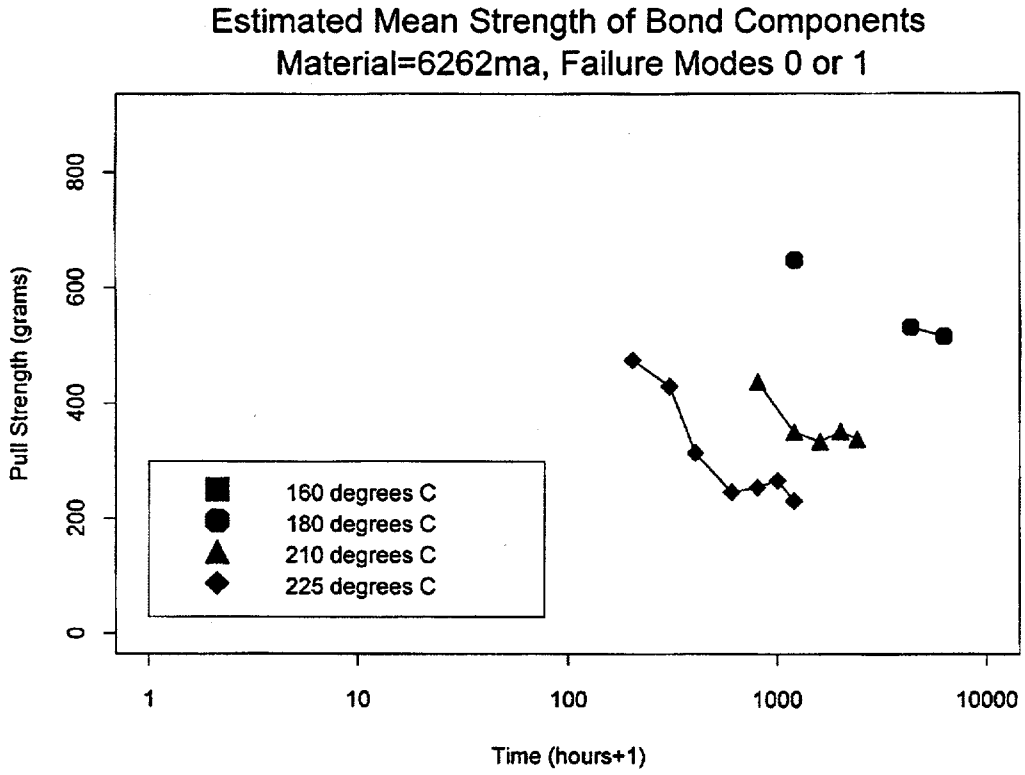

Figure D-9

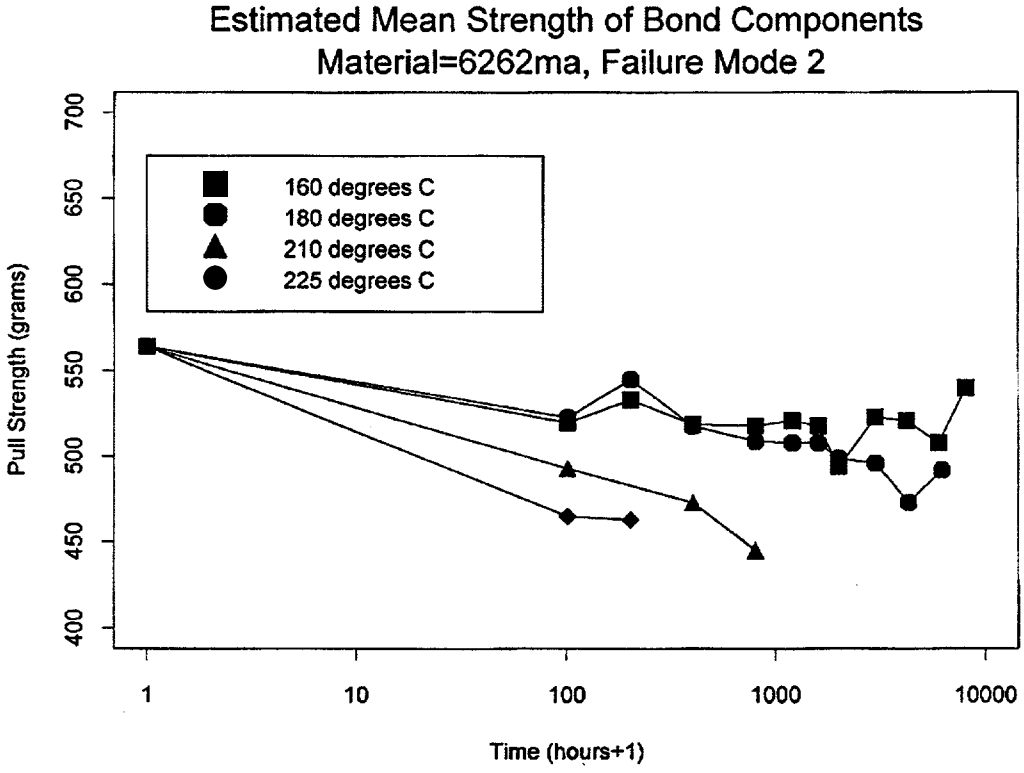

Figure D-10

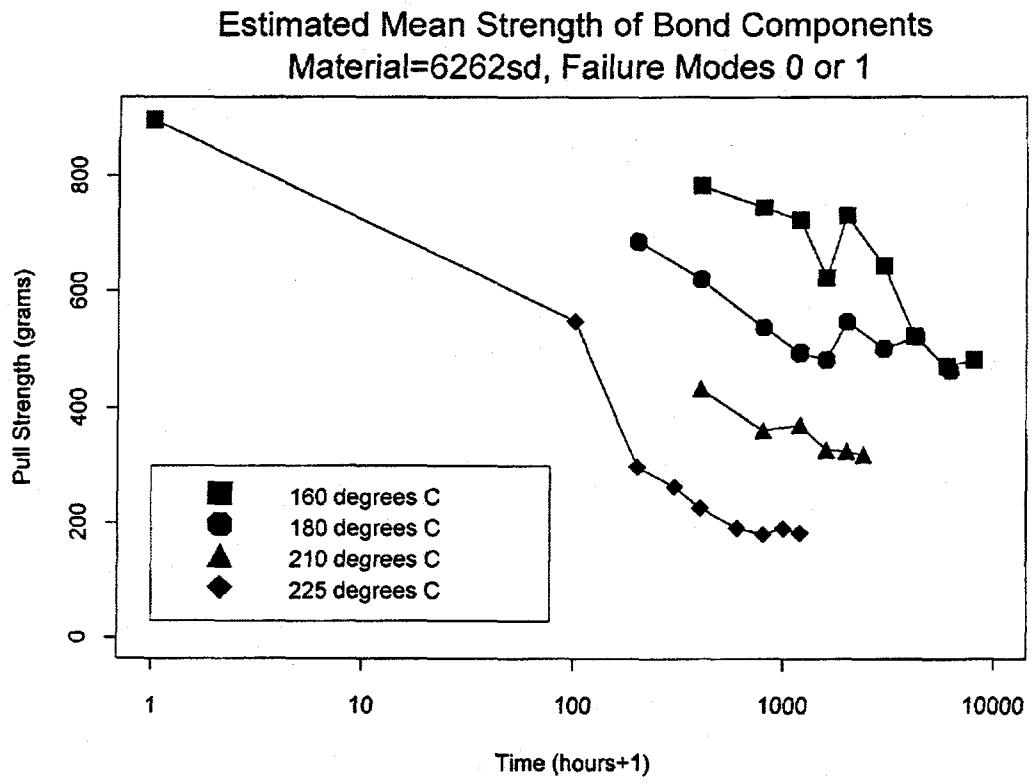

Figure D-11

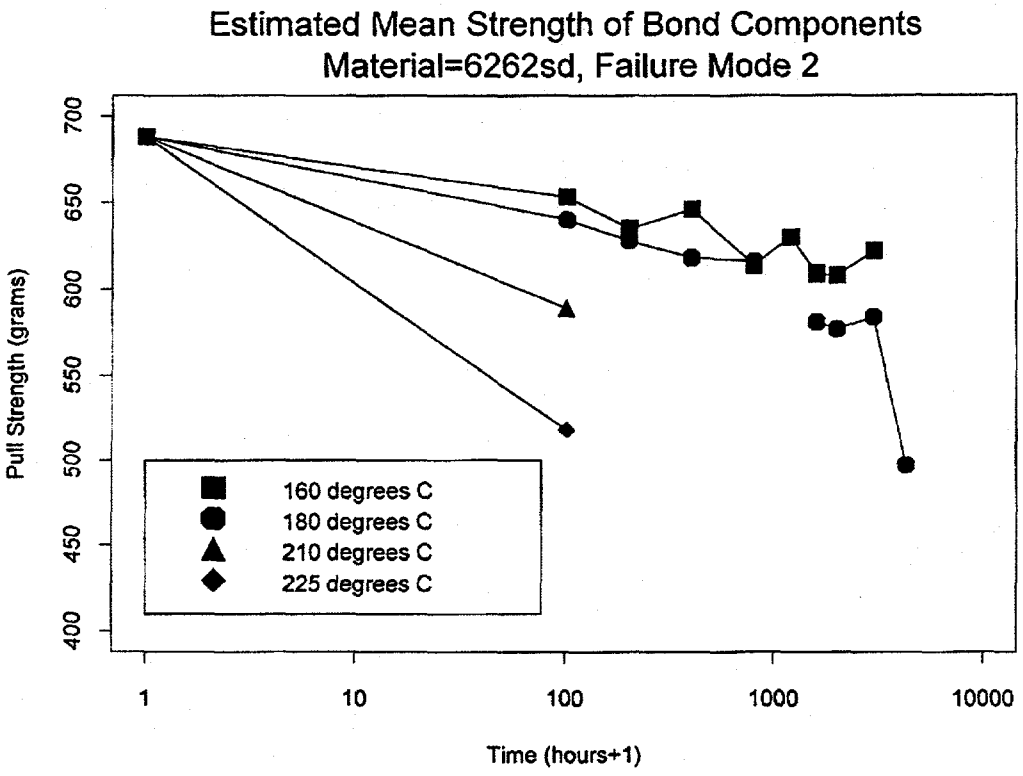

Figure D-12

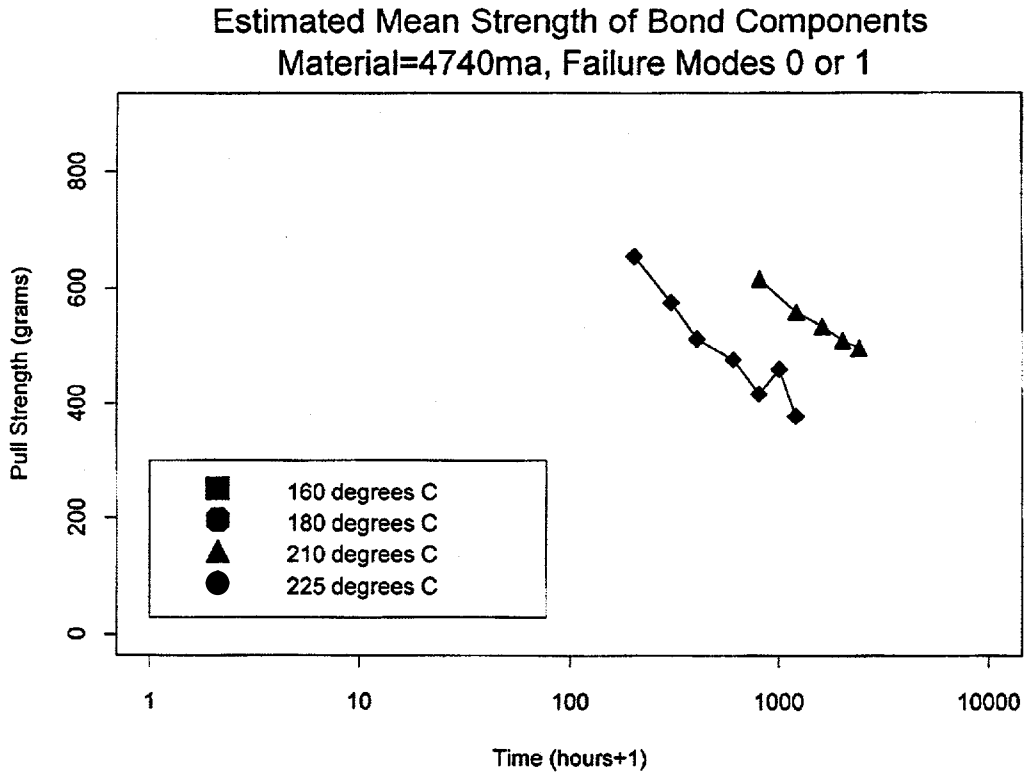

Figure D-13

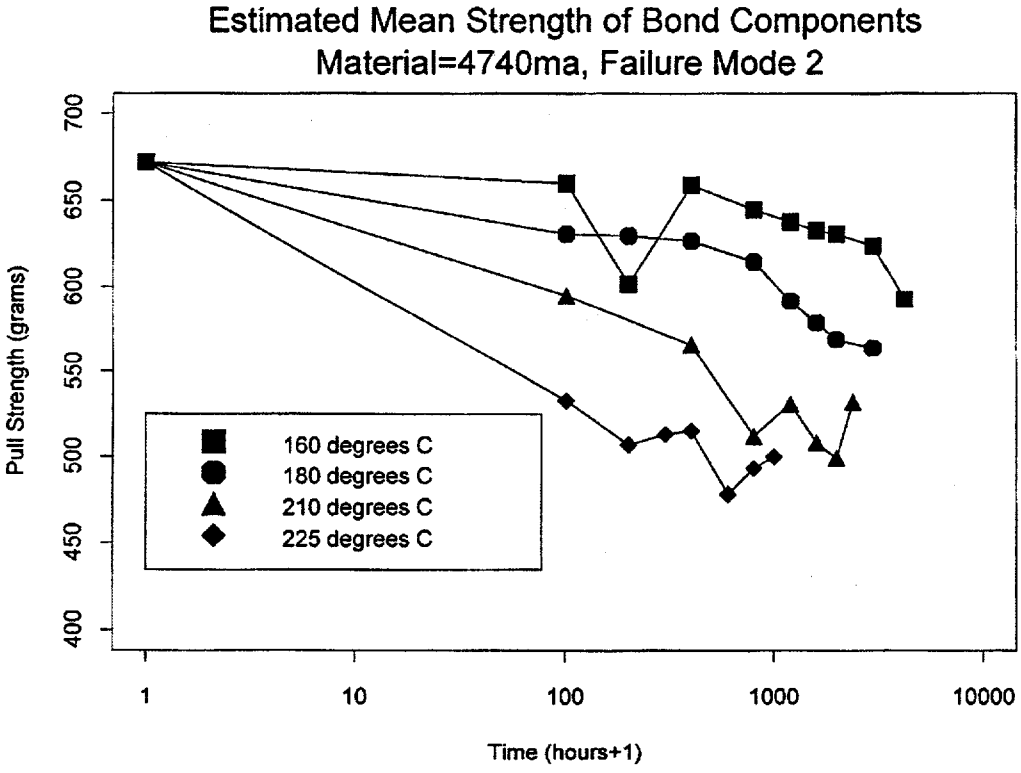

Figure D-14

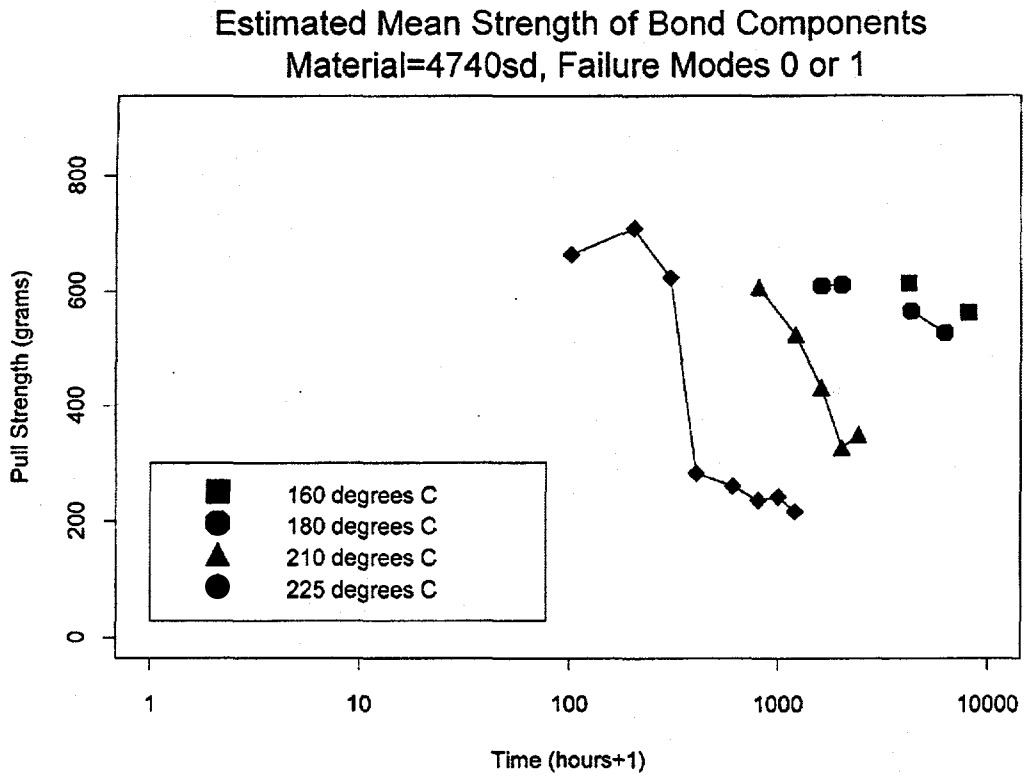

Figure D-15

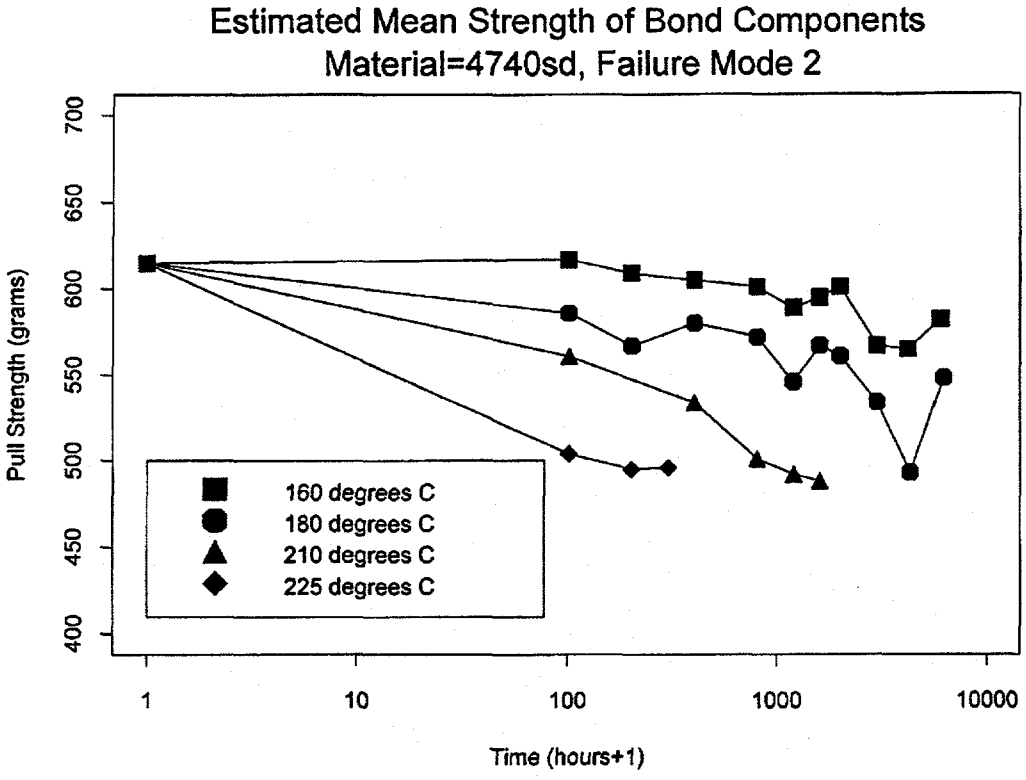

Figure D-16

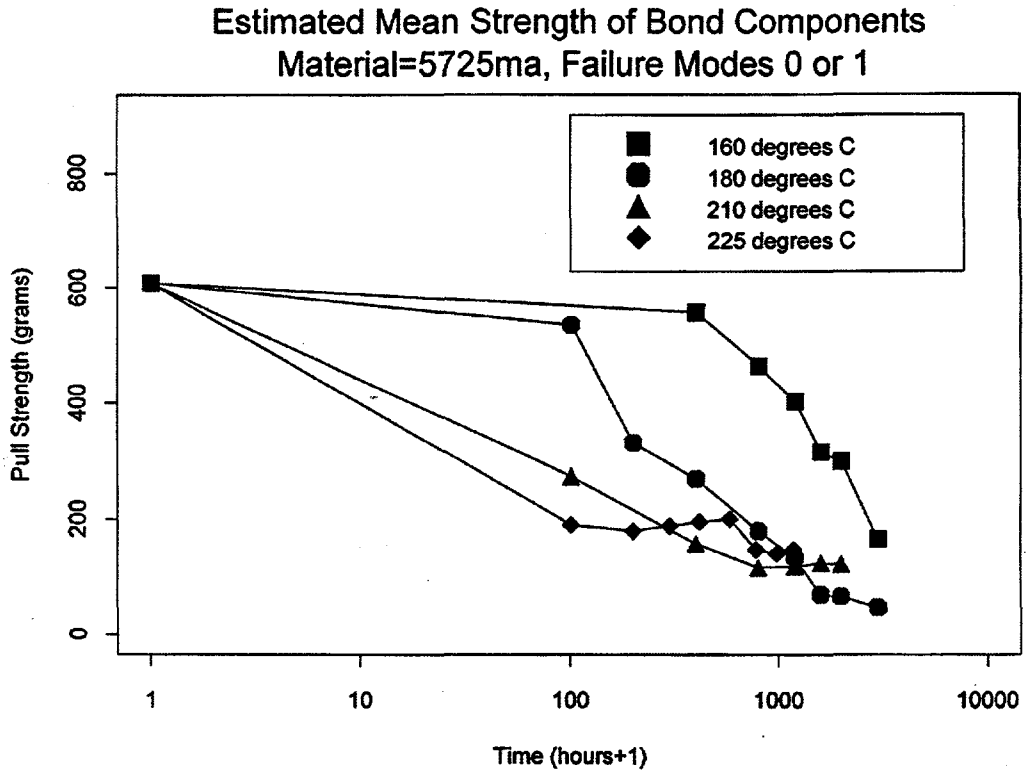

Figure D-17

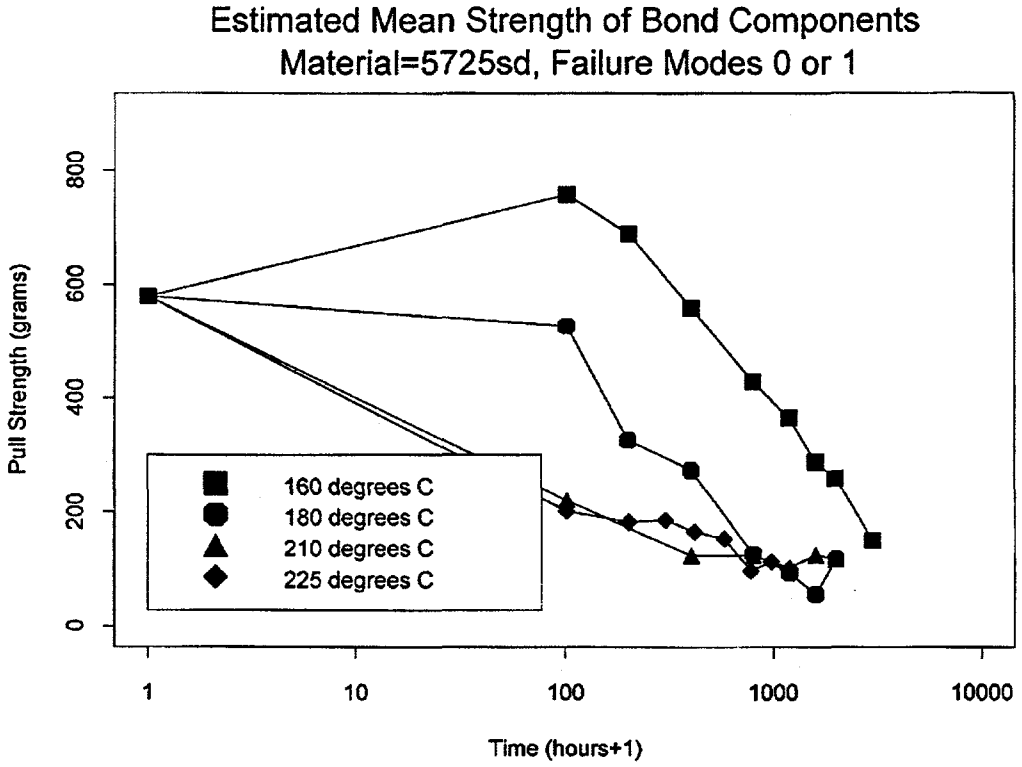

Figure D-18

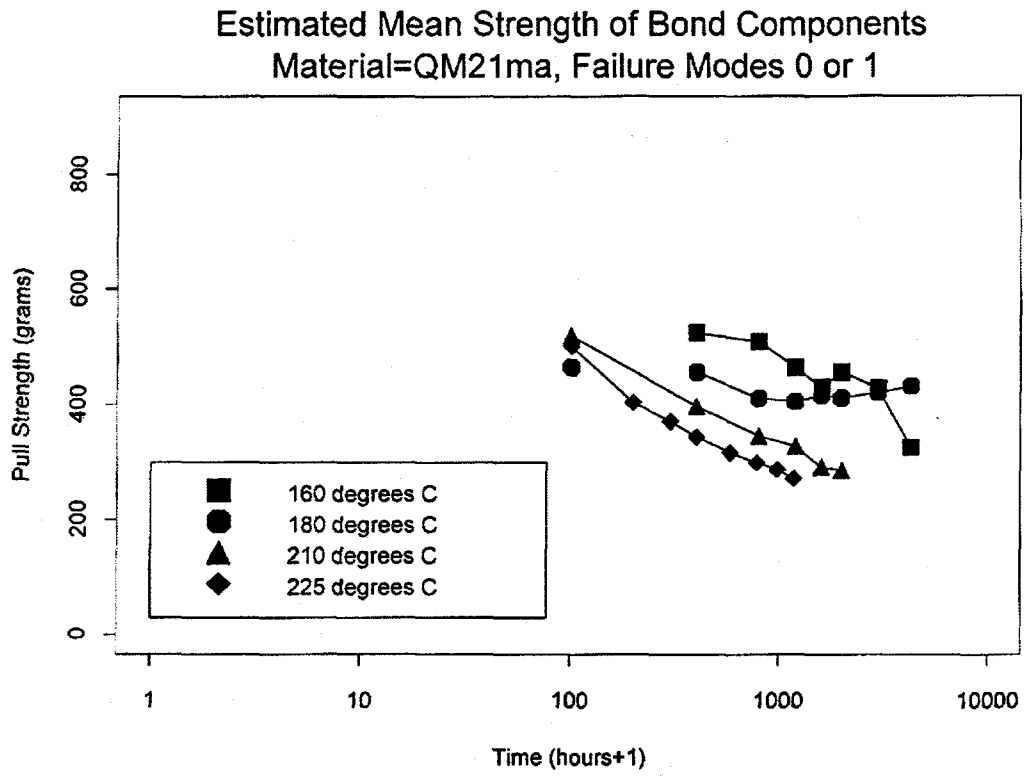

Figure D-19

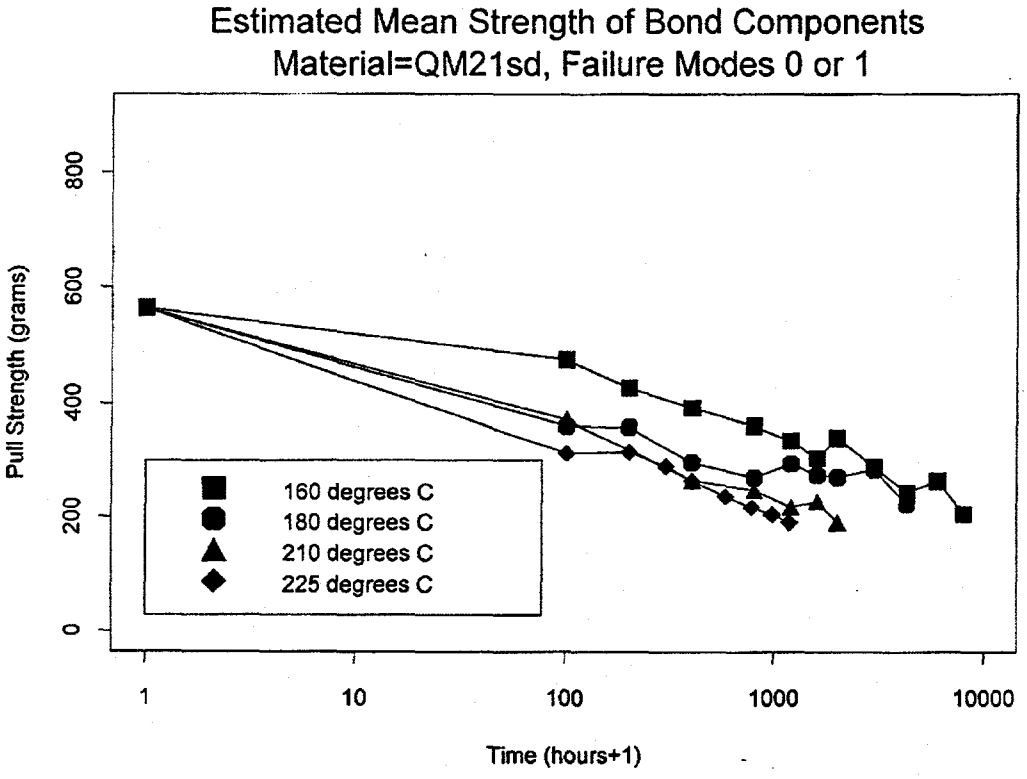

Figure D-20

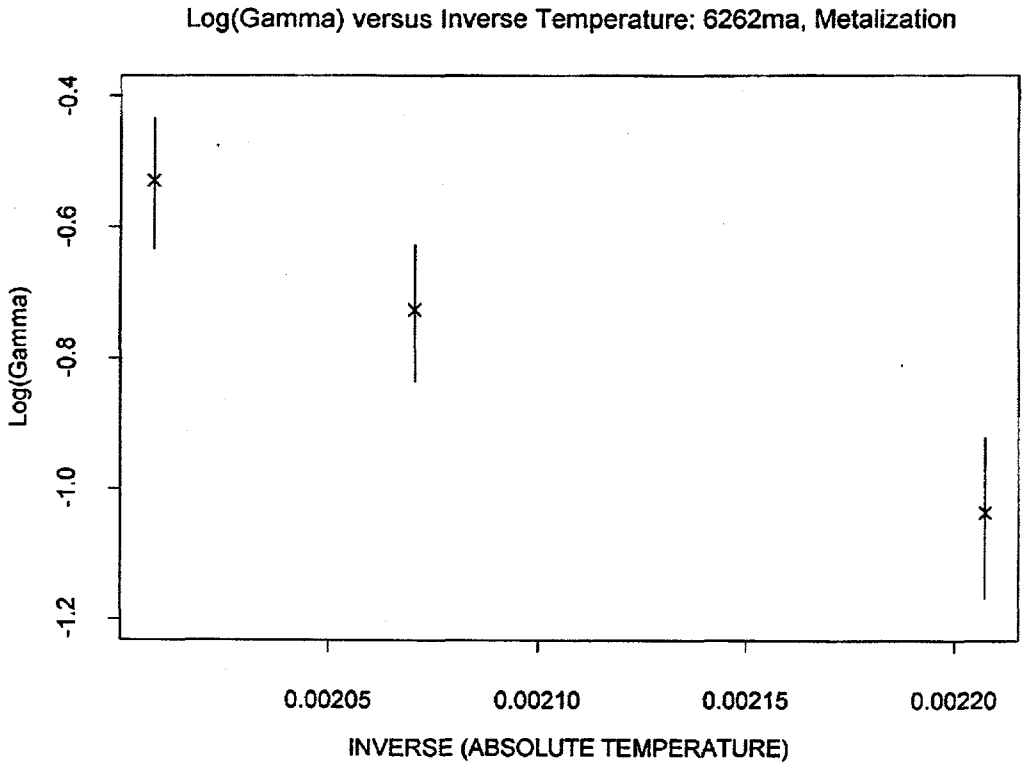

Figure D-21

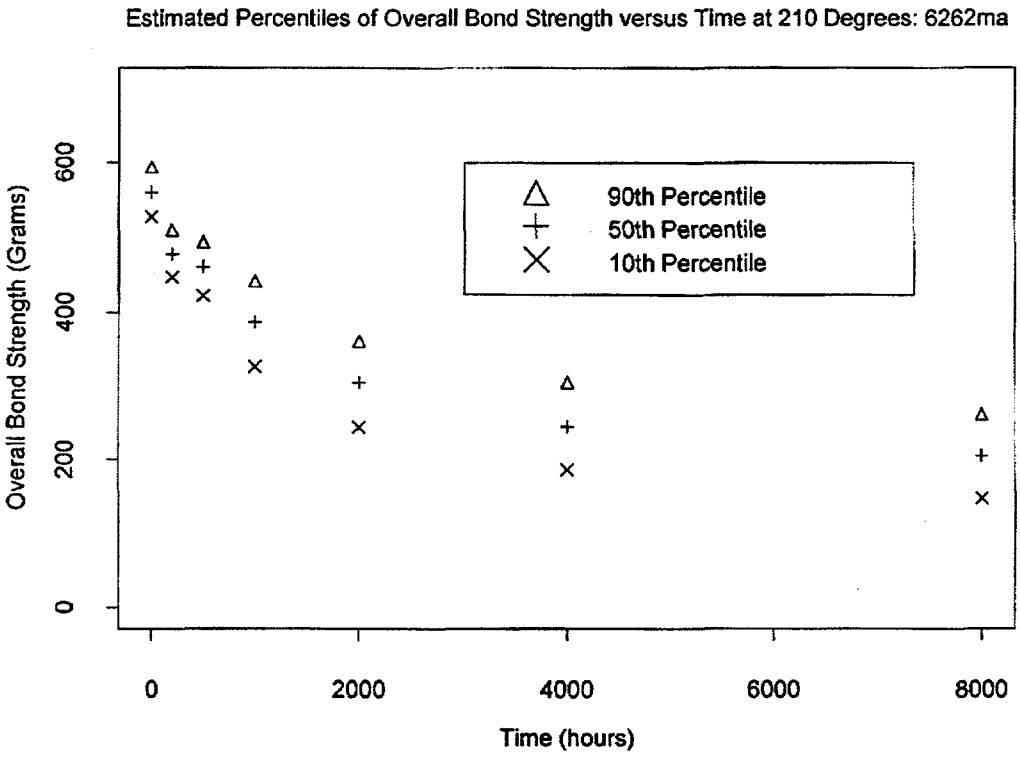

Figure D-22

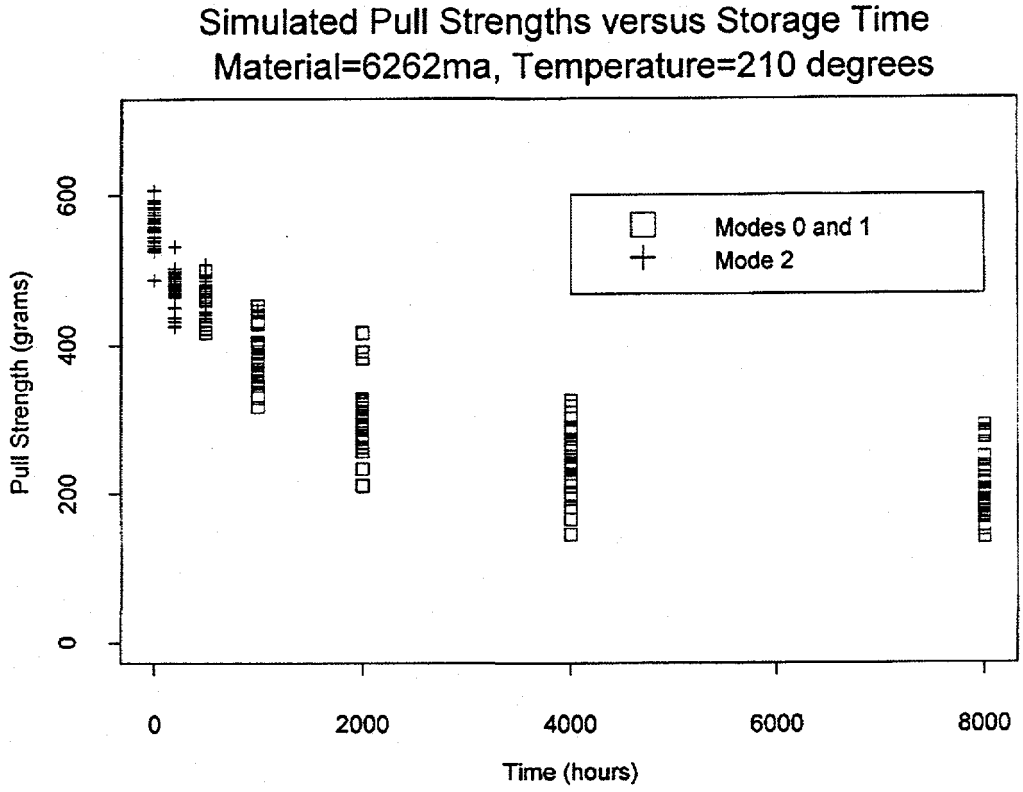

Figure D-23

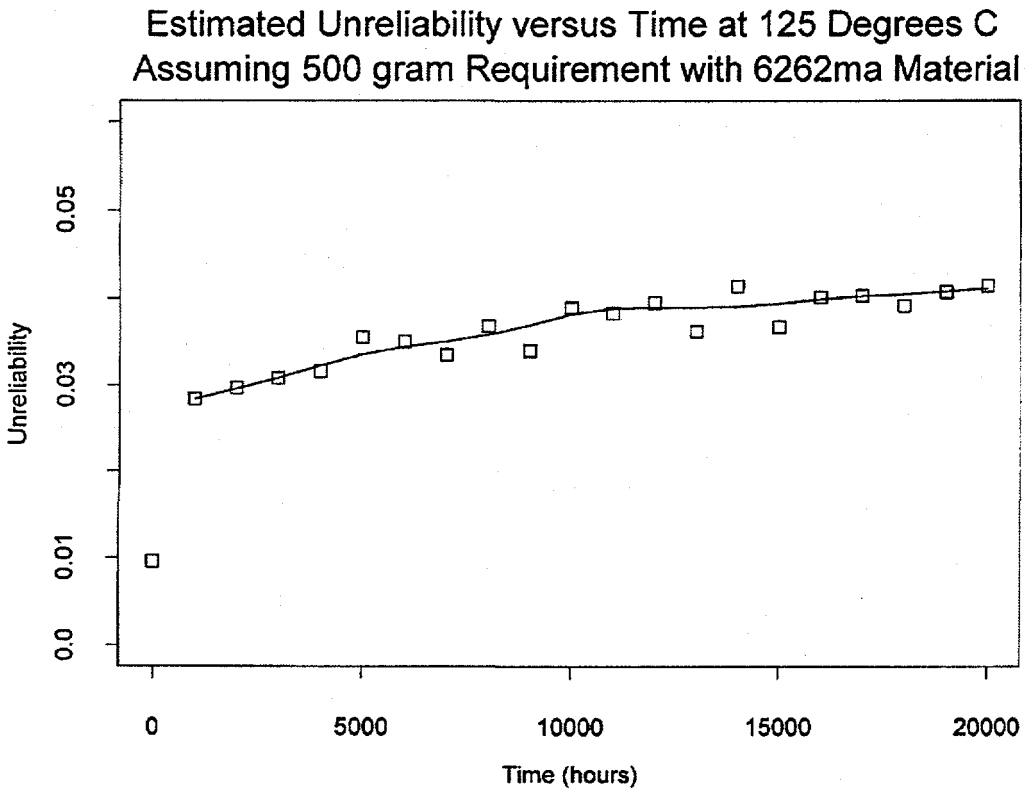

Figure D-24

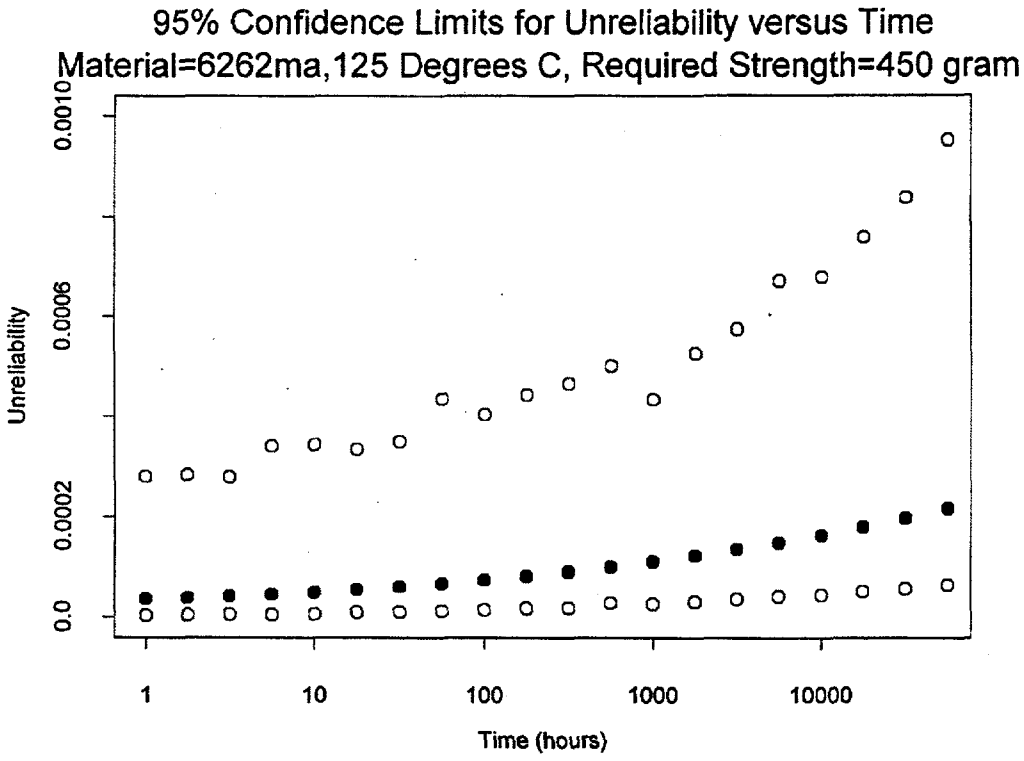

Figure D-25

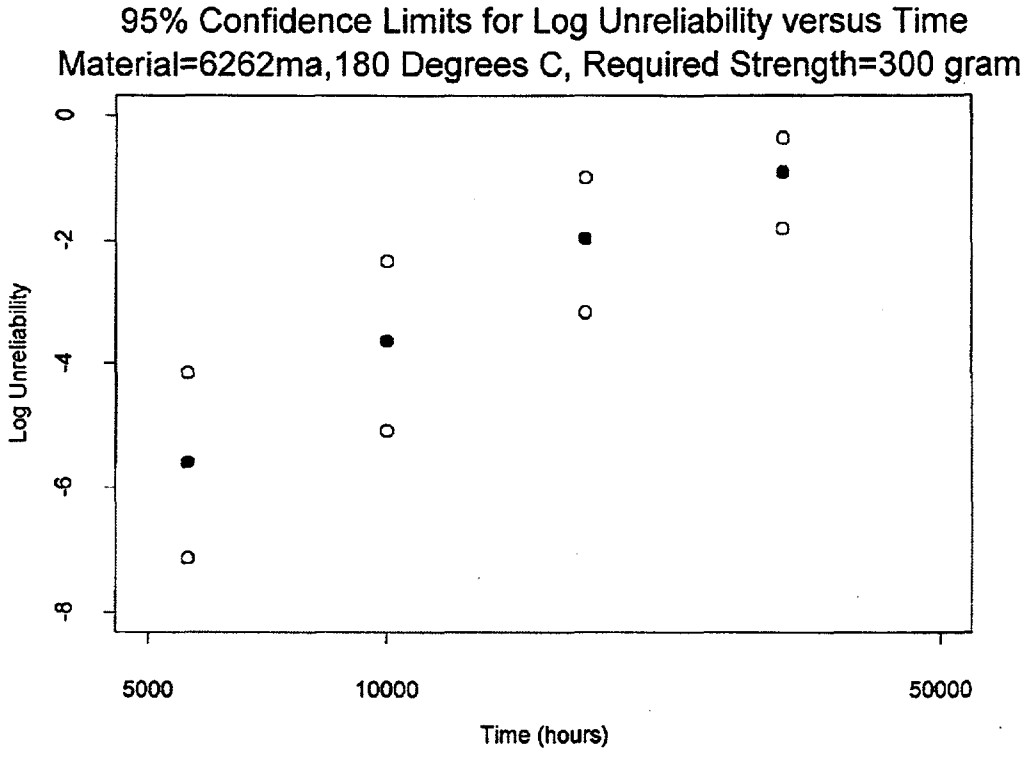

Figure D-26

Table D-2: Estimated Model Parameters: 6262ma

Failure Mode	Temperature	Time (hours)	$\hat{\mu}(\hat{\sigma}_{\hat{\mu}})$	$\hat{\sigma}(\hat{\sigma})_{\hat{\sigma}}$
FM={0,1}	180°C	4300	531 (36)	46 (25)
	180°C	6200	515 (21)	51 (18)
	180°C	7215	503 (16)	48 (14)
	180°C	8260	486 (35)	105 (32)
	210°C	800	437 (8)	23 (7)
	210°C	1200	350 (13)	41 (9)
	210°C	1600	334 (14)	44 (10)
	210°C	2000	351 (22)	70 (16)
	210°C	2400	338 (11)	66 (8)
	225°C	200	474 (9)	37 (8)
	225°C	300	429 (6)	35 (5)
	225 C	400	315 (10)	53 (7)
	225 C	600	246 (12)	63 (9)
	225°C	800	254 (9)	49 (6)
	225°C	1000	266 (9)	47 (6)
	225°C	1200	231 (6)	42 (5)
FM=2	n/a	0	564 (3)	27 (2)
	160°C	100	520 (4)	21 (3)
	160°C	200	533 (5)	30 (4)
	160°C	400	519 (5)	29 (4)
	160°C	800	518 (4)	21 (3)
	160°C	1200	521 (7)	39 (5)
	160°C	1600	518 (7)	39 (5)
	160°C	2000	494 (4)	21 (3)
	160°C	3000	523 (5)	25 (3)
	160°C	4200	521 (10)	22 (7)
	160°C	6000	508 (13)	27 (10)
	160°C	8060	540 (4)	9 (3)
	180°C	100	523 (5)	30 (4)
	180°C	200	545 (4)	23 (3)
	180°C	400	518 (5)	25 (3)
	180°C	800	509 (5)	26 (3)
	180°C	1200	508 (6)	29 (4)
	180°C	1600	508 (6)	32 (4)
	180°C	2000	499 (5)	28 (4)
	180°C	3000	496 (4)	23 (3)

Table D-2: Estimated Model Parameters: 6262ma (continued)

Failure Mode	Temperature	Time (hours)	$\hat{\mu}(\hat{\sigma}_{\hat{\mu}})$	$\hat{\sigma}(\hat{\sigma})_{\hat{\sigma}}$
	180°C	4300	473 (7)	27 (5)
	180°C	6200	492 (8)	27 (6)
	180°C	7215	500 (6)	17 (4)
	180°C	8260	475 (8)	23 (5)
FM=2	210°C	100	493 (9)	27 (6)
	210°C	400	473 (5)	23 (4)
	210°C	800	445 (7)	15 (5)
	225°C	100	465 (3)	17 (2)
	225°C	200	463 (5)	25 (4)

Table D-3: Estimated Model Parameters: 6262sd

Failure Mode	Temperature	Time (hours)	$\hat{\mu}(\hat{\sigma}_{\hat{\mu}})$	$\hat{\sigma}(\hat{\sigma})_{\hat{\sigma}}$
FM={0,1}	n/a	0	897 (67)	200 (48)
	160°C	400	783 (82)	107 (54)
	160°C	800	745 (72)	185 (59)
	160°C	1200	723 (54)	153 (45)
	160°C	1600	623 (25)	102 (22)
	160°C	2000	731 (64)	47 (50)
	160°C	3000	644 (46)	166 (41)
	160°C	4200	522 (57)	124 (46)
	160°C	6000	471 (23)	51 (16)
	160°C	8060	482 (15)	88 (11)
	180°C	200	686 (34)	109 (30)
	180°C	400	621 (19)	83 (17)
	180°C	800	537 (15)	80 (12)
	180°C	1200	494 (15)	80 (11)
	180°C	1600	482 (17)	91 (13)
	180°C	2000	547 (17)	86 (15)
	180°C	3000	501 (20)	92 (15)
	180°C	4300	521 (20)	48 (16)
	180°C	6200	463 (14)	94 (11)
	210°C	400	433 (18)	82 (13)
	210°C	800	361 (14)	44 (10)
	210°C	1200	371 (18)	57 (13)
	210°C	1600	327 (8)	25 (6)
	210°C	2000	325 (21)	66 (15)
	210°C	2400	319 (12)	75 (8)
	225°C	100	548 (23)	85 (20)
	225°C	200	298 (14)	79 (10)
	225°C	300	263 (9)	51 (7)
	225°C	400	226 (4)	24 (3)
	225°C	600	191 (8)	44 (6)
	225°C	800	180 (6)	31 (4)
	225°C	1000	190 (5)	25 (3)
	225°C	1200	182 (6)	41 (5)

Table D-3: Estimated Model Parameters: 6262sd (continued)

Failure Mode	Temperature	Time (hours)	$\hat{\mu}(\hat{\sigma}_{\hat{\mu}})$	$\hat{\sigma}(\hat{\sigma})_{\hat{\sigma}}$
FM=2	n/a	0	688 (2)	17 (1)
	160°C	100	653 (3)	17 (2)
	160°C	200	635 (6)	34 (4)
	160°C	400	646 (3)	14 (2)
	160°C	800	614 (5)	24 (3)
	160°C	1200	630 (4)	18 (3)
	160°C	1600	609 (7)	32 (5)
	160°C	2000	608 (5)	24 (3)
	160°C	3000	622 (5)	20 (4)
	180°C	100	640 (3)	14 (2)
	180°C	200	628 (3)	14 (2)
	180°C	400	618 (6)	27 (5)
	180°C	800	616 (12)	33 (8)
	180°C	1600	581 (10)	23 (8)
	180°C	2000	577 (8)	28 (6)
	180°C	3000	584 (13)	30 (10)
	180°C	4300	497 (5)	17 (4)
	210°C	100	589 (10)	33 (7)
	225°C	100	518 (5)	21 (3)

Table D-4: Estimated Model Parameters: 4740ma

Failure Mode	Temperature	Time (hours)	$\hat{\mu}(\hat{\sigma}_{\hat{\mu}})$	$\hat{\sigma}(\hat{\sigma})_{\hat{\sigma}}$
FM={0,1}	160 C	1600	665 (15)	32 (12)
	210°C	800	616 (79)	204 (69)
	210°C	1200	559 (43)	136 (39)
	210°C	1600	534 (40)	127 (36)
	210°C	2000	510 (11)	35 (9)
	210°C	2400	497 (15)	97 (13)
	225°C	200	655 (83)	113 (54)
	225°C	300	576 (32)	75 (26)
	225°C	400	513 (27)	120 (24)
	225°C	600	477 (17)	74 (14)
	225°C	800	417 (17)	92 (13)
	225°C	1000	460 (18)	91 (15)
	225°C	1200	378 (17)	111 (13)
FM=2	n/a	0	672 (3)	26 (3)
	160°C	100	660 (3)	15 (2)
	160°C	200	602 (11)	48 (8)
	160°C	400	659 (4)	20 (3)
	160°C	800	645 (4)	17 (3)
	160°C	1200	638 (5)	22 (3)
	160°C	1600	633 (5)	21 (4)
	160°C	2000	631 (4)	17 (3)
	160°C	3000	624 (3)	13 (2)
	160°C	4200	593 (7)	15 (5)
	180°C	100	631 (3)	15 (2)
	180°C	200	630 (4)	16 (3)
	180°C	400	627 (4)	16 (2)
	180°C	800	615 (3)	15 (2)
	180°C	1200	592 (4)	17 (3)
	180°C	1600	579 (6)	26 (4)
	180°C	2000	569 (5)	21 (3)
	180°C	000	564 (5)	14 (4)
	210°C	100	595 (5)	23 (4)
	210°C	400	566 (5)	23 (4)
	210°C	800	512 (8)	30 (6)
	210°C	1200	531 (3)	10 (2)
	210°C	1600	508 (12)	44 (9)
	210°C	2000	499 (8)	30 (6)

Table D-4: Estimated Model Parameters: 4740ma (continued)

Failure Mode	Temperature	Time (hours)	$\hat{\mu}(\hat{\sigma}_{\hat{\mu}})$	$\hat{\sigma}(\hat{\sigma})_{\hat{\sigma}}$
	210°C	2400	532 (5)	12 (3)
FM=2	225°C	100	533 (4)	20 (3)
	225°C	200	507 (5)	26 (4)
	225°C	300	513 (4)	23 (3)
	225°C	400	515 (6)	23 (4)
	225°C	600	478 (10)	44 (8)
	225°C	800	493 (7)	17 (5)
	225°C	1000	500 (7)	23 (5)

Table D-5: Estimated Model Parameters: 4740sd

Failure Mode	Temperature	Time (hours)	$\hat{\mu}(\hat{\sigma}_{\hat{\mu}})$	$\hat{\sigma}(\hat{\sigma})_{\hat{\sigma}}$
FM={0,1}	160°C	8000	562 (30)	60 (27)
	180°C	1600	609 (33)	122 (30)
	180°C	2000	611 (33)	103 (29)
	180°C	4300	565 (85)	204 (77)
	180°C	6200	527 (21)	119 (18)
	210°C	800	607 (130)	234 (116)
	210°C	1200	524 (67)	150 (61)
	210°C	1600	431 (33)	99 (28)
	210°C	2000	326 (23)	73 (16)
	210°C	2400	349 (15)	96 (11)
	225°C	300	624 (68)	177 (55)
	225°C	400	282 (8)	44 (6)
	225°C	600	260 (10)	52 (7)
	225°C	800	236 (8)	45 (6)
	225°C	1000	242 (8)	45 (6)
	225°C	1200	216 (8)	30 (5)
FM=2	n/a	0	615 (6)	51 (4)
	160°C	100	617 (3)	15 (2)
	160°C	200	609 (4)	21 (3)
	160°C	400	605 (3)	15 (2)
	160°C	800	601 (3)	15 (2)
	160°C	1200	589 (3)	19 (2)
	160°C	1600	595 (4)	19 (3)
	160°C	2000	601 (3)	14 (2)
	160°C	3000	567 (5)	27 (4)
	160°C	4200	565 (4)	8 (3)
	160°C	6000	582 (4)	8 (3)
	180°C	100	586 (4)	19 (2)
	180°C	200	567 (5)	26 (3)
	180°C	400	580 (3)	18 (2)
	180°C	800	572 (4)	20 (3)
	180°C	1200	546 (7)	35 (5)
	180°C	1600	567 (4)	16 (3)
	180°C	2000	561 (3)	16 (2)
	180°C	3000	534 (7)	34 (5)
	180°C	4300	493 (6)	18 (4)
	180°C	6200	548 (7)	23 (5)

Table D-5: Estimated Model Parameters: 4740sd (continued)

Failure Mode	Temperature	Time (hours)	$\hat{\mu}(\hat{\sigma}_{\hat{\mu}})$	$\hat{\sigma}(\hat{\sigma})_{\hat{\sigma}}$
FM=2	210°C	100	561 (5)	21 (3)
	210°C	400	534 (6)	26 (4)
	210°C	800	501 (5)	13 (4)
	210°C	1200	492 (6)	16 (4)
	210°C	1600	488 (8)	15 (6)
	225°C	100	504 (3)	17 (2)
	225°C	200	495 (4)	20 (3)
	225°C	300	496 (5)	26 (4)

Table D-6: Estimated Model Parameters: 5725ma

Failure Mode	Temperature	Time (hours)	$\hat{\mu}(\hat{\sigma}_{\hat{\mu}})$	$\hat{\sigma}(\hat{\sigma})_{\hat{\sigma}}$
FM={0,1}	n/a	0	608 (15)	81 (13)
	160°C	400	557 (26)	55 (20)
	160°C	800	464 (13)	66 (12)
	160°C	1200	402 (9)	49 (6)
	160°C	1600	315 (7)	38 (5)
	160°C	2000	299 (7)	38 (5)
	160°C	3000	165 (8)	45 (6)
	180°C	100	536 (27)	88 (23)
	180°C	200	331 (11)	58 (8)
	180°C	400	269 (6)	33 (4)
	180°C	800	179 (9)	51 (7)
	180°C	1200	133 (9)	50 (7)
	180°C	1600	69 (5)	27 (3)
	180°C	2000	66 (6)	36 (4)
	180°C	3000	47 (5)	26 (4)
	210°C	100	273 (9)	28 (6)
	210°C	400	157 (4)	18 (3)
	210°C	800	116 (4)	12 (3)
	210°C	1200	118 (3)	10 (2)
	210°C	1600	124 (3)	10 (2)
	210°C	2000	122 (5)	17 (4)
	225°C	100	190 (3)	17 (2)
	225°C	200	179 (3)	16 (2)
	225°C	300	188 (3)	18 (2)
	225°C	415	195 (3)	16 (2)
	225°C	580	200 (3)	19 (2)
	225°C	780	147 (4)	23 (3)
	225°C	980	140 (3)	18 (2)
	225°C	1180	147 (4)	15 (2)
FM=2	n/a	0	569 (3)	26 (2)
	160°C	100	525 (4)	24 (3)
	160°C	200	496 (5)	26 (3)
	160°C	400	499 (6)	30 (4)
	160°C	800	493 (5)	17 (3)
	180°C	100	490 (6)	30 (4)

Table D-7: Estimated Model Parameters: 5725sd

Failure Mode	Temperature	Time (hours)	$\hat{\mu}(\hat{\sigma}_{\hat{\mu}})$	$\hat{\sigma}(\hat{\sigma})_{\hat{\sigma}}$
FM={0,1}	n/a	0	579 (13)	122 (11)
	160°C	100	759 (54)	123 (42)
	160°C	200	690 (49)	190 (44)
	160°C	400	559 (11)	61 (8)
	160°C	800	429 (13)	73 (10)
	160°C	1200	365 (10)	56 (7)
	160°C	1600	288 (12)	64 (8)
	160°C	2000	259 (11)	60 (8)
	160°C	3000	150 (8)	47 (6)
	180°C	100	527 (14)	75 (11)
	180°C	200	326 (11)	59 (8)
	180°C	400	273 (9)	49 (6)
	180°C	800	127 (8)	43 (5)
	180°C	1200	95 (8)	43 (6)
	180°C	1600	57 (5)	24 (3)
	180°C	2000	118(4)	13 (3)
	210°C	100	221 (15)	47(11)
	210°C	400	124 (4)	19 (3)
	210°C	800	124 (3)	9 (2)
	210°C	1200	103 (7)	24 (5)
	210°C	1600	125 (5)	17 (4)
	210°C	2000	118 (4)	13 (3)
	225°C	100	202 (4)	21 (3)
	225°C	200	183 (3)	18 (2)
	225°C	300	186 (3)	17 (2)
	225°C	415	166 (3)	16 (2)
	225°C	580	154 (5)	29 (4)
	225°C	780	98 (4)	20 (3)
	225°C	980	114 (4)	20 (3)
	225°C	1180	100 (5)	20 (4)
FM=2	n/a	0	569 (3)	26 (2)
	160°C	100	525 (4)	24 (3)
	160°C	200	496 (5)	26 (3)
	160°C	400	499 (6)	30 (4)
	160°C	800	493 (5)	17 (3)
	180°C	100	490 (6)	30 (4)

Table D-8: Estimated Model Parameters: QM21ma

Failure Mode	Temperature	Time (hours)	$\hat{\mu}(\hat{\sigma}_{\hat{\mu}})$	$\hat{\sigma}(\hat{\sigma})_{\hat{\sigma}}$
FM={0,1}	160°C	400	524 (32)	66 (24)
	160°C	800	509 (24)	62 (19)
	160°C	1200	464 (13)	58 (11)
	160°C	1600	430 (12)	59 (10)
	160°C	2000	456 (11)	52 (10)
	160°C	3000	428 (12)	56 (10)
	160°C	4300	326 (17)	37 (12)
	180°C	100	465 (15)	49 (13)
	180°C	400	456 (18)	73 (16)
	180°C	800	411 (13)	67 (11)
	180°C	1200	405 (11)	56 (9)
	180°C	1600	416 (10)	46 (8)
	180°C	2000	411 (9)	47 (8)
	180°C	3000	421 (7)	34 (6)
	180°C	4300	432 (22)	60 (20)
	210°C	100	519 (82)	61 (54)
	210°C	400	397 (13)	55 (10)
	210°C	800	346 (8)	27 (7)
	210°C	1200	328 (10)	30 (7)
	210°C	1600	292 (10)	32 (7)
	210°C	2000	286 (9)	29 (6)
	225°C	100	501 (42)	69 (29)
	225°C	200	404 (7)	32 (6)
	225°C	300	371 (6)	34 (5)
	225°C	400	344 (6)	33 (5)
	225°C	580	317 (9)	47 (7)
	225°C	780	300 (8)	46 (6)
	225°C	980	288 (6)	32 (4)
	225°C	1180	272 (12)	45 (8)
FM=2	n/a	0	508 (5)	26 (4)
	160°C	100	469 (4)	21 (3)
	160°C	200	439 (8)	41 (6)
	160°C	400	458 (4)	20 (3)
	160°C	800	466 (5)	21 (3)
	160°C	1200	467 (6)	26 (5)
	160°C	1600	446 (6)	22 (5)
	160°C	2000	461 (5)	19 (4)

Table D-8: Estimated Model Parameters: QM21ma (continued)

Failure Mode	Temperature	Time (hours)	$\hat{\mu}(\hat{\sigma}_{\hat{\mu}})$	$\hat{\sigma}(\hat{\sigma})_{\hat{\sigma}}$
	160°C	3000	444 (4)	15 (3)
	180°C	100	438 (3)	17 (3)
	180°C	200	434 (6)	32 (4)
	180°C	400	442 (5)	20 (4)
	180°C	800	441 (7)	24 (5)
	180°C	1200	440 (6)	18 (4)
	180°C	1600	435 (9)	33 (7)
FM=2	180°C	2000	443 (5)	12 (4)
	180°C	3000	429 (3)	11 (2)
	180°C	4300	420 (4)	12 (3)
	210°C	100	442 (3)	8 (2)
	210°C	400	428 (4)	9 (3)
	225°C	100	442 (3)	7 (2)

Table D-9: Estimated Model Parameters: QM21sd

Failure Mode	Temperature	Time (hours)	$\hat{\mu}(\hat{\sigma}_{\hat{\mu}})$	$\hat{\sigma}(\hat{\sigma})_{\hat{\sigma}}$
FM={0,1}	n/a	0	564 (36)	66 (21)
	160°C	100	476 (11)	48 (10)
	160°C	200	427 (19)	92 (17)
	160°C	400	392 (8)	43 (6)
	160°C	800	361 (9)	47 (6)
	160°C	1200	335 (8)	42 (6)
	160°C	1600	304 (10)	52 (7)
	160°C	2000	340 (6)	31 (4)
	160°C	3000	288 (6)	36 (5)
	160°C	4300	244 (17)	39 (12)
	160°C	6000	264 (5)	11 (3)
	160°C	8000	205 (15)	33 (10)
	180°C	100	361 (15)	82 (12)
	180°C	200	359 (8)	46 (6)
	180°C	400	296 (10)	57 (7)
	180°C	800	270 (6)	32 (4)
	180°C	1200	294 (8)	45 (6)
	180°C	1600	275 (5)	29 (4)
	180°C	2000	271 (5)	27 (4)
	180°C	3000	284 (6)	36 (5)
	180°C	4300	222 (8)	29 (5)
	210°C	100	372 (9)	27 (6)
	210°C	400	265 (15)	46 (10)
	210°C	800	248 (11)	34 (8)
	210°C	1200	218 (13)	40 (9)
	210°C	1600	228 (7)	24 (5)
	210°C	2000	191 (12)	37 (8)
	225°C	100	313 (9)	47 (6)
	225°C	200	315 (6)	34 (4)
	225°C	300	290 (6)	32 (4)
	225°C	400	264 (6)	30 (4)
	225°C	580	237 (5)	29 (4)
	225°C	780	218 (6)	35 (4)
	225°C	980	205 (6)	34 (4)
	225°C	1180	191 (10)	37 (7)
FM=2	n/a	0	503 (10)	45 (8)
	160°C	100	475 (4)	17 (3)

Table D-9 Estimated Model Parameters: QM21sd (continued)

Failure Mode	Temperature	Time (hours)	$\hat{\mu}(\hat{\sigma}_{\hat{\mu}})$	$\hat{\sigma}(\hat{\sigma})_{\hat{\sigma}}$
	160°C	200	455 (9)	33 (7)
	180°C	100	447 (9)	22 (7)

Table D-10a: Arrhenius Model Parameter Estimates, by Material and Failure Mode

Material/FM	$\hat{\beta}_0(\hat{\sigma}_{\hat{\beta}_0})$	$\hat{\beta}_1(\hat{\sigma}_{\hat{\beta}_1})$	$\hat{\beta}_2(\hat{\sigma}_{\hat{\beta}_2})$	$\hat{E}(eV)$
6262ma/01	8.92 (.34)	.56 (.06)	2706 (170)	.23
6262ma/2	4.69 (.10)	.38 (.07)	6354 (1100)	.55
6262sd/01	6.46 (.11)	.27 (.02)	8379 (1300)	.72
6262sd/2	5.48 (.05)	.21 (.03)	5141 (710)	.44
4740ma/01	7.98 (.30)	.32 (.05)	3548 (300)	.31
4740ma/2	5.47 (.06)	.24 (.02)	6073 (740)	.52
4740sd/1	--	--	--	--
4740sd/2	5.21 (.06)	.25 (.02)	6336 (710)	.55

Table D-10b: Correlation Among Model Parameter Estimates, by Material and Failure Mode

Material/FM	Corr (β_0, β_1)	Corr (β_0, β_2)	Corr (β_1, β_2)
6262ma/01	.995	-.480	-.431
6262ma/2	.089	-.648	.634
6262sd/01	.904	-.930	-.789
6262sd/2	.325	-.574	.507
4740ma/01	.997	-548	-.500
4740ma/2	.437	-.809	.025
4740sd/01	--	--	--
4740sd/2	.293	-773	.263

This page intentionally left blank

APPENDIX E

	TOLERANCES ARE TO ± 1/16 in UNLESS SPECIFIED	DIMENSIONS ARE IN inches	SCALE: 1 TO 1	DESIGNED BY: GEOFF MUNSON
			DATE: 4/10/95	CHECKED BY: MARTIN WEISER

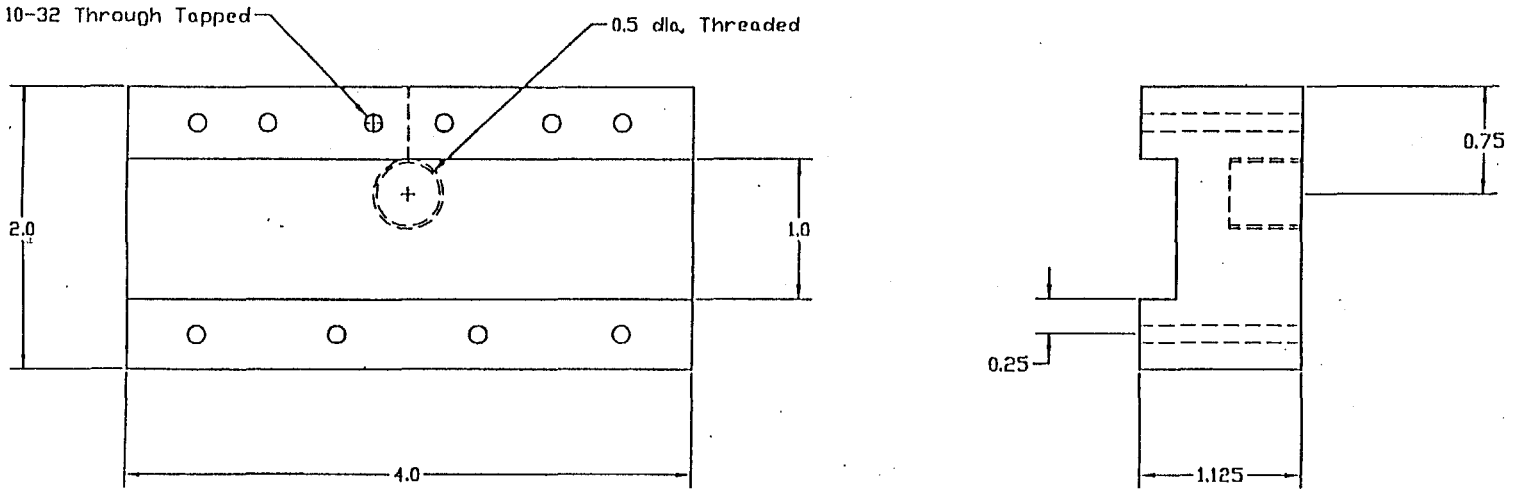

TITLE Solder Tester	FIND NO.	PART NO.	QTY	DESCRIPTION	MATERIAL
DRAWING NUMBER 2	1	1	1	Bottom Mount	6061 - T6 Aluminum or Similar

	TOLERANCES ARE TO ± 1/16 in UNLESS SPECIFIED	DIMENSIONS ARE IN inches	SCALE: 1 TO 1	DESIGNED BY: GEOFF MUNSON
			DATE: 4/10/95	CHECKED BY: MARTIN WEISER

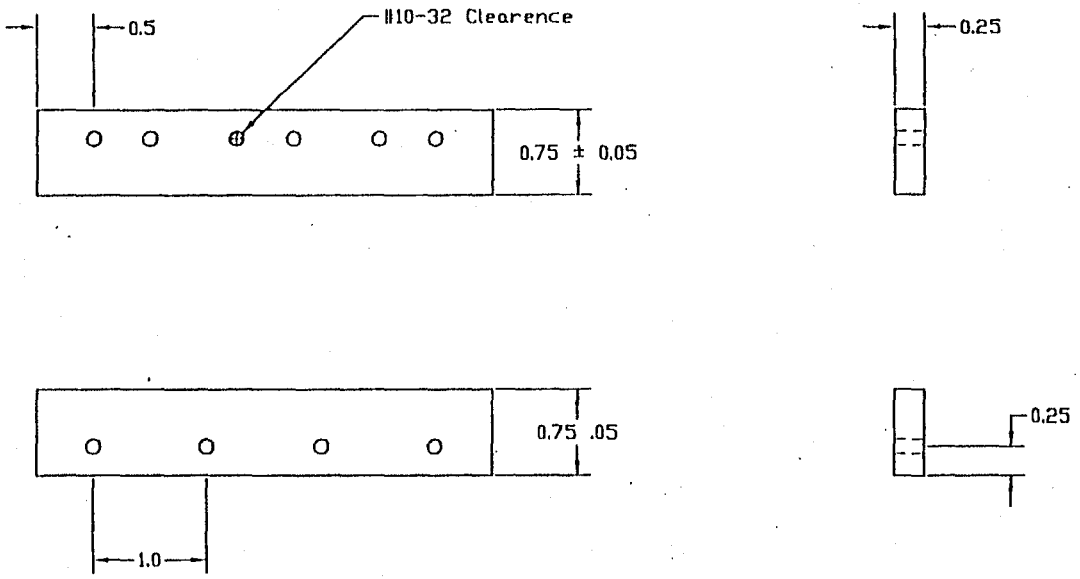

TITLE Solder Tester	FIND NO.	PART NO.	QTY	DESCRIPTION	MATERIAL
DRAWING NUMBER 3	2	2	1	Bottom Retainer	304 Stainless Steel or Similar

	TOLERANCES ARE TO ± 1/16 in UNLESS SPECIFIED	DIMENSIONS ARE IN inches	SCALE: 1 TO 1	DESIGNED BY: GEOFF MUNSON
			DATE: 4/10/95	CHECKED BY: MARTIN WEISER

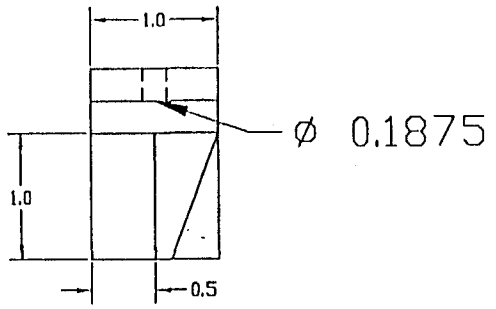

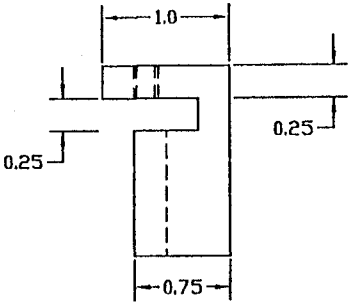

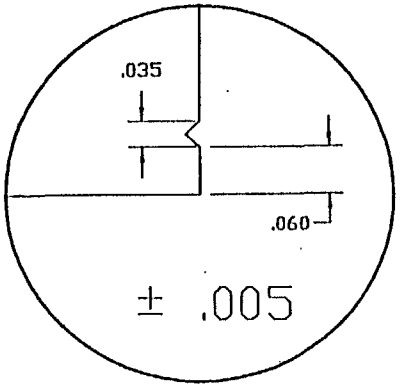

Section A

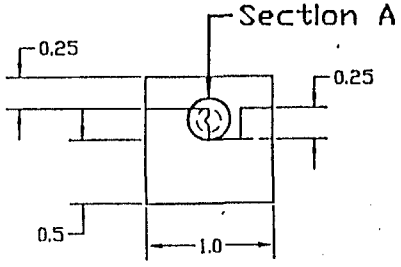

TITLE	FIND NO.	PART NO.	QTY	DESCRIPTION	MATERIAL
Solder Tester					
DRAWING NUMBER 4	3	3	1	Top Mount	304 Stainless Steel or Similar

	TOLERANCES ARE TO ± 1/16 in UNLESS SPECIFIED	DIMENSIONS ARE IN inches	SCALE: 1 TO 1	DESIGNED BY: GEOFF MUNSON
			DATE: 4/10/95	CHECKED BY: MARTIN WEISER

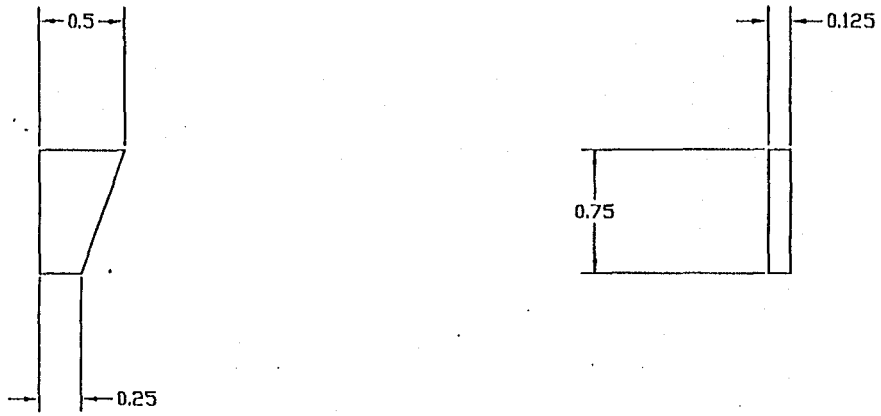

TITLE Solder Tester	FIND NO.	PART NO.	QTY	DESCRIPTION	MATERIAL
DRAWING NUMBER 5	4	4	1	Top Retainer	304 Stainless Steel or Similar

	TOLERANCES ARE TO ± 1/16 in UNLESS SPECIFIED	DIMENSIONS ARE IN inches	SCALE: 1 TO 1	DESIGNED BY: GEOFF MUNSON
			DATE: 5/4/95	CHECKED BY: MARTIN WEISER

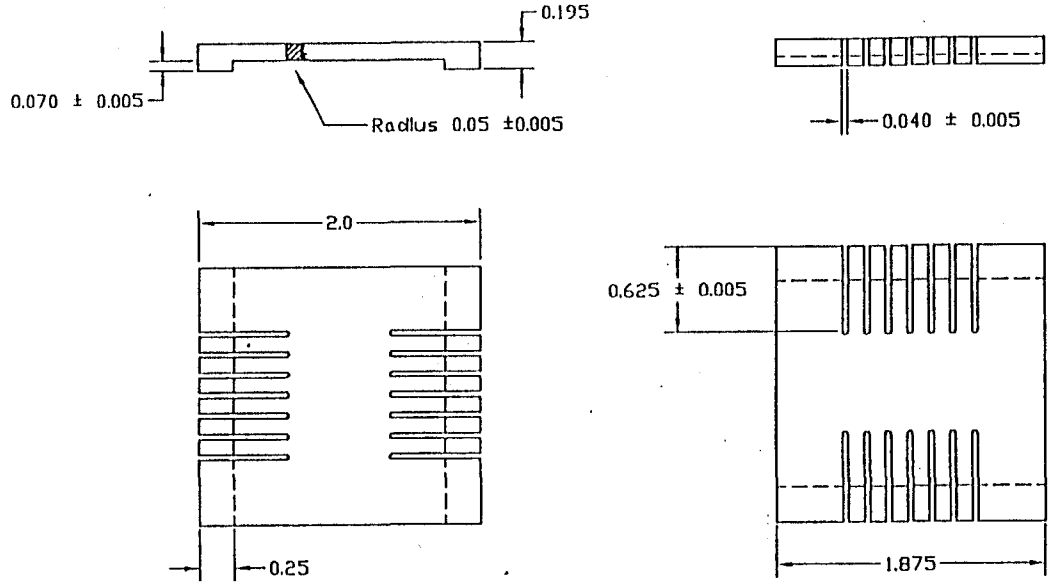

TITLE	FIND NO.	PART NO.	QTY	DESCRIPTION	MATERIAL
Solder Tester					
DRAWING NUMBER 6	N/A	N/A	1	Bend Fixture	304 Stainless Steel or Similar

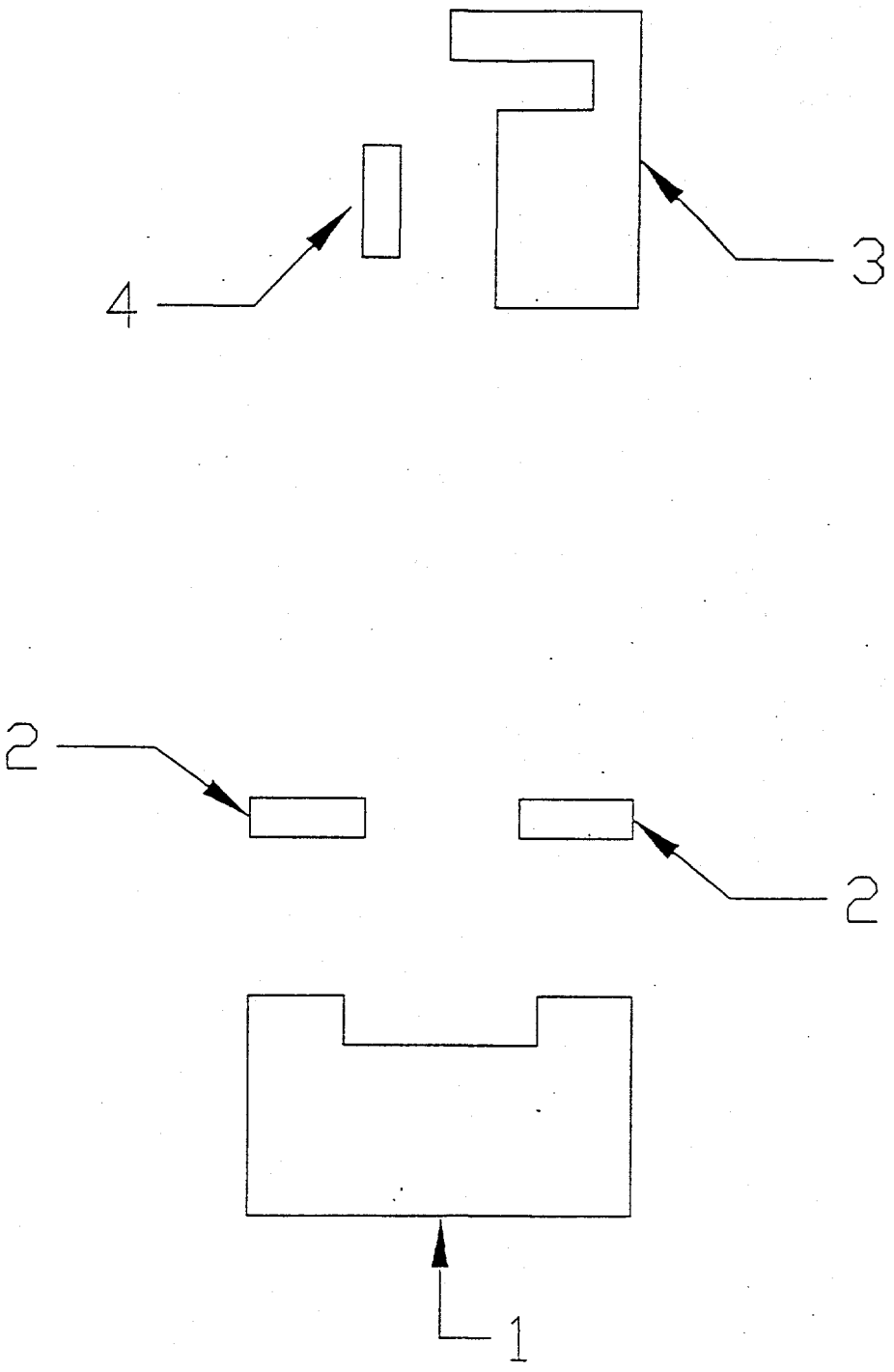
4
3
2
2
1

DISTRIBUTION:

1 US Department of Energy, Headquarters
Attn: Diane Bird, DP-17
Forrestal Building
1000 Independence Avenue, SW
Washington, DC 20585

1 DELPHI Energy & Engine Management Systems
Attn Carl Miller MC 485-301-150
PO Box 1360
Flint, Michigan 48501-1360

1 DELPHI Energy & Engine Management Systems
Attn Daniel A Crawford MC 485-301-150
PO Box 1360
Flint, Michigan 48501-1360

1 DELPHI Energy & Engine Management Systems
Attn Lary R Hocken MC 485-301-150
PO Box 1360
Flint, Michigan 48501-1360

1 DELPHI Energy & Engine Management Systems
Attn Larry D Hazelton MC 485-301-150
PO Box 1360
Flint, Michigan 48501-1360

1	MS1380	David Larson, 4231
1	MS0521	Tom Young, 1567
2	MS1071	Jim Jorgensen, 1202
1	MS1072	Dan Sprauer, 1274
2	MS1071	TJ Allard, 1205
5	MS0957	Fernando Uribe, 1411
3	MS0957	Stephen Garrett, 1411
1	MS1082	Dave Palmer, 1333
1	MS0835	Vicente Romero, 9113
1	MS0825	Bruce Bainbridge, 9113
1	MS1081	William Miller, 1276
1	MS0443	Vicki Porter, 9117
1	MS0829	Edward Thomas, 12323
1	MS1405	Paul Hlava, 1822
1	MS0959	Larry Kovacic, 1492

DISTRIBUTION (continued):

1	MS1411	David Keicher, 1831
1	MS0443	Robert Chambers, 9117
1	MS0835	Steven Gianoulakis, 9113
1	MS1411	Fred Yost, 1841
1	MS1405	Celeste Drewien, 1822
1	MS1411	Susan Sackinger, 1831
1	MS9018	Central Tech Files, 8940-2
5	MS0899	Technical Library, 4414
2	MS0619	Review & Approval Desk, 12690 for DOE/OSTI
1	MS1380	Technology Transfer, 4212